DEVELOPING MICROSTRUCTURE- AND DISLOCATION-BASED CONSTITUTIVE NUMERICAL MODELS FOR PREDICTING THE MECHANICAL BEHAVIOUR OF DMLS TI6AL4V(ELI) AT VARIOUS STRAIN RATES

By

Amos Mwangi Muiruri

A thesis submitted in fulfilment of the requirements for the degree

Doctor of Engineering in Mechanical Engineering

in the

Department of Mechanical and Mechatronics Engineering

Faculty of Engineering, Built Environment and Information Technology

at

Central University of Technology, Free State

***Promoter**: Dr Maina Maringa, Ph.D.*

***Co-Promoter**: Prof Willie du Preez, Ph.D. Pr. Sci. Nat.*

BLOEMFONTEIN, FREE STATE, SOUTH AFRICA
SEPTEMBER 2021

© Central University of Technology, Free State

DECLARATION OF INDEPENDENT WORK

DECLARATION WITH REGARD TO INDEPENDENT WORK

I, **AMOS MWANGI MUIRURI**, passport number [redacted] and student number [redacted], do hereby declare that this research thesis submitted to Central University of Technology, Free State for the award of a **DOCTOR OF ENGINEERING IN MECHANICAL ENGINEERING**, is my own independent work; and complies with the Code of Academic Integrity, as well as other relevant policies, procedures, rules and regulations of Central University of Technology, Free State; and has not been submitted before to any institution by myself or any other person in fulfilment of the requirements for the attainment of any qualification.

SIGNATURE OF STUDENT

7th September 2021

DATE

© Central University of Technology, Free State

ABSTRACT

Direct metal laser sintering (DMLS) is among the new technologies being pursued by many academic research centres, materials scientists and engineers in the aerospace and biomedical industries as a potential replacement of conventional manufacturing technologies. A scrupulous understanding of the DMLS processes and related post-processes is crucial for establishment of this technology as the better alternative manufacturing route for Ti6Al4V(Extra Low Interstitial-ELI), an alloy commonly used in these industries. The success of such processes depends on the achievement of good structural mechanical properties of Ti6Al4V(ELI), comparable or even superior to those of the conventionally produced alloy. The macroscopic properties of materials are largely affected by the microstructure. The microstructure is a very intricate feature with various aspects that influence specific properties in both a synergistic and competing manner. The morphologies and size of grains, crystallographic texture, macro process-residual stresses and defects, which are largely dislocations in nature, are among these aspects.

To accelerate the acceptance of DMLS Ti6Al4V(ELI) in industry, numerical models that can quantitatively describe the interrelationships between the microstructural features, field variables, such as temperature and strain rate, and the mechanical properties are necessary. At the initial stage of the present study, an analytical constitutive model that is sensitive to the microstructure of Ti6Al4V was developed. Various microstructures of DMLS Ti6Al4V(ELI) were produced via heat treatment and characterised to determine critical microstructural parameters of the model. Experimental tests at selected strain rates and temperatures were then undertaken for these microstructures of DMLS Ti6Al4V(ELI) to acquire data for use in determining the critical parameters of this model. The arising refined and validated analytical constitutive model was then implemented as material user subroutine in ABAQUS/Explicit to generate numerical solutions. Simulation tests were then carried out to determine the predictive capacity of the developed model.

Various mechanisms that prevail during yielding and plastic flow in Ti6Al4V were examined. Using these mechanisms, an advanced analytical model was developed to

© Central University of Technology, Free State

provide a macroscopic description of the flow properties of various microstructures of DMLS Ti6Al4V(ELI) for a wide range of field variables. The critical microstructural features of average α-grain size and initial dislocation density that influence the plastic deformation were explicitly articulated in the formulation of this model.

The effects of the heat treatment processes on the morphologies, size and crystallographic texture of the microstructural grains were first investigated. The microstructures of the non-heat-treated and heat-treated samples of DMLS Ti6Al4V(ELI) were examined using an optical microscope (OM) and a scanning electron microscope (SEM). A SEM equipped with a backscattered electron detector for electron backscatter diffraction (EBSD) analysis was used for crystallographic texture analysis. The β-phase texture from this data was ascertained based on a reconstruction method using the Automatic Reconstruction of Parent Grain for EBSD data (ARPGE) program. The average α′/α grain-size was observed to increase from a value of < 1.5 μm for the non-heat-treated samples to a value of about 9 μm for the samples that were heat-treated above the α→β grain transformation temperature. The intensity of texture was also seen to increase because of heat treatment, with the maximum unit density (MUD) of the α′/α-phase in the basal plane (0001) increasing from 4.9 in the non-heat-treated samples to 24 for samples that were heat-treated at the highest temperature. The non-heat-treated samples and those samples that were heat-treated to just below the α→β-grain transformation temperature showed a strong fibrous texture of the reconstructed β-grains with the ⟨100⟩ directions almost parallel to the build direction. The alignment of the fibrous texture in the build direction disappeared after heat treatment above the α→β-grain transformation temperature.

An analysis of the X-ray diffraction (XRD) profiles of the non-heat-treated and heat-treated microstructures of DMLS Ti6Al4V(ELI) was carried out to determine the level of defects in these microstructures. The modified Williamson-Hall and modified Warren-Averbach methods of analysis were used to evaluate the dislocation densities in these microstructures. The results obtained showed a 73% reduction of dislocation density in DMLS Ti6Al4V(ELI) upon stress-relieving heat treatment at a temperature of 650°C for a period of 3 hours. The density of dislocations further declined in microstructures that were annealed at elevated temperatures, with the microstructures that were heat-

© Central University of Technology, Free State

treated just below the α→β-grain transformation temperature recording the lowest dislocation densities.

The high cooling rate gradient normally associated with the DMLS process leads to formation of a non-equilibrium martensitic microstructure. Our previous study demonstrated that this microstructure possesses inferior dynamic deformation properties compared to the microstructure arising from use of conventional manufacturing processes. Thus, in the present study the compressive high-strain-rate properties and deformation behaviour of DMLS Ti6Al4V(ELI) were studied for samples that were heat-treated above the martensitic transformation temperature. High-strain-rate compression tests were carried out using a Split Hopkinson Pressure Bar (SHPB) test system at temperatures of 25 °C, 200 °C and 500 °C. The tests at each temperature were conducted at three different average plastic strain rates of 750 s^{-1}, 1500 s^{-1} and 2450 s^{-1} and flow stress curves at these test conditions were obtained. Comparative analyses of these flow stress curves for different categories of samples were then carried out. The flow stress curves of all samples tested generally showed the flow stress to increase with increasing strain rate and to decrease with increasing temperature. These observations showed that the microstructures of Ti6Al4V(ELI) are sensitive to both strain rate and temperature. The samples that were heat-treated at lower temperatures showed the highest dynamic yield stress at any temperature and strain rate compared to those that were heat-treated at elevated temperatures. An examination and analysis of the deformed surfaces of tested samples using SEM showed these surfaces to be dominated by adiabatic shear bands (ASBs) that were predominantly inclined at an angle of $\approx 45°$ to the loading axis. This suggested that the compressive fracturing of these samples at high strain rate was because of the development of ASBs.

The flow stress curves of different samples were then used to obtain and refine the calibration parameters of the analytical constitutive model that are sensitive to the microstructure of the samples developed here. In these equations, the strain hardening and dynamic recovery that are normally experienced by materials during high-strain-rate deformation were articulated by two model calibration parameters h and k_2, respectively. The influence of initial dislocation densities on the flow properties of

© Central University of Technology, Free State

Ti6Al4V(ELI) according to the models developed here was investigated. It was shown that for high initial dislocation densities, the shape of the stress-strain curve was that of a pronounced peak stress followed by a decreasing flow stress. Lower initial dislocation densities led to a decreased peak stress and, in some cases, this decrease was followed by a state where no strain hardening occurred. The expected decrease of flow stress with increasing temperature was demonstrated well by the model developed here. The upturn of flow stress at high strain rate was taken care of by the introduction of a viscous drag stress component that is sensitive to high strain rates. This stress component for different samples was calibrated with experimental data using two fitting parameters. The microstructure-based constitutive numerical model developed and validated here using experimental data showed good capacity to predict the high-strain-rate flow properties of additively manufactured Ti6Al4V(ELI) alloy. This was demonstrated by the statistical performance measures of the correlation coefficients (R^2) and the absolute average error (δ). The values of R^2 and δ obtained for correlation of the model and experimental values of various samples were > 0.976 and $< 6\%$, respectively. This high correlation is an indication of the robustness of the model developed here in predicting the high-strain-rate properties of DMLS Ti6Al4V(ELI).

The validated microstructure- and dislocation-based analytical constitutive model was then implemented as a user material subroutine in ABAQUS using VUMAT and VUHARD subroutines. This was followed by verification. Initially, the verification process was conducted for single and multiple element tests with varying prescribed loading conditions. The simulation results obtained were then compared with the analytical solutions which showed a good capacity of both the developed VUMAT and VUHARD subroutines to be used for high-strain-rate simulations. The verification process was then extended further for tests devised to study the dynamic properties of materials at high strain rates, in this case the SHPB test. Comparison between the SHPB simulation of numerical and experimental results showed excellent correlation, with the correlation coefficient and average absolute error being > 0.97 and $< 4\%$, respectively for various samples. This showed that the numerical model is suitable for use in designing the dynamic strength of DMLS Ti6Al4V(ELI) structures for high strain rate applications, by

© Central University of Technology, Free State

controlling the morphology of its microstructure and the initial dislocation density present in the alloy.

© Central University of Technology, Free State

ACKNOWLEDGMENTS

Foremost, I would like to thank my advisor Dr Maina Maringa for his invaluable support, guidance and encouragement throughout my studies. I would also like to extend my profound gratitude to my co-advisor Prof Willie du Preez for his strong support, commitment and constant availability for technical discussions involving my studies. I would like to acknowledge and thank the CRPM of the Central University of Technology, Free State, for allowing me access to the additive manufacturing facilities for production of the test samples used in my studies.

My deepest gratitude to the Centre for High Resolution Transmission Electron Microscopy (CHRTEM) of the Nelson Mandela University (NMU), where the EBSD analyses were carried out. Dr Roy Forbes of the Department of Chemistry at the University of the Witwatersrand is also acknowledged for his help in carrying out the XRD analysis. I acknowledge and thank Dr Johan Westraadt of the CHRTEM for his commitment and technical assistance in interpretation of EBSD and XRD data. The Department of Geology of the University of Free State is also acknowledged for providing the SEM for preliminary microstructural analysis and Ms Megan Purchase of the department for her assistance with the equipment.

My sincere gratitude to the Armaments Corporation of South Africa SOC Ltd (ARMSCOR), where the SHPB experiments were conducted. Many thanks to Mr Adriaan Steenkamp and Mr Pitso Mangoro for helping with the SHPB tests as well as letting me access and explore the testing facility at ARMSCOR. Many thanks also to Mr Emmanuel Zungu of CUT Library and Information Services for his constant support with accessing articles even during the national lockdown due to Covid-19.

I acknowledge the financial support given by the South African Department of Science and Innovation (DSI) through the Council for Scientific and Industrial Research (CSIR), for the Collaborative Program in Additive Manufacturing, Contract No.: CSIR -NLC-CPAM-18-MOA-CUT-01. The Directorate of Research and Development & Postgraduate Studies (RD & PGS) of CUT is also acknowledged for its financial support. Above all, I thank God for his mercy and protection throughout the duration of my doctorate studies.

© Central University of Technology, Free State

DEDICATIONS

This doctoral thesis is dedicated to my lovely wife Caroline Mwangi, my son James Mwangi, my parents, and my siblings, and to researchers in the field of additive manufacturing, computation materials science as well as modelling and simulation.

© Central University of Technology, Free State

LIST OF PUBLICATIONS

Papers Presented at International Conferences

1. **Muiruri Amos**, Maina Maringa, Willie du Preez, Application of phenomenological modeling in the development of a database for additively manufactured Ti6Al4V(ELI): A review, *Presented at the 10th International Conference of the African Materials Research Society (AMRS2019),* Arusha, Tanzania, 10th–13th December **2019**.

Peer Reviewed Conference Papers

1. **A M Muiruri**, M Maringa, W B du Preez, Constitutive numerical modelling in additive manufacturing: Challenges in predicting the yield strength and flow properties of alloys. *Proceedings of the 20th Annual RAPDASA International Conference*, Emoya Estate, Bloemfontein, 6th–8th November **2019**, pp.190–203, ISBN 978-0-6398390-0-4.

Peer Reviewed Journal articles

1. **Amos Muiruri,** Maina Maringa, Willie du Preez, Crystallographic texture analysis of as-built and heat-treated Ti6Al4V(ELI) produced by Direct Metal Laser Sintering, ***Crystals*** **2020, 10, 699**; *doi:10.3390/cryst10080699*
2. **Amos Muiruri**, Maina Maringa, Willie du Preez, Evaluation of dislocation densities in various microstructures of additively manufactured Ti6Al4V(ELI) by the method of X-ray diffraction, ***Materials*** **2020**, 13, 5355; doi:10.3390/ma13235355
3. **Muiruri, A**.; Maringa, M.; du Preez. High strain rate properties of various forms of Ti6Al4V(ELI) produced by direct metal laser sintering. ***Applied Sciences*** **2021**, 11(17), 8005; doi.org/10.3390/app11178005
4. **Muiruri, A**.; Maringa, M.; du Preez, W. Validation of a microstructure-based model for predicting the high strain rate flow properties of various forms of additively manufactured Ti6Al4V (ELI) alloy. ***Metals*** (submitted).

© Central University of Technology, Free State

TABLE OF CONTENTS

DECLARATION OF INDEPENDENT WORK ..... **II**

ABSTRACT ..... **III**

ACKNOWLEDGMENTS ..... **VIII**

DEDICATIONS ..... **IX**

LIST OF PUBLICATIONS ..... **X**

TABLE OF CONTENTS ..... **XI**

LIST OF FIGURES ..... **XVII**

LIST OF TABLES ..... **XXIX**

LIST OF SYMBOLS AND ABBREVIATIONS ..... **XXXI**

CHAPTER 1 - BACKGROUND OF THE STUDY **1**

1.1 Introduction 1

1.2 Problem Statement 5

1.2 Aim and Objectives of the Study 6

1.3 The Scope and Outline of the Thesis 7

1.4 References 9

CHAPTER 2 - LITERATURE SURVEY **12**

2.1 Introduction 12

2.2 Metal Additive Manufacturing 12

2.2.1 Directed Energy Deposition (DED) 13

2.2.2 Powder Bed Fusion (PBF) 14

2.3 Potential Applications of AM in the Aircraft Industry 15

2.4 Microstructure and Mechanical Properties of As-Built and Heat-Treated AM Ti6Al4V 19

2.4.1 Microstructure of as-built AM Ti6Al4V(ELI) parts and their inherent defects 19

© Central University of Technology, Free State

2.4.2 Heat-treatment processes and mechanical properties of AM Ti6Al4V 25
2.5 Dislocations and Plastic Deformation in Ti6Al4V 35
2.5.1 Dislocations – linear defects 36
2.5.2 Slip systems in Ti6Al4V 40
2.5.3 The α/β slip transfer and the role in plastic deformation of the Ti6Al4V 42
2.6 Microstructure Characterisation of Ti6Al4V 43
2.6.1 Electron backscatter diffraction (EBSD) 44
2.6.2 X-ray diffraction (XRD) 50
2.7 Modelling of Mechanical Properties with Specific Focus on Ti6Al4V 56
2.7.1 Artificial neural network models 56
2.7.2 Constitutive models for plastic flow behaviour of Ti6Al4V 58
2.8 A Review of the Theory of Plastic Deformation 67
2.9 The overview of radial return algorithm 71
2.10 Implementation of User's Defined Material in ABAQUS 73
2.11 High-Strain-Rate testing - Split Hopkinson Pressure Bar (SHPB) test 75
2.12 Summary 79
2.11 References 81
CHAPTER 3 – MATERIALS AND METHODS 94
3.1 Introduction 94
3.2 Production of Test Specimens and Heat Treatments 94
3.3 Microstructural Characterisation 98
3.3.1 Electron backscatter diffraction (EBSD) 99
3.3.2 Reconstruction of prior-β grains 101
3.3.3 X-ray diffraction (XRD) 102
3.4 Hardness Test 103
3.5 High-Strain-Rate Compression Testing 105

© Central University of Technology, Free State

3.5 Summary 107

3.6 References 108

CHAPTER 4 — DEVELOPMENT OF CONSTITUTIVE NUMERICAL MODELS TO PREDICT THE FLOW STRESS OF TI6AL4V OVER A WIDE RANGE OF STRAIN RATES... 110

4.1 Introduction 110

4.1.1 Prediction of the yield stress 111

4.1.2 Strain hardening and prediction of flow stress 114

4.2 Summary 118

CHAPTER 5 — MICROSTRUCTURE CHARACTERISATION OF AS-BUILT AND ANNEALED DMLS TI6AL4V(ELI) PARTS 122

5.1 Introduction 122

5.2 Microstructures of Heat-Treated DMLS Ti6Al4V(ELI) 122

5.3 Crystallographic Texture of As-built and Heat-Treated DMLS Ti6Al4V(ELI) 126

5.3.1 The percentage fraction and distribution of the α and β-phases 126

5.3.2 Crystallographic texture of transformed α phase 128

5.3.3 Reconstruction of prior-β grains 135

5.4 Variant Selection mechanism of the β→α Transformation in DMLS Ti6Al4V(ELI) 139

5.5 Misorientation Distribution in Various Microstructures of DMLS Ti6Al4V(ELI) 144

5.6 Hardness Test Results of the Various Microstructures of DMLS Ti6Al4V(ELI) 147

5.7 Summary 148

5.7 References 150

CHAPTER 6 — EVALUATION OF DISLOCATION DENSITIES IN VARIOUS MICROSTRUCTURES OF DMLS TI6AL4V(ELI) BY X-RAY DIFFRACTION..... 151

6.1 Introduction 151

6.2 The X-Ray Diffraction (XRD) Profiles of DMLS Ti6Al4V(ELI) Samples 151

6.3 Calculation of Dislocation Density in DMLS Ti6Al4V(ELI) Microstructures 156

© Central University of Technology, Free State

6.3.1 Analysis of DMLS Ti6Al4V(ELI) XRD peak broadening by the modified Williamson-Hall method 156

6.3.2 Calculation of Burgers vector population and average contrast Factor, $\boldsymbol{Chkl}$ in DMLS Ti6Al4V (ELI) 163

6.3.3 Evaluation of dislocation density by modified Warren-Averbach method 164

6.4 Summary 168

6.5 References 170

CHAPTER 7 – FLOW PROPERTIES OF DMLS TI6AL4V(ELI) OVER WIDE RANGES OF STRAIN RATES AND TEMPERATURES 172

7.1 Introduction 172

7.2 High Strain Rate – Time Test Characteristics 172

7.2 Stress–Strain Characteristics 173

7.3 Analysis of Microstructure and Fracture Surfaces of Various DMLS Ti6Al4V(ELI) Specimens Loaded at High Compressive Strain Rates and High Temperatures 183

7.3.1 Analysis of microstructure of deformed surfaces 183

7.3 2. Fractographic analysis of failure surfaces 190

7.4 Summary 195

7.5 References 197

CHAPTER 8 — VALIDATION OF MICROSTRUCTURE-BASED CONSTITUTIVE NUMERICAL MODEL FOR DMLS TI6AL4V(ELI) 199

8.1 Introduction 199

8.2 Prediction of the Yield Stress 200

8.2.1 Athermal stress ($\boldsymbol{\sigma a}$) 200

8.2.2 Temperature-dependent shear modulus 201

8.2.3 Thermal part of the yield stress 202

8.2 Prediction of the Flow Stress 204

8.3 Prediction of the Viscous Drag Stress Component of Flow Stress 210

© Central University of Technology, Free State

8.4 Summary 217

8.5 References 219

CHAPTER 9 — IMPLEMENTATION OF A MICROSTRUCTURE-BASED CONSTITUTIVE MODEL FOR DMLS TI6AL4V(ELI) IN ABAQUS 221

9.1 Introduction 221

9.2 Implementation of the VUHARD User Subroutine 222

9.3 Implementation of the VUMAT User Subroutine 223

9.4 Verification and Validation of the Implemented Models 226

9.4.1 The single element test 227

9.4.2 Multiple elements tests 236

9-5 Summary 247

9.6 References 248

CHAPTER 10 — APPLICATION OF THE NUMERICAL MODEL TO THE SPLIT HOPKINSON PRESSURE BAR TEST AT HIGH STRAIN RATES 249

10.1 Introduction 249

10.2 The Finite Element Model for the SHPB 249

10.3 Simulation of SHPB Tests using the Johnson-Cook model In-built in ABAQUS 258

10.3 Summary 264

10.4 References 266

CHAPTER 11 — CONCLUSIONS AND RECOMMENDATIONS 267

11.1 Introduction 267

11.2 Conclusions Arising in Various Chapters 267

11.2.1 Microstructure-sensitive constitutive model (Chapter 4) 267

11.2.2 Microstructural characterisation of various forms of DMLS Ti6Al4V(ELI) alloy (Chapters 5 & 6) 268

11.2.3 High-strain-rate testing and calibration of constitutive model (Chapters 7 & 8) 269

© Central University of Technology, Free State

11.2.4. Implementation, verification, and validation of constitutive model (Chapters 9 & 10) 271

11.3 Recommendations for Future Research 271

APPENDICES 273

Appendix A – The implicit integration scheme to compute for equivalent plastic strain (ABAQUS 2020) 273

Appendix B – Theory of one-wave propagation in SHPB test (Gray 2000) 274

Appendix C – Thermodynamics of SHPB test specimens 279

Appendix D – Integration of the Taylor hardening law (Jonas *et al*. 2009) 279

Appendix E – Method of calculating the average burgers vector and average contrast factor 280

Appendix F (1) – Code of the VUHARD subroutine developed here 281

Appendix F (2) – VUHARD subroutine user-defined material properties 284

Appendix G (1) – Code of the VUMAT Subroutine developed here 284

Appendix G(2) – VUMAT user-defined material properties 289

Appendix H(1) – Collective results for samples D using 8-node single brick elements 290

Appendix H (2) – Collective results for samples E using 8-node single brick elements 291

Appendix I (1) – Collective results for samples D using 8-node brick multiple elements 292

Appendix I (2) – Collective results for samples D using 8-node brick multiple elements 293

© Central University of Technology, Free State

LIST OF FIGURES

Figure 1-1. Projected titanium demand for commercial jet engines (Titanium USA 2018).....1

Figure 1-2. A section of a turbofan engine for aircraft showing various types of material used (Ikuhiro et al. 2014).....2

Figure 2-1. Various metal AM technologies, together with their commercial machine suppliers (Lewandowski et al. 2016).....13

Figure 2-2. Schematic diagram showing a laser DED technology (Courtesy of DM3D Technology).....13

Figure 2-3. Schematic diagram of PBF processes (a) DMLS (adapted from EOS GmbH) and (b) EBM (adapted from Arcam EBM). 14

Figure 2-4. Engine blade with transverse cooling passages produced via AM (Luibov et al. 2016).....17

Figure 2-5. (a) Phase diagram of Ti6Al4V (b) phase transformation of Ti6Al4V at different cooling rates (Ahmed and Rack 1998). 19

Figure 2-6. The DMLS Ti6Al4V microstructure, (a) the schematic diagram of martensitic α' hierarchical structure (Ter Haar and Becker (2018), (b) SEM SE image of a sample, (c) and (d) are magnification of the areas indicated by white boxes in (b) (Yang et al. 2016).....21

Figure 2-7. The microstructures of (a) and (c) the as-fabricated and (b) and (d) stress-relieved specimens for transverse and longitudinal sections with reference to the scan direction, respectively, observed in an optical microscope (Muiruri et al. 2019). 26

Figure 2-8. SE images (a) in BSE mode without etching and (b) in SE mode after etching, illustrating the partial decomposition of the α' martensite after annealing at 730 ℃ for 2 hours (Vilaro et al. 2011).....26

Figure 2-9. Scanning electron (SE) images of heat-treated SLM Ti6Al4V at 800 ℃ for 2 hours followed by (a) FC and (b) AC (Qianli et al. (2015).....27

Figure 2-10. SE images of heat-treated SLM Ti6Al4V at 950 ℃ for 2 hours followed by (a) FC and (b) (c) AC (Qianli et al. (2015). 28

Figure 2-11. Microhardness measurements of sub-transus heat-treated SLM samples. Attached is a typical microstructure at different heat-treatment temperatures (Markovitz et al. 2016).....28

© Central University of Technology, Free State

Figure 2-12. SE images of SLM Ti6Al4V heat-treated at 1050 ℃ (a) and (b) and 1200 ℃ (c) and (d) for 2 hours followed by air cooling (Qianli et al. 2015). 29

Figure 2-13. SE images of SLM Ti6Al4V, heat-treated at 1050 ℃ for 1 hour and WQ, followed by tempering at (a) 700 ℃ for 2 hours and (b) 950 ℃ for 2 hours, then furnace cooled (Vilaro et al. 2011). 30

Figure 2-14. Schematic diagram illustrating of the geometry and the build orientation of tensile test samples (Shunyu and Yung 2019). 32

Figure 2-15. Continuous cooling transformation diagram for Ti6Al4V with three different cooling rates (Mur et al. 1996). 33

Figure 2-16. Values of YS, UTS and % El for microstructures obtained by applying different cooling rates (Galaraga et al. 2016). 34

Figure 2-17. (a) Optical image of AM-produced Ti6Al4V component with prior-β grains oriented along the build direction, and schematic illustration of the same subjected to tension load applied along (b) horizontal direction (c) longitudinal direction (Caroll et al. 2015). 34

Figure 2-18. Illustration of the positions of atoms in a perfect crystal used to estimate theoretical critical shear stress (Hull and Bacon 2001). 35

Figure 2-19. Screw dislocation and (b) edge dislocation (Callister 2007, p.89) 36

Figure 2-20. (a) Schematic diagram of a mixed dislocation that has the character of both edge and screw dislocations (Callister 2007, p.89), and (b) diagrammatic illustration of dislocations in a well-annealed crystal (Hull and Bacon 2001). 37

Figure 2-21. (a) Tilt boundary, (b) twist boundary (c) twin boundary and (d) grain boundary (Callister 2007). 38

Figure 2-22. Slip systems in the α-phase crystal, basal (B), prismatic (P) and first-order pyramidal (Π1) planes containing < a > dislocations; and second-order (Π2) pyramidal slip planes containing < c + a > dislocation (Lütjering 1998). 40

Figure 2-23. (a) A transmission electron microscope image of Ti6Al4V with detailed view of a lamellar colony consisting of α_s and β plates and (b) schematic drawing of direct and indirect transmission of dislocations through grain boundaries (Kacher et al. 2014). 42

Figure 2-24. Schematic diagram illustrating the two stages in direct dislocation transmission through a phase interface or grain boundary (Zheng et al. 2018). 43

© Central University of Technology, Free State

Figure 2-25. (a) The experimental set up for EBSD and (b) schematic diagram illustrating the formation of backscatter Kikuchi lines (Zaefferer et al. 2007).....45

Figure 2-26. (a) Representation of a stereographic projection of crystallographic directions, (b) description of corresponding discrete pole figure, and (c) 0001 and (d) 1120 colour contour pole figures for Ti6Al4V (Simonelli et al. 2014, EBSD 2019).....47

Figure 2-27. (a) A hcp crystallographic orientation determined by three Euler angles θ_1, θ_2, and θ_3, (b) the orientations plotted in form of IPF, and (c, d & e) showing the colour in a unit triangle of which the crystal plane normal is parallel to a given specimen orientation (Simonelli et al. 2014).....48

Figure 2-28. Euler map showing orientation of grains in a metallic material (EBSD 2019).....49

Figure 2-29. Diffraction of X-rays by planes of atoms (Callister 2007).....50

Figure 2-30.The XRD profiles of SLM Ti6Al4V alloy after different heat treatments (Yang et al. 2017) and a schematic diagram showing the properties of a typical peak profile of a diffraction wave.....52

Figure 2-31.Schematic diagrams describing the method of analysis of (a) the modified Warren-Averbach plot following Equation 2-8, and (b) $YL2$ versus $In\ L$ (Dragomir et al. 2005).....55

Figure 2-32. Schematic diagram of the ANNM of mechanical properties as a function of microstructural feature parameters of Ti6Al4V alloy (Weidong et al. 2011, Sun et al. 2012).....57

Figure 2-33. Characteristics of hardening models (Stouffer and Dame 1996).....70

Figure 2-34. The radial return method for isotropic/von Mises hardening (Hibbitt et al. 2002).....72

Figure 2-35. A classical schematic diagram of a compressive SHPB setup (Gray 2000).....76

Figure 2-36. Wave propagation diagram showing the propagation of stress waves through the bars and specimen in SHPB apparatus (Ramesh 2008).....76

Figure 2-37. A thin metal specimen attached to the incident bar for pulse shaping (Frew et al. 2002).....78

Figure 3-1. Schematic diagram of the strip-scan pattern used in the EOSINT M 280 system showing raster scan vectors (arrows) within each stripe (each dashed line). For every new layer, the stripes rotate by 67 ° compared to the previous layer.....95

© Central University of Technology, Free State

Figure 3-2. A photographic image showing the manufactured test specimens on the EOS M 280 machine table. The insert schematic drawing shows the specifications of the specimens in millimetres.....96

Figure 3-3. Heat-treatment cycles for high-temperature-annealed DMLS Ti6Al4V(ELI) for (a) samples C, (b) samples D and (c) samples E, following initial stress-relieving heat treatment.....97

Figure 3-4. Typical ARPGE program main menu with set parameters for reconstruction of prior-β grains of Ti6Al4V.....101

Figure 3-5. Schematic diagram showing the theory of the Vickers hardness test. 104

Figure 3-6. The SHPB assembly at ARMSCOR, Pretoria.....105

Figure 3-7. Specimen placing and alignment fixture.....106

Figure 4-1. Microstructural variables-based constitutive model flow diagram for yield strength and flow stress. 110

Figure 4-2. Decomposition of macroscopic stress versus temperature (Kocks and Mecking 2003, Rusinek et al.2010).....112

Figure 4-3. A diagram illustrating the different stages of strain-hardening and the initial elastic-inelastic transition (Cheng et al. 2003). 116

Figure 5-1. Optical images (OI) of (a) non-heat-treated samples A and heat-treated samples (b) B, (c) C, (d) D and (e) E of DMLS TI6Al4V(ELI), with red arrows indicating the build direction. 123

Figure 5-2. Secondary electron images (SEI) of (a) non-heat-treated samples A, and heat-treated samples (b) B, (c) C, (d) D and (e) E of DMLS TI6Al4V(ELI). 124

Figure 5-3. The EBSD phase maps showing the typical α- and β-phase distributions and percentage fraction in (a) samples A, (b) samples B, (c) samples C, (d) samples D and (e) samples E. 127

Figure 5-4. The Euler orientation maps of (a) samples A, (b) samples B, (c) samples C, (d) samples D and (c) samples E, while (f) is the α-hcp principal planes and their depiction in the IPF key. 128

Figure 5-5. Schematic diagram illustrating the α/β BOR (Burgers 1934, Obasi 2012).....130

Figure 5-6. The (1010), (0110), (0001), (1120), (0111), (1011) and (1121) contour PFs of the α-phase for samples A. 132

© Central University of Technology, Free State

Figure 5-7. The (1010), (0110), (0001), (1120), (0111), (1011) and (1121) contour PFs of the α-phase for samples B. 132

Figure 5-8. The (1010), (0110), (0001), (1120), (0111), (1011) and (1121) contour PFs of the α-phase for samples C. 133

Figure 5-9. The (1010), (0110), (0001), (1120), (0111), (1011) and (1121) contour PFs of the α-phase for samples D. 133

Figure 5-10. The (1010), (0110), (0001), (1120), (0111), (1011) and (1121) contour PFs of the α-phase for samples E. 134

Figure 5-11. EBSD Euler map of reconstructed β-phase of (a) samples A (b) samples B, (c) samples C, (d) samples D, and (e) samples E, while (f) is the inverse pole figure (IPF) key for β-principal planes, with the black arrows in the figures indicating the build direction. 136

Figure 5-12. The (100), (110), and (111) pole figures of the β-phase of samples (a) A, (b) B, (c) C, (d) D, and (e) E. 137

Figure 5-13. Superimposed discrete pole figures of (110) poles of reconstructed prior-β grains (the red dots) and the (0001) poles of clustering α/α'-laths (the blue dots) for samples A–E. 140

Figure 5-14. Histograms of variant frequency distribution arising from the three selected grains of samples A and B. 141

Figure 5-15. The histograms of variant frequency distribution arising from the three selected grains of samples C, D and E. 142

Figure 5-16. Grain boundary misorientation angles of the samples (a) A, (b) B, (c) C, (d) D, and (e) E. The legend with colour scale related to misorientation angle is also shown. 144

Figure 5-17. Grain boundary misorientation angle distribution of the samples (a) A, (b) (c) B, (c) C, (d) D, (e) E, and (f) a linear graph plot for comparison. 145

Figure 5-18. The average Vickers microhardness of (a) various forms of DMLS Ti6Al4V(ELI) and (b) variation with heat-treatment temperature. 147

Figure 6-1. The X-ray diffraction patterns of the as-built samples, as-built and stress-relieved samples, and as-built and annealed samples of DMLS Ti6Al4V(ELI). 152

Figure 6-2. The magnification of selected peaks (110) β, (0002) α´/α, and (1011) α´/α. 153

Figure 6-3. The evolution of β-phase lattice parameter (a) with heat-treatment temperature. 153

© Central University of Technology, Free State

Figure 6-4. Comparative trend of average crystallite size and lattice strain for various samples of DMLS Ti6Al4V(ELI) as determined by Rietveld refinement method.....154

Figure 6-5. Typical measured XRD data and the Kα1 and Kα2 deconvoluted peaks using the Gaussian function of the (1011) reflection.....158

Figure 6-6.The (a) Gaussian and (b) Lorentzian FWHM against diffraction vector (K) for the five types of samples with instrumental broadening, referenced against results for a silicon (Si-640d) sample with no instrumental broadening.....159

Figure 6-7. The resulting FWHM values of the peaks obtained after convolution of Gaussian and Lorentzian functions in Equation 6-5 against diffraction vector (K) for the five types of DMLS Ti6Al4V(ELI) samples.....160

Figure 6-8. The relationship between $(\Delta K2 - \omega)/K2$ and x for various samples of DMLS Ti6Al4V(ELI).....161

Figure 6-9. The modified Warren-Averbach plots of DMLS Ti6Al4V(ELI) samples types (a) A, (b) B, (c) C, (d) D, and (e) E according to Equation 6-9, while (f) is a plot according to Equation 6-10. 166

Figure 6-10. Trend of dislocation density (a) with heat-treatment temperature and (b) in non-heat-treated- (samples A) and heat-treated- (samples B, C, D and E) microstructures of DMLS Ti6Al4V(ELI). 167

Figure 7-1. Strain-rate time graphs generated at different SHPB striker bar velocities.....172

Figure 7-2. The true stress-strain curves (a-c) at different strain rates and temperatures, and (d) true stress vs temperature curves at different strain rates and at strains of 0.1 and 0.2, all for samples C.....173

Figure 7-3. The true stress-strain curves (a-c) at different strain rates and temperatures, and (d) true stress vs temperature curves at different strain rates and at strains of 0.1 and 0.2, all for samples D. 174

Figure 7-4. The true stress-strain curves (a-c) at different strain rates and temperatures, and (d) true stress vs temperature curves at different strain rates and at strains of 0.1 and 0.2, all for samples E.....175

Figure 7-5. Comparison of (a-c) yield stresses under different high strain rates and (d) fracture strains at the strain rate of 2540 s^{-1} for samples C, D and E.....177

Figure 7-6. Plots (a-c) true stress vs. true strain rate on a log-log scale at a true strain of 0.1 and at different test temperatures and (d) the trend of strain rate sensitivity parameter m and its comparison in samples C, D and E.....179

© Central University of Technology, Free State

Figure 7-7. Viscous drag stress as a function of (a) strain rate for different grain sizes and (b) grain size at different strain rates.....182

Figure 7-8. Typical deformation features on cross sections through the surfaces of samples (a) C, (b) D, and (c) E observed under an optical microscope (the red arrows indicate the compression axis).....184

Figure 7-9. Secondary electron images showing adiabatic shear bands on sections of deformed surfaces of samples C at different temperatures and strain rates. (Note the different magnification at 750 s^{-1} and 25 °C). The red arrows indicate the loading axis. 186

Figure 7-10. Secondary electron images showing adiabatic shear bands on sections of deformed surfaces of samples D at different temperatures and strain rates (the red arrows indicate the loading axis).....187

Figure 7-11. Secondary electron images showing adiabatic shear bands on sections of deformed surfaces of samples E at different temperatures and strain rates (the red arrows indicate the loading axis).....188

Figure 7-12. Variation of the average width of adiabatic shear bands as a function of strain rate and temperature for samples C, D and E. 189

Figure 7-13. The photographic images of specimens deformed at a strain rate of 2450 s^{-1} and at temperatures of 25 °C, 200 °C and 500 °C.....191

Figure 7-14. The measured height of deformed specimens and estimated longitudinal plastic strain at a strain rate of 2450 s^{-1} and different temperatures for samples C, D, and E. 191

Figure 7-15. Typical characteristic features on the fracture surfaces of samples C at temperatures of (a) 25 °C, (b) 200 °C, and 500 °C at a magnification of X450. 192

Figure 7-16. Typical characteristic features on the fracture surfaces of samples D at temperatures of (a) 25 °C, (b) 200 °C, and 500 °C at a magnification of X450. 193

Figure 7-17. Typical characteristic features on the fracture surfaces of samples E at temperatures of (a) 25 °C, (b) 200 °C, and 500 °C at a magnification of X450. 194

Figure 8-1. Graphical description of the Hall-Petch relationship for DMLS Ti6Al4V(ELI). 200

Figure 8-2. The shear modulus of Ti6Al4V(ELI) as a function of temperature.....201

Figure 8-3. The normalised thermal-activated yield part of yield stress against the effects of temperature at a strain rate of 750 s^{-1}. 203

© Central University of Technology, Free State

Figure 8-4. Effects of parameter h, at a fixed parameter $k2$, initial dislocation density (ρo) and temperature (T). 206

Figure 8-5. Effects of parameter $k2$ at a fixed parameter h, initial dislocation density (ρo) and temperature (T)..... 206

Figure 8-6. Flow stress curves at different temperatures and constant parameters h and $k2$, and fixed initial dislocation density (ρo)..... 207

Figure 8-7. Effects of the initial dislocation density on the flow stress for fixed values of parameters h and k and temperature..... 207

Figure 8-8. Experimental flow stress curves and those predicted by the model represented by Equation 8-6 at a test temperature of 25 ℃ and different strain rates for samples (a) C, (b) D, and (c) E. 209

Figure 8-9. The viscous drag stress component against strain rate at various values of the curve-fitting parameters ζ and α. 211

Figure 8-10. Evolution of the viscous drag stress as a function of strain rate for samples C, D, and E. 212

Figure 8-11. Comparison of the modified model prediction and experimental results for samples C, at three high strain rates and at test temperatures of (a) 25 °C, (b) 200 °C and (c) 500 °C, and (d) correlation between the predicted values and those obtained from experimentation at yielding and at a strain of 0.2. 213

Figure 8-12. Comparison of the modified model prediction and experimental results for samples D at three high strain rates and at test temperatures of (a) 25 °C, (b) 200 °C and (c) 500 °C, and (d) correlation between the predicted values and those obtained from experimentation at yielding and at a strain of 0.2. 214

Figure 8-13. Comparison of the modified model prediction and experimental results for samples E, at three high strain rates and at test temperatures of (a) 25 °C, (b) 200 °C and (c) 500 °C, and (d) correlation between the predicted values and those obtained from experimentation at yielding and at a strain of 0.2. 215

Figure 9-1. Algorithm developed here to solve for equivalent plastic strain increments and updating of the related stress tensors. 224

Figure 9-2. (a & b) A single element model with boundary conditions, (c) typical set temperature in the predefined field and (d) the 8-node linear brick element. 227

Figure 9-3. A typical VUHARD deformed 8-node linear brick element at a temperature of 298 K and velocity of 4 m/s in (a & b) compression and (c & d) tension for

© Central University of Technology, Free State

samples type C. The arrows show the loading direction while the red dots are the roller supports. *228*

Figure 9-4. A typical VUMAT deformed 8-node linear brick element at a temperature of 298 K and velocity of 4 m/s in (a & b) compression and (c & d) tension for samples type C. The arrows show the loading direction while the red dots are the roller supports. *229*

Figure 9-5. The equivalent von Mises stress, plastic strain and strain rate against simulation time history generated in VUMAT and VUHARD subroutines developed here for a test velocity of 4 m/s and a temperature of 298 K. *230*

Figure 9-6. The effects of model parameters (a) $k2$ and (b) h on the numerical solutions derived from VUMAT and VUHARD subroutines and compared with analytical solution at the same conditions of 350 s^{-1} and 298 K. *231*

Figure 9-7. The effects of (a) initial dislocation density (ρo) and (b) temperature on the numerical solutions derived from VUMAT and VUHARD subroutines, compared with analytical solutions at the same average strain rate of 350 s^{-1}. *232*

Figure 9-8. Comparison between the analytical and numerical solutions in VUMAT and VUHARD at three different test velocities and temperatures of (a) 298 K and (b) 773 K for the case of an 8-node linear brick element in compression for samples C. *234*

Figure 9-9. Comparision between the analytical and numerical solutions in VUMAT and VUHARD at three different test velocities and temperatures of (a) 298 K and (b) 773 K for an 8-node linear brick element in tension for samples C. *235*

Figure 9-10. (a) A three-dimensional (3D) numerical model for the necking of a circular bar with, (b) imposed loading and boundary conditions, (c) 2 mm mesh size (475 elements), (d) 1 mm mesh size (3550 elements), (e) 0.5 mm mesh size (28320 elements) and (d) 0.25 mm mesh size (126038 elements). *237*

Figure 9-11. Numerical estimation of (a& c) equivalent plastic strain and (b and d) equivalent von Mises stress distribution in (a & b) VUHARD and (c & d) VUMAT subroutines developed here, using 2 mm mesh size, at a test velocity of 4 m/s and temperature of 298 K. *238*

Figure 9-12. Numerical estimation of (a & c) equivalent plastic strain and (b and d) equivalent von Mises stress distribution in (a and b) VUHARD and (c & d) VUMAT

© Central University of Technology, Free State

subroutines developed here, using 1 mm mesh size, at a test velocity of 4 m/s and temperature of 298 K. *238*

Figure 9-13. Numerical estimation of (a & c) equivalent plastic strain and (b & d) equivalent von Mises stress distribution in (a & b) VUHARD and (c & d) VUMAT subroutines developed here, using 0.5 mm mesh size, at a test velocity of 4 m/s and temperature of 298 K. *239*

Figure 9-14. Numerical estimation of (a & c) equivalent plastic strain and (b & d) equivalent von Mises stress distribution in (a and b) VUHARD and (c & d) VUMAT subroutines developed here, using 0.25 mm mesh size, at a test velocity of 4 m/s and temperature of 298 K. *239*

Figure 9-15. A typical equivalent (a) plastic strain and (b) von Mises stress distribution along the length of the numerical model with different mesh densities simulated at a velocity of 4 m/s for 0.001 s and at a temperature of 298 K. *241*

Figure 9-16. The mesh convergence analysis for equivalent (a) plastic strain at model normalised lengths of 0.2, 0.7 and 1, and (b) von Mises stress at normalised lengths of the models of 0.03, 0.3 and 0.7 for the VUMAT and VUHARD subroutines. *242*

Figure 9-17. The numerical equivalent von Mises stresses against equivalent plastic strains at a temperature of 298 K and imposed velocity of 4 m/s for different mesh densities obtained from the VUMAT and VUHARD subroutines developed here. *244*

Figure 9-18. Comparison between the analytical and numerical solutions in the VUMAT and VUHARD subroutines at three test velocities and a temperature of (a) 298 K and (b) 773 K for multiple elements cylindrical model of samples type C. *246*

Figure 10-1. (a) A longitudinal section of a numerical model for the SHPB test and (b) the velocity (expressed in mm/s) in the predefined field imposed along the z-axis. *250*

Figure 10-2.Numerical simulation of a compressive wave in a SHPB test. *251*

Figure 10-3. The equivalent plastic strain contours for a simulated SHPB test at striker velocities of 8 m/s for 1 mm, 0.5 mm, 0.25 mm and 0.18 mm mesh sizes (the red and blue arrows indicate the direction of incident and reflected waves, respectively). *252*

Figure 10-4. Curves of the numerical equivalent von Mises stress against plastic strain at a temperature of 298 K and imposed velocity of 8 m/s for different mesh sizes in

© Central University of Technology, Free State

numerical simulation of the SHPB test using the VUMAT and VUHARD subroutines developed in the present work. 253

Figure 10-5. The equivalent von Mises stress, plastic strain and strain rate against time history generated during the simulation of the SHPB test using the VUMAT and VUHARD subroutines at imposed striker velocities of 15 m/s and at a temperature of 298 K. 254

Figure 10-6. Graphs of the numerical model prediction and the experimental results for samples C, at three high strain rates and at temperatures of (a) 298 K, (b) 473 K and (c) 773 K, and correlation between the numerically predicted values and those obtained from experimentation at strains of 0.1 and 0.2 in (d). 255

Figure 10-7. Graphs of the numerical model prediction and the experimental results for samples D, at three high strain rates and at temperatures of (a) 298 K, (b) 473 K and (c) 773 K, and correlation between the numerically predicted values and those obtained from experimentation at strains of 0.1 and 0.2 in (d). 256

Figure 10-8. Graphs of the numerical model prediction and the experimental results for samples E, at three high strain rates and at temperatures of (a) 298 K, (b) 473 K and (c) 773 K, and correlation between the numerically predicted values and those obtained from experimentation at strains of 0.1 and 0.2 in (d). 257

Figure 10-9. A typical material properties module for the J-C model in-built in ABAQUS. 259

Figure 10-10. Results of SHPB test simulation at an impact velocity of 8 m/s and temperature of 298 K with the test samples modelled using various sets of J-C model parameters (Note B and L stand for bimodal and lamellar microstructures, respectively) and the numerical models developed in the present work. 261

Figure 10-11. Results of SHPB test simulation at an impact velocity of 15 m/s and temperature of 298 K with the test samples modelled using various sets of J-C model parameters (Note B and L stand for bimodal and lamellar microstructures, respectively) and the numerical models developed in the present work. 262

Figure 10-12. Results of SHPB test simulation at an impact velocity of 25 m/s and temperature of 298 K with the test samples modelled using various sets of J-C model parameters (Note B and L stand for bimodal and lamellar microstructures, respectively) and the numerical models developed in the present work. 262

Figure B-1. Schematic diagram illustrating the tensile and compressive SHPB set up. 276

© Central University of Technology, Free State

Figure H-1. Comparison between the analytical and numerical solutions in VUMAT and VUHARD at three different test velocities and temperatures of (a and c) 298 K and (b and d) 773 K for an 8-node linear brick element in (a and b) tension and (c and d) compression for samples D. *290*

Figure H-2. Comparision between the analytical and numerical solutions in VUMAT and VUHARD at three different test velocities and temperatures of (a and c) 298 K and (b and d) 773 K for an 8-node linear brick element in (a and b) tension and (c and d) compression for samples E. *291*

Figure I-1. Comparison between the analytical and numerical solutions in the VUMAT and VUHARD subroutines at three test velocities and a temperature of (a) 298 K and (b) 774 K for multiple elements cylindrical model of samples type D. *292*

Figure I-2. Comparison between the analytical and numerical solutions in the VUMAT and VUHARD subroutines at three test velocities and a temperature of (a) 298 K and (b) 773K for multiple elements cylindrical model of samples type E. *293*

© Central University of Technology, Free State

LIST OF TABLES

Table 2-1. Hierarchical structure of α' (Ter Haar and Becker 2018) 22

Table 2-2. Tensile properties of Ti6Al4V(ELI) parts built by SLM/DMLS as compared to traditional manufacturing processes 31

Table 2-3. Slip systems in the α-phase crystal of Ti6Al4V (Lütjering and Williams 2007) 40

Table 2-4. Critical resolved shear stress (CRSS) for different slip systems of α-titanium (Mayeurs and McDowell 2007) 41

Table 2-5. JC model parameters 60

Table 2-6. The mKHL-model material constants determined for 3 different forms of Ti6Al4V alloy (Khan et al. 2004) 61

Table 2-7. The material model parameters evaluated by Picu-Majorell (2002) 65

Table 2-8. The estimated Nemat-Nasser model parameters (Nemat-Nasser et al. 2001) 67

Table 3-1. Chemical composition of Ti6Al4V(ELI) alloy powder supplied by TLS Technik GmbH (wt.%) as determined in Thejane et al. 2017 and that of ASTM F3001-14 94

Table 3-2. EOSINT M 280 DMLS processing parameters 95

Table 3-3. Heat-treatment strategies and sample designations 97

Table 3-4. Grinding and polishing procedures 98

Table 3-5. SEM settings used for EBSD data acquisition 100

Table 3-6. The XRD-Bruker D2 Phaser specifications 103

Table 5-1. Twelve possible variants produced by the β→α-phase transformation through the BOR (Wang et al. 2014) 130

Table 5-2. A summary of the maximum MUD densities of different planes for samples A to E 134

Table 5-3. Summary of the maximum-MUD densities of different planes of the samples A to E 138

Table 6-1.The average crystallite size and lattice strain calculated from Rietveld refinement 154

Table 6-2. The measured value of parameters $q1(m)$ *and* $q2(m)$ 162

Table 6-3. Numerical calculated values of $Chk.0$, $q1$ *and* $q2$ *for the most common slip systems in titanium (Dragomir and Ungar 2002)* 162

Table 6-4. The fractions of Burgers vector population and the contrast factor $b2Chk.0(m)$ *for five different samples of DMLS Ti6Al4V(ELI) based on q values obtained using the modified Williamson-Hall method* 163

© Central University of Technology, Free State

Table 6-5. The density of dislocations and effective outer cut-off radius of dislocations resulting from the m-WA method *167*

Table 7-1. The analysis of the dynamic flow curves of samples C, D and E *176*

Table 7-2. Strain rate sensitivity (m) and correlation coefficient ($R2$) of the log-log plots of true stress and strain for samples C, D and E at various test temperatures *179*

Table 7-3. The range of dimple lengths in different DMLS Ti6Al4V(ELI) samples fractured at a strain rate of 2450 s^{-1} and at different temperatures *195*

Table 8-1. Evaluated model-fitting parameters describing the thermal part of the yield stress of samples C, D, and E *203*

Table 8-2. The initial density of dislocations for different microstructures of DMLS Ti6Al4V(ELI) *208*

Table 8-3. Calibrated curve-fitting parameters for the viscous drag component of yield and flow stress for DMLS Ti6Al4V(ELI) samples *212*

Table 8-4. Absolute error (δ) and correlation coefficient (R^2) for the correlation of experimental and predicted values of yield stress for various forms of DMLS Ti6Al4V(ELI) *216*

Table 8-5. A summary of constitutive flow stress model parameters for DMLS Ti6Al4V(ELI) *217*

Table 9-6. Computation time and number of increments for different mesh densities *240*

Table 10-1. Computation time for different mesh sizes *253*

Table 10-2. Absolute percentage error (δ) and correlation coefficient ($R2$) between the experimental and numerical model values of flow stress for various forms of DMLS Ti6Al4V(ELI) *258*

Table 10-3. A summary of J-C model parameters used to model the SHPB Ti6Al4V(ELI) samples *260*

Table F-1. The VUHARD subroutine and the ABAQUS material property definition *284*

Table G-1. The VUMAT subroutine and the ABAQUS material property definition *289*

© Central University of Technology, Free State

LIST OF SYMBOLS AND ABBREVIATIONS

3D	Three dimensional
AB	As-Built
AC	Air Cooling
AM	Additive Manufacturing
ANNMs	Artificial Neural Network Models
ASBs	Adiabatic Shear Bands
ASTM	American Society for Testing and Materials
$\boldsymbol{b}$	Burgers vector
BCC	Body Centered Cubic
CAD	Computer Aided Design
D	Crystallite size
DMLS	Direct Metal Laser Sintering
E	Young's modulus
EBM	Electron Beam Melting
EBSD	Electron Back Scatter Diffraction
ELI	Extra Low Interstitial
FC	Furnace Cooling
FEA	Finite Element Analysis
FWHM	Full Width at Half Maximum
h	Strain hardening coeffient
HAGBs	High Angle Grain Boundaries
HCP	Hexagonal Closed Packed
HD	Horizontal Direction
HIP	Hot Isostatic Pressing
IPF	Inverse Pole Figure
JC	Johnson Cook
K	Bulk modulus
k_2	Dynamic recovery coefficient
LAGBs	Low Angle Grain Boundaries
LD	Longitudinal Direction
L	Fourier length
PBF	Powder Bed Fusion
PF	Pole Figure

© Central University of Technology, Free State

$\boldsymbol{q}$	Equivalent von Mises stress
R_e	Effective outer cut-off radius of dislocation
SDV	Solution dependent variable
SEM	Scanning Electron Microscope
SHPB	Split Hopkinson Pressure Bar
SLM	Selective Laser Melting
SR	Stress Relieved
TEM	Transmission Electron Microscope
UTS	Ultimate Tensile Strength
XRD	X-Ray Diffraction
YS	Yield Strength
α	Alpha
β	Beta
$\overline{C_{hkl}}$	Average contrast factor
$\overline{\varepsilon_P}$	Equivalent plastic strain
$\overline{\dot{\varepsilon}_p}$	Equivalent plastic strain rate
ε_l	Lattice strain
ε_{ij}	Strain tensor
e_{ij}	Deviatoric strain
ε_m	Hydrostatic strain
ρ	Dislocation density
ΔG	Change in activation energy
θ	Theta
$\bar{\sigma}$	Von Mises equivalent stress
σ_m	Hydrostatic stress
σ_{ij}	Stress tensor
S_{ij}	Deviator stress
μ	Shear modulus
ν	Poisson's ratio
χ	Effective damping coeffient
ζ	Material constant

© Central University of Technology, Free State

CHAPTER 1 - BACKGROUND OF THE STUDY

1.1 INTRODUCTION

It is anticipated that by the year 2031, the demand for new large commercial aircraft will exceed more than 28,000 in the global market (Leahy 2013). This is expected to accelerate the demand for titanium, one of the aero-structural materials used in engines. In the proceedings of the 34th International Titanium Association (ITA) Conference (2018) in Las Vegas (see Figure 1-1), it was projected that the total titanium demand for commercial jet engines will reach more than 25,000 metric tonnes by the year 2030.

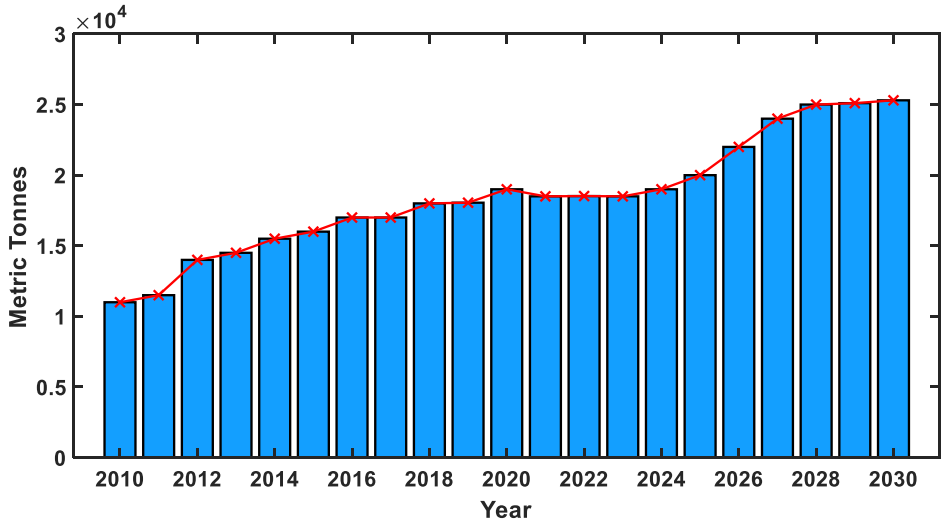

Figure 1-1. Projected titanium demand for commercial jet engines (Titanium USA 2018).

Titanium alloys are widely used in the aerospace and biomedical industries, mainly due to their excellent combination of unique properties, such as high specific strength (strength normalised by density), fracture toughness, high fatigue performance, outstanding corrosion resistance and superior biocompatibility (Leyens and Peter 2003, Ikuhiro et *al*. 2014). The properties of light weight and high specific strength, particularly at elevated temperatures, render these alloys highly desirable materials in the construction of aircraft (Ikuhiro *et al.* 2014). These alloys find increasing preference over aluminium-based alloys and steel in some areas of aircraft utilization. One of the reasons for this is because aluminium alloys lose their strength rapidly at elevated temperatures, while titanium alloys have a distinct high temperature strength advantage at temperatures of up to 426 ℃ (Azo

© Central University of Technology, Free State

Materials 2020). Such elevated operational temperature could occur at high speeds due to aerodynamic heating. The advantage of titanium alloys over steel in aircraft comes from their accompanying weight reduction with no loss in strength (Leyens and Peter 2003). Therefore, the utilization of titanium alloys in the construction of aircraft ranges from engines and airframes to skins and fasteners. Turbofan engines are widely employed by commercial aircraft to improve combustion efficiency, thereby improving fuel consumption. Turbofan engines consist of four sections. These are in order from the front: the fan, compressor, combustion chamber and turbine, as shown in Figure 1-2.

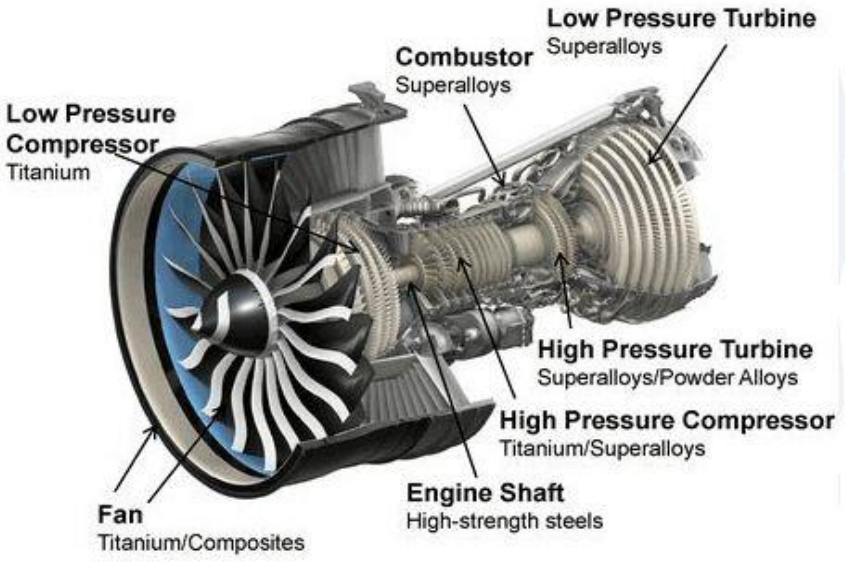

Figure 1-2. A section of a turbofan engine for aircraft showing various types of material used (Ikuhiro et al*. 2014).*

In jet turbo-engines, such as the one shown in this Figure 1-2, titanium alloys are chiefly used in compressor blades and turbine disks. The alloy Ti6Al4V, which comprises 50% of all titanium alloys in industrial usage (Frazier 2014), is mainly used in these parts in the front section of the engine where the temperature is relatively low (< 500 °C) (Ikuhiro *et al*. 2014).

The fabrication of complex parts of the engine, such as the blades and turbine discs, generally requires high dimensional accuracy and good surface integrity. Thus, the common metal-shaping technologies of machining (Zhang 2001) that include forging, turning, milling

© Central University of Technology, Free State

and drilling have been used to produce such parts. Machining titanium alloys is not easy (Ruibin 2016) because of its (a) low thermal conductivity, (b) low elastic modulus, (c) maintenance of high strength at high temperature, and (d) acute chemical reactivity. These factors give rise to low material removal rate, short tool life, and poor machining quality (Modgil 2003, Ruibin 2016). Furthermore, casting of titanium and its alloys is problematic due to its acute reactivity in molten form with crucible and mould materials during the process, as well as its reaction with atmospheric gases (Saha and Jacob 2014).

Over the recent decades, the aerospace and biomedical industries have undergone considerable technological advancement in relation to new processes of manufacturing that can partially or wholly replace the traditional manufacturing methods along the production chain. Additive manufacturing (AM) is among these new technologies that have been pursued by materials scientists and engineers in these industries, as well as in many academic research centres around the globe, as a potential replacement for conventional manufacturing technologies. It is important to note that the current state of research is not essentially about influencing the choice of AM over conventional manufacturing methods, but rather to establish how the AM process may be implemented at different stages in product development where the process is deemed advantageous. In view of this, the AM process has the following advantages over conventional manufacturing processes:

a) The AM process is highly advantageous in the fabrication of parts with geometric complexity. This is because AM processes are not constrained by complexity and undercuts and internal features can easily be built from 3D CAD models. Unlike AM, certain sophisticated parts cannot be fabricated by traditional manufacturing processes, such as CNC (computer numerical controlled) machining technology, unless they are broken up into components and reassembled at a later stage (Gibson *et al*. 2010).
b) The AM process can be used to produce parts in a single stage, therefore significantly reducing the energy usage by eliminating assembly steps in the production process. For instance, through a conventional manufacturing process 20 parts are welded to produce the LEAP fuel nozzle, while AM produces a single piece that is 20% lighter, five times more durable and reduces fuel burn by 15% (Keller 2017).

© Central University of Technology, Free State

c) AM is primarily an additive process rather than subtractive; thus, the process generates significantly less waste than conventional methods which are subtractive in nature (Gibson *et al*. 2010). Therefore, when dealing with expensive alloys, such as titanium alloys, little wastage can significantly reduce cost. Machining processes can have a buy-to-fly ratio of 10 or higher on large aerospace components, while for AM processes it is close to 2 (Gibson *et al*. 2010, Hendrixson 2020).

The AM technology was initially known as rapid prototyping (RP). More recently, its fast-growing application in the fabrication of parts for final products has led to broader acceptance of AM. For instance, it has shown greater success and potential and has already been used in fabrication of functional complex parts with good geometric accuracy such as novel turbine blades (Boris 2006) and LEAP fuel nozzles for aircraft engines (Kellner 2017). The ability of the technology to manufacture final product parts rather than prototypes is a breakthrough and is the most important part of AM's future (Campbell *et al.* 2011).

With the low machinability of titanium and problematic nature of handling molten titanium (Modgil 2003, Saha and Jacob 2014, Ruibin 2016) and the advantages offered by AM, this technology offers a better alternative and has attracted the attention of manufacturers of titanium alloy parts. Due to its wide usage in the aerospace and biomedical industries, Ti6Al4V is the most common alloy produced via AM, not only among titanium alloys, but also among the limited range of alloys processed via AM (Frazier 2014, Al-Sheebeb 2020). The AM process is characterised by a high input of energy over a very short period. This leads to very fast cooling, steep thermal gradients, fast solidification, and the formation of martensitic microstructure in AM produced titanium alloy parts with resultant low ductility and high macro- process residual stresses. To improve the mechanical properties and thus reliability of functional components, these fabricated parts are subsequently heat-treated to reduce macro- process residual stresses and achieve desirable microstructures with suitable mechanical properties. To this end, extensive research (Semiatin *et al*. 2003, Vilaro *et al.* 2011, Vrancken *et al*. 2012, Qianli *et al.* 2015, Markovitz *et al.* 2016, Yang *et al.* 2016) has focused on exploring suitable heat-treatment strategies for as-built AM Ti6Al4V parts to meet mechanical properties required for specific industrial applications.

The existing pool of knowledge on deformation and failure behaviour of metals and alloys provides industry with a strong basis for testing the suitability of the materials to bear

© Central University of Technology, Free State

different mechanical and thermo-mechanical loads. In the design of aircraft structural parts, such as undercarriage (landing gear beams) and turbo engines (turbine blades and their containment casings), as well as military and automotive structural parts, accurate knowledge of thermo-plastic behaviour of metals and alloys in use is required.

1.2 PROBLEM STATEMENT

The challenges of understanding the interrelationships between microstructure, post-processing, mechanical properties and performance of new AM materials has occupied materials researchers the world over (Uriondo *et al*. 2015). Methodologies for improving the performance and mechanical properties of AM materials can be developed through proper quantitative understanding of these attributes and those of their variables that can be controlled.

The macroscopic properties of materials are largely affected by the microstructure. On the other hand, the microstructure is a very intricate feature with various aspects that influence specific properties in a synergistic manner (Jaimie and Tiley 2002, Sun *et al.* 2012). These aspects include grain morphology and size, crystallographic texture, macro process-residual stresses and defects, which are largely dislocations in nature (Dieter 1986). The specific properties include strength, ductility and toughness.

Though strength and ductility are the most important properties of metals and alloys considered in the development of energy-efficient structural components, improving strength often results in degradation of ductility and vice versa, in what is commonly referred to as the strength-ductility trade-off (Jaimie and Tiley 2002, Kasperovich and Hausmann 2015). The strength of materials increases monotonically with the increase in dislocation density, and as noted above, comes at the cost of reduced ductility. Traditionally, strength in metals and alloys has been obtained via cold working and thermo-mechanical processing that introduce very high dislocation densities in materials and grain refinement because of the evolution of high-angle grain boundaries (Zhang *et al.* 2011). According to the Hall-Petch equation, decreasing the grain size will increase the yield strength and attendant decrease the ductility of a material if other variables are not a design consideration (Hall 1951). The Ti6Al4V alloy is complex and contains multiple

© Central University of Technology, Free State

variables which are competing and/or synergistically enhance its properties (Jaimie and Tiley 2002, Sun *et al.* 2012).

Other external factors, such as the prevailing level of strain rate and temperature, also affect the yield stress and subsequent deformation properties of metals and metal alloys (Dieter 1986). The exact relationships between the microstructural features and the tensile and compression high-strain-rate behaviour of AM Ti6Al4V (Extra Low Interstitial-ELI) are still unknown (Uriondo *et al*. 2015). This lack of information could result in the slow acceptance of the AM material for applications such as in aircraft turbo engines and landing gear beams, where firm design provisions are required for the integrity of structures (Armendáriz *et al.* 2016). Design provisions are based upon large databases whose statistics furnish engineers with the necessary confidence to consider the use of new materials (Sinha and Dorbala 2009). To address this challenge, there is a need to expedite the acceptance of new AM parts by promoting the development of numerical models. Such models will provide quantitatively descriptive interrelationships between microstructure, strain rate and temperature with the mechanical performance, represented by various properties, one of these being flow stress which is studied in the present research.

A major part of the aircraft industry throughout the production chain is supported by modelling and numerical simulation (Armendáriz *et al.* 2016). A manufacturing chain simulation can be used to compute the progressive effect of different processes. By pursuing the material state throughout the entire production chain from the initial state of the material, the mechanical properties of the final product can be predicted realistically (Sun *et al.* 2012). Numerical modelling and simulations can be useful to predict mechanical properties of materials, such as yield stresses and flow stresses, in those circumstances where actual experiments are too costly or even difficult to perform (Jaimie and Tiley 2002, Sun *et al.* 2012). Therefore, developing a model based on the dominant mechanisms of deformation of microstructures of AM Ti6Al4V(ELI) for various uses, over a broad-spectrum of temperatures and strain rates, will be useful (Uriondo *et al*. 2015).

1.2 AIM AND OBJECTIVES OF THE STUDY

The aim of this study was to develop a numerical model that can be used to tailor the microstructures of heat-treated Direct Metal Laser Sintered (DMLS) Ti6Al4V(ELI) to desired

© Central University of Technology, Free State

mechanical flow behaviour over a broad-spectrum of temperatures and strain rates. This aim was achieved through the following objectives:

- To develop three different microstructures of DMLS Ti6Al4V(ELI), through heat treatment of as-built parts.
- To quantify the metallographic parameters, such as phase fractions and grain sizes of the microstructures, using standard stereological procedures, which then form primary input data for the model to be developed.
- To study the initial length distribution and distribution density of dislocations, their dynamic recovery and influence on the yield stress and subsequent initial strain hardening for the three developed microstructures, using the methods of X-Ray Diffraction (XRD) and Electron Backscattered Diffraction (EBSD).
- To develop physics-based material models based on the microstructural data for use in predicting the flow stress behaviour of the material over a broad-spectrum of temperatures and strain rates.
- To calibrate and validate the physical model using experimental data.
- To implement the validated model as user subroutines in the commercial finite element software ABAQUS /Explicit.

1.3 THE SCOPE AND OUTLINE OF THE THESIS

This study reports on the production of various microstructures of AM Ti6Al4V(ELI) with improved deformation and fracture properties for high-strain-rate applications. This is part of wider studies that include investigation of the behaviour of the material under low and medium strain rates, whose inclusion here was considered too widening in scope. In the research work presented here, the metallographic parameters, such as grain sizes and density of dislocations of the microstructures, as well as various phenomenological aspects of strain hardening and dynamic recovery were used to develop numerical solutions for modelling the strain rate behaviour of the material.

The thesis comprises eleven chapters and appendices. References are presented at the end of every chapter in which they are cited for closer relevance. The first chapter is an outline containing the background and the aim of study. The second chapter contains a review of the concepts of AM and the general metallurgy of AM-produced Ti6Al4V(ELI). Theories of

© Central University of Technology, Free State

several techniques used for microstructural characterisation of metals and alloys are introduced and discussed in this chapter. In this chapter also are reviews of different models used to predict the mechanical properties of metals and alloys with a special focus on Ti6Al4V. The theory of plasticity used to calculate stress and strain in materials under deformation is also discussed in the chapter.

Materials and experimental methods are presented in Chapter 3. These include production and heat treatment of test specimens. Experimental methods, such as EBSD, XRD and the Split Hopkinson Pressure Bar (SHPB) test, are discussed here.

The development of a constitutive physical model that is sensitive to the microstructure of DMLS Ti6Al4V(ELI) is presented in Chapter 4. Chapters 5 and 6 contain results and discussion of microstructure, crystallographic texture and dislocation densities of the five different forms of DMLS Ti6Al4V(ELI) produced in this research. Chapter 7 details the results and discussion of high-strain-rate testing at different temperatures, while in Chapter 8, the resident material on calibration and validation of the developed physical constitutive model using the experimental results presented in the previous chapter are examined. Chapter 9 contains detailed description of the implementation of material constitutive models into FORTRAN codes, as well as testing and verification through the simulation of single and multiple element models in ABAQUS/Explicit. The detailed description of these FOTRAN codes lie in the appendices. In Chapter 10, there is a detailed description of the SHPB test simulation of high-strain rate properties of heat-treated microstructures of DMLS Ti6Al4V(ELI) at different temperatures that is validated using the experimental results in Chapter 7. Finally, in Chapter 11, the conclusions and recommendations for further work and a summary of arising knowledge created in this work is presented.

© Central University of Technology, Free State

1.4 REFERENCES

1. Al-Shebeeb, O.A. 2020. An investigation of the metal additive manufacturing issues and perspective for solutions approach. *Concept, Applications and Emerging Opportunities in Industrial Engineering,* Gary Moyniham, IntechOpen, London, UK.
2. Armendáriz, I., Millán, J., Encinas, J, Olarrea, . 2016. Strategies for dynamic failure analysis on aerospace structures. Handbook of Materials Failure Analysis: With Case Studies from the Aerospace and Automotive Industries, Salam, A., Makhlouf, H., Mahmood A., editors, Elsevier Ltd, Amsterdam, Netherlands, pp.29–55.
3. Azo Materials. 2020. *Properties: Titanium Alloys—Ti6Al4V Grade 5—AzoM.com.* Available online: https://www.azom.com/ properties.aspx?ArticleID=1547 (accessed on 28th April 2020).
4. Campbell, I., Bournell, D., Gibson, I. 2011. Additive manufacturing: Rapid prototyping comes of age. *Rapid Prototyping Journal,* 18(4) pp.255–258.
5. Dieter, E.G. 1986. Mechanical Metallurgy 3rd Edition. *Materials science and engineering series*, McGraw-Hill, New York, USA, pp.103–184.
6. Frazier, W.E. 2014. Metal additive manufacturing: A review. *Journal of Materials Engineering and Performance,* 23(6), pp.1917–1928.
7. Gibson, I., Rosen, D., Stucker, B. 2010. Additive manufacturing technologies. *Rapid Prototyping to Direct Digital Manufacturing*, Springer, Heidelberg, New York, USA, p.8.
8. Hall, E.O. 1951. The deformation and ageing of mild steel: Discussion of results. *Proceedings of the Physical Society B,* 64 (9), p.747.
9. Hendrixson, S. 2019. Lower Buy-to-Fly Ratios with Near-Net Additive Manufacturing. *https://www.mmsonline.com/blog/post/lower-buy-to-fly-ratios-with-near-net-additive-manufacturing.* (Accessed on 15th June 2019).
10. Ikuhiro, I., Tsutomu, T., Yoshihisa, S., Nozomu, A. 2014. Application and Features of Titanium for Aerospace Industry. *Technical Review—Nippon Steel Technical Report No 106*; Nippon Steel Corporation: Osaka, Japan.
11. Jaimie, S, Tiley, M.S. 2002. *Modelling of microstructure property relationships in Ti6Al4V.* Dissertation presented in partial fulfilment of the requirements for the

© Central University of Technology, Free State

degree Doctor of Philosophy in the Graduate School of the Ohio State University, USA.

12. Kasperovich, G., Hausmann, J. 2015. Improvement of fatigue resistance and ductility of TiAl6V4 processed by selective laser melting. *Journal of Material Processing Technology,* 220, pp.202–214.
13. Kellner, T. 2017. An Epiphany of Disruption: GE Additive Chief Explains How 3D Printing Will Upend Manufacturing. https://www.ge.com/news/reports/epiphany-disruption-ge-additive-chief-explains-3d-printing-will-upend-manufacturing. (Accessed on 10 th July 2019).
14. Leahy, J. 2013. Airbus: Global market forecast 2013–2032, s.1: *www.airbus-group.cp.* (Accessed on 28th July 2019).
15. Leyens, C., Peter, M. 2003. Titanium and its alloys: Fundamental and applications*, Wiley-VCH, Germany, ISBN 3-527-30534-3, pp.4–35.*
16. Markovitz, D., Katsman, A., Shirizly, A., Bamberger, M. 2015. Microstructure and mechanical properties of heat-treated selective laser melting manufactured Ti6Al4V. *Proceedings of the ICANM: International Conference & Exhibition on Advanced & Nano Materials,* 10th–12th August*,* Ottawa, Canada, pp.33–42*.*
17. Modgil, A. 2003. Effects of high-speed machining on surface topography of titanium alloy (TI6AL4V). *A master's thesis submitted to University of Florida*, USA.
18. Ruibin, X., Wu, H. 2016. Study on cutting mechanism of Ti6Al4V in ultra-precision machining. *International Journal of Advanced Manufacturing Technology*, 86, pp.1311–1317.
19. Saha, R., Jacob, K. 2014. Casting of Titanium and its Alloys. *Defence Science Journal,* 36, pp.121–141. https://doi.org/10.14429/dsj.36.5967
20. Semiatin, S., Kinsley, P., Fagin, P., Barker, D., Zhang, F. 2003. Microstructure evolution during alpha-beta heat treatment of Ti6Al4V. *Metallurgical and Material Transactions A,* 34(10), pp.2377–2386.
21. Sinha, S.K., Dorbala, S., 2009. Dynamic loads in the fan containment structures of a turbofan engine. *Journal of Aerospace Engineering*, 22(3). https://doi.org/10.1061/(ASCE)0893-1321(2009)22:3(260)
22. Sun, Y., Weidong, Z., Yuanfei, H., Xiong, M., Yongqing, Z., Ping, G., Wang, G., Dargusch, S. 2012. Determination of the influence of processing parameters on the

© Central University of Technology, Free State

mechanical properties of the Ti6Al4V alloy using an artificial neural network. *Computational Materials Science*, 60, pp.239–244. https://doi.org/10.1016/j.commatsci.2012.03.047

23. Titanium USA. 2018. Executive summary of the *34th Annual International Conference and Exhibition* at Bellagio Resort, Las Vegas, USA.
24. Uriondo, A., Esperson-Miguez, M., Perinpanyangam, S. 2015. The present and future of additive manufacturing in the aerospace sector: A review of important aspects. *Journal of Aerospace Engineering,* 229(11), pp.2132–2147. https://doi.org/10.1177/0954410014568797
25. Vilaro, T., Colin, C., Bartout, J.D. 2011. As-fabricated and heat-treated microstructures of the Ti 6Al4V alloy processed by selective laser melting. *Metallurgical and Materials Transactions A*: *Physical Metallurgy and Materials Science,* 42(10), pp.3190–3199.
26. Yang, J., Hanchen, Y., Yin, J., Ming, G., Zemin, W., Xianoyan, Z. 2016. Formation and control of martensite in Ti6Al4V alloy produced by selective laser melting. *Materials and Design, 108, pp.308–318.*
27. Zhang, L.C. 2001. Precision Machining of Advanced Materials. Key Engineering Materials, vol.196, Trans Tech Publications Ltd, Bäch SZ, Switzerland, pp.31–42.
28. Zhang, X., Godfrey, A., Huang, X., Hansen, N., Liu, Q. 2011. Microstructure and strengthening mechanisms in cold drawn pearlitic steel wire. *Acta Materialia*. 59(9), pp.3422–3430. https://doi.org/10.1016/j.actamat.2011.02.017

© Central University of Technology, Free State

CHAPTER 2 - LITERATURE SURVEY

Part of material contained in this chapter has been published in peer-reviewed media as detailed below:

1. ***A M Muiruri**, M Maringa, W B du Preez, Constitutive numerical modelling in additive manufacturing: Challenges in predicting the yield strength and flow properties of alloys. Proceedings of the 20th Annual RAPDASA International Conference, Emoya Estate, Bloemfontein, 6th–8th November **2019**, pp.190–203, ISBN 978-0-6398390-0-4.*
2. ***Muiruri Amos**, Maina Maringa, Willie du Preez, Application of phenomenological modeling in the development of a database for additively manufactured Ti6Al4V(ELI): A review, Proceedings of the 10th International Conference of the African Materials Research Society (AMRS2019), Arusha, Tanzania, 10th–13th December **2019**.*

2.1 INTRODUCTION

In this chapter, the relevant AM technologies in existence today are introduced briefly and the potential application of these in the aerospace industry discussed. The microstructures of as-built and heat-treated DMLS TI6Al4V(ELI) are discussed and their respective mechanical properties presented. Further in the chapter, various modelling approaches in literature that are used to predict the mechanical properties of Ti6Al4V are presented and their limitations stated briefly. Subsequently, towards the end of the chapter, the theory of plasticity that is used in the implementation of constitutive models in FE software is discussed and the radial return algorithms that are used to compute for equivalent plastic strain are introduced.

2.2 METAL ADDITIVE MANUFACTURING

Currently, there are several metal AM processes available, classified according to the source of heat, such as electron beam (Dutta and Froes 2014, Frazier 2014) and laser (Collins *et al.* 2014), and how the raw material is supplied. Material supply can occur via powder or wire feed. In cases where metal powder is supplied, selected regions are melted at different combinations of absorbed power and beam velocity and then solidified. For wire-feed AM systems, the laser generates a melt pool on the substrate material, into which metal wire is fed and melted, forming a metallurgical bond with the substrate (Collins *et al.* 2014).

Figure 2-1 shows the AM processes in the two major metal AM process classifications, namely directed energy deposition (DED) and powder bed fusion (PBF). The figure also

© Central University of Technology, Free State

includes the technology trademark names presently available within each major process group and current commercial machine suppliers, in bold.

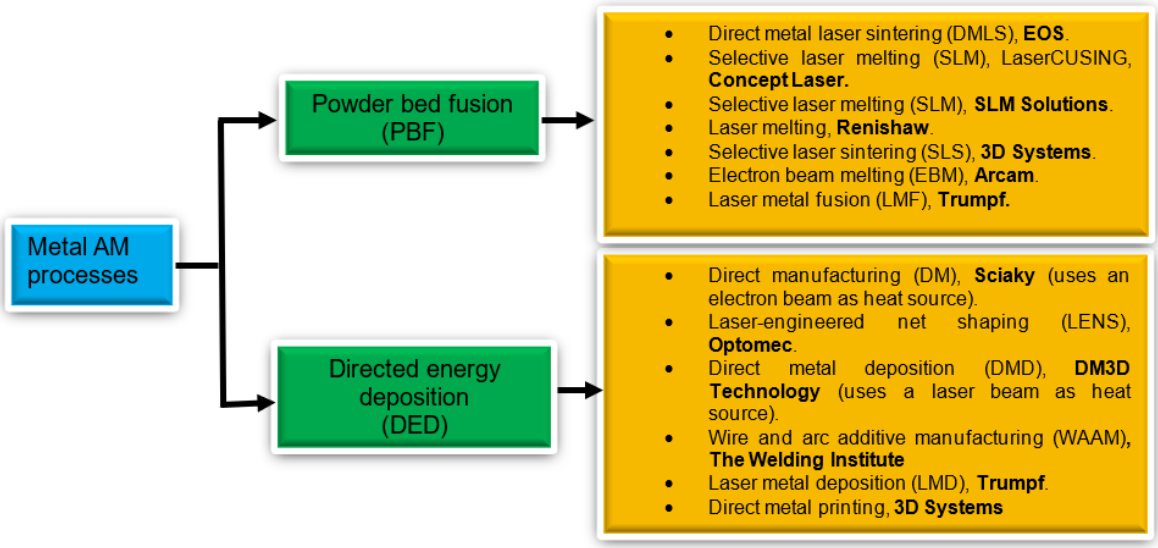

Figure 2-1. Various metal AM technologies, together with their commercial machine suppliers (Lewandowski et al. 2016).

2.2.1 Directed Energy Deposition (DED)

A schematic diagram of the DMD technology (laser-based metal deposition) is shown in Figure 2-2.

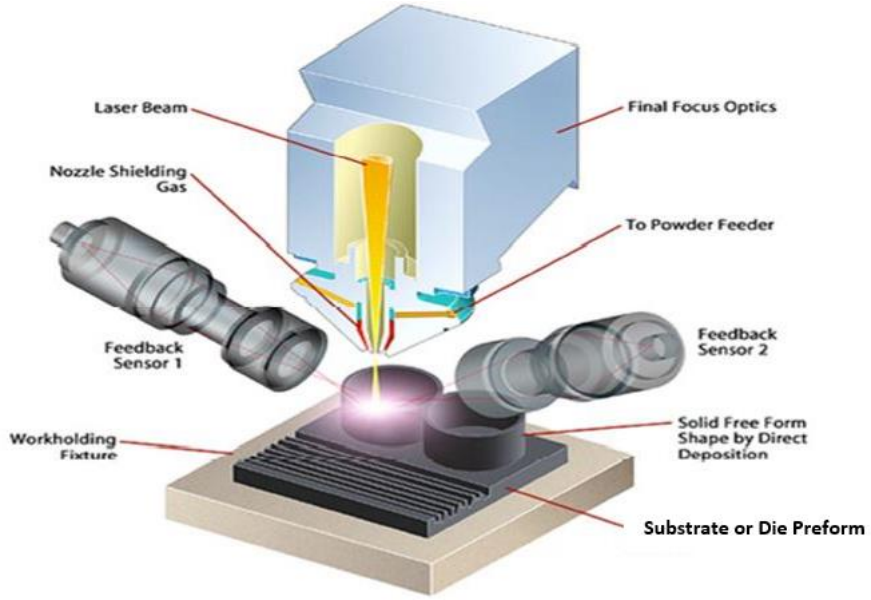

Figure 2-2. Schematic diagram showing a laser DED technology (Courtesy of DM3D Technology).

© Central University of Technology, Free State

The DED technologies use powder or wire material injection into a melt pool on a workpiece at the same time as a laser beam, electron beam or plasma arc impacts on the workpiece, instead of scanning on a powder bed, as happens in PBF technologies. A substrate or pre-existing part is placed on a worktable and as the nozzle (tooltip) moves away, the melt pool solidifies, forming a layer of metal. Successive layers are used to build up parts layer by layer until completion.

2.2.2 Powder Bed Fusion (PBF)

Figure 2-3 shows a schematic diagram of PBF laser melting (DMLS/SLM) and electron beam melting (EBM) machines.

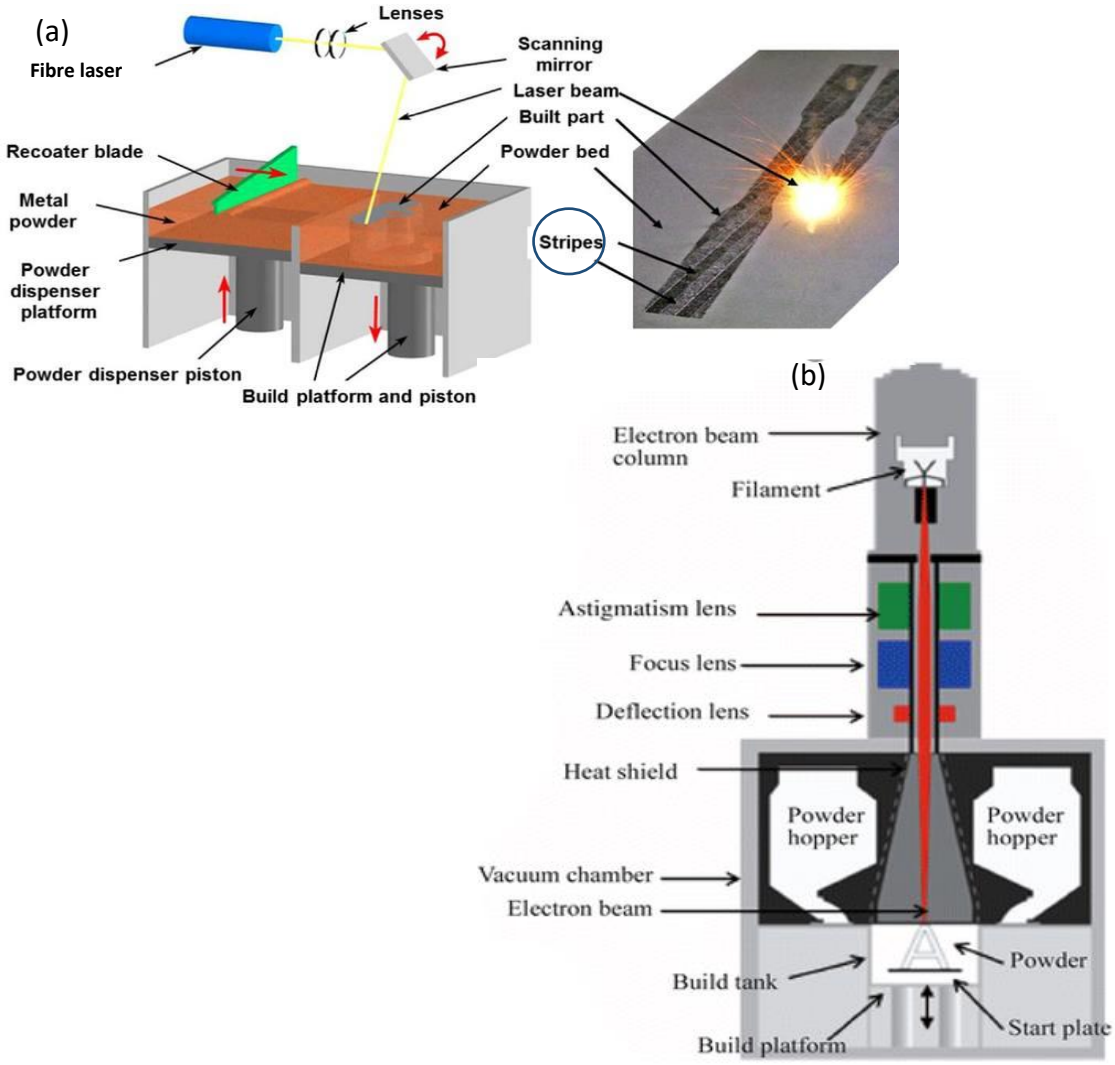

Figure 2-3. Schematic diagram of PBF processes (a) DMLS (adapted from EOS GmbH) and (b) EBM (adapted from Arcam EBM).

© Central University of Technology, Free State

The PBF technologies include any process where focused energy (laser beam or electron beam) is used to selectively melt or sinter a layer of powder on a powder bed. For metals, melting is now typically used instead of sintering. Originally, metals and alloys AM was done through sintering of powder, but with time, improvements in technology have led to full melting of metals and alloys (Sames *et al.* 2016). Re-melting of previous layers during the melting of the current layer allows fusion of the current layer to the previous layers.

Powder Bed Fusion machines require a build substrate or base plate to give mechanical and thermal support to the built part. In the DMLS/SLM process, the base plate is bolted down, whereas in the EBM process, powder surrounding the base plate is typically melted to stabilise it and prevent it from being displaced by the rake or recoater blade (Dutta and Froes 2014). When consecutive layers of powder are added and raked out or rolled, the previous, solidified layers of the build should not move. The mechanical support is provided by the substrate to this end. The substrate also provides a thermal path to dissipate heat away from the build during the process of manufacture. The excess powder must be removed from the build chamber upon completion of the build process. For EBM parts, this powder is passed through a powder recovery system to remove and recover sintered powder from around the parts. For a DMLS/SLM process, the powder surrounding the built parts does not sinter as much and can be sorted directly and then sifted to remove sintered clusters. Thereafter, the built parts are cut off from the substrate/ base plate with wire-electro discharge machining (EDM). The stripes shown (circled) in Figure 2-3(a) are a result of scanning strategy where each layer is divided into series of parallel stripes that run across the entire length of the cross section of any closed contour within a layer.

2.3 POTENTIAL APPLICATIONS OF AM IN THE AIRCRAFT INDUSTRY

Additive manufacturing has four primary applications within the aircraft industry: the manufacture and repair of components, and the manufacture and repair of tooling (Kobryn *et al*. 2006). Repair and manufacture of parts can generate significant financial benefits for the aerospace industry because of the benefits associated with AM, such as reduced lead time, zero hard tooling required and reduction in material wastage. The major subsets of parts for which AM is considered to holds promise include:

© Central University of Technology, Free State

i. **Rib-web structural components:** These comprise parts such as spars, longerons, ribs, and bulkheads. They are normally made of titanium or aluminium-based alloys. These components predominately form planar 'webs' reinforced with sparsely spaced, perpendicular 'ribs' to efficiently carry aircraft loads. They are generally machined from plate stock or die forgings, leading to buy-to-fly ratios of 10:1 or higher (Hendrixson 2019). The near-net-shape process of AM provides numerous potential advantages such as reduced usage of raw material, reduced size of material stock, reduced or lack of machining, and when compared to forgings, reduced requirements for hard tooling (Arcella *et al.* 2000).

ii. **Turbine engine cases:** These are main structural parts which house the engines and are typically made of nickel or titanium-based alloys. The cases mainly consist of thick cylindrical sections with a small number of low-volume, asymmetric protruding sections. The height of these protuberances determines the thickness of the forging performed and hence the level of the buy-to-fly ratio (Hendrixson 2019). The buy-to-fly ratio for engine cases can even be more than those for rib-web parts. Therefore, similar benefits are anticipated for AM of these parts as in the case of rib-web components.

iii. **Engine vanes and blades:** These are generally composed of complex aerofoil-shaped sections with internal cooling passages in some. Large vanes and blades contain internal cooling channels. The processes of investment casting or die forging are used to make these parts using nickel or titanium-based alloys, which gives them low buy-to-fly ratios (Kobryn *et al*. 2006). The limitations of these conventional technologies prevent the application of effective complex internal cooling passages, such as deflector-type systems (because of the considerable curvature along the chord lines) or penetrating-type systems (Pochuev *et al.* 2006, Riznyk *et al.* 2013). Fortunately, rapidly advancing AM facilitates the production of single-piece blades of much more complex shapes, such as the one shown in Figure 2-4.

© Central University of Technology, Free State

Figure 2-4. Engine blade with transverse cooling passages produced via AM (Luibov et al. 2016).

The engine blades and vanes are very costly to buy and generally experience significant wear and/or damage throughout their service life (Frazier 2014, Boris 2016). The potential advantages of AM technology in the manufacture of vanes and blades are significant since these parts are usually refurbished or repaired during the general aircraft engine overhaul (Luibov *et al.* 2016). The technology also has the capacity to compete with the traditional methods of repair and to enable previously difficult repair to be carried out in certain intricate circumstances.

Currently, parts produced through AM processes are already in use in modern engines. General Electric Aviation (GE Aviation 2019) has reported that the next generation GE9X series (high-bypass turbofan aircraft engine) will use 19 AM-printed fuel nozzles to help power the next generation of wide-body aircraft, like the Boeing 777X. The low-pressure turbine blades and large parts, such as heat exchangers and separators, in the GE9X series will also be additively manufactured. Rolls-Royce (Rolls-Royce Global Flight 2015) reported that a 1.5-metre diameter and 0.5-metre-thick front bearing housing containing 48 aerofoils was manufactured using AM for a Trent XWB-97 engine.

Of considerable interest is the ability of these AM materials to withstand the harsh environments imposed on the different parts and sections that eventually provide energy and thrust. One of the major safety concerns in a modern commercial aircraft is the failure of fan or compressor blades resulting in damage to the airplane (Australian Transport Safety Bureau 2002). The Federal Aviation Authority (FAA) certification (General Electric 2005) requires that every commercial engine line be tested to demonstrate the engine's ability to contain a detached blade/blades without catching and without failure and

© Central University of Technology, Free State

fragmentation of other parts. One of the flight safeties that is considered during the design of an aircraft engine is the likelihood of detachment of rotating fan blade when the engine is running, a phenomenon commonly known as fan blade-out. It involves a very intricate high-energy and high-speed interaction of numerous locally and remotely located engine components, such as a failed blade, other attached blades, containment structure, bearings, shafts and other externally mounted components. The incident involves progressive plastic deformation, failure and fragmentation of these interacting components (Sinha and Dorbala 2009). More critical is the need to avert damage of other independent systems, such as controls, which could lead to loss of control of the aircraft and consequent catastrophic losses or unsafe landing. Due to the nature of the impact type of loading in cases of blade-out events, the solution to the problem addresses characteristics of the material behaviour measured by parameters, such as yield stress and flow stress, as a function of strain rates and temperatures.

Uriondo *et al*. (2015) presented specific challenges that need to be addressed before these AM materials can be fully accepted in aircraft applications, as follows:

- The need to understand and control the differences in mechanical properties and quality of AM materials produced by different AM machines/techniques.
- The need to establish specific methods for Qualification of AM parts.
- The development, for inspection of critical flaws and defects in aircraft AM parts, of reliable non-destructive testing (NDT) methods.
- Improvement of properties of AM materials through heat treatment and better surface quality is needed.
- Physics-based models are required to predict the properties and microstructure of AM materials.

Of considerable interest in this research work are the last two items. It is crucial that the resulting microstructures of heat-treated AM materials are well characterised and constitutive models developed to predict the mechanical properties of the parts.

© Central University of Technology, Free State

2.4 MICROSTRUCTURE AND MECHANICAL PROPERTIES OF AS-BUILT AND HEAT-TREATED AM TI6AL4V

The grain structures and phases in a metal or metallic alloy are referred to as microstructure, and directly determines the mechanical properties of parts. The type of grain structures and phases present in a microstructure are a function of the manufacturing route used. In this section, the as-built and subsequently heat-treated microstructures of DMLS Ti6Al4V are discussed with a focus on phase formations as well as, the coarsening and transformation of grains. The inherent defects in the alloy's AM parts are also discussed, as well as the mechanical properties of various microstructures of the alloy.

2.4.1 Microstructure of as-built AM Ti6Al4V(ELI) parts and their inherent defects

The titanium alloy, Ti6Al4V, contains the primary alloying elements, 6 wt.% aluminium and 4 wt.% vanadium. The titanium element exists in two different crystal structures depending on temperature: α-titanium with atoms arranged in hexagonal close-packed (hcp) arrays is found below the β-transus temperature, while body-centred cubic (bcc) β-titanium is found above the β-transus temperature. Since aluminium is an α-phase stabilizer and vanadium stabilises the β-phase, Ti6Al4V maintains α+β dual phase at room temperature (Lütjering and Williams 2007). The α/β transformation in the Ti6Al4V alloy depends on the thermal history and cooling rates experienced during the manufacturing process (Banerjee and Williams 2013). In a complete melting and solidification, Ti6Al4V experiences α'/α+β → β and β → α + β/α' phase transformation. The phase transformation diagram of Ti6Al4V is shown in Figure 2-5 (Ahmed and Rack 1998).

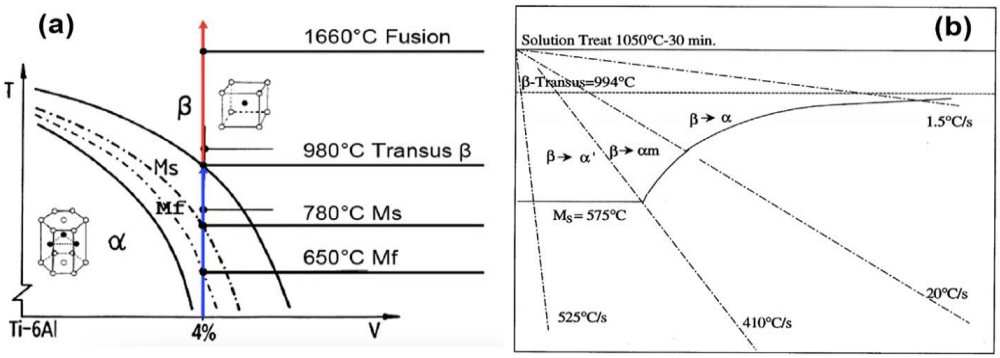

Figure 2-5. (a) Phase diagram of Ti6Al4V (b) phase transformation of Ti6Al4V at different cooling rates (Ahmed and Rack 1998).

© Central University of Technology, Free State

The α+β dual phase only exists after slow to moderate solidification processes. Upon fast cooling from above the β-transus temperature, the β-phase decomposes to form an α′ (acicular) martensite phase instead of the α+β phase mentioned above. The acicular martensite phase is produced by high cooling rates through diffusionless transformation, while the α+β transformation is a diffusional process (Lütjering and Williams 2007). Generally, the rapid cooling rate ($\geq 410\,℃/s$) and build temperature lower than the martensite start temperature (M_s) for Ti6Al4V produced by any manufacturing processes will lead to the formation of α′ martensite, as shown in Figure 2-5 (Ahmed and Rack 1998). Various values of M_s have been reported for Ti6Al4V in the range of 575 ℃–800 ℃ (ASM 1994, Ahmed and Rack 1998). The composition homogeneity, initial microstructure and impurity elements were suggested in ASM (1994) and by Reisgen *et al.* (2017) to affect the M_s. Additive manufacturing processes and particularly DMLS/SLM processes are characterised by highly focused energy sources and extremely short interaction times, and therefore, high temperatures and cooling rates are normally experienced in the molten pools formed. A maximum temperature of approximately 2710 K in the Ti6Al4V molten pool produced by the DMLS process was reported in Yadroitsev *et al*.(2014). In the separate works of Qiu *et al*. 2013, Gokuldoss and Kolla 2017, the cooling rate in this process was reported to lie in the range of about 10^4–10^6 K/s. Shunyu and Yung (2019) developed a model to exactly discern the thermal behaviour of AM processes during the interaction of the alloy with the laser beam. In their model, a maximum temperature of approximately 2600 K was produced in the molten pool. As the laser beam moved away, this temperature then decreased to ambient temperature in about 0.25 s as the laser beam moved away. This translates to an average cooling rate of approximately 10^4 K/s, which is consistent with the value reported in Qiu *et al.* (2013) and Gokuldoss and Kolla (2017). Due to these high cooling rates of the DMLS/SLM process, α′ martensite normally prevails in the as-built microstructure of AM-fabricated Ti6Al4V parts.

Yang *et al.* (2016) and Ter Haar and Becker (2018) reported the microstructure of DMLS Ti6Al4V to consist of four different groups of martensite at high magnifications. These include primary, secondary, tertiary and quartic α′, as shown in Figure 2-6(a). The primary α′ in Figure 2-6(b) extends across the entire prior-β grain whose minor axis is about 25 µm. Numerous fine secondary α′ martensite grains (Figure 2-6(c)), with major axis measuring

© Central University of Technology, Free State

several micrometres and minor axis measuring hundreds of nanometres, exist with orientations that are parallel or perpendicular to the primary α′ martensite.

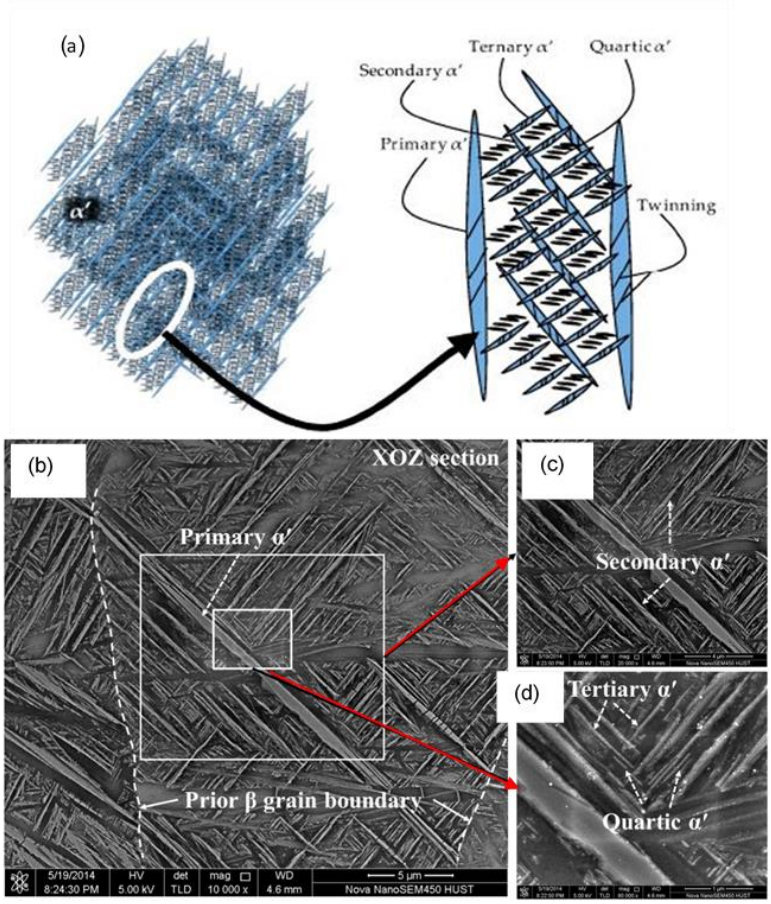

Figure 2-6. The DMLS Ti6Al4V microstructure, (a) the schematic diagram of martensitic α′ hierarchical structure (Ter Haar and Becker (2018), (b) SEM SE image of a sample, (c) and (d) are higher magnifications of the areas indicated by white boxes in (b) (Yang et al. 2016).

Finer tertiary α′ martensite grains are found between the secondary α′ martensite grains, as shown in Figure 2-6(c). Finally, the finest quartic α′ martensite grains with major and minor axis at nanometre-scale exist between these tertiary α′ martensite grains, as seen in Figure 2-6(d).

Ter Haar and Becker (2018) measured these hierarchical α′ structures in samples built using a LaserCUSING machine by Concept Laser GmbH, with the results shown in Table 2-1. Yang *et al.* (2016) suggested that the primary α′ and secondary α′ martensite in micrometre-size level nucleated and grew during the early stage of the thermal history and then grew further during subsequent thermal cycles.

© Central University of Technology, Free State

Table 2-1. Hierarchical structure of α' (Ter Haar and Becker 2018)

Type of α'	Length of major axis	Length of minor axis
Primary α'	(> 20 µm)	(1–3 µm)
Secondary α'	(> 10–20 µm)	(10–900 nm)
Ternary α'	(2–10 µm)	(10–90 nm)
Quartic α'	(< 1 µm)	(< 10 nm)

In contrast, the tertiary and quartic α' martensite grains were believed to be formed during the later stage of the thermal history and thus the growth process is inhibited by the boundaries of previously precipitated α' martensite, as well as the absence of subsequent thermal cycles. Rombouts *et al.* (2012) measured values of the lattice parameter of α' grains by X-ray diffraction of a = 0.293 nm and c = 0.469 nm, which are the same as the values reported for α titanium (Leyens and Peter 2003).

Parts produced by most of AM technologies exhibit the inherent limitations such as rough surfaces, presence of pores and high macro process-residual stresses. These inherent limitations have detrimental effects on the mechanical performance of their as-built components. Pores in AM parts exist mainly in the form of lack-of-fusion and gas pores (Li *et al.* 2015). Gas pores are usually spherical or elliptical in shape with diameters of about 1–100 µm and are irregularly distributed in the material (Qiu *et al.* 2013). The shape of these pores shows that they are formed because of the entrapment of gas in the molten pool that is consequently stuck in the solidified bead (Kobryn *et al* 2000, Qiu *et al.* 2013). It has been demonstrated that gas pores can be reduced but not eliminated entirely by the reduction of scanning speed and increase of laser power (Kobryn *et al* 2000). The lack-of-fusion pores are larger than gas-pores and show random wedge shapes with sharp tips at the ends (Gaytan *et al.* 2009). These pores are normally found along the boundary of two adjacent layers, forming interface cracks. Lack-of-fusion pores arise from failure to melt powder because of non-optimal melting conditions, which leads to the formation of weak inter layer (Tammas *et al.* 2015, Gaytan *et al.* 2009). The long axis of these pores is usually aligned in a direction orthogonal to the build direction with the sharp tips prone to concentration of local stresses. This could cause premature failure, particularly under tensile uniaxial loads parallel to the build direction (Li *et al.* 2015). The most appropriate

© Central University of Technology, Free State

way to alleviate lack-of-fusion pores is to raise the laser energy density expressed as (Gaytan *et al.* 2009):

$$E = \frac{ב P}{v.h.t} \qquad 2\text{-}1$$

where the symbols ב, P, h, t and v denote the absorptivity, laser power in Js^{-1}, hatch spacing in m, layers thickness in m and v is scan speed in ms^{-1}, respectively. The work of Muiruri *et al*. (2019) showed that pores act as nucleation sites for the formation of adiabatic shear bands and microcracks.

Leuders *et al*. (2013) determined the porosity of SLM specimens to be 0.23%. The porosity of DMLS Ti6Al4V(ELI) parts has been reported as 0.004%, with specific pore volume < 0.001 mm^3, using X-ray tomography, which translates to a densification of DMLS parts of ≅100% (Muiruri *et al*. 2020). The as-built AM components are often subjected to post-processes to reduce the porosity. The combined and not separate processes of heat treatment and hot isostatic pressing (HIP) are used to this end (Kasperovich and Hausmann 2015, Qiu *et al.* 2013). Kasperovich and Hausmann (2015) reported reduction of porosity from 0.077% to 0.012% after subsequent HIP treatment for SLM specimens produced by optimised parameters. However, it is not clear whether HIP treatment can be effective in improving the mechanical properties of DMLS parts and whether it can lower their porosity further, from the prevailing low value of 0.004%. Further research focusing on HIP treatments of DMLS parts, therefore, is needed to clarify these questions.

Additively manufactured Ti6Al4V shows relatively rough surfaces, like that of sand castings (Ra $\approx 12.5 - 25\ \mu m$) (Mead*info*, 2019). For example, the surface roughness of DMLS parts is typically in the range Ra$\approx 9 - 12\ \mu m$ (EOS material data sheet 2008), while the surfaces of EBM parts show much higher roughness with Ra values as high as 40 μm (Sun *et al.* 2016). Due to the roughness, as-built AM Ti6Al4V samples show distinctly lower tensile strength and ductility regardless of the AM process (Sun *et al.* 2016) as microcracks are found to initiate directly from surface defects (Sun *et al.* 2016, Muiruri *et al.* 2019). To improve the surface roughness and hence the mechanical properties of parts, post processes such as machining, surface polishing and acid etching have all proved to be effective (Qian *et al*. 2016). These additional processes applied to AM negate one of the important selling points for the technology, that of producing ready-to-use parts without

© Central University of Technology, Free State

the need for further treatment. Therefore, there is a need for further growth of AM technologies to improve parts' surface conditions and to improve their mechanical performance (Qian *et al.* 2016). This will be particularly beneficial in additive manufacturing of intricate Ti6Al4V components designed for load-bearing applications, due to the difficulty of modifying their internal surfaces.

The high thermal gradients occurring in parts produced by DMLS/SLM processes tend to generate high values of macro-process residual stresses in them (Bailey *et al*. 2017). The macro-process residual stresses in laser-based AM parts increase with the increasing number of layers (Mercelis and Kruth 2006). The highest macro-process residual stresses always occur in the last deposited layer along the build direction (Mercelis and Kruth 2006, Liu *et al.* 2016). Mercelis and Kruth (2006), reported values of macro-process residual stresses on the top regions of parts that were up to the material's tensile strength. Due to additional subsequent layers on the previously built layer, the tensile stress changes into compressive stresses because of thermal cycling process (Liu *et al.* 2016). Macro-process residual stresses along the build direction have been noted to be higher than in the transverse direction due to high prevailing temperature gradients along the build direction (Mugwagwa *et al.* 2017). This leads to the emergence of an anisotropic stress distribution in the fabricated parts. (Liu *et al*. 2016, Mugwagwa *et al.* 2017). Furthermore, macro-process residual stresses also increase with the increase in the dimension of parts along the build direction (Mercelis and Kruth 2006, Liu *et.al* 2016, Mugwagwa *et al.* 2017). Macro-process residual stresses are a major concern since they can negatively affect the mechanical properties of as-built parts, such as toughness, (Muiruri *et al.* 2020) or even lead to geometrical distortions and failure at low loads.

A way to alleviate the macro-process residual stresses originating from thermal gradients in AM processes is by post-process heat treatments. Desired microstructure and attendant mechanical properties of AM parts are also achieved using post-AM treatment. Heat treatments have been used to reduce the macro-process residual stresses and improve the mechanical properties of AM materials (Vilaro *et al*. 2011, Sercombe *et al.* 2008, Zadpoor 2018). Research has been conducted to investigate various heat-treatment strategies of AM Ti6Al4V(ELI) with the aim of improving its mechanical properties (Vilaro *et al.* 2011, Vrancken *et al*. 2012, Qianli *et al.* 2015, Markovitz *et al.* 2016, Yang *et al*. 2017).

© Central University of Technology, Free State

2.4.2 Heat-treatment processes and mechanical properties of AM Ti6Al4V

2.4.2.1 Heat-treatment processes

There is a need to modify the metastable α' martensite microstructure of AM Ti6Al4V, which is achieved through heat-treatment processes to satisfy industrial requirements of mechanical performance. The heat treatment of Ti6Al4V is basically done in the sub-transus region (below ~ 996 ℃ in the α-β region) and super-transus region (above ~ 996 ℃ in the β region), which may be followed by HIP, a process that concurrently applies high gas pressure (mostly argon) and temperature to close pores. The α→β/β→α transformation temperature of Ti6Al4V varies in the range 996 ± 18 ℃, depending on the actual Al (5.5–7.5) and V (3.5–4.5) contents (Ahmed and Rack 1998). This transformation temperature for the SLM Ti6Al4V(ELI) has been identified as 980 ℃ through measurement of the point of inflection in the linear thermal expansion curve evaluated using a dilatometer (Yang *et al.* 2017).

Conventional heat treatment of titanium alloys is designed for specific purposes, starting from a given microstructure, e.g., heavily deformed microstructures before heat treatment (Semiatin *et al*. 2003). Vilaro *et al.* (2011) and Vrancken *et al*. (2012) showed that application of standard heat-treatment processes, such as duplex annealing, mill annealing, recrystallizing annealing and β-annealing, do not yield expected results for AM parts. This is because the starting microstructure of AM Ti6Al4V parts is α' martensite obtained by high cooling rates, which is not usually achieved by conventional manufacturing routes. More so, the phase transformation kinetics of AM α'-martensite Ti6Al4V are different from those of traditional microstructures such as lamellar, equiaxed and bimodal microstructures (Qianli *et al.* 2015). Therefore, various specific and suitable post-heat treatments of AM Ti6Al4V have been investigated to optimise their properties via the control of microstructure, as reported in Vilaro *et al.* (2011), Vrancken *et al*. (2012), Qianli *et al.* (2015) and Markovitz *et al.* (2016).

The low-temperature heat-treatment strategy in the sub-transus region is that which is normally used to reduce the macro-thermal residual stresses in Ti6Al4V(ELI) resulting from the AM process and has been shown to generate little effect on the microstructure of the material as shown in Figure 2-7 (Muiruri *et al.* 2019).

© Central University of Technology, Free State

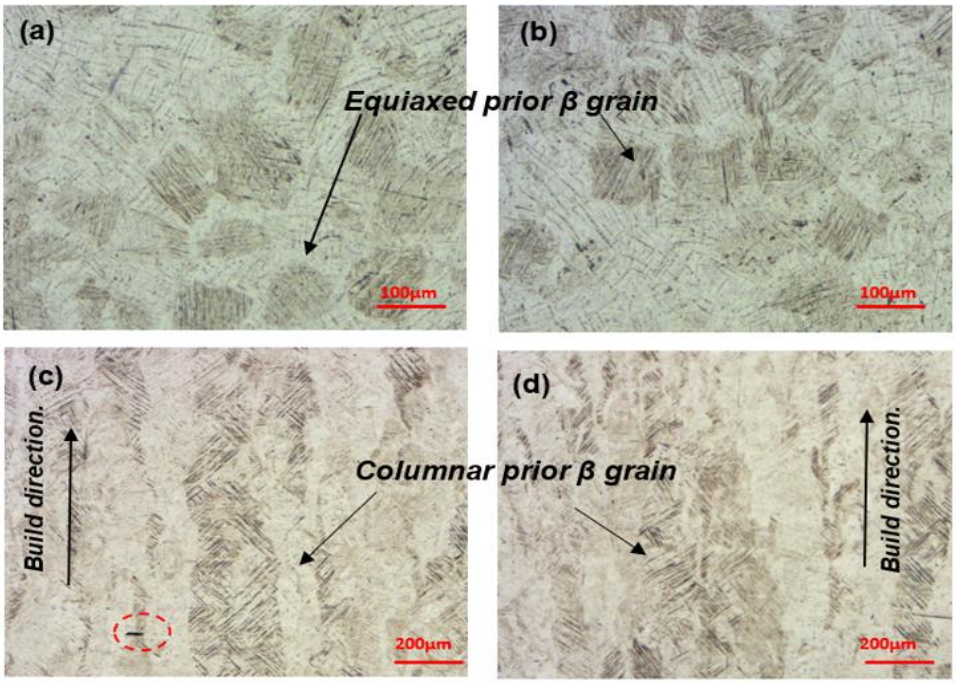

Figure 2-7. The microstructures of (a) and (c) the as-fabricated and (b) and (d) stress-relieved specimens for transverse and longitudinal sections with reference to the scan direction, respectively, observed in an optical microscope (Muiruri et al. 2019).

This stress-relieving heat treatment is commonly done at 650 ℃ and a residence time of 3 hours for DMLS Ti6Al4V(ELI) parts. The research work of Vilaro *et al*. (2011) showed that full relief of macro-process residual stresses could be achieved by soaking this material for 2 hours at a temperature of 730 ℃. However, this heat treatment temperature is sufficient to result in the partial decomposition of α' martensitic into stable α+β grains, as seen in Figure 2-8.

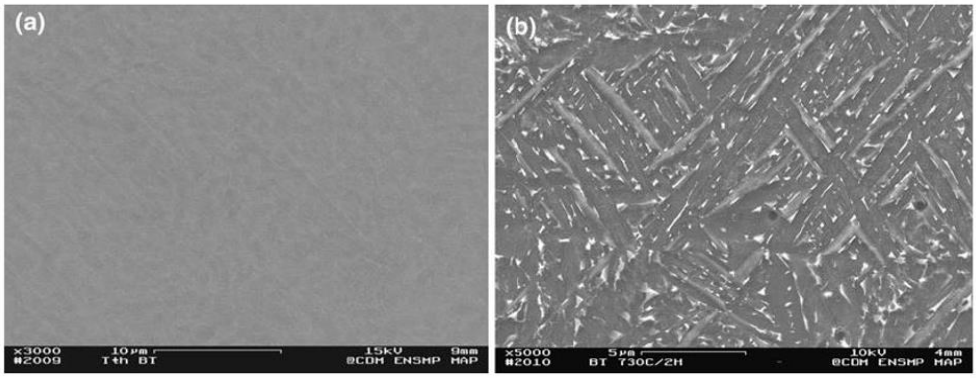

Figure 2-8. SE images (a) in BSE mode without etching and (b) in SE mode after etching, illustrating the partial decomposition of the α' martensite after annealing at 730 ℃ for 2 hours (Vilaro et al. 2011).

© Central University of Technology, Free State

The contrast of the α and β-phase seen as dark and bright regions in Figure 2-8(b) obtained through the secondary electron image mode (SEI), was confirmed by electron probe microanalysis, which highlighted the fact that the atoms of vanadium diffused favourably into the β-phase (Vilaro *et al.* 2011).

Complete decomposition of α' martensite of Ti6Al4V is only obtained for temperature treatments of 800 ℃ and above (Qianli *et al.* 2015, Markovitz *et al.* 2016), noting that complete decomposition is heat-treatment temperature and time dependent (Mur *et al.* 1996, Qianli *et al*. 2015). Mur *et al*. (1996) reported that complete decomposition of water-quenched α' martensite for wrought Ti6Al4V took place after 1 hour at 800 ℃. Complete decomposition of α' SLM martensite has been reported to take place after 4 hours at the same temperature (Qianli *et al*. 2015). High dislocations density and a high macro-process residual stress are created during SLM due to shrinkage of the molten pool and extremely rapid solidification. These defects act to impede the movement of phase boundaries and thus slow down the phase transformation process (Qianli *et al*. 2015). At a temperature of 800 ℃, α' martensite transforms to a mixture of equilibrium α and β phases. The α laths in the mixture have an average width that varies depending on the heat-treatment temperature and cooling rate (AC: air cooling or FC: furnace cooling), as seen in Figure 2-9 and Figure 2-10.

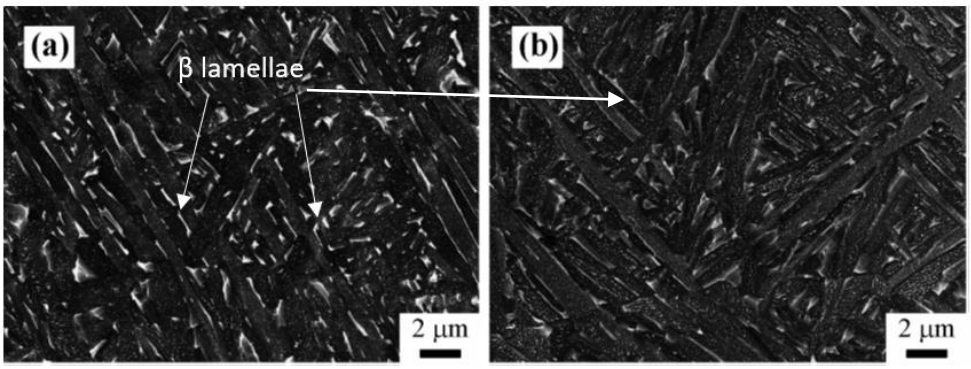

Figure 2-9. Scanning electron (SE) images of heat-treated SLM Ti6Al4V at 800 ℃ for 2 hours followed by (a) FC and (b) AC (Qianli et al. (2015).

With higher cooling rates (air cooling), the resulting microstructure consist of finer α laths. Qianli *et al.* (2015) reported the α laths having an average width of 0.7 μm for heat treatment at 800 ℃ for 2 hours followed by FC, seen in Figure 2-9(a), while at the higher

© Central University of Technology, Free State

heat-treatment temperature of 950 ℃, their widths were 2.4 µm, as shown in Figure 2-10(a).

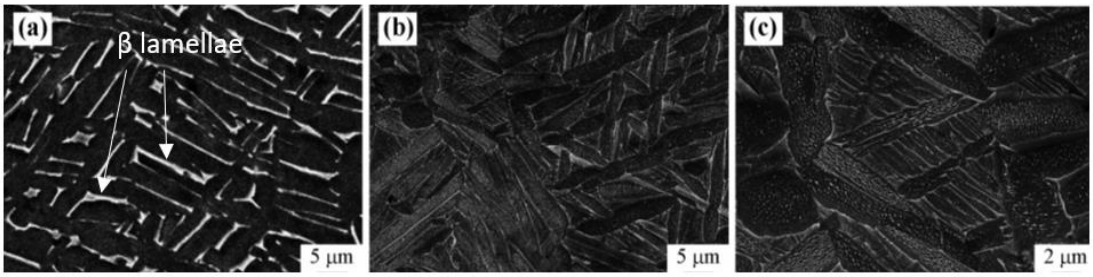

Figure 2-10. SE images of heat-treated SLM Ti6Al4V at 950 ℃ for 2 hours followed by (a) FC and (b) (c) AC (Qianli et al. *(2015).*

In the meantime, the shape of β-phase at 950 ℃ is more lamellae-like in comparison to the partial particle-like morphologies at 800 ℃ (see Figure 2-9(a) and Figure 2-10(a)). The β lamellae are uniformly distributed in the α matrix, largely along the grain boundaries of α-phase. Microhardness measurements for SLM Ti6Al4V samples heat-treated below the sub-transus region is characterised by a decrease of microhardness with the increase in heat-treatment temperatures from 650 ℃–850 ℃, followed by a sudden increase at 850 ℃ and a secondary decline at 900 ℃– 950 ℃ (Qianli et al. 2015, Markovitz *et al.* 2016). The trend is summarised in Figure 2-11.

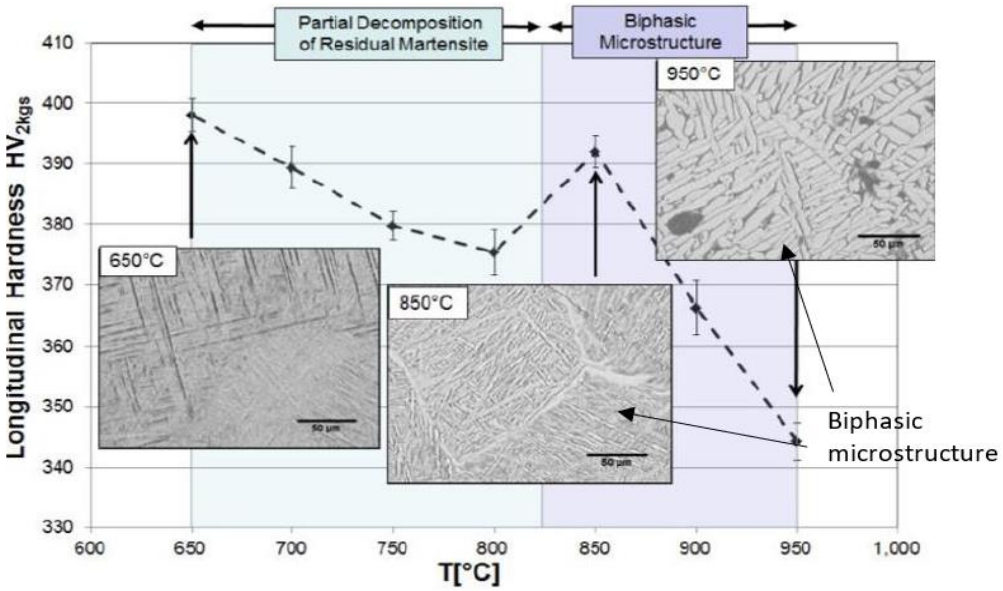

Figure 2-11. Microhardness measurements of sub-transus heat-treated SLM samples, with images of typical microstructures at different heat-treatment temperatures attached (Markovitz et al. 2016).

© Central University of Technology, Free State

The authors related the continuous drop in microhardness observed in the temperature range of 650 ℃–800 ℃ to the attendant, continuous coarsening microstructure and partial decomposition of the martensitic structure. They observed that the increase of microhardness obtained at 850 ℃ was due to decomposition of the martensite structure at this temperature and subsequent formation of a bi-phasic microstructure shown in the middle micrograph of Figure 2-11 (Markovitz *et al.* 2016). The resultant microstructure is composed of relatively fine α+β lamellar morphology within elongated needle-like α-grains. The subsequent decrease in microhardness is because of coarsening of the bi-phasic microstructure, as seen in micrograph labelled 950 ℃ of Figure 2-11.

It is worth noting here that sub-transus heat treatment does not lead to changes in the morphology of the prior-β grains. Rather, the α-phase arising from decomposition of α'-grains in the higher temperature range within this region prevents the movement of the grain boundaries and thus hindering the decomposition and coarsening of the columnar grains observed in Figure 2-7 (Vilaro *et al.* 2011). Figure 2-12 shows the microstructure resulting from heat treatment above the α→β transformation temperature.

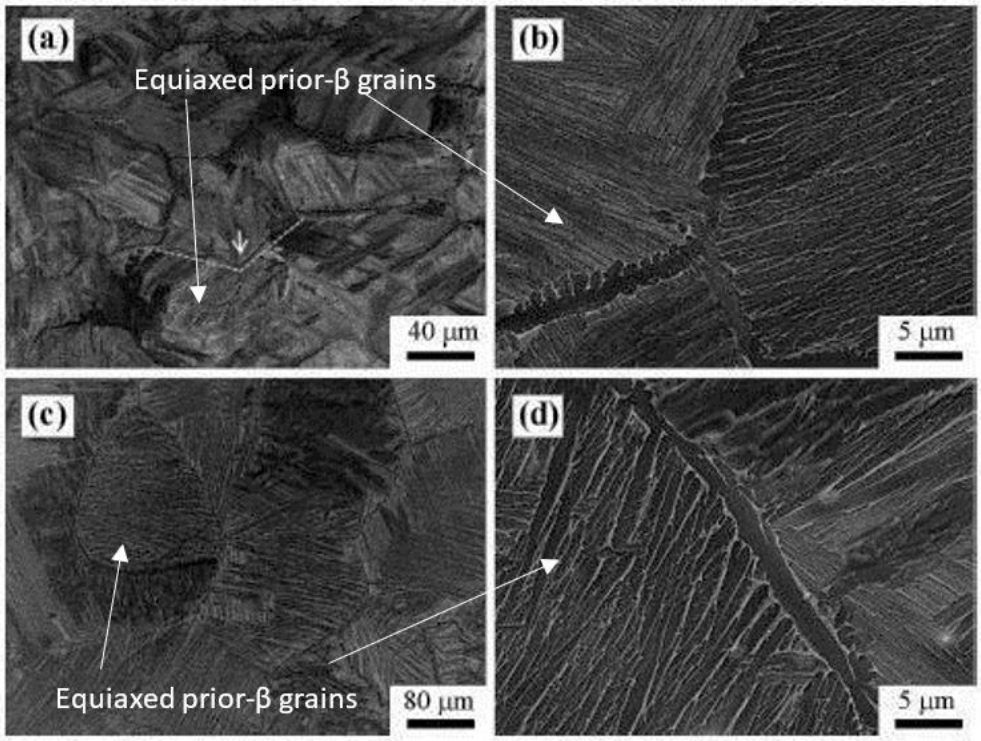

Figure 2-12. SE images of SLM Ti6Al4V heat-treated at 1050 ℃ (a) and (b) and 1200 ℃ (c) and (d) for 2 hours followed by air cooling (Qianli et al. 2015).

© Central University of Technology, Free State

Such heat treatment allows the columnar prior-β grain growth into equiaxed prior-β grains. From Figure 2-12(a), Qianli *et al*. (2015) observed that the diameter of the equiaxed prior-β grains (approximately 100 µm) arising from heat treatment at 1050 ℃ was close to the width of the columnar prior-β grains. Heat treatment at higher temperatures (1200 ℃) was found to further increase the size of the equiaxed prior-β grains, as shown in Figure 2-12(c & d). The combination of both super-transus and sub-transus heat treatments can be used to optimise the microstructure. This can be carried out on samples that are heat-treated in the super-transus region and then water quenched. Tempering then follows which can be varied from 700 ℃ to 950 ℃ for a fixed period of typically 2 hours. Typical microstructures from such heat treatment are shown in Figure 2-13.

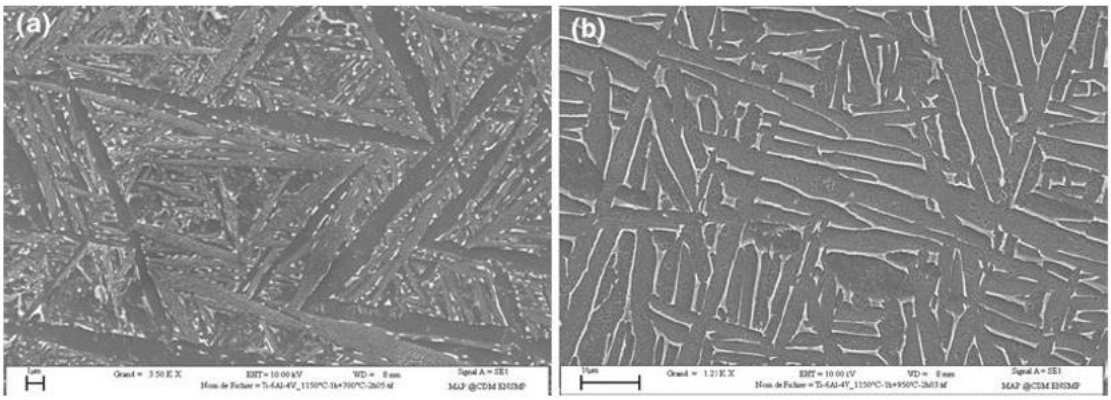

Figure 2-13. SE images of SLM Ti6Al4V, heat-treated at 1050 ℃ for 1 hour and WQ, followed by tempering at (a) 700 ℃ for 2 hours and (b) 950 ℃ for 2 hours, then furnace cooled (Vilaro et al. 2011).

A lamellar microstructure resulting from tempering and furnace cooling is seen in Figure 2-13(a) & (b). Thicker lamellae shown in Figure 2-12(b) arise from the higher tempering temperature.

2.4.2.2. Mechanical properties

A critical concern for AM techniques is whether parts produced this way will have better performance in comparison to those produced by conventional methods of manufacturing. The load-bearing capacity of most engineering materials is normally assessed from their tensile properties amongst other the mechanical properties. Table 2-2 provides a summary of the tensile properties of non-heat- treated, and heat-treated SLM/DMLS Ti6Al4V(ELI) parts compared to those for the alloy produced by traditional manufacturing methods.

© Central University of Technology, Free State

Table 2-2. Tensile properties of Ti6Al4V(ELI) parts built by SLM/DMLS as compared to traditional manufacturing processes

Process	Condition	Orientation	UTS (MPa)	YS (MPa)	El (%)	Ref
SLM	AB, not machined	LD	1040–1062	664–802	10.3±0.7	Kasperovich *et al.* 2015
	AB, not machined	HD	1035±29	910±9.9	3.3±0.79	Ramulu *et al.* 2014
	AB, machined	LD	1155±3	986±6	10.8±0.5	Koike *et al.* 2011
	AB, machined	LD	1166 ±25	962 ± 47	1.7± 0.3	Vilaro *et al.* 2011
	AB, machined	HD	1211±31	1100 ±12	6.5±0.6	Vilaro *et al.* 2011
	AB, machined	HD	1421±120	1273±53	3.2±0.5	Wysocki *et al.*2015
	AB, machined	LD	1265±5	1098±2	9.4±0.5	Moletsane *et al.* 2016
	SR, machined	LD	1170±6	1098±5	10.9±0.8	Moletsane *et al.* 2016
	SR, machined	LD	1052±11	937±9	9.6±0.9	Simonelli *et al.* 2014
	SR, machined	HD	1067±18	966±14	9.8±3.3	Simonelli *et al.* 2014
	HIP-900 °C/100MPa/2h followed by 700 °C/1h	-	973±1	885±	19.0±0.5	Kasperovich *et al.* 2015
	HT(730 °C/2h/AC) then machined	LD	1000±53	900±101	19±0.8	Vilaro *et al.* 2011
		HD	1046± 6	965±16	9.5±1	
	HT(950 °C/1h/WQ) then machined	LD	1040±4	925±14	7.5±14	Vilaro *et al.* 2011
		HD	1036±30	944±8	8.5±1	
	HT(1050 °C/1h/WQ then machined)	LD	951±55	836±64	7.9±2	Vilaro *et al.* 2011
		HD	1019±11	913±7	8.9±1	
	HT(800 °C/2h/AC)	-	1073±9	1010±11	17.1±1	Qianli *et al.* 2015
	HT(950 °C/2h/AC)	-	984±5	893±3	14.2±1.5	Qianli *et al.* 2015
	HT(1050 °C/1h/AC)	-	988±8	869±4	13.3±0.7	Qianli *et al.* 2015
	HT(1200 °C/1h/AC)	-	988±8	878±7	11.3±1.3	Qianli *et al.* 2015
	HT(1050 °C/1h/WQ, followed by 990 °C/0.5h/AC)	-	962±12	838±6	12±0.1	Qianli *et al.* 2015
	HT(850 °C/2h/FC)	-	1004±6	955±6	12.8±1.4	Vrancken *et al.* 2012
	HT(850 °C/5h/FC)	-	965±20	909±24	Premature failure	Vrancken *et al.* 2012
	HT(1015 °C/0.5h/AC, followed by 843 °C/2h/FC	-	874±23	801±20	13.5±1	Vrancken *et al.* 2012
	HT(1020 °C/2h/FC)	-	840±27	760±19	14.1±3	Vrancken *et al.* 2012
	HT(705 °C/3h/FC)	-	1082±34	1026±35	9.1±2	Vrancken *et al.* 2012
	HT(940 °C/1h/AC, followed by 650 °C/2h/AC)	-	948±27	899±27	13.6±0.3	Vrancken *et al.* 2012
	HT(1015 °C/0.5h/AC, followed by 730 °C/2h/AC)	-	902±19	822±25	12.7±0.6	Vrancken *et al.* 2012
Wrought	-	LD	942±8	836±9	12.5±1.2	Wysocki *et al.* 2017
	-	HD	933±7	832±10	13.0±1.5	Wysocki *et al.* 2017
Forged	Mill annealed	-	1006±10	960±10	18.37±0.9	Vrancken *et al.* 2012
As Cast	-	-	980	865	13.5	Vrancken *et al.* 2012

**AB: as-built, SR: stress-relieved, HT: heat-treated, AC: air-cooled, FC: furnace-cooled.*

It important to note here that the longitudinal direction (LD) and horizontal direction (HD) indicate the respective loading directions parallel and perpendicular to the build direction for the SLM process and rolling direction for the wrought (indicated by the arrows), shown in Figure 2-14.

© Central University of Technology, Free State

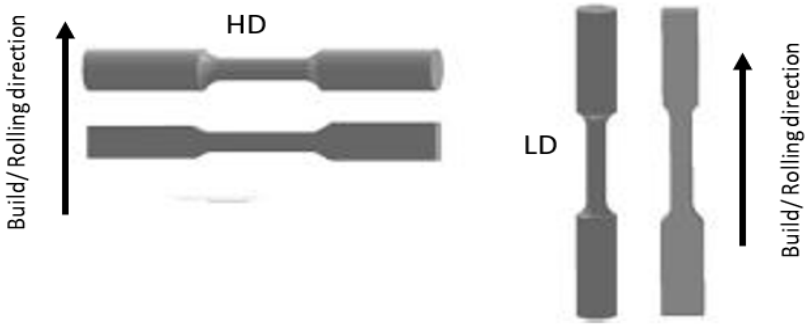

Figure 2-14. Schematic diagram illustrating of the geometry and the build orientation of tensile test samples (Shunyu and Yung 2019).

The yield and the ultimate tensile strength of the machined samples are higher than those of non-machined samples, as seen in Table 2-2. This is not surprising considering that the rough surfaces and micro-notches of the unmachined samples on the surfaces act as sites for the initiation of cracks (Muiruri *et al*. 2019). Non-heat-treated SLM/DMLS parts poses values of tensile strength well above those obtained from the wrought, as-cast and forged Ti6Al4V. This is attributed to an extremely fine martensitic α' microstructure caused by the very high cooling rates of the alloy from the β domain. As shown in Table 2-2, ductility shows the opposite trend in all cases, as the fracture of the AM alloy occurred well below the elongation to failure of the traditionally produced alloy.

Different heat-treatment strategies change the microstructure and therefore the properties of as-built parts differently. Stress-relieving heat treatment only, like the one commonly used for DMLS Ti6Al4V (650 ℃ for 3 hours followed by FC), will hardly transform the α' martensite (Muiruri *et al.* 2019) or coarsen its microstructure and therefore only slightly lower the tensile strength and slightly increase the ductility. Conversely, the high temperature annealing, will transform and grow the microstructure, leading to great improvements in elongation to failure even though at the expense of strength, as seen in Table 2-2. Use of HIPing process reduces porosity by densifying the microstructure of the alloy, and therefore, leads to an improvement of elongation to failure. However, despite a clear improvement in mechanical properties of HIPed Ti6Al4V, Kasperovich *et al.* (2015) found some minor defects appearing within the fracture surfaces of the alloy, which were suggested to act as origins of fracture.

© Central University of Technology, Free State

From the data presented in Table 2-2, it is evident that the mechanical properties of Ti6Al4V depend on the production and heat-treatment process adopted for the alloy. Heat treatment is known to affect the microstructural features of metals and metal alloys of, phase fractions, grain morphology, the presence of defects and the texture of prior-β grains (Vilaro *et al.* 2011, Kasperovich *et al.* 2015, Yang *et al.* 2017). Different cooling rates from the super-transus region lead to the formation of different microstructures, as shown in Figure 2-15. Galaraga *et al.* (2016) heat-treated EBM Ti6Al4V(ELI) at 1100 ℃ for 30 minutes followed by the three different cooling rates shown in Figure 2-15, all applied to different samples of the alloy. The analysis of the specimens revealed different microstructures and properties of the heat-treated samples due to the different cooling rates as compared to the as-built condition. The values of YS, UTS and % elongation (El) obtained for the different microstructures are illustrated in Figure 2-16.

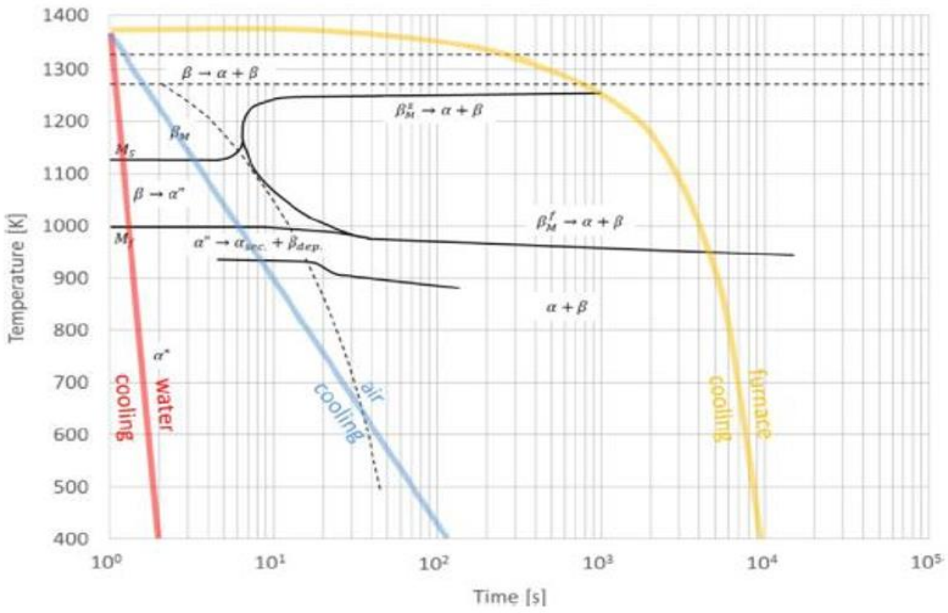

Figure 2-15. Continuous cooling transformation diagram for Ti6Al4V with three different cooling rates (Mur et al. 1996).

In Figure 2-16, columnar/lamellar α+β corresponds to the as-built condition, equiaxed α+β corresponds to FC, partially α' corresponds to AC and fully α' corresponds to WQ. The α' martensite has the highest value of strength among all the microstructures analysed in this work. The strength of lamellar/columnar α+β microstructure is higher in comparison to that of equiaxed α+β. Nevertheless, their ductility and strength exhibit opposite trends.

© Central University of Technology, Free State

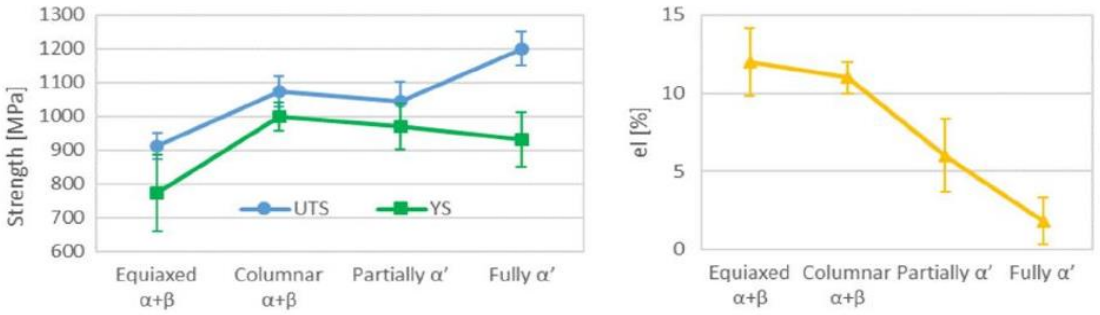

Figure 2-16. Values of YS, UTS and % El for microstructures obtained by applying different cooling rates (Galaraga et al. 2016).

As seen in Table 2-2, SLM Ti6Al4V parts show significant anisotropy of tensile properties in different orientations with respect to the build direction. The research work of Shunyu and Yung (2019) associated the difference in mechanical properties in the longitudinal (LD) and horizontal (HD) built orientations to the anisotropic microstructure: the elongated columnar β-grains seen in Figure 2-17 and the presence of grain boundary α grains.

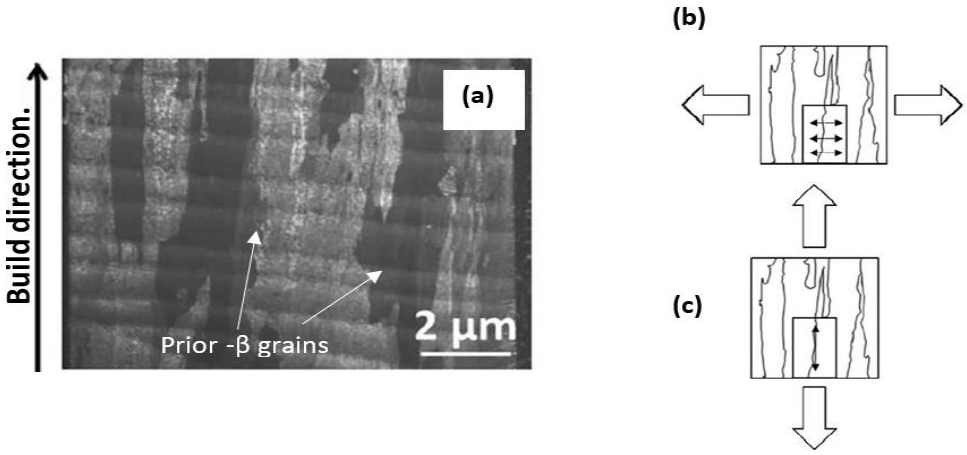

Figure 2-17. (a) Optical image of AM-produced Ti6Al4V component with prior-β grains oriented along the build direction, and schematic illustration of the same subjected to tension load applied along (b) horizontal direction (c) longitudinal direction (Caroll et al. 2015).

Along the build direction and between these columnar grains, a thin layer of grain boundary α grains normally forms upon heat treatment, delineating the prior-β grains. The presence of these grain boundary α-phase grains breaks the continuity of microstructure and acts like a weak band connector, through which failure can favourably initiate (Simonelli *et al 2014*, Shunyu and Yung 2019). Tensile loads acting orthogonal to the grain boundary act to separate adjacent prior-β grains. Thus, the morphology of the prior-β

© Central University of Technology, Free State

grains in the AM components leads in grain boundary α-grains being exposed to a tensile opening mode depending on whether tension is applied along the longitudinal or horizontal direction (Caroll *et al.* 2015, Shunyu and Yung 2019).

As shown in Figure 2-17(b), a specimen upon which a tensile load is applied in the horizontal direction subjects the entire length of the grain boundary α-grains/prior-β grains to Mode I (opening). Contrary, in Figure 2-17(c), when a tensile load is applied in the longitudinal direction, the prior-β grains with α-grain boundaries are not subjected to Mode I (opening). Thus, the anisotropic microstructure predisposes the horizontal specimens to Mode I, opening failure along the prior-β grain boundaries, but not the longitudinal specimens. Consequently, the longitudinal specimens will tend to have higher values of elongation to failure and strength. Nonetheless, when the lack-of-fusion pores dominate in the specimen the condition might reverse, or not be as prominent. In their work, Malefane *et al.* (2018) found that the fatigue properties of as-built DMLS Ti6Al4V parts did not exhibit any anisotropy. Elsewhere, Moletsane *et al.* (2016) had found that the tensile properties of DMLS Ti6Al4V samples were independent of the build orientation.

2.5 DISLOCATIONS AND PLASTIC DEFORMATION IN TI6AL4V

Figure 2-18 is a schematic illustration of atoms in a perfect crystal. In this figure, plastic deformation occurs when the shear stress τ moves a whole layer of atoms from one equilibrium position to another.

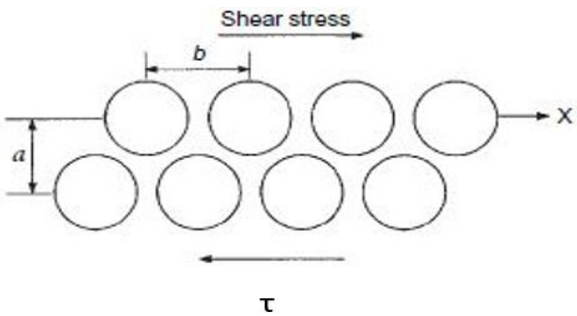

Figure 2-18. Illustration of the positions of atoms in a perfect crystal used to estimate theoretical critical shear stress (Hull and Bacon 2001).

In such a circumstance, the periodic shear stress would be given by the sinusoidal relation (Hull and Bacon 2001):

© Central University of Technology, Free State

$$\tau = \frac{\mu b}{2\pi a} sin \frac{2\pi x}{b} \qquad 2\text{-}2$$

where μ, τ, x, a and b are shear modulus, applied shear stress, shear translation of the two rows, spacing of the rows of atoms, spacing of between atoms in the direction of action of the shear stress, respectively. It has been shown experimentally that the yield stress is two to three orders of magnitude smaller than the theoretical value predicted by this equation (Hull and Bacon 2001). This is because plastic flow is expedited by the presence of dislocations and imperfections in the crystal structure. The propagation of dislocations requires less energy than breaking of atomic bonds along a plane of atoms (Hirth 2011).

2.5.1 Dislocations – linear defects

Dislocations are linear or one-dimensional defects in a crystal around which some of the atoms are misaligned. There are three types of dislocations in materials, namely the screw dislocation, the edge dislocation and the mixed dislocation (Dieter 1986, Hirth 2011).

(i) ***Screw dislocations*****:** These are imperfections whereby two parts of a plane in an atomic lattice structure move in opposite directions, thus causing movements of a dislocation in a perpendicular to the direction of the applied force, as shown in Figure 2-19(a).

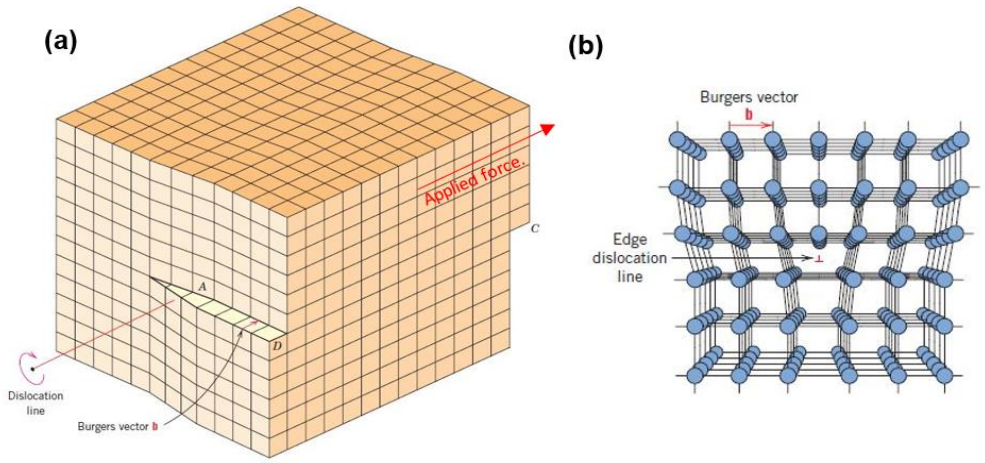

Figure 2-19. Screw dislocation and (b) edge dislocation (Callister 2007, p.89)

(ii) ***Edge dislocations:*** These are crystalline imperfections/linear defects in which an extra portion or a half plane of atoms have an edge which terminates within the crystal, as shown in Figure 2-19(b). This edge is sometimes referred to as a dislocation line. Around the dislocation line there is some localised lattice

© Central University of Technology, Free State

distortion. The atoms above the distortion line are squeezed together and those below are pulled apart, as seen in Figure 2-19(b).

(iii) ***Mixed dislocations:*** Large portion of dislocations in metals and their alloys exhibit parts of both screw and edge dislocations (Dieter 1989, Lütjering and William 2007). A mixed dislocation is presented schematically in Figure 2-20(a). The distortion of lattice normally produced away from the two faces is mixed, having different levels of edge and screw character.

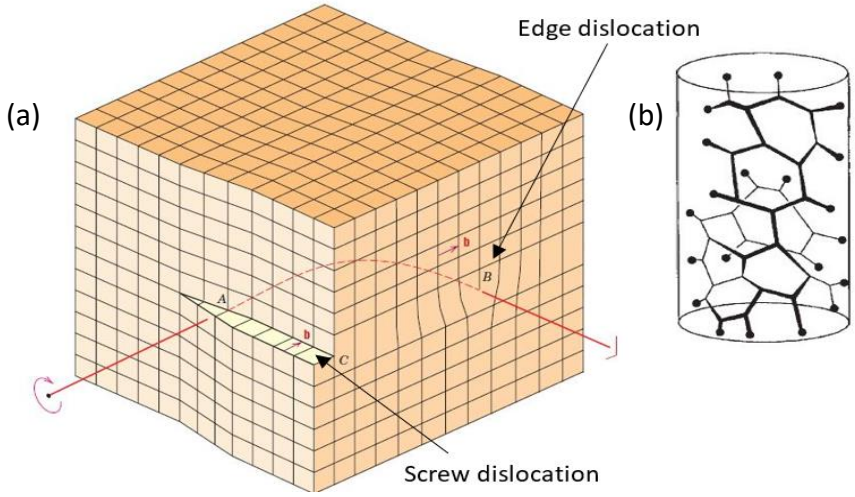

Figure 2-20. (a) Schematic diagram of a mixed dislocation that has the character of both edge and screw dislocations (Callister 2007, p.89), and (b) diagrammatic illustration of dislocations in a well-annealed crystal (Hull and Bacon 2001).

The magnitude and direction of the lattice distortion associated with a dislocation is expressed in terms of a Burgers vector denoted as $\boldsymbol{b}$ in Figure 2-19 and 2-20(a). Furthermore, the nature of a dislocation is defined by the relative orientations of the dislocation line and the Burgers vector. Thus, the following two important rules (Callister 2007):

a) The line of the edge dislocation is perpendicular to the Burgers vector.
b) The line of the screw dislocation is parallel to the Burgers vector.

Dislocations with the same line senses but opposite Burger vectors (or alternatively with opposite line senses and the same Burgers vector) are physical opposites in that if one is a positive edge, the other is a negative edge and if one is a right-handed screw, the other is left-handed. Dislocations which are physical opposites of each other annihilate and restore the perfect crystal if brought together (Hull and Bacon 2001).

© Central University of Technology, Free State

The dislocation density **ρ** is defined as the total length of dislocation lines per unit volume of a crystal and is usually quoted in units of cm^{-2} or m^{-2}. Dislocations occur in all crystals except for some nanowires (Lütjering and Williams 2007), and are usually arranged in an irregular network, commonly referred to as the *Frank net*, as illustrated in the schematic diagram in Figure 2-20(b). In annealing heat-treated crystalline material, the parameter **ρ** lies mainly within the range of 10^{10} - 10^{12} m^{-2} but quickly rises to about 10^{15} - 10^{16} m^{-2} with increased plastic strain (Hull and Bacon 2001).

Apart from these line defects, interfacial defects are also observed in crystalline materials. They are boundaries that have two dimensions and normally separate regions of the material that have different crystal structures and/or crystallographic orientations (Callister 2007, p.92). Such imperfections include grain, twist, tilt, twin and phase boundaries. Within these boundary regions, there is some atomic mismatch in a transition from the crystalline orientation of one grain to that of an adjacent one. Various degrees of crystallographic misalignment between adjacent grains are possible: thus, they are classified according to misorientation as low-angle grain boundaries (LAGBs) and high-angle grain boundaries (HAGBs) (Dieter 1987, Hull and Bacon 2001, Callister 2007, p.92). Low-angle grain boundaries occur where the angle of misorientation is lower than 15° (Dieter 1987) and include tilt and twist boundaries. Tilt boundaries are normally formed if edge dislocations are arranged in the manner shown in Figure 2-21(a) at a mismatch of less than approximately 15°.

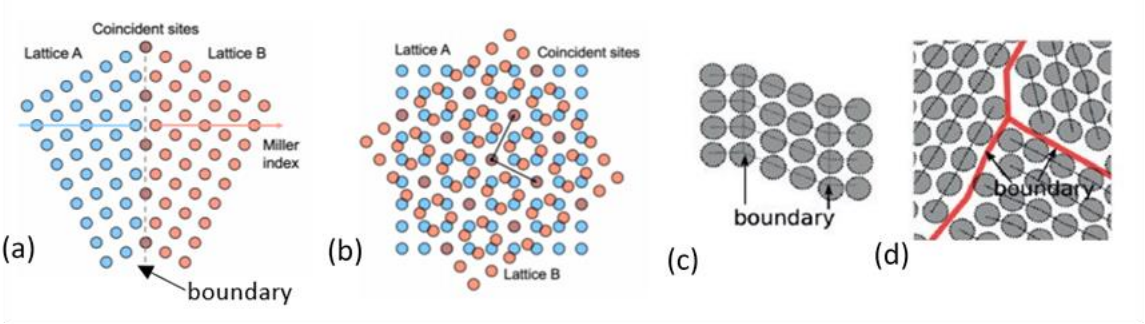

Figure 2-21. (a) Tilt boundary, (b) twist boundary (c) twin boundary and (d) grain boundary (Callister 2007).

A twist boundary is formed when the angle of misorientation is parallel to the boundary, which can be described in an array of screw dislocations and is shown in Figure 2-21(b). Twinning is a mechanical deformation mechanism that occurs when a certain section of

© Central University of Technology, Free State

lattice after shear, transforms itself into an orientation with mirror symmetry with reference to the parent lattice, as shown in Figure 2-21(c). High-angle grain boundaries occur when the angle of misorientation between two phases or lattice that share an interface is greater than approximately 15°, and such misorientation produces a phase or a high angle grain boundary. Coincident site lattices (CSLs) are another type of grain boundary formed whereby several lattices share the same lattice site. These kinds of boundaries have preferential misorientation angles and axes, such that adjacent crystallites are arranged in specific coincidence site lattices.

There are other common defects in materials such as vacancies and impurity atoms which are classified as point defects and stacking faults which are called planar defects. A vacancy is created when an atom in a crystal structure moves from a lattice position to an interstitial position or to a vacant lattice position. Impurity atoms can take up position in a crystal structure when an atom of the parent lattice is replaced by an atom of a different element. A stacking fault, on the other hand, occurs in a local region in a crystal structure, where the regular stacking sequence is interrupted (Hull and Bacon 2001). Point defects and stacking faults produce local distortions in otherwise perfect crystals (Dieter 1987).

The existence of dislocations in a material suggests that any crystal that contains a dislocation is not in its lowest energy state. The extra energy is referred to as strain energy (Dieter 1986). The total strain energy stored per unit length of dislocation, also referred to as the line energy of the dislocation, is given by the sum of the energy contained in the elastic field and the energy in the core of the dislocation. The energy stored in the core of the dislocation results from the distortion of lattice bonds (Dieter 1989, Callister 2007), while the elastic energy is due to the elastically strained bonds outside the radius of the dislocation core. The energy of line of dislocations (U) is approximately equal to (Hull and Bacon 2001):

$$U \approx \mu . b^2 \qquad 2\text{-}3$$

where μ is the material's shear modulus and b is the Burgers vector. Dislocations always tend to have the smallest possible Burgers vector and large dislocations are liable to dissociate to other smaller Burger vectors dislocations to reduce or conserve strain energy (Hull and Bacon 2001, Callister 2007).

© Central University of Technology, Free State

Macroscopic plastic flow occurs due to slip of many dislocations at a microscopic level. The applied stress required to overcome resistance of the lattice to movement of a dislocation, with no other obstacles present, is referred to as the Peierls-Nabarro stress (Peierls 1940), which is often described as the fundamental critical resolved shear stress (CRSS) at 0 K of a lattice (Hirth 2011).

2.5.2 Slip systems in Ti6Al4V

The α-phase is the dominant phase in the Ti6Al4V alloy; therefore, slip in the α-phase plays a critical role in the plastic flow of this alloy (Lütjering and Williams 2007). This literature survey thus focuses on the α-phase. Generally, slip can occur on the basal, prismatic and pyramidal planes by the movement of $< a >$, $< c >$ and $< c + a >$-type dislocations, respectively. The predominate slip planes and slip directions for α-titanium are shown in Table 2-3 and indicated in the hexagonal unit cell shown in Figure 2-22.

Table 2-3. Slip systems in the α-phase crystal of Ti6Al4V (Lütjering and Williams 2007)

Slip system type	Burgers vector type	Slip direction	Slip plane	No. of slip systems	
				Total	Independent
1	a	$\langle 11\bar{2}0 \rangle$	(0001)	3	2
2	a	$\langle 11\bar{2}0 \rangle$	$\{10\bar{1}0\}$	3	2
3	a	$\langle 11\bar{2}0 \rangle$	$\{10\bar{1}1\}$	6	4
4	c+a	$\langle 11\bar{2}3 \rangle$	$\{10\bar{1}1\}$	6	5

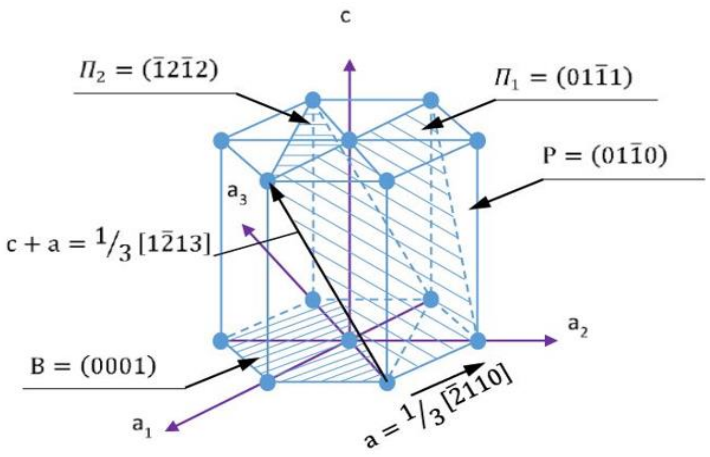

Figure 2-22. Slip systems in the α-phase crystal, basal (B), prismatic (P) and first-order pyramidal (Π1) planes containing < a > dislocations; and second-order (Π2) pyramidal slip planes containing < c + a > dislocation (Lütjering 1998).

© Central University of Technology, Free State

The $< a >$-type dislocations with a Burgers vector of $\frac{1}{3}\langle 11\bar{2}0\rangle$ are dominant in the three planes. The $< c + a >$-type dislocations with a Burgers vector of $\frac{1}{3}\langle 1\bar{2}13\rangle$, can slip on prismatic and first-order pyramidal planes. The type $< c >$ dislocations are restricted to prismatic planes only and do not glide (Dragomir and Ungar 2002). It is important to note that ideally the c/a ratio of the hcp lattice structure is 1.633. However, that of α-titanium with lattice parameters a = 0.295 nm and c = 0.468 nm is 1.587 (Hull and Bacon 2001). The reduced c/a ratio in α-titanium leads to a larger spacing between prismatic planes. This increases the packing density of the prismatic planes relative to the basal planes, thus favouring slip on prismatic planes rather than the basal planes (Leyen and Manfred 2003).

The low symmetry of the hexagonal closed-packed (hcp) structure leads to variation in the values of the CRSS for various slip systems. The CRSS is the resolved shear stress in the slip direction on the slip plane necessary to initiate slip. It is dependent on temperature as the motion of dislocation is a stress-assisted thermally activated phenomenon (Lütjering 1998). The CRSS also affects the probability of the activation of a particular slip system. Generally, the CRSS of < a >-type of dislocations is much lower than that of < c + a >-type of dislocations (Hull and Bacon 2001). Activation of prismatic and basal < a >-types of dislocations is easier due to low values of the CRSS. Large Burgers vector of < c + a >-type of dislocation on pyramidal planes results in high values of the CRSS on these planes (Singh *et al*. 2012). Therefore, the portion of grains deforming by < c + a > dislocations is very low in titanium alloys (Dragomir and Ungar 2002). The < c + a > dislocations are mostly activated when the dislocation mobility for < a > is minimal, the sample is exposed to a loading orientation that is almost parallel to the c-axis or is deformed at high strain rates and/or low temperatures (Mayeur and McDowell 2007). The estimated values of CRSS for the four slip systems of the hcp titanium seen in Table 2-3 and Figure 2-22 are presented in Table 2-4.

Table 2-4. Critical resolved shear stress (CRSS) for different slip systems of α-titanium (Mayeurs and McDowell 2007)

Slip system type	Slip plane	CRSS (MPa)
1	Basal	340
2	Prism	340
3	Pyramidal (П1)	640
4	Pyramidal (П2)	1035

© Central University of Technology, Free State

2.5.3 The α/β slip transfer and the role in plastic deformation of the Ti6Al4V

As discussed in section *2.3.2.1*, the α/β interfaces observed at room temperature are formed after β (bcc) → α (hcp) phase transformation. Taking the α/β lamellar microstructure as an example, the β-phase fills the gaps between α lamellae, as shown in Figure 2-23(a).

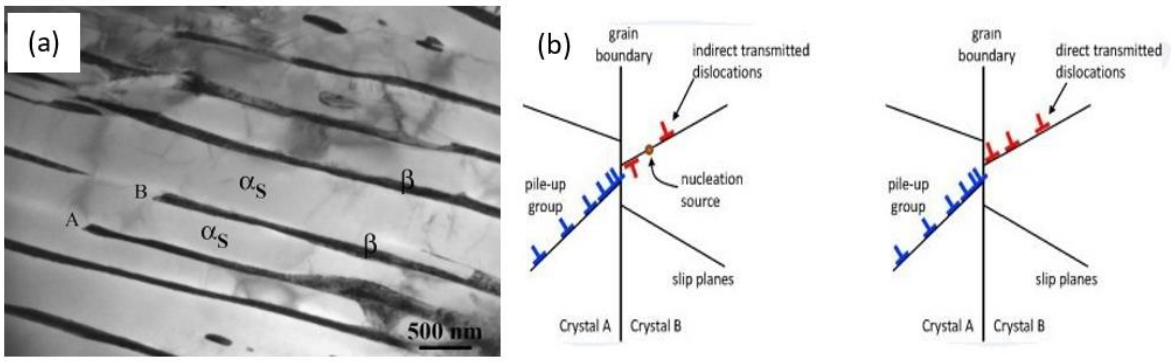

Figure 2-23. (a) A transmission electron microscope image of Ti6Al4V with detailed view of a lamellar colony consisting of α_s and β plates and (b) schematic drawing of direct and indirect transmission of dislocations through grain boundaries (Kacher et al. 2014).

The slip activation criteria across the α/β interface have been found to differ at the macro-scale and at the local interfaces (Lütjering and Williams 2007). At a macro-scale, activation of the slip system in a specimen is mostly determined by the Schmid factor, (Kacher *et al.* 2014), a factor based on iso-stress that satisfies equilibrium, or the Taylor factor, a factor based on iso-strain that satisfies compatibility and therefore is a reciprocal of the Schmid factor (Dieter 1987). Nonetheless, at a local interface, there are other factors that may influence the activation and transference of slip (Zhang *et al.* 2016). During plastic deformation, interfaces (grain and phase boundaries) usually act as barriers to the motion of dislocations and hence cause dislocations to pile up and give rise to stress concentrations. These interfaces enhance the strength of materials by preventing the extension of slip across the material. However, the movement of dislocations does also occur through grains and phase boundaries due to direct or indirect transmission, as illustrated in Figure 2-23(b). Indirect transmission mainly results from the nucleation at a *Frank-Read* source located in an area of stress concentration (Zhang *et al.* 2016). On the other hand, if the stress acting on the leading dislocation of a pile-up is high enough, the

© Central University of Technology, Free State

leading dislocation might be able to directly transfer to a new slip plane. The new slip plane should have low misorientation angles with respect to the originating plane for this slip transference (Kacher *et al*. 2014). The direct transfer of dislocations comprises of the two steps of re-nucleation and emission of dislocations, as shown in Figure 2-24. The figure shows an incoming dislocation with a Burgers vector $\boldsymbol{b_1}$ driven by external stress and moving into a phase interface or boundary.

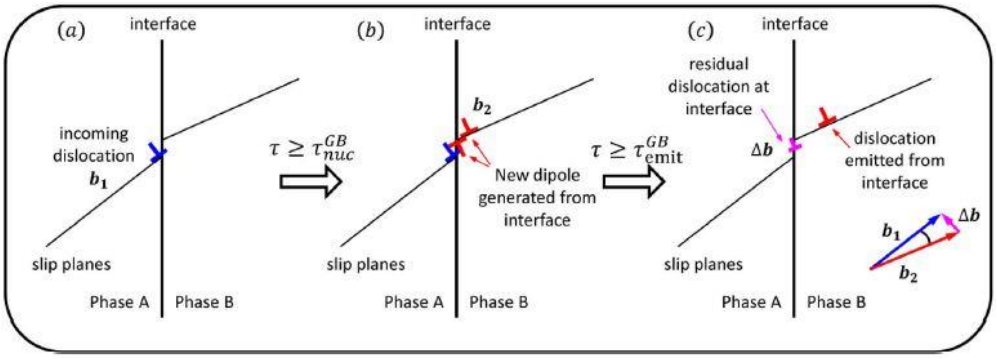

Figure 2-24. Schematic diagram illustrating the two stages in direct dislocation transmission through a phase interface or grain boundary (Zheng et al. 2018).

The discontinuity caused by the dislocation acts as a dislocation source located at the interface, and if the local stress is high enough, a new dislocation with a Burgers vector $\boldsymbol{b_2}$ may be generated. The external force can drive the new dislocation emitted from the interface and cause it to glide along the new slip plane (Zheng *et al.* 2018). Because of the inherent variation of the incoming and outgoing dislocation Burgers vectors, a residual dislocation $\Delta \boldsymbol{b}$ is formed and left at the boundary until it can cause dislocation re-emission (Li *et al*. 2009). Thus, the overall Burgers vector is conserved during the full process, as shown in Figure 2-21(c).

2.6 MICROSTRUCTURE CHARACTERISATION OF TI6AL4V

The attractive mechanical properties of Ti6Al4V of good toughness and high specific strength, are mostly determined by microstructural aspects such as dislocation density, texture, dislocation system activity and the individual α/β phase fractions. Therefore, to be able to predict the mechanical performance of the alloy and to design material with certain mechanical properties, such as optimal strength and ductility, a fundamental understanding of the flow process in terms of microstructural parameters of the alloy is crucial (Picu and Majorell 2002).

© Central University of Technology, Free State

The microstructural details of metals and metal alloys can be obtained by direct methods such as scanning electron microscopy (SEM), electron backscatter diffraction (EBSD), transmission electron microscopy (TEM) or indirect methods such as X-ray diffraction (XRD) or neutron diffraction (Dragomir *et al.* 2005). The techniques of TEM, XRD and neutron diffraction are appropriate for studying the evolution and distribution of dislocations in a material. Transmission electron microscopy reveals microstructural details in a very small area of a sample, which raises questions of how representative the TEM microstructure information is to the microstructure of the bulk specimen. Under such situations, XRD or neutron diffraction are the most effective techniques to study the microstructures since they give detail on the bulk material in a statistically averaged manner. The two techniques can be used to study the microstructure of two-phase materials, such as the α/β-phases in Ti6Al4V, as the peaks corresponding to constituent phases appear distinctly (Kniess *et al.* 2015).

Electron backscattered diffraction is a SEM-based technique which enables sample microstructures to be analysed, visualised and quantified (Oxford Instruments 2019). It is an appropriate technique for the visualization of grain sizes and grain subgrains, phase distribution, as well as local texture and misorientation of crystals (Zaefferer *et al.* 2007). This study's focus is on the bulk properties of microstructure; therefore, it uses the XRD and EBSD techniques as the primary tools for microstructural characterisation of non-heat-treated- and heat-treated DMLS Ti6Al4V(ELI) alloy.

2.6.1 Electron backscatter diffraction (EBSD)

The EBSD technique is based on acquiring and analysing the diffraction patterns of a flat surface of a sample. The EBSD analysis is executed on highly tilted crystalline samples, basically at an angle of 70° relative to normal incidence of the electron beam (Oxford Instruments 2019), as shown in Figure 2-25.

© Central University of Technology, Free State

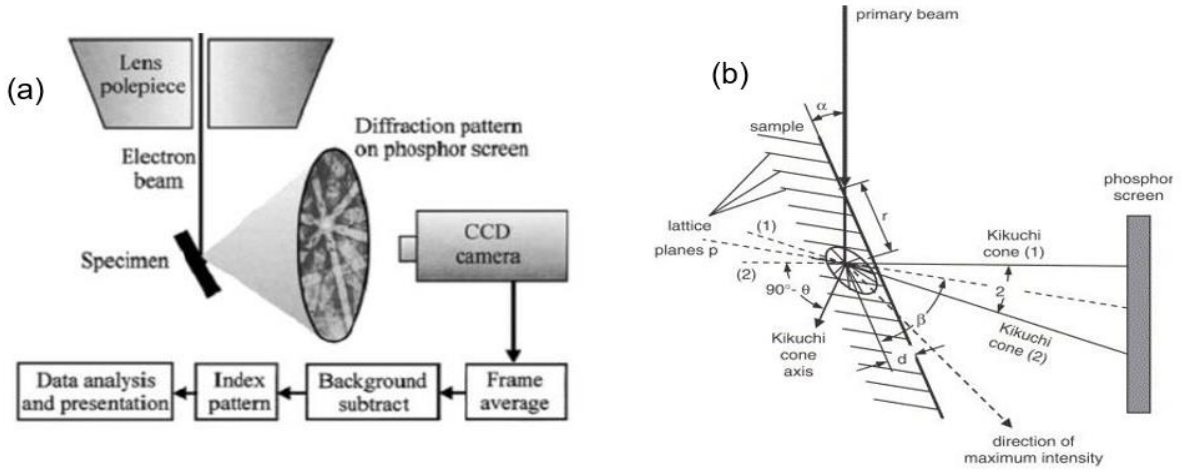

Figure 2-25. (a) The experimental set up for EBSD and (b) schematic diagram illustrating the formation of backscatter Kikuchi lines (Zaefferer et al. 2007).

The specimen is illuminated with a stationary focused primary electron beam. The back-scattered electrons are captured on a phosphor screen, positioned close to the sample and are then recorded by a highly light-sensitive camera. The camera images are then taken to a computer where the crystallographic phases and orientation (Zaefferer *et al.*2007) of the irradiated crystal are automatically determined by an *hkl*-EBSD system operating Channel 5 software (Oxford Instruments 2019). As seen in Figure 2-25(b), the primary beam gets into the specimen at an angle α. Then moves a distance $t_1 = {}^{r}/_{cos\,\alpha}$ in the sample to a maximum depth d from the surface. The symbol r in the figure shows the estimated spatial resolution of the method. The primary electrons are incoherently scattered with a distribution intensity indicated by the ellipse shown in the figure. The incoherently scattered electrons are subsequently coherently scattered by the lattice planes p into pairs of Kikuchi cones (1) and (2) with an opening angle $2(90° - \theta)$ (where θ is the Bragg angle) around the respective axes of the two Kikuchi cones. The cones leave the surface at an angle β. The path length which the electrons undergo for coherent scattering is $t_2 = {}^{d}/_{sin\beta}$ (Oxford Instruments 2019, Zaefferer *et al.* 2007).

A full random orientation of grains in most polycrystalline materials does not occur and the materials are thus said to have preferred texture or crystallographic orientations. The measurements of orientation collected by EBSD can be used to show the crystallographic texture of the sample. The details of orientation acquired from multiple points within a

© Central University of Technology, Free State

given phase enables a statistical check as to whether that phase has a preferred orientation. For interpretation of texture/orientation from EBSD data the following definitions are used:

a) ***Band contrast/EBSD pattern:*** These are greyscale images that give a measure of the quality of patterns for all the points in an EBSD map. A lighter shade of grey indicates a higher value of band contrast, and hence a better EBSP (electron back-scattering pattern) quality. The EBSD patterns form when the incident electrons of the electron beam collide and backscatter elastically from the atomic planes of the crystal grain that satisfy the Bragg's law (to be discussed in section 2.5.2) (Callister 2007). Any point in an EBSD map has a value of band contrast even if it has not been indexed. The band contrast is affected by numerous factors such as surface contamination, local crystalline imperfection, the phase and orientation as well as grain boundary (Oxford Instruments 2019). The band contrast shows features such as grain boundaries, grains and surface scratches where poor indexing occurs.

b) **Discrete/contour pole figures (PFs) and inverse pole figures (IPF) colouring:** Discrete pole figures are normally stereographic projections of the crystallographic directions present in the grains that constitute the material. Normally, the plot is built considering the projection of a specific crystal plane onto a unit sphere based on the sample coordinate system shown in Figure 2-26(a). The projected points are then connected to the southern hemisphere (opposite hemisphere pole) of the unit sphere. The intersections with the equatorial plane (circled in red hatched lines in this figure) thus consist of distinct unifocal points for a given crystallographic orientation shown in Figure 2-26(b). Contour pole figures are made in the same manner; however, they carry details relative to the whole set of grains in the data set and not to individual ones. Therefore, in this case the pole figures manifest regions of same pole density whose levels are defined by an equivalent colour legend scheme. Contour pole figures display a more quantitative analysis of the distribution of orientations in a material and are thus important to analyse the texture of metals and their alloys.

© Central University of Technology, Free State

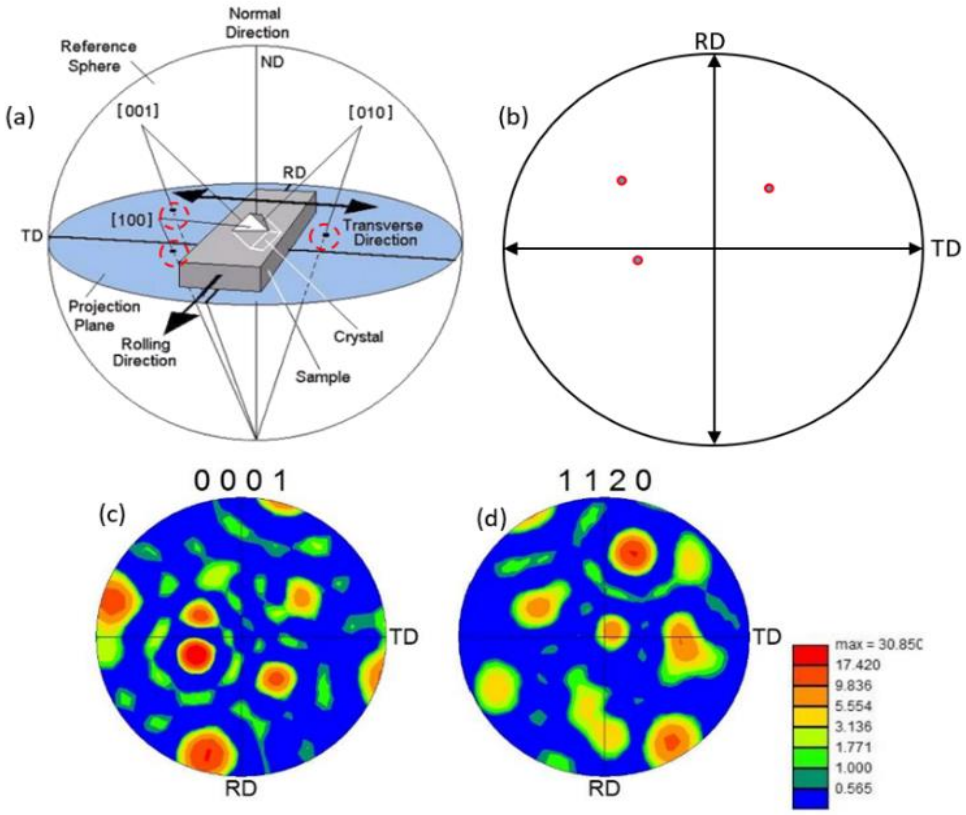

Figure 2-26. (a) Representation of a stereographic projection of crystallographic directions, (b) description of corresponding discrete pole figure, and (c) $\{0001\}$ and (d) $\{11\bar{2}0\}$ colour contour pole figures for Ti6Al4V (Simonelli et al. 2014, EBSD 2019).

The orientation density is usually displayed in regions of different colours or through density contours. Less spaced contours show high density and vice versa. A typical example of the coloured contours for hcpTi6Al4V is shown in Figure 2-26 (c & d). The inverse pole figure, on the other hand, shows the intensity of an orientation with reference to a single axis and is alternatively used to illustrate other types of symmetry of texture. The identification of crystallographic orientations with reference to sample coordinate systems is facilitated by IPF colouring scheme. Figure 2-27 is an illustration of an IPF colour coding for HCP crystal orientations with reference to a fixed frame (x, y, z). When the IPF is plotted along the *x*-direction (normally expressed in compact notation as [100]), the $\{0001\}$ HCP crystal orientation of Figure 2-27(a) can be assigned a red colour as seen in (b) and (c) of this figure.

© Central University of Technology, Free State

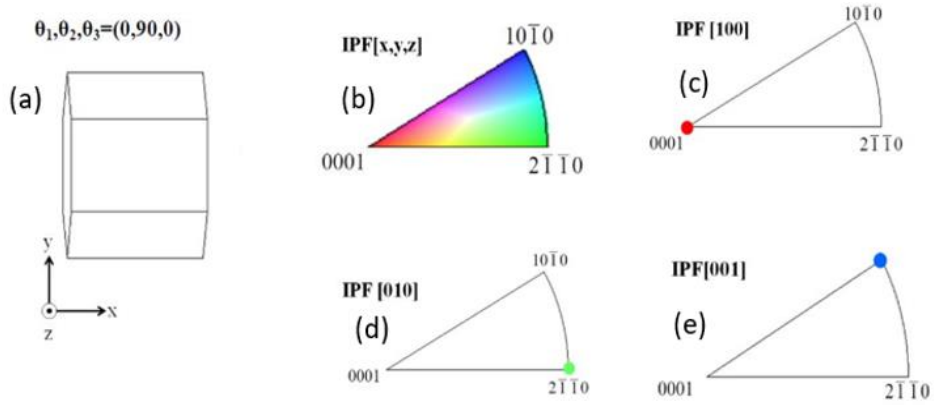

Figure 2-27. (a) A hcp crystallographic orientation determined by three Euler angles θ_1, θ_2, and θ_3, (b) the orientations plotted in form of IPF, and (c, d & e) showing the colour in a unit triangle of which the crystal plane normal is parallel to a given specimen orientation (Simonelli et al. 2014).

The [010] IPF of the same plot would show a different colour such as green, as seen in Figure 2-27(a) & (d). In this case, the planes $\{2\bar{1}\bar{1}0\}$ would be assigned a green colour on the triangle, as seen in Figure 2-27(b) & (d). Likewise, the [001] IPF would also be assigned a different colour such as blue, and since the $\{10\bar{1}1\}$ plane seen in Figure 2-27(a) is perpendicular to the *z*-direction, the vertex of the triangle corresponding to these planes would be assigned a blue colour. The IPF colouring does not display absolute texture, meaning that in this colouring scheme a small change of orientation does not have a considerable change in colour. Nonetheless, this colour scheme can easily be used to display information on the texture of a material.

c) Euler map: Euler colouring is a method of displaying absolute orientations. The method is used to interpret the orientation of the grain with reference to the geometry of a sample by rotation using three Euler angles labelled $\phi 1, \phi, \phi 2$. Contrary to the IPF colouring, an Euler map shows a distinctive colour that illustrate the spatial distribution of the various orientations of the grains, as shown in Figure 2-28. The orientation of each grain is shown on top of it in this figure. The [010] IPF of the same plot would show a different colour such as green, as seen in Figure 2-27(a) & (d). In this case, the planes $\{2\bar{1}\bar{1}0\}$ would be assigned a green colour on the triangle, as seen in Figure 2-27(b) & (d).

© Central University of Technology, Free State

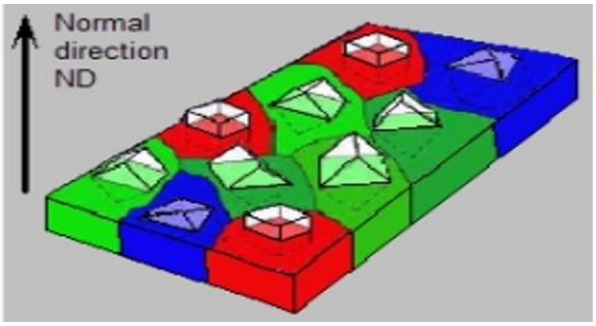

Figure 2-28. Euler map showing orientation of grains in a metallic material (EBSD 2019).

Likewise, the [001] IPF would also be assigned a different colour such as blue, and since the $\{10\bar{1}1\}$ plane, as seen in Figure 2-27(a), is orthogonal to the *z*-direction, the vertex of the triangle corresponding to these planes would be assigned a blue colour.

d) Misorientation map: This is a colouring scheme that colours EBSD points on the basis of the misorientation with neighbouring points with reference to a user-defined colour scheme. Low-angle grain boundaries with a misorientations in a range of 2° to 15° and, HAGBs with misorientation greater than 15° can be depicted in different colours in a misorientation map. Misorientation maps are thus useful in showing grain boundaries on the basis of misorientation angle.

To precisely measure the grain size in polycrystalline material, it is important that all the grain boundaries are shown: thus, the technique used must give the highest degree of delineation of grain boundaries. Conventionally, grain sizes were measured using optical microscopy (OM) and grain size standards, such as ASTM E112-13, still reference this method. Use of OM in measurement of grain parameters can be problematic for fine structured materials (Oxford Instrument 2019); thus, EBSD becomes the only practical alternative to measuring grain sizes. Identification of grains based on EBSD requires the definition of a critical misorientation angle < 10° and in some cases < 15° so that all boundary segments with angles higher than this are considered grain boundaries (Oxford Instrument 2019).

© Central University of Technology, Free State

2.6.2 X-ray diffraction (XRD)

X-rays are a form of electromagnetic radiation that have high energies and short wavelengths of the order of the atomic spacing for solids. They are produced artificially by acceleration of electrons by a metal anode inside an evacuated tube (Cullity 1978). When a beam of X-rays infringes on a solid material, part of this beam will be scattered in all directions by the electrons associated with each atom or ions that lie within the beam's path. (Kniess *et al.* 2015).

When an X-ray beam with a certain frequency focuses on an atom, it behaves as a scattering centre, spreading the X-ray beam in all directions. When the atoms are arranged in a lattice, the incident beam will undergo constructive interference in certain directions, as shown in Figure 2-29, and destructive interference in other directions (Callister 2007, Kniess *et al.* 2015). Bragg's law is a geometric interpretation of this kind of diffraction phenomena of atoms arranged in a lattice. Consider the two parallel planes of atoms A-A' and B-B' in Figure 2-29(a) having the same *h*, *k*, and *l* Miller indices and separated by the interplanar spacing d_{hkl}. If a parallel, monochromatic, and coherent (in-phase) beam of X-rays of wavelength λ is incident on these two planes at an angle θ, then the two rays in this beam, labelled 1 and 2, will be scattered by atoms A and B, as shown in Figure 2.29.

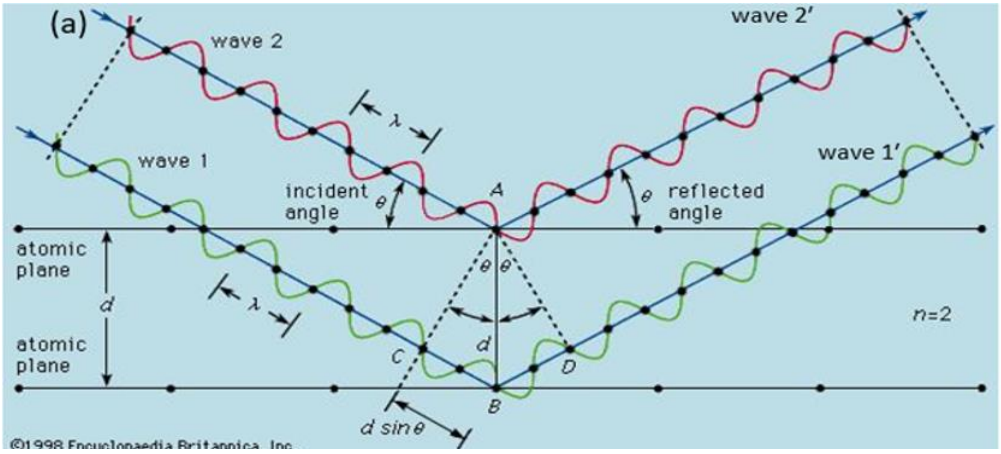

Figure 2-29. Diffraction of X-rays by planes of atoms (Callister 2007).

Constructive interference of the scattered rays 1' and 2' occurs also at an angle θ to the planes of diffraction, if the difference in the path length between 1-B-1' and 2-A-2' ($\overline{CB} + \overline{BD}$) is equal to a whole number, n, of wavelengths. Therefore, the condition for constructive interference of the diffracted waves is:

© Central University of Technology, Free State

$$n\lambda = \overline{CB} + \overline{BD} \qquad 2\text{-}4$$

Or

$$n\lambda = d_{hkl}\ sin\,\theta + d_{hkl}\ sin\,\theta = 2d_{hkl}\,sin\,\theta \qquad 2\text{-}5$$

Equation 2-5 is commonly referred to as Bragg's law and the symbol n in the equation stands for the order of reflection, which may be any integer (1, 2, 3…) consistent with sin θ not exceeding unity.

Phase identification from XRD is possible because diffraction from different planes of atoms produces different diffraction patterns, which contain details about the atomic arrangement within the crystal. According to Braggs' law (Equation 2-5), the diffraction peak position is a function of interplanar spacing (d_{hkl}), which can also be expressed as:

$$d = \frac{a}{\sqrt{h^2+k^2+l^2}}, \textit{ for cubic structure} \qquad 2\text{-}6(a)$$

$$d = \sqrt{\left(\frac{3a^2c^2}{4c^2(h^2+hk+k^2)+a^2l^2}\right)}, \textit{ for hcp structure} \qquad 2\text{-}6(b)$$

where the symbols *a* and *c* represent lattice parameters. Since in most diffractometers, the wavelength (λ) of the X-rays is fixed (Ungar 2004), a family of planes produces a diffraction peak only at a specific angle *2θ*. The quantification of phases from X-ray diffraction is related to the intensities (counts) of the peaks of the XRD pattern, which represents the characteristics (d_{hkl}) of the crystalline phases existing in the material and this way yields a ratio of the phases. The analysis is possible since the intensity counts of the diffraction pattern for a given phase in a mixture of phases depends on the concentration of that phase in the mixture.

While Bragg's Equation 2.5 gives the position of the diffraction peaks in terms of 2θ, it explains nothing about the peak intensities. The intensities of the diffraction peaks are dependent on the arrangement of atoms in the entire crystal and is proportional to the structure factor (F_{hkl}) (Birkholz 2006). The structure factor gives the *hkl* reflections which are present in a unit cell and those ones which are absent (Thomas 2012). In other words, F_{hkl} sums the results of scattering from all the atoms in a unit cell to form a diffraction peak from the *(hkl)* planes of atoms and is of the form (Birkholz 2006):

© Central University of Technology, Free State

$$F_{hkl} = \sum_{n=1}^{N} f_n exp[2\pi i(hx_n + ky_n + lz_n)] \quad 2\text{-}7$$

where the symbols x_n, y_n, z_n stand for the positional coordinates of the *nth* atom, and the symbol f_n is the scattering factor of the *nth* atom.

Every crystalline structure has a characteristic diffraction pattern, allowing their identification through the angular positions and relative intensities of the diffracted peaks, as shown in Figure 2-30 for SLM Ti6A4V. Different fraction peaks belonging to α′/α-titanium hcp-phase and β-titanium bcc-phase are indexed unambiguously in this figure. For sample A, the microstructure exhibits as 100% of α/α'-phase. Samples B microstructure, which experienced heat treatment higher than M_s, transformed fully to α with no detected β-phase peak. However, it should be noted that other studies have detected β phase for heat-treatment temperature of as low as 730 ℃ for AM Ti6Al4V(ELI) (Vrancken *et al.* 2012). With an increase in heat-treatment temperature, a small peak at $\sim 39.5°$ of the angle 2θ of the XRD profile was evidenced in samples' heat treatment C and D, indicating the precipitation of a small amount of β-phase at higher heat-treatment temperatures (Yang *et al.* 2017).

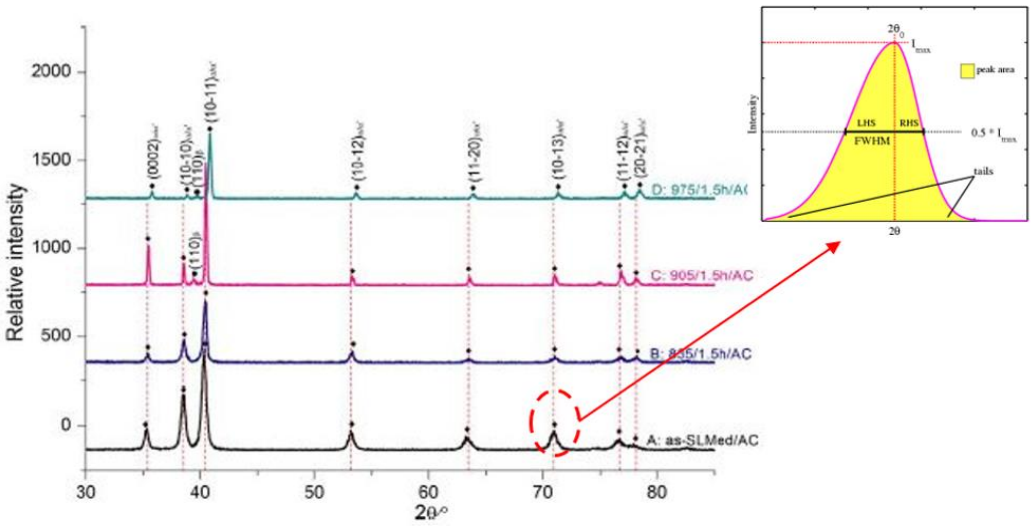

Figure 2-30.The XRD profiles of SLM Ti6Al4V alloy after different heat treatments (Yang et al. 2017) and a schematic diagram showing the properties of a typical peak profile of a diffraction wave.

The insert of the figure shows classical properties of a given peak. The ideal diffraction pattern consists of narrow, symmetrical, delta-function-like peaks, positioned according to a well-defined unit cell. The aberrations from the ideal powder pattern are referred to as peak broadening. The X-ray diffraction peaks broaden when the crystal lattice becomes

© Central University of Technology, Free State

imperfect due to the presence of defects in large numbers (< 5 x 10^{12} m^{-2}) (Ungar 2004). The art of correlating diffraction patterns and crystal defects is referred to as X-ray diffraction peak profile analysis (XDPPA) (Ungar and Borbely 1996). Defects distort the lattice in its neighbourhood in a characteristic way leading to different diffraction line profile shapes and very often to Miller indices $\{hkl\}$ dependent broadening. For example, the full width at half maximum (FWHM) value of the diffraction peak in Figure 2-30, which represents the crystalline imperfection of SLM Ti6Al4V, decreases with accompanying heat treatment. The larger FWHM in sample A can be ascribed to more defects and small grain size in the sample, thus leading to dispersion of crystallographic orientation (Yang *et al.* 2017). Thus, characteristic broadening is the basis for obtaining information on the nature and density of such defects (Dragomira *et al*. 2005).

Both the vectors describing dislocations and elastic properties of a materials determine the visibility of dislocations in XRD. This is quantified by what is commonly referred to as the contrast or orientation factor. It has been shown in the literature that in case of hcp and bcc structures for a given sub-slip system, the average contrast factor of a dislocation can be written as (Dragomir and Ungar 2002, Dragomir *et al.* 2005, Thomas 2012):

$$\overline{C_{hkl}} = \overline{C_{hk.0}}(1 + q_1 x + q_2 x^2) \qquad \textit{for hcp.} \qquad \textit{2-8}$$

$$\overline{C_{hkl}} = \overline{C_{h00}}(1 - qH^2) \qquad \textit{for bcc and fcc.} \qquad \textit{2-9}$$

where the symbols $x = (2/3)(l/ga^2)$, and $H^2 = \frac{h^2k^2+h^2l^2+k^2l^2}{(h^2+k^2+l^2)^2}$. The parameters *q*, q_1 and q_2 in these equations are determined by the elastic properties of a given material, while the parameters *g* and *a* are the diffraction vector and lattice parameter of HCP crystals, respectively. The symbols $\overline{C_{hk.0}}$ and $\overline{C_{h00}}$ are constants and represent average contrast factors at *hk0* and *h00* reflections, respectively, and in this case the symbols *h, k, l* are indices of given crystal planes. Different analytical functions have been developed to best fit the diffraction peaks to extract important information such as dislocation density in a material from the shape of a peak. These functions consist of those that use the normalised area under a peak (integral breath) or its width at FWHM, those that use the Fourier coefficients of the peak and those that use the intensity-values of the peaks to find restricted moments (Thomas 2012). The modified Williamson-Hall (MWH) and modified Warren-Averbach (MWA) that use integral breadth (IB) or FWHM and Fourier coefficients

© Central University of Technology, Free State

of the peaks, respectively, are the common methods used to determine the dislocation density in polycrystalline materials.

2.6.2.1 Evaluation of dislocation density by the Modified Williamson method

Williamson and Hall (1953) developed a method that simultaneously attributed size (crystalline size) and strain broadening of the peaks to their FWHM. The method is commonly referred to as the Williamson-Hall method and its formulation is of the form:

$$\Delta K \cong \frac{0.9}{D} + 0.263b\sqrt{\rho}\,K \qquad 2\text{-}10$$

where ΔK is the FWHM in nm^{-1} expressed as $\Delta K = 2cos\theta(\Delta\theta)/\lambda$ and K is the diffraction vectors expressed as $K = 2sin\theta/\lambda$. In this case, the parameters θ and $\Delta\theta$ stand for the diffraction angle and the FWHM in radians of the XRD peaks, respectively, while λ is the wavelength of the X-rays. The parameters *D, b* and *ρ* represent the crystalline size, Burgers vector and dislocation density in a material, respectively. In this method, the dislocation density in a material can be obtained from the gradient of a linear plot of ΔK obtained from XRD peaks against diffraction vectors, *K*, while the crystalline size is obtained from the y-intercept of the plot. Ungar and Borbely (1996) showed that in the case of materials that show strong strain anisotropy, ΔK is not a linear function of *K*. Strain anisotropy means that the broadening profiles of the peaks show an anisotropic behaviour as a function of the diffraction vectors/$hkil$ indices. They modified Equation 2-10 to account for the influence of strain anisotropy by introducing the average contrast factor of dislocations shown in Equation 2-8. The formulation is now commonly referred to as Modified Williamson-Hall method and is of the form (Dragomir and Ungar 2002, Dragomir *et al.* 2005, Thomas 2012):

$$(\Delta K)^2 \cong \left(\frac{0.9}{D}\right)^2 + \left(\frac{\pi M^2 b^2}{2}\right)\rho K^2 \overline{C_{hkl}} \qquad 2\text{-}11$$

The parameter M in Equation 2-11 is a dimensionless constant depending on the effective outer cut-off radius (R_e) of dislocations and the dislocation density ($M = R_e\sqrt{\rho}$).

2.5.2.2 Evaluation of dislocation density by the Modified Warren-Averbach method

Warren and Averbach (1952) developed a method that expresses the normalised Fourier transforms of the measured broadened peak profiles calculated for equidistant Fourier range *(L)* as the product of the size and the strain coefficient. The expression is normally expressed at a logarithmic scale as:

© Central University of Technology, Free State

$$ln\,A(L) = l\,n\,A^D(L) + ln\,A^s(L) \qquad 2\text{-}12$$

where the symbols $A(L)$, $A^D(L)$ and $A^s(L)$ represent the real, size and strain parts of the Fourier coefficients of the XRD peaks, respectively. When the strain coefficients are expanded and the terms with order higher than K^2 are ignored, this gives the standard formulation commonly known as the Warren-Averbach (WA) equation in the form of:

$$lnA_L = exp\left(-\frac{L}{D}\right) - 2\pi^2\,L^2K^2\langle\varepsilon^2\rangle \qquad 2\text{-}13$$

where the parameters L, D and ε^2 are the Fourier length, coherent domains of diffraction (crystalline size) and mean square strain, respectively. For materials that show strong strain anisotropic behaviour, Ungar *et al*. (1989) expanded Equation 2-13 with the theories of Wilkens *et al*. (1970) on the relationship between distortion and dislocation to account for strain anisotropy to formulate the Modified Warren-Averbach (MWA) equation. Thus, when the strain Fourier coefficients are caused by dislocations and for small values of L, the Fourier transform of the XRD profiles can be approximated as follows (Ungar *et al.* (1989):

$$lnA_L = lnA_L{}^D - \rho\frac{\pi b^2}{2}L^2 ln\left(\frac{R_e}{L}\right)K^2\overline{b^2C} \qquad 2\text{-}14$$

In this formulation, the product of the square of the average Burgers vectors ($\overline{b^2}$) and the average contrast factor $\overline{C_{hkl}}$ is not fitted but is fixed to a value obtained using Equation 2-8. As seen in Equation 2-14, lnA_L can be considered as a function of $K^2\overline{b^2C}$, thus dislocation density can be determined from a plot of lnA_L vs. $K^2\overline{b^2C}$, as shown in Figure 2-31.

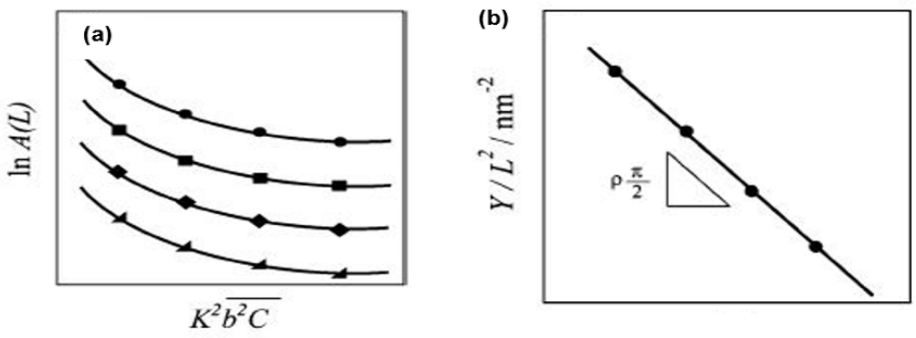

Figure 2-31.Schematic diagrams describing the method of analysis of (a) the modified Warren-Averbach plot following Equation 2-8, and (b) Y/L^2 versus $In\ L$ (Dragomir et al. 2005)

© Central University of Technology, Free State

The gradient of this plot, *Y*, is the coefficient of the second term of Equation 2-14, which can further be expressed as:

$$\frac{Y}{L^2} = \rho\frac{\pi}{2}lnR_e - \rho\frac{\pi}{2}lnL \qquad 2\text{-}15$$

Thus, values of ρ in Equation 2-15 are estimated from the slope of the linear relationship between Y/L^2 and $ln\ L$, such as the one shown in Figure 2-31(b), while the cut-off radius is evaluated from the Y-intercept of the plot in the figure.

2.7 MODELLING OF MECHANICAL PROPERTIES WITH SPECIFIC FOCUS ON TI6AL4V

As previously discussed in this chapter, Ti6Al4V occurs as complex two-phase microstructures, with microstructural features that span across length scales and which are interconnected in a way that strongly influences the mechanical properties (Qianli *et al*. 2015, Caroll *et al.* 2015, Shunyu and Yung 2019). For instance, relatively small α-laths result in high ultimate tensile strength (Jaimie and Tiley 2002, Yang *et al.* 2017). The ductility increases and the toughness decreases as the morphology of the primary α phase changes from acicular to lamellar or equiaxed structure (Lütjering and Williams 2007, Galaraga *et al.* 2017). Thus, it is imperative to control the microstructure of this alloy to obtain the desired mechanical properties for a desired functional structure.

Conventionally, many experiments are required to study the effect of processing parameters on the mechanical properties of materials and to obtain corresponding data. Nonetheless, materials are costly and experimental work time consuming (Sun *et al.* 2012). Modelling and simulation are alternative powerful methods that can be used to this end. Various modelling approaches have been developed to characterise the mechanical properties of wrought and cast Ti6Al4V, ranging from artificial neural networks to numerical models.

2.7.1 Artificial neural network models

Artificial neural network models (ANNMs) use machine learning algorithms to predict the mechanical properties of materials based on certain inputs (Jamie and Tiley 2002, Weidong *et al*. 2011, Sun *et al.* 2012). In principle, an ANN is a computing system consisting of several simple, highly organised processing subsystems that process data dynamically in

© Central University of Technology, Free State

response to external inputs (Jamie and Tiley 2002). A typical artificial neural network basically comprises numerous layers of artificial neurons. The first layer is referred to as the input layer and the last, the output layer. In-between these two layers are the hidden layers.

Generally, ANNMs include the following steps: (a) collection of data; (b) determination of input/output parameters; (c) analysis and pre-processing of data; (d) training of the ANN; (e) verification of the trained ANN, and finally (f) application of established models for evaluation and prediction. The input and the output nodes of the ANNMs may consist of several variables, such as shown in Figure 2-32.

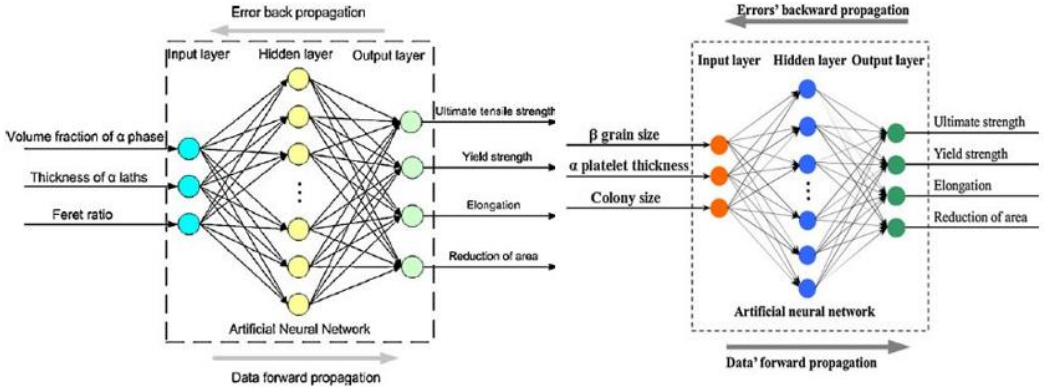

Figure 2-32. Schematic diagram of the ANNM of mechanical properties as a function of microstructural feature parameters of Ti6Al4V alloy (Weidong et al. 2011, Sun et al. 2012).

It is seen from this figure that the ANNMs receive input signals from an input layer, sums them according to their weight, then passes them through a function and produces an output. The output is compared with experimental values. After that, the error is calculated and propagated backwards to adjust the weight of each of the neurons, which is called a training procedure for the ANNMs.

The ability to model nonlinear and complex relationships between the inputs and outputs is one of the key advantages of ANNMs (Jamie and Tiley 2002, Weidong *et al*. 2011, Sun *et al.* 2012). Nevertheless, ANNMs are supervised systems that require input of huge amounts of data arising from experimental work or existing literature for training purposes. For instance, the works of Sun *et al.* (2012) used 54 experimental data sets while that of Tao *et al*. (2019) used 285 experimental data sets in total to accurately predict the mechanical

© Central University of Technology, Free State

properties of Ti6Al4V. This makes the use of the ANNMs very expensive and unreliable, the latter in cases where required input data is scant. Moreover, artificial neural network models are not based on specific mathematic equations, making it difficult to integrate these models into Finite Element Modelling (FEM) software due to lack of single transfer functions to characterise various relevant phenomena.

The alternative approach to ANNMs is the use constitutive numerical models. Material constitutive numerical models can be used to describe the relationship between microstructure and external state variables, such as strain, temperature and strain rate to the mechanical properties of materials (Picu and Majorell 2002, Kocks and Mecking 2003, Khan *et al.* 2004). Such models are the foundation for finite element analysis (FEA) modelling of thermo-mechanical deformation (ABAQUS 2006b).

2.7.2 Constitutive models for plastic flow behaviour of Ti6Al4V

Constitutive numerical models are used widely to describe flow stress of materials during plastic deformation and have conventionally been implemented into Finite Element (FE) methods to simulate engineering processes such as metal cutting and forming (Picu and Majorell 2002, Kocks and Mecking 2003, ABAQUS 2006).

There are various models available to predict the flow stress of Ti6Al4V alloys where macro-scale uniaxial tests are used to verify/determine materials' constants (Johnson and Cook 1983, Zerilli and Armstrong 1987, Nemat-Nasser *et al*. 2001, Khan *et al.* 2004). These models can be classified into two broad categories: (a) the empirical/phenomenological models and the (b) analytical models. The empirical models are based on experimental observations rather than on mathematically describable relationships of the phenomenon being modelled in contrast to the case of analytical models. The models are developed by fitting model equations and the parameters to experimental data without necessarily considering the physical processes causing the behaviour observed. On the other hand, models that are based on the physical properties of a material, commonly referred to as analytical models, are models where knowledge of the underlying physical properties and processes such as size, orientation and distribution of grains and dislocations, and their processes of growth and movement are used to formulate the constitutive behaviour of a

© Central University of Technology, Free State

material (Zerilli and Armstrong 1987). Even though both categories of models can be and are used to predict the stress-strain curves of materials, empirical models are subject to extrapolation, which assumes specific trends of the models. Analytical models that are based on the physical properties of a material are useful as predictive tools to characterise plastic deformation using parameters such as dislocation density and the microstructural morphologies (Picu and Majorell 2002).

2.7.2.1 Empirical models

The empirical models used to simulate the mechanical constitutive behaviour of Ti6Al4V in the literature include Johnson-Cook (JC), modified Khan-Huang-Liang (mKHL), polynomial, power law and Cowper-Symonds models.

(i) Johnson-Cook (JC) model

The Johnson and Cook, (1983) model is commonly used to predict the plastic flow of metal and alloys over a wide range of temperature and strain rate. It presents the von Mises flow stress (σ) as a function of strain, strain rate and temperature. The von Mises flow stress can be written as:

$$\sigma = (A + B\varepsilon^{n})\left(1 + CIn\frac{\dot{\varepsilon}}{\dot{\varepsilon}_0}\right)(1 - (T^{*})^{m}) \qquad 2\text{-}16$$

where

$$T^{*} = \begin{cases} 0 & for\ T < T_r \\ \frac{T - T_r}{T_m - T_r} & for\ T_r \leq T \leq T_m \\ 1 & for\ T > T_m \end{cases}$$

where $\dot{\varepsilon_o}$ is the reference strain rate taken for normalisation; A the yield stress and B the strain hardening factor, and C a dimensionless strain rate hardening coefficient. Parameters n and m are strain hardening and thermal softening exponents, respectively. Parameters, $T, T_m,$ and T_r are working, melting and room temperatures of the material, respectively. The temperature rise experienced due to adiabatic heating during shear strain is an additive to the working temperature T and can be computed using the equation:

$$\Delta T = \frac{\beta}{\rho C}\int \sigma(\varepsilon)\delta\varepsilon \qquad 2\text{-}17$$

© Central University of Technology, Free State

where β is the portion of plastic work converted to heat, ρ the mass density of the material and C the specific heat of the material. Fracture strain is calculated from the damage model expressed in Lesuer (2000) as:

$$D = \sum \frac{\Delta\varepsilon^p}{\varepsilon_f} \qquad 2\text{-}18$$

The strain at fracture, ε_f, is expressed as:

$$\varepsilon_f = (D_1 + D_2 exp D_3 \acute{\sigma})(1 + D_4 In\acute{\varepsilon})(1 + D_5 T^*) \qquad 2\text{-}19$$

where $\Delta\varepsilon^p$ is the increment of plastic strain with load, σ' the mean stress normalised by the effective stress and D_1, D_2, D_3, D_4, D_5 are material constants. The various sets of J-C model parameters from the literature are presented in Table 2-5.

Table 2-5. JC model parameters

JC model parameter	A(MPa)	B(MPa)	*n*	C	*m*
Lee and Lin (1997)	728.7	498.4	0.28	0.028	1
Lee and Lin (1997)	724.7	683.1	0.47	0.035	1
Seo and Min (2005)	997.9	653.1	0.45	0.0198	0.7
Calamaz *et al.* (2008)	968	380	0.421	0.0197	0.577
Meyer *et al.* (2001)	896	656	0.0128	0.8	0.5
Meyer *et al.* (2001)	862.5	331.2	0.012	0.8	0.34
Lesuer *et al.* (2000)	1098	1092	0.93	0.014	1.1
Khan *et al.* (2004)	1104	1036	0.6349	0.0139	0.7794
Khan *et al.* (2004)	1080	1007	0.5975	0.01304	0.7701
Khan *et al.* (2004)	1119	838.6	0.4734	0.01921	0.6437
Khan *et al.* (2004)	984	520.3	0.5102	0.015	0.8242

The advantages of the JC model are its ease of calibration and implementation; hence, it is the most widely used model to characterise the behaviour of materials over a wide range of strain rates and temperatures. However, as shown in Table 2-5, large inconsistencies exist between various sets of JC model parameters. Sun and Guo (2009) suggested that the three possible reasons for these discrepancies include (a) differences in the composition of alloys, (b) different procedures of preparation for the specimens and (c) different methods of testing. Reasons (a) and (b) will ultimately lead to variations in the microstructure of samples. The difference in the relative amounts of α and β-phases present in Ti6Al4V alloy has also been found to affect the calculated parameters of the JC model (Khan *et al.* 2004).

© Central University of Technology, Free State

(ii) Modified Khan-Huang-Liang (mKHL) model

Flow stress in the mKHL model is expressed as (Khan *et al.* 2004):

$$\sigma = \left(A + B\left(1 - \frac{In\dot{\varepsilon}}{InD_p}\right)^{n1} \varepsilon_p^{n0}\right)\left(\frac{\dot{\varepsilon}}{\dot{\varepsilon}^*}\right)^{C}\left(\frac{T_m - T}{T_m - T_{ref}}\right)^{m} \qquad 2\text{-}20$$

where ε_p is the true plastic strain, and T_m , T , T_{ref} the melting, ambient and reference temperatures, respectively. The upper-bound of the plastic strain rate is set at D_p = 10^6 s^{-1}, and the reference strain rate at a reference temperature of T_{ref} at which material constant A, B and n_o are determined $\dot{\varepsilon}^*$= 0.01 s^{-1}. The symbol $\dot{\varepsilon}$ stands for the current strain rate and the symbols n_0, n_1, C and m are additional material constants. To the knowledge of the author, the parameters of this model for Ti6Al4V are only those given by Khan *et al.* (2004), presented here in Table 2-6.

Table 2-6. The mKHL-model material constants determined for 3 different forms of Ti6Al4V alloy (Khan et al. 2004)

A	B	n_0	n_1	C	m
1069	874.8	0.4987	0.5456	0.02204	1.3916
1097	1004.7	0.6268	0.4993	0.02219	1.4796
1004	325.1	0.5263	1.9015	0.02204	1.1206

A main characteristic of this model, contrary to the JC model, is that the phenomenon of decreasing strain hardening with increasing strain rate that is commonly observed at high strain rates can be accommodated through the constant parameter n_1. However, due to the empirical nature of this model, similar drawbacks as in JC model will also be present.

(iv) Cowper-Symonds model

To define high-strain-rate deformation of materials in this model, the dynamic effects of strain rates are considered by scaling the dynamic yield stress of a material with the static yield stress as (Klemene and Andrej 2016):

$$\frac{\sigma_d}{\sigma_s} = 1 + \left(\frac{\dot{\varepsilon}}{C}\right)^{1/p} \qquad 2\text{-}21$$

where σ_d is the dynamic yield stress, σ_s the static yield stress, $\dot{\varepsilon}$ the strain rate, and C and p constants for the Cowper-Symonds relation. Based on the Cowper-Symonds relation, it is

© Central University of Technology, Free State

clear from Equation 2-20 that the dynamic and static yield stress ratio is determined by the deformation strain rate. The Cowper-Symonds materials' model can be further adjusted to incorporate contributions of isotropic and kinematic hardening to become:

$$\sigma_d = 1 + \left(\frac{\dot{\varepsilon}}{C}\right)^{1/p} \left(\sigma_o + \beta E_p \varepsilon^{ef}\right) \qquad 2\text{-}22a$$

$$E_p = \frac{E_{tan} E}{E - E_{tan}} \qquad 2\text{-}21b$$

where β is the work hardening parameter, which adjusts the contribution of kinematic and isotropic hardening, ε^{ef} the effective plastic strain and E_p the plastic hardening modulus, which is given in terms of elastic modulus E and the tangent elastic modulus E_{tan}.

This model is a phenomenological material equation; thus, the parameters must be determined from experimental observations. It shows the typical configuration of strain-rate-dependant empirical models in which the yield stress is modified by constant parameters. However, the model does not take into consideration the thermal softening phenomenon due to flow localization which lowers the flow stresses below the maximum flow stress.

(v) Power Law

The general form of the power-law stress-strain curve model is as follows (Hollomon 1945):

$$\sigma = K\varepsilon^n \qquad 2\text{-}23$$

where *n* is the strain-hardening exponent, K a constant which is adjusted to best fit measured stress-strain data (and is also referred to as a strength coefficient). The value of *n* ranges from 0–1 and the value of flow stress (σ) is always greater than the yield stress (σ_y). The power law is used extensively because of its mathematical simplicity, despite its shortcomings around the yield strength (Hollomon 1945). It is important to note that this equation is a summarised form of the Zener-Hollomon creep equation for constant temperature (Zener and Hollomon 1944).

The power equation that expresses the behaviour of material when strain rate is controlling plastic deformation is of the form:

$$\sigma = K\dot{\varepsilon}^m \qquad 2\text{-}24$$

© Central University of Technology, Free State

where the symbol m is the index of strain rate sensitivity. When m = 0, then the stress is not dependent on the strain rate. For most metals, m = 0.2. However, when m = 0.4 - 0.9, the material may exhibit superplastic behaviour. The major drawback of the power law is that Equations 2-23 and 2-24 relate two variable parameters at a time and neglect the effect of other variable parameters that may have a bearing on the behaviour of materials, such as strain rate in the first equation, strain in the second equation and temperature in both equations.

In summary, the major drawback of all these empirical models is that none include the effects of the various mechanisms occurring during deformation and instead, the material constants in them are fitted from specific experimental data. Therefore, the set of parameters used is distinct for a given material with a specific processing history; thus, different microstructures yield different sets of model parameters. For instance, this is very clear in the extensive list of JC materials' constants reported in Table 2-5, as well as the Modified KHL-model material constants shown in Table 2-6. However, the model parameters can be obtained easily and thus has a wide application of the models.

2.7.2.2 Analytical models

The analytical models used in the literature to predict the flow stress of Ti6Al4V include the Armstrong-Zerilli (AZ), Picu-Majorell and Nemat-Nasser models.

(i) Armstrong-Zerilli model

This model was developed by Zerilli and Armstrong (1987) and was initially used to model the flow stress in metals with fcc and bcc crystal structures. For bcc crystal structures, the model expresses the flow stress as:

$$\sigma = C_o + C_1 exp(-C_3 T + C_4 T \, In \, \dot{\varepsilon}_e) + C_5 \varepsilon^n \qquad 2\text{-}25$$

A similar equation for fcc crystal structures is:

$$\sigma = C_o + C_1 (\varepsilon)^{0.5} exp(-C_3 T + C_4 T \, In \, \dot{\varepsilon}_e) \qquad 2\text{-}26$$

where ε is the strain, $\dot{\varepsilon}_e$ effective strain rate, and T the temperature. The symbols C_0, C_1, C_2, C_3, C_4, C_5 are all constants. Later the authors developed the localising strength model predominantly for hcp Ti6Al4V that is somewhat different from that for bcc and fcc crystal structures, of the form:

© Central University of Technology, Free State

$$\sigma = C_0 + C_1 e^{-\beta T} + C_2 \sqrt{(\varepsilon_r(1 - e^{-\varepsilon/\varepsilon_r}))} e^{-aT} \quad 2\text{-}27$$

where the symbols α and β are parameters dependent of strain rate and the absolute temperature, and C_0, C_1 and C_2 are material parameters. The symbol ε_r stands for a material parameter that influences the strain at which saturation of the flow stress is attained.

The simple square root of strain in Equation 2-27 is derived from theoretical considerations of the motion of dislocations during deformation of metals given by Taylor (1934). In this work, Taylor deduced that the simple yield stress is a function of the square root of strain (and in addition to external factors such as temperature and strain rate). The challenge of this simple square root formulation is that stress cannot saturate at high strains in a formulation of the form $\sigma = k\sqrt{\varepsilon}$. This form of work-hardening behaviour poses a problem when modelling of localisation is desired. This is because localisation is dependent on thermal softening overtaking the work- hardening effects.

(ii) Picu-Majorell model

In all the aforementioned material models, the material is considered homogenous. None of these models account for the differences in mechanical behaviour between the hcp α phase and the bcc β phase. Picu and Majorell (2002) proposed a model to account for the individual phases during deformation. The model is composed of two parts of stress, namely the thermally activated component of stress (σ^*) and the athermal component of stress (σ_G). Generally, the flow stress is given by the sum of these two components of stress. The thermally activated component of stress for each phase of Ti6Al4V is expressed as a superposition of terms corresponding to the deformation mechanism. Two components are considered: one due to the interactions of dislocations with interstitial impurity atoms (C, N, H and O) and the other representing both the activation of dislocations over the Peierls barriers and the interaction of dislocations with alloying aluminium atoms. The thermally activated stress for the α phase is therefore given as:

$$\sigma_\alpha^* = \tau^o_{(C_{Oeq})}\left(1 - \left(\frac{kT}{\Delta G_{Oeq}} In\ \frac{\dot{\gamma}_0}{\dot{\gamma}}\right)^{1/q_{Oeq}}\right)^{1/P_{Oeq}} + \tau^o_{(C_{Al})}\left(1 - \left(\frac{kT}{\Delta G_{Al}} In\ \frac{\dot{\gamma}_0}{\dot{\gamma}}\right)^{1/q_{Al}}\right)^{1/P_{Al}} \quad 2\text{-}28$$

© Central University of Technology, Free State

where the symbols $\tau^{o}_{(C_{Oeq})}$ and $\tau^{o}_{(C_{Al})}$ are the mechanical threshold stresses at 0 *K*, that vary with the equivalent concentration of oxygen for the impurities and the concentration of aluminium, respectively. The symbol $C_{O\,eq}$ is taken as the equivalent oxygen concentration given by the expression $C_{O\,eq} = O + 2N + 0.75C$. The symbol ΔG is the activation energy for deformation, *k* the Boltzmann's constant, *p* and *q* fitting constants, and $\dot{\gamma}_o$ the reference strain rate. Similarly, the thermally activated component of stress for the *β* phase is given by:

$$\sigma^{*}_{\beta} = \tau^{o}_{\beta}\left(1 - \left(\frac{kT}{\Delta G_{\beta}} In\ \frac{\dot{\gamma}_{0\beta}}{\dot{\gamma}}\right)^{1/q_{\beta}}\right)^{1/P_{\beta}} \qquad 2\text{-}29$$

The stress contribution due to interaction of dislocations with vanadium atoms is neglected in Equation 2-29. The model parameters of the Picu-Majorell model are given in Table 2-7.

Table 2-7. The material model parameters evaluated by Picu-Majorell (2002)

$\tau^{o}_{(C_{Oeq})}$	$\tau^{o}_{(C_{Al})}$	τ^{o}_{β}	ΔG_{Oeq}	ΔG_{β}	$\dot{\gamma}_0$	$\dot{\gamma}_{0\beta}$	$p_{O_{eq}}$	$q_{O_{eq}}$	p_{Al}	q_{Al}	p_{β}
1050	1080	1200	150	200	10^7	10^7	0.45	1.7	0.7	2.7	0.4

The thermally active stresses capture the temperature and rate-dependence of flow stress. On the other hand, the athermal component of stress accounts for strain hardening and can be written as:

$$\sigma_{G_{\alpha}} = \zeta \mu b \sqrt{\rho} + \frac{k}{\sqrt{d}} \qquad 2\text{-}30$$

where the symbols ζ and *k* are material parameters, μ the shear modulus which depends on temperature, *b* the Burger's vectors, *d* the grain size and *ρ* the dislocation density. The second term in Equation 2-30 is the Hall-Petch term which represents the strengthening effect due to grain sizes. In the absence of recrystallization and grain growth, the only deformation- dependent parameter in Equation 2-30 is the dislocation density (*ρ*). The evolution of dislocations is therefore computed as follows:

$$\frac{d\rho}{d\bar{\varepsilon}^{p}} = \left|\frac{d\rho}{d\bar{\varepsilon}^{p}}\right|_{pr} + \left|\frac{d\rho}{d\bar{\varepsilon}^{p}}\right|_{re} \qquad 2\text{-}31a$$

$$\left|\frac{d\rho}{d\bar{\varepsilon}^{p}}\right|_{pr} = a_1 \sqrt{\rho} \qquad 2\text{-}30b$$

© Central University of Technology, Free State

$$\left|\frac{d\rho}{d\bar{\varepsilon}^p}\right|_{re} = -a_2 \frac{\dot{\varepsilon}_0^{ath}}{\dot{\bar{\varepsilon}}^p} \rho \left(1 - e^{-0.7R_C^4\rho^2}\right) exp^{-Q/kT} \quad \textit{2-30c}$$

The term $\left|\frac{d\rho}{d\bar{\varepsilon}^p}\right|_{pr}$ is the term for the accumulation (or production) of dislocations and $\left|\frac{d\rho}{d\bar{\varepsilon}^p}\right|_{re}$ the term for the recovery of dislocations. The symbols $\dot{\varepsilon}_0^{ath}$ and $\dot{\bar{\varepsilon}}^p$ are the reference and applied strain rates, *Q* the activation energy of cross slip, R_c the radius of dislocation to climb or annihilate and a_1 and a_1 constants of proportionality. The total flow stress in the α and β phases is given by:

$$\sigma = \left(1 - X_\beta\right)^{0.8} \left(\sigma_\alpha^* + \sigma_{G_\alpha}\right) + X_\beta^{0.8}\sigma_\beta^* \quad \textit{2-32}$$

where X_β is the percentage fraction of the β-phase, which can be obtained directly from the phase equilibrium diagram. The role of α and β-phases in plastic deformation of Ti6Al4V is captured well in this model. The model formulation has many material constants that require large amounts of resources and time to determine. It is also necessary to carry out extrapolation to 0 K so as determine some parameters.

(iii) Nemat-Nasser model

This model was developed by Nemat-Nasser *et al.* (2001). The flow stress, σ, in a state of uniaxial stress in this model, is divided into two parts; one due to the athermal resistance to motion of dislocations, denoted by the symbol σ_a, and the other associated with the thermally activated crossing of obstacles by dislocations, denoted by the symbol σ^*. The total flow stress is the sum of these two components ($\sigma = \sigma^* + \sigma_a$). It was assumed in this work that σ_a is only dependent on the dislocation density ρ while σ^* is dependent on the strain rate, and dislocation density. This model recognises and corrects the fact that in most of the empirical models the dependence of the flow stress on the dislocation density, ρ, is replaced by the dependence on plastic strain (ε). The error arising from this assumption in most empirical models is that while the dislocation density is related to the microstructural state of the material, the plastic strain may not be the sole determinant. The flow stress as a function of absolute temperature (T), effective plastic strain ($\bar{\varepsilon}^p$) and strain rate ($\dot{\bar{\varepsilon}}^p$) in the Nemat-Nasser formulation is written as:

© Central University of Technology, Free State

$$\sigma\left(\dot{\bar{\varepsilon}}^p, \bar{\varepsilon}^p, T\right) = \tau_a^0 \bar{\varepsilon}^{p^n} + \tau^0 \left\{1 - \left(\frac{kT}{G_0}\left(In\ \frac{\dot{\bar{\varepsilon}}^p\ f(\bar{\varepsilon}^p, T)}{\dot{\varepsilon}_0}\right)\right)^{1/q}\right\}^{1/p} + f\left(\bar{\varepsilon}^p, T\right) \qquad 2\text{-}33(a)$$

$$f = 1 + a_0\left(1 - \left(\frac{T}{T_m}\right)^2\right)\bar{\varepsilon}^{p^{1/2}} \qquad 2\text{-}33(b)$$

where the symbol τ^0 is the empirically determined effective stress, G_0 the energy barrier of dislocations (taken as 1.4eV for Ti6Al4V), $\dot{\varepsilon}_0$ the reference strain rate, $\tau_a^0 \bar{\varepsilon}^{p^n}$ the athermal part of the flow stress and a_0 a constant depending on the initial (reference) dislocation density. This model was developed with reference to three different microstructures produced with different manufacturing techniques; commercial Ti-64 (CP-Ti64), hot isostatic pressed Ti64 (HIP Ti64) and hot isostatic pressed material made with milled powder (MIL-HIP Ti64). The material model parameters estimated by Nemat-Nasser *et al.* (2001) for the three forms of the titanium alloy are shown in Table 2.8.

Table 2-8. The estimated Nemat-Nasser model parameters (Nemat-Nasser et al. 2001)

Parameter	*p*	*q*	k/G_0 ($x10^{-5}K^{-1}$)	$\dot{\varepsilon}_0$ ($x\ 10^{10}s^{-1}$)	a_0	τ^0	τ_a^0	*n*
CP-Ti64	1	2	6.2	1.32	2.4	1560	685	0.05
HIP Ti64	1	2	6.2	1.32	2.4	1620	680	0.04
Mil-HIP Ti64	1	2	6.2	1.32	2.4	1900	710	0.03

As is evident in this table, the model parameter k/G_0 associated with the thermally activated component of flow stress is the same for the three forms of the alloy, while the parameters that are associated with the athermal component of stress are different. This is an indication that the initial microstructure (initial dislocation density, grain sizes and their distributions) only affects the athermal part of the flow stress.

2.8 A REVIEW OF THE THEORY OF PLASTIC DEFORMATION

The most widely known theory of plasticity is the flow theory, which is comprised of a yield criterion, a hardening law and a flow rule (Stouffer and Dame 1996). The stress at which yielding occurs is defined by the yield criterion, the increase in plastic strain post yielding is described by the flow rule, and the hardening law describes the evolution of the flow stress with increased plastic strain.

© Central University of Technology, Free State

In continuum mechanics, a stress tensor that consists of nine components σ_{ij} is used to completely define the state of stress at a point/element inside a material under application of the load (Fridtjov 2008). For a given element of a material, the stresses $\sigma_{xx}, \sigma_{yy}\ \sigma_{zz}$, $\tau_{xy}\ \tau_{yz}$ and τ_{zx} acting on that element may be conveniently resolved into a mean, or average component and the deviatoric components. The mean stress, which is also known as hydrostatic or equivalent pressures stress, is expressed as (Fischer-Cripps 2007):

$$\sigma_m = \frac{1}{3}\left(\sigma_{xx} + \sigma_{yy} + \sigma_{zz}\right) \qquad 2\text{-}34$$

The deviatoric stress tensor (S_{ij}) is given by the difference between the stress tensor (σ_{ij}) and the hydrostatic stress ($\sigma_m \delta_{ij}$) (Stouffer and Dame 1996) expressed as:

$$S_{ij} = \sigma_{ij} - \sigma_m \delta_{ij} \qquad 2\text{-}35$$

The deviatoric stress tensor has its own coordinate-independent stress invariant. The three invariants of the deviatoric stress obtained from the determinant of Equation 2-35 are (Lubliner 1990):

$$\boldsymbol{J_1} = S_{ii} = 0 \qquad 2\text{-}36(a)$$

$$\boldsymbol{J_2} = \frac{1}{2} S_{ij} S_{ij} = \frac{1}{6}((\sigma_1 - \sigma_2)^2 + (\sigma_2 - \sigma_3)^2 + (\sigma_3 - \sigma_1)^2) \qquad 2\text{-}36(b)$$

$$\boldsymbol{J_3} = \frac{1}{3} S_{ij} S_{jk} S_{ki} = \frac{1}{27}(2\sigma_1 - \sigma_2 - \sigma_3)(2\sigma_2 - \sigma_3 - \sigma_1)(2\sigma_3 - \sigma_1 - \sigma_2) \qquad 2\text{-}36(c)$$

where σ_1, σ_2 and σ_3 are principal stresses at a given point. The deviatoric stress state can therefore be represented by only two variables, $\boldsymbol{J_2}$ and $\boldsymbol{J_3}$.

In a similar manner to the deviatoric stress tensor, the deviatoric strain tensor (e_{ij}) is given by the difference between the strain tensor(ε_{ij}) and the mean strain ($\varepsilon_m \delta_{ij}$):

$$e_{ij} = \varepsilon_{ij} - \frac{1}{3}\varepsilon_{kk}\delta_{ij} = \varepsilon_{ij} - \varepsilon_m \delta_{ij} \qquad 2\text{-}37$$

where $\varepsilon_m = \frac{1}{3}(\varepsilon_{xx} + \varepsilon_{xx} + \varepsilon_{xx})$ is the mean strain and ε_{kk} is the volumetric strain or dilatation.

In homogeneous and isotropic materials, the elastic stress tensor is defined by two Lame constants which are material-dependent quantities denoted by the symbols λ (lambda) and

© Central University of Technology, Free State

μ (shear modulus) that arise in stress-strain relationships (Stouffer and Dame 1996). The stress tensor for such materials is expressed using the Lame constants as:

$$\sigma_{ij} = 2\mu\varepsilon_{ij} + \lambda\varepsilon_{kk}\delta_{ij} \qquad 2\text{-}38$$

Equation 2-38 can further be expressed in terms of mean, deviatoric stress and strain values. The bulk modulus K can be expressed from the stress tensor or hydrostatic stress as:

$$K = \frac{\sigma_{ij}}{3\varepsilon_{kk}} = \frac{\sigma_m}{\varepsilon_{kk}} \qquad 2\text{-}39$$

This allows the tensor to be expressed as:

$$\sigma_{ij} = S_{ij} + \sigma_m\delta_{ij} = 2\mu e_{ij} + K\varepsilon_{kk}\delta_{ij} \qquad 2\text{-}40$$

The rate of deformation can be described as the sum of the elastic ($\dot{\varepsilon}_{ij}^{e}$) and plastic ($\varepsilon_{ij}^{p}$) components given as:

$$\dot{\varepsilon}_{ij} = \dot{\varepsilon}_{ij}^{e} + \dot{\varepsilon}_{ij}^{p} \qquad 2\text{-}41$$

For the plasticity model to distinguish between the elastic and plastic responses, some formulation is required to define (a) the yield surface – when yielding occurs, (b) flow rule – which describes the direction of the plastic deformation, and (c) hardening law – that explains how the flow varies with plastic deformation (Hibbitt *et al.* 2002, ABAQUS 2020). The yield surface is defined by a yield function which is of the form (Hibbitt *et al.* 2002):

$$f\left(\sigma_{ij}, \varepsilon_{ij}^{p}, T, k^{n}\right) = 0 \qquad 2\text{-}42$$

The yield surface is thus a function of the stress state (σ_{ij}), the plastic strain state (ε_{ij}^{p}), the temperature (T) and hardening parameter k^{n}. The step for which $f \leq 0$ indicates that the material is within the elastic region. On the other hand, the condition $f > 0$ exists in the case of rate-dependent plasticity resulting in stress states that lie outside the yield surface (Lubliner 1990, ABAQUS 2020).

For materials that obey $\boldsymbol{J_2}$-flow plasticity (flow controlled by shear), their plasticity behaviour is characterised by the (von Mises) equivalent stress-strain curve that can be obtained by conducting a uniaxial compression test, a tension test, or a torsion test (Dieter 1986, Hibbitt *et al.* 2002, Fischer-Cripps 2007). The stress-strain curves obtained from

© Central University of Technology, Free State

either one of these tests is normally used to predict the material's plastic response under various states of stress.

While the von Mises yield criterion is used to define the yield function, there are three general models for hardening post yielding shown in Figure 2-33, which describe changes of the yield function during deformation (Stouffer and Dame 1996):

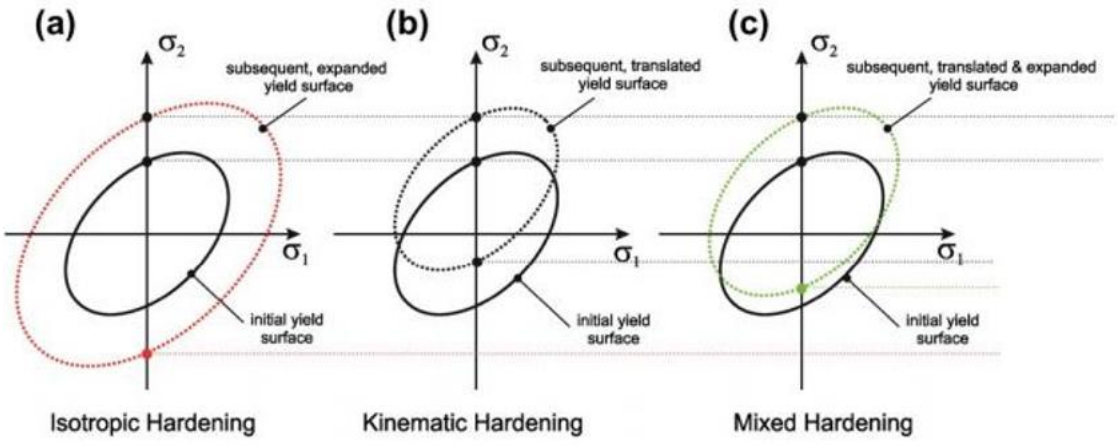

Figure 2-33. Characteristics of hardening models (Stouffer and Dame 1996).

i. ***Isotropic hardening*** – the centre of the yield surface is fixed while the surface expands uniformly.
ii. ***Kinematic hardening*** – the yield surface translates with no change of shape.
iii. ***Combined isotropic and kinematic hardening*** – involves both a yield surface expansion and translation.

The isotropic hardening model cannot be valid for cyclic loading conditions as it has been found that any strain-hardening in tension reduces the subsequent yield stress in compression a phenomenon known as the Bauschinger effect (Dieter 1986). The kinematic hardening shown in Figure 2-33 accounts for the Bauschinger effect in cyclic loading. The model formulation considered in the present study is based on the isotropic hardening model since the loading conditions to be studied are monotonic in nature.

If the yielding surface of a material is isotropic, the yield function can be expressed in terms of a deviatoric stress invariant $\boldsymbol{J_2}$. Then, the yield function f can be written as (Stouffer and Dame 1996, ABAQUS 2006):

© Central University of Technology, Free State

$$f(\boldsymbol{J_2}) = 0 \qquad 2\text{-}43$$

From the von Mises failure criterion (Dieter (1986)) and $\boldsymbol{J_2}$ in Equation 2-35b, Equation 2-43 can be written as:

$$\sigma_y - \sqrt{3\boldsymbol{J_2}} = 0 \quad or \quad \sigma_y - \sqrt{\frac{3}{2}S_{ij}S_{ji}} = 0 \qquad 2\text{-}44$$

This scalar quantity of stress obtained from the deviatoric stress is commonly referred to as the von Mises equivalent stress, $\boldsymbol{q}$ computed in most Finite Element Analysis packages such as ABAQUS *viz*:

$$\boldsymbol{q} = \sqrt{\frac{3}{2}S_{ij}S_{ji}} \qquad 2\text{-}45$$

Likewise, the scalar quantity of strain from the deviatoric strain, commonly referred to as equivalent strain, is expressed as:

$$\boldsymbol{\varepsilon_{eq}} = \sqrt{\frac{2}{3}e_{ij}e_{ij}} \qquad 2\text{-}46$$

When $\sigma_y - \sqrt{\boldsymbol{q}} > 0$ the state of the material is no longer elastic and therefore a plastic correction must be performed. In other words, the equivalent increment in inelastic strain must be calculated to return the isotropic stress state to a von Mises yield surface. The radial return algorithm introduced by Wilkins (1963) is the common method that uses the von Mises yield surface to define the increment of plastic strain necessary to return the stress state to the yield surface an after increment of trial stress (S_{ij}^t).

2.9 THE OVERVIEW OF RADIAL RETURN ALGORITHM

If the rate of change of the flow stress with plastic strain, $\boldsymbol{H}$ = 0 (perfectly plastic), the yield surface is constant. However, this is a rare situation for most materials and the yield surface normally expands during plastic deformation, as defined by the relationship, $\boldsymbol{H} > 0$. In radial return mapping, the stress is updated with an assumption that the response is elastic, and if it is outside the yield surface, the stress is projected onto the closest point on the yield surface.

© Central University of Technology, Free State

In elastoplastic deformation, the total change in strain can be expressed as the sum of the elastic ($\Delta\varepsilon^e$) and plastic strain ($\Delta\varepsilon^p$):

$$\Delta\varepsilon = \Delta\varepsilon^e + \Delta\varepsilon^p \qquad 2\text{-}47$$

If the $\Delta\varepsilon_{ij}$ has been derived for the Gauss point (integration point) from the current iteration procedure, then the trial stress S_{ij}^t can be obtained as:

$$S_{ij}^t = S_{ij}^{(1)} + 2\mu\Delta\varepsilon_{ij} \qquad 2\text{-}48$$

where S_{ij}^1 is the old trial stress obtained from previous iteration and μ is the shear modulus. The actual stress due to plastic deformation, obtained at the end of increment, is not the trial stress but rather the one returned to the yield surface, as seen in Figure 2-34.

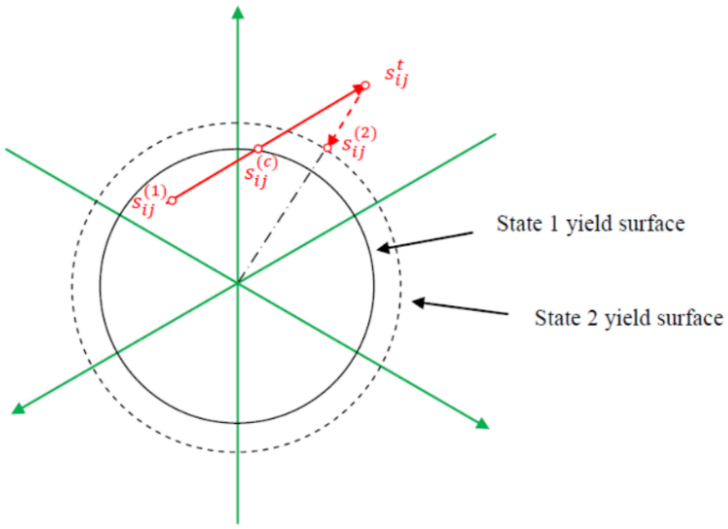

Figure 2-34. The radial return method for isotropic/von Mises hardening (Hibbitt et al. 2002).

Thus, the actual deviatoric stress can be expressed as:

$$S_{ij}^{(2)} = S_{ij}^{(1)} + 2\mu\Delta\varepsilon_{ij}^e = S_{ij}^{(1)} + 2\mu\left(\Delta\varepsilon_{kl} - \Delta\varepsilon_{kl}^p\right) = S_{ij}^t - 2\mu\Delta\varepsilon_{kl}^p \qquad 2\text{-}49$$

$$S_{ij}^r = 2\mu\Delta\varepsilon_{kl}^p \qquad 2\text{-}50$$

The 'correction' stress in Equations 2-49 and 2-50 is called the return stress (S_{ij}^r) which leads to the name "radial return" method. An implicit integration scheme (ABAQUS 2020) presented in Appendix A is used to evaluate the increment of the plastic strain component.

© Central University of Technology, Free State

From this integration scheme, the increment in equivalent plastic strain and the new stress tensor are obtained as:

$$\Delta\epsilon_e^p = \frac{\sigma_e^t - \sigma_y^{(1)}}{3\mu + \boldsymbol{H}} \qquad 2\text{-}51$$

$$factor = \frac{\sigma_y^{(2)}}{\sigma_e^t} = \frac{\sigma_y^{(2)}}{\left(\sigma_y^{(2)} + 3\mu\Delta\epsilon_e^p\right)} \qquad 2\text{-}52(a)$$

$$S_{ij}^{new} = factor\ x\ S_{ij}^t \qquad 2\text{-}52(b)$$

$$\sigma_{ij}^{new} = S_{ij}^{new} + \sigma_m \qquad 2\text{-}52(c)$$

Once the increase in equivalent plastic strain is computed, the proportionality factor $\left(\sigma_y^{(1)} / \sigma_e^t\right)$ is calculated using Equation 2-52(a) and the trial deviatoric stresses scaled back to the yield surface using Equation 2-52(b). The new stress tensor is updated by adding the scaled trial deviatoric stresses to the hydrostatic stress in Equation 2-52(c).

2.10 IMPLEMENTATION OF USER'S DEFINED MATERIAL IN ABAQUS

Several types of constitutive models have been implemented into the commercial finite element (FE) software such as ABAQUS (Hibbitt *et al*. 2002, ABAQUS 2020). Most material models implemented in FE software are incremental in nature, and the total strain in them expressed as the sum of elastic and inelastic strain. Generally, these incremental plasticity laws are described by a yield function, a flow rule and a hardening law, as discussed in section 2.8 of this chapter.

FE programs such as ABAQUS have two yield criteria apt for predicting the flow stress in metals and alloys, that is the (i) Hill criterion and (ii) the von Mises criterion. The Hill criterion is basically a form of the von Mises function that allows for anisotropic response. It also allows for perfectly plastic response, isotropic hardening and kinematic hardening, and has a nonlinear isotropic/kinematic hardening function intended to model cyclic loading in materials. While strain-rate effects can be accounted for in ABAQUS' simple isotropic hardening scheme, they cannot be applied to kinematic hardening and combined isotropic and kinematic hardening (ABAQUS 2006b).

© Central University of Technology, Free State

The basic approach in ABAQUS to solutions of nonlinear constitutive laws, such as plastic deformation, is to apply the loading in small steps, with the load in each step being sub-divided into increments. Constitutive models which are nonlinear in form, constituting the response of the structure/material to a load increment, are solved by iteration. The Newton-Raphson or Bisection method is adopted, with carefully checking of progress towards convergence to ensure a computationally efficient solution (ABAQUS 2020). During plastic deformation, the stress tensor is updated for the use in the next increment using an implicit or explicit integration scheme.

The explicit integration scheme, also commonly known as the forward Euler method, calculates the state of the system later from the state of the system at the current time without the need to solve algebraic equations. Generally, decreasing the size of the step (Δt) increases the accuracy of the approximate solutions even though this increases the computation resources (time and space). Graphical series of line segments are produced by this method, which thereby approximates the solution curves. For t_k, where $k = 1, 2, 3, \dots\dots\dots$ is the sequence of time with $t_{k+1} = t_k + \Delta t$, and the slope of the solution at the point (t_k, y_k) represented by the function $f(t_k, y_k)$, the explicit integration scheme determines the point (t_{k+1}, y_{k+1}) by presupposing that it lies on the line through (t_k, y_k) with the slope $f(t_k, y_k)$. Therefore:

$$y_{k+1} = y_k + \Delta t(t_k, y_k) \qquad \textit{2-53}$$

For this integration scheme, the error between the actual and approximate solution can be reduced by decreasing the step size or Δt.

The implicit integration method is also commonly known as the backward Euler's method. Contrary to the explicit method, this method finds the solution by solving an equation involving the current state of the system and the ensuing one, more accurately stated as:

$$y_{k+1} = y_k + f(t_k, y_{k+1})\Delta t \qquad \textit{2-54}$$

This method is usually numerically more stable for solving a stiff equation with a large step size (Δt). Nevertheless, it takes more time to generate a solution in comparison to the explicit method (ABAQUS, 2006b).

© Central University of Technology, Free State

The user-defined material models are necessary to carry out simulations where standard constitutive models that are in-built in FEA packages, are inadequate. Most commercial FE programs such as ABAQUS provide user interfaces via a FORTRAN compiler linking to the main program to allow the user to formulate and incorporate user-defined material laws (ABAQUS 2020). These subroutines include VUHARD or UHARD for the hardening flow law (plastic deformation) and VUMAT or UMAT for the full/complete behaviour law (elastic – plastic). The user subroutines for classical metal plasticity, applicable for ABAQUS/Standard (Implicit) are UMAT and UHARD, while the equivalent versions for ABAQUS/Explicit are called VUMAT and VUHARD. The major difference between ABAQUS explicit and implicit being that explicit subroutines do not need evaluation of the consistent Jacobian matrix, but only the stress tensor at the end of an increment (ABAQUS 2020).

2.11 HIGH-STRAIN-RATE TESTING - SPLIT HOPKINSON PRESSURE BAR (SHPB) TEST

Deformation of materials is fundamentally different at high-strain rates (10^2 – 10^4 s^{-1}) in comparison to that in low strain rate conditions (< 10^{-1} s^{-1}) (Picu and Majorell 2002, Kocks and Mecking 2003). At low strain rates, any element in a specimen has a summation of forces acting on it, tending to zero, what is commonly referred to as static equilibrium state. Nonetheless, at high-strain rates, deformation stresses travel through materials, leading into varying loading states for various regions at any one time (Lee and Lin 1997, Lesuer 2000). Moreover, high strain rates affect thermally-activated mechanisms in materials and may result in microstructural changes through adiabatic heating, which make them behave perfectly plastic (Zerilli and Armstrong 1987, Lee and Lin 1997, Seo *et al*. 2005). The Split Hopkinson Pressure Bar (SPHB) also known as Kolsky Bar apparatus is commonly applied in uniaxial loading configurations in tension, torsion and compression for high-strain-rate tests (Gray 2000, Ramesh 2008). The apparatus consists of the incident/input bar, the transmitted/output bar and the striker bar. The classical SHPB is shown in Figure 2.35. The incident and transmitted bars are usually made of steel or Inconel. The striker bar is generally made from the same material and cross-sectional area as the incident and transmitted bars.

© Central University of Technology, Free State

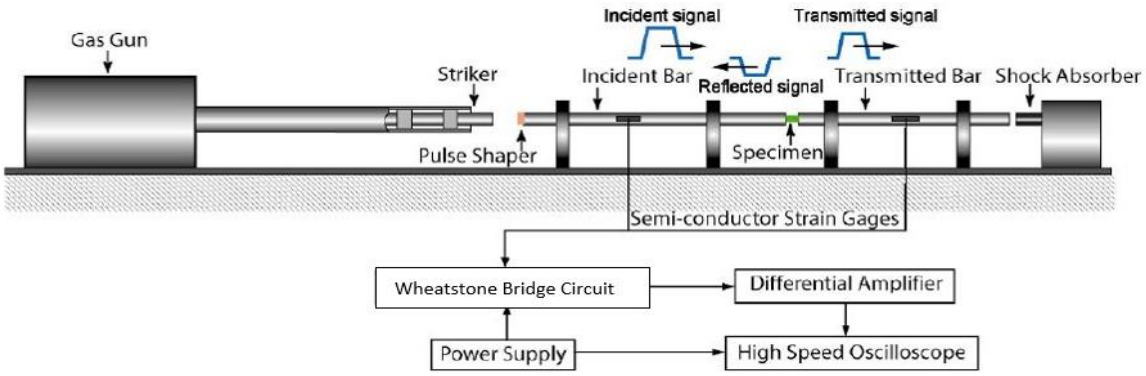

Figure 2-35. A classical schematic diagram of a compressive SHPB setup (Gray 2000).

The mechanical support with bearings in the SHPB provide accurate uniaxial alignment and enables free axial motion while preventing transverse motion of the loading axis. The test specimen is normally sandwiched between the incident and transmitted bars. During testing, the striker bar (see Figure 2-35) is fired from a pneumatic launcher/gas gun and impacts the free end of the incident bar at a high velocity.

The impact of the striker bar on the incident bar sends a compressive stress wave/incident wave towards the specimen and moves the bars with the specimen towards the shock absorber shown in Figure 2-36. Upon reaching the specimen, the incident wave becomes partially reflected due to impedance mismatch of the bar-specimen interface, and partially transmitted to the transmitted bar. A typical propagation of the waves across the loading bars and specimen is illustrated in a time-position diagram is shown in Figure 2-37.

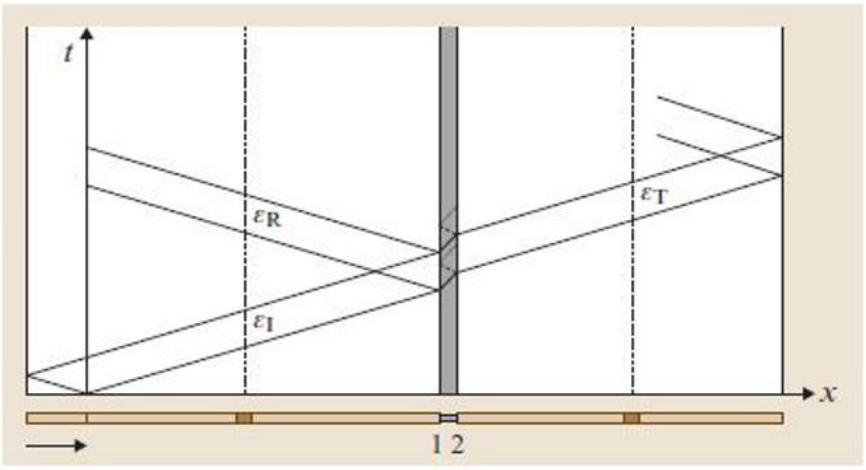

Figure 2-36. Wave propagation diagram showing the propagation of stress waves through the bars and specimen in SHPB apparatus (Ramesh 2008).

© Central University of Technology, Free State

The symbols ε_I, ε_R and ε_T in the figure denote the incident, reflected and transmitted waves, respectively. Upon the application of the impact load, reverberation of reflected waves occur across the length of the specimen, due to differences of impedance at both bar-sample interfaces, until the stress build-up is sufficient to cause plastic deformation (Gray 2000).

The strain in the incident and transmitted bars is measured by strain gauges that are attached at the centre of the surface of each bar such that the incident and reflected waves do not overlap (Ramesh 2008). The change in resistance of the strain gauges is measured by a Wheatstone bridge circuit which converts the strain in the bars to voltage signals displayed on an oscilloscope. Using the known strain gauge data (voltage, resistance and gauge factor), the voltage signals are converted into strain as follows (Gray 2000):

$$Strain = \frac{Gauge\ resistance\ x\ Voltage\ reading}{Calibrated\ voltage\ x\ Gauge\ factor(Calibrated\ resistance + Gauge\ resistance)} \qquad 2\text{-}55$$

Using the measured strain data and the theory of one-dimensional elastic wave propagation in a cylindrical specimen, the equations for determining the specimen stress, strain and strain rate are obtained. These derivations are presented in Appendix B and lead to the following equations for determining the stress, strain and strain rate:

$$\sigma_s = \frac{EA_0\epsilon_T}{A_s} \qquad 2\text{-}56$$

$$\dot{\epsilon}_s = \frac{2\epsilon_R C_0}{l_s} \qquad 2\text{-}57$$

$$\epsilon_s = 2\frac{C_0}{l_s}\int_0^t \epsilon_R\, dt \qquad 2\text{-}58$$

where the symbols A_o , A_s, l_s, C_0 and E stand for the cross-sectional area of the bars, initial cross-sectional area of the specimen, length of the specimen, bar wave velocity and Youngs's modulus of the bars, respectively.

To ensure accurate measurements of wave signals, two aspects must be considered (Song and Chen 2006, Ramesh 2008):

- The incident and transmitter bars should have high slenderness ratio of length (l_b) to diameter (D_d). Classical setups consist of (l_b / D_d) of the order 100 to ensure axial stress distribution over the bar cross sections (Ramesh 2008).

© Central University of Technology, Free State

- The slenderness ratio of cylindrical test specimens, (l_s/ d_s), should be in range of 0.5 to 1. The range represents an optimal balance between reducing the longitudinal inertia effect by using a shorter sample and reducing radial inertia and interface friction effects by using thinner specimens (Song and Chen 2006).

Stress triaxiality in this method normally arises due to friction at the specimen/bar interfaces and leads to spuriously stiff solutions (Bertholf and Karnes 1975). Lubricants are normally applied at the interfaces of the bars and specimen to minimise friction. Surface friction between the bars and the specimen is dependent on several factors such as the materials used for the specimen and bars, magnitude of impact, conditions of the specimen/bar interface, lubricant used and temperature (Ramesh 2008). The most frequently used lubricants for the SHPB test include molybdenum disulphide and lithium greases (Wang and Lenard 1992).

The analysis of dynamic stress and strain involves important assumptions of uniform stress and strain rate. The incident, reflected and transmitted stress waves change due to dispersion as they travel through the pressure bars and specimen (Ramesh 2008). Ignoring the effects of dispersion allows the assumption of uniform stress and strain rate to be made. However, two dispersion effects of superimposition of oscillations in the loading of the specimen remain a critical factor. Moreover, shorter stress pulses with rapid rise periods, lead to greater dispersion due to a greater high-frequency content and wider range (Song and Chen 2006, Ramesh 2008). The SHPB setup is normally modified to minimise the effects of dispersion. Dispersion can be minimised through the use of pulse-shaping materials or buffer materials placed between the striker and incident bars (Frew *et al.* 2002, Ramesh 2008), as shown in Figure 2-38.

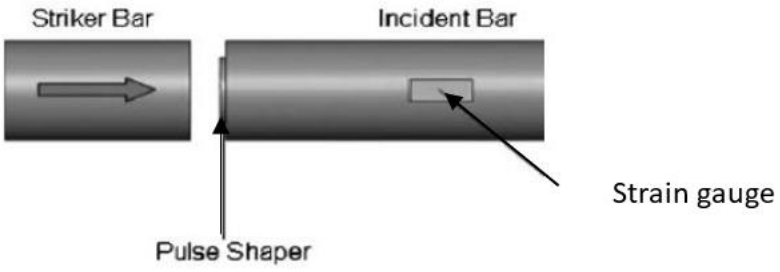

Figure 2-37. A thin metal specimen attached to the incident bar for pulse shaping (Frew et al. 2002).

© Central University of Technology, Free State

This leads to the shaping of the incident pulse with a longer rise period due to elastic and plastic deformation of the thin metal insert and thus lowers dispersion. Some modifications of the SHPB apparatus allow for high-temperature experiments. Heating the test specimen, commonly inside a tube furnace, whilst in contact with the incident and transmitter bars is the most frequently method for high- temperature SHPB experiments. Often this allows a strong temperature gradient to develop within the bars. The effects of temperature gradient are usually accounted for by adjusting the longitudinal wave velocity where the Young's modulus of the bar material is expressed as a factor dependent on temperature. To carry out an adjustment using this approach, the rise in temperature in the pressure bars must be measured/estimated (Ramesh 2008). The limitations of such a technique is the drop in temperature in the specimen due to the heat conduction through the bars. Usually, an insulating layer is placed between the pressure bars and test specimen to counter this shortcoming (Song and Chen 2006). A more recently developed method involves heating the specimen in a furnace, and then bringing it into contact with the pressure bars just prior to the SHPB high-temperature testing. A synchronised mechanical actuation system aligns the specimen with the loading bars after heating and launches the striker bars as soon as the bars close onto the sample (Frew *et al.* 2002). The advantage of this setup is reduced temperature gradients in the bars. However, the major design issue is the amount of time in which the pressure bars are in contact with the specimen before impact. Over this contact period, temperature gradients develop in the specimen, and overall, the temperature of the specimen decreases by an amount that is mostly never recorded (Ramesh 2008). However, this can be taken care of by considering the amount of time between placing the specimen and firing the bars and thereafter adjusting for this drop in temperature.

2.12 SUMMARY

The aim of this chapter was to provide a review of various topics that are relevant to the current research work. Metal AM technologies were briefly introduced and their operation discussed. The various microstructures produced upon the heat treatment of the as-built Ti6Al4V(ELI) alongside their mechanical properties were presented and discussed. It was evident from discussion that AM Ti6Al4V(ELI) exhibits a wide range of mechanical properties due to a wide variation of microstructure upon heat treatment. Moreover,

© Central University of Technology, Free State

various modelling approaches to predicting the mechanical properties of alloys such as Ti6Al4V were presented and discussed. It was clear from these discussions that the use of ANNMs can offer accurate correlation between the microstructures and mechanical properties of the Ti6Al4V alloy. However, the ANNMs are supervised systems that require input of huge amounts of data arising from the experimental work or existing literature. This makes the use of such models very expensive and unreliable, the latter in cases where the required input data is scant. The alternative use of constitutive numerical models that are based on specific mathematic equations was discussed. The capability of these existing constitutive models in predicting the mechanical properties of materials is questioned as most of the models are empirical in nature. Furthermore, in the few analytical models discussed, the microstructural aspects of materials, such as dislocations and grain sizes, are not explicitly accounted for. This limits the use of such models to predict the deformation properties of AM Ti6Al4V for a wide range of microstructures.

The theory of plasticity and the radial return method of computing the plastic strain components have been introduced and briefly discussed. The implementation of a material user subroutine in ABAQUS was also introduced and the implicit and explicit methods of integration applied to update variables discussed. The theory of the SHPB equipment devised for high-strain-rate testing was also discussed in this chapter with its modification for high-temperature tests also briefly given.

© Central University of Technology, Free State

2.11 REFERENCES

1. ABAQUS. 2006b. *ABAQUS User Subroutines Reference Manual*.
2. ABAQUS.2020. Documentation. https://help.3ds.com/2020/English/DSSIMULIA_Established/SIMULIA_Established_FrontmatterMap/HelpViewerDS.aspx?version=2020&prod=DSSIMULIA_Established&lang=English&path=SIMULIA_Established_FrontmatterMap%2fsim-r-DSDocAbaqus.htm&ContextScope=all (accessed on 12th Nov 2020).
3. Ahmed, T., Rack, H.J. 1998. Phase transformations during cooling in α+β titanium alloys. *Materials Science and Engineering: A,* 243 (1), pp.206–211. https://doi.org/10.1016/S0921-5093(97)00802-2
4. Arcam EBM. 2019. *Additive manufacturing machines.* https://www.ge.com/additive/additive-manufacturing/machines (accessed on 23rd May 2019).
5. Arcella, F.G., Abbott, D.H., House, M.A. Titanium alloy structures for airframe application by the laser forming process. *AIAA-2000-1465, 41st AIAA/ASME/ASCE/AHS/ASC Structures, Structural Dynamics, and Materials Conference and Exhibit,* Atlanta, Georgia, 3rd-4th April 2000.
6. ASM International. 1994. *Material Properties Handbook: Titanium alloys*. Material Park, OH. ISBN: 978-0-87170-481-8.
7. Australian Transport Safety Bureau, Canberra ACT. 2002. Examination of a failed Rolls-Royce RB211-524 turbofan engine. Boeing Commercial Aircraft Group, 747-436, G-BNLD, *Technical Analysis Rep. No. 20/02*, *Occurrence File No. BO/200200646*, *Australian Transport Safety Bureau,* Canberra, Australia.
8. Bailey, N.S., Katinas, C., Shin Y.C. 2017. Directed energy deposition of AISI H13 tool steel powder with numerical modelling of solid phase transformation, hardness, and residual stresses. *Journal of Material Processing Technology,* 247, pp.223–233.
9. Banerjee, D., Williams, J.C. 2013. Perspectives on titanium science and technology. *Acta Materialia* 61(3), pp.844–879. https://doi.org/10.1016/j.actamat.2012.10.043
10. Bertholf, L.D., Karnes, C.H. 1975. Two-dimensional analysis of the split Hopkinson pressure bar system. *Journal of Mechanics and Physics of Solids*, 23(1), pp.1–19. https://doi.org/10.1016/0022-5096(75)90008-3

© Central University of Technology, Free State

11. Birkholz, M. 2006. Thin film analysis by X-ray scattering. *Journal of Applied Crystallographic*, 8(6), pp.925–926. https://doi.org/10.1107/S0021889806034698
12. Boris, V. Novel designs of turbine blades for additive manufacturing. *Proceedings of ASME Turbo Expo: Turbine Technical Conference and Exposition*, Seoul, South Korea, 13th–17th June 2016.
13. Calamaz, M., Coupard, D., Girot, F. 2008. A new material model for 2D numerical simulation of serrated chip formation when machining titanium alloy Ti6Al4V. *International Journal of Machine Tool Manufacturing*, 48, pp.275–288.
14. Callister, W.J. 2007. *Materials science and engineering*. 7th Edition, Wiley Publisher, New York, USA, pp.*39–129*.
15. Caroll, B., Todd A., Beese, M. 2015. Anisotropic tensile behaviour of Ti6Al4V components fabricated with directed energy deposition additive manufacturing. *Acta Materialia,* 87, pp.309–320.
16. Collins, P.C., Haden, C.V., Ghamarian, I., Hayes, B.J., Ales, T. 2014. Progress toward an integration of process-structure-property-performance models for 'three-dimensional (3-D) printing' of titanium alloys. *JOM* 66(7), pp.1299–1309. https://link.springer.com/article/10.1007%2Fs11837-014-1007-y
17. Cullity, B.D. 1978. *Elements of X-Ray Diffraction.* 2nd Edition, Addison-Wesley Publishing Company Inc., Philippines, p.96.
18. Dieter, E.G. 1986. Mechanical Metallurgy. 3rd Edition, *Materials science and engineering series*, McGraw-Hill, New York, USA, p.184.
19. DM3D Technology. 2019. The next generation of additive manufacturing. https://www.dm3dtech.com/technology (accessed on 23rd May 2019).
20. Dragomir, I.C., Ungar, T. 2002. Contrast factors of dislocations in the hexagonal crystal system. *Journal of Applied Crystallography,* 35, pp.556–564. https://doi.org/10.1107/S0021889802009536
21. Dragomira, T., Lia, D.S., Castello, B., Garmestania, H., Snydera, R.L. 2005. Evolution of dislocation density and character in hot rolled titanium determined by X-ray diffraction. *Material Characterization,* 55(1), pp.66–74.

© Central University of Technology, Free State

22. Dutta, B., Froes, F. 2014. Additive manufacturing of titanium alloys. *Advanced Material Research,* 1019, pp.19–25. https://doi.org/10.4028/www.scientific.net/AMR.1019.19
23. EBSD. 2019. *Electron Backscatter Diffraction Analysis*. https://nano.oxinst.com/products/ebsd/
24. EOS GmbH. 2019. *Metal 3D printers.* https://www.eos.info/en/additive-manufacturing/3d-printing-metal/eos-metal-systems (accessed on 23rd May 2019).
25. EOS material data sheet (2008). http://www.crpm.co.za/wpcontent/uploads/2017/07/M280-Titanium_Material_data_sheet_10-11_en.pdf (accessed on 12th June 2018).
26. Fischer, C., Antony, C. 2007. *Introduction to contact mechanics*. 2nd edition, Springer Science Business Media, New York, p.36.
27. Frazier, W.E. 2014. Metal additive manufacturing: A review. *Journal of Material Engineering and Performance,* 23(6), pp.1917–1928.
28. Frew, D.J., Forrestal, M.J., Chen, W. 2002. Pulse shaping techniques for testing brittle materials with a split Hopkinson pressure bar. *Experimental Mechanics*, 42(1), pp.93–106.
29. Fridtjov, I. 2008. *Continuum mechanics*. Springer-Verlag, Berlin Heidelberg. ISBN-3-540-74297-2, pp.123–164.
30. Galarraga, H., Lados, D.A., Dehoff, R.R., Kirka, M.M., Nandwana, P. 2016. Effects of the microstructure and porosity on properties of Ti-6Al-4V ELI alloy fabricated by electron beam melting (EBM). *Additive Manufacturing,* 10, pp.47–57. https://doi.org/10.1016/j.addma.2016.02.003
31. Gaytan, S.M., Murr, L.E., Medina, F., Martinez, E., Lopez, M.I., Wicker, R.B. 2009. Advanced metal powder-based manufacturing of complex components by electron beam melting. *Materials Technology*, 24 (3), pp.180 –190. https://doi.org/10.1179/106678509X12475882446133
32. GE Aviation 2019. The GE brief. https://www.ge.com/news/reports/ge-brief-june-18-2019 (accessed on 23rd June 2019).
33. GE. 2005. Smart fan containment system. *Rep. No. NASA/CR-2005-213969*, NASA Glenn Research Center, Cleveland. http://gltrs.grc.nasa.gov. (Accessed on 8th July 2019).

© Central University of Technology, Free State

34. Gokuldoss, P.K., Kolla, S., Eckert, J. 2017. Additive manufacturing processes: selective laser melting, electron beam melting and binder jetting-selection guidelines. *Materials, 10 (6), p.672. https://doi.org/10.3390/ma10060672*
35. Gray, G.T. 2002. Classic Split-Hopkinson Pressure Bar Testing. Materials Park, *OH: ASM International*, pp.462–476.
36. Hendrixson, S. 2020. Lower Buy-to-Fly Ratios with Near-Net Additive Manufacturing. https://www.mmsonline.com/blog/post/lower-buy-to-fly-ratios-with-near-net-additive-manufacturing (accessed on 18th June 2019).
37. Hibbitt, Karlsson and Sorensen. 2002. *ABAQUS Theory Manual*. ABAQUS 6.3-1 Documentation.
38. Hirth, J.P. 2011. *Dislocations in solids: A tribute to F.R.N. Nabarro*. Revised ed. vol.14, Elsevier Science, Hereford, USA, p.484.
39. Hollomon, J.H. 1945. Tensile deformation. Transactions of the Metallurgical Society of AIME, 162, pp.268-290.
40. Hull, D., Bacon, D.J. 2011. *Introduction to dislocations*. 5th Edition, Elsevier, Boulevard, Oxford, p.13.
41. Jaimie, S, Tiley, M.S. 2002. *Modelling of microstructure property relationships in Ti6Al4V.* Dissertation presented in partial fulfilment of the requirements for the degree Doctor of Philosophy in the Graduate School of the Ohio State University, USA.
42. Johnson, G.R., Cook, W.H. A constitutive model and data for metals subjected to large strains, high strain rates and high temperatures. *Proceedings of the 7th International Symposium on Ballistics,* The Hague, Netherlands 19th – 21st April 1983.
43. Kacher, J., Eftink, B.P., Cui, B., Robertson, I.M. 2014. Dislocation interactions with grain boundaries. *Current Opinion in Solid State and Materials Science,* 18(4) pp.227–243.
44. Kasperovich, G., Hausmann, J. 2015. Improvement of fatigue resistance and ductility of TiAl6V4 processed by selective laser melting. *Journal of Material Processing Technology,* 220, pp.202–214.

© Central University of Technology, Free State

45. Khan, A.S., Sung, S., Kazmi, R. 2004. Quasi-static and dynamic loading responses and constitutive modelling of titanium alloys. *International Journal of Plasticity*, 20, pp.2233–2248. https://doi.org/10.1016/j.ijplas.2003.06.005
46. Klemene, J., Andrej, S. 2016. Estimating the strain rate dependent parameters of the Cowper-Symonds and Johnson-Cook material models using Taguchi arrays. *Journal of Mechanical Engineering*, 62(4) pp.220–230. https://doi.org/10.5545/sv-jme.2015.3266
47. Kniess, C., Cardoso, L., Prates P. 2015. The quantifications of crystalline phases in materials: Applications of Rietveld method. *Sintering – Methods and Products,* In Tech Publisher, London, UK, pp.294–313.
48. Kobryn, P.A., Ontko, N.R., Perkins, L.P., Tiley, J.S. 2006. Additive Manufacturing of Aerospace Alloys for Aircraft Structures. In Cost Effective Manufacture via Net-Shape Processing, *Meeting Proceedings RTO-MP-AVT-139, Paper 3*. Neuilly-sur-Seine, France: RTO, pp.3.1–3.14. Available from: http://www.rto.nato.int/abstracts.asp
49. Kocks, U.F, Mecking, H. 2003. Physics and phenomenology of strain hardening: the FCC case. *Progress in Materials Science,* 48, pp.171–273. https://doi.org/10.1016/S0079-6425(02)00003-8
50. Koike, M., Greer, P., Owen, K., Lilly, G., Murr, L.E., Gaytan S.M., Martinez E., Okabe, T. 2011. Evaluation of titanium alloys fabricated using rapid prototyping technologies electron beam melting and laser beam melting. *Materials,* 4(10), pp.1776–1792. https://doi.org/10.3390/ma4101776
51. Lee, W.S., Lin, M.T. 1997. The effects of strain rate and temperature on the compressive deformation behaviour of Ti-6Al-4V alloy. *Journal of Material Processing and Technology,* 71(2), pp.235–246.
52. Lesuer, D.R. 2000. Experimental investigations of material models for Ti-6Al-4V Titanium and 2024-T3 Aluminum. *Technical report, Federal Aviation Administration*, Aviation Research, Washington DC, USA.
53. Leuders, S., Thöne, M., Riemer, A., Niendorf, T., Torstar, T., Richard, H.A., Maier, H.J. 2013. On the mechanical behaviour of titanium alloy TiAl6V4 manufactured by selective laser melting: fatigue resistance and crack growth performance.

© Central University of Technology, Free State

International Journal of Fatigue, 48, pp.300–307. https://doi.org/10.1016/j.ijfatigue.2012.11.011

54. Lewandowski, J.J., Seifi, M., Salem, A., Beuth, J., Harrysson, O. 2016. Overview of materials qualification need for metal additive manufacturing. *JOM* 68(3), pp.747–764.
55. Leyens, C., Manfred, P.2003. Titanium and titanium alloys: Fundamentals and Application. WILEY-VCH, Germany ISBN 3-527-3053-3, p.6.
56. Leyens, C., Peter, M. 2003. *Titanium and titanium alloys: Fundamental and applications*. Wiley-VCH, Germany, ISBN 3-527-30534-3, pp.1–50.
57. Li, P.H., Guo, W.G., Huang, W.D., Su, Y, Lin, X., Yuan, K.B. 2015.Thermomechanical response of 3D laser-deposited Ti–6Al–4V alloy over a wide range of strain rates and temperatures. *Materials Science and Engineering* A 647, pp.34–42.
58. Li, Z., Hou, C., Huang, M., Ouyang, C. 2009. Strengthening mechanism in micro-polycrystals with penetrable grain boundaries by discrete dislocation dynamics simulation and Hall–Petch effect. *Computation Materials Science,* 46, pp.1124–1134.
59. Liu, Y., Yang, Y., Wang, D. 2016. A study on the residual stress during selective laser melting (SLM) of metallic powder. *International Journal of Advance Manufacturing and Technology,* 87 (1), pp.647–656.
60. Lubliner J., 1990, *Plasticity Theory.* Macmillan Publishing Company, New York, USA, pp.69– 82.
61. Luibov, M., Vasilyev, B., Vladimir, K. 2016. Novel designs of turbine blades for additive manufacturing. *Proceedings of ASME Turbo Expo: Turbine technical conference exposition,* Seoul, South Korea.
62. Lütjering, G., Williams, J.C. 2007. *Titanium: Engineering Materials and Processes Series*, Springer-Verlag Heidelberg Berlin. ISBN 978-3-642-09054-7, pp.125–156.
63. Malefane, L.B., Du Preez, W.B., Maringa, M. 2017. High cycle fatigue properties of as-built Ti6Al4V(ELI) produced by direct metal laser sintering. *South African Journal of Industrial Engineering*, 28(3), pp.188–199. http://dx.doi.org/10.7166/28-3-1861
64. Markovitz, D.D., Katsman, A., Shirizly, A., Bamberger, M. 2015. Microstructure and mechanical properties of heat-treated selective laser melting manufactured

© Central University of Technology, Free State

Ti6Al4V, *Proceeding the ICANM: International Conference & Exhibition on Advanced & Nano Materials, Ottawa, Canada,* 10th – 12th August 2015, pp.33–42.

65. Mayeur, J.R., McDowell, D.L. 2007. A three-dimensional crystal plasticity model for duplex Ti-6Al-4V. *International Journal of Plasticity,* 23(9), pp.1457–1485.
66. Mead*info*. 2019. Surface roughness produced by different manufacturing processes. https://www.meadinfo.org/2009/06/surface-finish-roughness-ra.html (accessed on 12th April 2019).
67. Mercelis, P., Kruth, J.P. 2006. Residual stresses in selective laser sintering and selective laser melting. *Rapid Prototyping Journal,* 12 (5), pp.254–265.
68. Meyer, H.W., Kleponis, D.S. 2001. Modelling the high strain rate behaviours of titanium underdoing ballistic impact and penetration. *International Journal of Impact Engineering*, 26, pp.509–521.
69. Moletsane, G., Krakhmalev, P., Du Plessis, A., Yadroitsava, I., Yadroitsev, I., Kazantseva, I. 2017. Tensile properties and microstructure of direct metal laser-sintered Ti6Al4V(ELI) alloy. *South African Journal of Industrial Engineering,* 2016, 27(3), pp.110–121.
70. Mugwagwa, L., Dimitrov, D., Matope, S., Venter, A.M. Residual stress distributions within components manufactured using selective laser melting. *Proceedings of the 18th Rapdasa Conference*, Durban, South Africa, 7th–10th November 2017.
71. Muiruri, A.M., Maringa, M, du Preez, W.B, Masu, L. 2020. Effects of stress relieving heat treatment on impact toughness of direct metal laser sintering (DMLS) produced Ti6Al4V(ELI) parts. *JOM,* 72, pp.1175–1185.
72. Muiruri, A.M., Maringa, M., du Preez, W.B., Masu, L. Effect of stress relieving heat treatment on high strain rate tensile properties of direct melting laser sintered (DMLS) parts. *Proceedings of 7th International Conference on Competitive Manufacturing (COMA-19)*, Wallenberg Centre (STIAS), Stellenbosch, South Africa, Jan 30th–February 1st, 2019.
73. Mur, F.X.G., Rodriguez, D., Planell, J.A. 1996. Influence of tempering temperature and time on the α'-Ti-6Al-4V martensite. *Journal of Alloys and Compounds*, 234, pp. 287–289.

© Central University of Technology, Free State

74. Nemat-Nasser S., Wei-Guo, G., Vitali, F., Yai-Bei, G. 2001. Dynamic response of conventional and hot isostatically pressed Ti6Al4V alloys: experiments and modelling. *Mechanics of Materials*, 33, pp.425–439.
75. *Oxford Instruments,* EBSD.http://www.ebsd.com/ebsd-explained/principle-components-of-an-ebsd-system (accessed on 3rd May 2019).
76. Peierls, R. 1940. The size of a dislocation. *Proceedings of Physical Society*, 52, pp.34–37.
77. Picu, P.C., Majorell, A. 2002. Mechanical behaviour of Ti6Al4V at high and moderate temperatures – Part II: constitutive modelling. *Materials Science and Engineering:* A, 326, pp.306–316.
78. Pochuev, V.P., Muhin, A.A., Kharkovsky, S.V., Svetlov, I.L. 2006. Cooled turbine blade. (In Russian) // *Ru patent #2267616,* Published on 10th January 2006.
79. Qian, M., Xu, W., Brandt, M., Tang, H. 2016. Additive manufacturing and post processing of Ti6Al4V for superior mechanical properties. *Metallic materials for 3D printing,* 41(10), pp.775–785.
80. Qianli, H., Xujie, L., Xing, Y., Ranran, Z., Zhijian, S., Qingling, F. 2015. Specific heat treatment of selective laser melted Ti6Al4V for biomedical applications. *Frontiers of materials science,* 9(4) pp.373–381.
81. Qiu, C., Adkins, E., Attallah, M. 2013. Microstructure and tensile properties of selectively laser-melted and of HIPed laser-melted Ti6Al4V. *Materials Science and Engineering:* A 578, pp.230–239.
82. Ramesh, K.T. 2008. High Rates and Impact Experiments. In: W.N. Sharpe (Ed.), *Handbook of Experimental Solid Mechanics*, Springer US, Boston, MA, pp.929–960.
83. Ramulu, M., Edwards, P. 2014. Fatigue performance evaluation of selective laser melted Ti–6Al–4V. *Materials Science and Engineering: A,* 598, pp.327–337.
84. Reisgen, U., Olschok, S., Sharma, R., Gach S. 2018. Influence on martensite-start temperature and volume expansion of low-transformation-temperature materials used for residual stress relief in beam welding. *Materials Science & Engineering Technology,* 48 *(12), pp.1276–1282.* https://doi.org/10.1002/mawe.201700159
85. Riznyk, S., Artushenko, A. Aero engine high pressure turbine blade cooling system concept. ASME Turbo Expo: *Turbine Technical Conference and Exposition. American*

© Central University of Technology, Free State

Society of Mechanical Engineers, San Antonio, Texas, USA, 3rd – 7th June 2013. https://doi.org/10.1115/GT2013-95789

86. Rolls-Royce Global Flight. 2015. Building first XWB-97 for Flight Tests. https://www.flightglobal.com/rolls-royce-to-fly-trent-xwb-with-largest-ever-3d-printed-part/115957.article (accessed on 24th June 2019).
87. Rombouts, M., Yu, J., Maes, G., Motmans, F. 2012. Material properties of Ti6Al4V parts produced by laser metal deposition. *Physics Procedia,* 39, pp.416–424.
88. Sames, W.J., List, F.A., Pannala, S., Dehoff, R.R., Babu, S.S. 2016. The metallurgy and processing science of metal additive manufacturing. *International Materials Reviews*, 61(5), pp.315–360. https://doi.org/10.1080/09506608.2015.1116649
89. Semiatin, S.L., Kinsley, P.S., Fagin, P.N., Barker, D.R., Zhang. F. 2003. Microstructure evolution during alpha-beta heat treatment of Ti6Al4V. *Metallurgical and Material Transactions A,* 34 (10), pp.2377–2386.
90. Seo, S., Min, O., Yang. H. 2005. Constitutive equation for Ti6Al4V at high temperatures measured using the SHBP technique. *International Journal of Impact Engineering*, 31, pp.735–754.
91. Sercombe, T., Jones, N., Day, R., Kop, A. 2008. Heat treatment of Ti-6Al-7Nb components produced by selective laser melting. *Rapid Prototyping Journal,* 14 (5), pp.300–304.
92. Shunyu, L., Yung, S. 2019. Additive manufacturing of Ti6Al4V alloy: A review. *Material and Design*, 164, 107552. https://doi.org/10.1016/j.matdes.2018.107552
93. Simonelli, M., Tse, Y.Y., Tuck, C. 2014. The formation of α + β microstructure in as-fabricated selective laser melting of Ti6Al4V. *MRS: The Materials Science of Additive Manufacturing*, 29(17) pp.2028–2035.
94. Singh, G., Sen, I., Gopinath, K., Ramamurty, U. 2012. Influence of minor addition of boron on tensile and fatigue properties of wrought Ti-6Al-4V alloy. *Materials Science and Engineering: A,* 540, pp.142–151. https://doi.org/10.1016/j.msea.2012.01.119
95. Sinha, K.S., Dorbala, S. 2009. Dynamic loads in the fan containment structure of a turban engine. *Journal of Aerospace Engineering*, 22 (3) p.260. https://doi.org/10.1061/(ASCE)0893-1321(2009)22:3(260)

© Central University of Technology, Free State

96. Song, B., Chen, W. 2006. Energy for specimen deformation in a split Hopkinson pressure bar experiment. *Experimental Mechanics,* 46(3), pp.407–410.
97. Stouffer, D.C., Dame, L.T. 1996. *In: Elastic Deformation of Metals: Models, Mechanical Properties and Metallurgy*, John Wiley & Sons Inc., general reference, pp.120–145.
98. Sun, J., Guo, B. 2009. Material flow stress and failure in multiscale machining titanium alloy Ti6Al4V. *International Journal of Advanced Manufacturing Technology*, 41 (7–8), pp.651–659.
99. Sun, Y., Weidong, Z., Yuanfei, H., Xiong, M., Yongqing, Z., Ping, G., Wang, G., Dargusch, S. 2012. Determination of the influence of processing parameter on the mechanical properties of the Ti6Al4V alloy using an artificial neural network. *Computational Materials Science*, 60, pp.239–244. https://doi.org/10.1016/j.commatsci.2012.03.047
100. Sun, Y.Y., Gulizia, S., Fraser, M. 2016. The influence of as-built surface conditions on mechanical properties of Ti6Al4V additively manufactured by selective electron beam melting. *JOM*, 68(3), pp.791–798.
101. Tammas, W.S., Zhao, H., Léonard, F., Derguti, F., Todd, I., Prangnell, P.B. 2015. XCT analysis of the influence of melt strategies on defect population in Ti6Al4V components manufactured by selective electron beam melting. *Materials Characterization, 102,* pp.47–61.
102. Tao, P., Jiangwei, Z., Huaixue, L., Quandong, H., Shuili, G., Qingyan, X. 2019. Microstructure, mechanical properties and constitutive models for Ti6Al4V alloy fabricated by selective laser melting (SLM), Metals, 9(4) pp.447. https://doi.org/10.3390/met9040447
103. Taylor, G.I. 1934. The mechanism of plastic deformation of crystals. Part 1– Theoretical. *Proceeding of the Royal Society of London. Series A*, 145(855), pp.362–387. https://doi.org/10.1098/rspa.1934.0106
104. Ter Haar, G., Becker, T.H. 2018. Selective laser melting produced Ti6Al4V: Post-process heat treatments to achieve superior tensile properties. *Materials* 11(1), p.146. https://doi.org/10.3390/ma11010146

© Central University of Technology, Free State

105. Thomas, H.S. 2012. *The use of diffraction peak profile analysis in studying the plastic deformation of metals*. A thesis submitted to the University of Manchester for the degree of Ph.D. in Faculty of Engineering and Physical Sciences.
106. Ungar, T. 2004. Microstructural parameters from X-ray diffraction peak broadening. *Scripta Materialia,* 51(8), pp.777–781. https://doi.org/10.1016/j.scriptamat.2004.05.007
107. Ungar, T., Borbely, A. 1996. The effect of dislocation contrast on X-ray line broadening: A new approach to line 665 profile analysis. *Applied Physics Letters,* 69(21), 3173. https://doi.org/10.1063/1.117951
108. Ungar, T., Groma, I., Wilkens, M. 1989. Asymmetric X-ray line broadening of plastically deformed crystals. II. 680 Evaluation procedure and application to [001] - Cu crystals. *Journal of Applied Crystallography*, 22, pp.26–34. https://doi.org/10.1107/S0021889888009720
109. Uriondo, A., Esperson-Miguez, M., Perinpanyangam, S. 2015. The present and future of additive manufacturing in aerospace sector; A review of important aspects. *Journal of Aerospace Engineering,* 229(11), pp.2132–2147. https://doi.org/10.1177/0954410014568797
110. Vilaro, T., Colin, C., Bartout, J.D. 2011. As-fabricated and heat-treated microstructures of the Ti-6Al-4V alloy processed by selective laser melting. *Metallurgical and Materials Transactions* A, 42(10), pp.3190–3199. https://link.springer.com/article/10.1007/s11661-011-0731-y
111. Vrancken, B., Thijs. L., Kruth, J.P. 2012. Heat treatment of Ti6Al4V produced by Selective Laser Melting: Microstructure and mechanical properties. *Journal of Alloys and Compounds,* 541, pp.177–185.
112. Wang, F., Lenard, J.G. 1992. An experimental study of interfacial friction-hot ring compression. *Journal of Engineering Materials and Technology,* 14(1), pp.13–18. https://doi.org/10.1115/1.2904133
113. Warren, B.A., Averbach, B.L. 1952. The separation of cold-work distortion and particle size broadening in X-ray 678 patterns. *Journal of Applied Physics,* 23, 497. https://doi.org/10.1063/1.1702234
114. Weidong, Z., Sun, Y., Yuanfei, H., Yongqing, Z., Gui, W., Matthew, S.D, Ping, G. 2011. Modelling the correlation between microstructure and the properties of the Ti6Al4V

© Central University of Technology, Free State

alloy based on an artificial neural network. *Materials Science and Engineering*: A, 528(29), pp. 8757–8764. https://doi.org/10.1016/j.msea.2011.08.059

115. Wilkens, M. 1970. Theoretical aspects of kinematical X-ray diffraction profiles from crystals containing dislocation distributions. In: *Fundamental Aspects of Dislocation Theory* Simmons, J.A.; deWit, R.; Bullough, R., National Bureau of Standards, Washington, DC, USA, 1970; vol. II, pp.1195–1219.
116. Wilkins, M.L. 1963. Calculations of elastic- plastic flow, Tech rep., Alder, B.(Ed), *Methods in Computations Physics*, vol.3, Academic Press, pp.211–263.
117. Williamson, G.K., Hall, W.H. 1953. X-ray line broadening from filed aluminium and wolfram. *Acta Metallurgica*, 1(1), pp.22–31. https://doi.org/10.1016/0001-6160(53)90006-6
118. Wysocki, B., Maj, P., Sitek, R., Buhagiar, J., Kurzydłowski, K., Święszkowski, W. 2017. Laser and electron beam additive manufacturing methods of fabricating titanium bone implants. *Applied Science,* 7 (7), 657. https://doi.org/10.3390/app7070657
119. Yadroitsev, I., Krakhmalev, P., Yadroitsava, I. 2014. Selective laser melting of Ti6Al4V alloy for biomedical applications: Temperature Monitoring and Microstructural Evolution. *Journal of Alloys and Compounds,* 583 pp.404–409. http://dx.doi.org/10.1016/j.jallcom.2013.08.183
120. Yang, J., Hanchen, Y., Yin, J., Ming, G., Zemin, W., Xianoyan, Z. 2016. Formation and control of martensite in Ti6Al4V alloy produced by selective laser melting. *Material and Design,* 108, pp.308–318.
121. Yang, Y., Liu, Y., Chen, J., Wang, H., Zhang, Z., Lu, Y. 2017. Crystallographic features of α variants and β phase for Ti6Al4V alloy fabricated by selective laser melting. *Materials Science and Engineering:* A, 707, pp.548–558. https://doi.org/10.1016/j.msea.2017.09.068
122. Zadpoor, A. 2018. Frontier of additively manufactured metallic materials. *Materials*, 11 (9), 1566. https://doi.org/10.3390/ma11091566
123. Zaefferer, S. 2007. On the formation mechanisms, spatial resolution and intensity of backscatter Kikuchi patterns. *Ultramicroscopy,* 107 (2–3), pp.254–266.
124. Zener, C., Hollomon, J.H. 1944. Effect of strain rate upon plastic flow of steel. Journal of Applied Physics, 15(1), pp. 22-32. *https://doi.org/10.1063/1.1707363*

© Central University of Technology, Free State

125. Zerilli, F., Armstrong, R. 1987. Dislocation-mechanics-based constitutive relations for material dynamics calculations. *Journal of Applied Physics*, 61, pp.1816–1825.
126. Zhang, Z., Jun, T.S., Britton, T.B., Dunne, F.P. 2016. Determination of Ti-6242 α and β slip properties using micro-pillar test and computational crystal plasticity. *Journal of the Mechanics and Physics of Solids*, 95, pp.393-410. https://doi.org/10.1016/j.jmps.2016.06.007
127. Zheng, Z., Waheed S., Balint, D., Dunne, F. 2018. Slip transfer across phase boundaries in dual phase titanium alloys and effect on strain rate sensitivity. *International Journal of Plasticity,* 104, pp.23–38. https://doi.org/10.1016/j.ijplas.2018.01.011

© Central University of Technology, Free State

CHAPTER 3 – MATERIALS AND METHODS

3.1 INTRODUCTION

To verify and validate microstructural-based constitutive laws that can accurately predict the yield strength and subsequent flow stress of DMLS Ti6Al4V(ELI) over a wide range of field variables, some experimental tests were designed. These tests were divided into three main areas that include:

(i) Production of test samples and generation of various microstructures of the alloy by heat treatment.

(ii) Microstructural characterisation – quantification of important microstructural features.

(iii) Design of mechanical tests that were used to generate stress-strain curves under a wide range of field-state variables (strain rate and temperature).

3.2 PRODUCTION OF TEST SPECIMENS AND HEAT TREATMENTS

The test samples used for this work were fabricated from gas-atomised spherical Ti6Al4V(ELI) (ASTM grade 23) alloy powder, supplied by TLS Technik GmbH, Germany, through the DMLS AM process. The alloy powder had an average diameter of < 40 µm. The chemical composition of the powder, as determined in Thejane *et al.* (2017), is shown in Table 3-1 and complied with the ASTM F3001-14 standard. The samples were fabricated in an EOSINT M 280 DMLS machine with parameters shown in Table 3-2. This optimised set of parameters was selected based on previous research carried out with this equipment and its process capability to attain superior solid Ti6Al4V(ELI) products (Els 2016). A back-and-forth raster scanning with rotated stripe pattern, having a shift angle of 67° after each layer, was used in the production of specimens. A schematic illustration of the scanning pattern is shown in Figure 3-1.

Table 3-1. Chemical composition of Ti6Al4V(ELI) alloy powder supplied by TLS Technik GmbH (wt.%) as determined in Thejane et al. (2017) and that of ASTM F3001-14

Element	Al	V	Fe	O	C	N	H	Ti
Composition (wt.%)	6.34	3.944	0.25	0.082	0.006	0.006	0.001	Bal.
ASTM F3001-14	5.50-6.50	3.50-4.50	<0.25	<0.13	<0.08	<0.05	<0.012	Bal.

© Central University of Technology, Free State

Table 3-2. EOSINT M 280 DMLS processing parameters

Processing variable	Value
Laser power setting	175 W
Laser diameter	80 µm
Hatch spacing	100 µm
Layer thickness	30 µm
Scanning speed	1400 mm/s

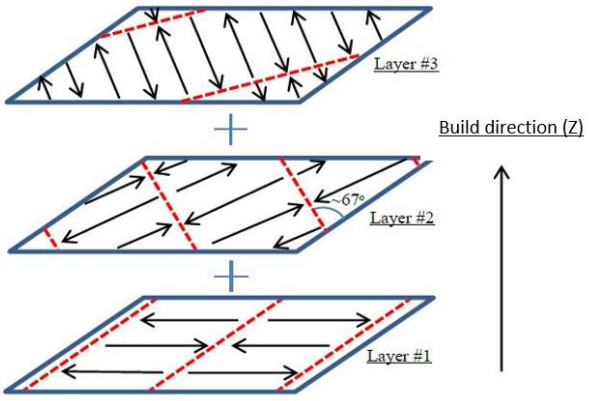

Figure 3-1. Schematic diagram of the strip-scan pattern used in the EOSINT M 280 system showing raster scan vectors (arrows) within each stripe (each dashed line). For every new layer, the stripes rotate by 67 ° compared to the previous layer.

During the fabrication process, each layer section was initially offset about 100 µm from the external edges, forming an internal area. The laser initially scans this region with parallel to-and-fro scan vectors. It then scans along the offset border and the outer border of the part to improve the component surface finish and reduce the number of defects near the surface of the component.

The DMLS process takes place in a chamber filled with argon gas to deplete the oxygen level to 500 ppm or less as well as other impurities (EOSINT M 280 2010, Analox Sensor Technology 2019). In other words, this gas helps to create an inert environment suitable for DMLS. The oxygen level in the chamber during the melt process needs to be minimised, as titanium is highly reactive with oxygen at process temperatures. Oxygen enrichment in titanium causes embrittlement and reduces fatigue life and toughness due to formation of an alpha-case, an oxygen enriched region directly beneath the surface (Bauristhene *et al.* 2013). Other benefits of the inert atmosphere during the melt process include reducing the fire hazard by making combustible dust inert (Analox Sensor Technology 2019).

© Central University of Technology, Free State

A total of 24 cylindrical specimens, each with diameter and length of 6 mm and 80 mm, respectively, were fabricated for use in the present research. A photographic image of typical manufactured specimens of DMLS Ti6Al4V(ELI) on the machine table is shown in Figure 3-2.

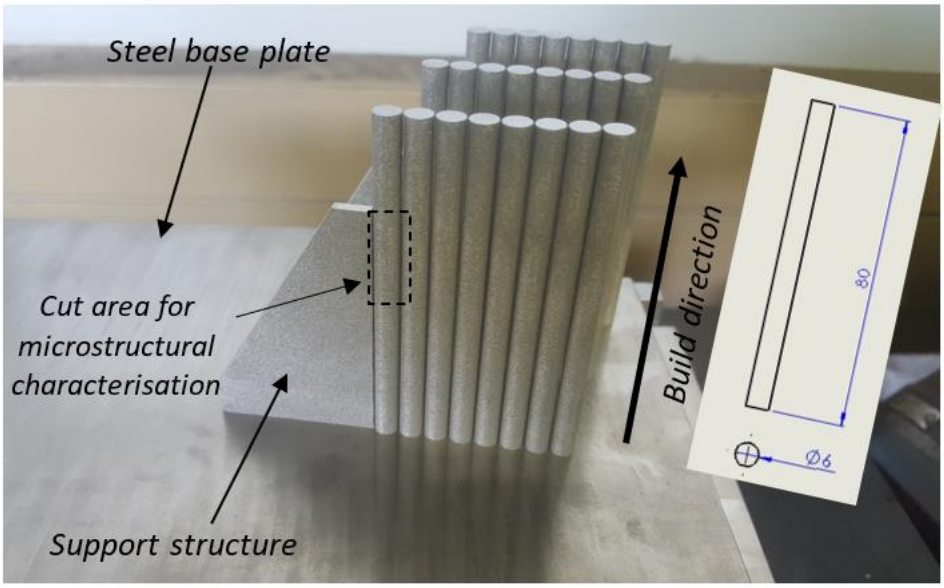

Figure 3-2. A photographic image showing the manufactured test specimens on the EOS M 280 machine table. The insert schematic drawing shows the specifications of the specimens in millimetres.

The manufactured specimens for microstructural characterisation and experimental tests were subdivided into five groups, designated hereinafter as samples A, B, C, D and E. Among these five groups of as-built samples, samples B, C, D and E were further heat-treated in a SuperSeries™ vacuum furnace system Model SS12-24/13MX with a horizontal vacuum chamber. Samples B were just stress-relieved, while samples C, D and E were first stress-relieved and subsequently heat-treated at different high temperatures to allow for microstructural transformation. The stress-relieving heat treatment was executed in a vacuum chamber at a temperature of 650 °C, with a residence time of 3 hours, and thereafter these specimens were furnace-cooled (FC) to room temperature. The subsequent heat-treatment cycles for samples C, D and E are summarised in Table 3-3, together with the values obtained of the cooling rate extracted from the furnace heat-treatment profile shown in Figure 3-3.

© Central University of Technology, Free State

Table 3-3. Heat-treatment strategies and sample designations

Designation	Temperature (℃)	Residence Time (h)	Cooling rate
A	As-built	-	-
B	650	3 h	FC
C	800	2.5 h	CC
D*	940 and 750	2.5 h and 2 h	CC
E	1020	2.5 h	CC

*duplex annealed, FC-Furnace cooled, CC-controlled cooling.

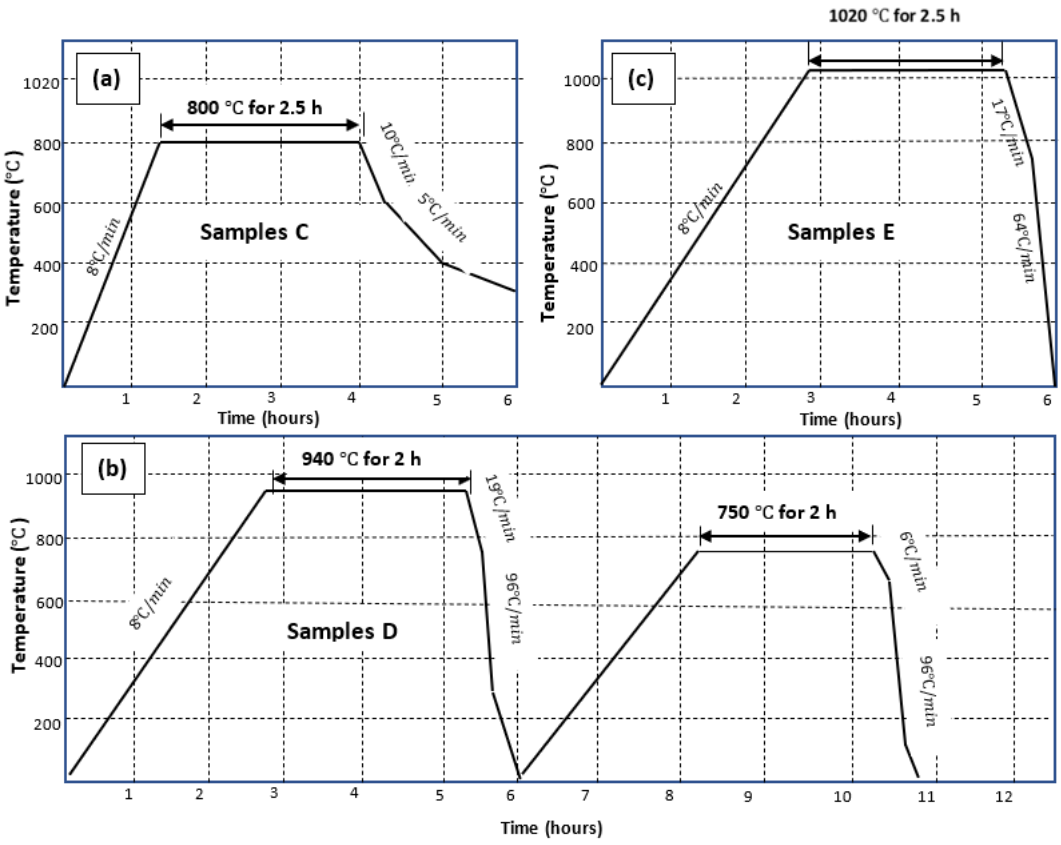

Figure 3-3. Heat-treatment cycles for high-temperature-annealed DMLS Ti6Al4V(ELI) for (a) samples C, (b) samples D and (c) samples E, following initial stress-relieving heat treatment.

Cooling rates affect the growth of α-laths for temperatures just below, and any temperature above the β-transus temperature (980 ℃) (Yang *et al.* 2017), including formation of a martensitic microstructure for very rapid cooling. However, the cooling rate has been shown to have minimal effect on α growth for temperatures near and below the Ms temperature (780 ℃) (Ahmed and Rack 1998). Therefore, samples C that were heated slightly above the Ms temperature were cooled at the furnace-cooling rate, which was relatively lower, obtained by switching off the furnace after a set residence time and

© Central University of Technology, Free State

allowing the chamber to then cool to room temperature. The higher cooling rates for samples D and E were achieved by an accelerated stream of argon gas through the furnace chamber. The initial slower cooling rates, as shown in Figure 3-3(d) and (e), ensured there was sufficient grain growth, while slightly higher cooling rates thereafter ensured minimal excessive coarsening of the grains formed during cooling, which could otherwise have led to lower strength of the final microstructure. It is pertinent to note that samples A and B were used as reference material and only microstructural analysis was performed on them. On the other hand, samples C, D and E were used for microstructural analysis and for mechanical tests (to be discussed later in this chapter).

3.3 MICROSTRUCTURAL CHARACTERISATION

The non-heat-treated samples (samples A) and heat-treated samples (samples B, C, D and E) for microstructural analysis were cut from the middle area along the height of the samples. Small pieces, with a height of 12 mm, were cut through the diameter from this area (see Figure 3-2) of the samples and then sectioned into halves across the diameter in the build direction. The cutting was executed using an electrical discharge machine (wire cutting). The cut surfaces were then mounted using a Citopress mounting machine, where the specimens were placed in a mounting cylinder together with Multifast resin (conductive Bakelite). The mounting was followed by grinding and chemical-mechanical polishing in the four steps, as shown in Table 3-4.

Table 3-4. Grinding and polishing procedures

Process	Wheel/Cloth	Lubricant	Force	Speed	Time
Plane grinding	320 Grit SiC	Water	25 N	300 rpm	1.4 min
Fine grinding	MD- Largo	DiaPro-Largo- 9 µm diamond	30 N	150 rpm	5.0 min
Fine grinding	MD-Mol	DiaPro Mol- 3 µm diamond	25 N	150 rpm	2.2 min
Polishing	MD-Chem	Colloidal silica (OP-S)/ water	20 N	150 rpm	1.5 min

Finally, chemical-mechanical polishing using a mixture of colloidal silica (OP-S) and water on an MD-Chem cloth was carried out. The use of water in this step ensures a constant removal of the reaction product between the titanium and silica suspension, thus ensuring no mechanical deformation on the surface. The polished surfaces were then cleaned individually under tap water and thereafter dried using a stream of compressed air. For the

© Central University of Technology, Free State

initial microstructural investigation with an optical microscope, the surfaces were etched in an ESCO Ductless Fume Hood, using a solution of Kroll's reagent that is commonly used for commercial titanium alloys. The chemical composition of the Kroll's reagent used was:

- 2 ml of HF
- 92 ml of H_2O
- 6 ml of HNO_3

The samples for electron backscatter diffraction (EBSD) analysis were not etched to delineate the grain boundaries, since in EBSD the grain boundaries are delineated by processing of orientation measurement data.

A ZEISS Axio Scope A1 optical microscope equipped with Axio Vision SE6E software was used to capture the optical images of etched samples. Further detailed information regarding the microstructures was obtained via a scanning electron microscope (SEM) equipped with an EBSD detector and through X-ray diffraction (XRD) techniques. The two techniques are discussed here.

3.3.1 Electron backscatter diffraction (EBSD)

Texture analysis and grain-size distribution of the samples were studied, examined and measured using a JEOL JSM-7001F SEM that was also equipped with an EBSD detector as well as other analytical detectors such as an energy dispersive X-ray spectrometer (EDS) and a wavelength dispersive X-ray spectrometer (WDS).

The EBSD system was equipped with a low-light-sensitive camera (CCD) and HKL Channel 5 acquisition and data manipulation software. The mounted samples were glued onto a holder pre-tilted at an angle of 70° from the horizontal towards the EBSD detector. This angle is normally used to optimise both the contrast in the diffraction pattern and the fraction of electrons backscattered from the sample (Oxford Instruments 2019). Prior to setting up for acquisition of EBSD scans, it was important to ensure optimal selection of certain parameters that influence the quality of material characterisation. Basically, EBSD data is collected using a sampling grid and the user must specify both the size of the grid (horizontally and vertically) and the spacing between measurement points; a process termed as step size. The combination of these parameters determines the total number of

© Central University of Technology, Free State

acquisition points for a given scan. Obviously, the number of points in a scan plays a critical role regarding the time required to collect the data.

The number of grains measured is defined by the scan area and the grain size, however the number of points per grain is defined by the step size. The ASTM E2627 (2010), the standard for determining the average grain size of polycrystalline material using EBSD, requires the setup of the scan in such a way that the average grain contains about 500 points. A measurable critical number of grains are significant for quantitative texture and grain-size analysis. Increasing the number of points per grain also helps to better describe the grain size and shape, as well as any interior sub-grain structure. The initial average grain sizes were estimated via visual examination of scanning electron images (SEI) and thereafter the scanning step size for the EBSD map was selected to be between 400–500 nm. The other settings used in EBSD data collection are given in Table 3-5.

Table 3-5. SEM settings used for EBSD data acquisition

Variable	Value
Spot size	3–5 µm
Accelerating voltage	15 kV
Working distance	14 mm
Magnification	200X
Sampling grid (X,Y)	980 x 755 µm
Step size	0.5 µm

The orientation distributions of various microstructures from EBSD were acquired and processed in the HKL Channel 5 software. Post-processing of the EBSD data in the form of CFT files was conducted in MTEX, a Matlab toolbox for analysing and modelling crystallographic textures from EBSD data. Orientation maps were coloured and analysed using the variety of ways presented in section 2.6.1 of Chapter 2 *viz.,* PFs, IPF and Euler maps. The PFs were generated for various key crystallographic orientations for the α phase and β phase of Ti6Al4V. The scattered PFs were used to indicate the orientation of specific crystal planes, while a contouring step clustered the data to indicate regions of similar/preferred orientations. The units for contouring were multiples of density normally abbreviated as MUD (Multiple Unit Density).

© Central University of Technology, Free State

3.3.2 Reconstruction of prior-β grains

As detailed in section 2.4.1 of Chapter 2, the high-temperature β-bcc phase of Ti6Al4V transforms to α-hcp platelets upon cooling down to room temperature. This transformation of β→α obeys the Burgers Orientation Relationship (BOR) of $(110)_\beta//(0002)_\alpha$ and $[111]_\beta//[11\bar{2}0]_\alpha$. During this transformation, the β-phase is obscured by the α-phase formed due to its relatively low volume. Therefore, the retained β-phase may not be sufficient to study and characterise the texture of the β-grains. However, using the BOR it is possible to reconstruct the orientations of the parent grains based solely on the knowledge of the room temperature orientations of the α/α'-phase.

Based on the above, a computer program ARPGE was developed (Cayron 2007) for grain reconstruction using the orientations measured from daughter variants in EBSD scans. The program is written in Python, which is a multi-platform, interpreted and object-oriented language. In this research work, the ARPGE program was used to carry out the automatic reconstruction of the β-phase. The typical appearance of the program is shown in Figure 3-4.

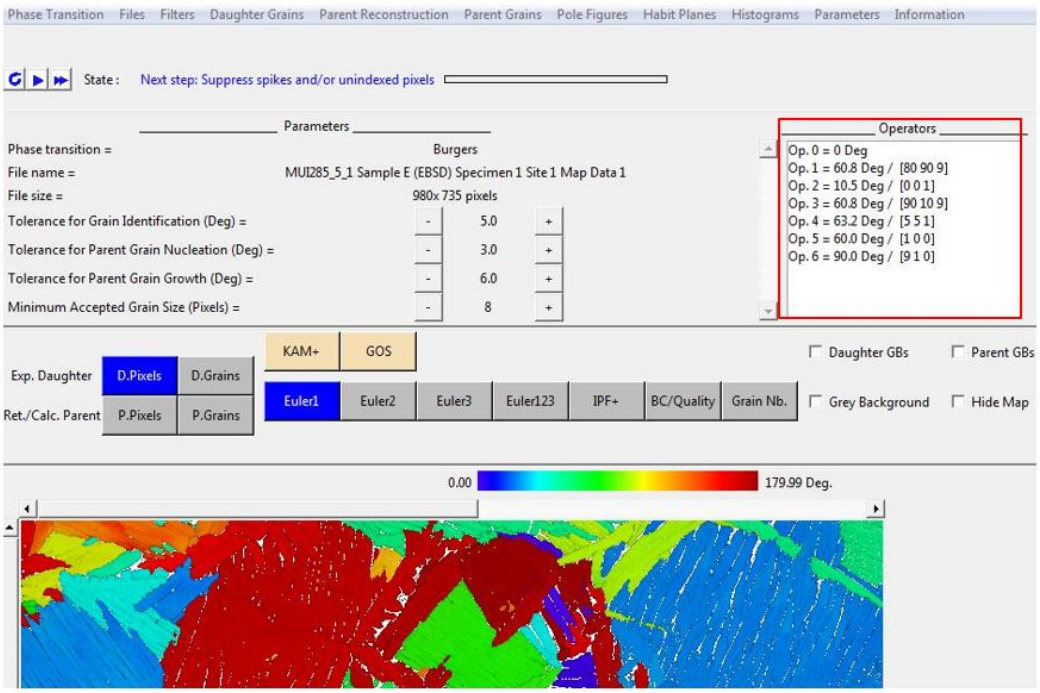

Figure 3-4. Typical ARPGE program main menu with set parameters for reconstruction of prior-β grains of Ti6Al4V.

© Central University of Technology, Free State

Steps were taken to identify the α/α' belonging to the same mother-β grain by considering specific misorientation angles and axes between the adjoining grains. The α/α' variants inherited from the same mother-β grain were assumed to have a specific misorientation related to the BOR. Consequently, five characteristic misorientation types between α/α' inherited from the same β-grain were possible (shown by the operators in Figure 3-4): 60.8°, 10.5°, 63.2°, 60.0° and 90°. Further details of these misorientation angles and axes can be found in Gey and Humbert (2003). The reconstruction was performed by only comparing the Euler angles and by checking if the misorientation between the grains were close to the theoretical operators. Identification of α-variants belonging to the same β-grains assumed that if the misorientation between two neighbouring points were $\geq 5°$, the points belonged to different variants. On the other hand, if the deviation of misorientation angle between the neighbouring variants was within a certain tolerance (3° to 5°) to any of the theoretical operators, there was a likelihood that the different variants belonged to the same β-grain. However, if the deviation was above the mentioned value (≥ 6), the variants were deemed to belong to a different β grain. The reconstructed β-grains were then exported to a file compatible with Mtex (*.ctf*) for plotting of orientation maps. The (0001) pole figures of the daughter grains (α/α') and the (110) pole figures of parent (β) grains were then constructed on the same plot for comparison.

3.3.3 X-ray diffraction (XRD)

An important aspect of the present research work was to determine the proportions of the α and β-phases, as well as the initial dislocation density of the non-heat-treated and heat-treated samples of DMLS Ti6Al4V(ELI). These qualitative and quantitative analyses were performed using the XRD technique. The background information and the principles of this method were outline and discussed in section 2.6.2. The XRD analyses were carried out on the surfaces that were initially analysed using the EBSD method for samples A, B, C, D and E.

The XRD-Bruker D2 Phaser was used and the instrument's specifications are listed in Table 3-6. The Bruker D2 Phaser is a low-power desktop diffractometer with a Co/Cu X-ray source, a secondary nickel filter and primary and secondary Söller slits. The Söller slits are used to limit the axial (vertical/out-of-plane) divergence of the incident and diffracted X-

© Central University of Technology, Free State

ray beams and, therefore, improve peak shape and resolution in 2θ-type scans, especially at low scattering angles. The diffractometer was set up to scan between the angles $40°$ to $120°$ in 2θ and take measurements at distinct values in $\Delta 2\theta$.

Table 3-6. The XRD-Bruker D2 Phaser specifications

	Parameter		Value
Goniometer Radii	Primary radius		70.7 mm
	Secondary radius		70.7 mm
Detector	2theta angular range		5.638°
Slits	Primary Söller		2.5°
	Secondary Söller		2.5°
X-ray source	Co Kα1/Kα2	Operational setting	30 KV; 10 mA
		Wavelength	0.179 nm

Some of the difficulties encountered with XRD are the overlapping of peaks due to (a) symmetric conditions such as in cubic space groups, (b) non-random distribution of the crystallite in the specimen, generally known as preferred orientation, and (c) accidental overlapping because of limited experimental resolution (Rietveld 1967, Kniess *et al.* 2015). A method developed by Rietveld (1967) is normally applied to the total angular range of diffraction patterns to minimise the problem of overlapping peaks, thus increasing the accuracy of the data obtained and allowing maximum extraction of information from the diffraction patterns (Kniess *et al.* 2015).

In essence, the Rietveld refinement technique is a multi-parameter curve-fitting procedure for diffraction data. The analysis is conducted by fitting a calculated diffraction pattern to the observed data, obtained from the diffraction scan, by adjusting each of the variables that describe the diffraction pattern. The computations are relatively intensive and require minimising the sum of the weighted, squared differences between observed and calculated intensities at every step in a digital pattern (Rietveld (1967). The Rietveld refinement technique that is normally implemented in the Bruker AXS TOPAS software version 5 of 2014 was used to fit the diffraction patterns.

3.4 HARDNESS TEST

Hardness is described as the resistance of a material to undergo plastic deformation as result of indentation, wear, abrasion or even scratching. Values of hardness from hardness

© Central University of Technology, Free State

tests are directly related to values of ultimate tensile strength (UTS) from tensile tests because both tests measure the resistance of a material to plastic flow, for stresses beyond the yield stress in the latter case. In the present research, the Vickers hardness test was used to measure the hardness of the five different forms of DMLS Ti6Al4V(ELI). The Future Tech Vickers hardness tester was used to this end. In principle, this instrument consists of a diamond indenter, in the form of a right pyramid with a square base and an angle of 136° between opposite faces, as shown in Figure 3-5. A load is then applied, as seen in this figure, to cause indentation on the surface of the material.

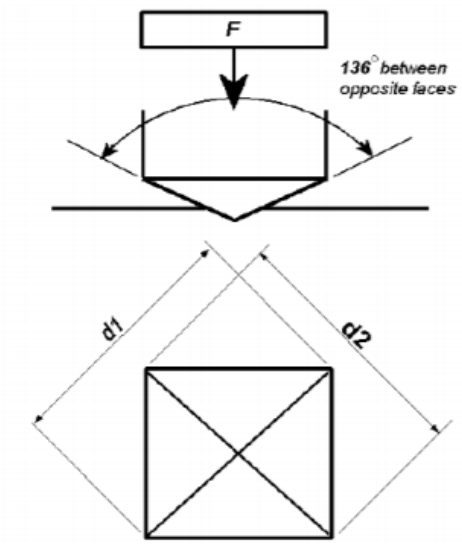

Figure 3-5. Schematic diagram showing the theory of the Vickers hardness test.

The Vickers hardness of a material is then calculated from the dimensions shown in Figure 3-5 based on Equation 3-1, thus:

$$HV = \frac{2Fsin\frac{136^{\circ}}{2}}{d^2} \qquad 3\text{-}1$$

where *F* is the applied load in kilogram-force (kgf), *d* the mean of the two diagonals (d1 and d2) and HV the Vickers hardness.

In the present research, the diagonals of the indentation that were left on the surface of the DMLS Ti6Al4V(ELI) specimens after taking away the load were measured using an optical microscope and then used to calculate the Vickers hardness of the samples using Equation 3-1. A minimum of 30 indentations were made randomly on the polished surfaces of each sample using a 200 g load with a dwell time of 10 s.

© Central University of Technology, Free State

3.5 HIGH-STRAIN-RATE COMPRESSION TESTING

The compression Split Hopkinson Pressure Bar (SHPB) test described in section 2.10 was used in the present research for high-strain-rate tests. These tests were conducted at the Armaments Corporation of South Africa (ARMSCOR) in Pretoria. A photographic image of the SHPB at the ARMSCOR testing facility is shown in Figure 3-6.

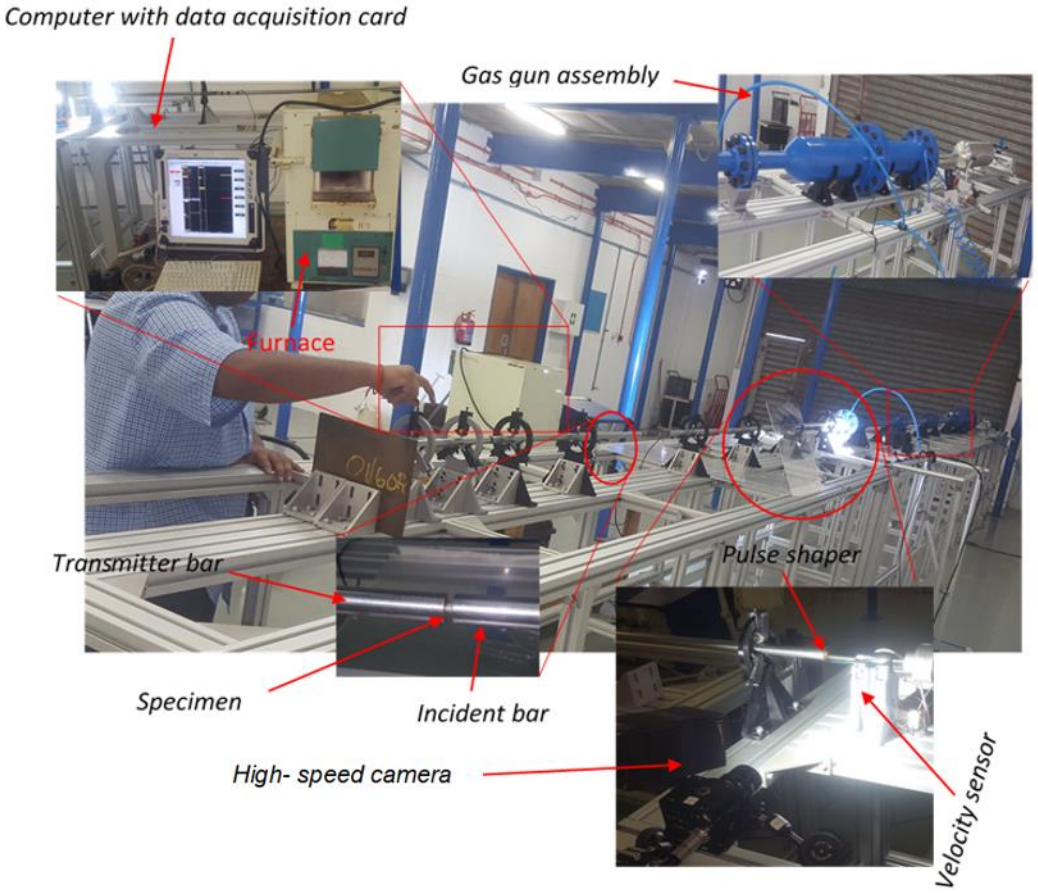

Figure 3-6. The SHPB assembly at ARMSCOR, Pretoria.

The incident and transmitter bars (pressure bars) of this equipment for testing Ti6Al4V(ELI) material were made of tool steel and were 2000 mm long with a diameter 20 mm. The striker bar was made of the same material and same diameter as the pressure bars but was 500 mm long. Another tool steel bar of length 250 mm was used at the end of the output bars to damp the oscillations and therefore quickly bringing the bars to rest during testing. The data acquisition system consisted of strain gauges with a gauge factor of 1.88, calibrated voltage of 1.00 V, amplifier and data acquisition cards fixed in a computer. Hottinger Baldwin Messtechnik GmbH (HBM) strain gauges were arranged in a full

© Central University of Technology, Free State

Wheatstone bridge configuration to eliminate the effects of bending and only measure the axial strain, and then glued at the centre of the incident and transmitter bars (1000 mm from one end) before being wired to the data acquisition card in the computer. The high-speed camera and the velocity sensors shown in Figure 3-6 were used to measure the velocity of the projectile (striker bar) just before it strikes the incident bar.

To minimise the effects of wave dispersion, oxygen-free high thermal conductivity (OFHC) copper was used as a pulse-shaping material or buffer material and was put between the striker bar and the incident bar. The pulse shaper was 3 mm thick and with a diameter of 10 mm. The pulse shaper ensured that the rising time of the incident pulse during the test exceeded the time needed by the test specimen to attain the stress equilibrium state and thus ensure that the plastic deformation of the specimen occurred after attainment of the equilibrium state (Frew *et al.* 2002).

The SHPB test specimens used here were those cut off from samples C, D and E, which were heat-treated according to the profiles shown and discussed in Figure 3-3. These heat-treated samples were cut into SHPB test specimens with a diameter and a height of 6 mm. This specification was chosen to ensure a height-to-diameter ratio of 1 to facilitate equilibrium dynamic forces. The effects of the height to diameter ratio on the SHPB test were briefly discussed in section 2-10. The ends of these specimens were faced off on a lathe machine to ensure that they were flat and parallel to achieve the best possible contact between specimen and pressure bars during impact loading. The method to carry out the SHPB high-temperature tests was to heat the test specimen alone in a furnace, shown in Figure 3-6, and then bring the bars into contact with the specimen a short moment before impact. The fixture shown in Figure 3-7 was used to align the samples with the loading bars before launching the striker bars to ensure perfect alignment between the bars and test specimens.

Figure 3-7. Specimen placing and alignment fixture.

© Central University of Technology, Free State

To minimise friction and therefore maintain a uniaxial state of compression, lithium based NLGI 3 grease (Castrol WB) was used to lubricate the interface between the pressure bars and the test specimen. As briefly stated in section 2.10 of Chapter 2, the separate heating of the specimens has an advantage of ensuring minimal thermal gradients develop in the pressure bars. However, the major drawback of this approach is the amount of time in which the pressure bars are in contact with the test specimen just before the arrival of the striker bar since prolonged times may reduce the test temperature of the specimen.

Prior to the actual testing, thermodynamic analysis was done of the heat lost by the specimens from the time the specimens were taken from the furnace to the time the projectile was launched. The results of this analysis are presented in Appendix C. Following this analysis and to compensate for any temperature drop by the specimen before impact, the test samples were soaked at a temperature 30 °C higher than the intended test temperatures.

The test samples were tested at three different impact velocities of 8 m/s, 15 m/s, and 25 m/s generated by firing the striker bar at pressures of 4 bars, 7 bars, and 13 bars, respectively. The tests at each strain rate were conducted at the three different temperatures of 25 °C, 200 °C, and 500 °C. At least three sets of specimens were loaded at each strain rate and temperature.

3.5 SUMMARY

This chapter presented information on the production of test samples via the DMLS process and the subsequent heat-treatment strategies that were applied to them. The methods of preparation of test samples for microstructural characterisation have also been outlined. The XRD and the EBSD methods that were used to study the microstructures of the as-built and heat-treated DMLS Ti6Al4V(ELI) alloy and their experimental step-ups were discussed. The SHPB apparatus used in the present research to study the mechanical properties of AM Ti6Al4V(ELI) at high-strain-rate and temperature was presented and its experimental set-up discussed.

© Central University of Technology, Free State

3.6 REFERENCES

1. Ahmed, T., Rack, H.J. 1998. Phase transformations during cooling in α+β titanium alloys. *Materials Science and Engineering. A* 243 (1), pp.206–211. https://doi.org/10.1016/S0921-5093(97)00802-2
2. Analox Sensor Technology: https://www.analoxsensortechnology.com/blog/2016/12/13/argon-used-3d-printing/ (accessed on 24th October 2019).
3. ASTM E2627. 2010. Standard Practice for Determining Average Grain Size Using Electron Backscatter Diffraction (EBSD) in Fully Recrystallized Polycrystalline Materials. *ASTM International.*
4. ASTM F3001-14.2014. Standard specification for additive manufacturing Titanium-6 Aluminium-4 Vanadium ELI (Extra Low Interstitial) with powder bed fusion. *ASTM International.*
5. Bauristhene, A.M., Mutombo, K., Stumpf, W.E. 2013. Alpha case formation mechanism in Ti6Al4V alloy investment castings using YFSZ shell moulds, *Journal of the Southern African Institute of Mining and Metallurgy,* 113(4), pp.357–361.
6. Cayron, C. 2007. ARPGE: A computer program to automatically reconstruct the parent grains from electron backscatter diffraction data. *Journal of Applied Crystallography*, 40 (6), pp.1183–1188. https://doi.org/10.1107/S0021889807048777
7. Els, J. 2016. *Optimal Process Parameters for Direct Metal Laser Sintering of Ti6Al4V for Medical Implant Production.* Master's Thesis submitted to the Department of Mechanical Engineering, Central University of Technology, Free State, South Africa.
8. EOS.2010. Technical description of EOSINT M 280. https://webbuilder5.asiannet.com/ftp/2684/TD_M280_en_2011-03-29.pdf (accessed on 17th June 2019).
9. Frew, D.J., Forrestal, M.J., Chen, W. 2002. Pulse shaping techniques for testing brittle materials with a split Hopkinson pressure bar. *Experimental Mechanics*, 42(1), pp.93–106.
10. Gey, N., Humbert, H. 2003. Specific analysis of EBSD data to study the texture inheritance due to the β→α phase transformation. *Journal of Materials Science*, 38, pp.1289–1294.

© Central University of Technology, Free State

11. Kniess, C., Cardoso, L., Prates, P. 2015. The quantifications of crystalline phases in materials: Applications of Rietveld method. *Sintering – Methods and Products,* In tech Publisher, London UK, pp.294–313.
12. Oxford Instruments, EBSD. Available online: http://www.ebsd.com/ebsd-explained/calibrating-an-ebsdsystem (accessed on 3rd May 2019).
13. Rietveld, H.M. 1969. A profile refinement method for nuclear and magnetic structures. *Journal of Applied Crystallographic*, 2(2), pp.65–71. https://doi.org/10.1107/S0021889869006558
14. Thejane, K., Chikosha, S., du Preez, W.B. 2017. Characterisation and monitoring of Ti6Al4V(ELI) powder used in different selective laser melting systems. *South African Journal of Industrial Engineering,* 28(3), pp.161–171.
15. Yang, Y., Liu, Y., Chen, J., Wang, H., Zhang, Z., Lu, Y. 2017. Crystallographic features of α variants and β phase for Ti6Al4V alloy fabricated by selective laser melting. *Materials Science and Engineering* A, 707, pp.548–558. https://doi.org/10.1016/j.msea.2017.09.068

© Central University of Technology, Free State

CHAPTER 4 — DEVELOPMENT OF CONSTITUTIVE NUMERICAL MODELS TO PREDICT THE FLOW STRESS OF TI6AL4V OVER A WIDE RANGE OF STRAIN RATES

4.1 INTRODUCTION

As discussed in Chapter 2, mechanical properties of Ti6Al4V are complicated by the fact that the alloy exhibits complex two-phase microstructures that are rich with morphological features that strongly influence its mechanical properties. The material in this chapter is predicated on the hypothesis that a single expression for stress can be developed to accurately predict the yield stress and subsequent flow stress of DMLS Ti6Al4V(ELI), upon post-process heat treatment. The constitutive model to account for microstructural variables should be of such a nature as to provide a bridge between sub-microscale phenomena and macroscale continuum mechanics.

This kind of model should connect the morphological aspects of microstructure to the stress-strain relationships of the material as a function of the prevailing levels of strain rate and temperature. A logical flow of the model is shown in Figure 4-1.

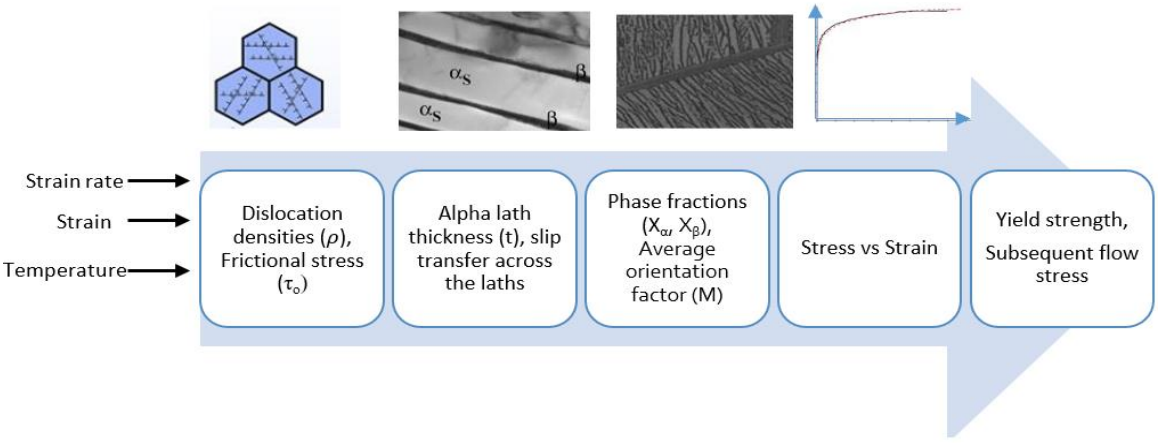

Figure 4-1. Microstructural variables-based constitutive model flow diagram for yield strength and flow stress.

The envisaged microstructural variables-based model is classified into two parts: (a) for the prediction of yield strength and (b) for subsequent prediction of the flow stress. The total stress is the sum of the yield stress and the flow stress, which automatically arises from a combination of these two solutions.

© Central University of Technology, Free State

4.1.1 Prediction of the yield stress

It is known that yield-stress-enhancing mechanisms during loading include grain-boundary strengthening, solid-solution strengthening as a function of prevalent alloy phases, work-hardening and the related pile-up of dislocations (Dieter 1986, Hull and Bacon 2010).

The Hall-Petch relationship (Hall 1951) was used to determine the yield stress (σ_y) of a material as a function of grain size based on the expression:

$$\sigma_y = \sigma_i + \frac{K_{H-P}}{\sqrt{d}} = \sigma_i + \sigma_a \qquad 4\text{-}1$$

where the symbol σ_i stands for the lattice friction stress required to initiate slip along slip planes in grains/phases. The second term of Equation 4-1 is independent of temperature and strain rate and is referred to as an athermal component of stress (σ_a). The symbol K_{H-P} is a material constant taken as equal to $328\,MPa\,\mu m^{1/2}$ for Ti6Al4V (Kohn and Ducheyne 1991), and d is the average grain size of the α-phase. In Equation 4.1, the parameter d is represented by the length across a grain for equiaxed grain structures, whereas this parameter is represented by the average width of a lath for lamellar microstructures that possess a typical lath shape. For bimodal microstructures, the parameter d is determined from the rule of mixtures (RoM) that considers the contribution of representative grain size, $d_{\alpha p}$, for the primary α grains, the representative grain size, $d_{\alpha s}$, for the secondary alpha laths and the relative percentage fraction, $V_{\alpha s}$, of the secondary α- phase. In this case the athermal stress component is given by (Galindo *et al.* 2018):

$$\sigma_a = K_{H-P}\left(\frac{V_{\alpha s}}{\sqrt{d_{\alpha p}}} + \frac{1-V_{\alpha s}}{\sqrt{d_{\alpha s}}}\right) \qquad 4\text{-}2$$

It important to note that the strength of the α-phase is higher in comparison to that of the β-phase (Semiatin and Bieler 2001). Taking the α/β lamellar microstructure as an example, the β- phase fills in the small gap between α lamellae. Consequently, during plastic deformation these interfaces (β-phase) usually act as barriers to the motion of dislocations causing a pile-up of dislocations and creation of stress concentration. In other words, plastic deformation will initiate in the α-phase and with subsequent strain-hardening, plastic flow starts on the opposite side of the α-phase upon slip transference across the β

© Central University of Technology, Free State

phase (interphase) (Semiatin *et al.* 2003, Zheng *et al*. 2018). Thus, the characteristic Hall-Petch mechanisms are likely to occur in the α-phase, rather than the β-phase (Zheng *et al*. 2018) and it may be speculated that the α/β interface and β layers themselves are analogous to grain boundaries in a single-phase material. Therefore, the Hall-Petch mechanism was assumed here to be controlled by the properties and thickness of the α-laths/platelets, and the contribution of the β-phase to the Hall-Petch mechanism was ignored (Kohn and Ducheyne 1991).

The lattice friction stress was assumed to be due to the contribution of the respective phases in a material and similarly follows the rule of mixtures, thus (Galindo *et al*. 2018):

$$\sigma_i = \sigma_{\alpha i} V_\alpha + \sigma_{\beta i}(1 - V_\beta) \qquad 4\text{-}3$$

The component σ_i in this equation is sensitive to temperature and strain rate. In other words, energy must be provided to initiate slip and for dislocations to overcome the barriers (short-range obstacles) they encounter during slip (Nemat-Nasser *et al*. 2001). A schematic diagram illustrating the evolution of the yield stress components with the increase in temperature is shown in Figure 4-2.

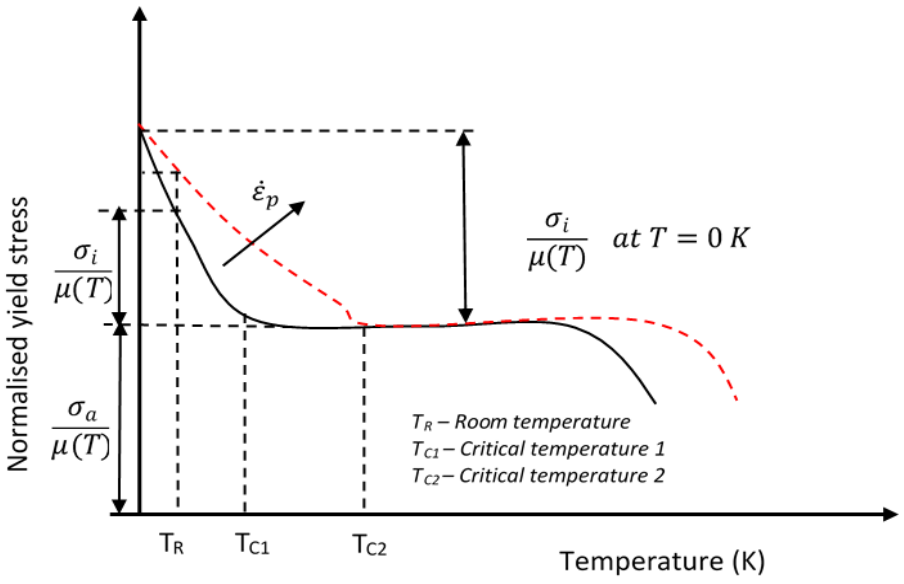

Figure 4-2. Decomposition of macroscopic stress versus temperature (Kocks and Mecking 2003, Rusinek et al.2010).

The lattice friction stress (σ_i) decreases with increase in temperature up to a critical temperature (T_c), above which there is enough thermal energy to overcome barriers by

© Central University of Technology, Free State

thermal activation alone. Furthermore, a rise in applied strain rate will increase the yield stress and shift T_c to higher temperatures (Kocks 1976). Therefore, the yield stress is dependent on strain rate and temperature and can be expressed as (Follansbee and Kocks 1988):

$$\sigma_y(\dot{\varepsilon}, T) = \sigma_a + (S\sigma_i)\frac{\mu(T)}{\mu_o} \qquad 4\text{-}4$$

where the symbol S is the temperature and strain rate -dependent scaling factor of the yield stress, μ is the shear modulus dependent on temperature, and μ_o is the shear modulus at absolute zero temperature (0 K).

The thermal stress part of the yield stress can be expressed by combination of the existing relation between free energy and the mechanical threshold stress (MTS), and Arrhenius-type equation as follows (Mecking and Kocks 1981, Rusinek *et al.*2010):

$$\begin{cases} \dot{\varepsilon} = \dot{\varepsilon_o} exp\left(\frac{-\Delta G}{k_b T}\right) \\ \Delta G = g_o \mu b^3 \left(1 - \left(\frac{\sigma_i}{\sigma_o}\right)^p\right)^q \end{cases} \qquad 4\text{-}5$$

Combination of the two expressions in Equations 4-5 gives rise to:

$$\sigma_i = \sigma^o \left(1 - \left(\left(\frac{k_b T}{\Delta G}\right) ln\ \frac{\dot{\varepsilon}_o}{\dot{\varepsilon}}\right)^{1/q}\right)^{1/p} = \sigma^o \left(1 - \left(\left(\frac{k_b T}{g_{oi}\mu b^3}\right) ln\ \frac{\dot{\varepsilon}_o}{\dot{\varepsilon}}\right)^{1/q}\right)^{1/p} \qquad 4\text{-}6$$

where the symbol σ^o the mechanical threshold stress, or the value of the thermal stress at 0 K, ΔG is the activation energy for deformation, k_b the Boltzmann's constant (1.38 x 10^{-23} J/K), b the Burgers vector (taken as 2.95 x 10^{-10} m for Ti6Al4V) (Lütjering and Williams 2007), and $p, q\ and\ \dot{\varepsilon}_o$ are fitting constants. The term g_{oi} in the equation is a material constant of proportionality for $\Delta G \propto \mu b^3$ reported in (Kocks 1976) and is generally the normalised activation energy for dislocations to overcome the intrinsic barrier(s) or to unpin from impurities or solutes (Picu and Majorell 2002). From Equations 4.4 and 4.6, the strain rate – temperature scaling factor (S) can be expressed as (Kocks 1976, Follansbee and Kocks 1988).

$$S = \left(1 - \left(\frac{kT}{g_{oi}\mu b^3} In\frac{\dot{\varepsilon}_o}{\dot{\varepsilon}}\right)^{1/q}\right)^{1/p} \qquad 4\text{-}7$$

© Central University of Technology, Free State

Combining Equations 4.4 and 4.7 allows the total thermally activated stress to be expressed as:

$$\left(\frac{\sigma_y-\sigma_a}{\mu}\right)^p = \left(\frac{\sigma_o}{\mu_o}\right)^p \left(1-\left(\frac{1}{g_{oi}}\right)^{1/q}\left(\frac{kT}{\mu b^3}\left(In\frac{\dot{\varepsilon}_o}{\dot{\varepsilon}}\right)\right)^{1/q}\right) \quad 4\text{-}8$$

This is a linear equation of the form of $y = mx + c$ where the y-intercept is equal to the term $\left(\frac{\sigma_0}{\mu_o}\right)^p$ and the material constant g_{oi} can be computed from the gradient m. The superscripts $0 < p \leq 1$ and $1 \leq q \leq 2$ are material constants related to the energy barrier profile (Mecking and Kocks 1981). For Ti6Al4V, the parameters p and q were determined experimentally as 1 and 2, respectively, by Nemat-Nasser *et al*. (2001). The same values were used elsewhere in Majorell and Picu (2002) and separately in Park *et al.* (2012) for ELI-graded alloy.

4.1.2 Strain hardening and prediction of flow stress

The proposed model for work-hardening and flow stress starts from the point that the flow stress is a function of the average dislocation density as expressed in the Taylor (1934) equation. For single crystals, shear flow stress is controlled by interactions of dislocations and is expected to follow the relation:

$$\tau = \alpha\mu(T)b\sqrt{\rho} \quad 4\text{-}9$$

where the symbol α is a dimensionless parameter of magnitude ranging from 0.2–0.4, for different materials and reported as 0.2 for Ti6Al4V (Galindo *et al*. 2018). The symbol μ is the shear modulus which is dependent on temperature (*T*), and ρ the average dislocation density. Using the Taylor factor, *M*, which relates the shear flow stress τ of a single crystal to the uniaxial flow stress σ of a polycrystal, the Taylor equation can be rewritten for the uniaxial loading of polycrystals as (Kassner 2003):

$$\sigma - \sigma_y = \alpha\mu(T)bM\sqrt{\rho} \quad 4\text{-}10$$

where the symbol σ_y stands for the yield stress. At the onset of plastic flow and for subsequent work-hardening, the strain-hardening rate θ_p for a polycrystalline material can be derived by differentiating Equation 4-10 and is written as (Kocks and Mecking 2003):

© Central University of Technology, Free State

$$\theta_p = \frac{d\sigma}{d\varepsilon_p} = \alpha\mu(T)bM \frac{d}{d\varepsilon_p}\sqrt{\rho} \quad 4\text{-}11$$

Thus, determination of the strain-hardening rate requires an expression for the term $\frac{d}{d\varepsilon_p}\sqrt{\rho}$. As plastic flow continues, the dislocation density increases in the crystals of the material and the stress required to continue deformation increases, due to the interaction of mobile dislocations with an increasingly dense network of dislocations stored due to plastic strain. Strain-hardening must, however, be understood to be a result of competition between the accumulation of dislocations in the material and reduction in the number of and total line length of dislocations, the latter, which is often referred to as dynamic recovery, therefore (Dieter 1986, Cheng et al. 2003):

$$d\rho = d\rho_{accumulation} - d\rho_{recovery} \quad 4\text{-}12$$

The increase in dislocations is due to the multiplication (such as at Frank-Read sources) and nucleation of dislocation lines at other sources (such as at precipitates, dispersed phases and nucleation of dislocation line lengths at grain boundaries) and trapping of dislocations (Dieter 1986, Zheng *et al*. 2018). Trapping of mobile dislocations can occur due to forest interaction which generates shear stresses that can oppose their motion (Zheng *et al*. 2018). Dislocations of opposite sign can annihilate one another if they are very close. This leads to a decrease in the dislocation density as part of what is termed thermal softening, which is a dynamic recovery occurring simultaneously with plastic strain. At the saturation limit of flow stress, the accumulation and recovery terms are assumed to be equal. The flow stress starts decreasing when the term for dynamic recovery becomes greater than the accumulation (*i.e.*, $d\rho_{recovery} > d\rho_{accumulation}$). The distinction between the accumulation component and recovery component becomes clear from understanding that the generation of dislocations is mildly dependent on temperature and strain rate while the annihilation of dislocations is greatly dependent on both (Kocks 1976). Annihilation is mainly a thermally activated process. However, during gliding of dislocations at low temperature, dislocations annihilate mutually with dislocations of opposite sign approaching on closely neighbouring glide planes (Hull and Bacon 2011).

© Central University of Technology, Free State

From Equation 4.12, a single differential equation with separate terms for the generation (k_1 factor) and annihilation (k_2 factor) of dislocations can be used to define the evolution of dislocation density with plastic strain, ε_p as proposed in Kocks and Mecking (2003):

$$\frac{d\rho}{d\varepsilon_p} = M\left(k_1\sqrt{\rho} - k_2\rho\right) \qquad 4\text{-}13$$

The work-hardening rate, Equation 4-11, can be expressed as a product of the differentials, $d\sigma/d\rho$ and $d\rho/d\varepsilon$, (via the chain rule) of Equation 4-13 as:

$$\theta_p = \frac{d\sigma}{d\rho}.\frac{d\rho}{d\varepsilon_p} = \frac{M^2\alpha\mu b}{2\sqrt{\rho}}\left((k_1\sqrt{\rho} - k_2\rho)\right) \qquad 4\text{-}14$$

A plot of the variation of work-hardening rate versus true stress was illustrated in various stages by Cheng *et al.* (2003), as shown in Figure 4-3.

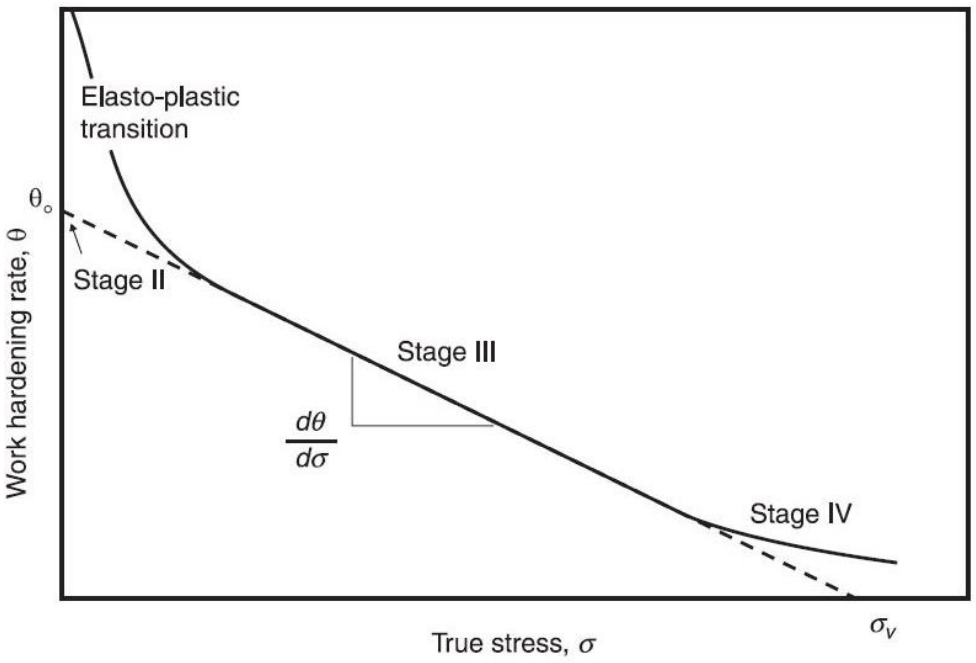

Figure 4-3. A diagram illustrating the different stages of strain-hardening and the initial elastic-inelastic transition (Cheng et al. 2003).

From Equation 4-14, the strain-hardening rate can be rewritten as follows:

$$\theta_P = \frac{M^2\alpha\mu b k_1}{2} - \frac{M^2\alpha\mu b\sqrt{\rho}\,k_2}{2} \qquad 4\text{-}15$$

Equation 4-15 gives rise to a linear curve in stage III, as shown in Figure 4-3. In this stage, the equation takes the form: $\theta = C_o - C_1.\sigma_v$, where $C_o = \theta_o = \mathrm{M}^2\alpha\mu\mathrm{b}k_1/2$, $C_1 = Mk_2/2$

© Central University of Technology, Free State

and σ_v is the steady state/saturation stress. The constant parameters k_1 and k_2 can be determined from the stage III, linear plot of θ vs σ_{true} using experimental data.

The expression of the flow stress with plastic strain, as represented by Equation 4-10, requires the expression of average dislocation density, thus integration of Equation 4-13. The assumption in the present study is that the accumulation of dislocations (strain-hardening rate) is mildly dependent on temperature and strain rate, while rate of annihilation of dislocations is strongly dependent on both (Kocks 2001). In other words, the production term, $k_1\sqrt{\rho}$ in Equation 4-13, is associated with the athermal storage of moving dislocations which become immobilised after having moved a length proportional to the mean spacing between the dislocations. The length travelled by these dislocations is known as the mean free path of dislocations (L). Therefore, the rate of accumulation of dislocations with strain ($k_1\sqrt{\rho}$) can be written as (Chan *et al*. 2012):

$$\frac{d\rho}{d\varepsilon_p} = \frac{1}{bL} \qquad 4\text{-}16$$

The assumptions can be made here that the mean free path of dislocations is the space between impenetrable obstacles (sinks of dislocation) such as grain boundaries. Thus, one may reasonably argue that the mean free path of dislocations, *L*, is proportional to a characteristic length, such as the average grain size for a material. Consequently, the term describing the rate of accumulation of dislocations becomes constant, thus allowing Equation 4-13 to be rewritten as (Kock and Mecking 2003, Davoudi and Vlassak 2018):

$$\boldsymbol{\frac{d\rho}{d\varepsilon_p}} = (h - k_2\rho) \qquad 4\text{-}17$$

where the constant $h = k_1\sqrt{\rho}$ stands for the athermal work-hardening coefficient, while the parameter k_2 specifies the rate of annihilation of dislocations at a given temperature and strain rate. The increase of dislocation density in a material with plastic strain requires evaluation of the integral for Equation 4-17, and thus the increase/decrease of flow stress with plastic strain can be evaluated from Equation 4-10. The integration of Equation 4-17 is presented in Appendix D (Jonas *et al*. 2009). Therefore, the increase in flow stress with plastic strain is given by:

© Central University of Technology, Free State

$$\sigma - \sigma_y = \alpha\mu(T)bM\left(\frac{h}{k_2}\left(1 - exp(-k_2\varepsilon_p)\right) + \rho_o\, exp(-k_2\varepsilon_p)\right)^{\frac{1}{2}} \quad 4\text{-}18$$

where ρ_o is the initial dislocation density for a given microstructure.

The total flow stress is now expressed by the following equation:

$$\sigma = \left(\frac{\mu(T)}{\mu_0}\right)\sigma^o\left(1 - \left(\left(\frac{k_bT}{g_{0i}\mu(T)b^3}\right)ln\,\frac{\dot{\varepsilon}_o}{\dot{\varepsilon}}\right)^{1/q}\right)^{1/p} + \frac{K_{H-P}}{\sqrt{d}} + \alpha\mu(T)bM\left(\frac{h}{k_2}\left(1 - exp(-k_2\varepsilon_p)\right) + \rho_o\, exp(-k_2\varepsilon_p)\right)^{1/2} \quad 4\text{-}19$$

This microstructural-based constitutive equation contains many adjustable parameters that can easily be tuned to fit experimental curves.

4.2 SUMMARY

This chapter of the thesis documented an examination of various mechanisms in play at the yield point and initiation of plastic flow in Ti6Al4V(ELI). Using these mechanisms, an advanced constitutive relationship was adopted to provide a macroscopic description of flow properties of various microstructures of DMLS Ti6Al4V(ELI) for varying strain rates and temperatures. The formulated constitutive model is sensitive to the microstructure in that the effects of the average grain size and initial dislocation density on deformation behaviour of DMLS Ti6Al4V(ELI) are explicitly articulated. Thus, this constitutive model requires the average grain size and initial dislocation density of any given microstructure as an input, besides the other constant parameters that can be obtained from the literature.

Chapters 5 and 6 of this thesis are devoted to estimating these microstructural aspects using the methods outlined in Chapter 3. Furthermore, calibration and validation of this model with the experimental data for DMLS Ti6Al4V(ELI) material is presented in Chapter 8 of the thesis. This is followed by the implementation of the model into FE code in ABAQUS/Explicit in Chapter 9 and the codes used to simulate high-strain-rate SHPB experimental tests in Chapter 10.

© Central University of Technology, Free State

4.3 References

1. Cheng, L.M., Poole, W.J., Embury, J.D., Lloyd, D.J. 2003. The influence of precipitation on the work-hardening behaviour of the aluminium alloys AA6111 and AA7030. *Metallurgical and Materials Transactions A* , 34(11), pp.2473–2481.
2. Davoudi, K.M., Vlassak, J.J. 2018. Dislocation evolution during plastic deformation: Equations vs. discrete dislocation dynamics study. *Journal of Applied Physics*, 123 (8), 10.1063/1.5013213.
3. Dieter, E.G. 1986. Mechanical Metallurgy 3rd Edition – *Materials science and engineering series*, McGraw-Hill, New York, USA. p.184.
4. Follansbee, P.S., Kocks, U.F. 1988. A constitutive description of the deformation of copper based on the use of the mechanical threshold stress as an internal state variable. *Acta Metallurgica* 36(1), pp.81–93. https://doi.org/10.1016/0001-6160(88)90030-2
5. Galindo, M.A., Mumtaz, K., Rivera, P.E., Galindo-Nava, J.E., Ghadbeigi, H. 2018. A microstructure sensitive model for deformation of Ti6Al4V describing cast-and-wrought and additive manufacturing morphologies. *Material & Design,* 160, pp.350–362. https://doi.org/10.1016/j.matdes.2018.09.028
6. Hall, E.O. 1951. The deformation and ageing of mild steel: Discussion of results. *Proceedings of the Physical Society B,* 64 (9), p.747.
7. Hull, D. and Bacon, D.J. 2011. *Introduction to dislocations*. 5th Edition, Elsevier, Boulevard Oxford, pp.205–217.
8. Jonas, J.J., Quelennec, X., Jiang, L., Étienne, 2009. The Avrami kinetics of dynamic recrystallization. *Acta Materialia,* 57(9), pp.2748–2756.
9. Kassner, M.E. 2003. Taylor hardening in five-power-law creep of metals and class M alloys. *Acta Materialia*, 52(1), pp.1–9 https://doi.org/10.1016/j.actamat.2003.08.019
10. Kocks, U. 1976. Laws for work-hardening and low-temperature creep. *Journal of Engineering Materials and Technology*, 98, pp.76–85. http://dx.doi.org/10.1115/1.3443340
11. Kocks, U.F. 2001. Realistic constitutive relations for metal plasticity. *Materials Science and Engineering A*, 317(1–2), pp.181–187.

© Central University of Technology, Free State

12. Kocks, U.F., Mecking, H. 2003. Physics and phenomenology of strain hardening: the FCC case. *Progress in Materials Science,* 48, pp.171–273.
13. Kohn, D.H., Ducheyne, P. 1991. Tensile and fatigue strength of hydrogen-treated Ti6Al4V alloy. *Journal of Materials Science*, 26(2) pp.328–334.
14. Lütjering, G., Williams, J.C. 2007. *Titanium* 2nd edition, Springer Verlag, Berlin, pp.203–258.
15. Mecking, H., Kocks, U. 1981. Kinetics of flow and strain-hardening. *Acta Metallurgica*, 29(11), pp.1865–1875.
16. Nemat-Nasser, S., Wei-Guo, G., Vitali, F., Yai-Bei, G. 2001. Dynamic response of conventional and hot isostatically pressed Ti6Al4V alloys: Experiments and Modelling. *Mechanics of Materials*, 3(8), pp.425–439.
17. Park, C.H., Son, Y.I., Lee, C.S. 2012. Constitutive analysis of compressive deformation behaviour of ELI-grade Ti6Al4V with different microstructures. *Journal of Materials Science,* 47, pp.3115–3124.
18. Picu, P.C., Majorell, A. 2002. Mechanical behaviour of Ti6Al4V at high and moderate temperatures – Part II: Constitutive modelling. *Materials Science and Engineering A,* 326, pp.306–316.
19. Rusinek, A., Rodrıguez-Martınez, J.A., Arias, A. 2010. A thermo-viscoelastic constitutive model for FCC metals with application to OFHC copper. *International Journal of Mechanical Sciences*, 52(2), pp.120–135.
20. Semiatin, S.L., Bieler, T.T. 2001. The effect of alpha platelet thickness on plastic flow during hot working of Ti6Al4V with a transformed microstructure. *Acta Materialia,* 49(17), pp.3565–3573. https://doi.org/10.1016/S1359-6454(01)00236-1
21. Semiatin, S.L., Kinsley, P.S., Fagin, P.N., Barker, D.R., Zhang, F. 2003. Microstructure evolution during alpha-beta heat treatment of Ti6Al4V. *Metallurgical and Material Transactions A,* 34 (10), pp.2377–2386.
22. Taylor, G.I. 1934. The mechanism of plastic deformation of crystals. Part 1– Theoretical. *Proceeding of the Material Society A, Mathematical, Physical and Engineering Sciences, 145(855).* https://doi.org/10.1098/rspa.1934.0106
23. Zheng, Z., Waheed, S., Balint, D., Dunne, F. 2018. Slip transfer across phase boundaries in dual phase titanium alloys and effect on strain rate sensitivity.

© Central University of Technology, Free State

International Journal of Plasticity, 104, pp.23–38. https://doi.org/10.1016/j.ijplas.2018.01.011

© Central University of Technology, Free State

CHAPTER 5 — MICROSTRUCTURE CHARACTERISATION OF AS-BUILT AND ANNEALED DMLS TI6AL4V(ELI) PARTS

The material contained in this chapter has been published in peer-reviewed media as detailed below:

Amos Muiruri, *Maina Maringa, Willie du Preez, Crystallographic texture analysis of as-built and heat-treated Ti6Al4V(ELI) produced by Direct Metal Laser Sintering,* ***Crystals 2020, 10, 699****; doi:10.3390/cryst10080699*

5.1 INTRODUCTION

During the DMLS process, the β (bcc) to α (hcp)-phase transition in Ti6Al4V occurs by displacive transformation to form an α′ (acicular) martensitic structure and is accompanied by a build-up of high macro-thermal residual stresses, thus requiring post-process heat treatment. On this account, it was deemed necessary to study the effect of such heat treatment on the microstructure, crystallographic texture, and misorientation distribution of this alloy, as these three intrinsic variable factors do influence the mechanical performance of the alloy. The details and analysis of the microstructures, the crystallographic texture, the grain-boundary misorientation distribution of various forms of Ti6Al4V(ELI) alloy produced via the DMLS process, and selected heat-treatment processes are discussed in this chapter.

5.2 MICROSTRUCTURES OF HEAT-TREATED DMLS TI6AL4V(ELI)

The various microstructures of DMLS Ti6Al4(ELI) that were obtained after the heat-treatment strategies described in Table 3-3 and Figure 3-3 of Chapter 3 are presented in Figure 5-1 (using an optical microscope) and Figure 5-2 (higher magnification using a scanning electron microscope). As expected, the microstructure of non-heat-treated material (samples A) is characterised by the prior-β columnar grains shown in Figure 5-1(a), with lengths of several millimetres epitaxially grown through multiple DMLS layers along the build direction. The width of these β-grains is about 100–250 µm. Within the β-grains, acicular α′-martensite phase which has needle-like grains is found, as shown in the micrograph obtained at high magnification in Figure 5-2(a). This phase arises from the high thermal gradients and rapid solidification conditions during the DMLS process. The typical lath thickness of these martensitic grains is about 0.5–1.5 µm, while the lengths extend to several hundreds of micrometres, while confined by the width of β-prior grains. This

© Central University of Technology, Free State

microstructure remains unchanged upon stress-relieving heat treatment, as seen in Figures 5-1(b) and 5-2(b). Samples C were heat-treated at 800 °C followed by FC and during the process, the fine acicular α' microstructure transformed to an equilibrium mixture of α and β-phases in which the α-phase is present as fine needles, as seen in Figure 5-1(c). The prior-β-grain boundaries in this micrograph, as well as in Figure 5-2(c), are starting to become visible in some grains, which is associated with the precipitation of grain boundary α as opposed to the original/reference microstructure.

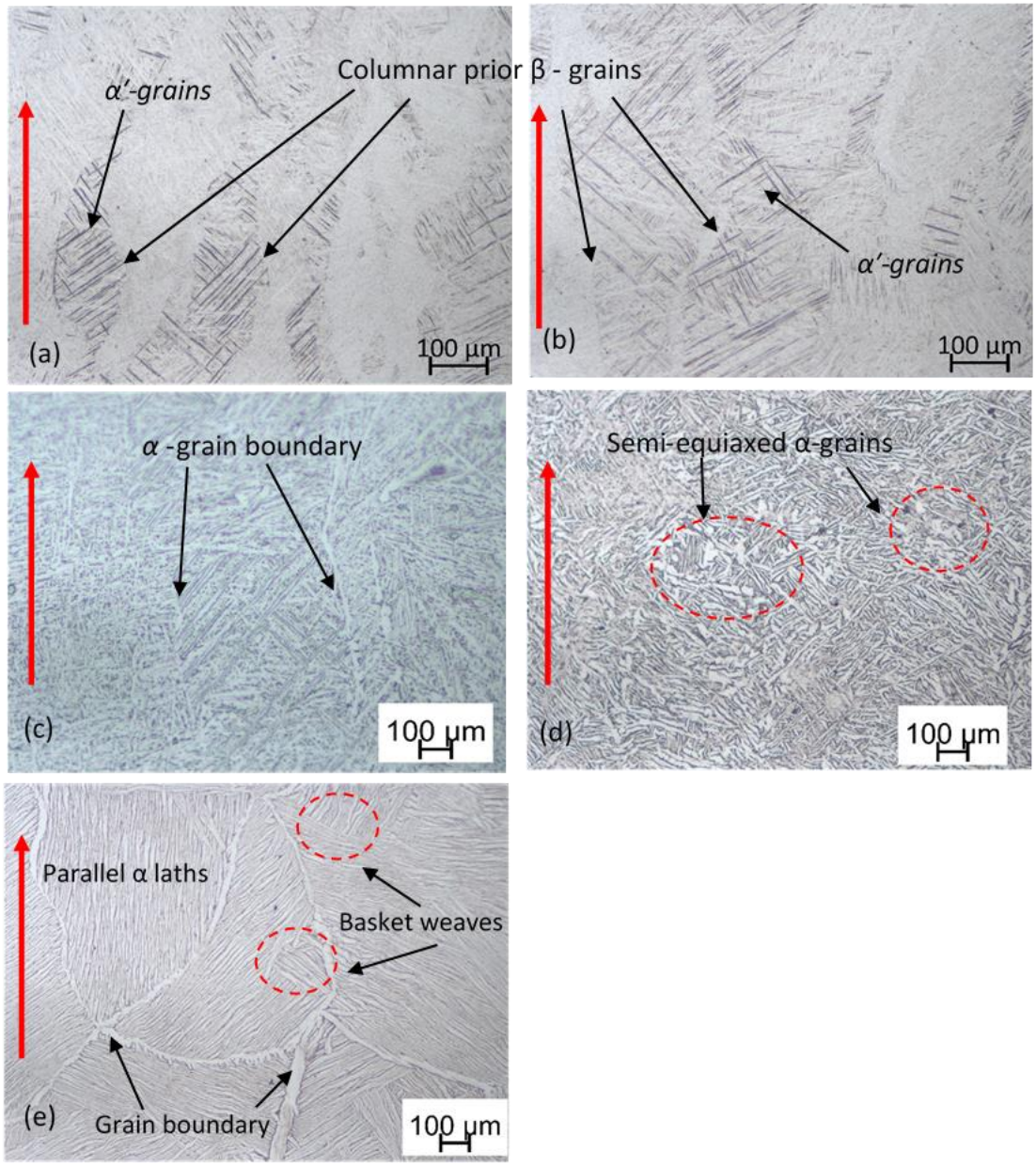

Figure 5-1. Optical images (OI) of (a) non-heat-treated samples A and heat-treated samples (b) B, (c) C, (d) D and (e) E of DMLS TI6Al4V(ELI), with red arrows indicating the build direction.

© Central University of Technology, Free State

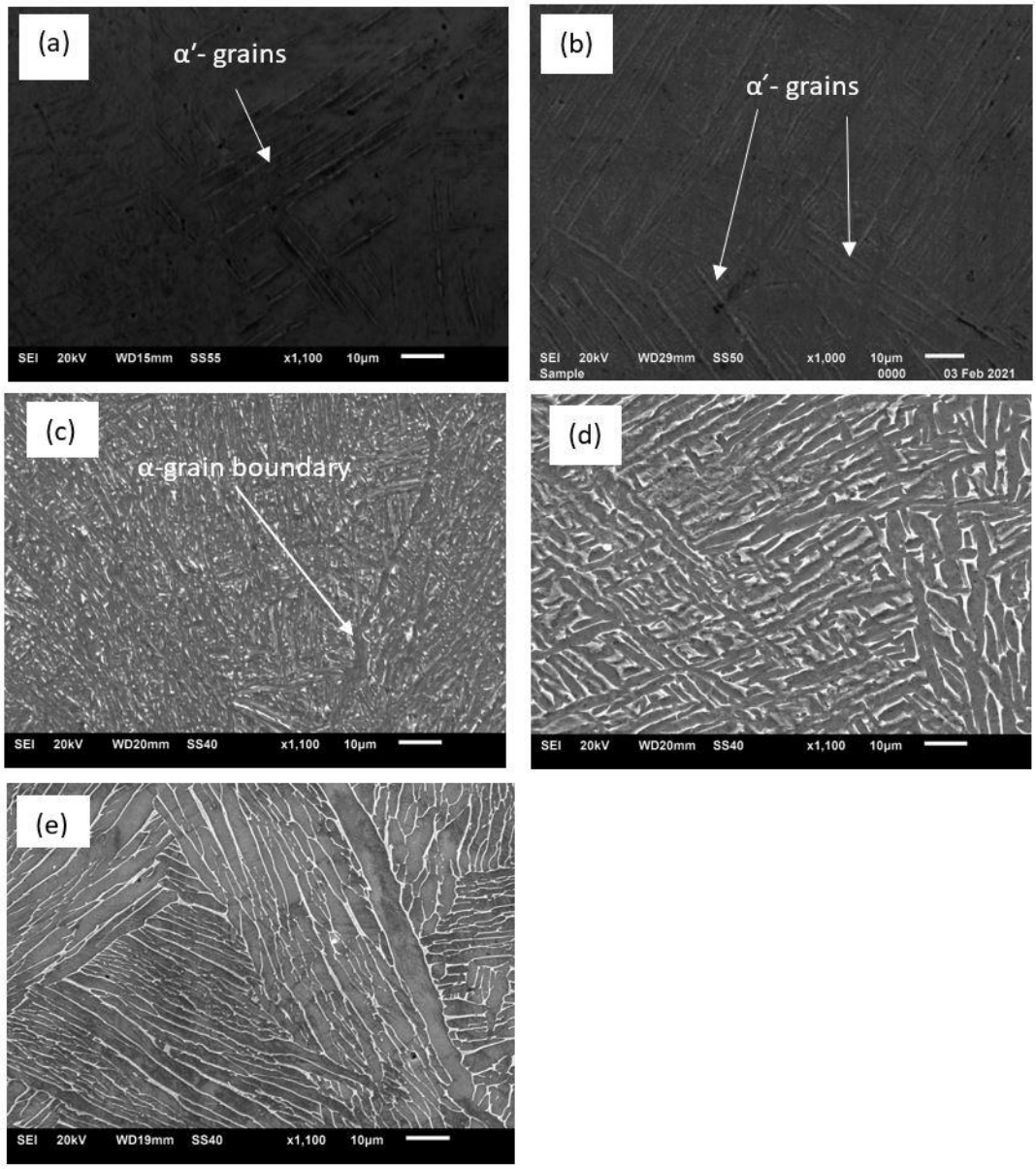

Figure 5-2. Secondary electron images (SEI) of (a) non-heat-treated samples A, and heat-treated samples (b) B, (c) C, (d) D and (e) E of DMLS TI6Al4V(ELI).

The β-phase is clearly shown in Figures 5-2(c–f) as brighter regions that are rich in vanadium, while regions that are low in vanadium content (α-phase) appear darker. The brighter and the darker contrast of SEI is associated with different crystallographic orientations of the hcp (α-phase) and bcc (β-phase). The brighter and darker contrast is absent in Figure 5-2(a and b), indicating the absence of β-phase in samples A and B. The α-laths have an average width of about 2.5 µm, while the length seems unchanged in samples C. The β-phase in the particle and lamellar-like morphology in samples C is distributed uniformly in the α matrix, especially along the grain boundaries of α laths, as seen in Figure 5-2(c).

© Central University of Technology, Free State

Hypothetically, it is expected that this microstructure, shown in Figures 5-1(c) and 5-2(c), will have the optimum/best combination of ductility and strength among the three microstructures. The fine size of α-laths and the α/β lamellar morphologies are the reason behind the postulation. It is broadly accepted that the mechanical properties of titanium alloys with a lamellar structure are determined by the effective slip length which is influenced by the size of α-laths. The laths in this regime are very small and inclined at varying angles (different orientations) to each other. This variation in inclination of interfaces between laths enhances the strength of the material by hindering the extension of slip across the material. However, this has a detrimental effect on ductility. Thus, the contribution of short effective slip lengths of the α/β lamellae could lead to a desirable combination of strength and ductility.

Samples D that were exposed to duplex annealing (940 ℃/FC followed by 750 ℃/FC) resulted in a coarse bi-phasic microstructure, as seen in Figures 5-1(d) and 5-2(d). The α-laths in this case have an average thickness and length of about 6 µm and 150 µm, respectively. The shape of the α/β-grains is more lamellae-like compared to the partial particle-like morphology in samples C. A few patches of semi-equiaxed grains are observed, as shown in Figure 5-1(d), while a larger portion of the microstructure consists of the lamellar α and β. Stefansson *et al.* (2002) suggested that to achieve at least 50% globularisation of the α phase in this heat-treatment regime, a residence time of approximately eight hours is necessary. However, in their work, the starting microstructure was equiaxed and deformed at local strains of 0.49. Therefore, for a starting fine martensitic microstructure of as-built DMLS Ti6AL4V(ELI), the globularisation time is expected to be higher. The microstructure obtained in this heat-treatment regime is expected to have lower strength but higher ductility in comparison to those discussed for samples A, B and C, due to the larger sizes of both the α- laths and the α and β lamellae.

Samples E, that were heat-treated at a temperature above the α→β transformation temperature (1020 ℃ for 2 hours and 30 minutes followed by CC) have the columnar epitaxial prior-β grains replaced by equiaxed and semi-equiaxed prior-β grains. The diameters of these prior-β grains are in the range of 150–500 µm, as seen in Figure 5-1(e), indicating extensive grain growth of the material when heat-treated above the β-transus for an extended period. Typical Widmanstätten structure with large α colonies can be seen

© Central University of Technology, Free State

in Figure 5-1(e) and 5-2(e). These colonies contain several parallel α plates where their sizes are limited by the adjacent α colonies. However, in some areas within the β-grains, as seen in Figure 5-1(e), the Widmanstätten α-lath structures change to basket-weave. The width of the α laths within these colonies ranged between 7–15 µm, while the average width of these laths was determined through the line-intercept method as 9 µm. Additionally, a much thicker continuous grain boundary α can also be observed at prior-β boundaries, having a thickness of about 10 µm.

The equiaxed and semi-equiaxed grains that were created by splitting of columnar prior-β grains can be seen in Figure 5-1(a), (b) and (c). The high thermal energy prevalent in this regime causes a reduction in the interfacial energy, thus causing the movement of the initial-β-grain boundaries. These induced recovery and nucleation processes account for the new semi-equiaxed and equiaxed grain morphology. This kind of microstructure could result in loss of material strength due to coarsening of the grains. However, it is expected to give the highest ductility among all the samples discussed here if the logic behind the slip path is to be considered. Hence, lath thickness > 7 µm can yield higher ductility in comparison to those of thickness of 2.5 µm and 6 µm obtained in the case of samples C and D, respectively. Even so, it may be argued that this microstructure may show the lowest ductility or even premature failure, since the large incessant grain boundary α layers with low ductility could even be the favourably areas of inelastic deformation leading to intergranular fracture.

5.3 CRYSTALLOGRAPHIC TEXTURE OF AS-BUILT AND HEAT-TREATED DMLS TI6AL4V(ELI)

5.3.1 The percentage fraction and distribution of the α and β-phases

Figure 5-3 shows the distribution and percentage proportions of the α-phase and the β-phase in Ti6Al4V(ELI) for the samples as-built, stress-relieved and heated-treated in various regimes. The EBSD mappings shown in Figure 5-3(a) highlight the absence of the β-phase in the Ti6Al4V(ELI) alloy microstructure immediately after production in the as-built state. In Figure 5-2(b), the percentage of β-phase detected in the stress-relieved microstructure via this method is seen to be below 1%. This is confirmation that stress-relieving heat treatment has little or no effect on the microstructural constitution of the alloy.

© Central University of Technology, Free State

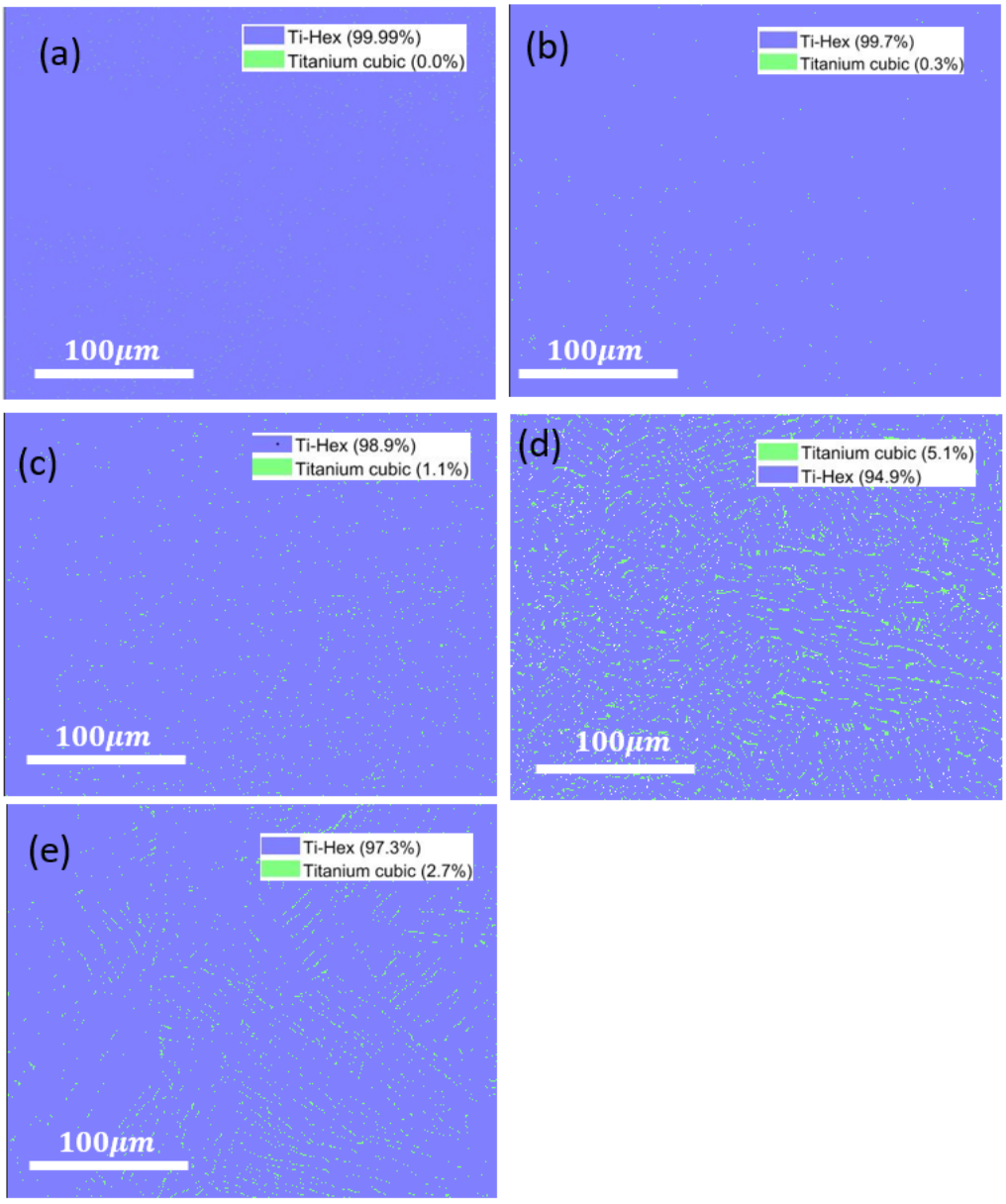

Figure 5-3. The EBSD phase maps showing the typical α- and β-phase distributions and percentage fraction in (a) samples A, (b) samples B, (c) samples C, (d) samples D and (e) samples E.

From the images in Figure 5-3, the fraction of β-phase is seen to have increased at higher annealing temperatures that were below the β-transus temperature, with sample C and D recording 1.1% and 5.1% of this phase, respectively, with a proportionate decrease in the α-phase. A value of 2.7% of the β-phase was detected for sample E that was heat-treated above the α→β transformation temperature and then cooled down to room temperature. This ties well with the expected deposition of the α phase upon cooling from the pure β-phase existing above the β-transformation temperature.

© Central University of Technology, Free State

5.3.2 Crystallographic texture of transformed α phase

The Ti6Al4V alloy is generally composed of crystalline grains with each grain (either α or β) having a crystal structure with a uniform crystallographic orientation relative to a reference frame. Grain orientation distributions in polycrystals are generally dependent on processing history and any alignments of these crystals are referred to as texture. To understand well the micro-texture of various microstructures of DMLS Ti6Al4V(ELI), EBSD orientation maps for various microstructures were obtained and are presented in Figure 5-4.

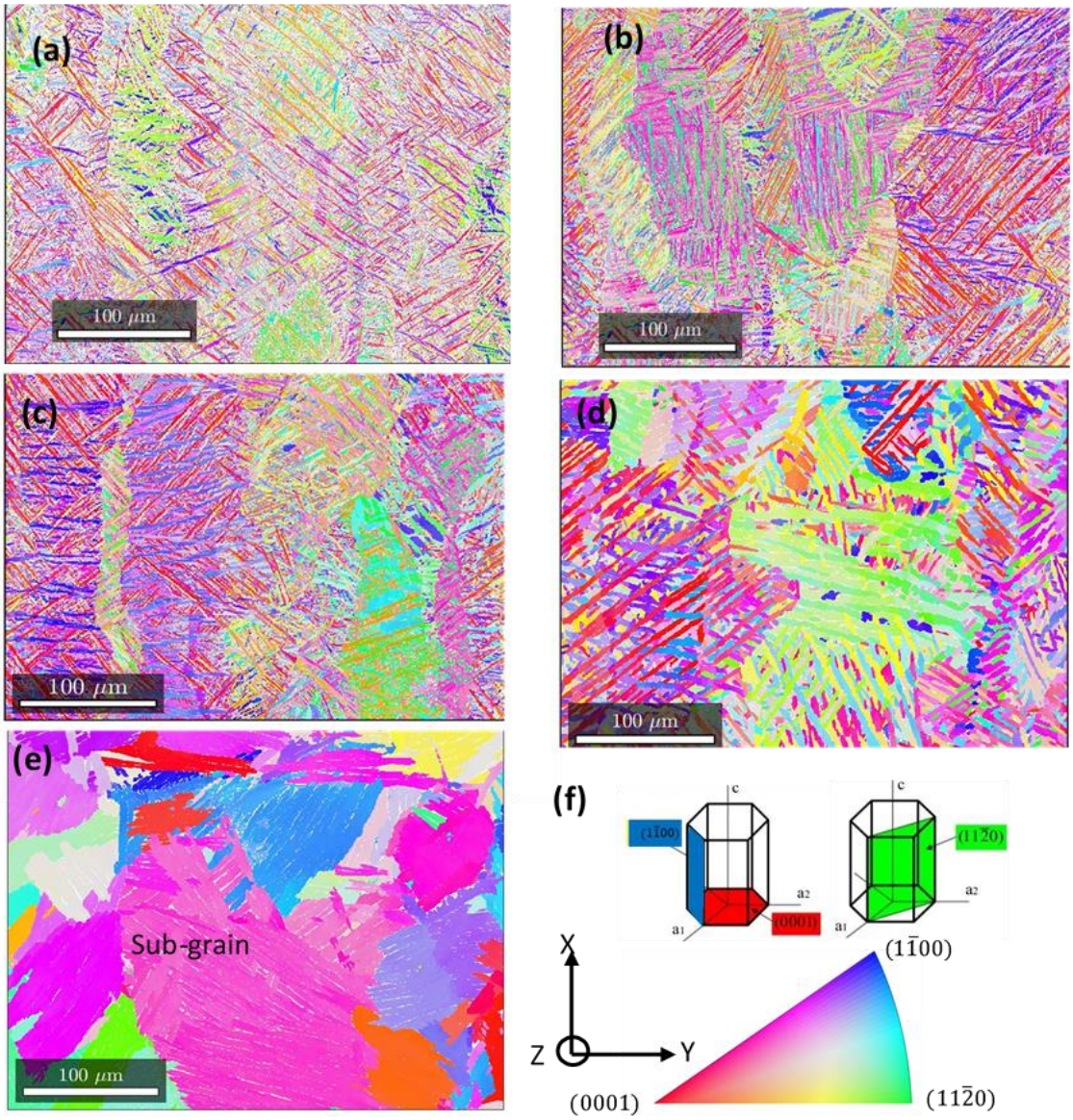

Figure 5-4. The Euler orientation maps of (a) samples A, (b) samples B, (c) samples C, (d) samples D and (c) samples E, while (f) is the α-hcp principal planes and their depiction in the IPF key.

© Central University of Technology, Free State

The EBSD orientation maps shown in Figure 5-4 on the X-Y section of the samples were indexed by the cell parameters of the α and β phases (taken as *a* = 2.954 and *c* = 4.729 for Ti-Hex and *a* = 3.192 for Ti-cubic). The sample coordinates were defined by *X*, *Y* and *Z* directions. The Z-coordinate was the normal to the sample surface (out of plane of the image), which was the direction of the EBSD scans, while the X-coordinate of the sample was aligned to the build direction of the samples during the DMLS process. The crystallographic orientations of the α/α' needles are illustrated by Euler angles for all samples shown in Figure 5-4. Prior-β grains elongated along the build direction are distinct along the build direction in Figure 5-4 (a, b and c), while in (d) and (e), the columnar grains seem to disappear. This relates to the heat treatment at a temperature just below the β-transformation temperature in the case of samples D and above the β-transformation temperature in case of the samples E. As seen in Figure 5-3(e), the equiaxed and semi-equiaxed morphologies of the prior-β grains have orientation maps showing sub-grains within them, each consisting of crystals with a similar orientation, shown by the same colour. This orientation distinguishes the α colonies (parallel α laths shown in Figure 5-4(e)), since these colonies are composed of α-laths with the same crystal orientation.

It is important to note that the inverse pole figure's (IPF) key shown in Figure 5-4(f) has the colour codes related to the specific orientations: the colours red, green and blue represent the family of planes $\{0001\}$, $\{11\bar{2}0\}$ and $\{1\bar{1}00\}$, respectively, parallel to the surface X-Y. The α' martensitic needles previously described in Figure 5-1(a and b) are conspicuous in Figure 5-4(a and b) with random prevailing texture. High numbers of orientations or variants within each prior-β grain that are elongated along the build direction can be seen in these orientation maps. However, some crystal orientations of the α'-needle-shaped grains tend to repeat within the same prior-β grains, as indicated by the repetition of the same colour of the α' acicular martensitic grains. It is clear from the EBSD orientation map in Figure 5-4(c and d) that extensive growth of α-laths occurred after heat treatments C and D. But, like the as-built and stress-relieved samples, the samples C and D exhibited random texture with mixed overall α-lath configurations, largely in-between the $\{0001\}$, and $\{1\bar{1}00\}$ planes, with some α/α' laths within the same prior grains exhibiting similar crystal orientations. The randomness/weak texture of the α/α'-laths in samples A, B, C, and D can be elucidated by the fact that the phase transformation of the β→α during cooling

© Central University of Technology, Free State

proceeds randomly with twelve definite orientation relationships between the prior-β grain (mother) and the α-phase (daughter) in the so-called Burgers Orientation Relationship (BOR). The BOR between the α and β-phase of the Ti6Al4V alloy is shown in Figure 5-5, as described by Burgers (1934).

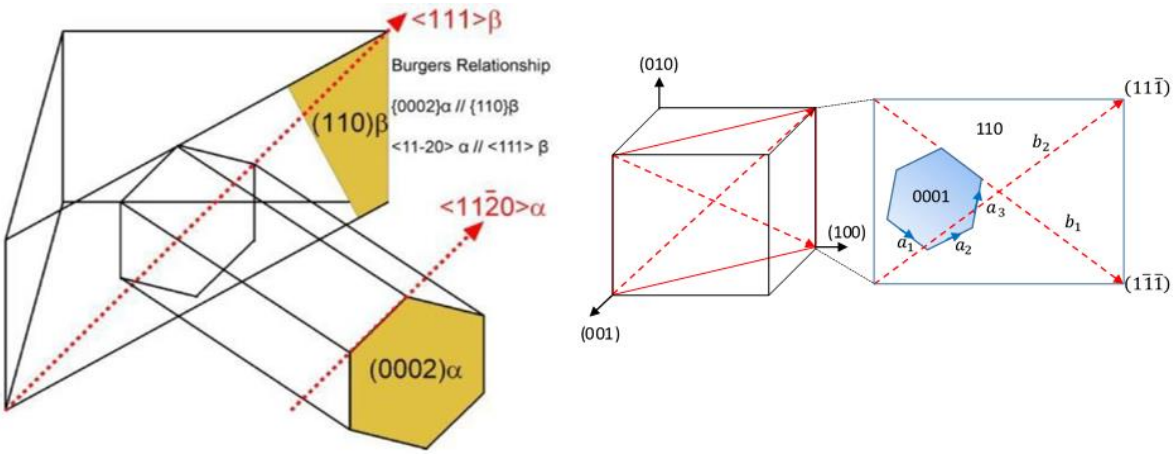

Figure 5-5. Schematic diagram illustrating the α/β BOR (Burgers 1934, Obasi 2012).

Table 5-1. Twelve possible variants produced by the β→α-phase transformation through the BOR (Wang et al. 2014)

	Variant plane parallel	Direction parallel	Rotation angle/axis from V1	Type
V1	$(1\bar{1}0)_\beta \| \| (0001)_\alpha$	$[111]_\beta \| \| [11\bar{2}0]_\alpha$	-	Type 0
V2	$(10\bar{1})_\beta \| \| (0001)_\alpha$	$[111]_\beta \| \| [11\bar{2}0]_\alpha$	$60°/[11\bar{2}0]$	Type II
V3	$(01\bar{1})_\beta \| \| (0001)_\alpha$	$[111]_\beta \| \| [11\bar{2}0]_\alpha$	$60°/[11\bar{2}0]$	Type II
V4	$(110)_\beta \| \| (0001)_\alpha$	$[\bar{1}11]_\beta \| \| [11\bar{2}0]_\alpha$	$90°/[1\overline{2.38}\ 1.38\ 0]$	Type V
V5	$(101)_\beta \| \| (0001)_\alpha$	$[\bar{1}11]_\beta \| \| [11\bar{2}0]_\alpha$	$63.26°/[\overline{10}\ 5\ 5\ \bar{3}]$	Type IV
V6	$(01\bar{1})_\beta \| \| (0001)_\alpha$	$[\bar{1}11]_\beta \| \| [11\bar{2}0]_\alpha$	$60.83°/[\overline{1.377}\ \bar{3}\ 2.377\ 0.359]$	Type III
V7	$(110)_\beta \| \| (0001)_\alpha$	$[1\bar{1}1]_\beta \| \| [11\bar{2}0]_\alpha$	$90°/[1\ \overline{2.38}\ 1.38\ 0\ ]$	Type V
V8	$(10\bar{1})_\beta \| \| (0001)_\alpha$	$[1\bar{1}1]_\beta \| \| [11\bar{2}0]_\alpha$	$60.83/[\overline{1.377}\ \bar{1}\ 2.377\ 0.3595]$	Type III
V9	$(011)_\beta \| \| (0001)_\alpha$	$[1\bar{1}1]_\beta \| \| [11\bar{2}0]_\alpha$	$63.26°/[\overline{10}\ 5\ 5\ \bar{3}]$	Type IV
V10	$(1\bar{1}0)_\beta \| \| (0001)_\alpha$	$[11\bar{1}]_\beta \| \| [11\bar{2}0]_\alpha$	$10.53°/[0001]$	Type I
V11	$(101)_\beta \| \| (0001)_\alpha$	$[11\bar{1}]_\beta \| \| [11\bar{2}0]_\alpha$	$60.83/[\overline{1.377}\ \bar{1}\ 2.377\ 0.3595]$	Type III
V12	$(011)_\beta \| \| (0001)_\alpha$	$[11\bar{1}]_\beta \| \| [11\bar{2}0]_\alpha$	$60.83/[\overline{1.377}\ \bar{1}\ 2.377\ 0.3595]$	Type III

Between the twelve variants shown in Table 5-1, five different types (excluding Type 0 which is the reference) can be formed based on the misorientation angle between a pair of

© Central University of Technology, Free State

α-grains. The details of these misorientation angle distributions are discussed further in section 5.2.4.

It would be expected that during the β→α-phase transformation, all twelve variants of orientation would occur with equal probability. However, as described in Figure 5-4, some α/α'-lath orientations tend to repeat within the same prior-β grain. This preference of certain variants can be attributed to variant selection (Simonelli *et al*. 2014). Further details of variants at a scale of a single prior-β grain are discussed in section 5.2.3.

One of the most important tools in crystallographic textural analysis are pole figures, which were described well in Chapter 2 section 2.6.2. In overview, a pole figure (PF) is a two-dimensional stereographic projection of a crystallographic plane normal onto the equatorial plane of an imaginary sphere. It shows the variation of pole density with pole orientation from a selected set of crystal planes with respect to a reference direction. To study and compare the texture of the five different samples from the pole figures, orientation densities from various crystal planes of α-phase, namely $(10\bar{1}0)$, $(01\bar{1}0)$, (0001), $(11\bar{2}0)$, $(01\bar{1}1)$, $(10\bar{1}1)$ and $(11\bar{2}1)$ were plotted. The intensities of the pole distributions were visualised in terms of contours and colour, then expressed as multiple unit density (MUD). Here, the pole figure contours are analogous to topographic maps, where an increasing value would correspond to higher elevation in a topographic map. For instance, a higher value of MUD corresponds to stronger texture; MUD 3 means thrice as many grains are aligned with corresponding lattice planes in this direction than MUD 1. Figures 5-6 to 5-10 show the α/α' contour pole figures for samples A to E.

© Central University of Technology, Free State

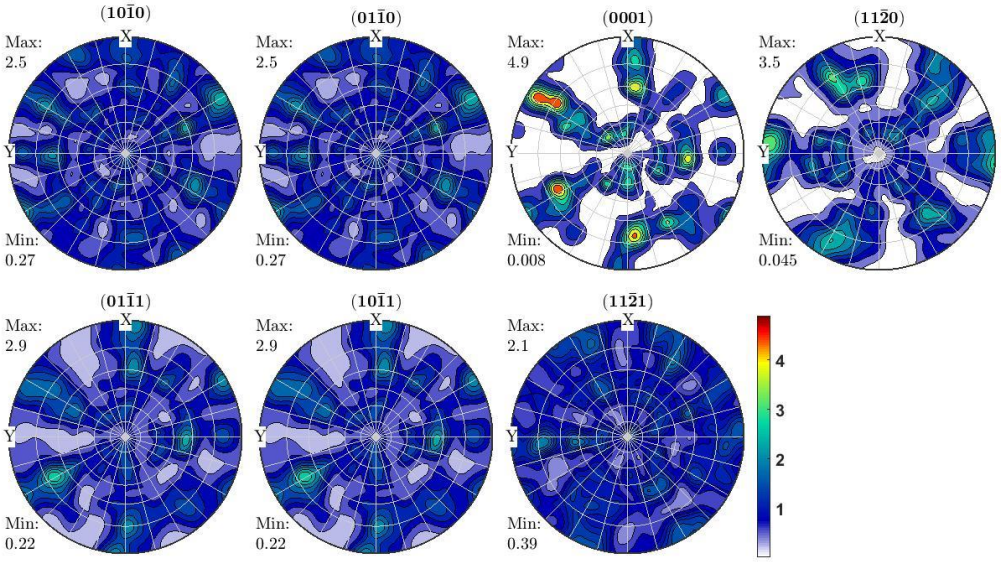

Figure 5-6. The (10$\bar{1}$0), (01$\bar{1}$0), (0001), (11$\bar{2}$0), (01$\bar{1}$1), (10$\bar{1}$1) and (11$\bar{2}$1) *contour PFs of the α-phase for samples A.*

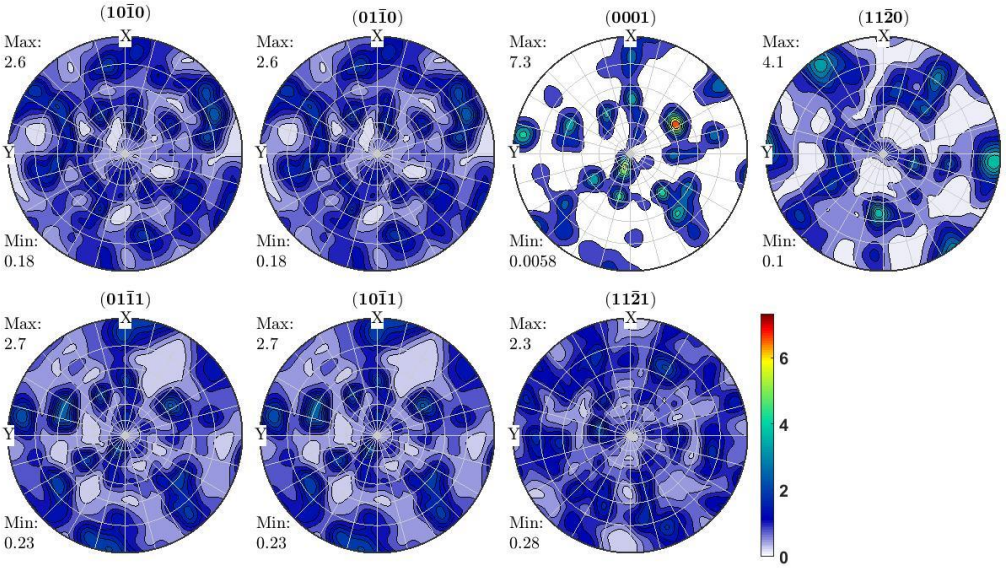

Figure 5-7. The (10$\bar{1}$0), (01$\bar{1}$0), (0001), (11$\bar{2}$0), (01$\bar{1}$1), (10$\bar{1}$1) and (11$\bar{2}$1) *contour PFs of the α-phase for samples B.*

© Central University of Technology, Free State

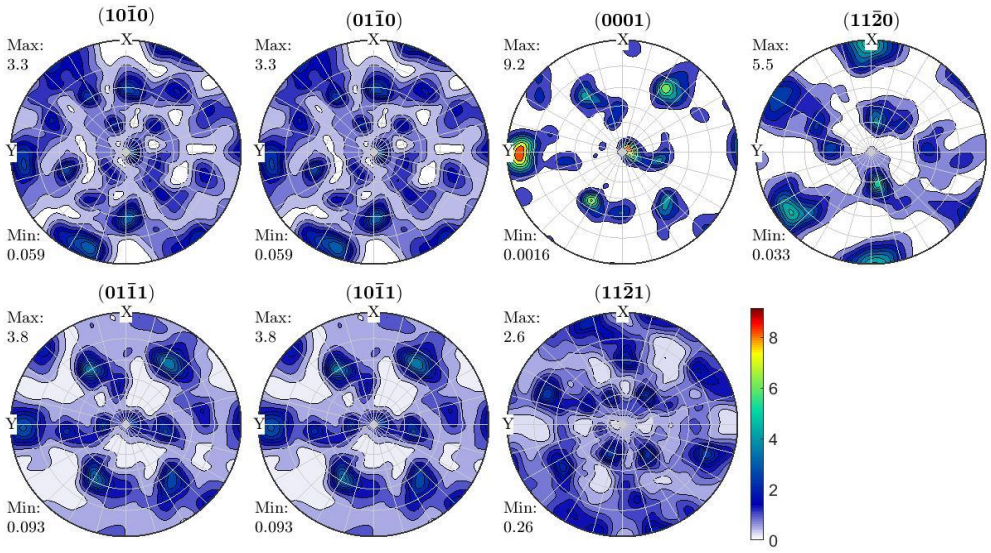

Figure 5-8. The (10$\bar{1}$0), (01$\bar{1}$0), (0001), (11$\bar{2}$0), (01$\bar{1}$1), (10$\bar{1}$1) and (11$\bar{2}$1) *contour PFs of the α-phase for samples C.*

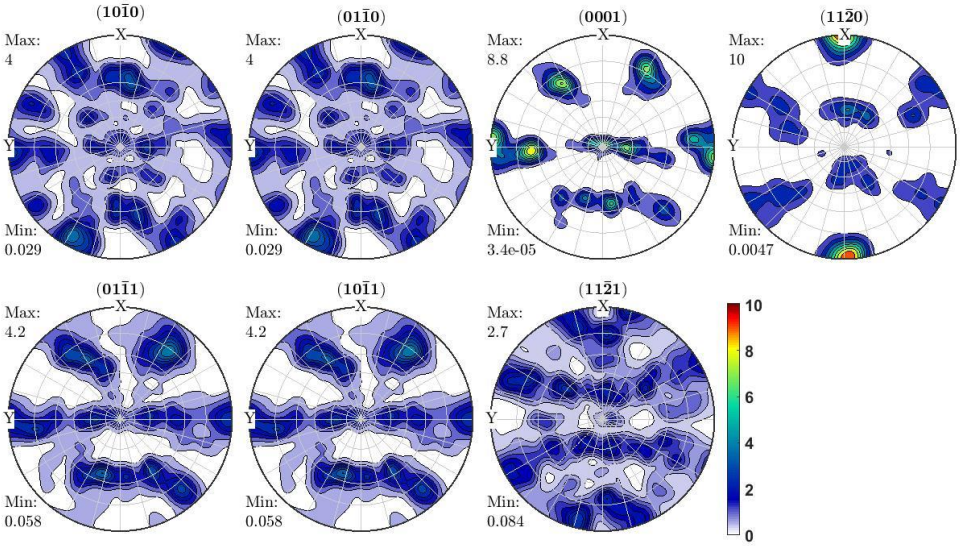

Figure 5-9. The (10$\bar{1}$0), (01$\bar{1}$0), (0001), (11$\bar{2}$0), (01$\bar{1}$1), (10$\bar{1}$1) *and* (11$\bar{2}$1) *contour PFs of the α-phase for samples D.*

© Central University of Technology, Free State

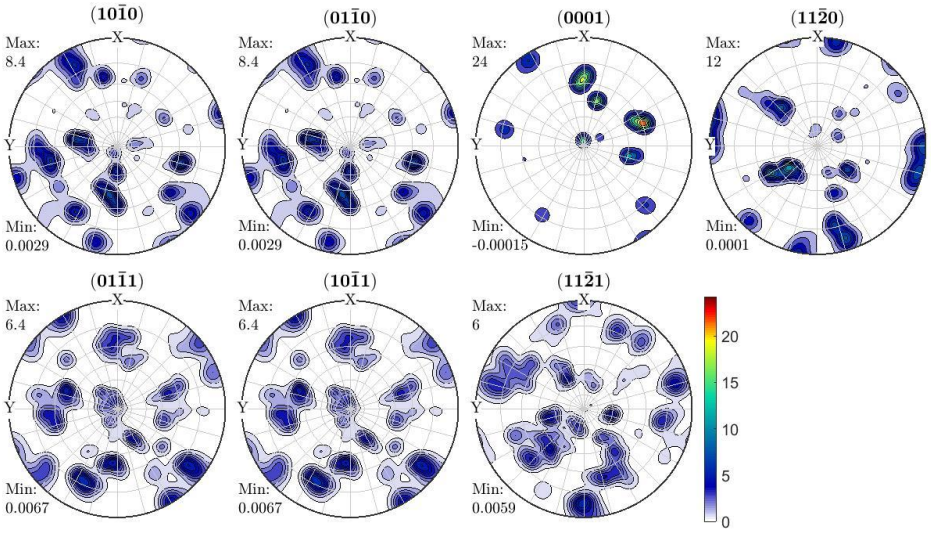

Figure 5-10. The $(10\bar{1}0)$, $(01\bar{1}0)$, (0001), $(11\bar{2}0)$, $(01\bar{1}1)$, $(10\bar{1}1)$ and $(11\bar{2}1)$ *contour PFs of the α-phase for samples E.*

A summary of the maximum values of the texture in the form of MUD for the different planes in these Figures 5-6 to 5-10 are summarised in Table 5-2.

Table 5-2. A summary of the maximum MUD densities of different planes for samples A to E

Plane	$(10\bar{1}0)$	$(01\bar{1}0)$	(0001)	$(11\bar{2}0)$	$(01\bar{1}1)$	$(10\bar{1}1)$	$(11\bar{2}1)$
sample				**Max-MUD**			
A	2.5	2.5	**4.9**	3.5	2.9	2.9	2.1
B	2.6	2.6	**7.3**	4.1	2.7	2.7	2.3
C	3.3	3.3	**9.2**	5.5	3.8	3.8	2.6
D	4.0	4.0	8.8	**10.0**	4.2	4.2	2.7
E	8.4	8.4	**24.0**	12.0	6.4	6.4	6.0

It is worth mentioning here that all the EBSD scans for the five groups of samples were carried out on an equal grid area on each sample of 980 µm by 735 µm and hence the influence of heat treatment on the micro-texture could be deduced. The α/α'-phase texture of the five different samples is quite different. As noted in Figure 5-4(a–d), no packets of α'/α laths share the same crystallographic orientation, which appears as a spread in the foregoing pole figures, but the spread decreases with heat treatment across all the Miller planes. As previously stated, there are a few orientations that tend to repeat within the same prior-β grains and give rise to clustering, resulting in maximum MUDs around a specific orientation. The maximum intensities of texture for samples A are significantly weaker (maximum values ranging from 2.1 to 4.9) in comparison to the rest. There is a

© Central University of Technology, Free State

slight improvement of the maximum texture values of samples A to D. Heat treatments C and D led to decomposition of the unstable α'-martensitic phase into stable α+β with significant increase of the widths of the α laths. It can also be argued that while the sampling grid area is constant, the remarkable growth of α-laths from about 0.5 µm in the as-built state to about 2.5 µm and 6 µm after heat treatment for samples C and D, respectively, could contribute to the increased frequency of orientations of planes seen in Table 5-2. This inference is because an increase in the size of α-grains could mean an increase in the number of α crystals packed within the grains, since the crystal lattice constants remain relatively unchanged after heat treatment.

A significant improvement in texture from the pole figure is noted in samples D to E (maximum value ranging from 6 to 24). It is noted that samples E were exposed to heat treatment above the β-transus temperature then cooled down, whilst the rest of the samples that were heat-treated, were heat-treated below the transformation temperature. Heat treatment above the transformation temperature was accompanied by decomposition of the elongated prior-β grains into semi-equiaxed grains that consist of a typical Widmanstätten microstructure. This microstructure is characterised by large α colonies that contain numerous parallel α-laths with the same crystallographic orientations, as explained in Figure 5-4(e). This, together with the effect of an increase in the width of α-laths discussed in the preceding paragraph explains the remarkable improvement of the intensity of texture of α-grains for samples E in comparison with the rest of the samples. This shows that significant effective aggregation of the variants occurred after this heat treatment. Of all the planes, the maximum values of MUD of the (0001) plane is the highest for all the samples except for samples D where the $(11\bar{2}0)$ plane shows the maximum value. It is also noted in Figures 5-6 to 5-10 that a remarkable change in position of the $\{0001\}$ and $\{11\bar{2}0\}$ poles took place after heat treatment. This is possibly due to restoration of the microstructure that occurred after heat treatment and furnace cooling to room temperature.

5.3.3 Reconstruction of prior-β grains

As previously seen in Figure 5-3, the β→α-phase transformation occurred in DMLS Ti6Al4V(ELI) in such a manner that the percentage volume of the retained β-phase was

© Central University of Technology, Free State

statistically very small (< 6%) at ambient temperature. This low percentage volume of the β-phase was not sufficient to be taken as representative of the β-phase texture. Therefore, reconstruction of prior-β grains was executed using ARPGE program (Cayron 2007). Figures 5-11 and 5-12 show the orientation maps and (100), (110), and (111) pole figures of the resulting reconstructed prior-β grains of the five different samples of DMLS Ti6Al4V(ELI), respectively.

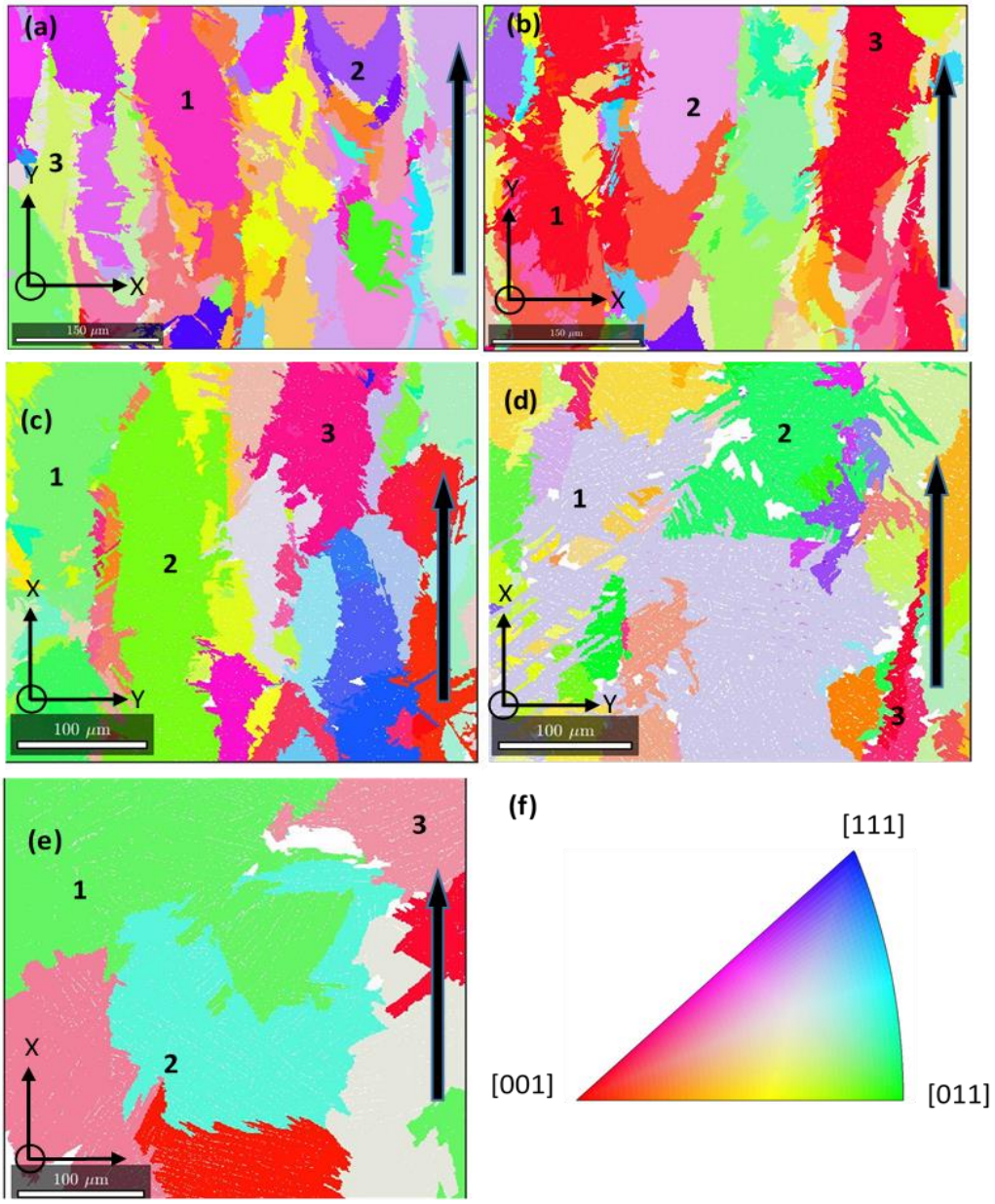

Figure 5-11. EBSD Euler map of reconstructed β-phase of (a) samples A (b) samples B, (c) samples C, (d) samples D, and (e) samples E, while (f) is the inverse pole figure (IPF) key for β-principal planes, with the black arrows in the figures indicating the build direction.

© Central University of Technology, Free State

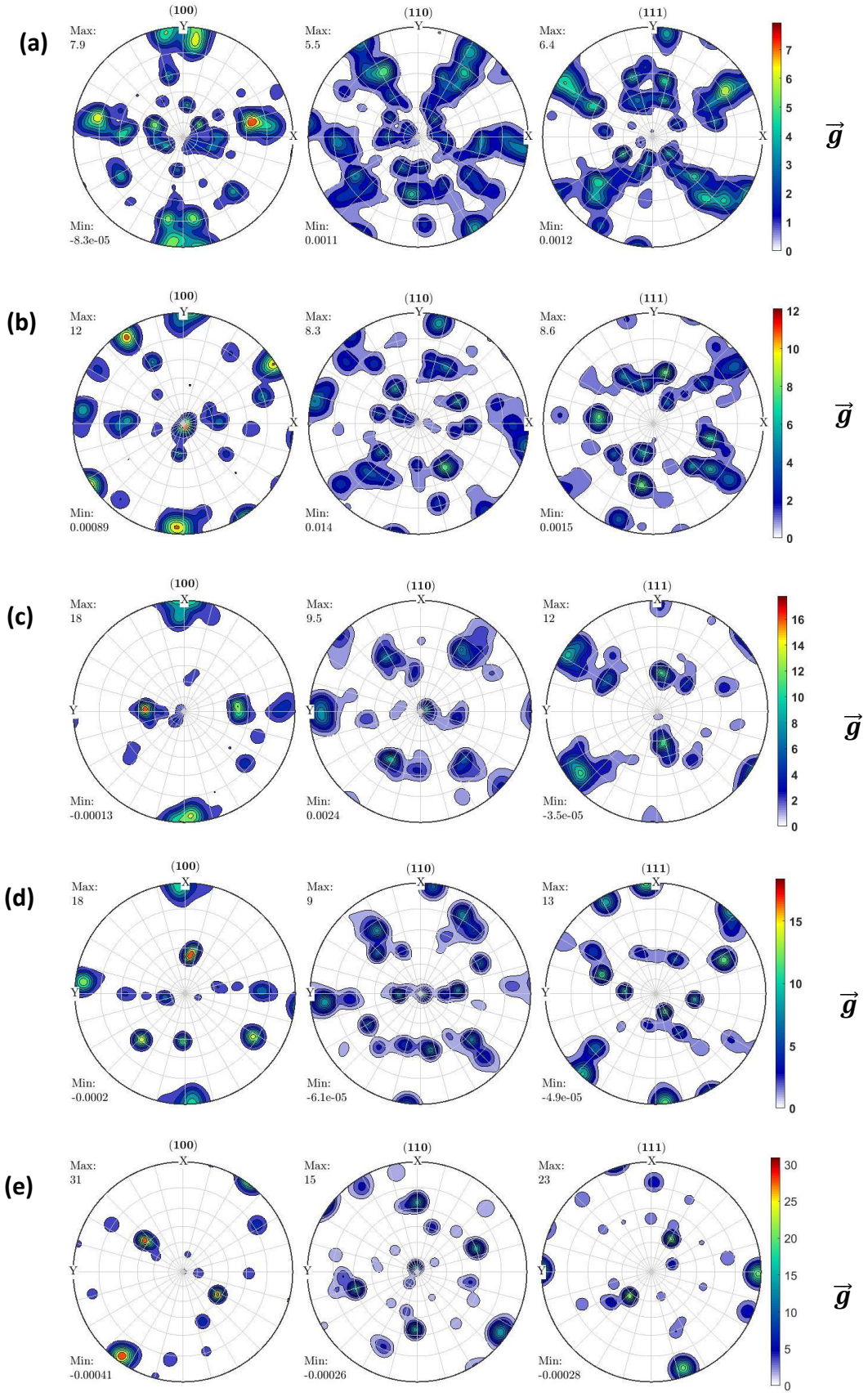

Figure 5-12. The (100), (110), and (111) pole figures of the β-phase of samples (a) A, (b) B, (c) C, (d) D, and (e) E.

© Central University of Technology, Free State

As shown in Figure 5-11, the prior-β grains are now apparent and extended along the build orientation for samples A to C and less pronounced in the case of samples D. The analysis of pole figures in Figure 5-12 shows the (100) poles to be mainly concentrated approximately in the build direction, $\vec{g}$, with the intensity of these poles being higher than the rest, as shown in Table 5-3.

Table 5-3. Summary of the maximum-MUD densities of different planes of the samples A to E

Plane	**(100)**	**(110)**	**(111)**
Sample	**Maximum - Multiple Unit Density (MUD)**		
A	*7.9*	*5.5*	*6.4*
B	*12*	*8.3*	*8.6*
C	*18*	*9.5*	*12*
D	*18*	*9*	*13*
E	*31*	*15*	*23*

The development of typical fibre texture of the prior-β grains with the $\langle 100 \rangle$ directions parallel or near parallel to the build direction has been reported in the recent literature for AM material (De Formanoir *et al.* 2016, Xufel and Xin 2017). Grain re-orientation has been reported to occur during the columnar growth of the β phase, giving rise to a preferred $\langle 100 \rangle_{\beta}$ orientation aligned with the maximum thermal gradient (Obasi *et al.* 2012, Simonelli *et al.* 2014). It is important to note here that during the DMLS process, the base plate and subsequently deposited layers act as heat sinks during deposition, while the laser beam provides the source of heat from above. Consequently, the maximum thermal gradient during the DMLS process is along the build direction. While this elucidates the alignment of the fibrous texture in the build direction of the prior-β grains in DMLS parts, this fibrous texture disappeared in samples E. This was a result of decomposition of the columnar prior-β grains upon heat treatment.

As also seen in Table 5-3, samples E showed a strong $\langle 100 \rangle_{\beta}$ texture with an intensity of about 31, whereas for samples A, the intensity was only 7.9 indicating a more random texture in the former. One possible explanation of this is the lateral growth of the β-grains, as seen in Figure 5-11(e). It is also to be noted that, overall, the texture of the transformed α′/α-phase shown in Table 5-2 was weaker than those of the β-phase texture shown in Table 5-3 for all the samples. Obviously, this suggests there was variant selection during the

© Central University of Technology, Free State

β→α transformation. The α texture was diluted since there are twelve possible variants that could form from a single prior-β grain, as previously shown in Table 5-1.

5.4 VARIANT SELECTION MECHANISM OF THE β→α TRANSFORMATION IN DMLS Ti6Al4V(ELI)

As previously seen in Table 5-1, there are six β poles, which are $(110)_{\beta}$, $(1\bar{1}0)_{\beta}$, $(101)_{\beta}$, $(10\bar{1})_{\beta}$, $(011)_{\beta}$, $(0\bar{1}1)_{\beta}$ in total for the β phase. Two $(0001)_{\alpha}$ poles amongst the twelve possibilities share a common $\{110\}_{\beta}$ pole. Therefore, six equivalent β variants can be gathered from the defined α/α′ orientation. The misorientation angles and axes between any two of the twelve α/α′-variants from the same β- grains are unique and are categorised into the five groups shown in Table 5-1. These groups are referred to as operators in the ARPGE program and are popularly used to work out the crystallographic orientations of parental β-grains (Cayron 2007).

The discrete pole figures and frequency of the α/α′-variant distribution of at least three reconstructed parent grains, labelled 1, 2, and 3 in Figure 5-11 for each sample, were obtained and presented in Figure 5-13. This was carried out in detail to study the orientation relationship between the α/α′-variants which formed within the prior-β grains and the parent-β phase. As shown in Figure 5-13, there are six variants that formed inside each parent-β grain. The (0001) planes (shown by blue dots) of the α/α′-phase are nearly parallel to one of the $\{110\}$ planes (shown by the red dots) of the β-phase. A keen observation of these pole figures shows that even if the (0001) poles are clustered around (110) poles, there is a remarkable spread in orientations between the two phases. This indicates deviations from the known BOR in the Ti6Al4V alloy.

It is interesting, however, to note that the BOR orientation spread in samples E that were heat-treated above α→β transformation temperature has drastically reduced with the α-(0001) and β-(110) perfectly superimposed. Since the α-phase is known to respect the BOR when it precipitates, the observations made from Figure 5-13 indicate that the orientation is gradually distorted during cooling in the DMLS process. The high cooling rate in the DMLS process leads to accumulation of micro-thermal residual stress and strain, which leads to deformation and slight rotation of crystalline lattices due to lattice strain.

© Central University of Technology, Free State

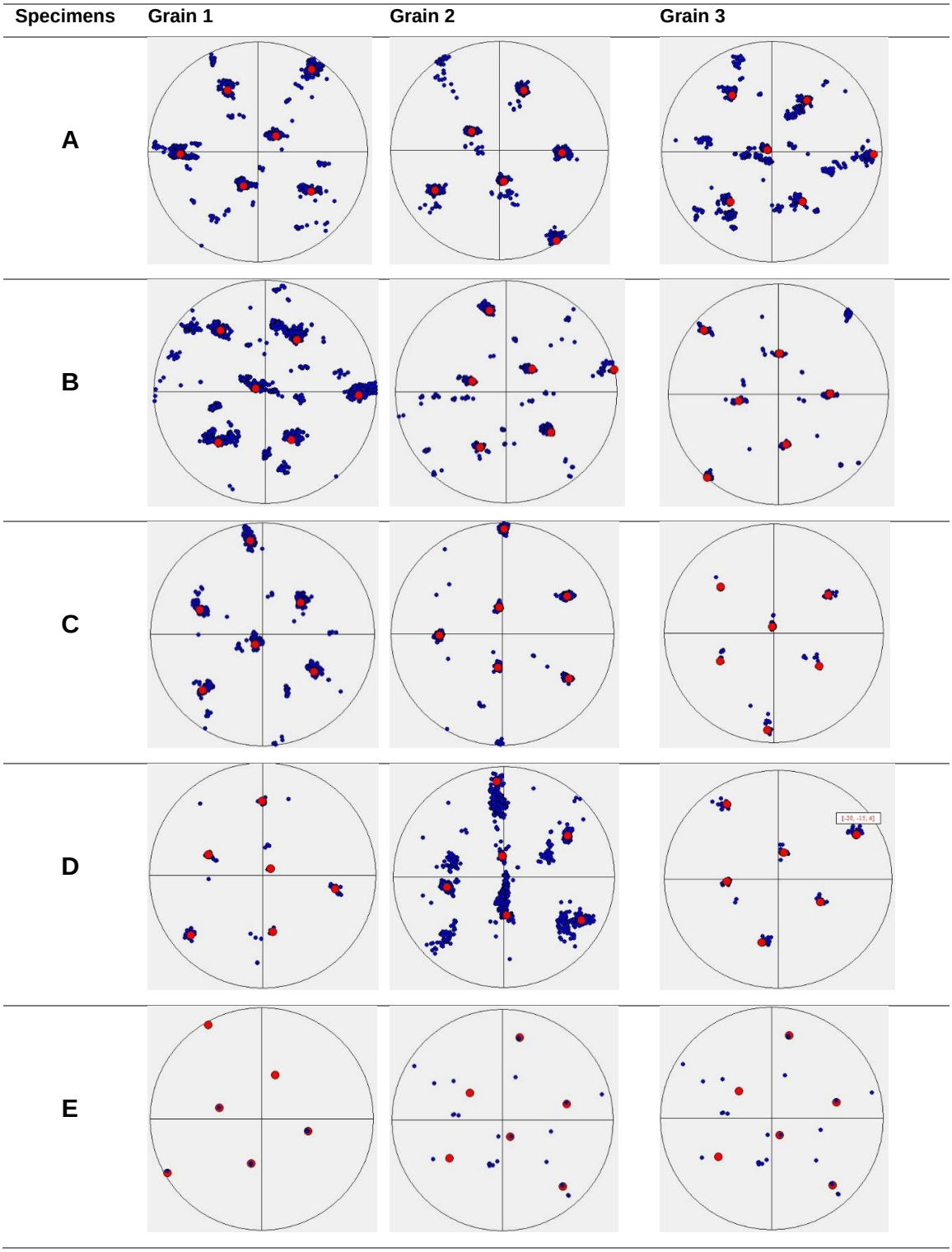

Figure 5-13. Superimposed discrete pole figures of (110) poles of reconstructed prior-β grains (the red dots) and the (0001) poles of clustering α/α'-laths (the blue dots) for samples A–E.

© Central University of Technology, Free State

To establish whether specific α'/α-variants were preferentially precipitated, statistics with reference to the variant frequencies were ascertained for at least three β-grains reconstructed in each group of samples. The frequency of α'/α-variants in a single β-grain in the samples were reported in Figures 5-14 and 5-15, since only the orientation information of the α-phase in a single β-grain can be used to study variant selection behaviour.

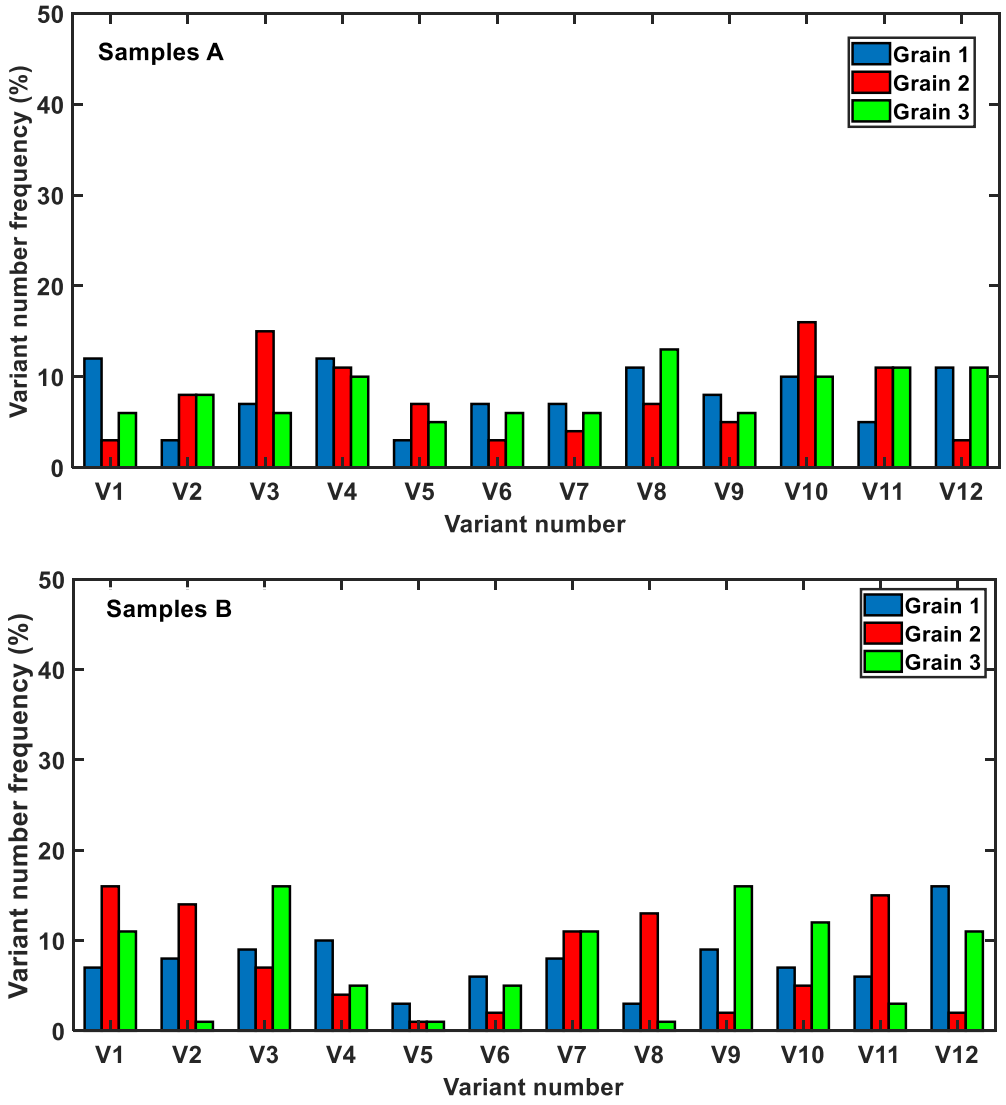

Figure 5-14. Histograms of variant frequency distribution arising from the three selected grains of samples A and B.

© Central University of Technology, Free State

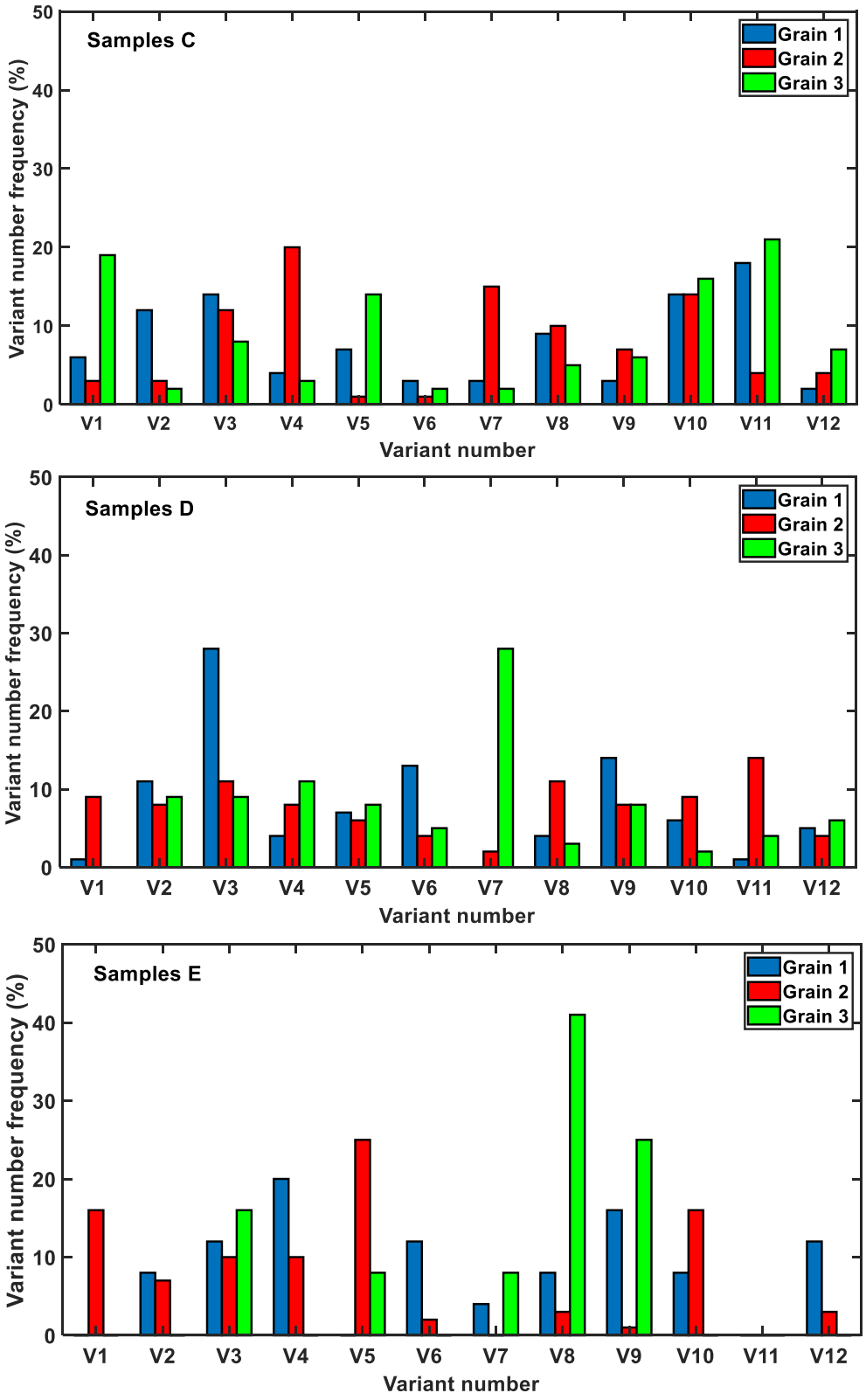

Figure 5-15. The histograms of variant frequency distribution arising from the three selected grains of samples C, D and E.

© Central University of Technology, Free State

During the β→α transformation, all twelve variants occurred in samples A, B and C, as seen in Figures 5-14 and 5-15, whereas in samples D and E, some variants were not precipitated in some grains, as seen in Figure 5-15. For instance, V1 and V7 are absent in grain 3 and grain 1, respectively, of samples D whilst in samples E at least one variant is absent, except V3, V8 and V9, which are present in the three grains.

Overall, there is no statistical trend among the twelve variants formed in the three grains analysed here for all the specimens. Nevertheless, some variants/orientations formed more frequently than others. When generally assessing the highest frequency in all the specimens, the variant selection intensified from sample A to E; that is 16%, 16% 21%, 28% and 41% in this order from samples A to samples E. A similar trend was observed in the texture strength of the (0001) pole figure presented in Table 5-2, where the slower cooling conditions of samples E from above the β-transus temperature revealed greater texture (24 times random) compared with the martensitic structure (4.9 times random).

Various factors have been cited in literature (Obasi *et al.* 2012, Beladi *et al.* 2014) to influence the extent of crystallographic variant selection during β→α-phase transformation. These factors include alloy composition (Beladi *et al*. 2014), prior-β grain size (Obasi *et al*. 2012), and phase transformation/cooling rate. Since the composition of the five forms of DMLS Ti6Al4V(ELI) alloy is the same and they only differ in microstructure, the effect of the composition in the variant selection can be winnowed out. Thus, the intensified crystallographic variant selection observed in the study for the samples annealed above the transformation temperature (E) as opposed to the as-built samples (A), is suggested to be because of emergence and coarsening of the parent-β grains and due to the slower cooling rate in comparison with the very fast cooling rate during the DMLS process.When the Ti6Al4V(ELI) alloy is heat-treated near or above the α→β transformation temperature followed by a moderate to slow cooling rate, the microstructure is characterised by competitive growth of α grains, and larger percentages of secondary α-Widmanstätten structure, as seen in Figures 5-1(e) and 5-4(e). This type of structure accounts for homogenous orientations, and thus, together with the growth of α-grains, could explain how the cooling rate contributed to the high preferential nucleation of certain variants more than others, which consequently dominated the texture of the transformed microstructure.

© Central University of Technology, Free State

5.5 MISORIENTATION DISTRIBUTION IN VARIOUS MICROSTRUCTURES OF DMLS TI6AL4V(ELI)

The boundaries between grains in polycrystalline materials are basically regions of disturbed lattice (dislocations) and are a few atomic diameters in width (Dieter 1986). Generally, crystallographic orientation changes abruptly in passing from one grain to the next across the grain boundary. Grain boundaries are conveniently categorised according to the extent of misorientation between adjoining grains. The EBSD orientation maps can be used as a tool to quantify restoration processes, because of heat treatment or even thermo-mechanical processes, by measuring the angles of grain boundaries. Figure 5-16 illustrates the grain boundary misorientation angle distribution obtained from the EBSD scanned surface of samples A, B, C, D, and E.

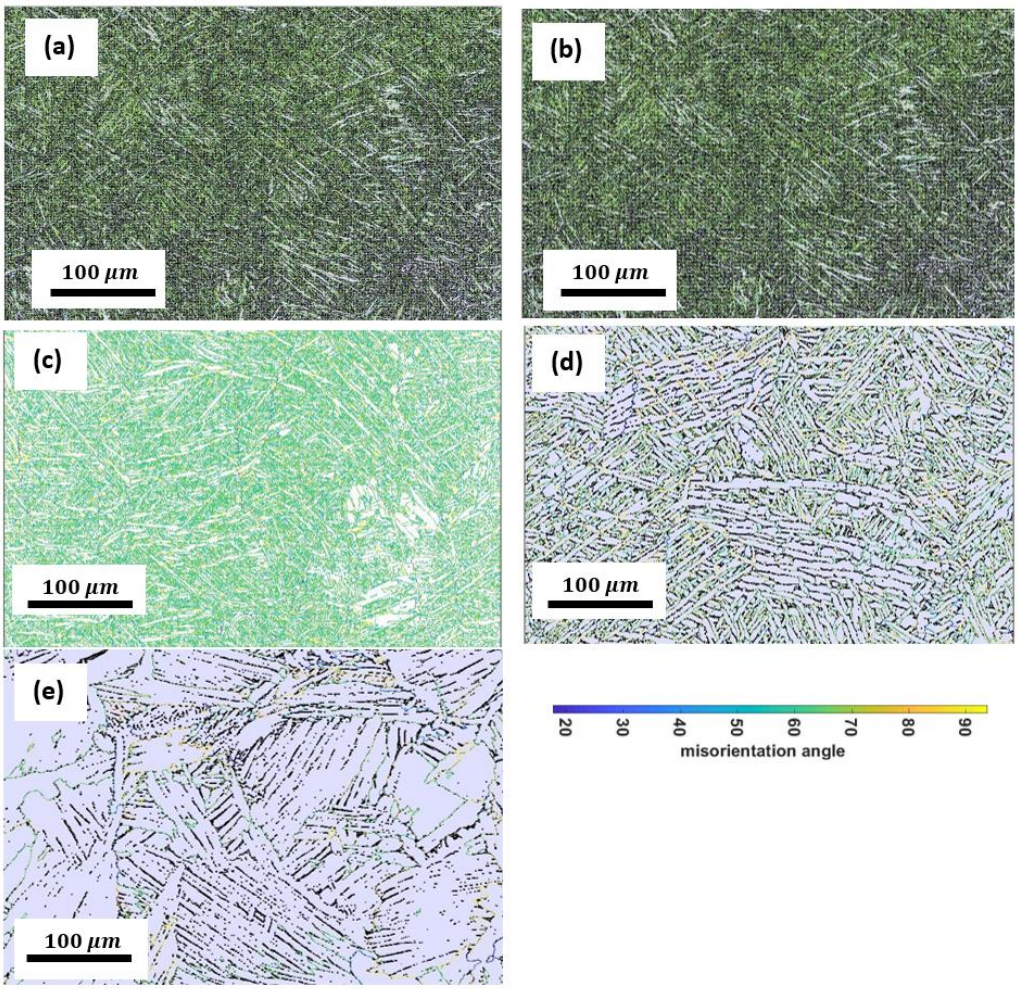

Figure 5-16. Grain boundary misorientation angles of the samples (a) A, (b) B, (c) C, (d) D, and (e) E. The legend with colour scale related to misorientation angle is also shown.

© Central University of Technology, Free State

The boundaries are colour-coded and the key provided is based on the misorientation angle size. Low-angle grain boundaries (LAGBs) or sub-grain boundaries are those with a misorientation less than about 15°, while high-angle grain boundaries (HAGBs) are those whose misorientation is greater than about 15°. Figure 5-17 provides a more intuitive regular distribution pattern of the grain boundary misorientation angles from Figure 5-16.

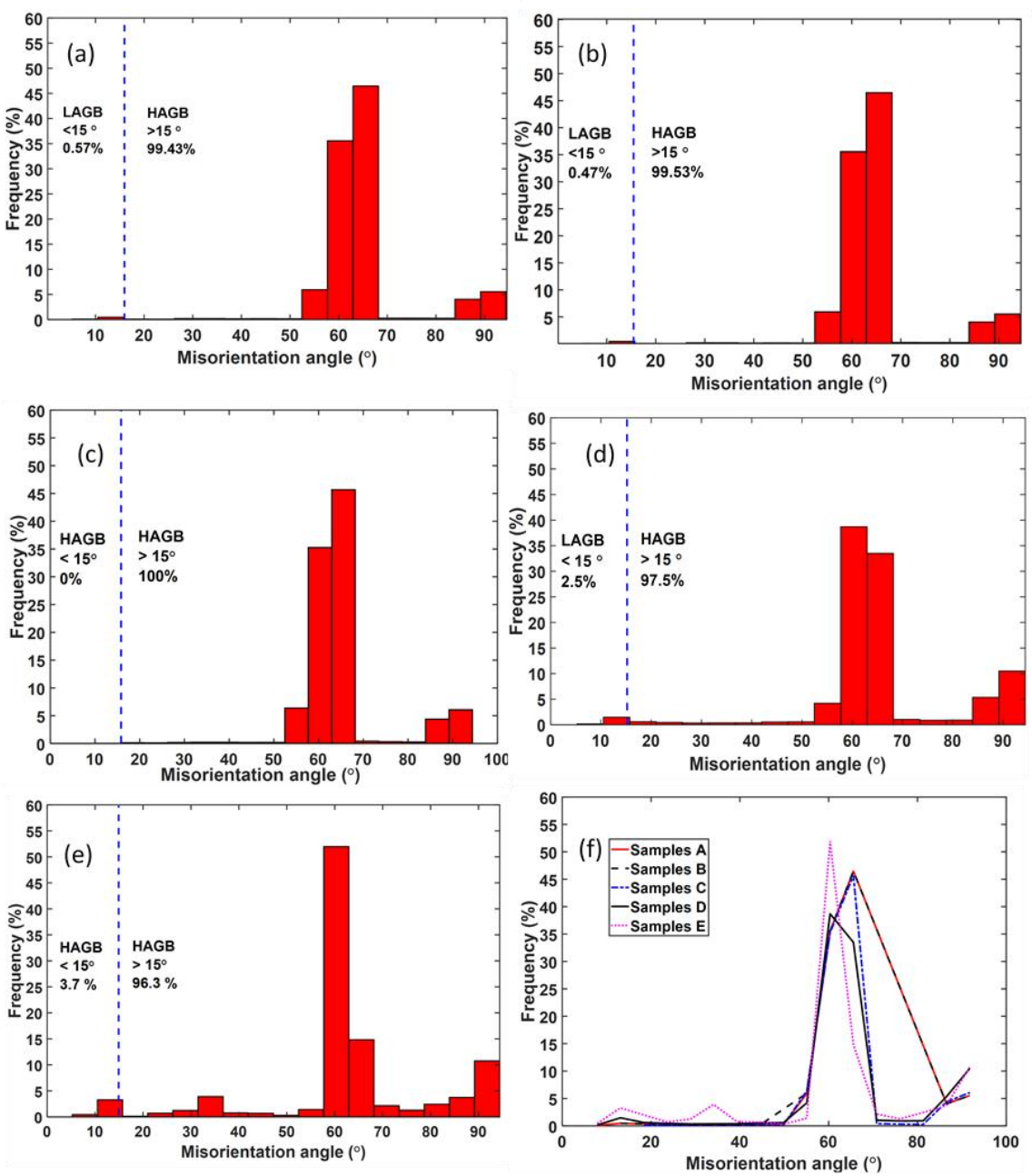

Figure 5-17. Grain boundary misorientation angle distribution of the samples (a) A, (b) (c) B, (c) C, (d) D, (e) E, and (f) a linear graph plot for comparison.

© Central University of Technology, Free State

The percentage fractions of HAGBs accounted for the majority of misorientation angles (> 95%) for all five groups of samples, with samples C not showing any traces of LAGBs, as seen in Figure 5-16(c) and Figure 5-17(c). The frequencies of LAGBs for samples A and B are less than 1%, while those of samples C and D are 2.5% and 3.7%, respectively. The initial decrease in the LAGBs in samples C that were annealed at an intermediate temperature of 800 ℃ is attributed to annihilation of dislocation arrays and HAGB growth at this temperature. Furthermore, the slow cooling rate of this heat treatment ensured minimal or no formation of residual strain, which may manifest as local variation in lattice orientation and therefore generate LAGBs.

The most significant fraction of misorientation is seen in Figure 5-17 to be at misorientation angles of between 55° and 70° in all cases of samples scanned. This is expected, since the misorientation types II, III, and IV shown in Table 5-1 consist of eight of the twelve possible variants (Type II: V2 & V3; Type III: V6, V8, V11 & V12; Type 1V: V5 & V9). In other words, the expected ratio between these misorientation types I, II, III, IV and V in the absence of any variant selection is 1:1:2:4:2:2. Between these angles, the misorientation frequencies of samples A and B, and that of samples C from 55° to 65° are equal, as shown by the coinciding linear curves in Figure 5-17(f) and peak at about 68° for these types of samples. The misorientation frequencies of samples D and E peak at about 60°, showing a decline from the rest. This decline was ascribed to remarkable grain growth that was associated with the two high-temperature annealing conditions of samples D and E. This decline would also suggest an ease of slip transfer in samples D and E in comparison to samples A, B and C. It is also noted that the highest peak frequency of misorientation angles for samples E is 53% compared to a value of 37% for samples D, which is the lowest value for all five types of samples. The higher peak frequency in samples E is suggested to be because of significant grain growth and thus, existence of relatively fewer grain boundaries in these samples in comparison to the other samples for an equal EBSD scanned area. In fact, the parallel α laths (colonies) seen in Figure 5-1(e) were confirmed to be sharing the same crystallographic orientation in Figure 5-4(e).

Generally, the impact toughness and strength of metals and alloys are strongly dependent on crack initiation and propagation and HAGBs play a critical role in hindering crack propagation. The presence of HAGBs at the interfaces of grains are known to lead to

© Central University of Technology, Free State

instability of microstructure (high number of atoms deviate) resulting in high energy accumulation at the grain boundaries (Dieter 1989). When cracks propagate towards HAGBs, their directions change many times due to random arrangement of the atoms, and therefore, demand higher amounts of energy to propagate cracks. Thus, samples C with the largest fraction of HAGBs will effectively impede the propagation of cracks more than the other samples studied here, thus reducing crack growth rate and therefore, improving their fracture toughness and impact energy.

5.6 HARDNESS TEST RESULTS OF THE VARIOUS MICROSTRUCTURES OF DMLS TI6AL4V(ELI)

The values of microhardness of non-heat-treated and heat-treated samples of DMLS Ti6Al4V(ELI) and their variation with heat-treatment temperature are plotted in Figure 5-18.

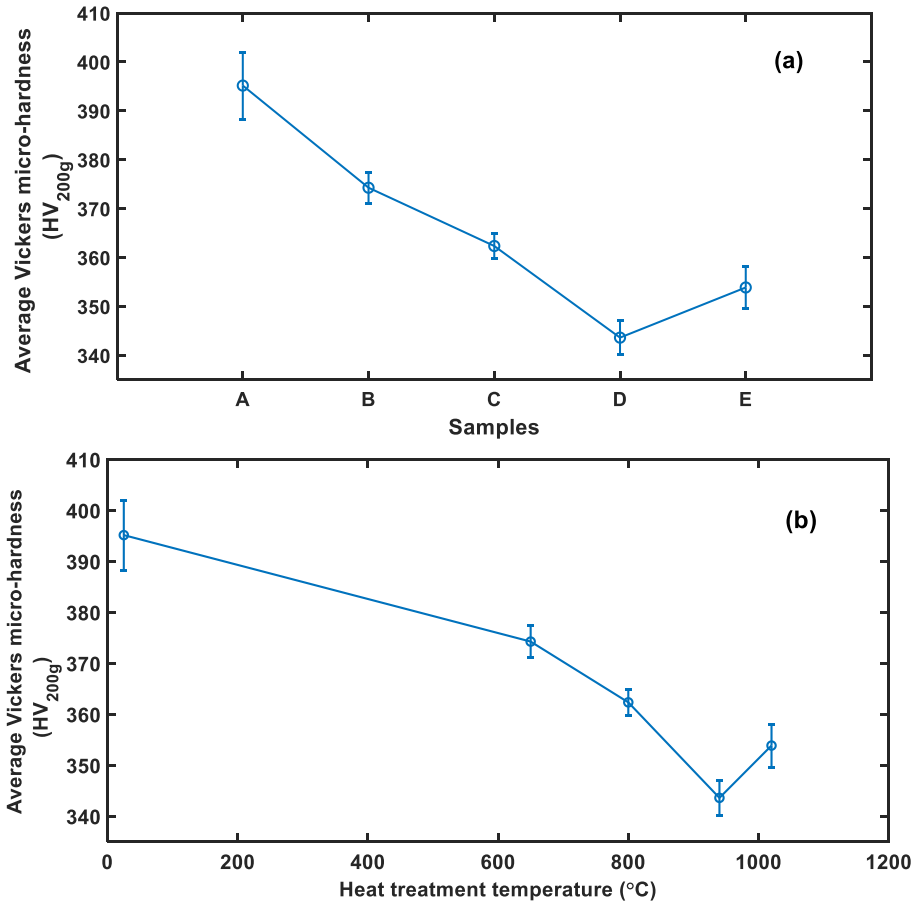

Figure 5-18. The average Vickers microhardness of (a) various forms of DMLS Ti6Al4V(ELI) and (b) variation with heat-treatment temperature.

© Central University of Technology, Free State

The Vickers microhardness of DMLS Ti6Al4V(ELI) is seen to decrease with 5% of the value recorded for the as-built samples upon stress-relieving heat treatment. This is expected due to the reduction of the large amount of tensile residual stress (created because of rapid solidification during the DMLS process) upon this heat treatment. Further loss of hardness is noted for samples C (heat-treated at 800 °C) and this was attributed to the dissolution of the α′-martenstic into more stable α+β-phases, as noted in Figures 5-1(c) and 5-2(c). The hardness is further seen to decline continously to a minimum in samples D that were heat-treated at 940 °C. This further decrease of hardness is ascribed to the growth/coarsening of α-phase experienced at a heat treatment temperature just below the α→β transformation temperature, as previously shown in Figures 5-1(d) and 5-2(d). Surpringly, a gain in hardness is then seen to occur in samples E that were heat-treated above the α→β transformtion temperature even though these samples recorded the higher average α grain sizes. It is surmised here that this gain in hardness was probably due to the increase in percentage of LAGBs seen in Figure 5-17(e). Since these LAGBs are dislocations in nature, their increase could possibly lead to an increase of hardness as they offer increased resistance to localised plastic deformation induced by the mechanical indentation. This hypothesis will be confirmed in Chapter 6 that generally aims at evaluating the dislocation densities in the five different forms of DMLS Ti6Al4V(ELI).

5.7 SUMMARY

In this chapter, the microstructures, crystallographic texture and grain boundary distribution of five different forms of DMLS Ti6Al4V(ELI) alloys formed after various heat-treatment strategies were presented and discussed. The results presented underscore the fact that this alloy of titanium shows a wide range of microstructures dependent on heat-treatment regime. For instance, the average α′/α-grain size increased from a value of < 1.5 µm for the as-built form to a value of about 9 µm for the samples heat-treated above the transformation temperature. The absence of β-phase was noted in the as-built and stress-relieved samples, however, a small portion of this phase (< 6%) was detected in heat-treated samples. The intensity of texture was observed to increase because of heat treatment with the MUD of the α′/α-phase in the basal plane (0001), increasing from 4.9 in the non-heat-treated samples to 24 for samples that were annealed at the highest temperature. The reconstruction of prior-β grains was successfully executed using the

© Central University of Technology, Free State

ARPGE program. The results obtained following the reconstruction process showed that the columnar β-grains disappeared in samples that were heat-treated at temperatures just below and above the α→β→α transformation temperature. The lateral growth of these decomposed β-grains was noted for the samples that were heat-treated above the transformation temperature. Examination of the $(0001)_{\alpha'/\alpha}$ and $(110)_{\beta}$ poles that were plotted on the same plots for the as-built samples and those samples that were heat-treated below the transformation temperature showed significant spread of orientation between these α- and β-phase orientations. This indicated deviations from the known BOR in the Ti6Al4V alloy. Interestingly, the BOR orientation spread in samples type E that were heat-treated above the β-transformation temperature drastically reduced with the α-(0001) and β-(110) perfectly superimposed. The percentage fractions of HAGBs accounted for the majority of misorientation angles (> 95%) for all five groups of samples with samples C not showing any traces of LAGBs. The frequencies of LAGBs in samples type A and B were less than 1% while that of samples C and D were recorded as 2.5% and 3.7%, respectively. The information from this chapter will be used as a reference for work on the high-strain-rate mechanical properties of these different forms of DMLS Ti6Al4V(ELI) to be presented in Chapter 7.

© Central University of Technology, Free State

5.7 REFERENCES

1. Beladi, H., Chao, Q., Gregory, S. 2014. Variant selection and intervariant crystallographic planes distribution in martensite in a Ti6Al4V alloy. *Acta Materialia*, 80, pp.478–489. https://doi.org/10.1016/j.actamat.2014.06.064
2. Burgers, W. 1934. On the process of transition of the cubic-body-centered modification into the hexagonal-close-packed modification of zirconium. *Physica* 1 (7–12) pp.561-586.
3. Cayron, C. 2007. ARPGE: A computer program to automatically reconstruct the parent grains from electron backscatter diffraction data. *Journal of Applied Crystallography*, 40 (6), pp.1183–1188. https://doi.org/10.1107/S0021889807048777
4. De Formanoir, C., Michotte, S., Rigo, O., Germain, L., Godet, S., A. 2016. Electron beam melted Ti6Al4V: Microstructure, texture and mechanical behaviour of the as-built and heat-treated material. *Materials Science and Engineering. A*, 652, pp.105–119. https://doi.org/10.1016/j.msea.2015.11.052
5. Dieter, E.G. 1986. Mechanical Metallurgy. *3rd Edition - Materials science and engineering series* McGraw-Hill, New York, USA, p.184.
6. Obasi, G.C., Birosca, S., Quinta, F.J., Preuss, M. 2012. Effect of β grain growth on variant selection and texture memory effect during α→β→α phase transformation in Ti6Al4V. *Acta Materialia* 60, pp.1048–1058.
7. Simonelli, M., Tse, Y.Y., Tuck, C. 2014. The formation of α + β microstructure in as-fabricated selective laser melting of Ti6Al4V. *MRS: The Material Science of Additive Manufacturing,* 29(17) pp.2028–2035.
8. Stefansson, N., Semiatin, S., Eylon, D. 2002. The kinetics of static globularization of Ti-6Al-4V. *Metallurgical and Material Transactions. A*, 33, pp.3527–3534.
9. Wang, Y., Fraser, H., Dixit, V., Shi, R. 2014. Variant selection of grain boundary α by special prior β grain boundaries in titanium alloys. *Acta Materialia*. 75, pp.156–166.
10. Xufel, L., Xin, L., Zhuang, Z., Jing, C., Hua, T., Weidong, H. 2017. Formation mechanism of the α variants and its influence on the tensile properties of laser solid formed Ti6Al4V titanium alloy. *Materials Science and Engineering A,* 691, pp.16–24. https://doi.org/10.1016/j.msea.2017.03.035

© Central University of Technology, Free State

CHAPTER 6 — EVALUATION OF DISLOCATION DENSITIES IN VARIOUS MICROSTRUCTURES OF DMLS TI6AL4V(ELI) BY X-RAY DIFFRACTION

The material contained in this chapter has been published in peer-reviewed media as detailed below:

***Amos Muiruri**, Maina Maringa, Willie du Preez, Evaluation of dislocation densities in various microstructures of additively manufactured Ti6Al4V(ELI) by the method of X-ray diffraction, Materials **2020**, 13, 5355; doi:10.3390/ma13235355*

6.1 INTRODUCTION

The average dislocation densities of five different microstructures of DMLS Ti6Al4V(ELI) were evaluated from X-ray diffraction (XRD) profile analysis. Although the method of transmission electron microscopy (TEM) can also be used for dislocation analysis, it was not used in the present study. It was realised that the inhomogeneity in the martensitic microstructures of samples type A, B and partially in samples C, could lead to variation in dislocation density from place to place within the microstructure. Furthermore, it has been shown in Cong and Murata (2011) that for a martensitic microstructure with high dislocation densities, applying TEM is difficult due to complicated image-contrasts from samples. Thus, it was decided to use the alternative XRD method in this analysis, which gives macroscopic average values. The quantification of dislocation density via the XRD method relies on broadening of diffraction peaks that occurs when the atoms are displaced from their ideal position due to small crystalline sizes, below one micrometre, and an abundance of lattice defects such as dislocations (Ungar 2004).

6.2 THE X-RAY DIFFRACTION (XRD) PROFILES OF DMLS TI6AL4V(ELI) SAMPLES

The XRD analyses were performed on polished samples type A, B, C, D and E using a Bruker D2 phaser equipped with a cobalt anode with wavelength $0.179\ \mathrm{nm}$. The diffraction profiles of the peaks were taken in the angular range $40°$ (2θ) to $120°$ (2θ). Bragg reflections of $\{10\bar{1}0\}$, $\{0002\}$, $\{10\bar{1}1\}$, $\{10\bar{1}2\}$, $\{11\bar{2}0\}$ and $\{10\bar{1}3\}$ planes for the α′/α-phase and the $\{110\}$ plane for the β-phase were measured. The peak profiles of these reflections are shown in Figure 6-1. The non-heat-treated- and stress-relieved microstructures of DMLS Ti6Al4V(ELI) (Samples A and B) all exhibit only α/α′-phase, as shown in the XRD profiles of Figure 6-1.

© Central University of Technology, Free State

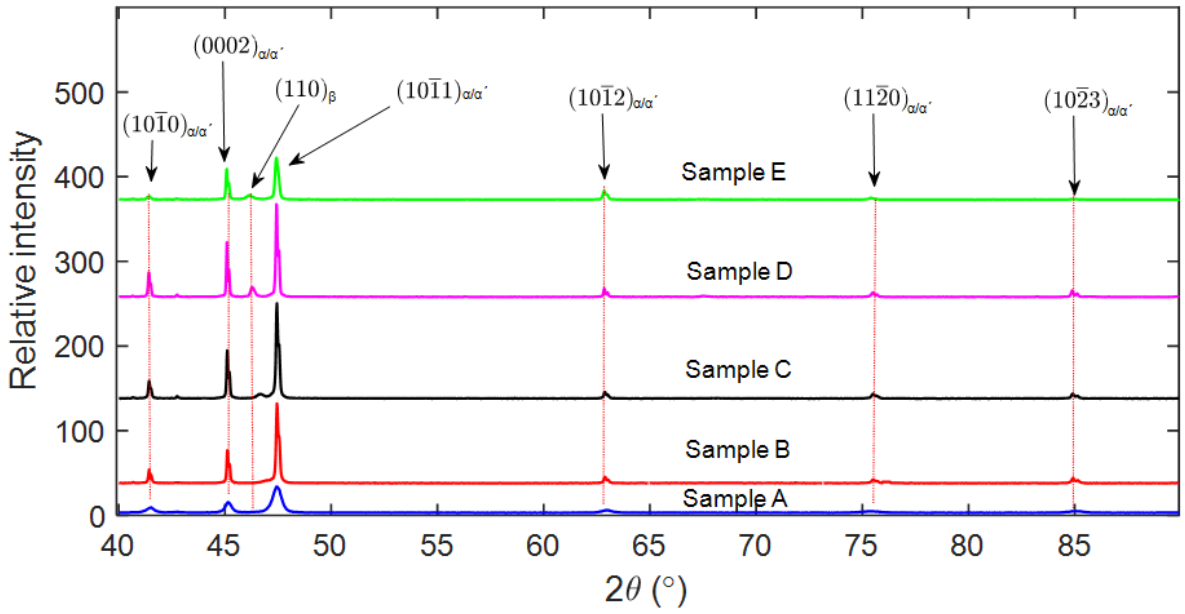

Figure 6-1. The X-ray diffraction patterns of the as-built samples, as-built and stress-relieved samples, and as-built and annealed samples of DMLS Ti6Al4V(ELI).

As further shown in this figure, the α and α'-phases, which crystallise in a hexagonal closed-packed structure (hcp), cannot easily be distinguished from one another from the XRD peak profiles, since their respective { $hkil$ }-planes are reflected at approximately the same angle in 2θ and thus these peaks are referred to as α/α'. It is also noted here that the two phases have similar lattice parameters (Rombouts *et al.* 2012). The presence of the β-phase is noted in Figure 6.1 in samples C, D and E judging from the reflection of β $\{110\}$ at angles 2θ between 46.10° and 46.69° of the XRD profile. Thus, from the peak intensities of these three types of alloys, the fraction of β-phase in samples C, D and E are seen in Figure 6-1 to be 3.6%, 6.4% and 6.6%, respectively. Figure 6-2 shows that the {110} Bragg peak positions of the precipitated β-phase in the samples have shifted to a lower angle (2θ) in the order from samples C to D to E. On the other hand, the Bragg reflections for the (0002) $_{\alpha'/\alpha}$, and $(110\bar{1})_{\alpha'/\alpha}$ planes in this figure demonstrate a larger integral width of the peaks of samples A compared to the rest of the samples. The shift in $(110)_{\beta}$ peak position demonstrates an increase in calculated values of the lattice parameter {a} of the β-phase with heat-treatment temperature, as presented in Figure 6-3.

© Central University of Technology, Free State

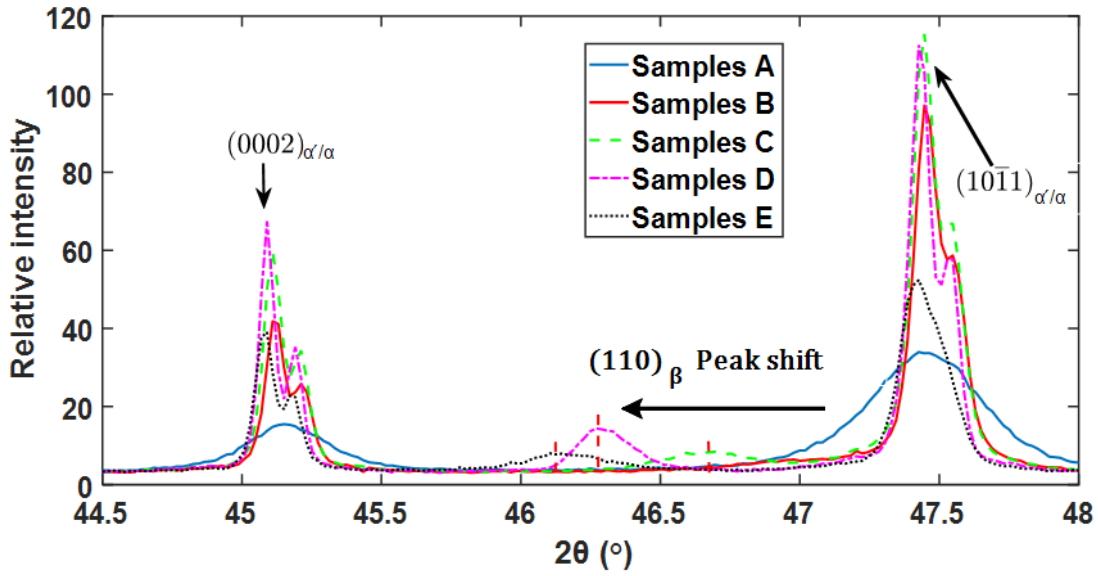

Figure 6-2. The magnification of selected peaks (110) β, (0002) α′/α, and $(10\bar{1}1)$ α′/α.

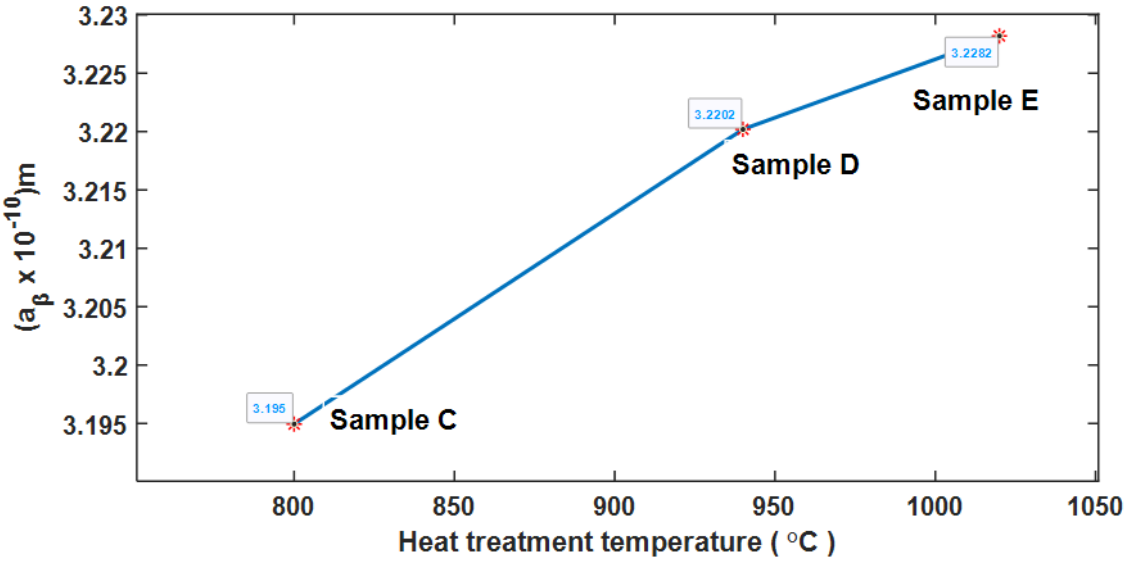

Figure 6-3. The evolution of β-phase lattice parameter (a) with heat-treatment temperature.

The trend observed in Figure 6-3 agrees well with a recent report from Haubrich *et al.* (2019), which showed the lattice parameter {a} of the β-phase in a Ti6Al4V alloy to increase at elevated annealing temperatures. This increase in the lattice parameter is attributed to the decrease in content of vanadium in the β-phase of Ti6Al4V at high temperatures.

For instance, Lasalmonie and Loubradou (1979) obtained a 10% vanadium content in the β-phase of a Ti6Al4V ingot annealed at 800 °C, while annealing at an elevated temperature of 900 °C decreased the content to 6%. Generally, vanadium has an atomic radius of 0.132 nm, while that of titanium is larger at 0.147 nm (Liang *et al.* 2012) and, therefore, a

© Central University of Technology, Free State

decrease in the content of the former in the β-phase will result in an increase in lattice spacing of β- titanium.

The values of average crystallite size and average lattice strain of the five categories of DMLS Ti6Al4V(ELI) samples were obtained through Rietveld refinement of data as implemented in the Bruker AXS TOPAS software (Version 5, 2014). It should be noted here that the crystallite sizes are different from grain sizes and the two should not be confused with one another. Crystallite sizes are sometimes referred to as apparent grain sizes and are generally coherent diffraction domains in XRD (Murata *et al*. 2008), while actual grain sizes are volumes inside crystallite materials with specific crystal orientations determined via optical or scanning electron microscopes. Table 6-1 shows the average crystallite size and lattice strain of various forms of DMLS Ti6Al4V(ELI) alloy. A comparative analysis of average crystallite size and lattice strain for different samples shown in this table is graphically presented in Figure 6-4.

Table 6-1.The average crystallite size and lattice strain calculated from Rietveld refinement

Alloy	Average crystallite size (nm)	Lattice strain (G) (%)
Samples A	66.6 ± 1.9	0.6059242 ± 0.01095
Samples B	249.6 ± 4.3	0.1083321 ± 0.00293
Samples C	254.0 ± 5.6	0.0866357 ± 0.00310
Samples D	833.6 ± 64.8	0.0963554 ± 0.00205
Samples E	521.7 ± 44.3	0.1419919 ± 0.00396

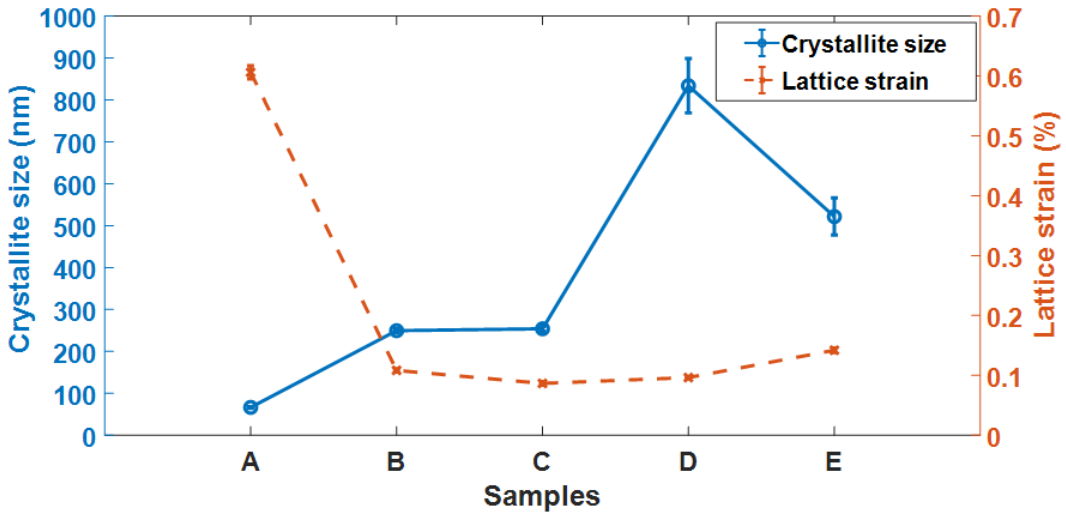

Figure 6-4. Comparative trend of average crystallite size and lattice strain for various samples of DMLS Ti6Al4V(ELI) as determined by Rietveld refinement method.

© Central University of Technology, Free State

It is apparent in Figure 6-4 that the lattice strain and crystalline size are highest and lowest, respectively, in non-heat-treated samples (samples A). This is consistent with the observation made in Figures 6-1 and 6-2 where samples A have a broader peak in comparison to the rest. This is expected from the DMLS process. During the DMLS process, the small diameter laser interacts with powder feedstock, momentarily producing a molten pool, which solidifies rapidly as the laser moves on. This highly localised heat input and short interaction time leads to larger thermal gradients and high cooling rates, which result in the formation of the fine acicular martensitic microstructure of Ti6Al4V(ELI) with high macro-process residual stresses and strains. Thus, the broader peaks observed in the as-built samples A are ascribed to (a) fine martensitic microstructure that results in a small coherent domain *i.e.,* small numbers of atoms contributing to constructive interference, and (b) assumed large numbers of defects in the material that create strain and distortion of the lattice. Each defect distorts the lattice in its immediate neighbourhood in a way that leads to a different diffraction profile shape (broadening). It has been shown in publications that the XRD peak broadening due to defects is very often dependent on the plane, *i.e.* $\{hkil\}$-dependent in this case for hcp structure (Wilkens 1970, Ungar and Borbely 1996, Dragomir and Ungar 2002).

A remarkable decrease in lattice strain and slight increase in crystallite size are noted from samples A to samples B, as seen in Figure 6-4. This is also consistent with the significant decrease in integral breadth of the (0002) $_{\alpha/\alpha'}$, and (11$\bar{2}$0) $_{\alpha'/\alpha}$ peaks shown in Figure 6-2. This is a clear indication of a notable reduction of macro-process residual stress in the as-built parts upon exposing them to stress-relieving heat treatment. Noteworthy, after annealing at 650 ℃ for 3 hours, there was no observable growth in grain size with respect to the as-built condition. However, the observed increase in scattering domain (crystalline size) could be as a result of lattice relaxation that increases scattering volume. It could also be argued that slight grain growth of the martensitic structure occurred after stress-relieving heat treatment that perhaps could not be detected at a magnification of X1100.

Samples C recorded the lowest lattice strain. This was attributed to full relief of stress fields associated with lattice distortion, which can be expected upon full transformation of strained fine α′-laths to the thermodynamically more stable α/β lamellae. This assertion is further supported by the fact that in the analysis of misorientation distribution of grain

© Central University of Technology, Free State

boundaries shown in Figures 5-16 and 5-17 of Chapter 5, samples C did not show any trace of LAGBs (< 15°) (identified by vertical blue hatched lines in Figure 5-17) but was rather characterised by 100% HAGBs. The LAGBs further increased from D to E, in that order, as shown in Figure 5-17 of Chapter 5. The LAGBs, as described in Dieter (1986), contain a simple arrangement of dislocations. Since dislocations contribute to the distortion of lattices, the increase in lattice strain in order from samples C to E, seen in Figure 6-4, could be attributed to the increasing percentage of LAGBs. The preceding discussion and the histograms presented in Figure 5-17 of Chapter 5 clearly underscore the fact of varying dislocation densities between these different microstructures of DMLS Ti6Al4V(ELI).

Based on the assumption of a random distribution of dislocation density, the relationship between lattice strain $\langle \varepsilon_l \rangle$, crystallite size (D) and dislocation density (ρ) can be expressed as (Krivoglaz 1996):

$$\langle {\varepsilon_l}^2 \rangle \cong \frac{\rho C b^2}{4\pi} ln \frac{L}{D} \qquad 6\text{-}1$$

where the parameters, *C* and *b* are the average contrast factor and the Burgers vector of dislocations, respectively. Even though this model shows the correlation between the three parameters, Wilkens (1970) showed that this form of a model cannot be applied to calculate dislocation density since the case $\langle {\varepsilon_l}^2 \rangle$ diverges logarithmically with increasing crystallite size. This is mainly due to long-range decay of strain fields created by dislocations. Therefore, in this research work, modified Williamson-Hall (Dragomir and Ungar 2002) and modified Warren-Averbach (Wilkens 1970) plots were used to evaluate the dislocation density. These two methods were described in detail in section 2.6.2 of Chapter 2 but will be stated briefly in section 6.3 on the evaluation of dislocation density of DMLS Ti6Al4V(ELI) microstructures, for ease of reference.

6.3 CALCULATION OF DISLOCATION DENSITY IN DMLS TI6AL4V(ELI) MICROSTRUCTURES

6.3.1 Analysis of DMLS Ti6Al4V(ELI) XRD peak broadening by the modified Williamson-Hall method

The contribution of dislocations to the broadening of different diffraction peaks occurs through what is known as the contrast factor (orientation factor) of dislocations (Dragomir

© Central University of Technology, Free State

and Ungar 2002). The modified Williamson-Hall (m-WH) method defines the broadening of diffraction peaks expressed in terms of full-width at half-maximum intensity (FWHM) as a function of crystallite size and dislocation density (lattice strain). To account for the influence of strain anisotropy in this method, a scaling parameter (contrast factor) $\bar{C}$, which is { $hkil$ }-plane dependent, is introduced, thus allowing the m-WH method to be written as (Ungar and Borbely 1996):

$$(\Delta K)^2 \cong \left(\frac{0.9}{D}\right)^2 + \left(\frac{\pi M^2 b^2}{2}\right)\rho K^2 \overline{C_{hkl}} \qquad 6\text{-}2$$

where the symbol ΔK in nm^{-1} is expressed as $\Delta K = 2cos\theta(\Delta\theta)/\lambda$ and K is the diffraction vector expressed as $K = 2sin\theta/\lambda$. In this case, the parameters θ and $\Delta\theta$ stand for the diffraction angle and FWHM in radians of the XRD peaks, respectively, while λ is the wavelength of the X-rays. The parameters *K*, *ρ* and *b* represent the diffraction vector, dislocation density and the magnitude of the Burgers vector, respectively. Here, the wavelength of the cobalt X-rays of $\lambda = 0.179$ nm and the average crystallite size for various samples, as calculated from the Rietveld refinement method, are presented in Table 6-1. The parameter, M in Equation 6-2 is a dimensionless constant depending on the effective outer cut-off radius (R_e) of dislocations and the dislocation density and is expressed as $M = R_e\sqrt{\rho}$. In the present work, the dislocation densities were calculated from the α/α′-phase (hexagonal crystals) peak broadening.

The diffraction peak profiles were fitted using either Gaussian or Cauchy (Lorentzian) functions. The present study is cognisant of the fact that the diffraction peaks of the diffraction measured are never exactly described by either one of these two functions, but instead fall somewhere between the two. The backgrounds of the profiles for the peaks were subtracted and the integral intensity of each reflection normalised first using the equation:

$$\int_{-\infty}^{\infty} I(\theta)d\theta = 1 \qquad 6\text{-}3$$

The normalised peaks were then fitted using Lorentzian and Gaussian functions with *Fityk*, an open-source curve-fitting program which yields peak positions and the FWHM, as well as the breadth of the integral.

© Central University of Technology, Free State

It is important to note that the XRD patterns consisted of the Kα1 and Kα2 peaks doublet, rather than just a single peak, as seen in Figure 6-2. This is due to the slight difference in wavelength of these two radiations (see Table 3-6 of Chapter 3), thus, according to the Braggs law, each of them will give rise to a diffraction peak. In the present research, only the Co Kα1 radiation was needed, thus individual peaks were separated into Kα1 and Kα2 using Lorentzian and Gaussian functions. A typical example of the deconvoluted peaks is shown in Figure 6-5.

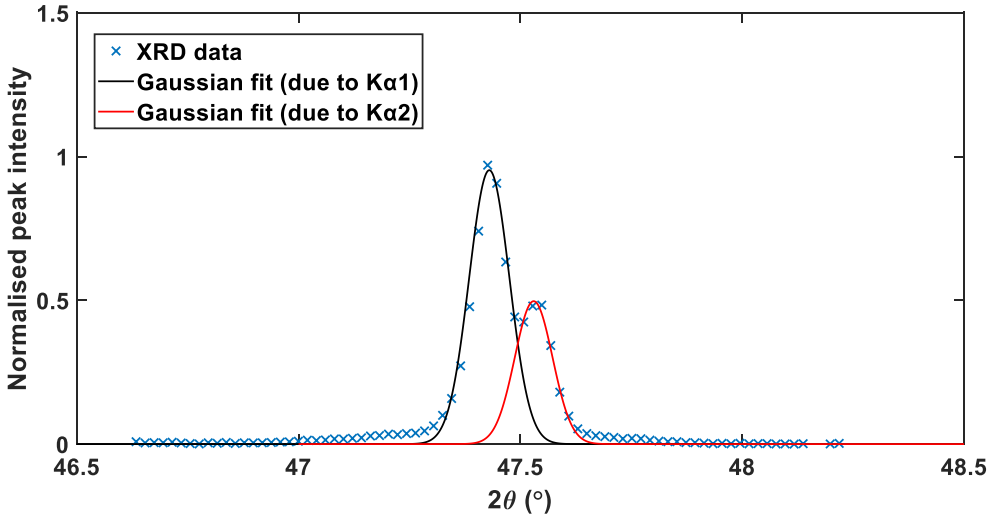

Figure 6-5. Typical measured XRD data and the Kα1 and Kα2 deconvoluted peaks using the Gaussian function of the $(10\bar{1}1)$ *reflection.*

Figure 6-6 shows the trends of the FWHM in nm for the various peaks of the five types of DMLS Ti6Al4V(ELI) microstructures studied here, and that of the National Institute of Standards and Technology (NIST) silicon Si-640d standard sample obtained from the same Bruker D2 Phaser XRD machine. It is apparent from this figure that samples A showed the highest FWHM over most of the diffraction vector positions. As seen in this figure, a remarkable decrease in FWHM was noted upon heat treatment, with samples type D recording the lowest FWHM values over the angular range of the diffraction. To remove instrumental broadening from the measured peak profiles of samples, it was necessary to measure the diffraction pattern of a free-strain sample that displayed no broadening of its own. A standard reference material, Si-640d, was used and its FWHM profile as a function of diffraction vector (K), both as a Gaussian and Lorentzian function, are shown in Figure 6-6 (a) and (b), respectively.

© Central University of Technology, Free State

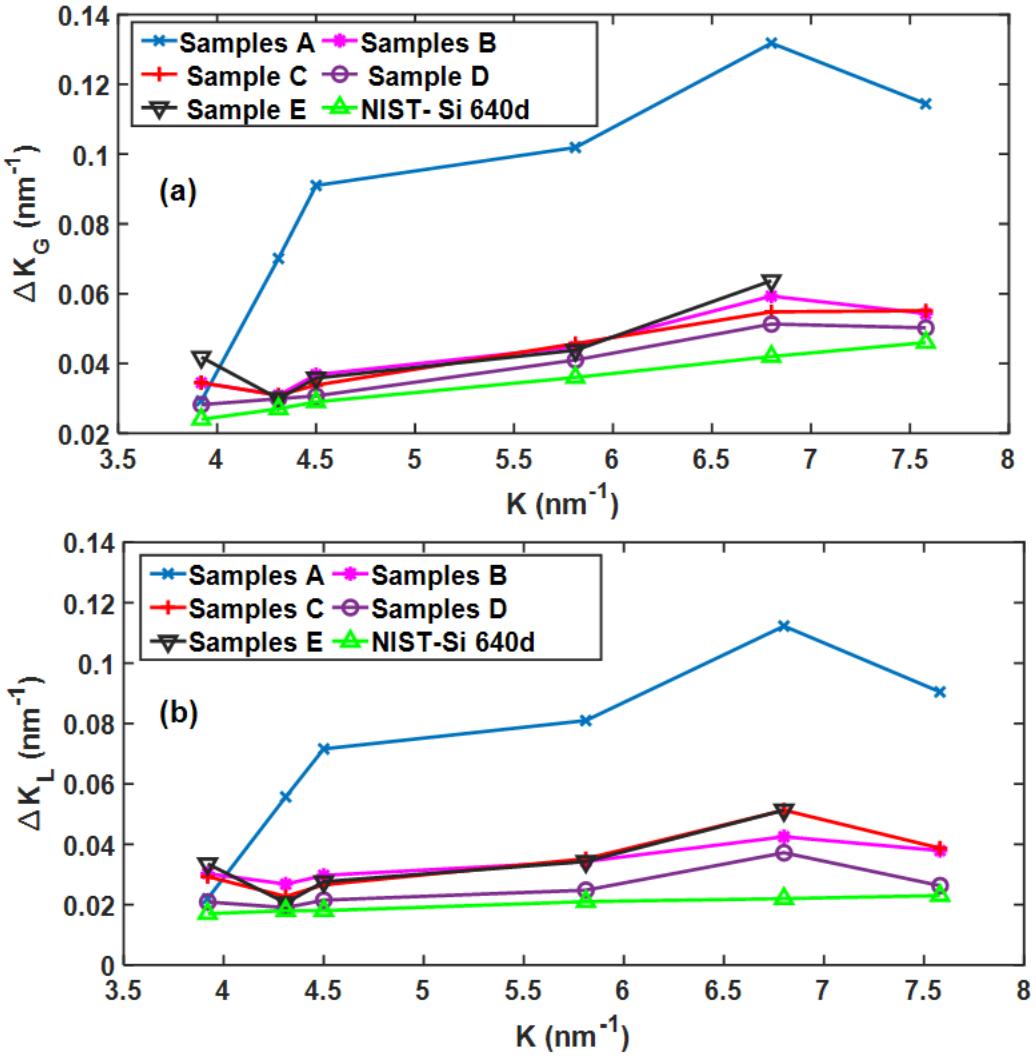

Figure 6-6.The (a) Gaussian and (b) Lorentzian FWHM against diffraction vector (K) for the five types of samples with instrumental broadening, referenced against results for a silicon (Si-640d) sample with no instrumental broadening.

Correction of the instrumental broadening was carried out by comparing the FWHM of each peak reflection of the test samples with that of the Si-640d standard for both the Gaussian and Lorentzian functions. This was done to remove instrumental broadening of the peaks to retain the true broadening of the samples using the following equations (Balzar and Ledbetter 1993):

$$(\Delta K_G^t)^2 = (\Delta K_G^m)^2 - (\Delta K_G^s)^2 \quad \text{6-4a}$$

$$\Delta K_L^t = \Delta K_L^m - \Delta K_L^s \quad \textit{6-4b}$$

© Central University of Technology, Free State

In these two equations, the parameters ΔK_G^t and ΔK_L^t are true Gaussian and Lorentzian FWHM, respectively. The parameters ΔK_G^m and ΔK_G^s are the measured FWHM for the samples and Si-640d in the Gaussian function, respectively, while the parameters ΔK_L^m and ΔK_L^s are the measured FWHM for the samples and Si-640d in the Lorentzian function, respectively.

The size- (due to crystallite size) and strain- (due to defects) broadening profiles are Lorentzian and Gaussian functions, respectively (Warren and Averbach 1952). Thus, the resulting values of FWHM and ΔK_R, due to strain and size, can be expressed from a convolution of each of these two functions and from values obtained from Equation 6-4 as follows (Balzar and Ledbetter 1993, Olivera and Longbothum 1977):

$$\Delta K_R = \frac{1}{2}\left\{1.0692\Delta K_L^t + \sqrt{0.86639(\Delta K_L^t)^2 + 4(\Delta K_G^t)^2}\right\} \qquad 6\text{-}5$$

Figure 6-7 shows the true FHWM values obtained from Equation 6-5 for the five types of DMLS Ti6Al4V(ELI) samples tested here.

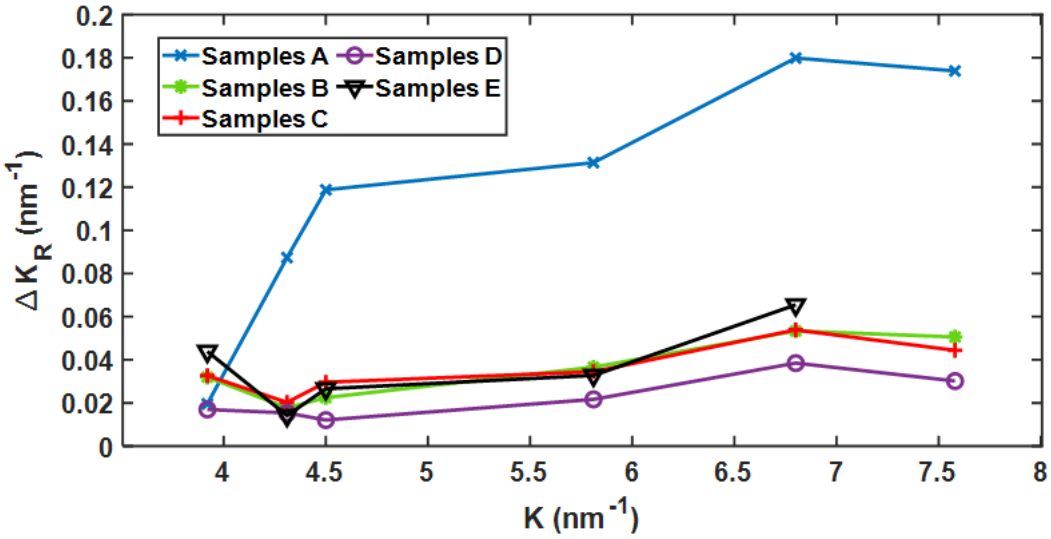

Figure 6-7. The resulting FWHM values of the peaks obtained after convolution of Gaussian and Lorentzian functions in Equation 6-5 against diffraction vector (K) for the five types of DMLS Ti6Al4V(ELI) samples.

As reported in Wilkens (1970) and Ungar (2004), the diffraction broadening caused by dislocations varies depending on the diffraction vector K($\{hkil\}$-plane). The contribution of a dislocation's strain field to the broadening of different diffraction profiles is through the orientation/contrast factor (Ungar and Borbely 1996) previously mentioned in the

© Central University of Technology, Free State

introductory paragraph of this section. Dragomir and Ungar (2002) gave the contrast factor for HCP metals for equally populated slip systems as:

$$\overline{C_{hkl}} = \overline{C_{hk.0}}(1 + q_1 x + q_2 x^2)\,, \text{where } x = \frac{2}{3}\left(\frac{l}{Ka}\right)^2 \qquad 6\text{-}6$$

where the parameters q_1 and q_2 are curve-fitting parameters that depend on the elastic properties of materials, while a and l are lattice constants in the basal plane (taken as 0.295 nm for Ti-Hex) and the last index of the $\{hkil\}$-peak reflection, respectively. The parameter $\overline{C_{hk.0}}$ is the average contrast factor corresponding to $(hk.0)$ reflections, which occur in the planes where the last lattice index, *l,* is zero.

To evaluate for q_1 and q_2, and therefore, $\overline{C_{hkl}}$, Equations 6-2 and 6-6 are normally combined to a quadratic function of the form:

$$((\Delta K)^2 - \omega)/K^2 \cong X\bar{C}_{hk.0}(1 + q_1 x + q_2 x^2) \qquad 6\text{-}7$$

where the parameters $X = \pi M^2 b^2 \rho/2$ and $\omega = \left(\frac{0.9}{D}\right)^2$. As Equation 6-7 is a quadratic function of x, the values of the parameters q_1 and q_2 in it can be determined from the coefficient of the curve of $((\Delta K)^2 - \omega)/K^2$ against x. Using the values of ΔK_R from Figure 6-7, analysis was done using Equation 6-7. A plot of the function $((\Delta K_R)^2 - \omega)/K^2$ vs. x for samples A to E is shown in Figure 6-8.

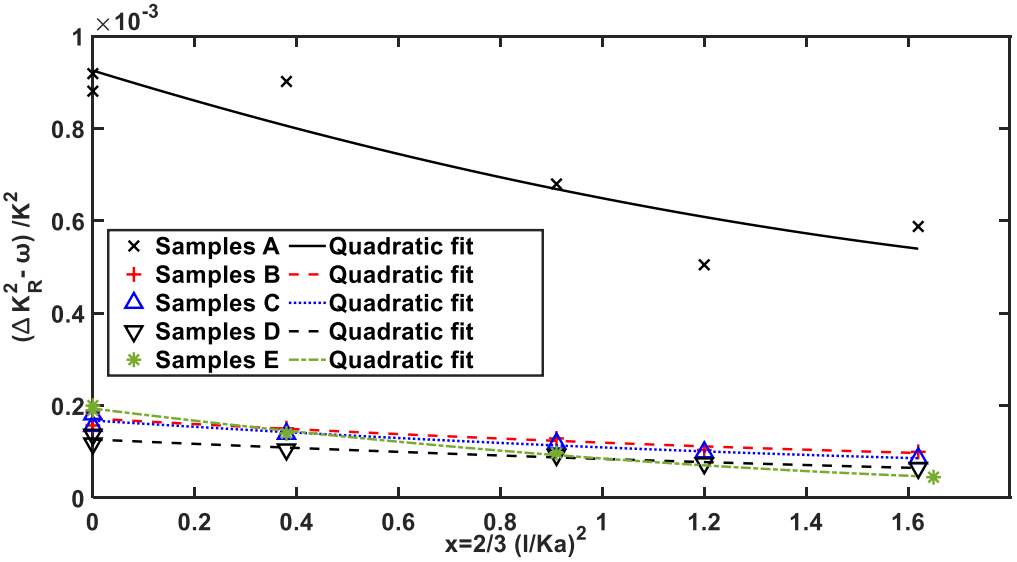

Figure 6-8. The relationship between $((\Delta K)^2 - \omega)/K^2$ and x for various samples of DMLS Ti6Al4V(ELI).

© Central University of Technology, Free State

By fitting the quadratic curves of Equation 6-7 to the experimental values obtained in this work, as shown in this figure, values of the parameters $q_1{}^{(m)}$ and $q_2{}^{(m)}$ in this equation that give the best curve fits were obtained and are presented in Table 6-2.

Table 6-2. The measured value of parameters $q_1{}^{(m)}$ and $q_2{}^{(m)}$

Alloy	$q_1{}^{(m)}$	$q_2{}^{(m)}$
Samples type A	-0.34	0.04
Samples type B	-0.37	0.05
Samples type C	-0.37	0.06
Samples type D	-0.38	0.05
Samples type E	-0.50	0.04

In hexagonal crystal systems, such as the ones for Ti6Al4V, there are three different major slip systems that are related to the three glide planes: basal, prismatic, and pyramidal (Lütjering and Williams 2007). When taking into consideration different slip directions and the character of dislocations (edge and screw) in hcp crystals, there are eleven sub-slip systems. The values of the parameters q and $\overline{C_{hk.0}}$ for these eleven sub-slip systems that were calculated numerically in work of Dragomir and Ungar (2002) are shown in Table 6-3.

Table 6-3. Numerical calculated values of $\overline{C_{hk.0}}$, q_1 and q_2 for the most common slip systems in titanium (Dragomir and Ungar 2002)

Slip system	Slip plane	Burgers vector	$\overline{C}_{hk.0}$	q_1	q_2
Edge dislocations					
Basal <a>	(0002)	$[11\bar{2}0]$	0.20227	-0.101142	-0.102623
Prismatic <a>	$(1\bar{1}00)$	$[11\bar{2}0]$	0.35387	-1.19272	0.355623
Prismatic <c>	$(1\bar{1}00)$	$[0001]$	0.04853	3.61619	1.226411
Prismatic <c+a>	$(1\bar{1}00)$	$[11\bar{2}3]$	0.10247	2.01717	-0.616631
Pyramidal1<a>	$(10\bar{1}1)$	$[11\bar{2}0]$	0.3118	-0.89401	0.183311
Pyramidal2 <c+a>	$(11\bar{2}2)$	$[11\bar{2}3]$	0.09227	1.29905	0.397247
Pyramidal3 <c+a>	$(11\bar{2}1)$	$[11\bar{2}3]$	0.09813	1.89412	-0.365739
Pyramidal4 <c+a>	$(10\bar{1}0)$	$[11\bar{2}3]$	0.09323	1.52702	0.146150
Screw dislocations					
Screw <a>	Multiple	$[11\bar{2}0]$	0.1444	0.59492	-0.710368
Screw <c+a>	Multiple	$[11\bar{2}3]$	0.41873	1.25714	-0.94015
Screw <c>	Multiple	$[0001]$	3.61×10^{-6}	165366	-98611

The fact that the experimental pair values of the parameter q for Ti6Al4V in Table 6-3 do not match any pair of the numerically calculated values in Table 6-3 suggests that more than one sub-slip system is activated during plastic deformation of this material.

© Central University of Technology, Free State

Dislocations may also be populated in more than one slip system. Therefore, the average contrast factor $\overline{C_{hkl}}$ (in Equation 6-6) for calculating the dislocation density should be evaluated based on the fractions of the three fundamental Burgers vectors in the material shown in Table 6-3 *i.e.* **b1** = 1/3<$11\bar{2}0$ > (Type < a >), **b2** =1/3<0001> (Type < c >) and **b3** = 1/3 <$11\bar{2}3$ > (Type < c+a >). The magnitude of these vectors in the case of hcp-titanium are 0.295 nm, 0.468 nm and 0.553 nm for Type < a >, Type < c > and Type < c+a >, respectively (Hull and Bacon 2011).

6.3.2 Calculation of Burgers vector population and average contrast Factor, $\overline{C_{hkl}}$ in DMLS Ti6Al4V (ELI)

The method of calculating the Burgers vector and average contrast factor used in numerous studies (Dragomir and Ungar 2002, Dragomir 2006 and Takashi *et al.* 2010) for hexagonal crystal structures was adopted for this research. This method is outlined in Appendix E. The values ${q_1}^{(m)}$ and ${q_2}^{(m)}$ for the five types of DMLS Ti6Al4V(ELI) samples that are presented in Table 6-2, while the numerical values of ${q_1}^{(i)}$, ${q_2}^{(i)}$ and $\overline{C_{hk.0}}^{(i)}$ for various sub-slip systems in hcp-titanium, are given in Table 6-3. These values were used to determine the unknown fractions of dislocation population h_a, h_c and h_{c+a}, using the three expressions in Equation E-5 (of Appendix E). The values of h_a, h_c and h_{c+a} for the five types of DMLS Ti6Al4V(ELI) samples obtained this way were then used to compute the product of the average Burgers vector over the three different slip systems with each Burgers vector and the average contrast factor $\overline{b^2C_{hk.0}}^{(m)}$, using Equation E-3 (in Appendix E). The results obtained from doing so are presented in Table 6-4.

Table 6-4. The fractions of Burgers vector population and the contrast factor $\overline{b^2C_{hk.0}}^{(m)}$ for five different samples of DMLS Ti6Al4V(ELI) based on q values obtained using the modified Williamson-Hall method

Samples	Burgers vector population (Fraction)			
	<a> ($\boldsymbol{h_a}$)	<c> ($\boldsymbol{h_c}$)	<c+a> ($\boldsymbol{h_{c+a}}$)	$\boldsymbol{\overline{b^2C_{hk.0}}^{(m)}}$
A	0.8800	0	0.1200	0.0253 nm^2
B	0.9088	0	0.0912	0.0245 nm^2
C	0.9077	0	0.0923	0.0245 nm^2
D	0.8819	0	0.1181	0.0252 nm^2
E	0.8925	0	0.1075	0.0249 nm^2
				Mean 0.0249 ± 0.00038 nm^2

© Central University of Technology, Free State

As seen in Table 6-4, the < a > dislocation types dominated the dislocation population in the five types of samples. The < c+a > dislocation types are relatively marginal while the absence of < c > dislocation types was noted in all samples. The results presented here are in good agreement with the work of Simm (2012), where the < a > dislocation types were most frequent (> 84%) while < c > dislocation types were absent. The computed values of the contrast factor $\overline{b^2C_{hk.0}}^{(m)}$ for the five different samples of DMLS Ti6Al4V(ELI) shown in Table 6-4 are very close to one another with a mean value of 0.0249 nm^2 and standard deviation of 0.00038 nm^2. These values are also all close to the value obtained in Dragomir and Ungar (2000) of 0.0222 nm^2 for dislocation population fractions of 0.75, 0.2 and 0.05 for < a >, < c > and < c+a > dislocation types, respectively. The very small standard deviation of the values shown in Table 6-4 justified use of the mean value of 0.0249 nm^2 for $\overline{b^2C_{hk.0}}^{(m)}$ to determine the dislocation densities in various microstructures of Ti6Al4V(ELI) using the modified Warren-Averbach (MWA) method.

6.3.3 Evaluation of dislocation density by modified Warren-Averbach method

According to Warren (1969), the Fourier coefficients of normalised broadened peaks are products of the size and strain coefficients expressed as follows:

$$lnA_L = lnA_L{}^S + lnA_L{}^D = exp\left(-\frac{L}{D}\right) - 2\pi^2 L^2 K^2 \langle \varepsilon^2 \rangle \qquad 6\text{-}8$$

where the parameters A_L, $A_L{}^S$ and $A_L{}^D$ are the real part, strain, and size Fourier coefficients, respectively, and the parameters L, D and ε^2 are the Fourier length, coherent domains of diffraction and mean square strain, respectively. When the strain Fourier coefficients are caused by dislocations and for small values of L, the Fourier transform of the XRD profiles can be approximated as follows (Wilkens 1970):

$$lnA_L = lnA_L{}^S - \rho\frac{\pi}{2}L^2 ln\left(\frac{R_e}{L}\right) K^2\overline{b^2C} \qquad 6\text{-}9$$

where the parameters ρ and R_e stand for the dislocation density and the outer cut-off radius of dislocations. Using this equation, the contrast factor parameter $\overline{b^2C}$ is not fitted, but is fixed to a value obtained using the modified Williamson Method (m-WM) in section 6.3.2. As seen in Equation 6-9, lnA_L can be considered as a function of $K^2\overline{b^2C}$, thus the

© Central University of Technology, Free State

dislocation density can be determined from a plot of lnA_L vs. $K^2\overline{b^2C}$. The gradient of this plot, *Y*, is the coefficient of the second term of Equation 6-9 which can be expressed as:

$$\frac{Y}{L^2} = \rho\frac{\pi}{2}lnR_e - \rho\frac{\pi}{2}lnL \qquad 6\text{-}10$$

The real part of Fourier coefficient (A_L) of the normalised peaks of the XRD profile can be obtained from FWHM of Gaussian and Lorentzian fitting as (HajyAkbary *et al.* 2015):

$$A_L = exp - \left\{\left(\frac{1}{2}L^2(\Delta K_G^t)^2\right) + L\Delta K_L^t\right\} \qquad 6\text{-}11$$

Figure 6-9 shows the modified Warren-Averbach (m-WA) plots for the five types of DMLS Ti6Al4V(ELI) specimens obtained by plotting the equation lnA_L *vs.* $K^2\overline{b^2C}$, at selected different values of Fourier length (*L*).

Equation 6-11 generates Fourier coefficients values that can be fitted with linear curves having gradients that are higher for higher values of Fourier length (*L*) as seen in Figure 6-9. The gradients of these fitting curves are seen to increase exponentially with increasing value of the Fourier length and thus, the visible divergence of the fitted curves at higher values of L. That the plotted data exhibits significant scatter for higher values of L and $K^2\overline{b^2C}$ is not all together surprising as the assumption of the small diffraction vector (K) and Fourier length (*L*) inherent in the modified Warren–Averbach method do not apply at these higher values (Warren and Averbach 1952, HajyAkbary *et al.* 2015).

© Central University of Technology, Free State

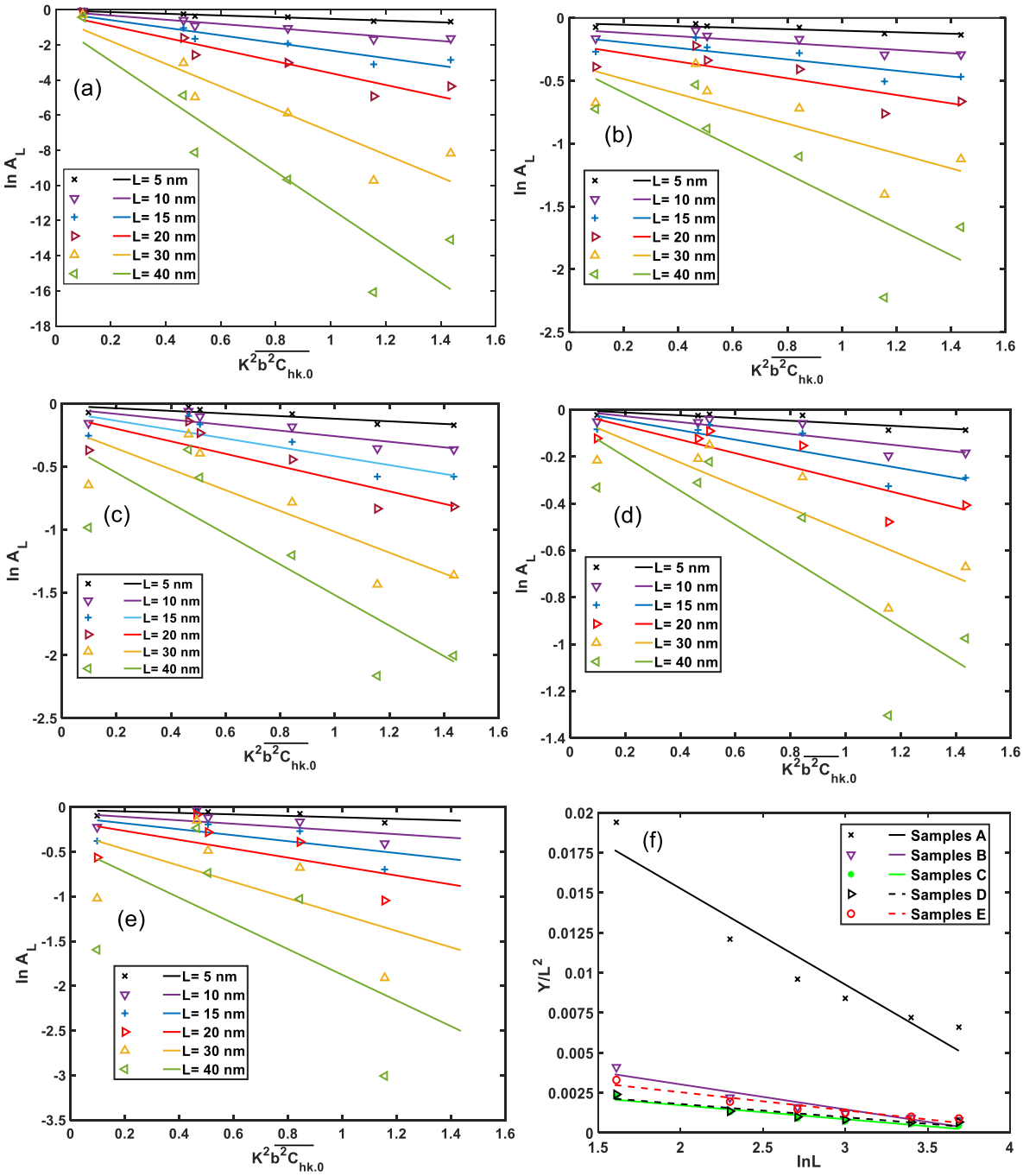

Figure 6-9. The modified Warren-Averbach plots of DMLS Ti6Al4V(ELI) samples type (a) A, (b) B, (c) C, (d) D, and (e) E according to Equation 6-9, while (f) is a plot according to Equation 6-10.

The slopes of the m-WA plots in Figures 6-9(a-e) give the values of *Y,* and the plots of the ratio, $\frac{Y}{L^2}$ against L for the various specimens are shown in Figure 6-9(f). The computed dislocation densities of the five different microstructures of DMLS Ti6Al4V(ELI) from Figure 6-9(f) are presented in Table 6-5 and for ease of comparison plotted in Figure 6-10.

© Central University of Technology, Free State

Table 6-5. The density of dislocations and effective outer cut-off radius of dislocations resulting from the m-WA method

Sample type	Dislocation density (m^{-2})	Outer cut-off radius of dislocations (Re) (nm)
A	3.82×10^{15}	93.06
B	1.02×10^{15}	70.02
C	5.73×10^{14}	46.12
D	5.09×10^{14}	48.81
E	7.00×10^{14}	78.54

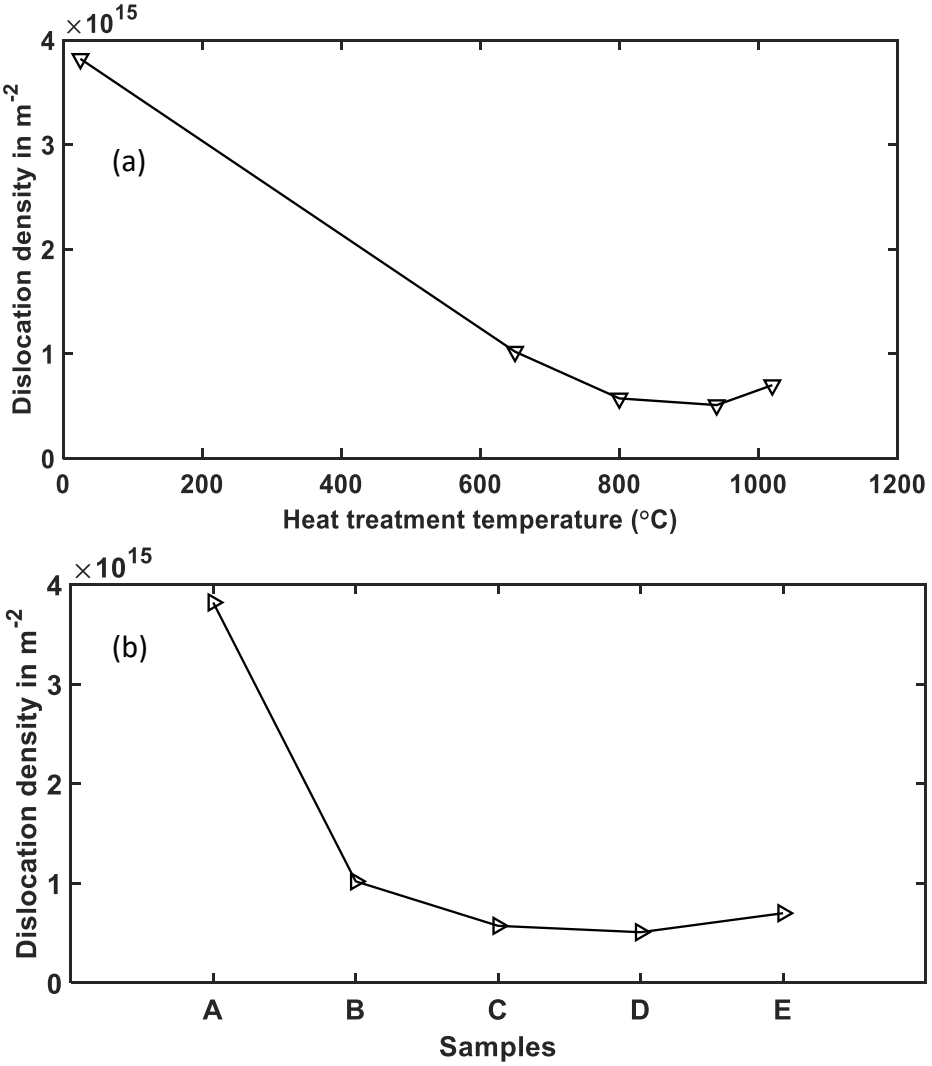

Figure 6-10. Trend of dislocation density (a) with heat-treatment temperature and (b) in non-heat-treated- (samples A) and heat-treated- (samples B, C, D and E) microstructures of DMLS Ti6Al4V(ELI).

As expected, Figure 6-10 shows the non-heat-treated- (samples type A) microstructure of DMLS Ti6Al4V(ELI) to have the highest dislocation density among the five different microstructures analysed in this study. This is anticipated due to distortion of the lattice because of the high cooling rates experienced during the DMLS process. The dislocation

© Central University of Technology, Free State

density is seen in the figure to reduce drastically, by almost 73%, after stress-relieving heat treatment (samples type B) conducted at a temperature of 650 ℃ for 3 hours. This reduction was attributed to relaxation of the microstructure and subsequent reduction in macro-process residual stresses and lattice strains. The change in dislocation density post stress-relieving heat treatment was strictly ascribed to microstructural change. At a heat treatment temperature of 800 ℃ (samples type C), complete decomposition of α'-martensite microstructure to an α+β mixture occurred, with an attendant lowering of the dislocation density, as seen in Table 6-5 and therefore, further lowering of the microhardness of the material as previously seen in Figure 5-18. The absence of LAGBs reported in Figures 5-16(c) and 5-17(c) of Chapter 5, which are dislocations in nature, could also explain the low dislocation density in samples type C. Growth of α laths after a heat treatment just below the α→β transformation temperature (samples D) resulted in a further decrease in dislocation density. This type of microstructure recorded the lowest dislocation density (a decrease of about 87% from the one recorded by non-heat-treated samples A) as determined by m-WA. Interestingly, samples E that were heat-treated above the transformation temperature and had the largest average α-laths thickness recorded a higher dislocation density than samples C and D, and as expected, lower than that of samples A and B. This higher dislocation density in samples E than samples C and D was proposed to be because of higher percentage of LAGBs (3.7%) in this microstructure, as shown in Figures 5-16(e) and 5-17(e) of Chapter 5.

6.4 SUMMARY

In this chapter, the XRD peak profile analytical methods were used to extract useful information for the five different microstructures of DMLS Ti6Al4V(ELI). This included information about the microstructures that could not be extracted in Chapter 5 *viz.* (i) the size of crystallites, (ii) lattice strain, and (iii) the density and the character of dislocations. The lattice strain and crystallite size were highest and lowest, respectively, in the non-heat-treated samples and the remarkable decrease in lattice strain and increase in crystallite size were noted upon heat treatment. The Burgers vector population and the average contrast factor of these microstructures were evaluated using the estimated parameters ${q_1}^{(m)}$ and ${q_2}^{(m)}$. It was noted that the < a > dislocation types dominated the dislocation population in

© Central University of Technology, Free State

the five types of samples. The < c+a > dislocation types were relatively marginal, while the absence of < c > dislocation types was noted in all samples. Using the obtained average value of the contrast factor $\overline{b^2 C_{hk.0}}^{(m)}$, the density and effective outer cut-off radius of dislocations were obtained. The non-heat-treated samples recorded the highest dislocation density and the highest outer cut-off radius of dislocations. The dislocation density drastically reduced by at least 73% after heat treatment, which is thought to be a result of reduction in macro-process residual stresses and strains due to heat treatment. The values of the dislocation density for the five different samples of DMLS Ti6Al4V(ELI) with other microstructural information obtained in Chapter 5 will be used in the calibration of the constitutive model, developed in Chapter 4, in Chapter 8 of this thesis.

© Central University of Technology, Free State

6.5 REFERENCES

1. Balzar, D., Ledbetter, H. 1993. Voigt – function modelling in Fourier analysis of size- and strain-broadened X-ray diffraction peaks. *Journal of Applied Crystal*lography, 26, pp.97–103. https://doi.org/10.1107/S0021889892008987
2. Cong, Z., Murata, Y. 2011. Dislocation density of lath martensite in 10Cr-5W heat-resistant steels. *Material Transactions* 52, pp.2151–2154. https://doi.org/10.2320/matertrans.M2011201
3. Dieter, G.E. 1986. *Mechanical metallurgy*, 3rd ed.; McGraw-Hill Inc., New York, USA, p.185.
4. Dragomir, I.C., Ungar, T. 2002. Contrast factors of dislocations in the hexagonal crystal system. *Journal of Applied Crystallography.* 35(5), pp.556–564. https://doi.org/10.1107/S0021889802009536
5. HajyAkbary, F., Sietsma, J., Böttger A.J., Santofimia M.J.2015. An improved X-ray diffraction analysis method to characterise dislocation density in lath martensitic structures. *Materials Science and Engineering A* 639, pp.208–218. https://doi.org/10.1016/j.msea.2015.05.003
6. Haubrich, J., Gussone, J., Barriobero-Vila, P., Kürnsteiner, P., Dierk, R., Norbert, S., Guillermo, R. 2019. The role of lattice defects, element portioning, and intrinsic heat effects on the microstructure in selective laser melted Ti6Al4V. *Acta Materialia*, 167, pp.136–148. https// doi.org/10.1016/j.actamat.2019.01.039
7. Hull, D., Bacon, D.J. 2011. *Introduction to dislocations.* 5th ed, Elsevier Ltd, Kidlington, Oxford, USA, p.111.
8. Krivoglaz, M.A. 1969. *Theory of X-ray and thermal neutron scattering by real crystals*. Springer-Verlag, Berlin, p.136.
9. Lasalmonie, A., Loubradou, M. 1979. The age hardening effect in Ti6Al4V due to ω and α precipitation in the β grains. *Journal of Materials Science*, 14(11), pp.2589–2595.
10. Liang, S.X., Ma, M.Z., Jing, R., Zhou, Y.K., Jing, Q., Liu, R. 2012. Preparation of the ZrTiAlV alloy with ultra-high strength and good ductility. *Materials Science and Engineering: A*, 539, pp.42–47. https://doi.org/10.1016/j.msea.2012.01.022

© Central University of Technology, Free State

11. Lütjering, G., Williams, J., Gysler, A. 2002. Microstructures and mechanical properties of titanium alloys. In the book, *Microstructure and properties of materials*, J.C.M. Li, World Scientific, Singapore, 2, pp.1–77.
12. Murata, Y., Ippei, N., Masahiko, M. 2008. Assessment of strain energy by measuring dislocation density in copper and aluminum prepared by ECAP and ARB. *Materials Transaction,* 49, pp.20–23. https://doi.org/10.2320/matertrans.ME200707
13. Olivera, J.J., Longbothum, R.L. 1977. Empirical fit to the Voigt line width: A brief review. *Journal of Quantitative Spectroscopy and Radiation Transfer,* 17(2), pp.233–236. https://doi.org/10.1016/0022-4073(77)90161-3
14. Rombouts, M., Yu, J., Maes, G., Motmans, F. 2012. Material properties of Ti6Al4V parts produced by laser metal deposition. *Physics Procedia*, 39, pp.416–424.
15. Simm, H.S. 2012. The use of diffraction peak profile analysis in studying the plastic deformation of metals. *Doctorate thesis*, submitted to the University of Manchester, UK.
16. Takashi, S., Yoshinori, M., Yoshihiro, T., Masahiko, M. 2010. Evaluation of dislocation density in a Mg-Al-Mn-Ca alloy determined by X-ray diffractometry and transmission electron microscopy. *Materials Transaction*, 51, pp.1067–1071.
17. Ungar, T. 2004. Microstructural parameters from X-ray diffraction peak broadening. *Scripta Mater,* 51(8), pp.777–781. https://doi.org/10.1016/j.scriptamat.2004.05.007
18. Ungar, T., Borbely, A. 1996. The effect of dislocation contrast on X-ray line broadening: A new approach to line profile analysis. *Applied Physics Letters* 69(21), pp.3173. https://doi.org/10.1063/1.117951
19. Warren, B.A., Averbach, B.L. 1952. The separation of cold-work distortion and particle size broadening in X-ray patterns. *Journal of Applied Physics,* 23(4), p.497. https://doi.org/10.1063/1.1702234
20. Wilkens, M. 1970. Theoretical aspects of kinematical X-ray diffraction profiles from crystals containing dislocation distributions. In *Fundamental aspects of dislocation theory.* Simmons, J.A., deWit, R., Bullough, R. National Bureau of Standards, Washington, DC, USA, Volume II, pp.1195–1219.

© Central University of Technology, Free State

CHAPTER 7 – FLOW PROPERTIES OF DMLS TI6AL4V(ELI) OVER WIDE RANGES OF STRAIN RATES AND TEMPERATURES

The material contained in this chapter has been published in peer-reviewed media as detailed below:

***Muiruri, A**.; Maringa, M.; du Preez. High strain rate properties of various forms of Ti6Al4V(ELI) produced by direct metal laser sintering. **Applied Sciences 2021**, 11(17), 8005; doi.org/10.3390/app11178005*

7.1 INTRODUCTION

As reported in Chapter 2, formation of non-equilibrium microstructure during the AM process leads to inferior deformation properties of fabricated Ti6Al4V(ELI) parts. Various heat-treatment processes are therefore pursued to improve the mechanical performance of these parts for industrial application. This chapter documents the high-strain-rate mechanical properties of various heat-treated microstructures of DMLS Ti6Al4V(ELI). The compressive high-strain-rate dynamic mechanical properties of the three different heat-treated samples C, D and E of DMLS Ti6Al4V(ELI), whose microstructures were reported and discussed in Chapter 5, are presented and discussed here.

7.2 HIGH STRAIN RATE – TIME TEST CHARACTERISTICS

To study the high-strain-rate properties of these different samples, the classical SHPB equipment was employed to establish the flow stress curves, under conditions of high-strain-rate loading. The tests were conducted in a range of temperatures from ambient temperature (25 ℃) to 500 ℃. The strain rates were controlled by regulating the pressures created to launch the SHPB projectile.

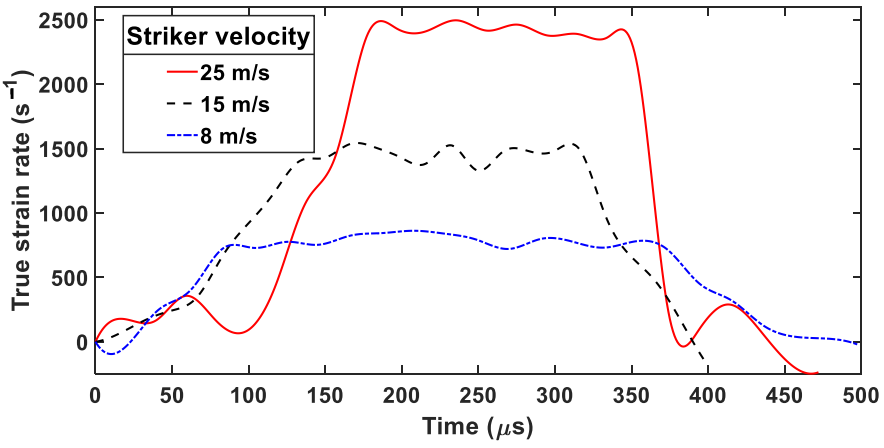

Figure 7-1. Strain-rate time graphs generated at different SHPB striker bar velocities.

© Central University of Technology, Free State

Different pressures affected the velocity of the striker bar differently, which led to a variation of the strain rate generated. Build-up pressures of 4 bars, 7 bars and 13 bars generated striker velocities recorded by velocity sensors and a high-speed camera of 8 m/s, 15 m/s and 25 m/s, respectively. Figure 7-1 shows that these velocities yielded and deformed the material at average true strain rates of about 750 s^{-1}, 1500 s^{-1}, and 2450 s^{-1}, respectively.

7.2 STRESS–STRAIN CHARACTERISTICS

Figures 7-2 to 7- 4 present the dynamic true stress-strain and true stress temperature curves of samples C, D and E deformed at average true strain rates of 750 s^{-1}, 1500 s^{-1}, and 2450 s^{-1}, and at temperatures of 25 °C , 200 °C and 500 °C.

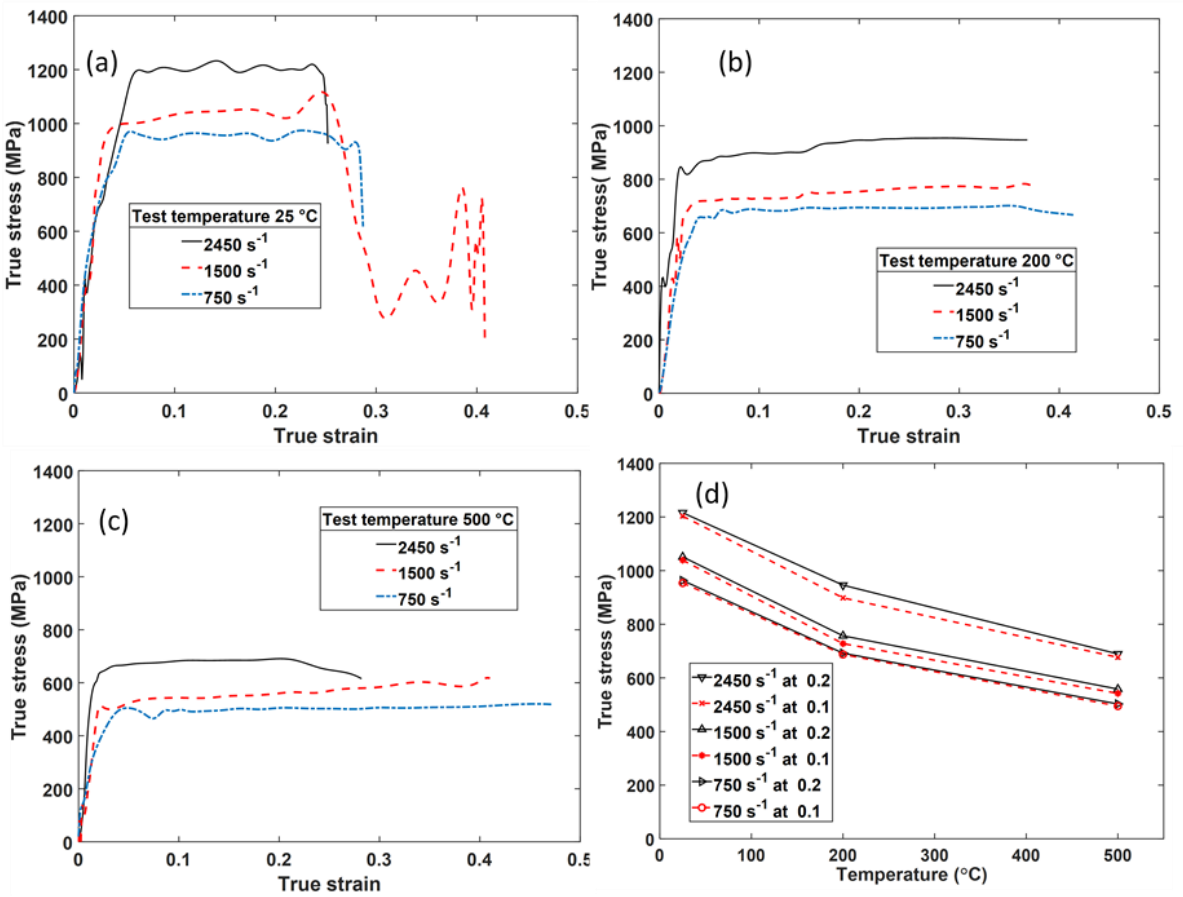

Figure 7-2. The true stress-strain curves (a-c) at different strain rates and temperatures, and (d) true stress vs temperature curves at different strain rates and at strains of 0.1 and 0.2, all for samples C.

© Central University of Technology, Free State

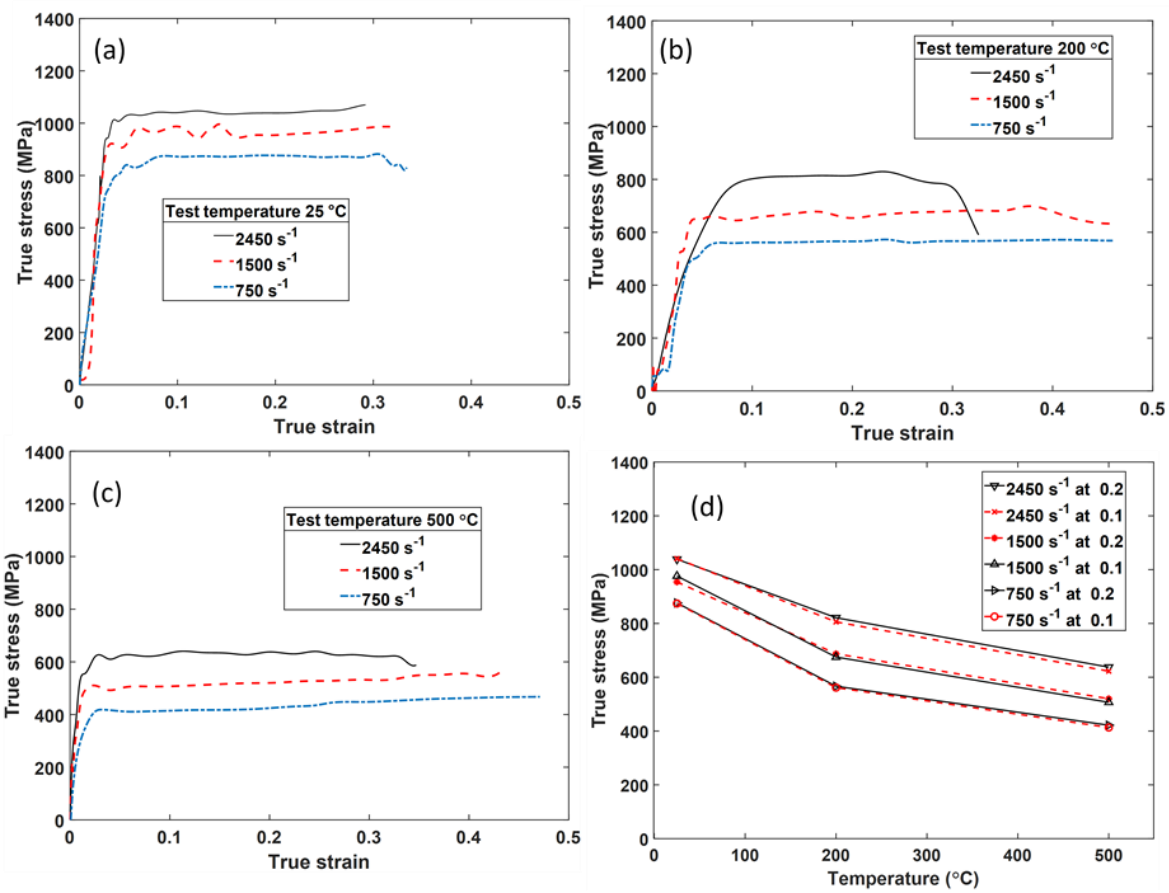

Figure 7-3. The true stress-strain curves (a-c) at different strain rates and temperatures, and (d) true stress vs temperature curves at different strain rates and at strains of 0.1 and 0.2, all for samples D.

© Central University of Technology, Free State

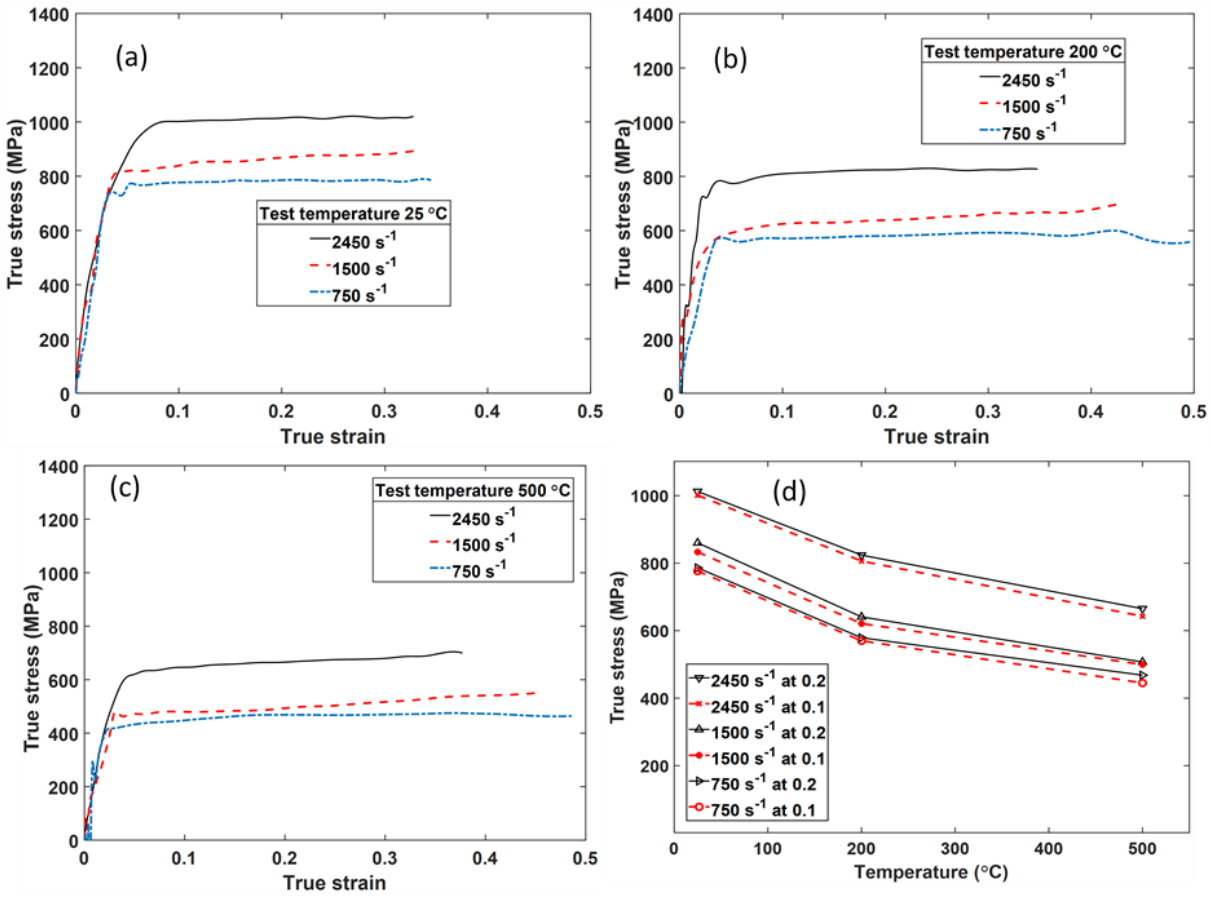

Figure 7-4. The true stress-strain curves (a-c) at different strain rates and temperatures, and (d) true stress vs temperature curves at different strain rates and at strains of 0.1 and 0.2, all for samples E.

The absence of a distinct yield point phenomenon for DMLS Ti6Al4V as seen in some of the plots in Figures 7-2 to 7-4 was also noted in the research work of Moletsane *et al*. (2017), who determined the tensile properties at low strain rate. A general observation in all the curves in Figures 7-2 to 7-4 (a-c) is that the flow stress increases with increasing strain rate, whereas as shown in Figures 7-2 to 7-4 (d), it decreases with increase in temperature. These observations clearly show that these three different microstructures of DMLS Ti6Al4V(ELI) are sensitive to both strain rate and temperature. The observed increase in flow stress with increase in strain rate can be attributed to increased generation and interaction of dislocations causing a higher instantaneous strain hardening at and beyond yielding, thereby increasing the flow stress in the material. Whereas, for tests conducted at elevated temperatures, the generation of dislocations is countered by the annihilation of dislocations, as a result of thermal softening, which leads to a decline of the magnitude of

© Central University of Technology, Free State

flow stress. It is also apparent that under these high-strain-rate dynamic loading conditions, the three different forms of DMLS Ti6Al4V(ELI) alloy yielded at different levels of stress for the same imposed strain rates and temperatures. Obviously, this is expected due to differences in microstructure among the three groups of samples. Further information on the curves shown in Figures 7-2 to 7-4 and observation made during testing are presented in Table 7-1. It is still doubtful if the elastic modulus of materials can be accurately determined under high strain rate using SHPB due to the difficulties in measurement of small strains. The work of Zhao *et al.* (2013) concluded that the SHPB analyses can induce significant errors in measurement of dynamic elastic properties of materials due to the transient effect in specimens. In the present research the values of yield strength reported in Table 7-1 were taken at the onset of plastic deformation and the off-set process was not used due to the stated limitation of the SHPB test.

Table 7-1. The analysis of the dynamic flow curves of samples C, D and E

Temperature (℃)	Alloy	Strain rate (s^{-1})	Dynamic yield stress (MPa)	Fracture state	Fracture strain
25	C	750	964	No fracture	-
		1500	1003	No fracture	-
		2450	1204	Fractured	0.25
	D	750	833	No fracture	-
		1500	923	No fracture	-
		2450	1014	Fractured	0.29
	E	750	739	No fracture	-
		1500	810	No fracture	-
		2450	958	Fractured	0.32
200	C	750	607	No fracture	-
		1500	690	No fracture	-
		2450	825	Fractured	0.36
	D	750	529	No fracture	-
		1500	639	No fracture	-
		2450	802	Fracture	0.32
	E	750	581	No fracture	
		1500	615	No fracture	
		2450	752	Fractured	0.34
500	C	750	498	No fracture	-
		1500	507	No fracture	-
		2450	641	Fractured	0.28
	D	750	414	No fracture	-
		1500	506	No fracture	-
		2450	616	Fractured	0.34
	E	750	457	No fracture	-
		1500	480	No fracture	-
		2450	626	Fractured	0.37

© Central University of Technology, Free State

For ease of comparison of the mechanical properties of the three types of samples, the results in Table 7-1 are presented in Figure 7-5. In the present high strain tests, not all the conditions of test strain rate and temperature resulted in specimen failure, as shown in Table 7-1. Only the specimens loaded at a strain rate of 2450 s^{-1} led to fracture. Generally, the specimens tested at strain rates of 750 s^{-1} and 1500 s^{-1} could not reach fracture strain simply because the waves generated by these strain rates were not sufficient to load the specimens to failure. As previously seen in Equation 2-57 (in page 77), the strain experienced by the SHPB test specimen is dependent on reverberations of the reflected signal. This suggests that if the duration of build-up of the reflected wave is limited due to low striker velocity the specimen may not necessarily reach the fracture strain.

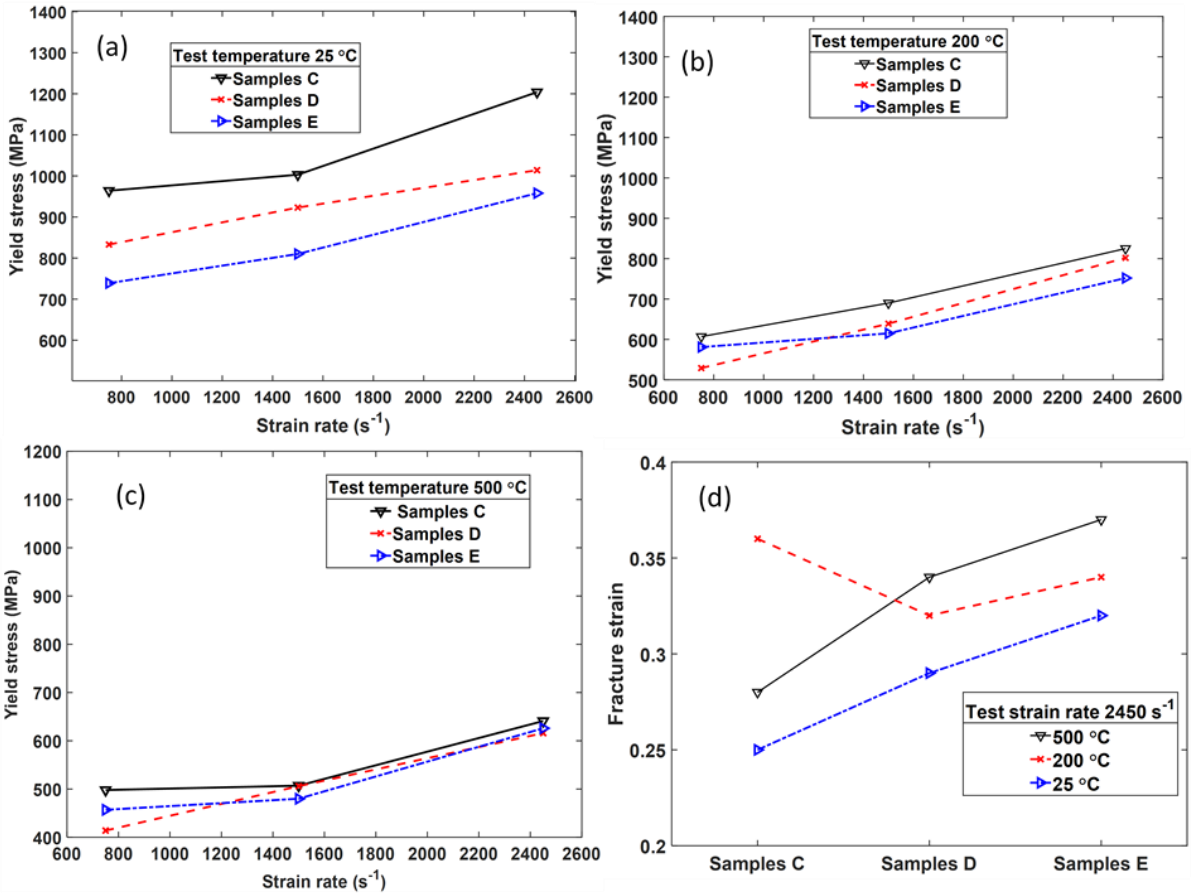

Figure 7-5. Comparison of (a-c) yield stress under different high strain rates and (d) fracture strains at the strain rate of 2540 s^{-1} for samples C, D and E.

As seen in Figure 7-5 (a-c), samples C showed the highest dynamic yield strengths at any given temperature and strain rate as compared to samples D and E. As seen in Figure 7-5(d), the fracture strains that were recorded for samples loaded at the highest strain rate of

© Central University of Technology, Free State

2450 s^{-1}, were lower at all temperatures except at 200 ℃, for samples C compared to the rest of the samples. Samples E showed the lowest dynamic yield stress compared to the other two samples for most of the test temperatures and strain rates. The fracture strains of samples E at the highest strain rate were the highest at two temperatures and second highest at the third temperature. The high dynamic flow stress in samples C in comparison to the samples D and E is attributed here to the small average α-lath thickness, recorded as 2.5 µm for samples C, which therefore leads to a short effective slip length during deformation, thus increasing the yield stress and subsequent flow stress.

To get clarity on the effect of strain rate and temperature on the dynamic response of the three different microstructures of DMLS Ti6Al4V(ELI), the variation of true stress with strain rate as a function of true strain and temperature was plotted. The effects of strain rate on the flow stress at a fixed strain and temperature can be quantified using the strain rate sensitivity parameter m expressed as:

$$m = \frac{\Delta log\sigma}{\Delta log\dot{\varepsilon}} \qquad 7\text{-}1$$

where the symbols σ and $\dot{\varepsilon}$ stand for true stress and true strain rate, respectively. The strain rate sensitivity is therefore given by the gradient of the linear plot of true stress *vs*. true strain rate in log-log graphs and at a given strain. Such plots for the samples tested in the present research are shown in Figure 7-6 (a-c). The increase of flow stress with strain rate of the curves presented in this figure at a log-log scale, shows a linear dependence as evidenced by the correlation coefficients of the plots presented in Table 7-2. The strain rate sensitivity parameter m for the three categories of samples at the three test temperatures is also shown in this table and for ease of comparison presented in (d) of Figure 7-6. As seen in Table 7-2 and Figure 7-6(d), the calculated values of strain rate sensitivity m are small at the lower temperature but increase with test temperature for all samples tested. Generally, plastic deformation in alloys is due to slip of dislocations.

© Central University of Technology, Free State

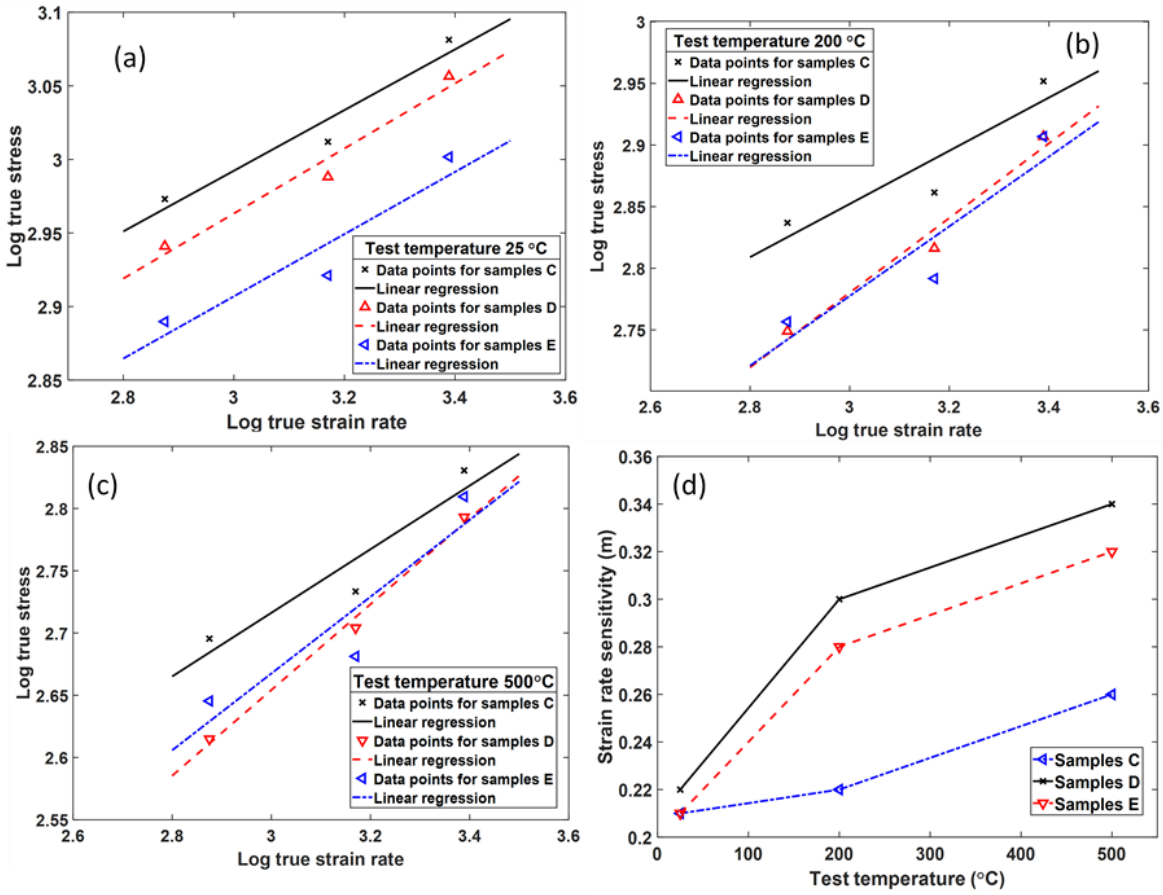

Figure 7-6. Plots (a-c) true stress vs. true strain rate on a log-log scale at a true strain of 0.1 and at different test temperatures and (d) the trend of strain rate sensitivity parameter m and its comparison in samples C, D and E.

Table 7-2. Strain rate sensitivity (m) and correlation coefficient (R^2) of the log-log plots of true stress and strain for samples C, D and E at various test temperatures

Test temperature	**25** ℃		**200** ℃		**500** ℃	
Alloy	***m***	***R²***	***m***	***R²***	***m***	***R²***
C	0.21	0.94	0.22	0.85	0.26	0.89
D	0.22	0.96	0.30	0.97	0.34	0.85
E	0.21	0.89	0.28	0.97	0.32	0.99

Furthermore, according to dislocation mechanics, the flow stress of materials consists of a thermal part (dependent on strain rate and temperature) and an athermal part (generally regarded as being independent of temperature and strain rate (Babu and Lindgren 2013). The thermal part is controlled by short-range barriers, such as mobile dislocations and the Peierls stress, and is sensitive to both temperature and strain rate. More so, at high temperature, the edge dislocations of the α-phase in Ti6Al4V(ELI) presented in Table 6-3 of

© Central University of Technology, Free State

Chapter 6, can climb along the direction perpendicular to their slip planes (Hull and Bacon 2012). Thus, the increase in the magnitude of the strain rate sensitivity parameter m with temperature seen in Table 7-2 is a sign of an attendant increase in the activity of dislocations.

High strain rates accelerate the multiplication of these mobile dislocations, resulting in the formation of dislocation tangles (Kocks 1976). On the other hand, higher temperatures will supply the dislocations with sufficient thermal energy to help overcome dislocation tangles, therefore enhancing the dislocation activities (Mecking and Kocks 1981). In fact, the increasing activity of the non-basal slip systems as a function of increasing temperature (200 ℃ to 500 ℃ in this case), in addition to basal slip systems of the hcp structure of this material, is another reason that could explain the higher m-value at higher deformation temperatures. The athermal part of the flow stress is controlled by long-range barriers such as the secondary precipitates and grain boundaries which are generally termed as being independent of strain rate and temperature during high-strain-rate deformation (Mecking and Kocks 1981, Kocks 2001). Even though this is the case, the effects of grain size on dislocation activity for this material cannot be ignored. A previous study by Conrands (2003) showed that the grain size effect on the strain rate sensitivity is mainly attributed to the thermally activated dislocation motion, since reducing the grain size leads to a decrease in the spacing of dislocation forests, thereby enhancing the parameter m. In fact, for α laths with small thickness, it means that dislocations inside them move a shorter distance before encountering obstacles (grain boundaries), increasing the material's potential of encountering serious dislocation pile-up and hence a higher value of parameter m. It is important to note here that a high-strain-rate sensitivity index could mean that the material exhibits a dramatic increase in strength with increase in strain rate, which is consistent with the results presented in Figures 7-6 and Table 7-2.

The calculated values of strain rate sensitivity index m shown in Table 7-2 and Figure 7-6(d) do not follow the analogy of grain size described in the preceding paragraph, namely that the strain rate sensitivity increases with decrease in grain size. At any given temperature, samples D (average laths thickness 6 µm) have the highest strain rate sensitivity parameter, showing the material to be more sensitive to high strain rate and temperature than the rest. On the other hand, samples C (average laths thickness 2.5 µm) show the lowest

© Central University of Technology, Free State

response to high strain rate and temperature depicted by a lower value of m. Samples E with the largest average α-thickness have higher values of m at all temperatures and strain rates than samples C, but lower than those of samples D.

A previous study by Mao *et al.* (2018) attributed opposite/reverse grain size dependence on strain rate sensitivity of copper at high strain rate because of a change in deformation mechanism from obstacle-controlled plasticity to a combination of obstacle and dislocation drag-controlled plasticity. A similar case was reported elsewhere in Lesuer (2000) for close-packed structures. At high strain rates, the interactions of mobile dislocations with phonons and electrons slow down the motion of dislocations and therefore more force is required to deform the material. Generally, a shock wave acting on a material crystal lattice generates mechanical waves within the crystal structure. The unit of vibrational energy that arises from oscillating atoms within a crystal is referred to as a phonon. A simple derivation of pure drag plasticity for a material is described here from the Orowan relationship (Kocks 1976). The relationship of strain rate ($\dot{\varepsilon}$), mobile dislocation density (ρ_m) and dislocation velocity (v) can be expressed as:

$$\dot{\varepsilon} = \frac{vb\rho_m}{M} \qquad 7\text{-}2$$

where M is the Taylor factor. The average dislocation velocity, as described in Frost and Ashby (1982), can be expressed as:

$$v = \frac{\sigma_{drag} b}{\mu_d} \qquad 7\text{-}3$$

where σ_{drag}, b and μ_d are the viscous drag flow stress due to the dislocation dragging effect, the Burgers vector and the drag coefficient, respectively. Dislocation density can be assumed to be proportional to the reciprocal of the grain size (d) (taking this as represented by the lath thickness in the case of DMLS Ti6Al4V(ELI)). Furthermore, the mobile dislocation density is part of the total dislocation density, and the scale factor can be assumed constant for the three material variants C, D and E. With these assumptions, Equations 7-2 and 7-3 can be combined to give:

$$\sigma_{drag} = \frac{\dot{\varepsilon}\, \mu_d M^2 d}{b^2} \qquad 7\text{-}4$$

© Central University of Technology, Free State

Taking the parameter M as equal to 3 and the ratio μ_d/b as a constant K, the graph of flow stress due to dislocation dragging effect against strain rate for different grain sizes and against grain sizes for different strain rates is presented in Figure 7-7. As seen in this figure, the relationship between flow stress and the grain size/lath thickness is one where thicker α-laths give a higher drag stress and vice versa. This could explain the higher values of index m for samples D and E than those of samples C. While comparing the strain rate sensitivity index of samples D and E, it is important to highlight the microstructural and textural differences between these samples, as discussed in Chapter 5. As previously noted in Figure 5.1 of Chapter 5, samples D are characterised by typical basket-weave microstructure, while samples E have largely typical Widmanstätten microstructure composed of colonies of α-laths with similar orientation.

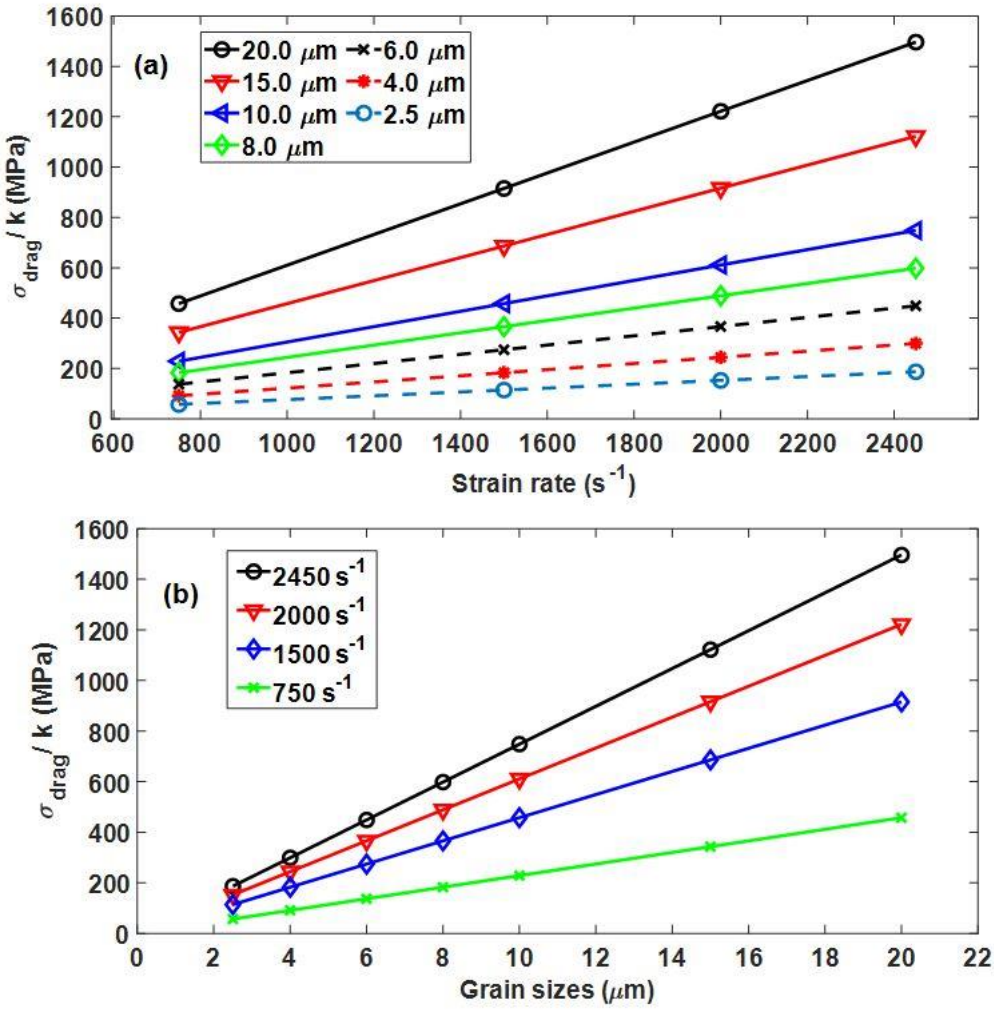

Figure 7-7. Viscous drag stress as a function of (a) strain rate for different grain sizes and (b) grain size at different strain rates.

© Central University of Technology, Free State

The ease of penetration of dislocations across the α/β interfaces depends upon the degree of alignment of slip directions in adjacent phases, as determined by the Burgers orientation relationship (BOR) (Burgers 1943). As reported previously, samples D with the typical basket-weave microstructure have a high number of different α variants in the microstructure making it difficult to transfer slip across the grains. However, for samples E, which are composed of colonies of parallel α-laths sharing the same crystallographic orientation, it is easier to transfer slip across the laths and therefore less force is required to initiate plastic deformation.

The foregoing discussion suggests that the morphology, texture, and atomic-level inherent dislocation mechanisms can play a prominent role in determining the flow response and strain rate sensitivity of DMLS Ti6Al4V(ELI) alloy.

7.3 ANALYSIS OF MICROSTRUCTURE AND FRACTURE SURFACES OF VARIOUS DMLS TI6AL4V(ELI) SPECIMENS LOADED AT HIGH COMPRESSIVE STRAIN RATES AND HIGH TEMPERATURES

7.3.1 Analysis of microstructure of deformed surfaces

As previously indicated in Table 7-1, not all the dynamic test conditions resulted in failure of specimens and only the samples that were tested at a strain rate of 2450 s^{-1} failed. As the specimens that were loaded at strain rates of 750 s^{-1} and 1500 s^{-1} at all test temperatures did not fail, they form a good basis for analysing the deformation characteristics of the various forms of DMLS Ti6Al4V(ELI) alloy. Figure 7-8 shows the quintessential deformation features of these samples observed under low magnification in an optical microscope.

© Central University of Technology, Free State

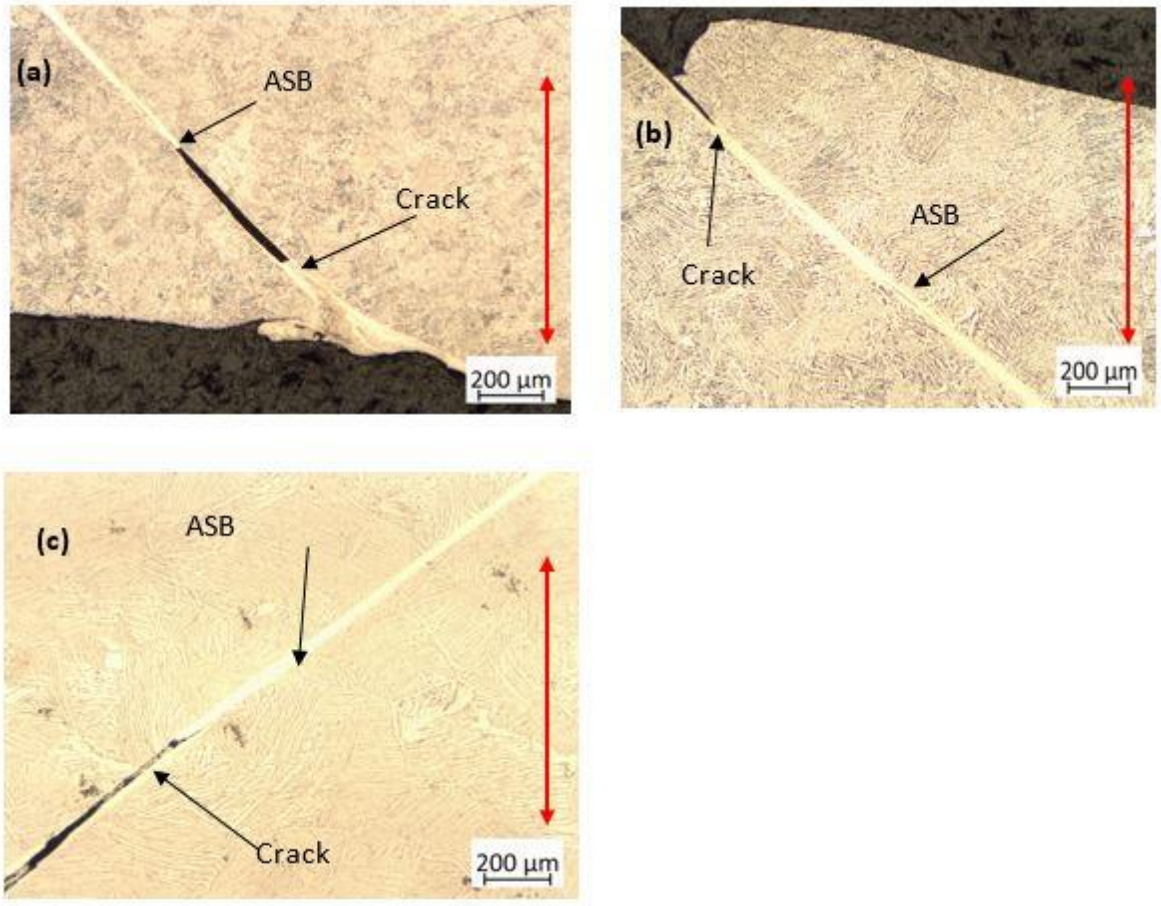

Figure 7-8. Typical deformation features on cross sections through the surfaces of samples (a) C, (b) D, and (c) E observed under an optical microscope (the red arrows indicate the compression axis).

A more detailed description of bulk microstructures, seen in Figure 7-8 for samples C, D and E, was presented in section 5.2 of Chapter 5. Generally, the microstructure of samples C that were heat-treated at 800 °C followed by furnace-cooling, consists of an equilibrium mixture of α and β-phases, where the α-phase is present as fine needles. Samples type D, that were heat-treated at 940 °C and furnace-cooled also consist of an equilibrium mixture of α and β- phases but the shape of the α/β-grains is more lamellae-like. The microstructure of samples E, that were heat-treated at 1020 °C and furnace-cooled, generally is comprised of Widmanstätten microstructure with large colonies of the α-phase.

It is apparent from the micrographs in Figure 7-8 that the deformed surfaces of various samples of DMLS Ti6Al4V(ELI) are characterised by bright bands and in some places the bright bands are replaced by dark elongated features. The bright bands are known as adiabatic shear bands (ASBs), while the dark elongated features are cracks propagating

© Central University of Technology, Free State

along the ASBs. The ASBs are seen in Figure 7-8 to be narrow and extend through the grains across the deformed surfaces at an angle of approximately 45° to the compression axis, which is the expected angle of maximum shear in cases of uniaxial loading.

Generally, plastic work during high-strain-rate deformation of materials is invariably transformed into thermal energy, which results in a rise in the local temperature in a material. Since the thermal conduction of Ti6Al4V(ELI) is very poor and at the same time its strain hardening, as seen in Figures 7-2 to 7-4 is low, the alloy is sensitive to strain localisation in the conditions of dynamic deformation (Chen *et al*. 2007). Due to low heat dissipation, the rise in temperature in the alloy in conditions of dynamic deformation lowers its strength, a phenomenon commonly known as “thermal softening”. As the strain increases, the thermal softening effect outweighs the strengthening effect due to strain hardening and shear instability occurs. Basically, if the stress in the primary shear zone is surpassed by the stress in the bulk material, a shear localisation event takes places forming narrow shear bands (Dodd and Bai 2012). Once formed, the ASBs become sites of subsequent failure by rapid nucleation and growth of cracks within them, as seen in Figure 7-8.

The ASBs in the three forms of DMLS Ti6Al4V(ELI) at different temperatures and strain rates were studied further at higher magnification in a scanning electron microscope (SEM), to give the secondary electron images (SEIs) presented in Figures 7-9 to 7-11.

© Central University of Technology, Free State

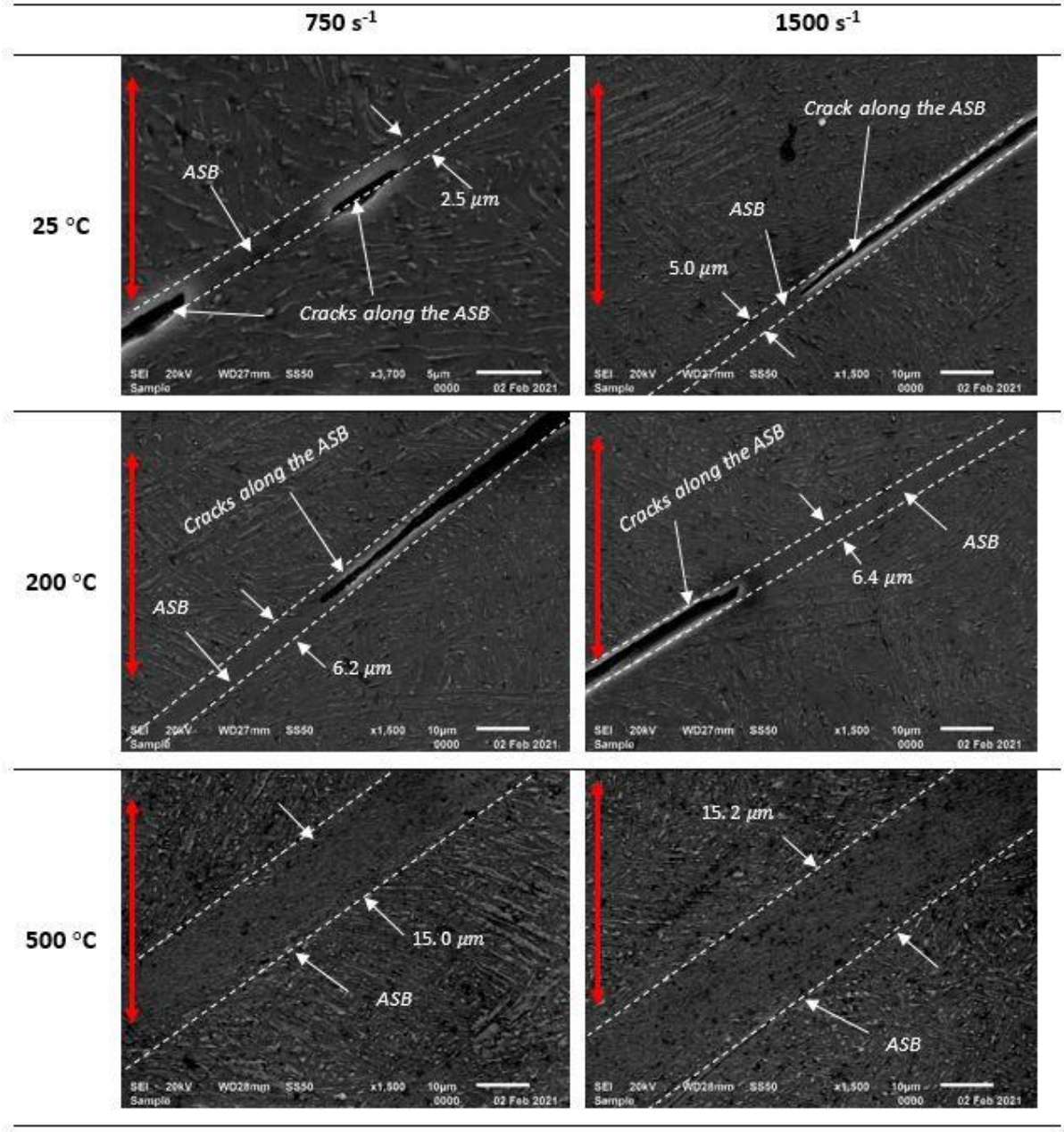

Figure 7-9. Secondary electron images showing adiabatic shear bands on sections of deformed surfaces of samples C at different temperatures and strain rates. (Note the different magnification at 750 s^{-1} and 25 °C). The red arrows indicate the loading axis.

© Central University of Technology, Free State

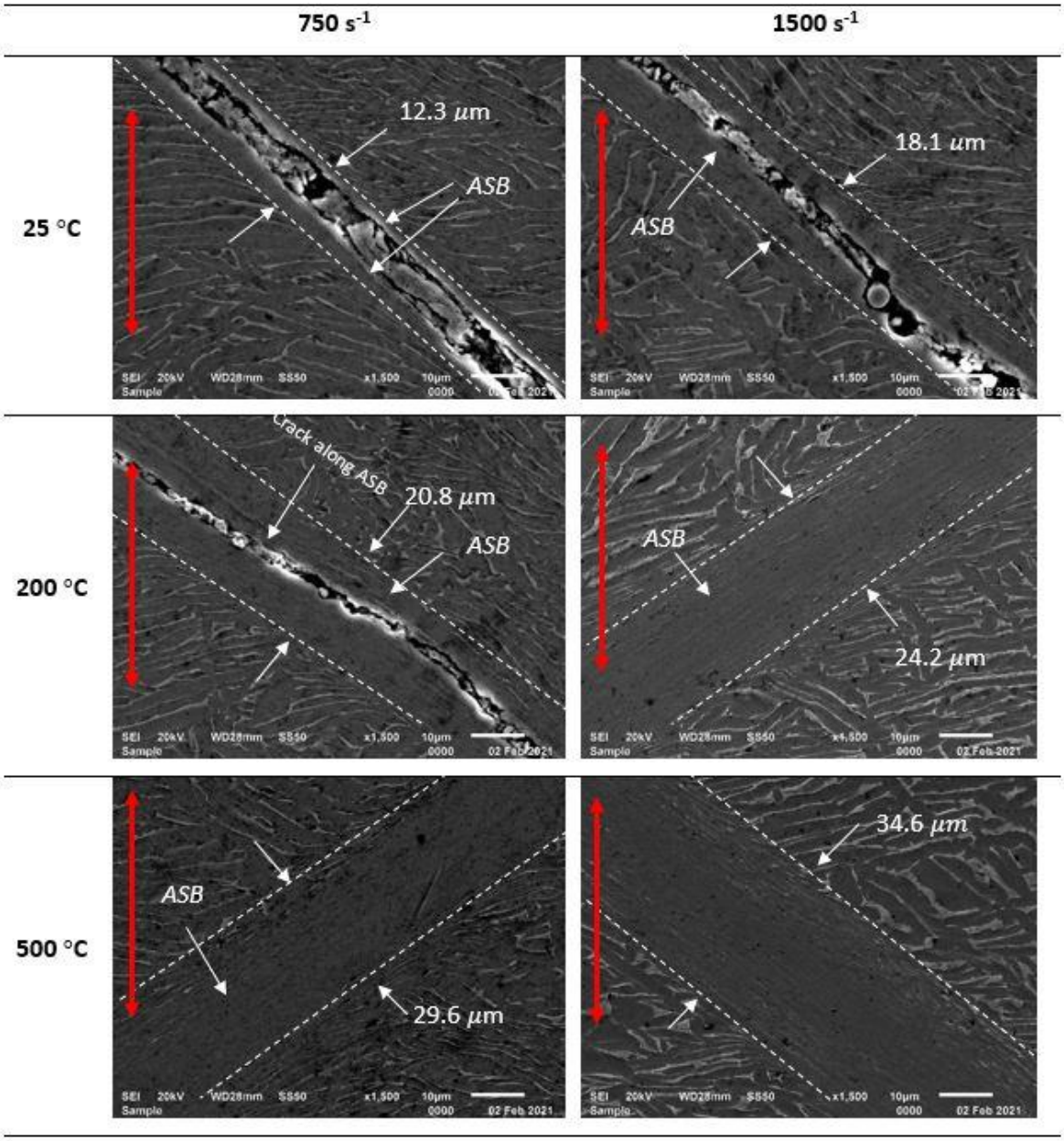

Figure 7-10. Secondary electron images showing adiabatic shear bands on sections of deformed surfaces of samples D at different temperatures and strain rates (the red arrows indicate the loading axis).

© Central University of Technology, Free State

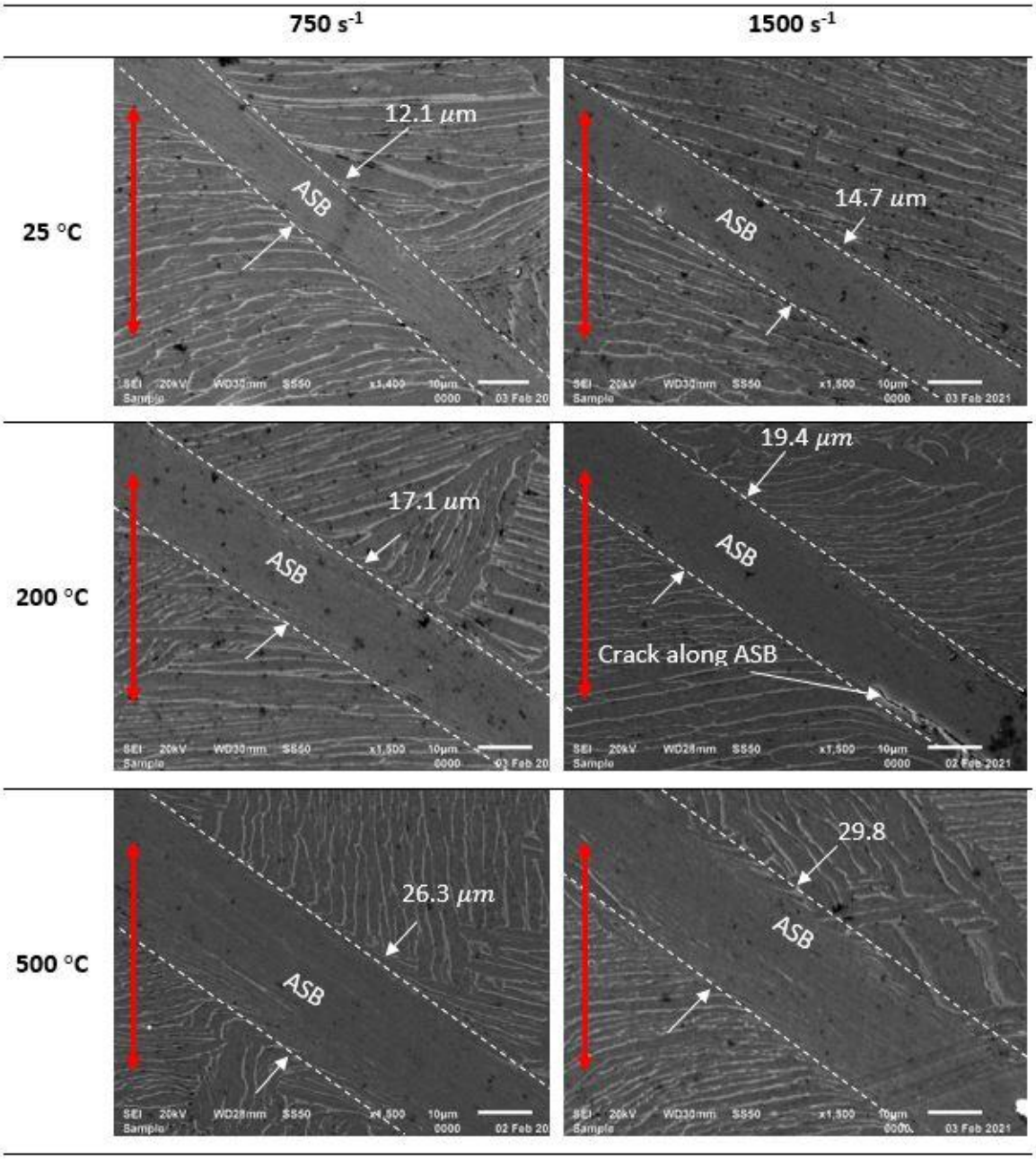

Figure 7-11. Secondary electron images showing adiabatic shear bands on sections of deformed surfaces of samples E at different temperatures and strain rates (the red arrows indicate the loading axis).

It is clear from observation of Figures 7-9 to 7-11 that the microstructures within the adiabatic shear bands are different from that of the bulk material, a difference thought to have arisen during the formation of these adiabatic shear bands. It is known from the literature (Xue *et al.* 2002, Dodd and Bai 2012) that microstructural changes such as dynamic recovery, recrystallisation and phase transformation do occur during formation of

© Central University of Technology, Free State

adiabatic shear bands. However, direct evidence of these microstructural changes could not be pinpointed from the SEIs presented in the three figures. The most appropriate method to study the microstructural changes along the ASBs is the EBSD technique. As part of future research, it is envisaged to establish the extent of phase transformation and recrystallisation in these ASBs. As previously mentioned, the formation of ASBs precedes failure mechanisms such as nucleation and propagation of cracks. As seen in these figures, well-developed adiabatic shear bands in some cases are accompanied by cracks which propagate within and along the bands. This suggests that the eventual failure of the different forms of DMLS Ti6Al4V(ELI) at high strain rate is because of the formation of ASBs which offer favourable regions for the initiation, growth and propagation of cracks.

The width of ASBs is seen in Figures 7-9 to 7-11 to vary for different forms of the DMLS Ti6Al4V(ELI) alloy and at different test conditions of temperature and strain rate. A summary of the average width of ASBs for different forms of the alloy and at different testing conditions is presented graphically in Figure 7-12, all together for ease of comparison.

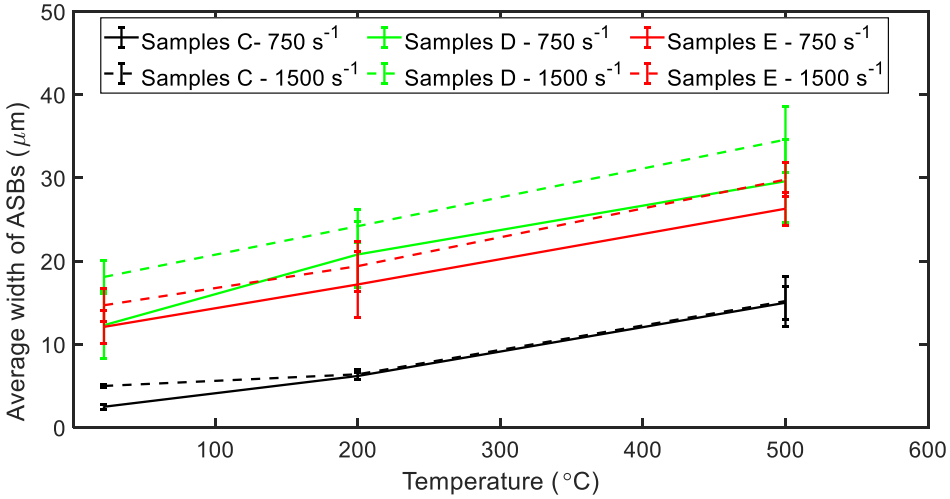

Figure 7-12. Variation of the average width of adiabatic shear bands as a function of strain rate and temperature for samples C, D and E.

It is evident from this figure that the average width of the ASBs increases with increasing test temperature, almost invariably in linear relationships. A similar observation was reported by Lee and Lin (1997) for wrought Ti6Al4V. The average width of the ASBs is also seen in the figure to increase with strain rate, however, the error bars are seen to overlap

© Central University of Technology, Free State

which could suggest that the increase in shear band width is not significant between the strain rate of 750 s^{-1} and 1500 s^{-1}.

A significant difference in the average width of ASBs is noted in the Figure 7-12 for different samples of DMLS Ti6Al4V(ELI). At the same strain rate and temperature, samples C and D show the lowest and the highest values of width, respectively. This suggests that the heat-treatment regimes of DMLS Ti6Al4V(ELI) do influence the width of ASBs formed at conditions of high-strain-rate deformation. A critical factor that influences the width of ASBs, as reported in the research of Dodd and Bai (2012), is the hardness of materials, as the width of the ASBs diminishes with increasing hardness of the material. Hardness is generally a measure of a material's resistance to localised plastic deformation and is normally proportional to material strength. The thermo-softening effect which results in the formation of ASBs is expected to reduce with increase in strength and related hardness of materials.

The reported values of Vickers hardness for samples C, D and E in Figure 5-18 of Chapter 5 were 362.36 $\pm$ 2.57 HV, 343.92 $\pm$ 3.52 HV and 353.88 $\pm$ 4.23 HV, respectively. This order of hardness is consistent with the order of width of ASBs observed here for the three microstructures. Therefore, the difference in the width of the ASBs observed in Figure 7-12 for samples C, D, and E is because of the different microstructures formed by the different heat-treatment processes and the arising values of strength and hardness.

7.3 2. Fractographic analysis of failure surfaces

Figure 7-13 presents photographic images of the specimens tested at a strain rate of 2450 s^{-1} and at different test temperatures. It is clear from this that the specimens failed in a catastrophic manner along a plane oriented at an angle of approximately 45° to the compression axis. From the observation made in the preceding section, it is plausible to deduce that the specimens fractured because of intensive localised plastic flow prompted by the formation of adiabatic shear bands, seen in Figures 7-8 to 7-11, which were also inclined at an angle of approximately 45°. The effects of temperature are also revealed in Figure 7-13, where at 200 °C and 500 °C, the specimens were seen to have undergone intensive plastic deformation in comparison to those deformed at a temperature of 25 °C.

© Central University of Technology, Free State

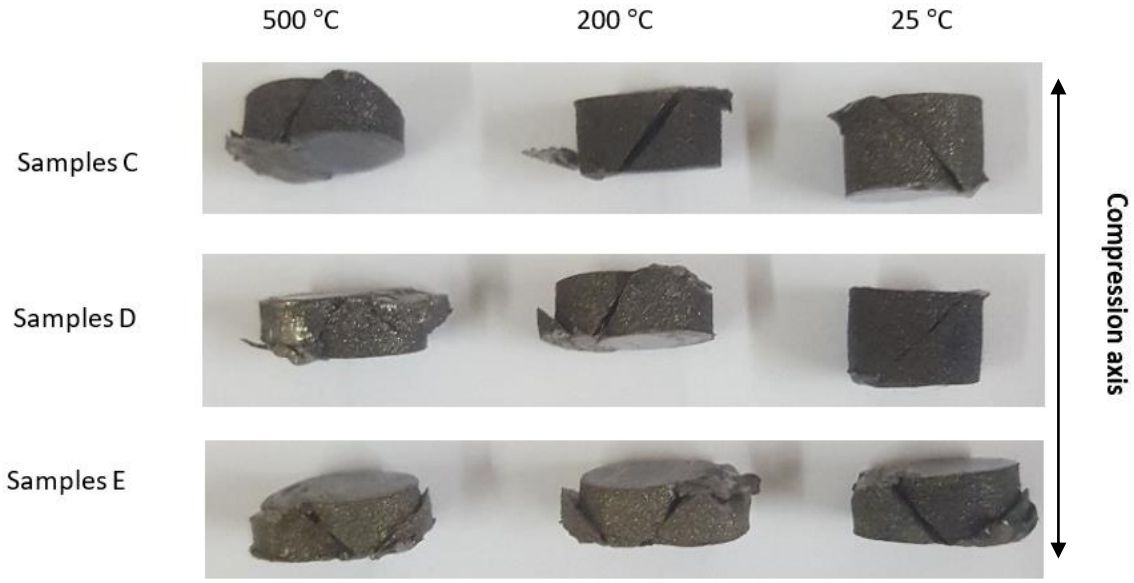

Figure 7-13. The photographic images of specimens deformed at a strain rate of 2450 s^{-1} and at temperatures of 25 °C, 200 °C and 500 °C.

Figure 7-14 shows the measured height of deformed specimens and corresponding longitudinal plastic strain at a strain rate of 2450 s^{-1} and at different temperatures. From Figure 7-14, the measured deformed height and corresponding longitudinal plastic strain for different specimens are seen to decrease and increase with temperature, respectively.

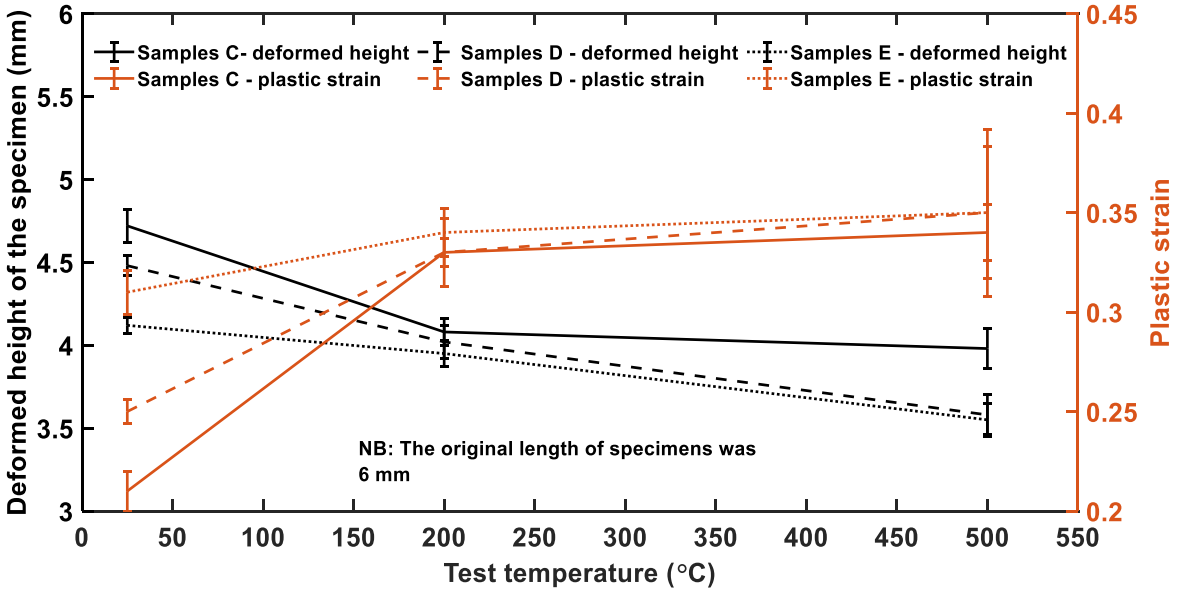

Figure 7-14. The measured height of deformed specimens and estimated longitudinal plastic strain at a strain rate of 2450 s^{-1} and different temperatures for samples C, D, and E.

© Central University of Technology, Free State

The observations made from Figures 7-13 and 7-14 are consistent with the results presented in Figures 7-2 to 7-4, where ductility of the specimens was seen to increase with increase in temperature. The ductility of samples E and C is seen to be highest and lowest, respectively, judging from the decrease in the height and increase in longitudinal plastic strain of each group of samples at different temperatures. The fracture surfaces of the samples that were tested at a strain rate of 2450 s^{-1} and at different temperatures are presented in Figures 7-17 to 7-19.

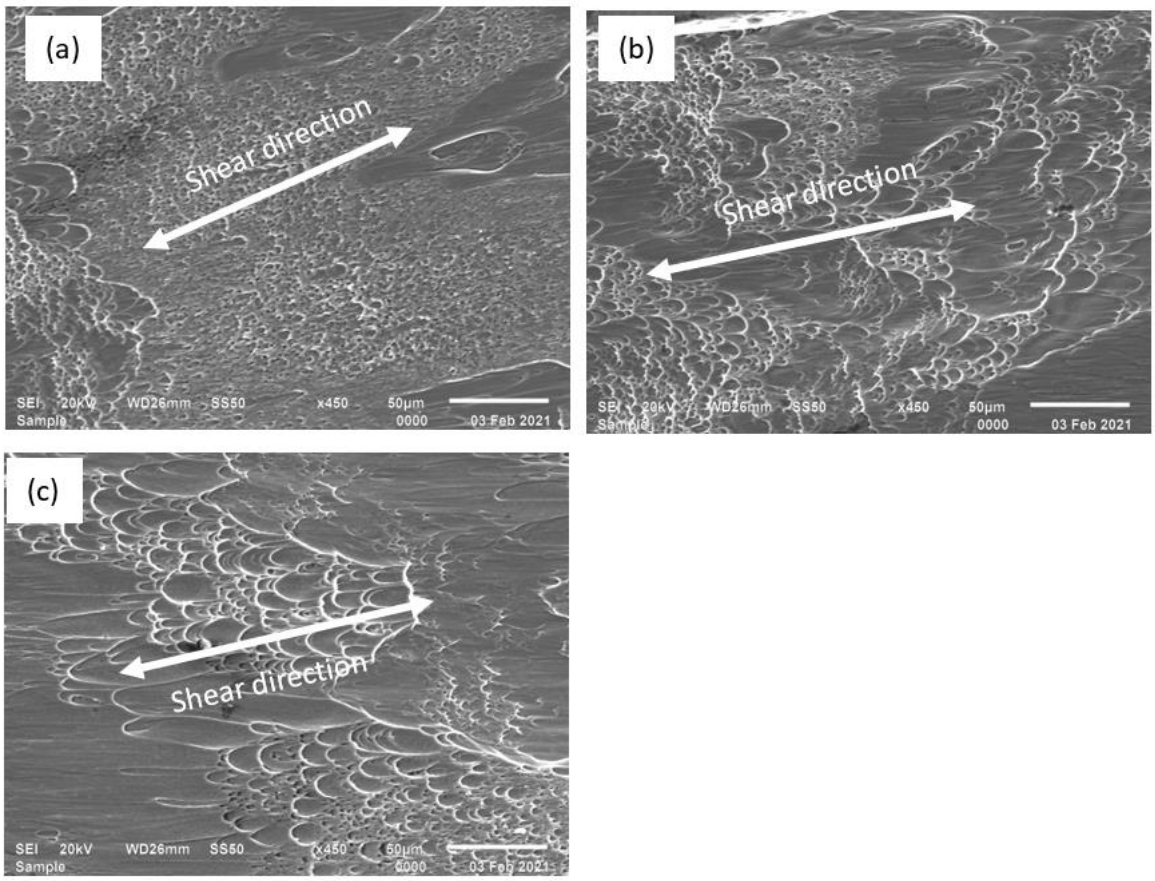

Figure 7-15. Typical characteristic features on the fracture surfaces of samples C at temperatures of (a) 25 °C, (b) 200 °C, and 500 °C at a magnification of X450.

© Central University of Technology, Free State

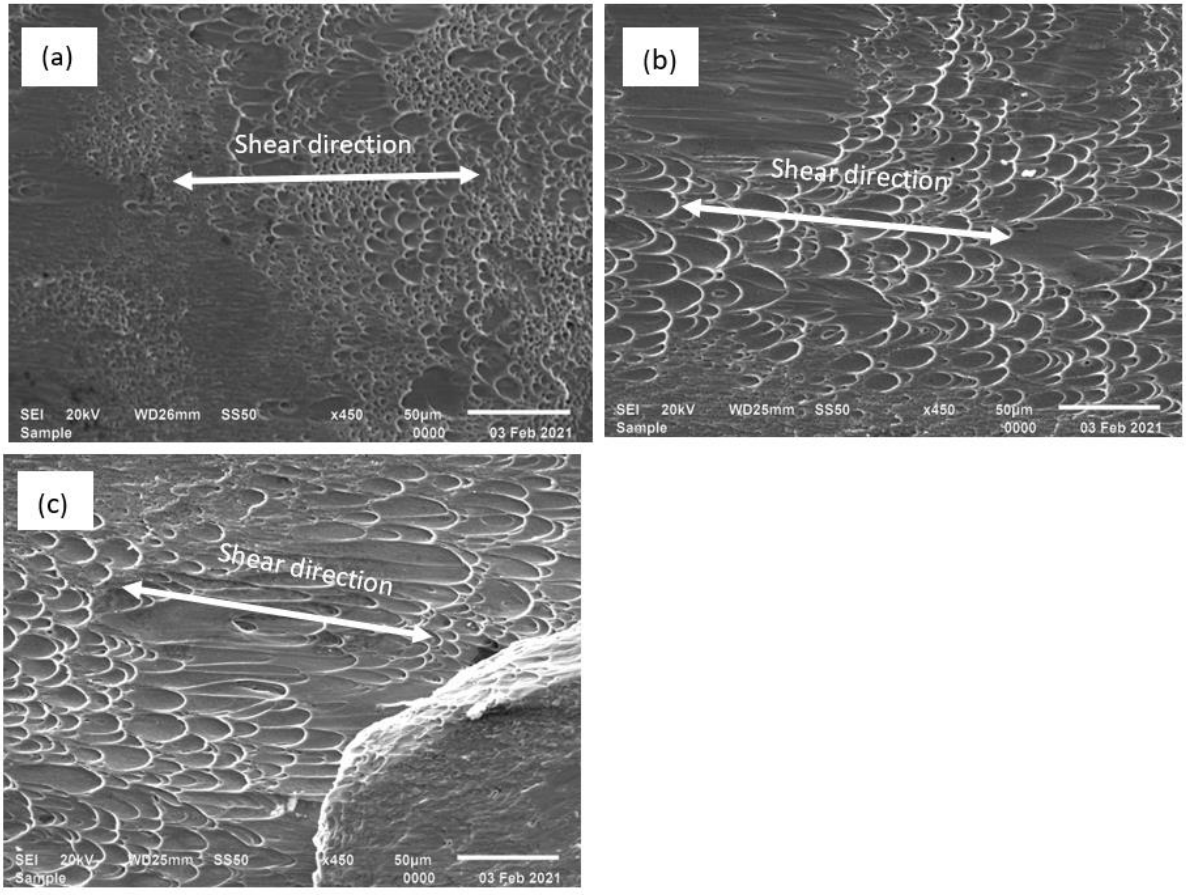

Figure 7-16. Typical characteristic features on the fracture surfaces of samples D at temperatures of (a) 25 °C, (b) 200 °C, and 500 °C at a magnification of X450.

© Central University of Technology, Free State

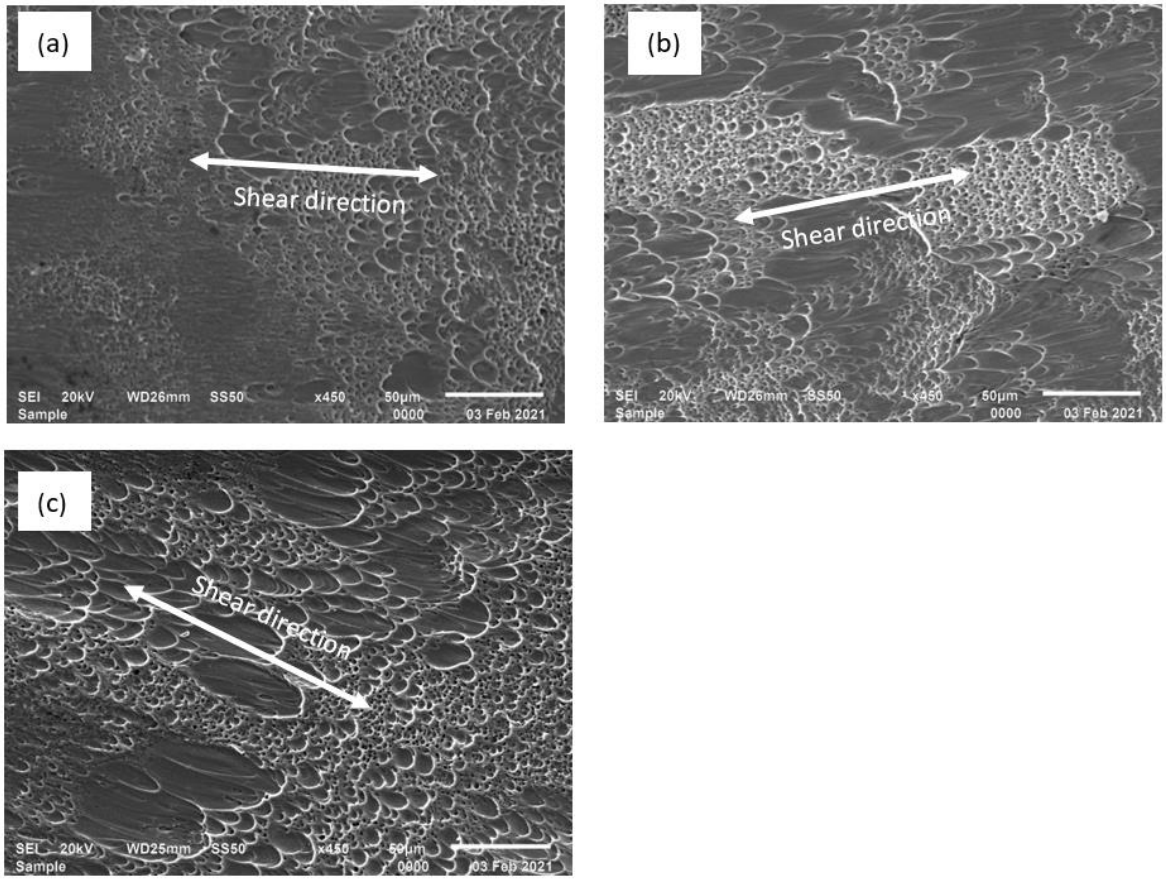

Figure 7-17. Typical characteristic features on the fracture surfaces of samples E at temperatures of (a) 25 °C, (b) 200 °C, and 500 °C at a magnification of X450.

The micrographs of the fracture surfaces of samples C, D and E shown in Figures 7-15, 7-16 and 7-17, respectively, show elongated dimples in all conditions of testing. The dimples are elongated along the directions of shear. These dimple features suggest that an array of microcracks/microvoids along the ASBs preceded the moment of fracture, with each microcrack/microvoid corresponding to a dimple. After dimples form from nucleated microvoids, their size increase with imposed flow stress, followed by their coalescence with other dimples to form larger dimples. This explains the multiple dimples of varying sizes on each fracture surface presented in Figures 7-15 to 7-17. The presence of dimples on the fracture surfaces denotes ductile fracture in contrast to smooth surfaces that are characterised by cleavages which are a sign of brittle fracture. It is intriguing to note that in every case of the test samples here, the extent of elongation of these dimples was influenced by the test temperature. At the temperatures of 200 °C and 500 °C, the dimples are seen to be more elongated in comparison with ones resulting from tests conducted at room temperature (25 °C). A summary of the major and the minor diagonal lengths of

© Central University of Technology, Free State

these dimples for different samples seen in Figures 7-15 to 7-17 at different temperatures is presented in Table 7-3.

Table 7-3. The range of dimple lengths in different DMLS Ti6Al4V(ELI) samples fractured at a strain rate of 2450 s^{-1} and at different temperatures

Temperature (°C)	**25**		**200**		**500**	
Alloy	Dimples size range (major & minor diagonals) in (μm)					
	Major	Minor	Major	Minor	Major	Minor
Samples C	1 - 10	1 - 7	8 - 25	5 - 20	20 - 60	15 - 24
Samples D	3 - 15	3 - 10	12 - 30	8 - 20	25 - 60	15 - 25
Samples E	3 - 15	3 - 10	6 - 25	6 - 20	17 - 60	10 - 40

As seen in this table, both the major and minor diagonal lengths of dimples increase with an increase in temperature for all cases of samples tested. This confirms that plastic deformation of the specimens increases with increased temperature and thus supports the inference of increased ductility with increasing temperature of the various microstructures of the DMLS Ti6Al4V(ELI) alloy tested here.

7.4 SUMMARY

The high-strain-rate properties of three different heat-treated forms of DMLS Ti6AL4V(ELI) were discussed in this chapter. It was shown that their microstructures are sensitive to temperature and strain rate. Samples C and E yielded at the highest and lowest value of stress at most of the test conditions, respectively. This was attributed to variation in microstructure, where samples C, with smaller grain sizes, resulted in a higher dynamic strength and samples E yielded at a lower stress due to coarse α-laths in the microstructure. The strain-rate sensitivity of these samples varied, with samples D showing the highest value followed by samples E, while samples C showed the lowest values, at any given temperature. This was also ascribed to microstructure, precisely the grain sizes and the texture. Coarse grain sizes of samples D and E will result in much higher viscous drag stresses at high strain rates, thus making the material more sensitive to strain rate. However, the presence of basket-weave microstructure in samples D suggests difficulty for dislocations to slip between adjacent phases, resulting in a high flow stress, making these samples more sensitive to strain rate than the case of samples E. All three different samples of DMLS Ti6Al4V(ELI) deformation surfaces were characterised by the formation of ASBs.

© Central University of Technology, Free State

The thickness of these ASBs increased with temperature and strain rate. It was also noted that the thickness of the ASBs also varied in different samples, due to variation of microstructure and therefore, strength and hardness in these samples, because of heat treatment.

© Central University of Technology, Free State

7.5 REFERENCES

1. Babu, B., Lindgren, L.E. 2013. Dislocation density-based model for plastic deformation and globularization of Ti-6Al-4V. *International Journal of Plasticity*, 50, pp.94–108. https://doi.org/10.1016/j.ijplas.2013.04.003
2. Burgers, W.G. 1943. On process of transition of cubic-body-centered modification into the hexagonal-close-packed modification of zirconium. *Physica*, 1 (7-12), pp.561–586. https://doi.org/10.1016/S0031-8914(34)80244-3
3. Chen, J., Zhao, Y., Yang, H., Hiu, L., Hong, Q. 2007. Investigation of adiabatic shear bands of Ti-B19 titanium alloy, Ti 2007: Science and Technology. *Proceeding of the 11th World Conference on Titanium, Kyoto International Conference Centre*, Kyoto, Japan, 3rd–7th June 2007.
4. Conrands, H. 2003. Grain size dependence of the plastic deformation kinetics in Cu. *Materials Science and Engineering* A, 341(1), pp.216–228. https://doi.org/10.1016/S0921-5093(02)00238-1
5. Dodd, B., Bai, Y. 2012. *Adiabatic shear localization—frontiers and advances*. 2nd edition Elsevier, Amsterdam, pp.183–200.
6. Frost, H.J., Ashby, M.F. 1982. *Deformation-mechanism maps: The plasticity and creep of metals and ceramics*. Elsevier Science Ltd, Michigan, USA, pp.134–147.
7. Hull, D., Bacon, D.J. 2011. *Introduction to dislocations* 5th edition, Elsevier Ltd, Kidlington, Oxford, USA, pp.53–57.
8. Kocks, U. 1976. Laws for work-hardening and low-temperature creep. *Journal of Engineering Materials and Technology*, 98, pp.76–85. http://dx.doi.org/10.1115/1.3443340
9. Kocks, U.F. 2001. Realistic constitutive relations for metal plasticity. *Materials Science and Engineering A,* 317, pp.81–187.
10. Lee, W., Lin, C. 1997. Adiabatic shear fracture of titanium alloy subjected to high strain rate and high temperature loadings. *Journal de Physique IV Colloque*, 1997, 7(C3), pp.855–860. https://doi.org/10.1051/jp4:19973144
11. Lesuer, D.R., Kay, G., LeBlanc, M. 2001. Modelling large-strain, high-rate deformation in metals. *Third Biennial Tri-laboratory Engineering Conference on Modelling and Simulation*, Pleasanton, California, USA.

© Central University of Technology, Free State

12. Mao, Z.N., An, X.N., Liao, X.Z., Wang, J.T. 2018. Opposite grain size dependence of strain rate sensitivity of copper at low *vs*. high strain rates. *Materials Science and Engineering A,* 738, pp.430–438.
13. Mecking, H., Kocks, U. 1981. Kinetics of flow and strain-hardening. *Acta Metallurgica*, 29(11), pp.1865–1875.
14. Moletsane, G., Krakhmalev, P., Du Plessis, A., Yadroitsava, I., Yadroitsev, I., Kazantseva, I. 2017. Tensile properties and microstructure of direct metal laser-sintered Ti6Al4V(ELI) alloy. *South African Journal of Industrial Engineering,* 2016, 27(3), pp.110–121.
15. Xue, Q., Meyers, M.A., Nesterenko, V.F. 2002. Self-organization of shear bands in titanium and Ti6Al4V alloy. *Act Materialia* 50(3), pp.575–596. https://doi.org/10.1016/S1359-6454(01)00356-1

© Central University of Technology, Free State

CHAPTER 8 — VALIDATION OF MICROSTRUCTURE-BASED CONSTITUTIVE NUMERICAL MODEL FOR DMLS TI6AL4V(ELI)

The material contained in this chapter has been submitted for publication in peer-reviewed media as detailed below:

***Muiruri, A**.; Maringa, M.; du Preez, W. Validation of a microstructure-based model for predicting the high strain rate flow properties of various forms of additively manufactured Ti6Al4V (ELI) alloy. **Metals** (submitted).*

8.1 INTRODUCTION

This chapter presents refinement and validation of the microstructure-sensitive constitutive model developed in Chapter 4, using the flow stress curves of DMLS Ti6Al4V(ELI) alloys at given temperatures and strain rates presented in Chapter 7. A constitutive model that combines the microstructural effects and the coupled effects of strain rate and temperature to describe the flow stress was derived in Chapter 4 as Equation 4-19 and is presented here as Equation 8-1 for ease of reference, thus:

$$\sigma = \left(\frac{\mu(T)}{\mu_0}\right)\sigma^o\left(1-\left(\left(\frac{k_bT}{g_{0i}\mu(T)b^3}\right)ln\ \frac{\dot{\varepsilon}_o}{\dot{\varepsilon}}\right)^{1/q}\right)^{1/p} + \frac{K_{H-P}}{\sqrt{d}} + \alpha\mu(T)bM\left(\frac{h}{k_2}\left(1-exp\left(-k_2\varepsilon_p\right)\right)+\rho_o\,exp\left(-k_2\varepsilon_p\right)\right)^{\frac{1}{2}} \quad 8\text{-}1$$

This constitutive model contains many adjustable parameters that can easily be tuned to fit experimental curves. Some of the parameters are categorised as “prescribed” and others as “fitted”. Among the prescribed parameters are those that are obtained from metallographic analysis such as grain size (presented in Chapter 5) and dislocation density (presented in Chapter 6), while others are obtained from literature.

Based on the procedure outlined in Chapter 4 for evaluation of fitted model parameters, refinement of the microstructure-based constitutive model developed in this chapter is divided into two, namely:

(a) Prediction of the yield stress.

(b) Prediction of subsequent flow stress.

© Central University of Technology, Free State

8.2 PREDICTION OF THE YIELD STRESS

8.2.1 Athermal stress (σ_a)

The Hall-Petch equation was used here to define the athermal stress and allowed the component of yield stress to be estimated using the equation $\sigma_a = K_{H-P} d^{-\frac{1}{2}}$. The Hall-Petch constant K_{H-P} is a stress concentration factor. This stress concentration arises from pile-ups of dislocations against the grain boundaries, which at a certain point yield enough stress to activate dislocation sources in neighbouring grains.

The grain size d determines the maximum distance dislocations travel before encountering an obstacle, defined by the thickness of α laths of Ti6A4V. The Hall-Petch equation for Ti6Al4V for a wide range of grain sizes, taking K_{H-P} as $328\ MPa\mu m^{1/2}$ (Kohn and Ducheyne 1991), is shown in Figure 8-1.

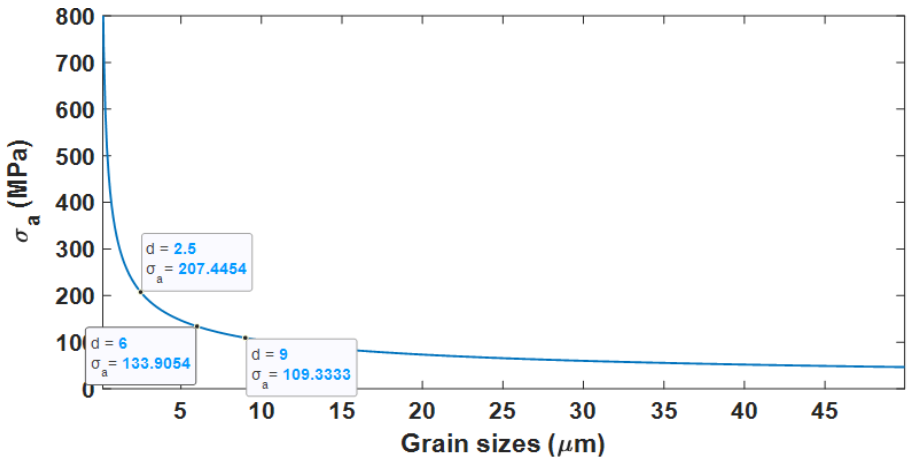

Figure 8-1. Graphical description of the Hall-Petch relationship for DMLS Ti6Al4V(ELI).

In this research, the Hall-Petch effect was assumed to be controlled by the properties and average thickness of the α-laths, since this is the shortest distance dislocations can travel before encountering obstacles. Owing to the low volume fraction of β-phase recorded in the three different sample types C, D and E of the DMLS Ti6Al4V(ELI) test specimens at various strain rates, the contribution of the β-phase to athermal stress in this study was ignored. It was assumed that the β layers themselves are like typical grain boundaries in a single-phase material. The average thicknesses of the α-lath of samples C, D and E were noted in Chapter 5 to be 2.5 µm, 6.0 µm and 9.0 µm, respectively. As seen in the insert labels in Figure 8-1, the contribution of the athermal stress to the yield strength for the

© Central University of Technology, Free State

three different microstructures of DMLS Ti6Al4V(ELI) is 207.45 MPa, 133.91 MPa and 109.33 MPa, for samples C, D and E, respectively.

8.2.2 Temperature-dependent shear modulus

The empirical temperature-dependent shear modulus of materials is often of the form (Majorell and Picu 2002, Chan *et al.* 2012):

$$\mu(T) = \mu_o - \frac{D}{exp\left(\frac{T_0}{T}\right)-1}(GPa) \qquad 8\text{-}2$$

where μ_o is the shear modulus at $0\ K$, and T_o and D are material constants. For Ti6Al4V, these parameters have values of 49.02 GPa, 181 K and 5.821, respectively (Majorell and Picu 2002). From the fact that the Ti6Al4V (grade 5) and Ti6Al4V(ELI) (grade 23) do not show significant difference in elastic properties (Azo Materials 2020), the constants used in Majorell and Picu (2002) were adopted in the present research. Thus, the formulation for the shear modulus of Ti6Al4V(ELI) becomes:

$$\mu(t) = 49.02 - \frac{5.821}{exp\left(\frac{181}{T}\right)-1}\ (GPa) \qquad 8\text{-}3$$

Figure 8-2 shows the shear modulus of Ti6Al4V(ELI) as a function of temperature. The shear moduli of this alloy at the test temperatures of 25 ℃, 200 ℃ and 500 ℃ are shown in the insert labels of the figure.

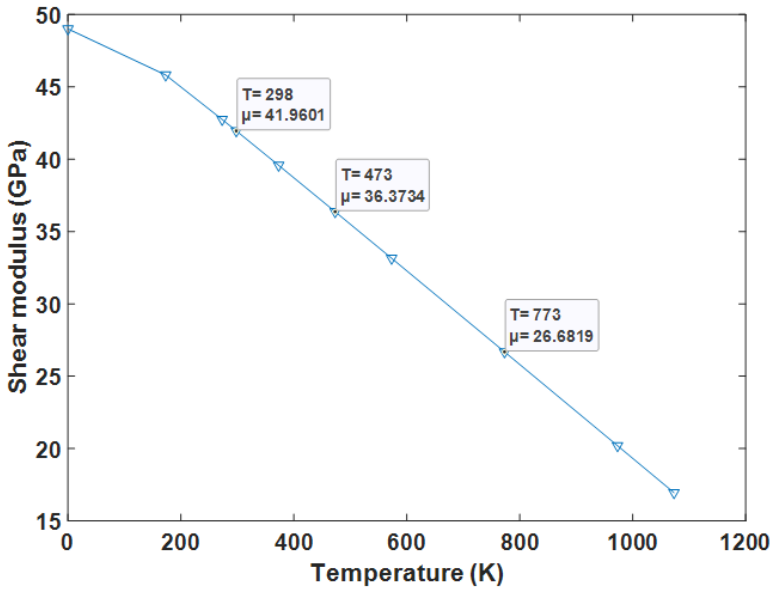

Figure 8-2. The shear modulus of Ti6Al4V(ELI) as a function of temperature.

© Central University of Technology, Free State

8.2.3 Thermal part of the yield stress

The expression for total thermally activated stress was adopted in Chapter 4 as:

$$\left(\frac{\sigma_y-\sigma_a}{\mu(t)}\right)^p = \left(\frac{\sigma_o}{\mu_o}\right)^p \left(1-\left(\frac{1}{g_{oi}}\right)^{1/q}\left(\frac{KT}{\mu(t)b^3}\left(ln\frac{\dot{\varepsilon}_o}{\dot{\varepsilon}}\right)\right)^{1/q}\right) \qquad 8\text{-}4$$

In this equation, the constant parameter $\dot{\varepsilon}_o$ is the reference strain rate, while p and q represent the energy barrier profile and are normally based on empirical observations. From literature, for Ti6Al4V, these constants have been determined as $p = 1$, $q = 2$ and $\dot{\varepsilon}_o = 10^7 s^{-1}$ (Nemat-Nasser *et al*. 2001, Majorell and Picu 2002, Chan *et al.* 2012). The constant parameters involving the Boltzmann constant (K) and Burgers vector (b) for Ti6Al4V are $K = 1.38\ x\ 10^{-23}\left(\frac{J}{k}\right)$ and $b = 2.95\ x\ 10^{-10}\ m$, giving rise to the ratio $K/b^3 = 537542.78\ Pa/k$ or $0.5375\ MPa/k$. Equation 8.4 can be expanded to a linear form as:

$$\left(\frac{\sigma_y-\sigma_a}{\mu}\right)^p = \left(\frac{\sigma_o}{\mu_o}\right)^p - \left(\frac{\sigma_o}{\mu_o}\right)^p . \left(\frac{1}{g_{oi}}\right)^{1/q}\left(\frac{kT}{\mu b^3}\left(ln\frac{\dot{\varepsilon}_o}{\dot{\varepsilon}}\right)\right)^{1/q} \qquad 8\text{-}5$$

It is of interest to note that in this formulation the viscous drag effect (σ_d) at high strain rate discussed in section 7.2 of Chapter 7 is not captured and its introduction in Equation 8-5 would further lower the term $\frac{\sigma_y-\sigma_a}{\mu}$. As previously seen with reference to Figure 7-7 (a) of Chapter 7, the viscous drag becomes significant at high strain rates above 10^3 s^{-1} (Kumar *et al*. 1968, Frost and Ashby 1982) and is therefore assumed to be insignificant at a strain rate of 750 s^{-1}. With this assumption, the variation of the normalised thermal-activated part of the yield stress, $\left(\frac{\sigma_y-\sigma_a}{\mu}\right)^p$, with the coupled effect of strain rate and temperature term $\left(\frac{kT}{\mu b^3}\left(ln\frac{\dot{\varepsilon}_o}{\dot{\varepsilon}}\right)\right)^{1/q}$, for samples C, D and E, was plotted at a strain rate of 750 s^{-1}, giving rise to the graphs shown in Figure 8-3.

© Central University of Technology, Free State

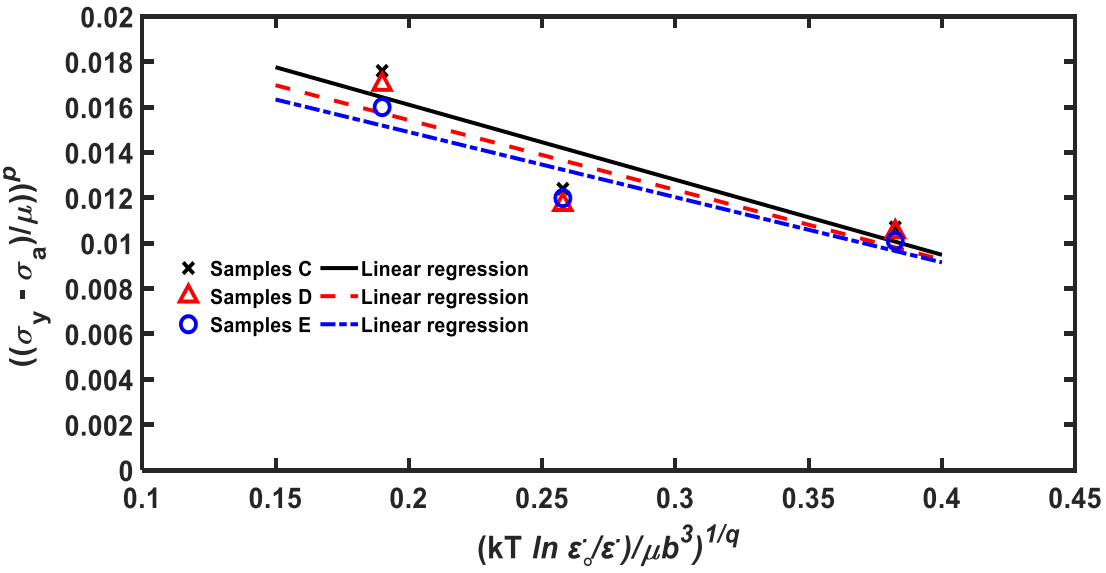

Figure 8-3. The normalised thermal-activated yield part of the yield stress against the effects of temperature at a strain rate of 750 s^{-1}.

The mechanical threshold stress (σ_o), which is the thermal-activated component of yield stress at $0\,K$, and the average value of normalised activation energy are given by the *y*-intercept and the gradient of the linear fitting of the plots in Figure 8-3, respectively. The values of these model-fitting parameters for samples C, D and E, obtained from Figure 8-3, are presented in Table 8-1.

Table 8-1. Evaluated model-fitting parameters describing the thermal part of the yield stress of samples C, D, and E

Samples	Mechanical threshold stress (σ_o)	Normalised activation energy (g_{oi})
C	1085.47 MPa	0.253
D	1064.39 MPa	0.251
E	1039.75 MPa	0.254

In the present research, Peierls barriers and short-range obstacles in the material are overcome by the motion of dislocations in a thermally activated manner during plastic deformation. Peierls stress is related to the temperature-sensitivity of the yield stress of a material by the fact that temperature weakens the atomic bond strength of a unit cell and therefore lowers the stress required to move a dislocation within the plane of atoms in a unit cell.

© Central University of Technology, Free State

Short-range obstacles to the motion of dislocations for Ti6Al4V(ELI) include aluminium and vanadium atoms and the clusters of low-percentage interstitial elements (Picu and Majorell 2002). As explained in section 8.2.1, and previously determined via EBSD (Chapter 5) and XRD methods (Chapter 6), the β-phase in samples C, D and E is limited in quantity, and thus can be assumed to play a minor role during deformation. The effect of vanadium atoms on dislocations can therefore be ignored. Thus, the total thermally activated stress can be expressed as a superposition of three components: (a) due to activation of dislocations over Peierls barriers, (b) the interaction of dislocations with aluminium and lastly, (c) the interaction of dislocations with interstitial elements. The three different alloys of DMLS Ti6Al4V(ELI) tested here are of the same chemical composition (Table 3-1 of Chapter 3) and only differ in microstructure. Following the reasoning in this paragraph, it can be assumed that both the mechanical threshold stress (σ_o) and the normalised activation energy (g_{oi}) for the three types of samples could be the same. Therefore, the average values of 1063.2 $\pm$ 22.8 MPa and 0.25 $\pm$ 0.0015 for σ_o and g_{oi}, respectively, obtained from Table 8-1 will be used to predict the flow stress of the DMLS Ti6Al4V(ELI) alloy.

8.2 PREDICTION OF THE FLOW STRESS

Dislocations play a critical role in determining the plastic behaviour of materials and their flow stress under various loading states of strain rate and temperature. Dynamic loading of materials in the inelastic range causes dislocations to be generated, moved and stored. The initiation of motion of dislocations shows that the material has exceeded the yield strength/ elastic limit and that inelastic strains are now generated. As noted in Chapter 7, at high strain rates Ti6Al4V(ELI) experiences instantaneous strain hardening which increases the yield stress of the material. The movement and storage of the dislocations during strain hardening is related to different loading states of strain rate and temperature. The model adopted in the present research assumes that the flow stress ($\sigma - \sigma_y$), due to the motion of dislocations, is dependent on temperature, plastic strain (ε_p) and the initial density of dislocations (ρ_o) and is in the form of the equation derived in Chapter 4 as:

$$\sigma - \sigma_y = \alpha\mu(T)bM\left(\frac{h}{k_2}\left(1 - exp\left(-k_2\varepsilon_p\right)\right) + \rho_o\, exp\left(-k_2\varepsilon_p\right)\right)^{1/2} \qquad 8\text{-}6$$

© Central University of Technology, Free State

where the dimensionless parameter α is a constant parameter dependent on the geometrical arrangement of dislocation whose magnitude varies from 0.2–0.4 for metals and is taken to be 0.2 for Ti6Al4V (Galindo *et al*. 2018). The parameter μ stands for the shear modulus of the material, which is dependent on temperature as seen in Figure 8-2, M is the Taylor orientation factor (reciprocal of Schmid factor). For polycrystals, M varies from grain to grain due to differences in texture with reference to the loading axis. Furthermore, Cáceres and Lukac (2008) found that for hcp crystal structures with texture that inhibits basal and prismatic slip while favouring pyramidal polyslip, M is estimated to be between 2.1 and 2.5 and increases to about 4.5 for randomly textured polycrystals. If all grains undergo the same deformation as the overall deformation and based on the use of the von Mises compatibility conditions, Taylor (1938) obtained the average value for M as 3 for hcp crystal structures. This is the value adopted in the present studies from the assumption that all grains undergo deformation. This is further supported by the relatively random texture of the α-phase in samples C, D and E reported in Chapter 5. The parameter ρ_o stands for the initial density of dislocations in a material, as determined via XRD in Chapter 6. The Burgers vector (*b*) is taken to be 0.295 nm for hcp Ti6Al4V (Hull and Bacon 2011). The constants h and k_2 are model calibration parameters that stand for the athermal work-hardening coefficient and rate of annihilation of dislocations, respectively, at given temperatures and strain rates and are determined from the experimental flow curves. The effects of these two parameters, as well as the temperature and initial dislocation density on the shape of the flow curve in the plastic range were investigated here by varying one of the two parameters, while holding all other parameters constant. The outcomes are discussed here.

The curves in Figures 8-4 and 8-5 show the sensitivity of the flow stress with respect to the parameters h and k_2. The two parameters are seen in these two figures to have opposing effects on the predicted flow stress. Variation of the parameter h with a fixed dynamic recovery coefficient k_2 results in parabolic strain hardening, which together with the saturated flow stress decreases with decreasing values of the parameter h, as seen in Figure 8-4.

© Central University of Technology, Free State

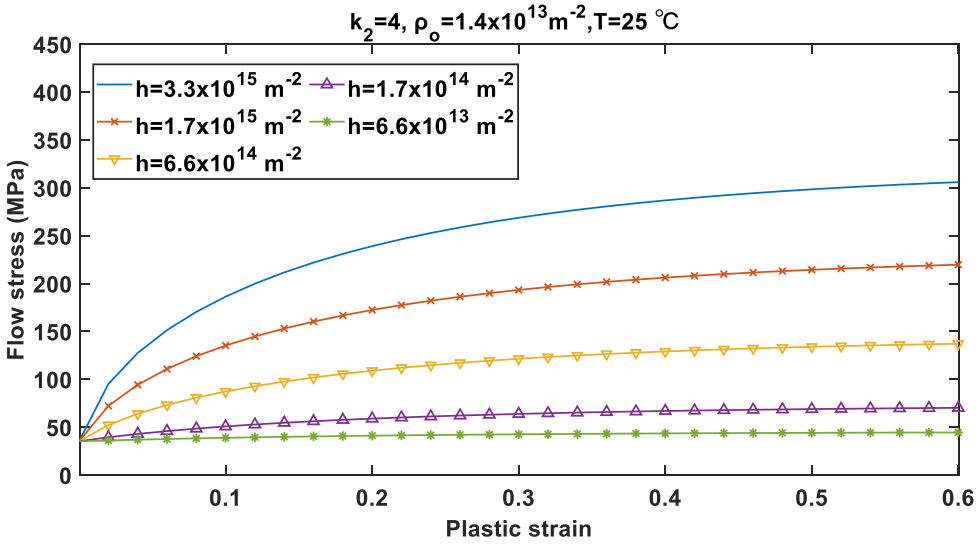

Figure 8-4. Effects of parameter h, at a fixed parameter k_2, initial dislocation density (ρ_o) and temperature (T).

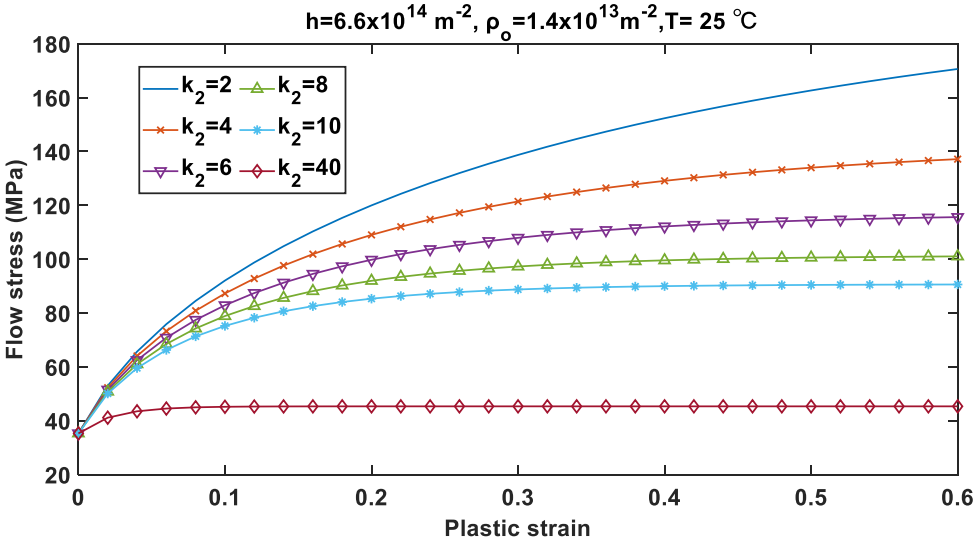

Figure 8-5. Effects of parameter k_2 at a fixed parameter h, initial dislocation density (ρ_o) and temperature (T).

At a fixed value of the parameter h of $6.6\,x10^{14}m^{-2}$ and fixed values of all other parameters in Equation 8-6, larger values of the parameter k_2 result in smaller strain hardening and saturation flow stresses, as seen in Figure 8-5. The model for flow stress represented by Equation 8-6 requires adjustment of the two parameters to fit the experimental data.

The effects of temperature on flow stress of Ti6Al4V is investigated using Equation 8-6 at temperatures ranging from -273 ℃ to 800 ℃ at a constant initial dislocation density (ρ_o) and calibration parameters h and k_2, as seen in Figure 8-6.

© Central University of Technology, Free State

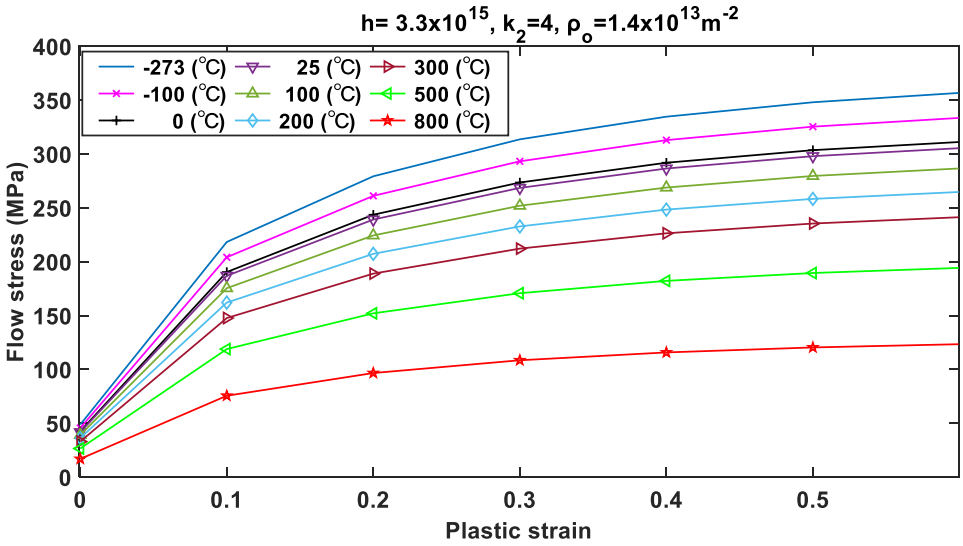

Figure 8-6. Flow stress curves at different temperatures and constant parameters h and k_2, and fixed initial dislocation density (ρ_o).

The curves in this figure show that increase of temperature gives rise to a drop in the flow stress. This is consistent with the physical reality that dictates an increase in the recovery rate with increasing temperature. It is necessary to note that formulation of flow stress in Equation 8-6 does not incorporate the failure criterion or damage growth of the alloy. Thus, the decrease in ductility that is expected to occur as the temperature decreases is not evident in Figure 8-6.

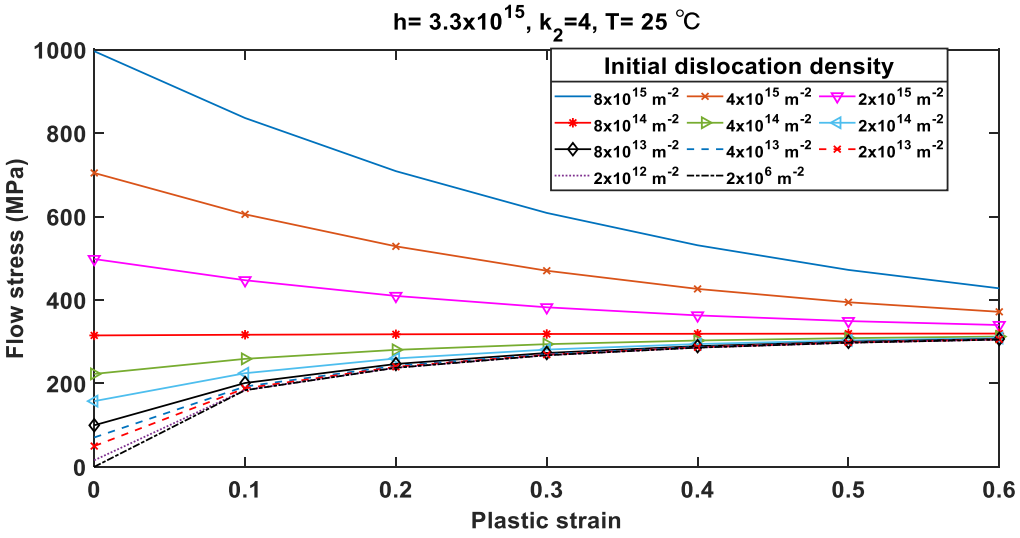

Figure 8-7. Effects of the initial dislocation density on the flow stress for fixed values of parameters h and k and temperature.

Figure 8-7 shows the effects of initial dislocation density on the flow properties of the Ti6Al4V alloy. The shape of the flow curves in this figure for very high initial dislocation

© Central University of Technology, Free State

densities in the material is a pronounced peak followed by a drop in the flow stress or strain softening of the material. The peak stress decreases with the decrease in the initial dislocation density, through to a case where no strain hardening occurs and cases where strain hardening occurs. Obviously, high density of dislocations in a material is known to increase its yield strength (peak stress). In fact, dislocations in such materials will rapidly pile up at barriers such as precipitates, grain boundaries, or even sessile dislocations. The leading dislocation in the pile-up is acted on, not only by applied shear stress but also by the interaction stress with other dislocations in the pile-up. High stresses initiate yielding on the other side of the barrier and can initiate cracks at the barriers (Shi and Zirky 2009), which could cause a decrease of the stress with strain softening at the onset of plastic flow, as seen in Figure 8-7.

For dislocation densities below $8\,x10^{14}m^{-2}$, the flow curves are characterised by the familiar strain hardening that decreases in magnitude with increasing plastic strain. This is the common scenario for Ti6Al4V(ELI) alloy, as previously reported in Chapter 7, and is the characteristic of metals and metal alloys. Further decrease in the initial dislocation density, according to the model, decreases the rate of instantaneous strain hardening and therefore the material has significant post-yielding strain hardening before forming a plateau. This is consistent with the physical reality where materials with large grain sizes and therefore low dislocation densities have significant post-yielding strain hardening (Xu *et.al* 2018).

The initial dislocation densities of the three different heat-treated microstructures of DMLS Ti6Al4V(ELI) tested under high strain rate that were determined via the XRD peak broadening analysis, as reported in Chapter 6, are shown here again in Table 8.2 for ease of reference. It is evident that all the values in this table are lower than the threshold of $8\,x10^{14}m^{-2}$ noted above. Therefore, the three microstructures should all lead to stress flow curves with strain hardening, beyond yield.

Table 8-2. The initial density of dislocations for different microstructures of DMLS Ti6Al4V(ELI)

Samples type	Dislocation density (m^{-2})
C	5.73 x 10^{14}
D	5.09 x 10^{14}
E	7.00 x 10^{14}

© Central University of Technology, Free State

Parameters h and k_2 of the model were the only unknown parameters in Equation 8-6 and were determined for Ti6Al4V(ELI) specimens by a process of adjustment to fit the model to experimental curves of true stress versus true strain for samples C, D and E. Figure 8-8 shows the flow stress curves of the three DMLS Ti6Al4V(ELI) specimen types and those predicted by the model by fine-tuning the model parameters h and k_2 to obtain the best fits values of $8.3x10^{15}m^{-2}$ and 10, respectively.

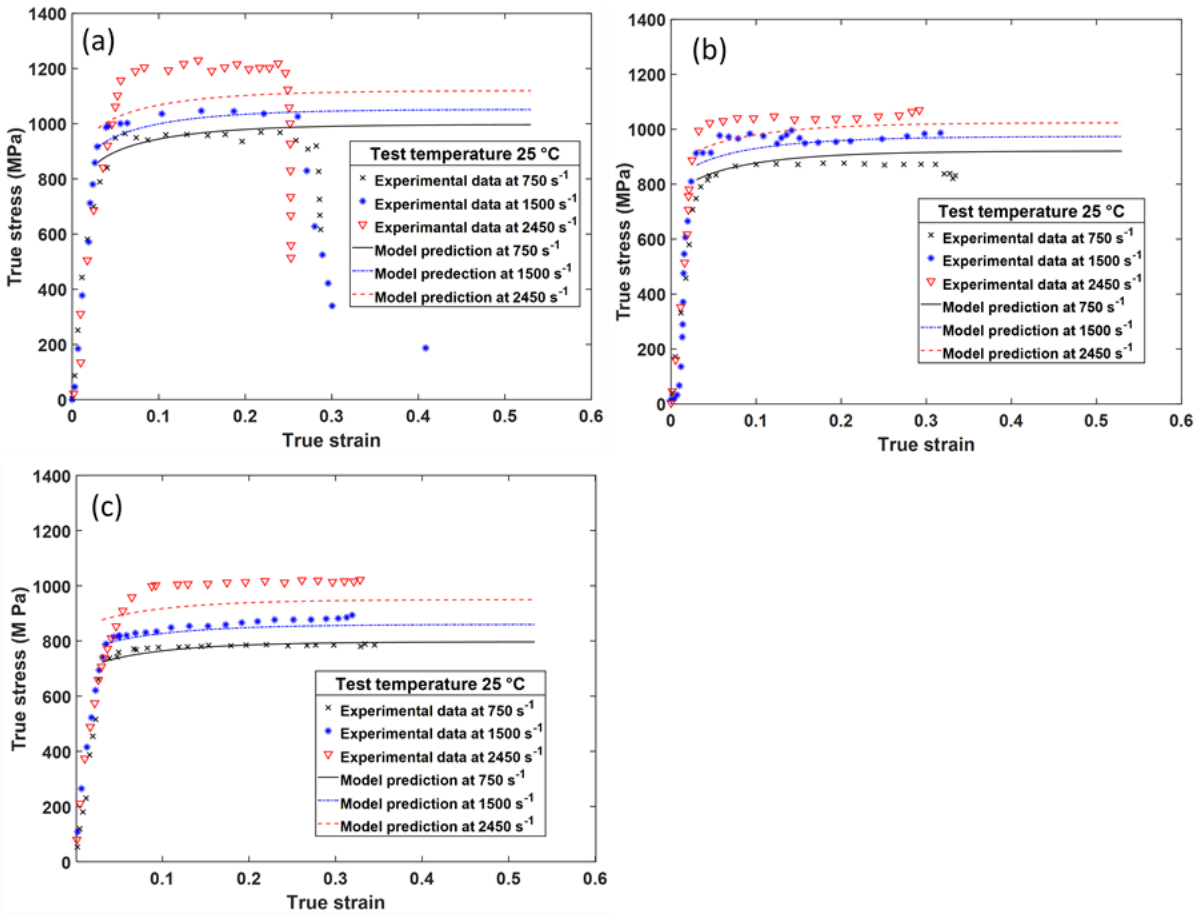

Figure 8-8. Experimental flow stress curves and those predicted by the model represented by Equation 8-6 at a test temperature of 25 ℃ and different strain rates for samples (a) C, (b) D, and (c) E.

One common observation made in Figure 8-8, for all three categories of samples, is that the deviation of the experimental curves from the ones predicted from Equation 8-6 increases with increasing strain rates. This suggests that the current state of the model cannot accurately describe the upturn of flow stress at high strain rates. As was explained in Chapter 7, the resistance to the flow of dislocations due to the drag mechanism at high

© Central University of Technology, Free State

strain rates does explain the upturn of the yield and flow stresses. This is not captured in the flow stress formulation presented by Equation 8-6.

8.3 PREDICTION OF THE VISCOUS DRAG STRESS COMPONENT OF FLOW STRESS

To increase the predictive capability of the model adopted in this research, a viscous drag component of stress is incorporated in the model to predict the deformation process of Ti6Al4V(ELI) at high strain rates. This component is assumed to be additive to the athermal component of yield stress, since the viscous drag effect resists the flow of dislocations and therefore increases the yield stress and subsequent flow stress. Generally, dislocation drag springs from electrons and phonons in materials and has a retarding effect on the moving dislocations as a Newtonian drag force (Kumar *et al*. 1968, Frost and Ashby 1982). Because of viscous drag, the kinetic energy of dislocations is reduced, which otherwise would help overcome obstacles, and more external force is thus required to keep the dislocations in motion. Therefore, by the introduction of a viscous drag component to the model represented by Equation 8-6, the physical mechanism behind the upturn of yield and flow stress at high strain rates can be accommodated. Other studies have studied the effects of viscous drag on the motion of dislocations in closed-packed structures and found that it has a profound influence (Vreeland and Jassby 1971, Frost and Ashby 1982, Kapoor and Nemat 2000).

The viscous drag stress can be expressed as (Kapoor and Nemat 2000, Lesuer *et al.* 2001):

$$\sigma_{drag}\left(\dot{\varepsilon}_p\right) = \zeta.\left(1 - exp\left(-\chi.\dot{\varepsilon}_p\right)\right) \qquad 8\text{-}7a$$

$$\chi = \left(\frac{M^2.\mu_d}{\rho_m.b^2.\sigma_a}\right) \qquad 8\text{-}7b$$

where the symbol χ represents the effective damping coefficient influencing the dislocation motion, while ζ is a material constant, both used as viscous drag curve-fitting parameters. The symbols $M, \sigma_a, \mu_d, b, \rho_m$ are Taylor factor, athermal stress, drag coefficient, Burgers vector and mobile dislocation density, respectively. A systematic approach was adopted to determine these two curve-fitting parameters. In this approach, the difference between the experimental flow stress and the one predicted by the model at a strain of 0.1 and at any given strain rate was first determined. This difference was then taken as a viscous drag

© Central University of Technology, Free State

component of stress and together with the corresponding strain rate then used in conjunction with Equation 8-7a to evaluate the material constants ζ and χ.

Figure 8-9 shows the evolution of the viscous drag stress as a function of strain rate and at different values of the curve-fitting parameters ζ and χ. It is evident in this figure that at low and moderate strain rates ($\dot{\varepsilon} \leq 100\ s^{-1}$), the viscous drag component is small and negligible at all values of ζ and χ. In such cases, the material strain rate sensitivity and deformation is mainly controlled by obstacles. As the strain rate increases ($\dot{\varepsilon} > 100\ s^{-1}$), the viscous drag becomes relevant and quickly rises with the deformation rate, as seen in Figure 8-9.

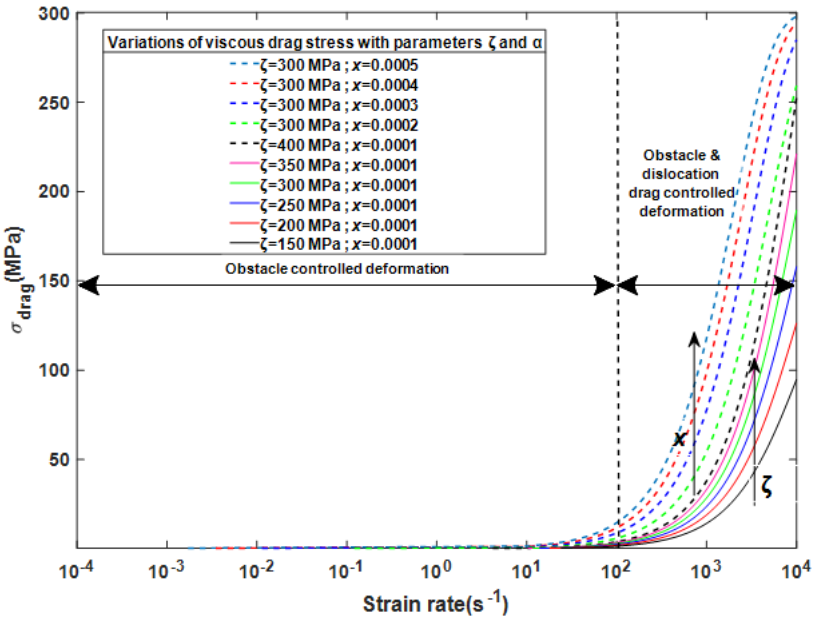

Figure 8-9. The viscous drag stress component against strain rate at various values of the curve-fitting parameters ζ and χ.

The increase in the strain rate and the two curve-fitting parameters ζ and χ, all lead to an increase in viscous drag stress, though the effect of strain rate is clearly seen in this figure to be more predominant. Equations 8-7a and 8-7b were then used together with experimental data for samples C, D, and E to evaluate the values of the curve-fitting parameters ζ and χ, as shown in Figure 8-10, with the results shown in Table 8-3.

© Central University of Technology, Free State

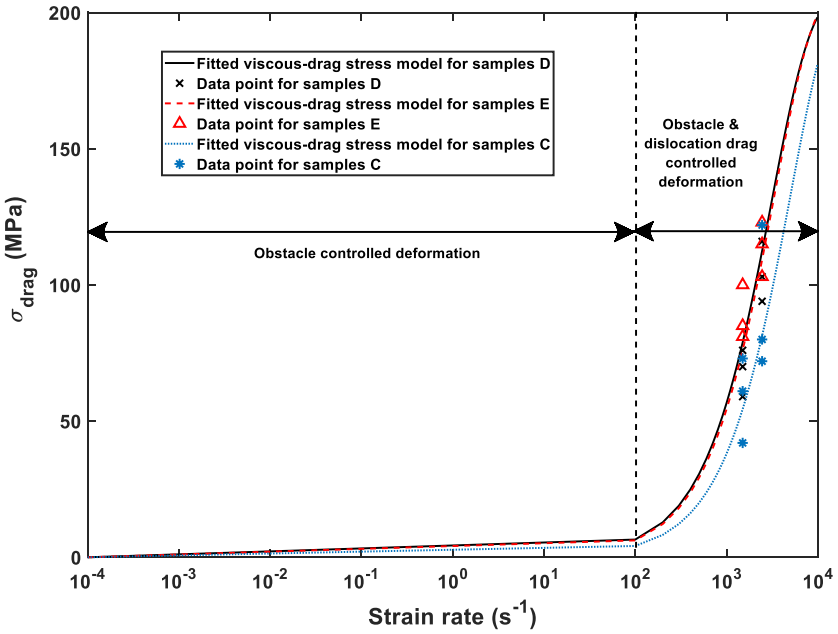

Figure 8-10. Evolution of the viscous drag stress as a function of strain rate for samples C, D, and E.

Table 8-3. Calibrated curve-fitting parameters for the viscous drag component of yield and flow stress for DMLS Ti6Al4V(ELI) samples

	Viscous drag stress fitting parameters	
Samples	**ζ (MPa)**	χ
C	207	0.00020
D	210	0.00032
E	210	0.00030

The experimental and predicted flow stress curves for various samples, with the viscous drag effect included, are presented in Figures 8-11 to 8-13. Curves of the constitutive model developed were plotted together with the experimentally obtained results to determine the effectiveness of the parameters determined, in replicating the experimental results.

© Central University of Technology, Free State

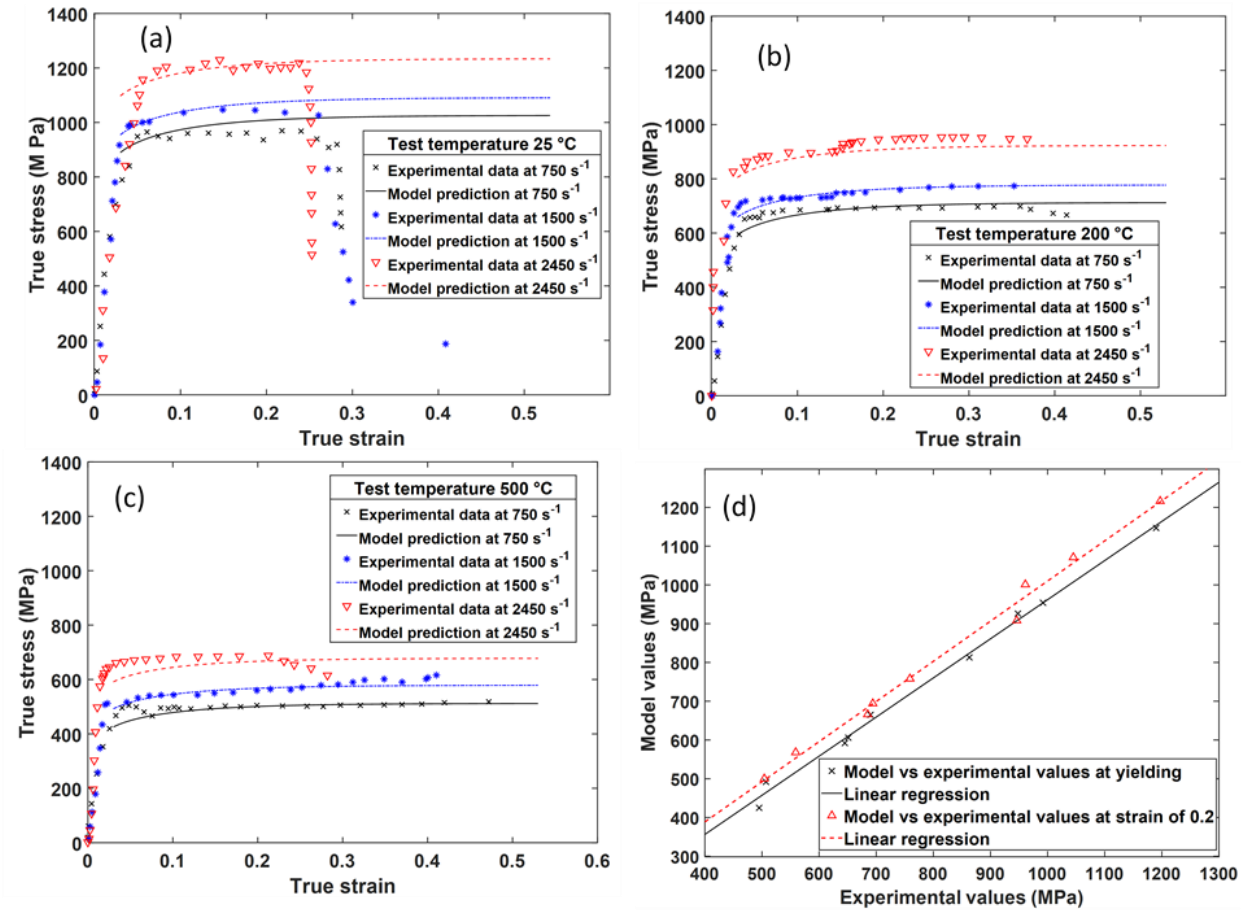

Figure 8-11. Comparison of the modified model prediction and experimental results for samples C, at three high strain rates and at test temperatures of (a) 25 °C, (b) 200 °C and (c) 500 °C, and (d) correlation between the predicted values and those obtained from experimentation at yielding and at a strain of 0.2.

© Central University of Technology, Free State

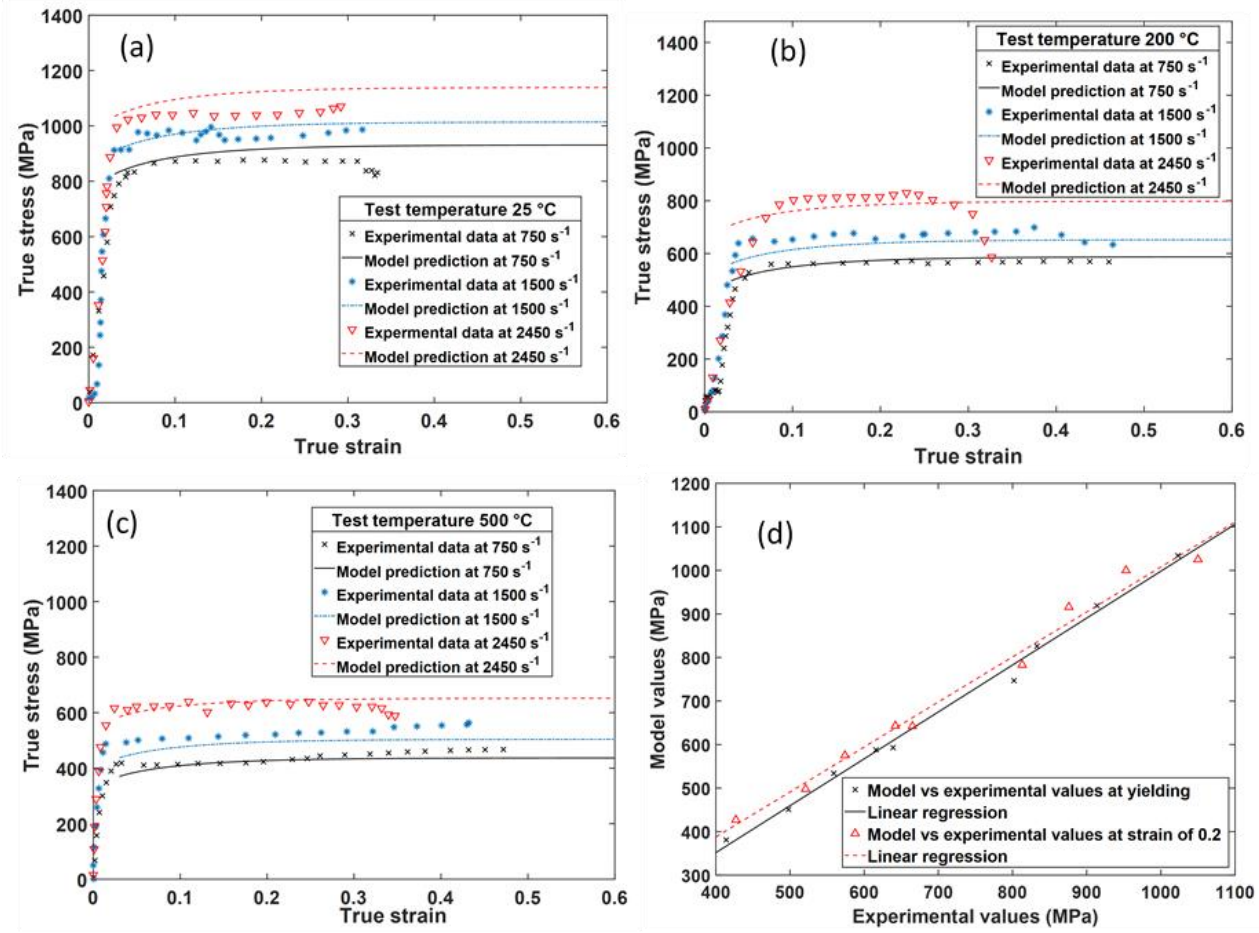

Figure 8-12. Comparison of the modified model prediction and experimental results for samples D at three high strain rates and at test temperatures of (a) 25 °C, (b) 200 °C and (c) 500 °C, and (d) correlation between the predicted values and those obtained from experimentation at yielding and at a strain of 0.2.

© Central University of Technology, Free State

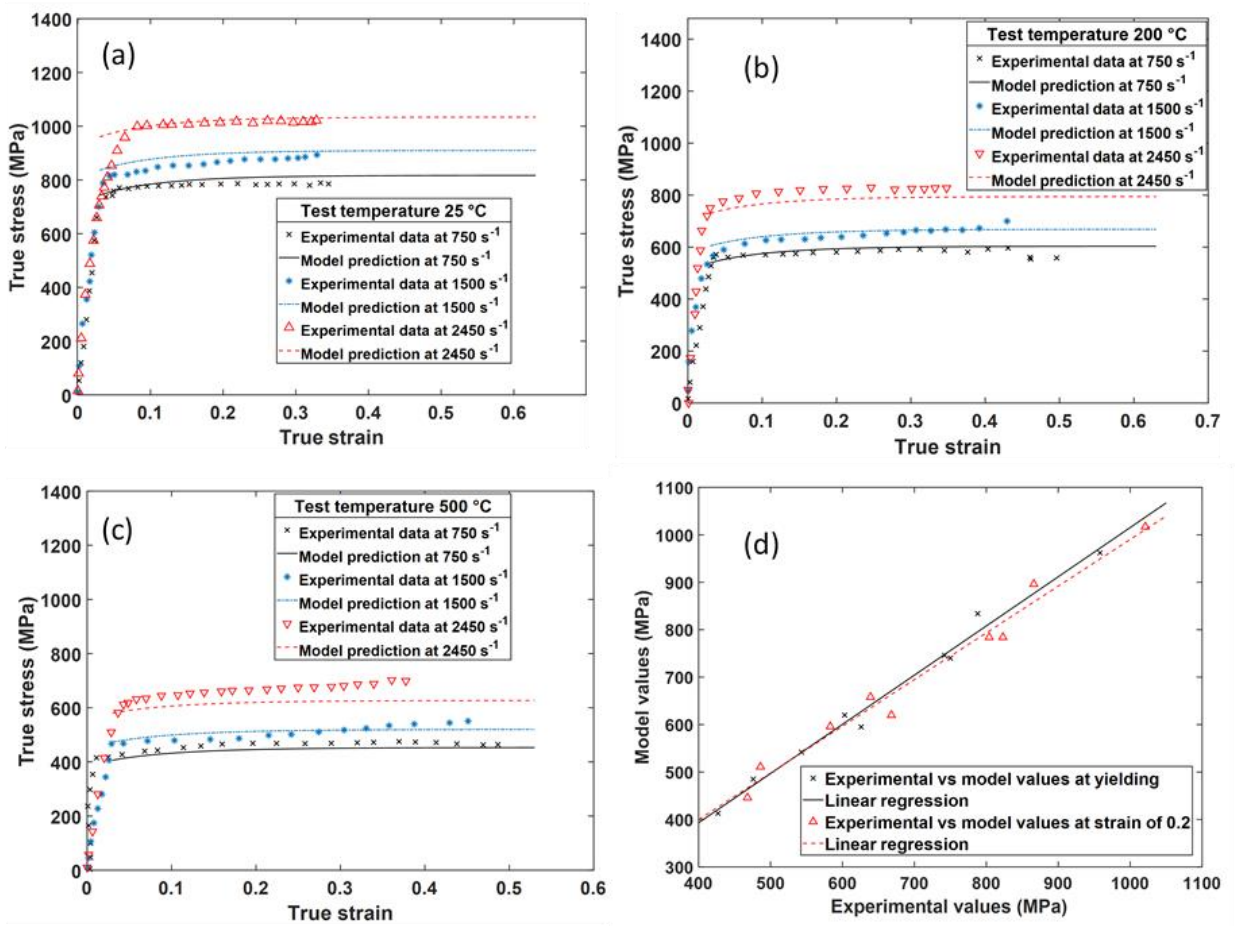

Figure 8-13. Comparison of the modified model prediction and experimental results for samples E, at three high strain rates and at test temperatures of (a) 25 °C, (b) 200 °C and (c) 500 °C, and (d) correlation between the predicted values and those obtained from experimentation at yielding and at a strain of 0.2.

To evaluate the overall capability of the model to predict the yield stress, the statistical measures of correlation coefficient (R^2) and absolute average error (δ) were obtained. This was done for the graphs comparing the experimental and predicted values from the modified model in Figures 8-11(d), 8-12(d) and 8-13(d). The correlation coefficient (R^2) in this case provides details on the strength of the linear relationship between the experimental and predicted values. It is important to note that R^2 may not certainly show better performance of the model, due to a tendency of the linear fit to be biased towards lower or higher values. This suggests that R^2 can be misleading if outlier values are present. The absolute average error, on the other hand, is calculated through a term-by-term comparison of the relative error and is thus an unbiased statistical parameter for measuring the predictability of the model. These standard statistical performance measures, the

© Central University of Technology, Free State

correlation coefficients (R^2) and absolute average error (δ), are expressed by the following respective equations:

$$R^2 = \frac{\sum_{i=1}^{N}(E_i-\bar{E})^2\,(P_i-\bar{P})^2}{\sum_{i=1}^{N}(E_i-\bar{E})^2\,\sum_{i=1}^{N}(P_i-\bar{P})^2} \qquad 8\text{-}8$$

$$\delta = \frac{1}{N}\sum_{i=1}^{N}\left|\frac{E_i-P_i}{E_i}\right| \qquad 8\text{-}9$$

where the symbol N stands for the total number of data points employed in the analysis, $E_i$and P_i represent the experimental and predicted yield stress values, and $\bar{E}$ and $\bar{P}$ are the mean values of E_i and P_i at the line of fit, respectively. Generally, when the R^2-value is close to 1 and the δ-value is close to 0, the model has the desired capacity to yield values close to the experimental values. Table 8-4 shows the statistical measures obtained from Figures 8-11(d), 8-12(d) and 8-13(d).

Table 8-4. Absolute error (δ) and correlation coefficient (R^2) for the correlation of experimental and predicted values of yield stress for various forms of DMLS Ti6Al4V(ELI)

Samples Type	R^2		δ	
	At yielding	At strain of 0.2	At yielding	At strain of 0.2
C	0.9949	0.9918	0.0571	0.0195
D	0.9937	0.9843	0.0477	0.0264
E	0.9862	0.9762	0.0236	0.0370

The values of correlation coefficient (R^2) are high and very close to 1, as seen in Table 8-4. It is also evident in the table that the absolute percentage errors between the predicted values of the proposed model and experimental values are all less than 6.0%, which is an acceptable range. This is a good indication that the modified microstructural constitutive model that was developed in the present study is reasonably good for use in predicting the high-strain-rate mechanical flow stress properties of the additively manufactured Ti6Al4V(ELI) alloy.

Finally, the microstructural constitutive model developed in the present study to describe the high-strain-rate mechanical flow stress of DMLS Ti6Al4V(ELI) for a range of temperatures, Equation 8-1 is therefore reformulated to include viscous drag as:

© Central University of Technology, Free State

$$\sigma = \left(\frac{\mu(T)}{\mu_0}\right)\sigma^o\left(1-\left(\left(\frac{k_bT}{g_{0i}\mu(T)b^3}\right)ln\,\frac{\dot{\varepsilon}_o}{\dot{\varepsilon}}\right)^{1/q}\right)^{1/p} + \zeta.\left(1-exp\left(-\chi\,.\,\dot{\varepsilon}_p\right)\right) +$$

$$\frac{K_{H-P}}{\sqrt{d}} + \alpha\mu(T)bM\left(\frac{h}{k_2}\left(1-exp\left(-k_2\varepsilon_p\right)\right)+\rho_o\,exp\left(-k_2\varepsilon_p\right)\right)^{\frac{1}{2}} \qquad 8\text{-}10$$

A summary of the physical constants, microstructural features and calibrated fitting parameters obtained from literature, experimental data and analytical modelling at this point is shown in Table 8-5.

Table 8-5. A summary of constitutive flow stress model parameters for DMLS Ti6Al4V(ELI)

Prescribed parameters	**Value and units**	**Fitted parameters**	**Values and units**
Boltzmann constant (k_b)	1.38 x 10^{-23} $m^2kgs^{-2}k^{-1}$	σ^o	1063.2 MPa
Shear modulus (μ)	$49.02-\frac{5.821}{e^{\frac{181}{T}}-1}\,(GPa)$	g_{0i}	0.25
Burgers vector (b)	$2.95\,x\,10^{-10}\,m$	h	8.3 x $10^{15}m^{-2}$
Reference strain rate ($\dot{\varepsilon}_o$)	10^7 s^{-1}	k_2	10
Grain sizes (d)	Measured value in (μm)	ζ	(MPa)
Samples C	2.5	Samples C	207
Samples D	6.0	Samples D	210
Samples E	9.0	Samples E	210
Initial dislocation density	Measured values in (m^2)	χ	
Samples C	5.73 x 10^{14}	Samples C	0.00032
Samples D	5.09 x 10^{14}	Samples D	0.00030
Samples E	7.00 x 10^{14}	Samples E	0.00020
Hall-Petch constant (K_{H-P})	$328\,MPa\mu m^{1/2}$		
p	1		
q	2		
Taylor factor (M)	3		
α	0.2		

8.4 SUMMARY

A constitutive model that is sensitive to microstructure has been calibrated and validated in this chapter. The strain hardening and dynamic recovery phenomena that are normally experienced by materials during dynamic deformation were articulated by the parameters h and k_2 of the model developed. These two constants were calibrated with the high strain rate and temperature experimental flow curves of samples type C, D and E. The influence of the initial dislocation density on the flow properties of the Ti6Al4V(ELI) alloy according to

© Central University of Technology, Free State

the model was investigated. It was shown that for dislocation densities below $8\ x10^{14}m^{-2}$, the shape of flow stress plastic curve was that of a pronounced peak, followed by a reduction in the flow stress or strain softening of the material. However, the reduction in the initial dislocation density decreased the peak stress and, in some cases, this decrease was followed by a state where no strain hardening occurs. Further decrease in initial dislocation density resulted in strain hardening post-yielding. The expected decrease of flow stress with increasing temperature was also demonstrated well by the model.

To take care of the upsurge of flow stress at high strain rates that is not captured in the mechanical threshold model (MTS), a viscous drag stress component that is sensitive to high strain rate (>100 s^{-2}) was introduced in the initial formulation. The viscous drag stress curve-fitting parameters ζ and χ were calibrated for different microstructure of DMLS Ti6Al4V(ELI) material.

The microstructural constitutive model developed in the present research was modified and validated in this chapter and showed good capacity to predict the high-strain-rate flow stress properties of the additively manufactured Ti6Al4V(ELI) alloy. In fact, standard statistical performance measures of correlation coefficients (R^2) and absolute average errors (δ) obtained between the model and experimental values were ≈ 1 and $< 6\%$ which are an indication of the accuracy of the model in predicting the high-strain-rate mechanical properties of DMLS Ti6Al4V(ELI).

© Central University of Technology, Free State

8.5 REFERENCES

1. AZO Materials; Titanium alloys – Ti6Al4V grade 5. https://www.azom.com/article.aspx?ArticleID=1547 (accessed on 7th Nov 2020).
2. Cáceres, C.H., Lukac, P. 2008. Strain hardening behaviour and the Taylor factor of pure magnesium. *Philosophical Magazine*, 88(7), pp.977–989.
3. Chan, H.P., Young, I.S., Chong, S.L. 2012. Constitutive analysis of compressive deformation behaviour of ELI-grade Ti6Al4V with different microstructures. *Journal of Materials Science*, 47(7), pp.3115–3124.
4. Frost, H.J., Ashby, M.F. 1982. Deformation-mechanism maps: *The plasticity and creep of metals and ceramics*, Elsevier Science Ltd, Michigan, USA, pp.134–147.
5. Galindo, M.A., Mumtaz, K., Rivera, P.E., Galindo-Nava, J.E., Ghadbeigi, H. 2018. A microstructure sensitive model for deformation of Ti6Al4V describing cast-and-wrought and additive manufacturing morphologies. *Material & Design* 160, pp.350–362. https://doi.org/10.1016/j.matdes.2018.09.028
6. Hull, D., Bacon, D.J. 2011. Introduction to dislocations, 5th edition, Elsevier, Boulevard Oxford, pp.109–110.
7. Kaapor, R., Nemat-Nasser, S. 2000. Comparison between high and low strain-rate deformation of tantalum. *Metallurgical and Materials Transactions A*, 31, pp.815–823.
8. Kohn, D.H., Ducheyne, P. 1991. Tensile and fatigue strength of hydrogen-treated Ti6Al4V alloy. *Journal of Materials Science*, 26(2), pp.328–334.
9. Kumar, A., Hauser, F.E., Dorn, J.E. 1968. Viscous drag on dislocations in aluminium at high strain rates. *Acta Metallurgica*, 16(9), pp.1189–1197. https://doi.org/10.1016/0001-6160(68)90054-0
10. Lesuer, D.R., Kay, G., LeBlanc, M. Modelling large-strain, high-rate deformation in metals. *Third Biennial Tri-laboratory Engineering Conference on Modelling and Simulation*, Pleasanton, California, , USA, 20th July 2001.
11. Majorell, A., Picu, R. 2002. Mechanical behaviour of Ti6Al4V at high and moderate temperatures – Part II: Constitutive modelling. *Materials Science and Engineering A*, 326(2), pp.306–316.

© Central University of Technology, Free State

12. Nemat-Nasser, S., Wei-Guo, G., Vitali, F., Ya-Bei, G. 2001. Dynamic response of conventional and hot isostatically pressed Ti6Al4V alloys: Experiments and Modelling. *Mechanics of Materials*, 33(8), pp.425–439.
13. Shi, J., Zirky, M.A. 2009. Grain-boundary interactions and orientation effects on crack behavior in polycrystalline aggregates. *International Journal of Solids and Structures*, 46(21), pp.3914–3925. https://doi.org/10.1016/j.ijsolstr.2009.07.019
14. Taylor, G.I. 1938. Plastic strain in metals. *Journals of the Institute of Metals*, 62, pp.307–324.
15. Vreeland, J., Jassby, K.M. 1971. Temperature dependent viscous drag in close-packed metals. *Materials Science and Engineering,* 7(2), pp.95–102. https://doi.org/10.1016/0025-5416(71)90029-2
16. Xu, D.M., Wan, X.L., Yu, J.X., Xu, G., Li, G.Q. 2018. Effect of grain refinement on strain hardening and fracture in austenitic stainless steel. *Materials Science and Technology*, 34(11), pp.1344–1352. https://doi.org/10.1080/02670836.2018.1451735

© Central University of Technology, Free State

CHAPTER 9 — IMPLEMENTATION OF A MICROSTRUCTURE-BASED CONSTITUTIVE MODEL FOR DMLS TI6AL4V(ELI) IN ABAQUS

9.1 INTRODUCTION

The analytical constitutive model developed in Chapter 4, then modified, refined, and validated in Chapter 8 was implemented separately in the two ABAQUS/Explicit subroutines available for defining the yield surface and isotropic plasticity of materials. These user subroutines are VUMAT and VUHARD, both briefly mentioned in Chapter 2. The VUMAT user subroutine is commonly used to describe the mechanical elastic-plastic constitutive behaviour of materials. The subroutine is called for blocks of a material's calculation/integration points for which the constitutive law is defined (ABAQUS documentation 2020). The equivalent plastic strain at the material integration point in this subroutine is generated in an iterative process and updated to the next integration point as the new value. Therefore, equivalent plastic strain is normally allocated space as a solution-dependent state variable (SDV).

The VUHARD user subroutine, on the other hand, is called at all material points of elements for which the material definition includes user-defined isotropic hardening (ABAQUS documentation). The user-defined isotropic hardening in this case includes material behaviour dependent on the field (strain rate and temperature) or even internal state (strain) variables. Unlike the VUMAT subroutine, this subroutine is straightforward since it only needs a definition of the flow stress and its derivatives with respect to the relevant field or state variables. Notably, the subroutine only takes care of the inelastic part of a material's behaviour; though with different implementation procedures, the expected outcome of these two subroutines are not expected to differ. This chapter presents discussion on the implementation and verification of these two subroutines. Verification was done using benchmark tests to determine if simulations using these subroutines can aptly produce results consistent with the microstructural analytical constitutive model developed in this work. These benchmark tests included:

(i) Single element tests at various prescribed loading conditions.

(ii) Multiple element tests at various prescribed loading conditions.

© Central University of Technology, Free State

9.2 IMPLEMENTATION OF THE VUHARD USER SUBROUTINE

Implementation of the VUHARD user subroutine for the microstructure-based constitutive formulation of flow stress was done by first obtaining the derivatives of this constitutive model with respect to appropriate variables. In this constitutive model, presented here as Equation 9-1 for ease of reference (Equation 8-10 of Chapter 8), the total flow stress is seen to be dependent on the three variables ($\varepsilon_p, \dot{\varepsilon}_p$ and T). The temperature-dependence of the constitutive model was taken care of by the decrease in shear modulus (μ) with increase in temperature using Equation 8-3 of Chapter 8 (presented here for ease of reference as Equation 9-2).

$$\sigma = \left(\frac{\mu(T)}{\mu_0}\right).\sigma^o\left(1-\left(\left(\frac{k_b T}{g_{0i}\mu(T)b^3}\right)ln\,\frac{\dot{\varepsilon}_o}{\dot{\varepsilon}}\right)^{1/q}\right)^{1/p} + \zeta.\left(1-exp\left(-\chi.\dot{\varepsilon}_p\right)\right) + \frac{K_{H-P}}{\sqrt{d}} + \alpha\mu(T)bM\left(\frac{h}{k_2}\left(1-exp\left(-k_2\varepsilon_p\right)\right)+\rho_o\,exp\left(-k_2\varepsilon_p\right)\right)^{\frac{1}{2}} \quad 9\text{-}1$$

$$\mu(t) = 49.02 - \frac{5.821}{exp^{\left(\frac{181}{T}\right)}-1}\,(GPa) \quad 9\text{-}2$$

Therefore, in this study, implementation of the VUHARD subroutine for the constitutive model required only two analytical derivatives of $\left(D\,1 = \partial\sigma/\partial\,\varepsilon_p\right)$ and $\left(D\,2 = \partial\sigma/\partial\dot{\varepsilon}_p\right)$, which were then evaluated numerically to allow quadratic convergence. These derivatives represented the change in the calculated total flow stress for inputs of equivalent plastic strain rate and equivalent plastic strain. The term “equivalent” is used here to denote the scalar quantity of strain and strain rate obtained from the transformation of the strain tensor using the von Mises criterion (presented and discussed in section 2.8 of Chapter 2), the common criterion used in ABAQUS.

The partial derivative $\partial\overline{\sigma^{n+1}}/\partial\overline{\varepsilon_p}^{n+1}$ was determined numerically from the equation:

$$\frac{\partial\overline{\sigma^{n+1}}}{\partial\overline{\varepsilon_p^{n+1}}} = \frac{\alpha\mu(T)bM}{2}\left(\frac{h}{k_2}\left(1-exp\left(-k_2\overline{\varepsilon_p^{n+1}}\right)\right)+\rho_o\,exp\left(-k_2\overline{\varepsilon_p^{n+1}}\right)\right)^{-1/2}.\left(h\,exp\left(-k_2\overline{\varepsilon_p^{n+1}}\right)-\rho_o k_2 exp\left(-k_2\overline{\varepsilon_p^{n+1}}\right)\right) \quad 9\text{-}3$$

Similarly, the other derivative, now with respect to $\dot{\varepsilon}_p^{n+1}$, was evaluated from the equation:

© Central University of Technology, Free State

$$\frac{\partial\overline{\sigma^{n+1}}}{\partial\dot{\varepsilon}_p^{n+1}} = \left(\frac{\mu(T)}{\mu_0}\right).\frac{\sigma_o k_b T^{n+1}}{pq\dot{\varepsilon}_p^{n+1}G^{n+1}b^3}\left(1-\left(\frac{k_b T^{n+1}}{g_{0i}G^{n+1}b^3}ln\left(\frac{\dot{\varepsilon}_o}{\dot{\varepsilon}_p^{n+1}}\right)\right)^{\frac{1}{q}}\right)^{\frac{1-p}{p}}.\left(\frac{k_b T^{n+1}}{g_{0i}G^{n+1}b^3}ln\left(\frac{\dot{\varepsilon}_o}{\dot{\varepsilon}_p^{n+1}}\right)\right)^{\frac{1-q}{q}} + \alpha exp\left(-\chi.\dot{\varepsilon}_p^{n+1}\right) \quad 9\text{-}4$$

The VUHARD user subroutine, as written in this work is included in Appendix F (1). The coding for this subroutine was generated using FORTRAN 90 and saved in a *.for* file, formatted to be compatible with ABAQUS 2020. The first algorithm for the subroutine was used to generate the user material properties described as user material constants. A total of 17 user material constants, derived from Equation 9-1 and listed in Appendix F (2), were generated. These excluded the material density, elastic modulus and Poisson's ratio that were provided separately in ABAQUS/CAE. The flow stress component that is dependent on the average thickness of α-lath, was computed based on the Hall-Petch constant and was input into the subroutine as an average variable of α-lath thickness (a variable that depends on the form of the alloy).

The previous and current values of equivalent plastic strain in a step were defined as old and new solution-dependent variables (SDV1), respectively. Thus, the increment of plastic strain was obtained as the difference between these two states. The equivalent plastic strain rate component of Equations 9-1 and 9-4 was expressed from the increment in equivalent plastic strain ($\Delta\overline{\varepsilon_p}$) for a time increment size (Δt) as follows:

$$\dot{\overline{\varepsilon_p}} = \frac{\Delta\overline{\varepsilon_p}}{\Delta t} \quad 9\text{-}5$$

Equations 9-1 to 9-3 were evaluated at given material points and arrays containing values of equivalent yield stress, plastic strain and strain rate, generated by related material points.

9.3 IMPLEMENTATION OF THE VUMAT USER SUBROUTINE

To make it easier to implement the microstructure- and dislocation-based constitutive model as a VUMAT user material subroutine, the implementation algorithm was written following the logic of the flow chart shown in Figure 9-1. Coding for this subroutine was based on the theory of plasticity and radial return mapping presented in section 2.8 of Chapter 2.

© Central University of Technology, Free State

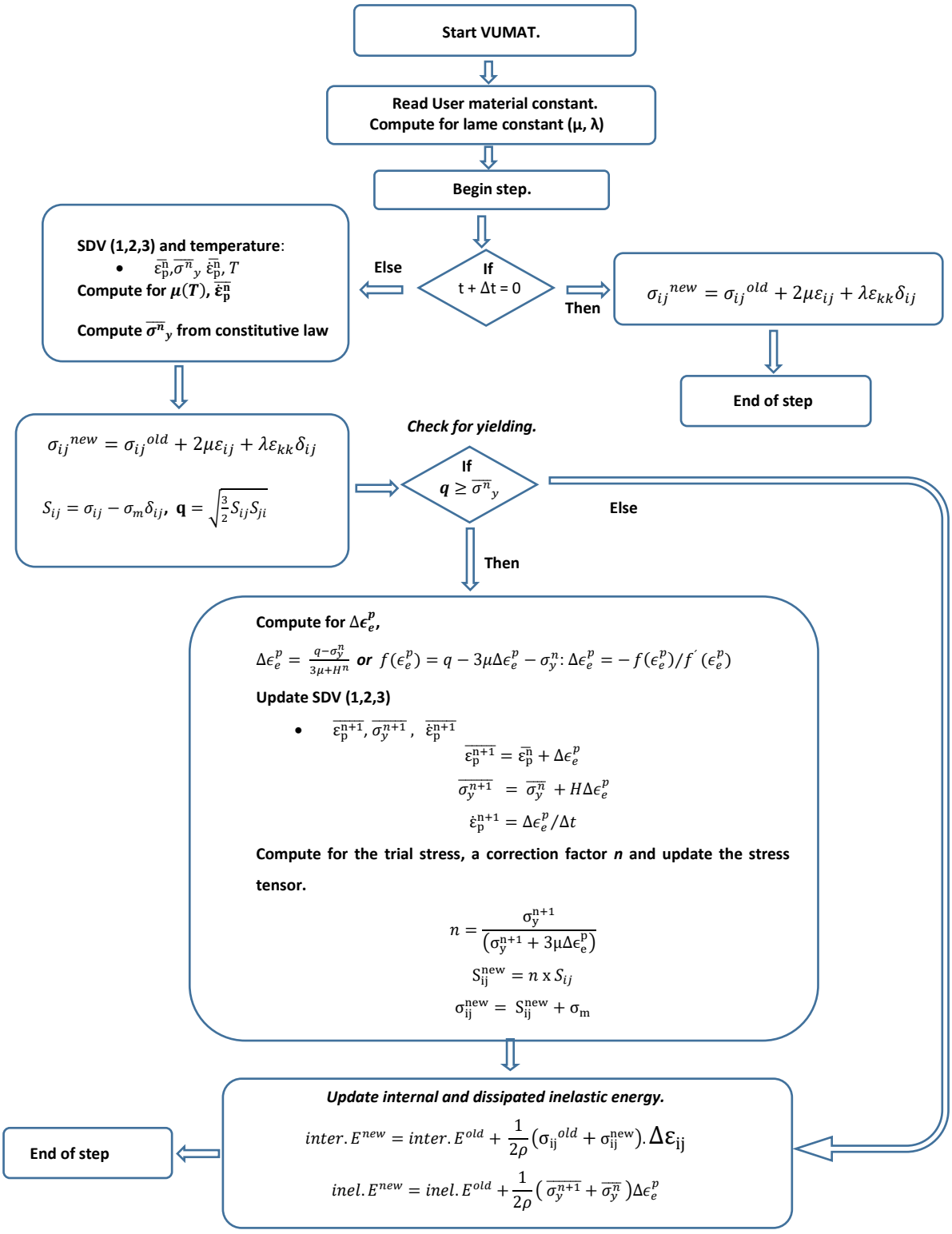

Figure 9-1. Algorithm developed here to solve for equivalent plastic strain increments and updating of the related stress tensors.

Similar to VUHARD, the coding for VUMAT was generated in FORTRAN 90 and saved as a *.for file* for execution in ABAQUS 2020. The codes written are presented in Appendix F (1).

© Central University of Technology, Free State

The second block in the algorithm was used to obtain the model constants of the material. Both elastic and plastic properties are required in this subroutine's main program, which is different from VUHARD where only the plastic properties are provided in the main program and the elastic properties are provided in ABAQUS/CAE. Thus, the 17 material constants from Equation 9-1 in addition to the material's elastic modulus (E) and Poisson's ratio (ν) were used for this subroutine. These material constants are presented in Appendix F (2). The two Lame's constants (μ and λ) were computed from E and ν using the following two expressions for isotropic hardening:

$$\mu = \frac{E}{2(1+\nu)} \text{ and } \lambda = \frac{\nu E}{(1-2\nu)(1+\nu)} \qquad 9\text{-}6$$

The principal components of the stress tensor were first obtained at the reference time, $t + \Delta t = 0$, from the following trace of principal strain increments:

$$trace(\Delta\varepsilon) = \Delta\varepsilon_{11} + \Delta\varepsilon_{22} + \Delta\varepsilon_{33} \qquad 9\text{-}7$$

At time, $(t + \Delta t > 0)$, the VUMAT algorithm was split in three parts. In the first part, the values of equivalent plastic strain ($\overline{\varepsilon_p^n}$), equivalent plastic strain rate ($\overline{\dot{\varepsilon}_p^n}$) and yield stress σ_y^n (given by the constitutive model at $\overline{\varepsilon_p^n}$ and $\overline{\dot{\varepsilon}_p^n}$, and at a prescribed test temperature (T)) at the beginning of the increments at each integration point, were defined as SDV1, SDV2 and SDV3, respectively. The values of shear modulus used in the constitutive model to define the flow stress were computed at prescribed test temperatures before obtaining the value of flow stress in this part. In the second part, the theory of plasticity presented in section 2.8 of Chapter 2, was used to compute equivalent von Mises trial stresses $\boldsymbol{q}$. The third part aimed at comparing the values of equivalent von Mises trial stresses obtained with the values of yield stress (from the constitutive model given by Equation 9-1) obtained at the beginning of each increment such that:

i. If $\boldsymbol{q} < \sigma_y^n$, then the state response was elastic and the radial return algorithm that is inherent in the subroutine to correct the plastic response was skipped. The stress tensor and related deviatoric stress remain unchanged at any value of $\boldsymbol{q}$. Therefore, the last step of the algorithm to compute internal energy and dissipation of inelastic energy was initiated. It is important to note that internal energy abbreviated as *ALLIE* in ABAQUS is the sum of the recoverable elastic strain energy and the energy

© Central University of Technology, Free State

dissipated through plastic deformation (ABAQUS documentation 2020). Since there was no plastic deformation, the inelastic energy remained zero and the internal energy only included the elastic strain energy component.

ii. If $\boldsymbol{q} \geq \sigma_y^n$, then the stress state was outside the yield surface and was plastic. Thus, the radial return mapping previously described in section 2.8.1 of Chapter 2 was initiated to compute the equivalent plastic strain and therefore return back the predicted stress to the expanded yield surface of the material. At this stage, strain hardening was expected since the loading was beyond the elastic limit.

The final part of this algorithm updated the SDVs and computed the new internal energy and inelastic dissipated energy. The updated SDV1, SDV2, SDV3 at each stage of computation, which were now the new values of equivalent plastic strain $\overline{\varepsilon_p^{n+1}}$, the new equivalent plastic strain rate $\overline{\dot{\varepsilon}_p^{n+1}}$, and the new yield stress σ_y^{n+1}, were stored and then used in the next increment as current values.

For linear isotropic materials undergoing small strains, the strain energy is of the form (Sadd 2009, ABAQUS 2020):

$$U = \frac{1}{2}\sum_{i,j=1}^{3} \sigma_{ij}\, \varepsilon_{ij} \qquad 9\text{-}8$$

From Equation 9-8, the total new specific internal energy ($inter.E^{new}$) and specific inelastic dissipation energy ($inel.E^{new}$) were expressed as:

$$inter.E^{new} = inter.E^{old} + \frac{1}{2\rho}\left({\sigma_{ij}}^{old} + \sigma_{ij}^{new}\right).\Delta\varepsilon_{ij} \qquad 9\text{-}9$$

$$inel.E^{new} = inel.E^{old} + \frac{1}{2\rho}\left(\overline{\sigma_y^{n+1}} + \overline{\sigma_y^{n}}\right)\Delta\epsilon_e^p \qquad 9\text{-}10$$

9.4 VERIFICATION AND VALIDATION OF THE IMPLEMENTED MODELS

The microstructure- and dislocation-based constitutive model developed in this work, implemented as VUHARD and VUMAT subroutines, was verified by determining the closeness of the results of simulation using ABAQUS to the analytical solutions based on Equation 9-1. The user material constants in this equation were those that were used to fit experimental results of samples C, D and E, which were presented in Table 8-5 of Chapter 8.

© Central University of Technology, Free State

Various benchmark tests were used ranging from single element tests to multiple element tests.

9.4.1 The single element test

The verification process adopted in the present research was to first test the material model developed in ABAQUS using single 8-node linear brick element tests. This is an easiest and practical technique to examine the sensitivity and accuracy of an element to external loading. Here, the single 8-node linear brick element tests were performed using the prescribed velocity loading conditions both in compression and tension, as shown in Figure 9-2(a & b), respectively.

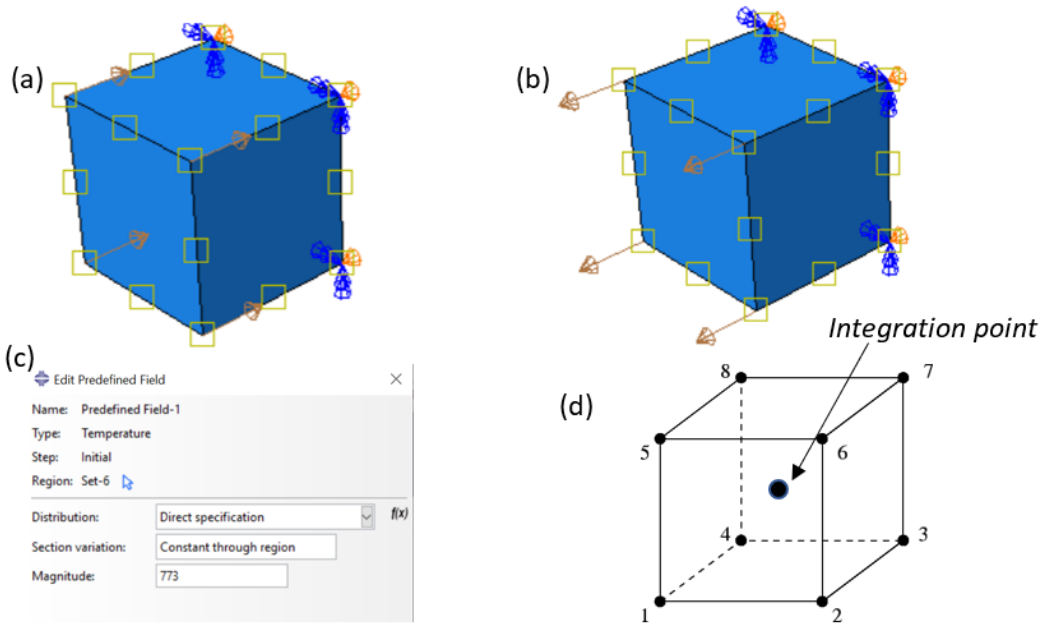

Figure 9-2. (a & b) A single element model with boundary conditions, (c) typical set temperature in the predefined field and (d) the 8-node linear brick element.

The roller support condition to restrain the surface in a direction parallel to the loading direction was applied to the four nodes of the surface opposite to the surface onto which load was applied. The absolute test temperature was defined in the predefined field in the software, as seen in Figure 9-1(c). The dimensions of the cube were arbitrarily taken as (10 x 10 x 10) mm and the cube meshed using the 8-node linear brick C3D8R element shown in Figure 9-2(d), with reduced integration and hourglass control settings. This type of mesh is simple and appropriate for the cubic element models of components with regular straight-edged shapes. The reduced integration elements normally have a single integration point

© Central University of Technology, Free State

located at the element's centroid rather than full integrated element types, hence giving rise to reduced computation time. However, reduced integration elements tend to be too flexible, since they suffer from their own numerical problem called hourglassing. Hourglassing arises where elements are unable to resist bending and hence cannot store strain energy for bending deformation. In ABAQUS hourglass control, a small amount of artificial stiffness is introduced in elements to limit the propagation of the hourglass phenomenon (ABAQUS documentation 2020).

Three different prescribed instantaneous velocities of 0.1 m/s, 1 m/s and 4 m/s were then applied onto the cube in both compression and tension. These different velocities were used to generate high equivalent plastic strain rates of approximately 10 s^{-1}, 123 s^{-1} and 350 s^{-1}. A typical deformed 8-node linear brick element at 4 m/s is shown in Figures 9-3 and 9-4. The shapes plotted in these figures are for superimposed undeformed and deformed shapes of the element under compressive and tensile load.

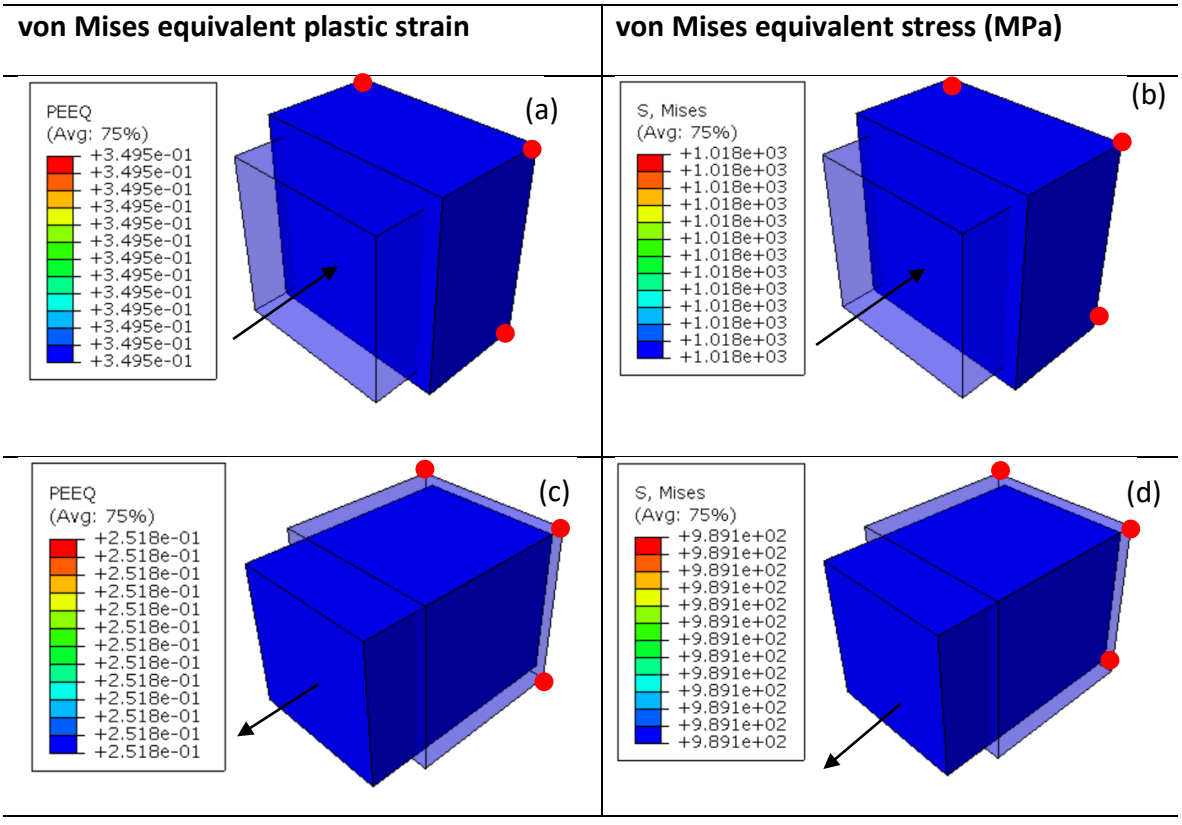

Figure 9-3. A typical VUHARD deformed 8-node linear brick element at a temperature of 298 K and velocity of 4 m/s in (a & b) compression and (c & d) tension for samples type C. The arrows show the loading direction while the red dots are the roller supports.

© Central University of Technology, Free State

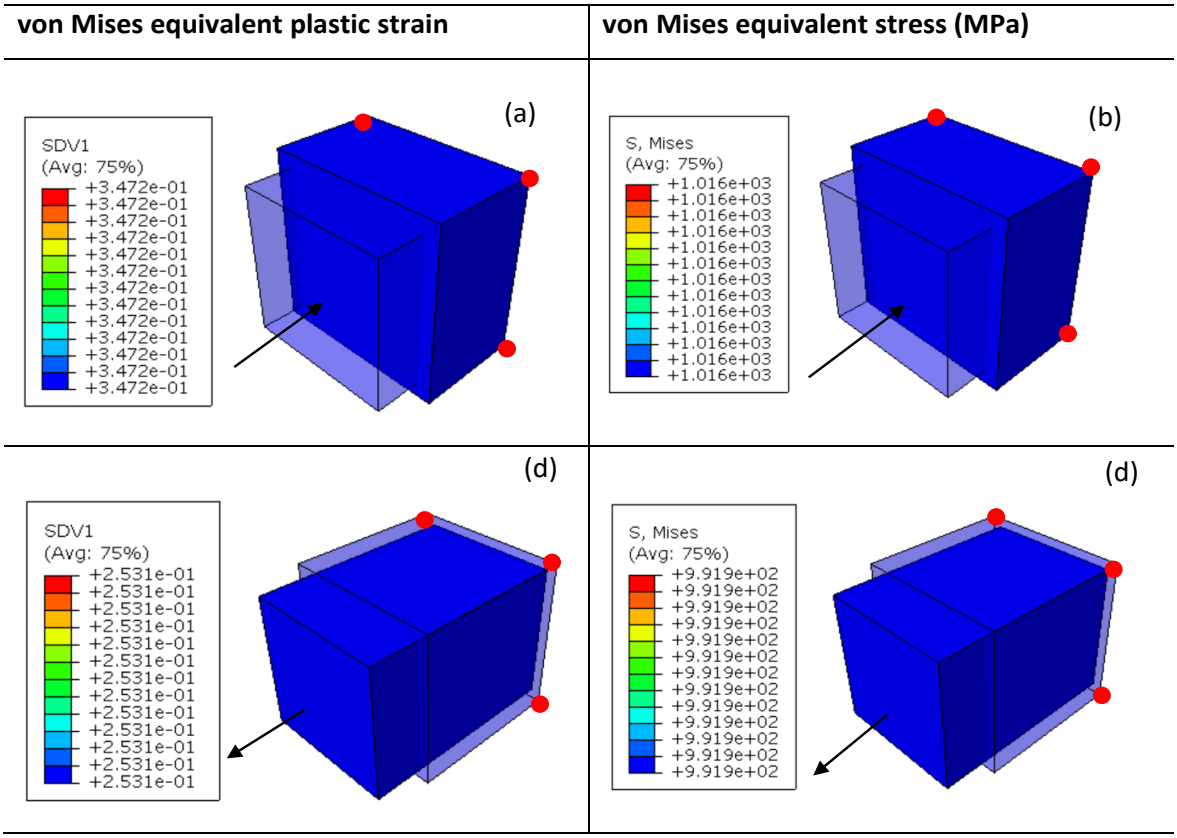

Figure 9-4. A typical VUMAT deformed 8-node linear brick element at a temperature of 298 K and velocity of 4 m/s in (a & b) compression and (c & d) tension for samples type C. The arrows show the loading direction while the red dots are the roller supports.

The values of equivalent plastic strain are normally expressed as PEEQ (this abbreviation stands for von Mises equivalent plastic strain in ABAQUS) in VUHARD, as shown in Figures 9-3(a and c), while in VUMAT they are allocated space as the solution-dependent variable, SDV1, seen in Figures 9-4(a and c). The equivalent plastic strain and equivalent von Mises stresses were obtained at the integration/Gauss point shown in Figure 9-2(d). Lateral expansion of the cube is realised in case of a compression test from the surface where load was applied to the surface under the constraints, as shown in Figures 9-3(a and b) and 9-4 (a and b). To the contrary and as expected, the deformed tensile element is characterised by lateral reduction in cross-sectional area, as shown in Figures 9-3(c and d) and 9-4(c and d). The values of equivalent von Mises stress and equivalent plastic strain shown in the keys of Figures 9-3 and 9-4 were obtained from the field output.

With dynamic explicit integration of instantaneous imposed velocities, step times are important since long step times could cause excessive deformation of elements. In some

© Central University of Technology, Free State

instances, the opposite faces may cross over each other (in compression) causing the job to exit with an error, whilst for very small step times, the elements may not reach the plastic deformation state. For single element tests, the dynamic explicit integration option with total step times (*t*) of 0.03 s, 0.003 s and 0.001 s for velocities of 0.1 m/s, 1 m/s and 4 m/s, respectively, were found to give sufficient deformation without excessive distortion of the element. For velocities beyond 4 m/s for this kind of numerical model, the simulation aborted even for very small step times due to excessive deformation of the model. Figure 9-5 shows the change in the values of equivalent von Mises stresses, plastic strains and plastic strain rates with increasing simulation time in VUHARD and VUMAT for a velocity of 4 m/s.

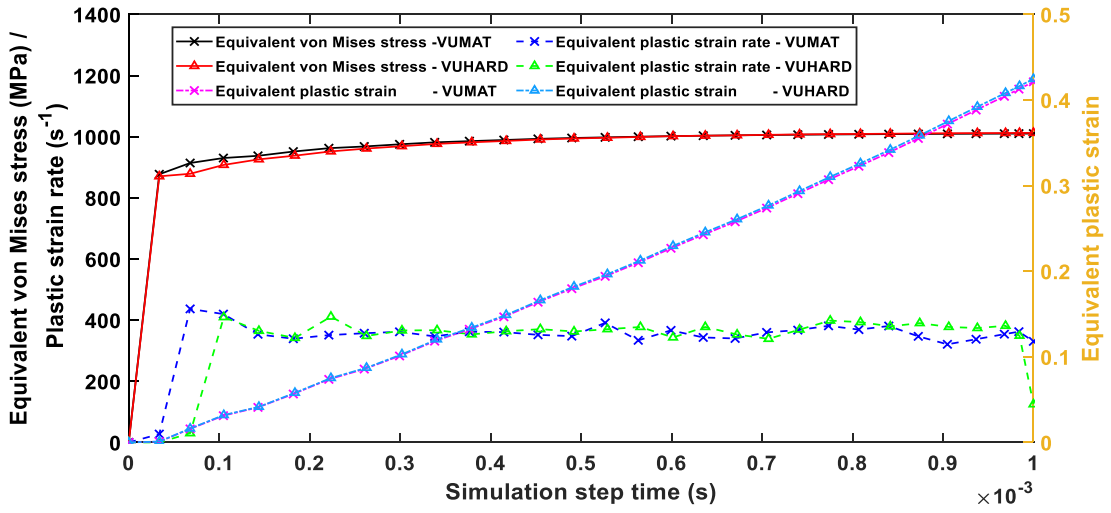

Figure 9-5. The equivalent von Mises stress, plastic strain and strain rate against simulation time history generated in VUMAT and VUHARD subroutines developed here for a test velocity of 4 m/s and a temperature of 298 K.

In both subroutines, the plastic strain is initially zero (during elastic deformation) before increasing uniformly to a maximum value and therefore the rate of deformation (plastic strain rate) is constant during this period, as seen in Figure 9-5. Both VUMAT and VUHARD show fairly similar values of average plastic strain rate of approximately 350 s^{-1} in the figure. The equivalent plastic strain and flow stress curves generated from the two subroutines also coincide for the entire and a large part of the simulation step time, respectively.

As previously discussed in Chapter 8, there are four critical parameters of the constitutive model developed in this work (Equation 9-1) that influence the shape of the flow stress

© Central University of Technology, Free State

curve, namely h, k_2, ρ_o and T. The symbols h and k_2 stand for the strain hardening and dynamic recovery parameters discussed in section 4.3 of Chapter 4 and calibrated for DMLS Ti6Al4V(ELI) in section 8.2 of Chapter 8. The parameter ρ_o represents the initial dislocation density in a material and T the test temperature. The sensitivity of these critical parameters in the numerical models developed here was investigated at a velocity of 4 m/s and the results compared with those of the analytical solutions developed here as well and at the same conditions for both cases. These results are presented in Figures 9-6 and 9-7. As seen in these figures, the results from the numerical models derived in VUMAT and VUHARD, and those from analytical solutions developed here coincide for the large part of the flow curves.

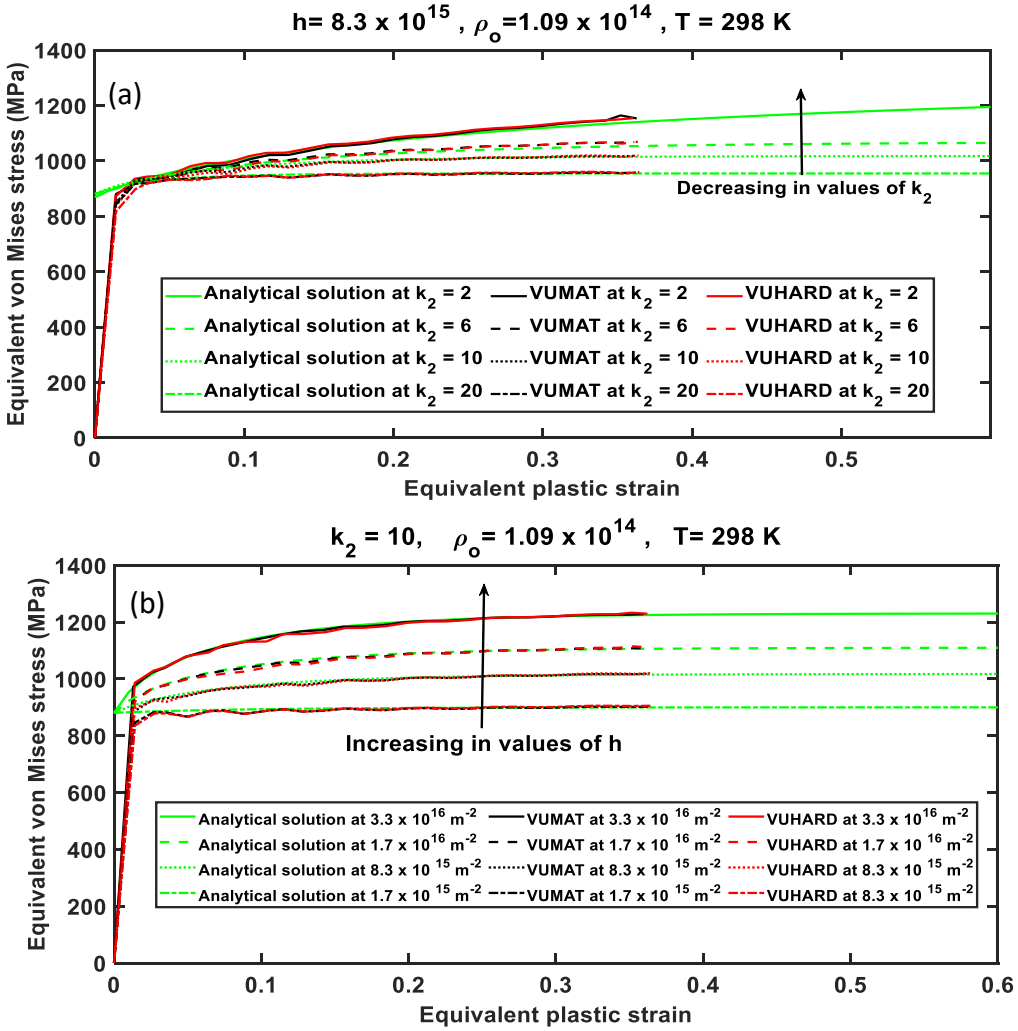

Figure 9-6. The effects of model parameters (a) k_2 and (b) h on the numerical solutions derived from VUMAT and VUHARD subroutines and compared with analytical solution at the same conditions of 350 s^{-1} and 298 K.

© Central University of Technology, Free State

The opposing effect of parameters h and k_2 is well articulated in the numerical model where the flow stress increases with decreasing values of the parameter k_2, whereas it increases with increasing values of the parameter h, as seen in Figure 9-6. Similar observations were reported in Figures 8-4 and 8-5 of Chapter 8. Figure 9-7 shows the effects of initial dislocation density and temperature on the numerical solutions obtained from the VUMAT and VUHARD subroutines developed here and the analytical solutions obtained in Chapter 8, all at the same strain rate of 350 s^{-1}. It is clear from Figure 9-7(a) that for very high initial dislocation densities, the flow stress curve is characterised by high initial peak stresses followed by a decrease in flow stress.

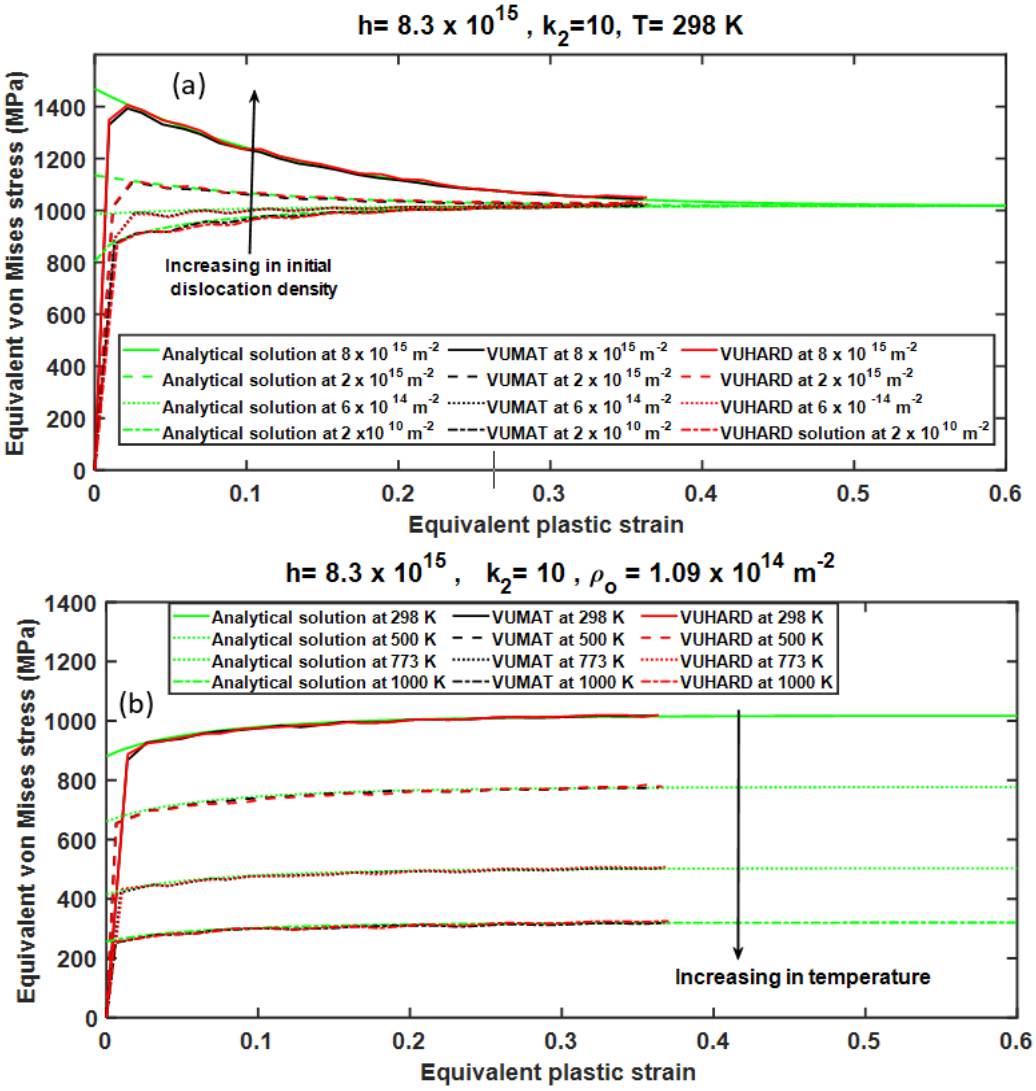

Figure 9-7. The effects of (a) initial dislocation density (ρ_o) and (b) temperature on the numerical solutions derived from VUMAT and VUHARD subroutines, compared with analytical solutions at the same average strain rate of 350 s^{-1}.

© Central University of Technology, Free State

For very low initial dislocation densities, the peak stresses are lower and the material experiences strain hardening. Similar observations were noted in Figure 8-7 and the theory behind this phenomenon presented.

The effects of simulation temperatures on the flow stress curve are very conspicuous in Figure 9-7(b), where the values of flow stress are seen to decrease with increase in temperature. This is consistent with observation made in Figure 8-6 of Chapter 8. The preceding discussion and the observations made from Figures 9-6 and 9-7 show good sensitivity of the numerical models developed here in VUMAT and VUHARD subroutines to the critical parameters that dictate the shape of the flow stress curve in the DMLS Ti6Al4V(ELI) alloy. The close coincidence of the curves for the numerical models with those for the analytical models is also noted. This creates confidence in the use of these models in the simulation of flow stresses for sample types C, D and E at various imposed velocities.

The preceding results for the 8-node linear brick element are for the numerical simulations of samples type C. Those for samples type D and E are presented in Appendix H. The values obtained from numerical simulation here were plotted and compared with those obtained from the analytical solutions based on Equation 9-1 at the same test conditions. The collective results for samples type C 8-node linear brick elements are shown in Figures 9-8 and 9-9.

As seen in these two figures, the scaling down and upturn of flow stress at high temperature and with an increase in strain rate, respectively, is well articulated. For the two cases of strain rate and temperature, the results from the numerical models based on the VUMAT and VUHARD subroutines and those derived from the analytical solution developed here are nearly overlapping over most of the equivalent plastic strain range. This confirms that the two subroutines work well in the loading conditions applied.

© Central University of Technology, Free State

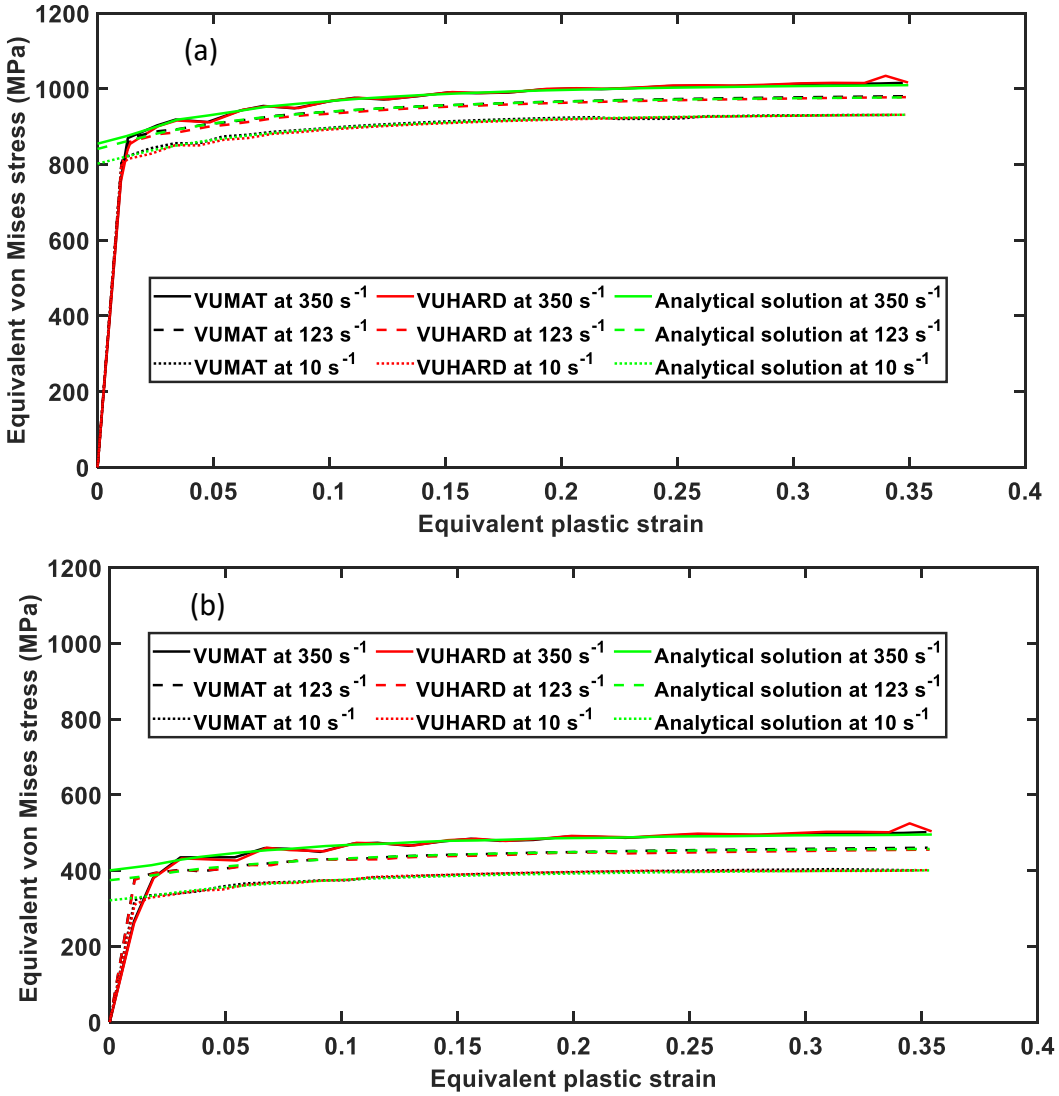

Figure 9-8. Comparison between the analytical and numerical solutions in VUMAT and VUHARD at three different test velocities and temperatures of (a) 298 K and (b) 773 K for the case of an 8-node linear brick element in compression for samples C.

© Central University of Technology, Free State

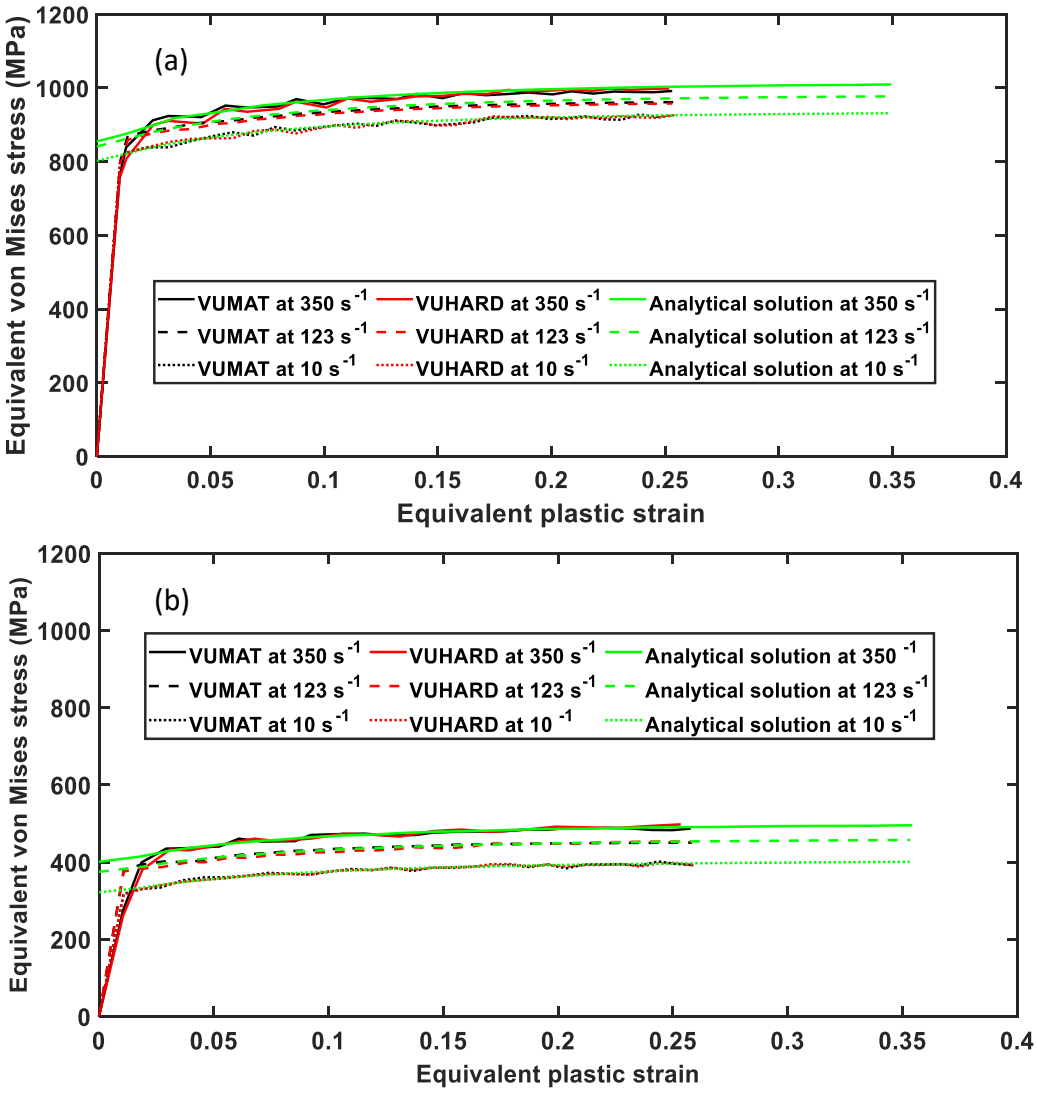

Figure 9-9. Comparision between the analytical and numerical solutions in VUMAT and VUHARD at three different test velocities and temperatures of (a) 298 K and (b) 773 K for an 8-node linear brick element in tension for samples C.

Both the compression and tensile test simulations showed the same values of flow stress at all strain rates and temperatures, which is anticipated considering the criterion for isotropic yielding used to develop and implement the constitutive models. Even though this was the case, for the same simulation time, there was a significant difference in the maximum equivalent plastic strains attained in the two load conditions, with values of about 0.35 in compression and about 0.25 in tension. The elastic moduli in tension and compression for metals and alloys are normally taken to be the same. Also, failure due to the formation of adiabatic shear bands (ASBs) occurs in both high-strain-rate compression and tension. Failure due to monotonic tensile stress occurs first through the formation of pores, cracks

© Central University of Technology, Free State

and their horizontal spread in the initial brittle fracture, and thereafter, necking before final tearing along the ASBs. Compressive stresses, on the other hand, cause materials to reduce in length and increase in cross section, and failure in most cases is because of initiation of ASBs. These distinct deformation mechanisms in compression and tension suggest different values of plastic strain for the same applied load, as seen in Figures 9-8 and 9-9.

The necking failure mechanism in tension can be studied better using multiple elements, since multiple element models consist of several integration points and therefore results from various sections of the model can be obtained. A specific geometry of the model can also be used to allow early necking.

9.4.2 Multiple elements tests

The necking of a circular bar test is an example commonly used in finite element analysis to investigate necking and softening of a tensile bar (Tvergaard and Needleman 1984). The test was used in the present research to investigate the performance of the VUHARD and VUMAT subroutines developed here under the conditions of necking in tensile loading. The numerical model used was that of the asymmetrical cylinder shown in Figure 9-10(a), with large and small diameters (on the fixed end and at the surface of application of load) of 10 mm and 8 mm, respectively, and a height of 10 mm. The roller boundary condition with y-axis rotational symmetry was applied on the side of the model with the large diameter to constrain the displacement only in the y-direction and to allow rotation only about the y-axis. Tensile loading of the cylinder was realised through imposed instantaneous velocities of 0.1 m/s, 1 m/s and 4 m/s along the y-axis (the axial direction of the cylinder), shown in Figure 9-10(b), each at a time.

For multiple elements tests, it is crucial to use a adequately refined mesh to ensure that the results from simulation are adequately accurate. Coarse meshes can yield inaccurate results, while the numerical solution provided by a model becomes more accurate with the increase of mesh density. However, the computational resources (time and space) required to run simulations increase with increasing mesh refinement. Therefore, mesh convergence studies on the performance of the two subroutines were first undertaken. Four different mesh global sizes of 2 mm (for coarse mesh), 1 mm (for moderate fine mesh), 0.5 mm (for

© Central University of Technology, Free State

fine mesh) and 0.25 mm (very fine mesh) were assigned to the model, as seen in Figure 9-10(c-e).

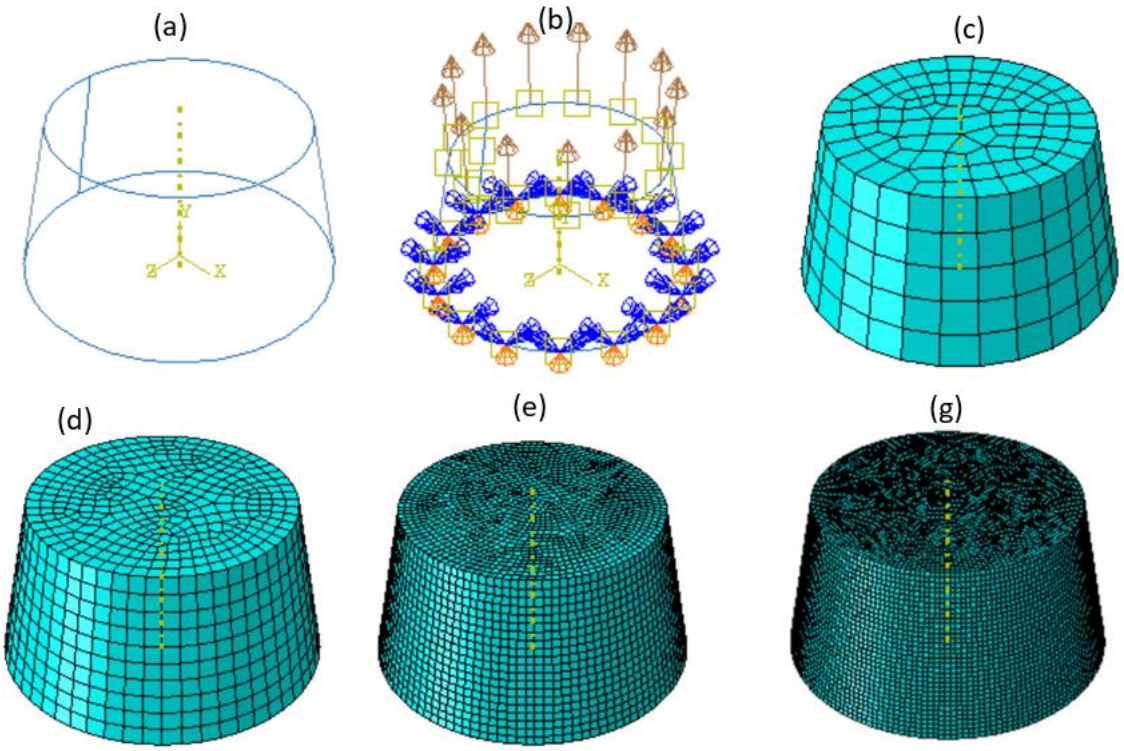

Figure 9-10. (a) A three-dimensional (3D) numerical model for the necking of a circular bar with, (b) imposed loading and boundary conditions, (c) 2 mm mesh size (475 elements), (d) 1 mm mesh size (3550 elements), (e) 0.5 mm mesh size (28320 elements) and (d) 0.25 mm mesh size (126038 elements).

These four different sizes of meshes yielded 475, 3550, 28320 and 126038 linear hexahedral elements of C3D8R type, in order from the largest mesh size to the smallest. Figure 9-11 to Figure 9-14 show the distribution of equivalent von Mises stresses and plastic strains obtained using the VUHARD and VUMAT subroutines developed here, for the four different mesh sizes.

© Central University of Technology, Free State

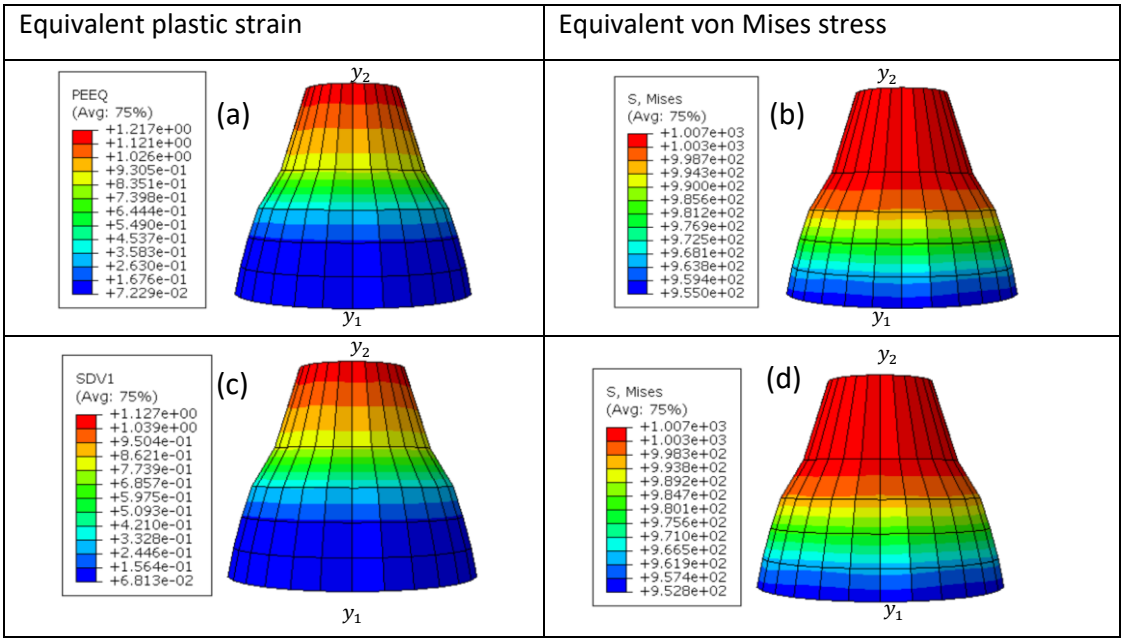

Figure 9-11. Numerical estimation of (a& c) equivalent plastic strain and (b and d) equivalent von Mises stress distribution in (a & b) VUHARD and (c & d) VUMAT subroutines developed here, using 2 mm mesh size, at a test velocity of 4 m/s and temperature of 298 K.

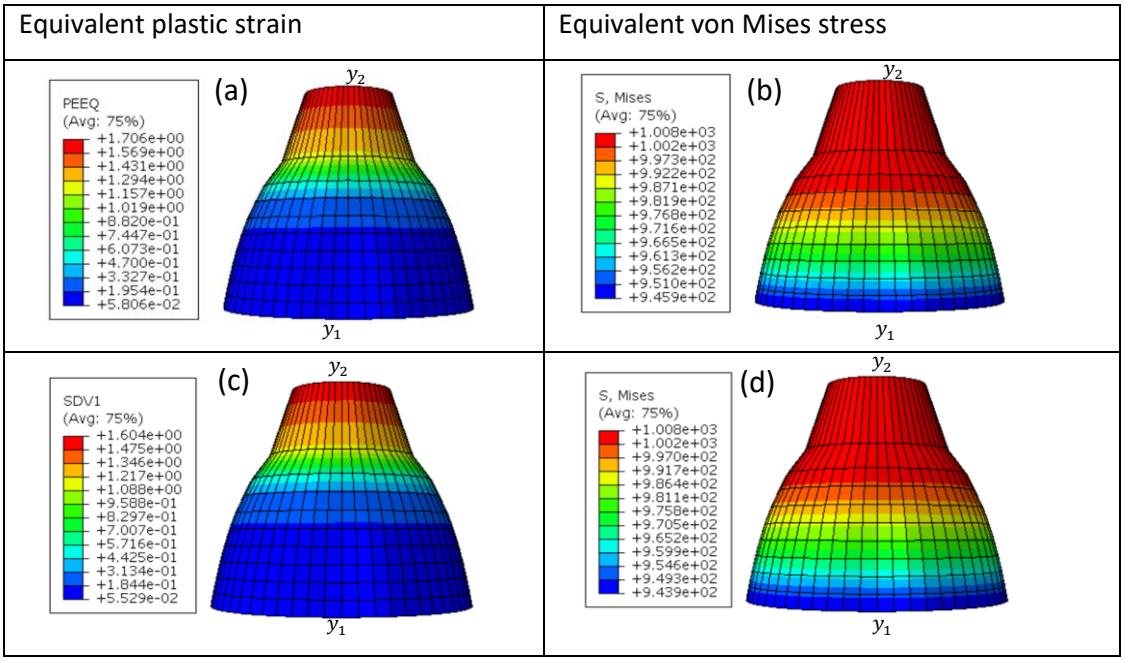

Figure 9-12. Numerical estimation of (a & c) equivalent plastic strain and (b and d) equivalent von Mises stress distribution in (a and b) VUHARD and (c & d) VUMAT subroutines developed here, using 1 mm mesh size, at a test velocity of 4 m/s and temperature of 298 K.

© Central University of Technology, Free State

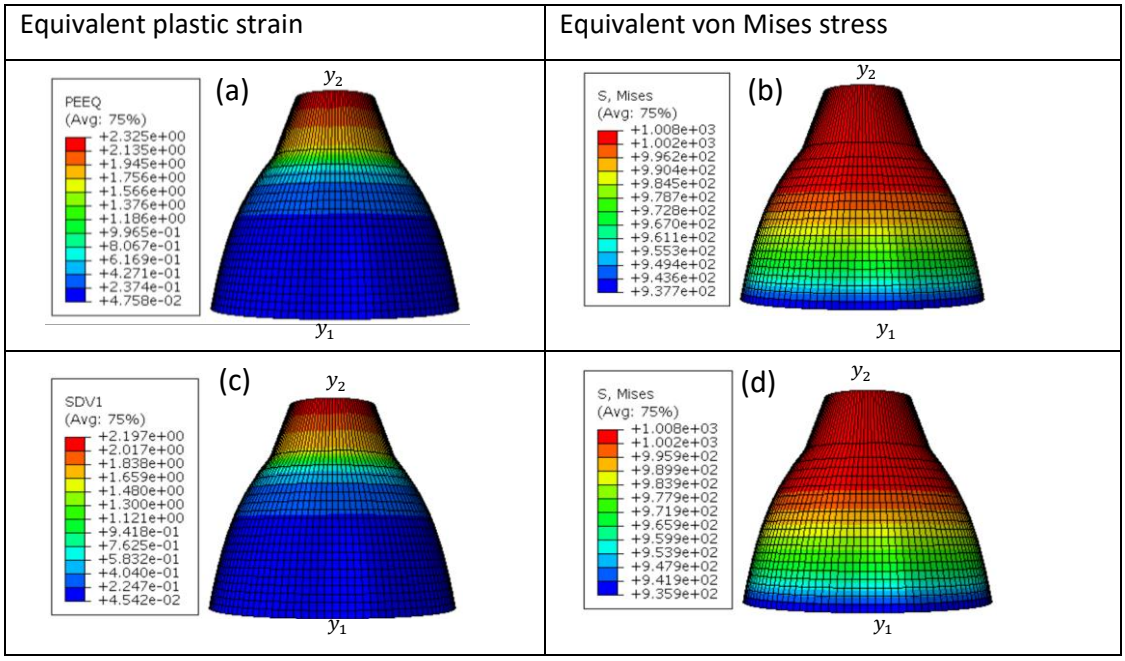

Figure 9-13. Numerical estimation of (a & c) equivalent plastic strain and (b & d) equivalent von Mises stress distribution in (a & b) VUHARD and (c & d) VUMAT subroutines developed here, using 0.5 mm mesh size, at a test velocity of 4 m/s and temperature of 298 K.

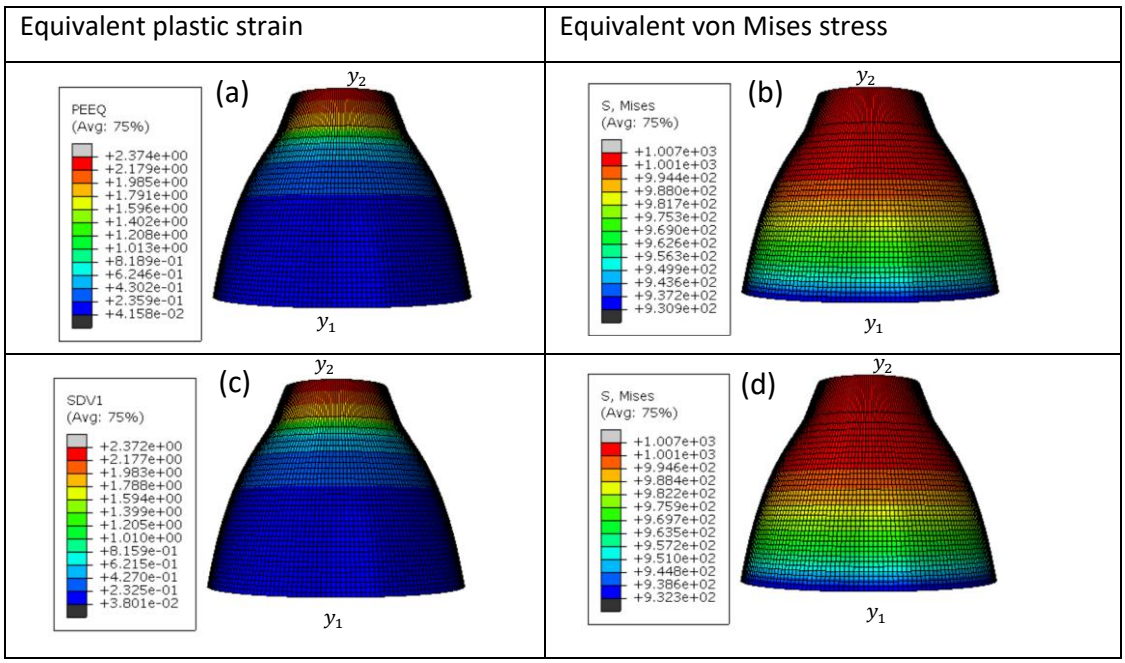

Figure 9-14. Numerical estimation of (a & c) equivalent plastic strain and (b & d) equivalent von Mises stress distribution in (a and b) VUHARD and (c & d) VUMAT subroutines developed here, using 0.25 mm mesh size, at a test velocity of 4 m/s and temperature of 298 K.

© Central University of Technology, Free State

A summary of computation times for simulation of the necking bar in this set of simulations is shown in Table 9-1. The VUMAT subroutine is seen in this table to have more computation time and increments in comparison to VUHARD. The computation time is also seen to increase with mesh density.

Table 9-6. Computation time and number of increments for different mesh densities

Subroutine	**VUHARD**		**VUMAT**	
Mesh size (mm)	**Time (s)**	**Increments**	**Time (s)**	**Increments**
2	6.3	92	9.2	96
1	59.3	200	63.2	219
0.5	177.2	447	396.6	629
0.25	1676	900	1876	1037

For all four sizes of mesh, the VUHARD and VUMAT subroutines display similar distributions of equivalent plastic strain ($\overline{\varepsilon_p}$) and von Mises stress ($\overline{\sigma_p}$). From the legends in (a) and (c) of Figures 9-11 to 9-14, all four numerical models are seen to experience plastic deformation. The maximum values of equivalent plastic strain and equivalent von Mises stress are located at the tip labelled y_2 and decline gradually towards y_1 where they are minimum, as seen in the contours in these figures. It should be noted that the shape of the undeformed model shown in Figure 9-10 is that of a truncated cone with the cross-section areas that decrease linearly towards the top surface. Thus, for a given load that is applied at the top surface of the model, the values of equivalent von Mises stress and strain will decline as the cross section increases towards the bottom surface of the original cone.

To better understand the distribution of these two variables for different mesh densities, their values were obtained from elements along the surface from y_1 to y_2 at the end of each simulation. These values were then plotted against the normalised length of the deformed model. The resulting curves for different mesh densities are shown in Figure 9-15, while the results of mesh convergence studies on various sections of the model are presented in Figure 9-16.

© Central University of Technology, Free State

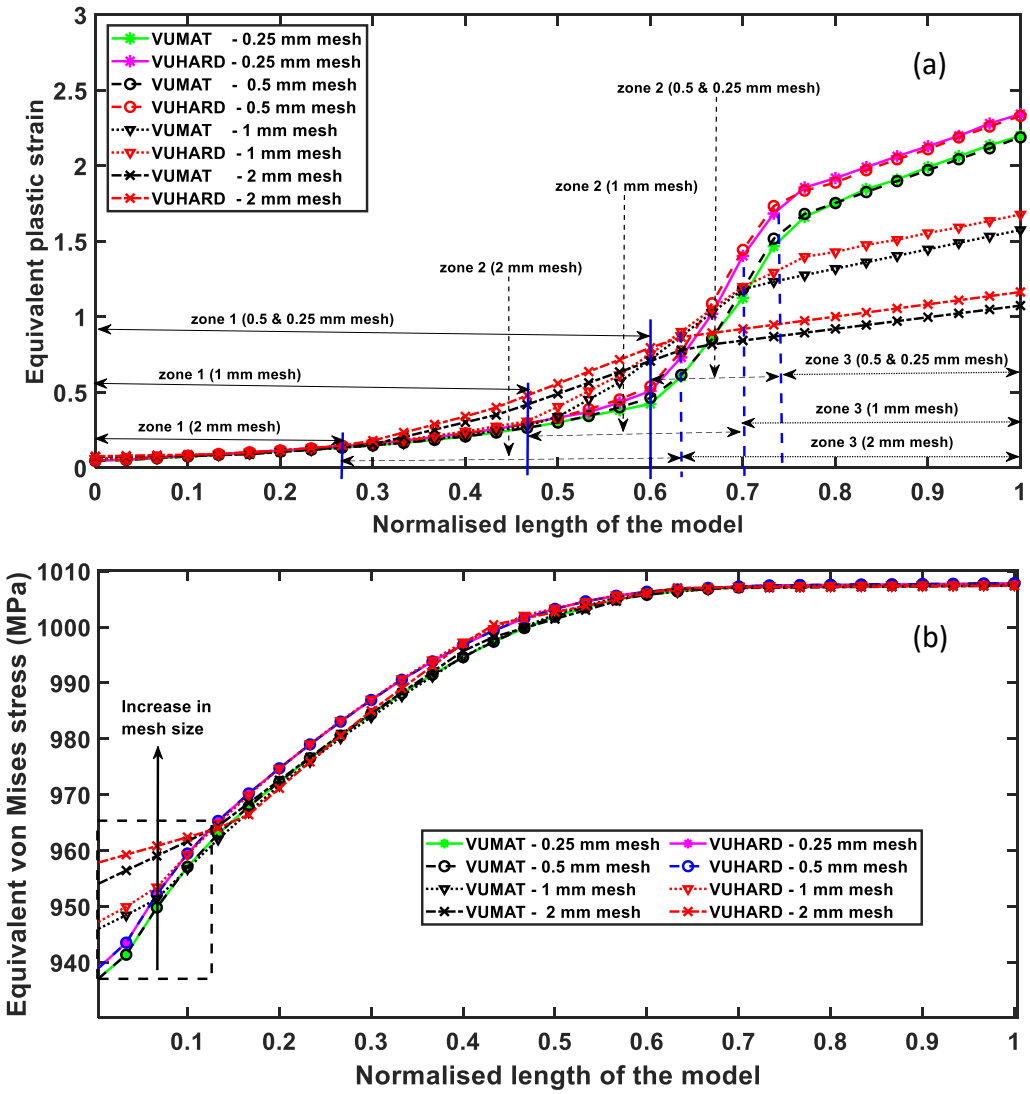

Figure 9-15. A typical equivalent (a) plastic strain and (b) von Mises stress distribution along the length of the numerical model with different mesh densities simulated at a velocity of 4 m/s for 0.001 s and at a temperature of 298 K.

Both the equivalent plastic strains ($\overline{\varepsilon_p}$) and von Mises stresses ($\overline{\sigma_p}$) show distinct profiles for the three different mesh densities of the model in Figure 9-15(a and b). The $\overline{\varepsilon_p}$ profiles exhibit three typical zones, as shown in Figure 9-15(a), which differ in range for different mesh sizes. The first zone shows slow increase of $\overline{\varepsilon_p}$ at increasing rates and its ranges from normalised lengths of 0 – 0.26, 0 – 0.47, 0 – 0.60 and 0 – 0.60 for models with 2 mm, 1 mm, 0.5 mm and 0.25 mm mesh sizes, respectively. The slow increase of equivalent strain in this zone is attributed to the large cross-section areas of the model and therefore, low equivalent von Mises stress acting on elements in the region. The second zone shows a higher increase in $\overline{\varepsilon_p}$ with points of inflexion. It ranges from normalised length of 0.26 – 0.63, 0.47 – 0.70, 0.60 – 0.73 and 0.60 – 0.73 in order of decreasing mesh size. This is the

© Central University of Technology, Free State

zone that precedes necking. Rapid decrease in cross-section area around this zone resulted in rapid increase in equivalent von Mises stress and strain. This stage forms the shoulder of the "neck". The third zone is the necking section of the model and shows an increase in $\bar{\varepsilon_p}$ at constant rates and it ranges from a normalised length 0.47 – 1, 0.70 – 1, 0.73 – 1 and 0.73 – 1 in order of increasing mesh density.

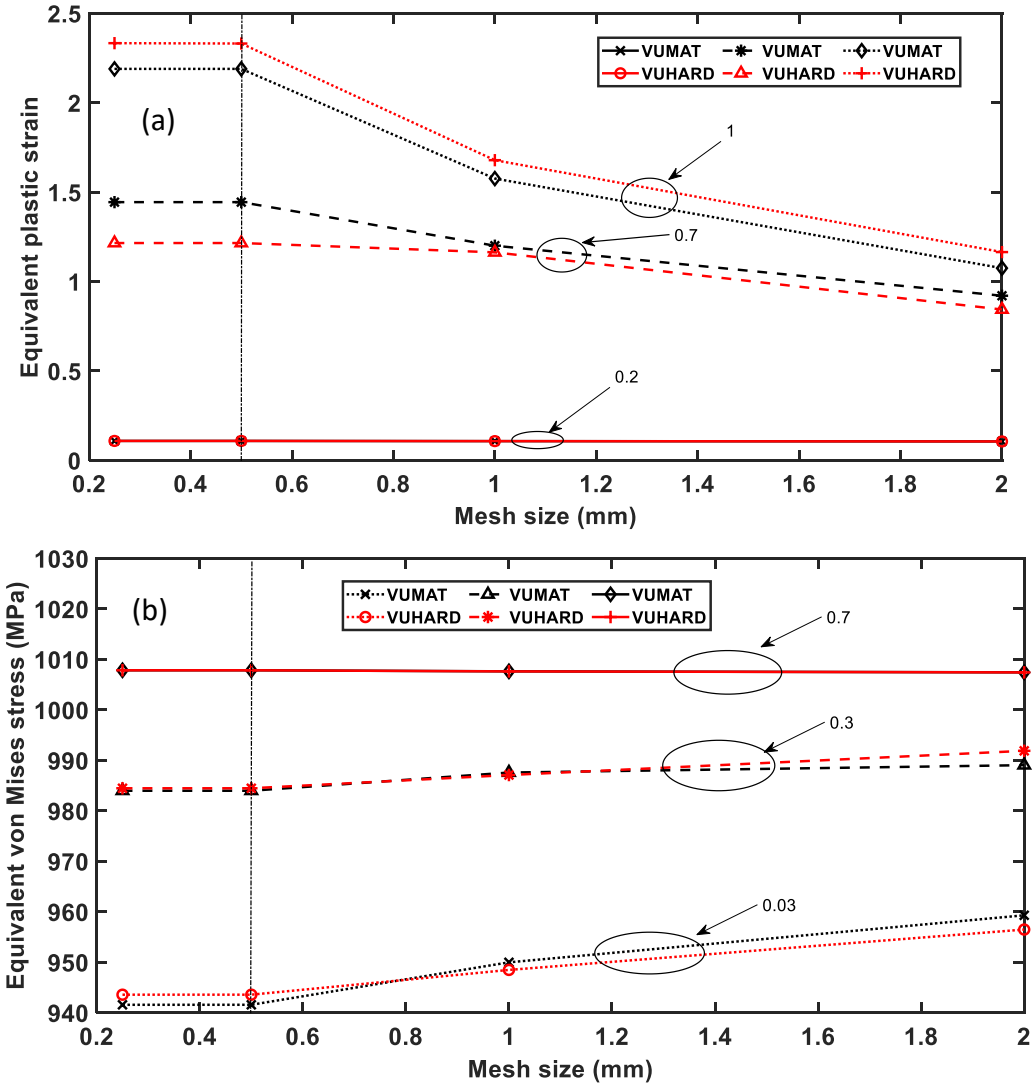

Figure 9-16. The mesh convergence analysis for equivalent (a) plastic strain at model normalised lengths of 0.2, 0.7 and 1, and (b) von Mises stress at normalised lengths of the models of 0.03, 0.3 and 0.7 for the VUMAT and VUHARD subroutines.

The mesh convergence analysis shown in Figure 9-16(a) for the values of equivalent plastic strain obtained at various sections of the model gives rise to several observations. There is convergence of the values of equivalent plastic strain as the mesh density increases in the second and third zones. Lower and higher values of equivalent plastic strain from the

© Central University of Technology, Free State

VUHARD subroutine in the second and third zones, respectively are also noted. There is insignificant variation of equivalent plastic strain as the mesh density increases in the first zone and the results from the VUHARD and VUMAT subroutines are perfectly superimposed in this zone.

From Figure 9-15(b), the influence of mesh density on the distribution of equivalent von Mises stresses is seen to be significant between the normalised lengths of 0 – 0.14. The values of equivalent von Mises stresses are seen to increase with increasing mesh size in this range for both the results obtained using the VUMAT and VUHARD subroutines. However, with 0.5 mm and 0.25 mm mesh sizes, the results from the two subroutines overlap. In the zone between normalised lengths of 0.14 – 0.57, there is a small spread of results obtained for different mesh densities. The variation between the values of equivalent von Mises stresses obtained with coarse and refined mesh models in this region are less than 0.1% of the former. Like the preceding zone, the 0.5 mm and 0.25 mm mesh sizes in this zone give results that are indistinguishable. The results obtained in the final zone, for normalised lengths of 0.57 to 1, are seen in Figure 9-15(b) to be superimposed on top of one another. It is important to note here that for large values of equivalent plastic strain, the flow stress given by the constitutive model developed in this study saturates (no strain hardening), which elucidates the convergence of all these curves in the final zone. This is clearly shown in Figure 9-16(b) at a normalised length of the model of 0.7.

The values of equivalent von Mises stresses obtained from the VUHARD subroutine are higher and lower than those from the VUMAT subroutine in the first and second zones at lower mesh densities. The reverse is true for higher mesh densities, with cross-over points at mesh densities of about 0.85 and 1.2 for the two zones, respectively, while in the last zone the results from the two subroutines are indistinguishable. Although, the results from these two subroutines are very close to one another, the small differences seen in the preceding two figures could be a result of the different integration scheme employed by these two subroutines. The VUHARD subroutine uses an explicit central difference time integration rule in-built in ABAQUS to generate plastic strain at Gauss points (Ming and Pantalé 2018), while the VUMAT subroutine uses the radial return method, which belongs to backward or forward integration algorithm methods, in which equivalent plastic strains are evaluated at Gauss points. The difference in their time integration schemes suggests

© Central University of Technology, Free State

variations in the results obtained due to inherent integration errors associated with each integration scheme. For instance, the error in the forward and backward integration algorithms is proportional to the size of the time step, while for the central difference method, the error is equal to the square of the size of the time step. This suggests that the central difference time integration scheme is more accurate than the forward and backward integration methods.

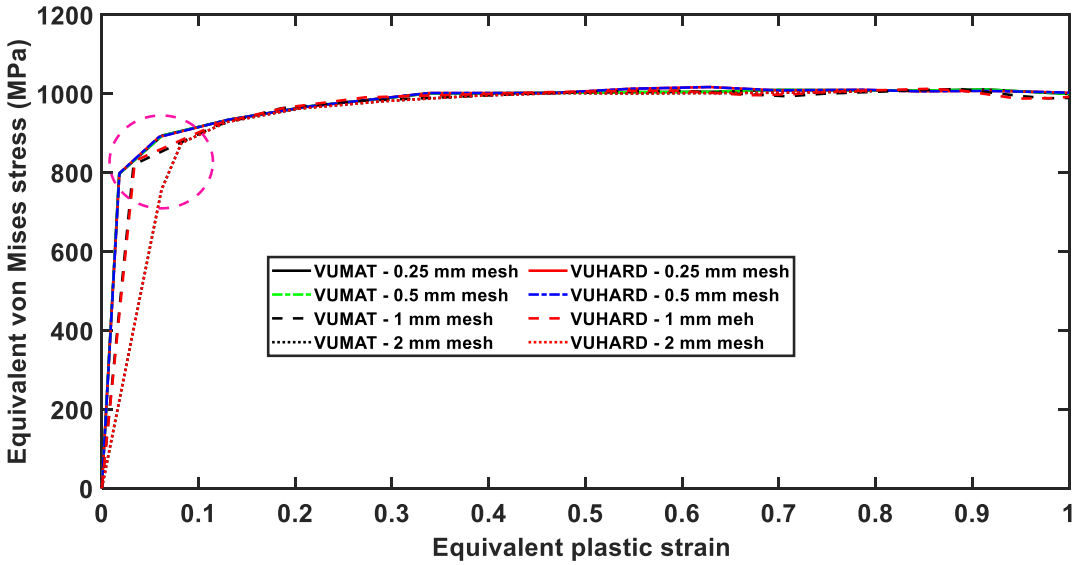

Figure 9-17. The numerical equivalent von Mises stresses against equivalent plastic strains at a temperature of 298 K and imposed velocity of 4 m/s for different mesh densities obtained from the VUMAT and VUHARD subroutines developed here.

The plots of equivalent plastic strains and equivalent von Mises stresses obtained from the two subroutines, shown in Figure 9-17 for four different mesh sizes, are nearly overlapping for the better part of the flow stress curves. The significant effects of mesh size is revealed at the initial values of equivalent plastic strain (circled in Figure 9-17), with the 2 mm mesh size giving a much higher value of about 0.083 equivalent plastic strain in comparison to the 0.25 mesh size, which has a value of about 0.02. However, the curves for 0.25 mm and 0.5 mm mesh size are indistinguishable at all values of strain, which is consistent with the observations made from Figures 9-15 and 9-16.

It is not surprising to see the flow stress saturating at the equivalent plastic strain of 0.4 and onward for the VUMAT and VUHARD subroutine, since the implemented model was not developed to take care of unloading conditions or even damage evolution. During the initial stage of deformation, materials experience work-hardening where flow stress increases

© Central University of Technology, Free State

with increasing strain. Work-hardening occurs normally due to generation and accumulation of dislocations with increasing plastic strain. However, as previously explained in section 7-3 of Chapter 7, materials loaded at high strain rate experience the "thermal softening" effect. The thermal softening mechanism causes dynamic recovery where dislocations begin to annihilate. If the rate of dislocation annihilation equals the rate of dislocation generation by strain hardening, the flow stress saturates. However, if the rate of dislocation annihilation exceeds the rate at which dislocations are generated, materials experience decreasing flow stress with increasing plastic strain, a phenomenon commonly referred to as "strain softening". The threshold value of dislocation accumulation for the three forms of DMLS Ti6Al4V(ELI) samples was calibrated as 8.3 x 10^{15} m^{-2} in Chapter 8. As also noted in section 7.3 of Chapter 7, formation of ASBs is the precursor to material failure due to formation and growth of microvoids and cracks along them. The failure processes at high strain rates that lead to instabilities can be reflected in the numerical models through extension of the analytical model to predict the evolution of such damage. However, this was not within the scope of the present research and future research is expected to focus on integrating the evolution of damage into the constitutive model developed here.

The foregoing graphs and related discussions suggest that mesh density does influence the strain and stress distribution in a numerical model. However, this does not appear to significantly affect the VUMAT and VUHARD subroutines differently. This is evident from the fact that for the four different mesh densities used here, the VUMAT and VUHARD subroutines' equivalent von Mises stress-strain curves are nearly superimposed on top of one another for most of the flow stress curves. Furthermore, the flow stress curves and the distribution of equivalent strain and von Mises stress given by the models with 0.25 mm and 0.5 mm mesh sizes are indistinguishable. The values of equivalent plastic of strain and von Mises stress at various sections of the model were also noted to correspond for these two mesh sizes. Given that more computation resources (space and time) are required as mesh density increases, the mesh of size of 0.5 mm was selected for simulation of the necking of a cylindrical numerical model at different temperatures and strain rates of 298 K and 773 K.

The results obtained from the last elements near the point y_2 (shown in Figure 9-13) were compared with the analytical solutions obtained from Equation 9-1 at different strain rates.

© Central University of Technology, Free State

The flow stress curves obtained from numerical simulation and the analytical constitutive model for samples type C, in this case, are summarised in Figure 9-18. The remainder of the results for samples type D and E can be found in Appendix I.

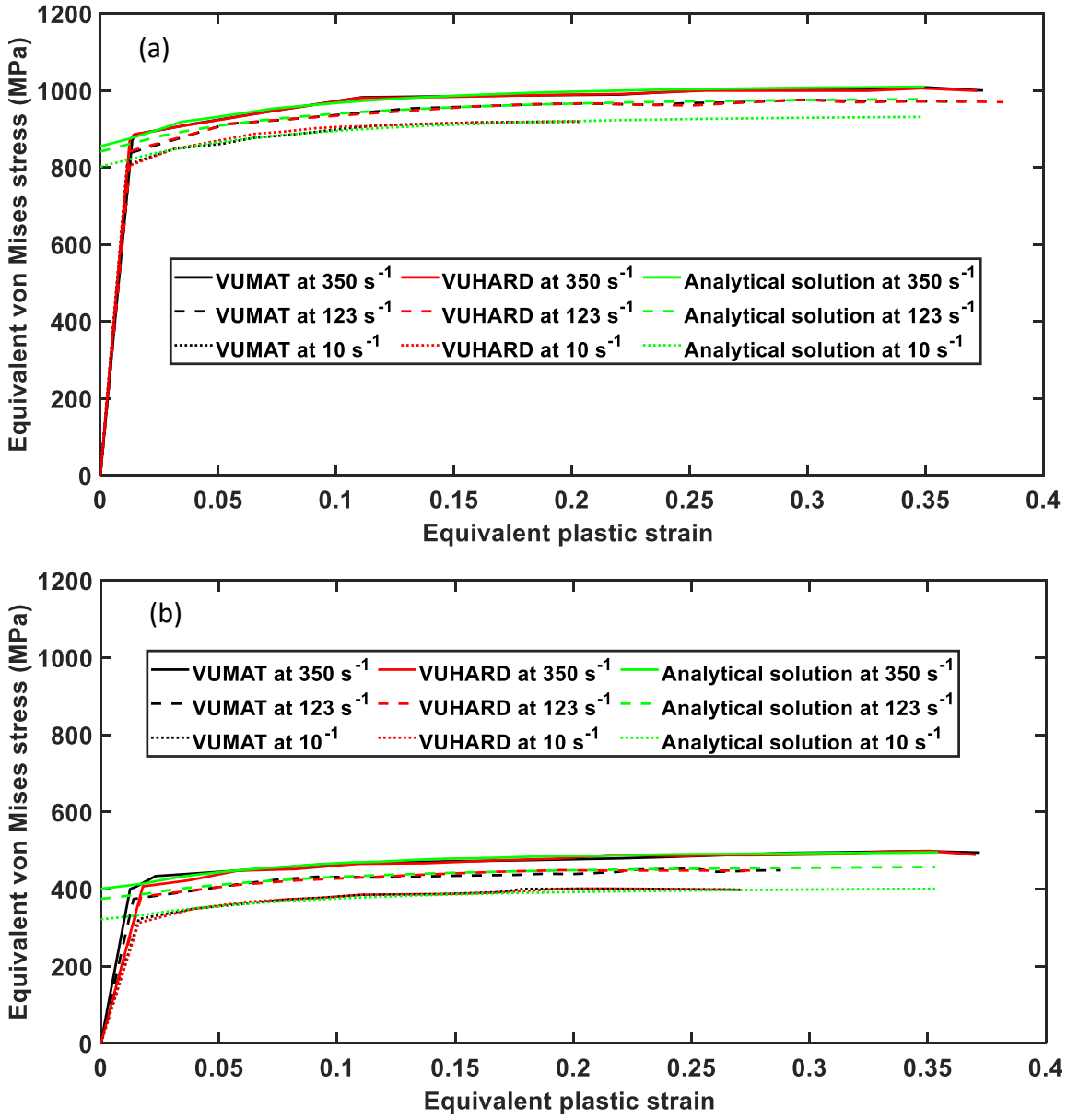

Figure 9-18. Comparison between the analytical and numerical solutions in the VUMAT and VUHARD subroutines at three test velocities and a temperature of (a) 298 K and (b) 773 K for multiple elements cylindrical model of samples type C.

Like the result from the single element test reported earlier on, the curves for the analytical solution and those from the VUMAT and VUHARD subroutines are nearly superimposed on top of one another at the temperatures of 298 K and 773 K, and respective strain rates, as

© Central University of Technology, Free State

seen in Figures 9-18. That the curves in this figure are nearly overlapping indicates that both subroutines are accurate in modelling a multiple element cylinder.

9-5 SUMMARY

The foregoing completes verification of the VUMAT and VUHARD subroutines using a single element and a multiple elements cylindrical specimen. The results from this, the verification, have shown successful implementation of the microstructure- and dislocation-based constitutive numerical model for DMLS Ti6Al4V(ELI) in ABAQUS. This then creates confidence in the numerical model and provides a foundation for simulating more complicated numerical experimental tests with contact interaction, such as the SHPB tests, to obtain much higher strain rates. This is reported in Chapter 10, where simulation of SHPB experiments and verification of numerical results using the experimental results obtained in Chapter 7 for various forms of DMLS Ti6Al4V(ELI) is done.

© Central University of Technology, Free State

9.6 REFERENCES

1. ABAQUS.2020. Documentation. https://help.3ds.com/2020/English/DSSIMULIA_Established/SIMULIA_Established_FrontmatterMap/HelpViewerDS.aspx?version=2020&prod=DSSIMULIA_Established&lang=English&path=SIMULIA_Established_FrontmatterMap%2fsim-r-DSDocAbaqus.htm&ContextScope=all (accessed on 12th Nov 2020).
2. Ming, L., Pantalé, O. 2018. An efficient and robust VUMAT implementation of elastoplastic constitutive laws in ABAQUS/Explicit finite element code. *Mechanics & Industry*, 19 (3). p.308. https://doi.org/10.1051/meca/2018021
3. Sadd, M.H. 2009. *Elasticity: Theory Applications and Numerics*. Elsevier Inc, Burlington, MA, USA, p.116.
4. Tvergaard, V., Needleman, A. 1984. Analysis of the cup-cone fracture in a round tensile bar. *Acta Metallurgica*, 32(1), pp.157–169. https://doi.org/10.1016/0001-6160(84)90213-X

© Central University of Technology, Free State

CHAPTER 10 — APPLICATION OF THE NUMERICAL MODEL TO THE SPLIT HOPKINSON PRESSURE BAR TEST AT HIGH STRAIN RATES

10.1 INTRODUCTION

To demonstrate the capacity of the numerical model, that was developed and tested in Chapter 9, in predicting the flow stress of various microstructures of DMLS Ti6Al4V(ELI) at various dynamic loading conditions, the Split Hopkinson Pressure Bar (SHPB) experiment is simulated in this chapter. A brief and the theory of this experiment were presented in section 2.10 of Chapter 2 and more details were placed in Appendix A. The results obtained from this simulation are verified in this chapter using the experimental results presented in Chapter 7 for various microstructures of DMLS Ti6Al4V(ELI).

10.2 THE FINITE ELEMENT MODEL FOR THE SHPB

The 3D finite element model (FEM) for the SHPB setup used here consisted of incident, transmitter and the striker bars modelled with tool steel. The incident and transmitter bars were set to lengths of 2000 mm and diameter 20 mm, while the striker bar was set to have the same diameter but with a length of 500 mm. The Poisson's ratio, elastic modulus and the density assigned to these bars were 0.3, 230 GPa and 8050 Kg/m^3, respectively. Cylindrical test specimens of DMLS Ti6Al4V(ELI), with a length of 6 mm and diameter of 6 mm were used throughout this simulation. The flow stress curves of these specimens was modelled using the constitutive numerical material model implemented in VUMAT and VUHARD in Chapter 9 of this thesis.

A "hard" contact that allows separation after contact was used as the normal interaction property between the specimen and the bars on either side of it. The hard contact relationship in ABAQUS is normally used to minimise the penetration of one surface into another at locations of contact (ABAQUS 2020). This provision in the simulation of the SHPB test between the specimens and adjacent bars ensures that neither the specimens nor bars penetrate one another upon impact. As noted in section 3.5 of Chapter 3, the interfaces between the test specimen and the two bars on either side of it in SHPB testing are normally lubricated to minimise friction. The friction between the specimen and bar interface during the SHPB compression test, acts as radial constraint. The radial constraint

© Central University of Technology, Free State

can produce a hydrostatic stress imposed over the assumed deviatoric stress state, resulting in a non-uniform tri-axial stress state in the specimen (Gray 2000). This could negate the assumption of uniform and one-dimensional stress in the SHPB experiment. Thus, the tangential behaviour at the interface between the specimen and bars on either side of it was modelled as frictionless in all simulations. Since the SHPB equipment works on the principle of one-directional wave propagation (Gray 2002), constraints were applied to the bars and specimen to allow the propagation of stress waves only in the z-direction. Figure 10-1 shows a longitudinal section of the components for the numerical model of the SHPB test.

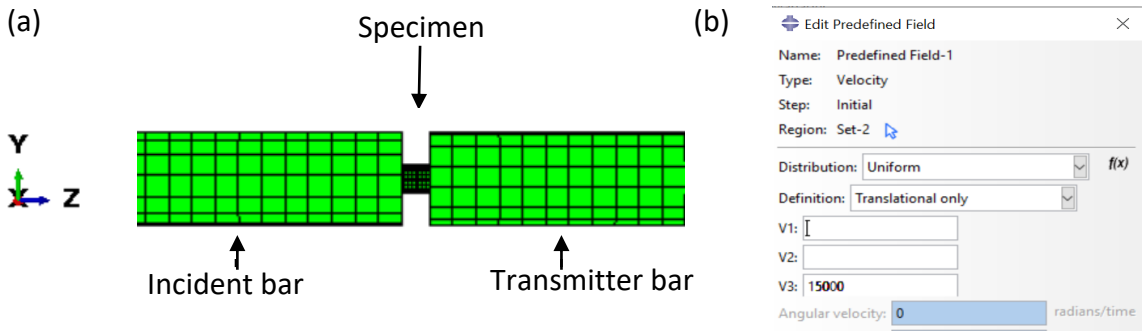

Figure 10-1. (a) A longitudinal section of a numerical model for the SHPB test and (b) the velocity (expressed in mm/s) in the predefined field imposed along the z-axis.

A uniform velocity was applied to the nodes of the striker bar to yield an impact loading in ABAQUS/Explicit. This velocity was set in the predefined field in ABAQUS shown in Figure 10-1(b). During the SHPB numerical test, the launched striker bar strikes the input bar with a pre-determined velocity to induce a desired strain rate. A compressive wave pulse is produced in the input bar which travels toward the test specimen. The compressive wave passes through the specimen to the output bar and part of it is reflected back to the incident bar due to the impedance mismatch between the specimen and the input bar. The incident wave in the incident bar at the beginning of simulation and the transmitted and reflected waves at the transmitter and incident bars, respectively, just after passing the specimen are shown in Figure 10-2.

© Central University of Technology, Free State

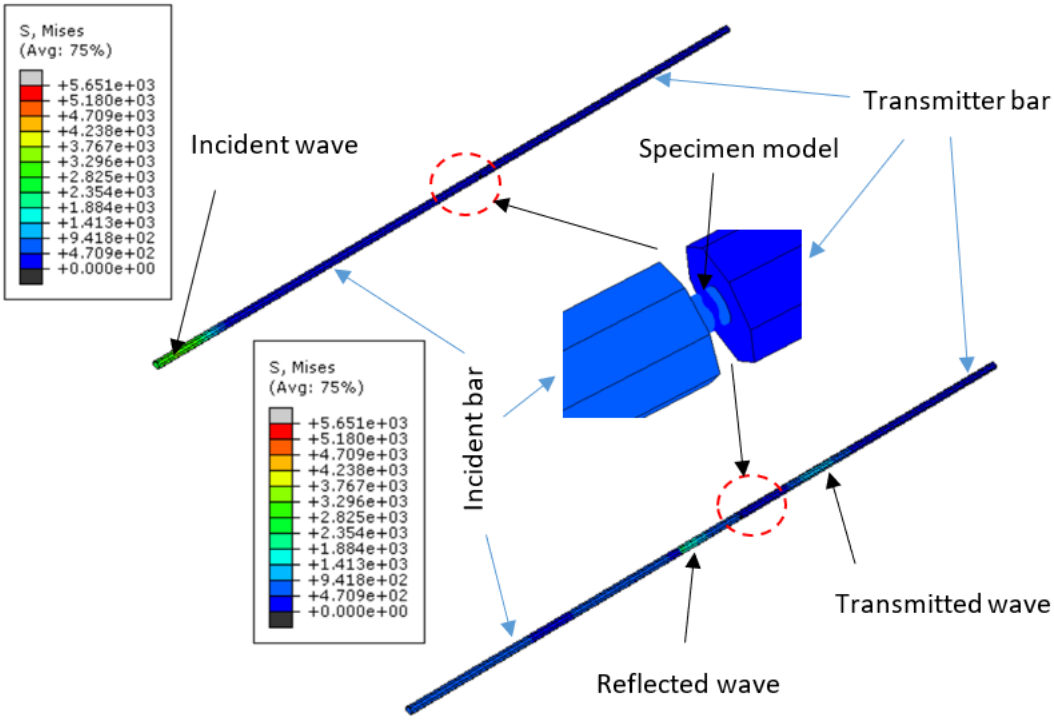

Figure 10-2.Numerical simulation of a compressive wave in a SHPB test.

A mesh convergency study was first carried out with the proposed VUMAT and VUHARD models to find the optimum mesh density to give the most accurate results in the simulation of dynamic properties of DMLS Ti6Al4V(ELI) using the SHPB test. Continuum elements C3D8R were used which have meshes with global sizes of 1 mm, 0.5 mm, 0.25 mm and 0.18 mm. The mesh convergence study was then undertaken by imposing an impact velocity of 8 m/s through the striker bar at a simulation temperature of 298 K. The corresponding arising equivalent plastic strain contours are shown in Figure 10-3, while the stress-strain curves resulting from the simulation using the four mesh sizes are shown in Figure 10-4. The summary of computation time in the SHPB test simulation using different mesh sizes is presented in Table 10-1.

The equivalent plastic strain profiles for the SHPB test specimen are seen in Figure 10-3 to be almost the same for all four mesh sizes. The maximum equivalent plastic strain on the test specimen is seen to be located at the surfaces in contact with the incident and transmission bars, and a distinct strain zone that forms an “X- shape” pattern through the diameter of the deformed model sample is visible in all cases.

© Central University of Technology, Free State

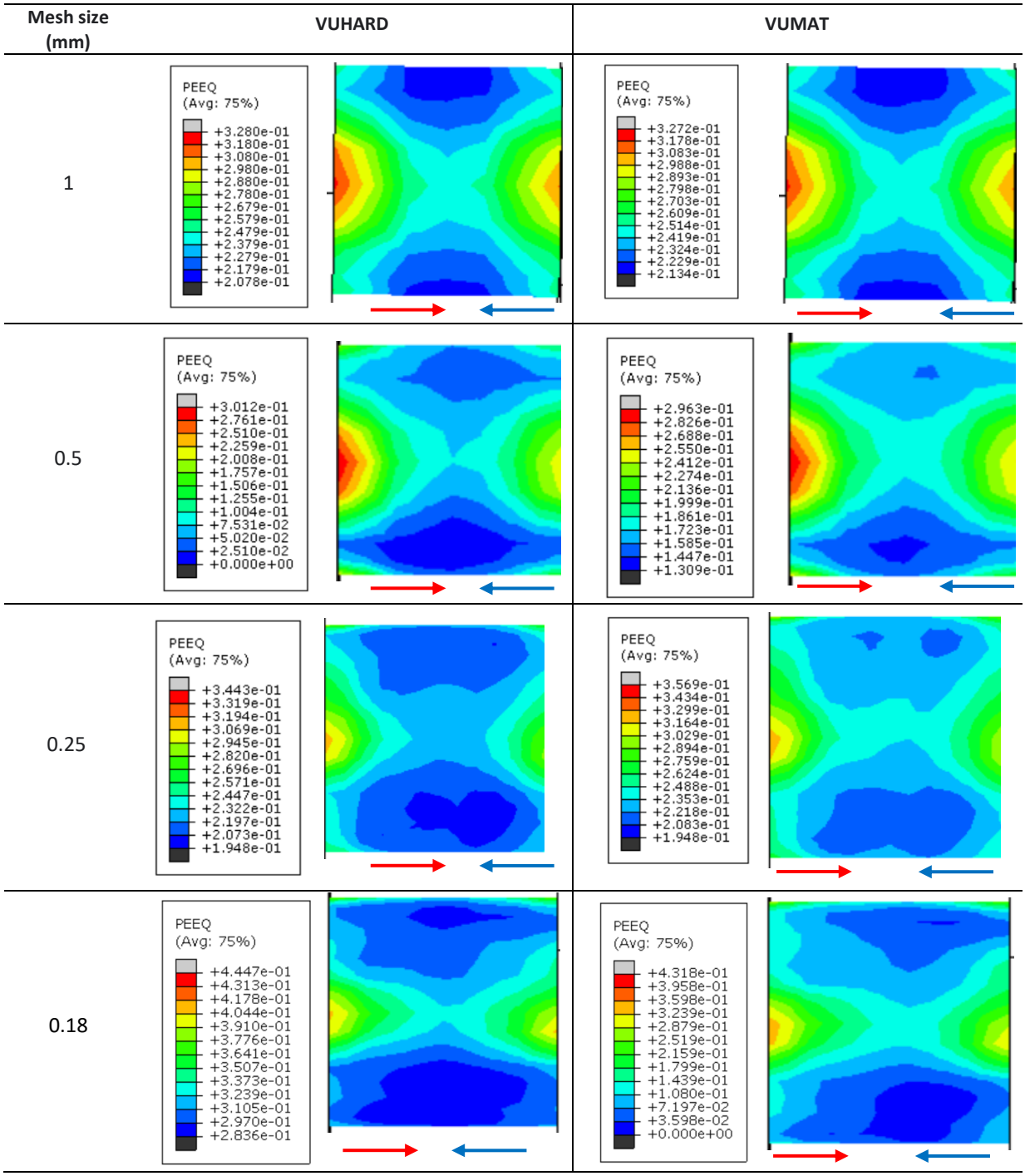

Figure 10-3. The equivalent plastic strain contours for a simulated SHPB test at striker velocities of 8 m/s for 1 mm, 0.5 mm, 0.25 mm and 0.18 mm mesh sizes (the red and blue arrows indicate the direction of incident and reflected waves, respectively).

© Central University of Technology, Free State

Table 10-1. Computation time for different mesh sizes

Subroutine	VUHARD	VUMAT
Mesh size (mm)	Time (s)	Time (s)
1	195.4	216.7
0.5	515.6	555.8
0.25	979.6	997.3
0.18	1627.1	1692.9

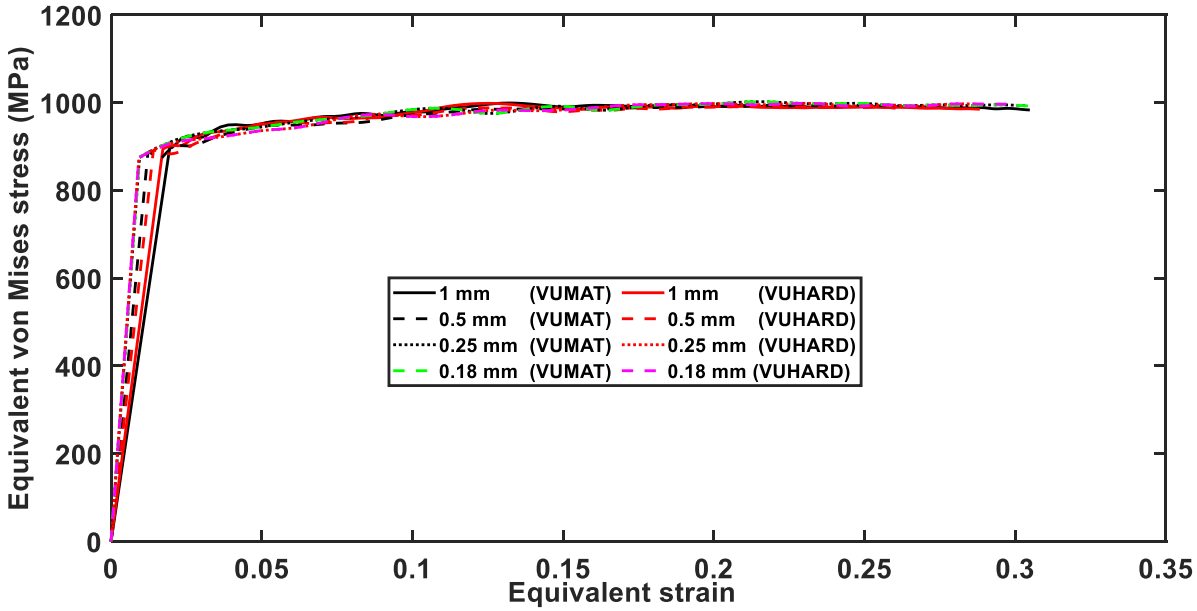

Figure 10-4. Curves of the numerical equivalent von Mises stress against plastic strain at a temperature of 298 K and imposed velocity of 8 m/s for different mesh sizes in numerical simulation of the SHPB test using the VUMAT and VUHARD subroutines developed in the present work.

Like previously observed in Table 9-1 of Chapter 9, the VUMAT subroutine is seen here to require more computation time compared to VUHARD. As expected, the computation time increases as the mesh size decreases. It is seen from Figure 10-4 that the stress-strain curves for various mesh sizes nearly overlap for the better part of the profiles and the curves for the 0.25 mm and 0.18 mm mesh sizes are indistinguishable.

The effect of mesh sizes in Figure 10-4 is seen to be significant at the initiation of equivalent plastic strain, which is consistent with the observations made in Figure 9-14 of Chapter 9. It is seen in Figure 10-4 that the value of initial plastic strain increases with the increase in mesh size. These initial values of strain are very small, thus the difference in computed initial von Mises stress from these strain values is 1.7% between 1 mm and 0.18 mm mesh

© Central University of Technology, Free State

sizes and 0.87% between 0.5 mm and 0.18 mm mesh sizes. Considering the computation time shown in Table 10-1 and the observation made with reference to Figure 10-4, it can be concluded that a 0.25 mm mesh size is sufficient to obtain a good prediction. This is because a smaller mesh size would show a negligible sensitivity improvement of the stress-strain curve and require more computation resources. Therefore, all ensuing simulations to generate stress-strain curves for various forms of DMLS Ti6Al4V(ELI) were conducted with a 0.25mm mesh size in the present study.

Simulations were carried out with striker velocities of 8 m/s, 15 m/s and 25 m/s and at temperatures of 298 K, 473 K and 773 K following the experimental setup used in Chapter 3 for SHPB tests. To ensure sufficient plastic deformation and at the same time avoid excessive model distortion, different total step times of 1000 μs, 300 μs and 200 μs for the velocities of 8 m/s, 15 m/s and 25 m/s respectively, were used. Typical curves of equivalent plastic strain, plastic strain rate and von Mises stress against simulation time at a velocity of 15 m/s is shown in Figure 10-5.

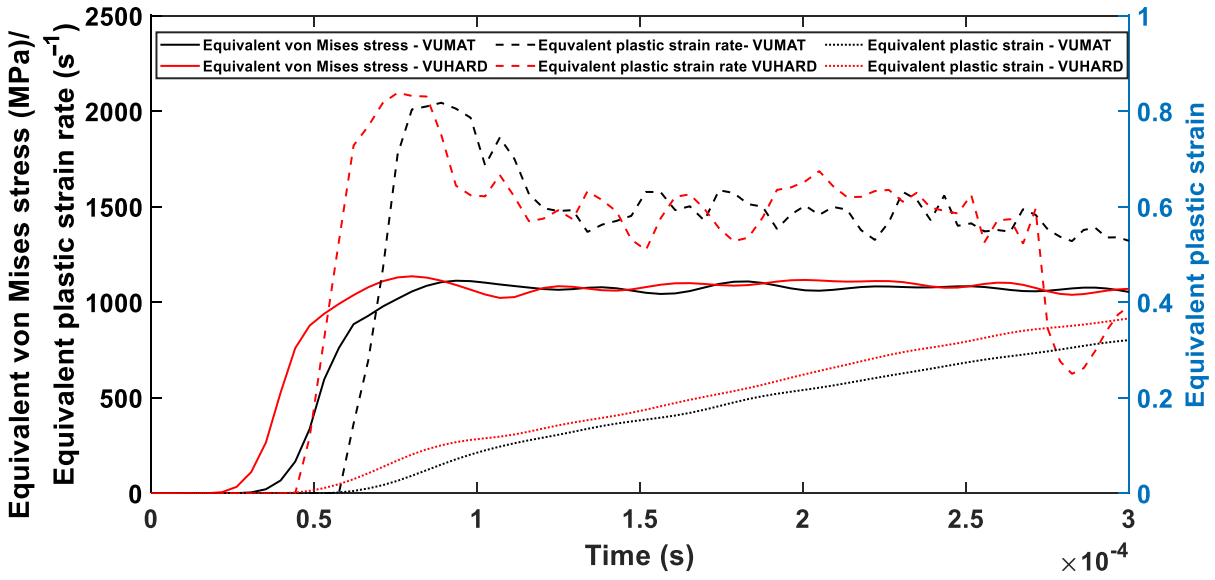

Figure 10-5. The equivalent von Mises stress, plastic strain and strain rate against time history generated during the simulation of the SHPB test using the VUMAT and VUHARD subroutines at imposed striker velocities of 15 m/s and at a temperature of 298 K.

From Figure 10-5, the model is seen to have experienced linearly increasing strains over most of the period of build-up of strain. During this period, the simulation results eventually average at an equivalent plastic strain rate of about 1500 s^{-1}, a value similar to

© Central University of Technology, Free State

that which was recorded during the experimental results reported in Figure 7-1 of Chapter 7. This demonstrates great confidence in the SHPB numerical model setup and the implemented subroutines developed in it in this work. Figures 10-6 to 10-8 show a comparison between the experimental results and results from the numerical model at average plastic strain rates of approximately 750 s^{-1}, 1500 s^{-1} and 2450 s^{-1} and temperatures of 298 K, 473 K and 773 K. The numerically predicted values using these subroutines developed in this thesis and the experimental values at the equivalent strains of 0.1 and 0.2 for same test conditions were next plotted against one another. These plots are presented in Figure 10-6(d) to 10-8(d) for DMLS samples C, D and E and their correlation tested.

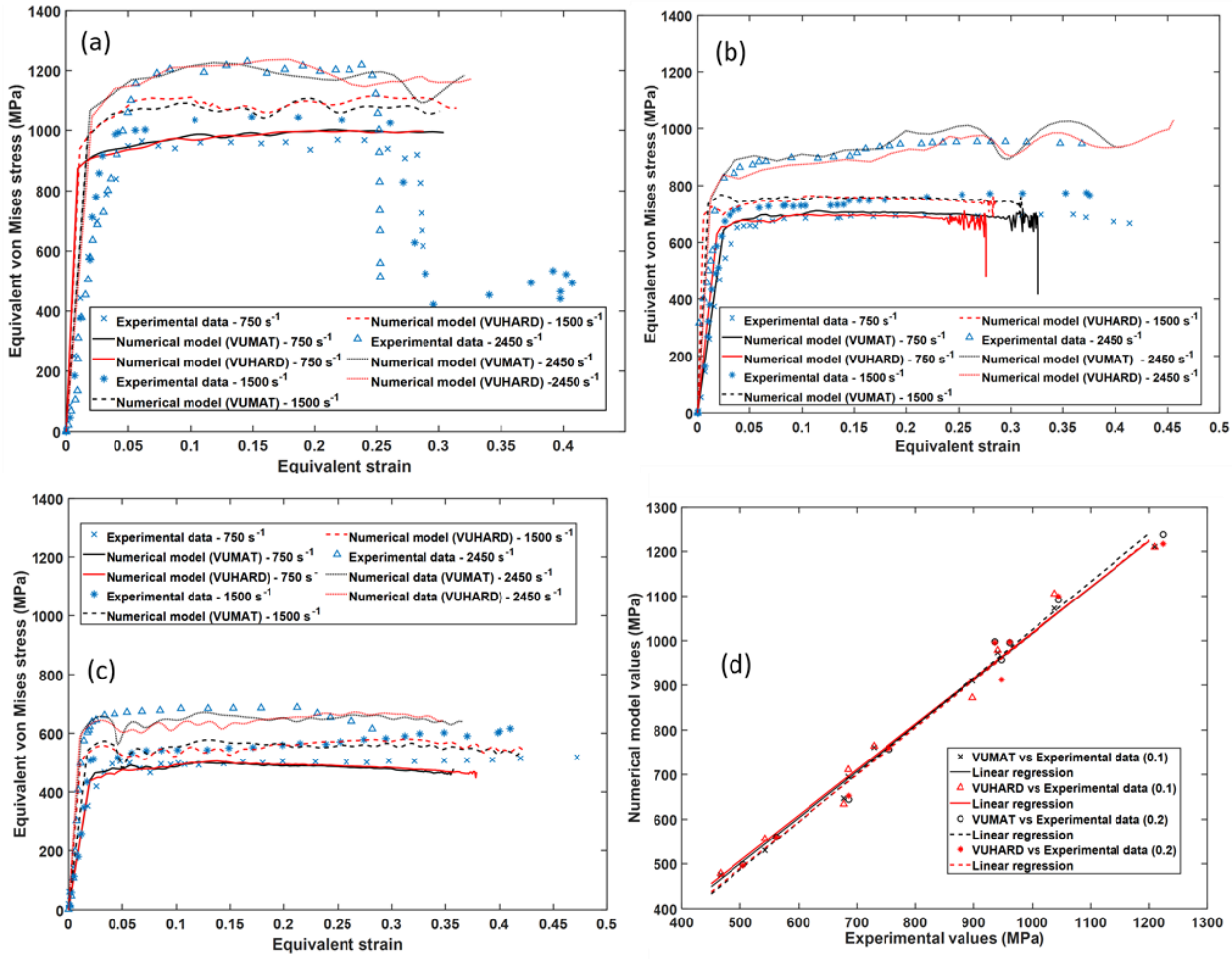

Figure 10-6. Graphs of the numerical model prediction and the experimental results for samples C, at three high strain rates and at temperatures of (a) 298 K, (b) 473 K and (c) 773 K, and correlation between the numerically predicted values and those obtained from experimentation at strains of 0.1 and 0.2 in (d).

© Central University of Technology, Free State

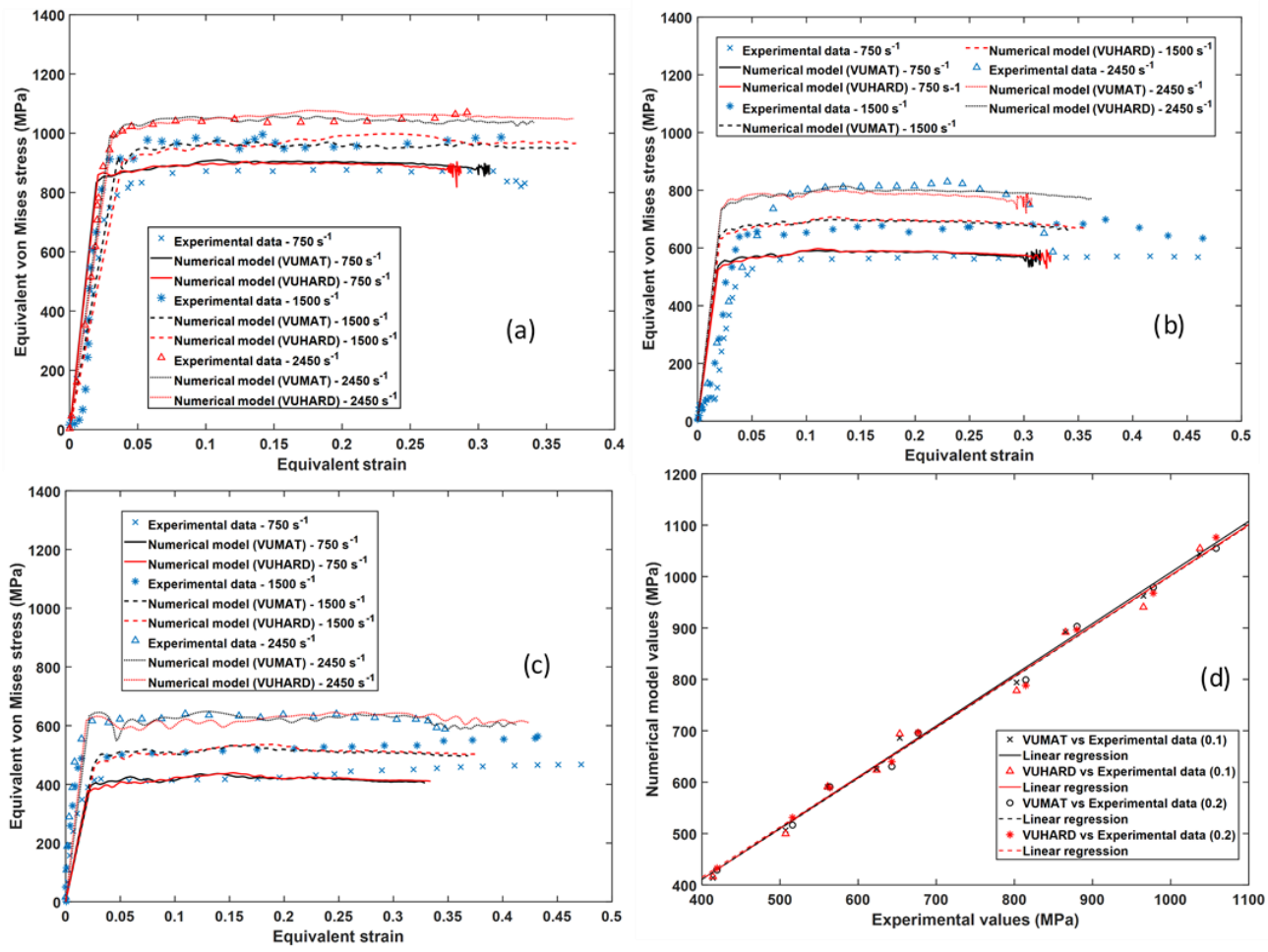

Figure 10-7. Graphs of the numerical model prediction and the experimental results for samples D, at three high strain rates and at temperatures of (a) 298 K, (b) 473 K and (c) 773 K, and correlation between the numerically predicted values and those obtained from experimentation at strains of 0.1 and 0.2 in (d).

© Central University of Technology, Free State

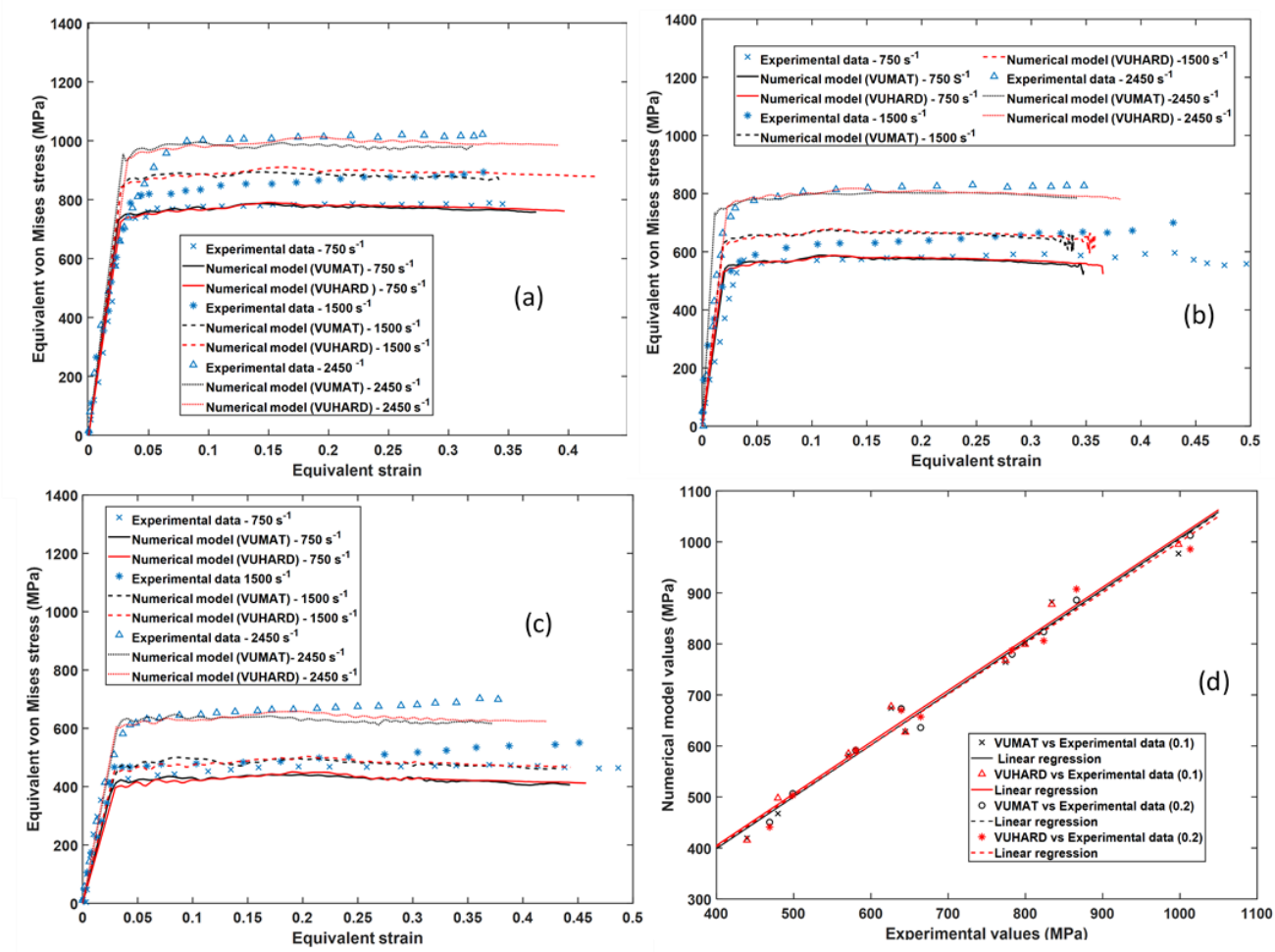

Figure 10-8. Graphs of the numerical model prediction and the experimental results for samples E, at three high strain rates and at temperatures of (a) 298 K, (b) 473 K and (c) 773 K, and correlation between the numerically predicted values and those obtained from experimentation at strains of 0.1 and 0.2 in (d).

The ability of the implemented numerical model in the VUMAT and VUHARD subroutines developed in this study to accurately predict flow stress of DMLS Ti6Al4V(ELI) was assessed from the statistical measures of correlation coefficient (R^2) and absolute average error (δ), based on the plots of Figures 10-6(d) to 10-8(d). These statistical measures were briefly introduced and discussed in section 8.3 of Chapter 8. The correlation coefficients and average absolute errors obtained from these plots are summarised in Table 10-2.

© Central University of Technology, Free State

Table 10-2. Absolute percentage error (δ) and correlation coefficient (R^2) between the experimental and numerical model values of flow stress for various forms of DMLS Ti6Al4V(ELI)

Measure	***R²***				***δ (%)***			
Strain	**0.1**		**0.2**		0.1		0.2	
Samples	VUMAT	VUHARD	VUMAT	VUHARD	VUMAT	VUHARD	VUMAT	VUHARD
C	0.993	0.982	0.978	0.983	2.54	3.73	2.74	3.01
D	0.994	0.987	0.995	0.994	1.77	2.66	1.89	2.44
E	0.978	0.981	0989	0.982	3.18	3.22	1.28	2.77

Considering the correlation coefficient shown in Table 10-2, the implemented microstructural- and dislocation-based model in the VUMAT and VUHARD subroutines shows a very high degree of correlation as the R^2values are above 0.97. It is also observed in this table that the absolute percentage errors between the numerical and the experimental values are all within 4%. These measures of correlation suggest that the numerical model developed in the present study does accurately predict the flow properties of the various microstructures of DMLS Ti6Al4V(ELI) tested here. The numerical model developed in this study is, therefore, suitable for use in designing the dynamic strength of DMLS Ti6Al4V(ELI) by controlling the morphology of its microstructure and the initial dislocation density present in the alloy.

10.3 SIMULATION OF SHPB TESTS USING THE JOHNSON-COOK MODEL IN-BUILT IN ABAQUS

There are numerous constitutive models used to define the isotropic flow properties of metals and metal alloys during plastic deformation. These models were presented and briefly discussed in section 2.8.2 of Chapter 2. Among these many constitutive models for isotropic hardening, only the Johnson-Cook model is in-built in ABAQUS/CAE due to its simplicity of use. For this reason, it is the only alternative model used for carrying out SHPB numerical test simulations here.

The Johnson-Cook model, previously introduced in section 2.7.2.1 of Chapter 2, is a special type of von Mises plasticity model that comprises an empirical form of the strain hardening law, rate dependence and thermal softening. For ease of referencing, the model is reproduced here as Equation 10-1.

© Central University of Technology, Free State

$$\sigma = \left(A + B{\varepsilon_{pl}}^{n}\right)\left(1 + CIn\frac{\dot{\varepsilon}}{\dot{\varepsilon}_0}\right)(1 - (T^*)^m) \qquad 10\text{-}1$$

where

$$T^* = \begin{cases} 0 & for\ T < T_r \\ \frac{T - T_r}{T_m - T_r} & for\ T_r \leq T \leq T_m \\ 1 & for\ T > T_m \end{cases}$$

where the parameters A, B, n, C and m are yield stress, strain hardening factor, strain hardening exponent, dimensionless strain rate hardening coefficient and thermal softening exponent, respectively. The symbol ε_{pl} stands for the equivalent plastic strain and $\dot{\varepsilon_o}$ the reference strain rate at which parameters A, B, n are determined. This is usually a low strain rate where the effects of such strain rate on the plastic flow are negligible. Parameters T, T_m and T_r are working, melting and room temperatures of the material, respectively. Transition temperature is usually defined as a temperature at or below which there is no temperature-dependence of the yield stress and is most of the time taken as room temperature. This is also the temperature used to determine the parameters A, B and n. This model is in-built in ABAQUS for modelling isotropic flow properties of materials and the user needs to provide the values of parameters A, B, n, m, T_m and T_t as part of the metal plasticity material definition. The user also needs to provide the values of parameters C and $\dot{\varepsilon}_o$ when defining Johnson-Cook rate dependence. A typical properties module for the J-C model with rate dependence is shown in Figure 10-9.

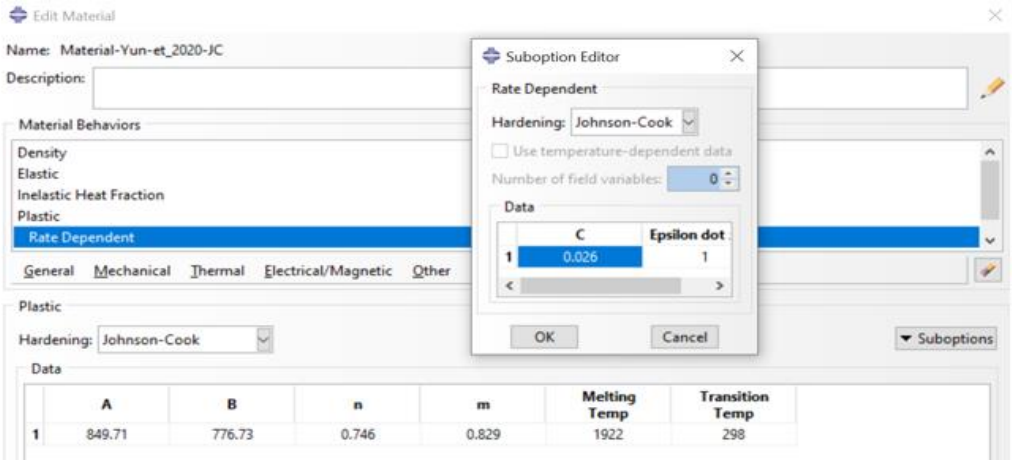

Figure 10-9. A typical material properties module for the J-C model in-built in ABAQUS.

© Central University of Technology, Free State

The J-C plasticity model is also used for high-strain-rate transient dynamic applications, where the temperature change (ΔT) in the model is generally computed internally by assuming adiabatic conditions using the following expression (ABAQUS 2020):

$$\Delta T = \frac{\beta}{\rho \mathrm{C}} \int \sigma(\varepsilon) \delta\varepsilon \qquad 10\text{-}2$$

Here the parameters β, ρ and C are inelastic heat fraction (% of plastic work converted into heat and is normally taken as 0.9 for metal), density and specific heat capacity, respectively. These three parameters must be provided for a simulation step that includes adiabatic heating effects.

The 3D finite element model of the SHPB test discussed in the preceding section, that was used to investigate the high-strain rate deformation behaviour of Ti6Al4V(ELI) samples, is now modelled using the set of J-C parameters derived from literature that is shown in Table 10-3. Besides these parameters, the specific heat, density, and inelastic heat fraction values of 560 J/Kg.K, 4420 Kg/m^3 and 0.9 were used (ABAQUS 2020, Material data 2021) since the simulation step was taken to include adiabatic heating effects. Interestingly, the sets of parameters in Table 10-3 differ considerably even though they describe the behaviour of the same material, Ti6Al4V(ELI), though with different microstructures in certain cases.

Table 10-3. A summary of J-C model parameters used to model the SHPB Ti6Al4V(ELI) samples

JC model parameter	Microstructure	α-lath size	A(MPa)	B(MPa)	*n*	C	*m*
Lee and Lin (1997a)	[-]	[-]	782.7	498.4	0.28	0.028	1
Lee and Lin (1997b)	[-]	[-]	724.7	683.1	0.47	0.035	1
Xin *et al.* (2018)	[-]	[-]	920	380	0.578	0.042	0.633
Yu *et al.* (2020)	Lamellar	0.5 μm	984.32	601.1	0.512	0.025	0.987
Yu *et al.* (2020)	Lamellar	2.0 μm	829.30	524.32	0.621	0.024	0.715
Yu *et al.* (2020)	Bimodal	0.4 μm	907.03	752.97	0.502	0.20	0.904
Yu *et al.* (2020)	Bimodal	2.1 μm	849.71	776.73	0.742	0.026	0.829

© Central University of Technology, Free State

As was the case for the numerical model developed in this work, three different striker velocities of 8 m/s, 15 m/s and 25 m/s, and a temperature of 298 K were used to perform simulations and determine the equivalent von Mises stress and strain reported for the model at each striker velocity. Figures 10-10 to 10-12 present the plots of the results obtained using different sets of J-C model parameters in Table 10-3 together with those from the numerical model developed in this work, using the VUMAT and VUHARD subroutines developed here.

It is worth noting that the shape of the flow stress curves (relationship between flow stress and plastic strain) seen in Figures 10-10 to 10-12 for the J-C model is established empirically by isolating effects of temperature and strain rate. The strain rate $(1 + \mathrm{C}In\frac{\dot{\varepsilon}}{\dot{\varepsilon}_0})$ and temperature $(1 - (\mathrm{T}^*)^{\mathrm{m}})$ parts are functions that scale the flow stress without necessarily influencing the shape of the flow stress curve. This implies that the J-C model is not adequate to represent flow characteristics of a material with the existence of recovery and recrystallisation that allow stress to saturate as strain increases, as seen for samples C, D and E in this study. A similar observation was reported in the work of Yingnan *et al.* (2017).

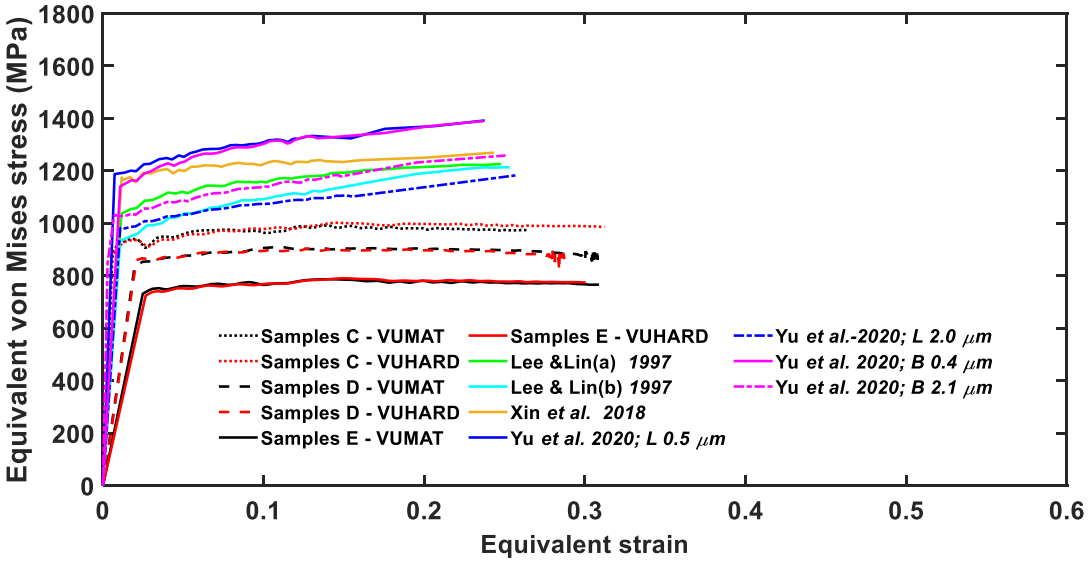

Figure 10-10. Results of SHPB test simulation at an impact velocity of 8 m/s and temperature of 298 K with the test samples modelled using various sets of J-C model parameters (Note B and L stand for bimodal and lamellar microstructures, respectively) and the numerical models developed in the present work.

© Central University of Technology, Free State

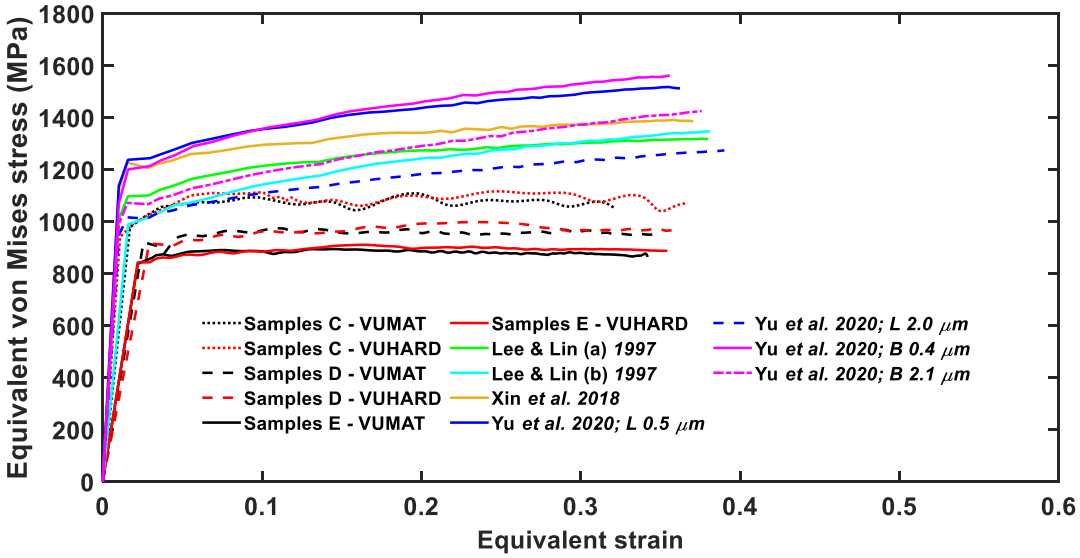

Figure 10-11. Results of SHPB test simulation at an impact velocity of 15 m/s and temperature of 298 K with the test samples modelled using various sets of J-C model parameters (Note B and L stand for bimodal and lamellar microstructures, respectively) and the numerical models developed in the present work.

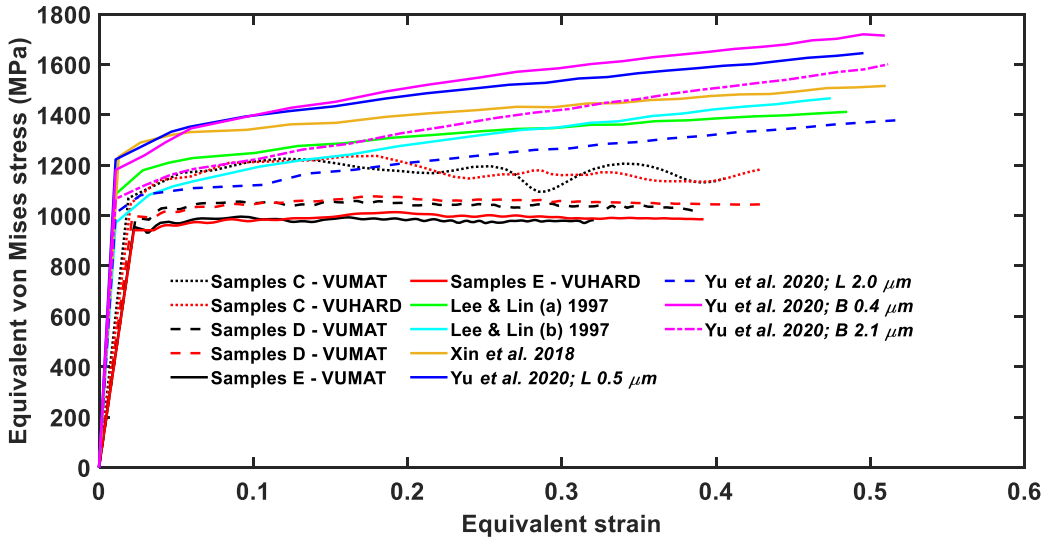

Figure 10-12. Results of SHPB test simulation at an impact velocity of 25 m/s and temperature of 298 K with the test samples modelled using various sets of J-C model parameters (Note B and L stand for bimodal and lamellar microstructures, respectively) and the numerical models developed in the present work.

© Central University of Technology, Free State

The Taylor strain hardening model that allows for strain hardening and dynamic recovery as strain increases through calibrated parameters h and k_2 was used in the model developed in the present research. This explains the flow stress saturation observed in samples C, D and E as opposed to continuous strain hardening for the J-C model curves seen in Figures 10-10 to 10-12.

It is very clear from these three figures that each set of J-C model parameters gives a different flow stress curve. The microstructural details of Ti6Al4V(ELI) from the work of Lee and Lin (1997a), Lee and Lin (1997b) and Xin *et al.* (2018) are not inserted in Table 10-3 as they are missing from these references. However, specific microstructural information of this alloy are available from the work of Yun *et al.* (2020). Each of these microstructures show different stress-strain curves in Figures 10-10 to 10-12. For instance, lamellar and bimodal microstructures with average α-lath grain sizes of 0.5 μm and 0.4 μm, respectively, show higher values of flow stress in comparison with similar microstructures with average α-lath grain sizes of 2.0 μm and 2.1 μm, respectively. The lamellar microstructure with an average α-lath grain size of 2.0 μm shows low values of flow stress in comparison to the bimodal microstructure with an average α-lath grain size slightly large at 2.1 μm. The initial values of flow stress at lower strain for the lamellar microstructure, with a 0.5 μm α-lath average grain size, are higher than those for the bimodal microstructure with a 0.4 μm α-lath average grain size. At higher strains, the lamellar microstructure with a 0.5 μm α-lath average grain size shows lower values of flow stress than those for the bimodal microstructure with a 0.4 μm α-lath average grain size, especially at the higher impact velocities of 15 m/s and 25 m/s in Figures 10-11 and 10-12.

As seen in Figures 10-11 and 10-12, at low values of strain and at striker velocities of 15 m/s and 25 m/s, the flow stress curves of samples type C (an average α-lath grain size of 2.5 μm) from the two subroutines developed here are close to those of Lee and Lin (1997b) and Yu *et.al* (2020) for lamellar microstructure (average α-lath grain size of 2.0 μm). Whereas the flow stress curves of samples D and E, with much larger average α-lath grain sizes of 6 μm and 9 μm, respectively, are much lower than the rest, as seen in Figures 10-11 to 10-12.

The preceding discussion suggests no single set of J-C model parameters can be adequate in accurately describing the flow properties of any given microstructure of Ti6Al4V(ELI). This is

© Central University of Technology, Free State

mainly due to the fact that each microstructure is related with a different set of J-C model parameters. In contrast, the microstructure- and dislocation-based constitutive numerical model developed, refined and validated in the present study can be used to predict the flow properties of alloys, such as Ti6Al4V(ELI), that show a wide range of microstructures. The model developed in the present work offers a few advantages including:

- The critical microstructural parameters of initial dislocation density and grain size are part of the few input parameters that are needed to adequately describe the flow stress.
- Both strain hardening and dynamic recovery that occur for deformation at high temperatures and high strain rates are articulated in this model through calibrated parameters h and k_2. These parameters are insensitive to the different microstructures of samples C, D and E as opposed to the case of the J-C model where its many parameters vary with microstructure.
- There are only four input parameters that are influenced by microstructure in the numerical model developed here. These include initial dislocation density and grain size which are determined directly from the microstructure, as well as two viscous drag stress-fitting parameters (χ and ζ) determined empirically from the experimental data. This is in sharp contrast to the five microstructure-sensitive parameters of the J-C model that are empirically determined from the experimental data.

10.3 SUMMARY

Three dimensional SHPB numerical tests were simulated in this chapter with test specimens modelled here using the VUHARD and VUMAT subroutines developed in the present study. The numerical results from this simulation and those obtained from experimental testing at the high strain rates of 750 s^{-1}, 1500 s^{-1} and 2450 s^{-1} and at temperatures of 298 K, 473 K and 773 K were compared for sample types C, D and E. The numerical and experimental results showed a high degree of correlation with correlation coefficients (R^2) above 0.97. The absolute percentage errors between the numerical and experimental results were for both subroutines and for all samples below 4%, which is acceptably low. The SHPB test Ti6Al4V(ELI) numerical samples modelled here were also modelled with various sets of J-C

© Central University of Technology, Free State

model parameters available in literature. The results for this simulation displayed a wide variety of stress-strain curves, with each set of parameters showing a different curve profile. This was ascribed to the wide range of microstructures associated with Ti6Al4V(ELI) alloy, which limits the utility of a single set of J-C model parameters to describe and simulate the flow properties of various forms of the alloy. The developed numerical model has advantages over the J-C model in that unlike the J-C model, the critical parameters of microstructures, such as grain size and dislocation density that influence the flow stress, form part of the numerical model inputs. Furthermore, the model gives good predictions of the strain hardening and dynamic recovery processes that prevail for deformations at high strain rates and high temperature, which is not the case for the J-C model.

© Central University of Technology, Free State

10.4 REFERENCES

1. ABAQUS.2020. Documentation.
2. Gray, G.T. 2002. Classic Split-Hopkinson Pressure Bar Testing, Materials Park, OH: ASM International, pp.462–476.
   https://help.3ds.com/2020/English/DSSIMULIA_Established/SIMACAEMATRefMap/simamat-c-johnsoncook.htm?ContextScope=all&id=295f6fbf2efc4b65921ffefab664d8bc#simamat-c-johnsoncook-t-HeatGenerationByPlasticWork-sma-topic7. *(Accessed on 24th November 2020)*
3. Lee, W.S., Lin, C.F. 1997a. High-temperature deformation behaviour of Ti6Al4V alloy evaluated by high strain-rate compression tests. *Journal of Materials Processing Technology,* 75, pp.127–136.
4. Lee, W.S., Lin, C.F. 1997b. Plastic deformation and fracture behaviour of Ti6Al4V alloy loaded with high strain rate under various temperatures. *Materials Science and Engineering* A, 241, pp.48–59.
5. Material Properties Data. 2021. Titanium Ti6Al4V (ELI) (Grade 23), Annealed. http://www.matweb.com/search/datasheet.aspx?matguid=c4297fb8f1094da189732c224e3be1ed&ckck=1 (accessed on 23rd Feb 2021).
6. Xin, H., Zhanqiang, L., Bing, W., Woyun, L., Xiaoliang Liang., Yang H. 2018. Stress-strain curves and modified material constitutive model for Ti6Al4V(ELI) over the wide ranges of strain rate and temperature. *Materials, 11, 938*. https://doi:10.3390/ma11060938
7. Yingnan, X., Zhang, C., Liwen, Z., Wenfei, S., Qianhong, X. 2017. A comparative study of constitutive models for flow stress behaviour of medium carbon Cr-Ni-Mo alloyed steel at elevated temperature. Journal of Material Research, 32(20), pp.3875–3884. https://doi.org/10.1557/jmr.2017.356
8. Yu, R., Yuantong, M., Qiyun, P. 2020. Effect of microstructure on the Johnson-Cook constitutive model parameters of Ti6Al4V alloy. *Journal of Physics: Conference Series, 1637, 012018. https://*doi:10.1088/1742-6596/1637/1/012018

© Central University of Technology, Free State

CHAPTER 11 — CONCLUSIONS AND RECOMMENDATIONS

11.1 INTRODUCTION

In this research study, a microstructure- and dislocation-sensitive constitutive model was developed from knowledge garnered in existing literature to describe the flow properties of various microstructures of DMLS Ti6Al4V(ELI) at high strain rate. Firstly, a clear understanding of the microstructures of the DMLS Ti6Al4V(ELI) was required to determine critical microstructural parameters of the model that influence the mechanical properties of this alloy. Therefore, characterisation of various microstructures of DMLS Ti6Al4V(ELI) achieved by heat treatment was carried out at the onset to determine these parameters. The flow stress curves of various microstructures of DMLS Ti6Al4V(ELI) were also required to calibrate the developed constitutive relations. The SHPB test devised for high-strain experimentation was used to generate high-strain-rate data and therefore, facilitate study of the deformation properties of three different categories of DMLS Ti6AL4V(ELI) samples. The high-strain-rate flow stress curves obtained thus were used to calibrate and validate the constitutive model developed here. The constitutive models developed were later implemented into finite element (FE) code as ABAQUS user subroutines and tested successfully for their predictive accuracy. Important conclusions and recommendations that were arrived at in various chapters of this thesis are now discussed briefly.

11.2 CONCLUSIONS ARISING IN VARIOUS CHAPTERS

The conclusions arising from the various chapters of the present work are best summarised in the four sections now presented.

11.2.1 Microstructure-sensitive constitutive model (Chapter 4)

The review of the various mechanisms that control yielding and plastic deformation of Ti6Al4V showed that the α-lath thickness and initial dislocation density in this alloy play an important role in determining its mechanical properties. Therefore, to explicitly describe the flow stress of this alloy, the constitutive relations that articulate the effects of microstructure by introducing the average grain α-laths thickness and dislocation density as model input parameters should be used. In addition, the mechanical threshold stress model

© Central University of Technology, Free State

(MTS) formulation and Hall-Petch relation to describe yielding, as well as the Taylor's hardening law are also necessary to completely describe the flow stress of the DMLS Ti6Al4V(ELI) alloy at high-strain rate and temperature.

11.2.2 Microstructural characterisation of various forms of DMLS Ti6Al4V(ELI) alloy (Chapters 5 & 6)

The microstructure of the as-built (samples A) and that of stress-relieving (samples B) parts were determined to consist of columnar prior-β grain with the interior filled with α′-acicular martensite grains. The size of these fine α′-grains were estimated to be between 0.5 μm and 2.5 μm. There was no β-phase detected in the two microstructures using both EBSD and XRD techniques. Even though there was no difference in microstructure detected, the hardness and dislocation density decreased by 5% and 75%, respectively upon stress-relieving heat treatment. Also, for the same EBSD scanned area, the maximum intensity texture of α′-phase, as determined from pole figures, increased from 4.9 to 7.3 after this heat-treatment plan.

Upon stress relieving followed by heat treatment at 800 °C (samples C), the α′-acicular martensite transformed to an equilibrium mixture of α and β-phase with the percentage of β-phase estimated as 1.1% and 3.6% using EBSD and XRD methods, respectively. The average size of α-laths remained at 2.5 μm, while both micro-hardness and dislocation density declined further by 8% and 85%, respectively. The maximum intensity texture of α′/α-phase further increased to 9.2 from 7.3 recorded for samples B.

The heat treatment performed at 940 °C (samples D) resulted in a coarse bi-phasic microstructure with average α-lath thickness increasing further to 6.0 μm. The β-phase also increased to 5.1% and 6.4%, as estimated using EBSD and XRD methods, respectively. Further decrease in micro-hardness and dislocation density was noted at this heat-treatment regime, with these samples recording the lowest values for these two variables as compared to the rest of the samples. The maximum texture intensity of the α-phase further increased to 10.0.

Heat treatment above the α→β transformation temperature (samples E) resulted in decomposition of prior-β grains into equiaxed and semi-equiaxed prior-β grains. The α-laths

© Central University of Technology, Free State

inside these prior-β grains formed the typical Widmanstätten structure. This type of structure consisted of α-colonies with each of them having α-laths with similar crystallographic orientation, as observed by EBSD. The average thickness of the α-laths in these colonies also increased to 9 μm. Thick and continuous grain boundary α was also observed at the prior β boundaries. The percentage of β-phase in this microstructure was estimated as 2.7% and 6.6% by the EBSD and XRD methods, respectively. The micro-hardness and the dislocation density in these samples were slightly higher compared to the values recorded for samples D that were heat-treated slightly below the α→β transformation temperatures. Significant improvement of the intensity of texture from the pole figures was noted in these samples, with the highest MUD being 24.

Different percentage fractions of β-phase were recorded using the EBSD and XRD methods for the same material, which was ascribed to the inhomogeneous distribution of the β-phase in these microstructures. The EBSD results were based on a micro-grid area of 980 μm x 735 μm, while the XRD scans were conducted on the bulk surface of the samples. Thus, the results from XRD were taken to be a better representation of the bulk microstructure of each group of samples.

It was noted from discrete pole figures used to study the orientation relationship between the α/α' variants, which formed within the prior-β grains and the parent-β phase, that six different misorientations of α/α' phase formed inside each parent-β phase, where (0001) planes of the α/α'-phase were clustered around the six $\{110\}$ planes of the parent-β phase. It was further noted that even if the (0001) poles were clustered around (110) poles there was a significant spread in orientations between the two phases in samples A, B, C and D. This was an indication of the deviations from the known BOR in the Ti6Al4V(ELI) alloy. However, the spread in BOR in samples E that were heat-treated above the α→β transformation temperature drastically reduced and the α-(0001) and β-(110) poles were perfectly superimposed.

11.2.3 High-strain-rate testing and calibration of constitutive model (Chapters 7 & 8)

The flow stress was observed from SHPB experiments to increase with increasing strain rate, whereas it decreased with increase in test temperature in the heat-treated samples C, D and E of DMLS Ti6Al4V(ELI). The three different samples, however, yielded at different

© Central University of Technology, Free State

levels of stress for the same imposed strain rates and temperatures. Samples type C and E showed the highest and lowest dynamic yield strength, respectively, at any given strain rate and temperature. The strain rate sensitivity was found to be less at low temperature but increased as the test temperature rose for all cases of samples tested. This was mainly attributed to an increase in dislocation activity at high temperatures. Samples C and D showed the lowest and the highest values of strain rate sensitivity parameter (m), respectively.

A typical deformed surface at high strain rate of these three groups of samples consisted of ASBs and elongated cracks propagating within these ASBs. The microstructure within these shear bands was found to be different from that of the bulk material for the three groups of samples. This suggested that microstructural changes occurred during the process of formation of these ASBs. The failure of all these samples at high strain rate was facilitated by the formation of ASBs, which formed favourable regions for growth of microvoids and initiation, growth, and propagation of cracks. The thickness of these ASBs was found to vary for different samples and at different testing conditions of strain rate and temperature. The thickness increased significantly with increase in temperature in an almost linear relationship. It also increased with strain rate, however, the increase between the strain rates of 750 s^{-1} and 1500 s^{-1} was not much significant, since the error bars were found to be overlapping. A significant difference in the width of ASBs was noted for different samples. Samples C and D recorded the lowest and the highest values of the width of ASBs, respectively. The difference in the thickness of ASBs for different samples was ascribed to variation in the micro-hardness among these various forms of DMLS Ti6Al4V(ELI) alloy.

The investigation of fracture surfaces of failed samples showed elongated dimples on the surfaces in all conditions of testing for the three groups of samples. The extent of elongation of these dimples was affected by temperature, where at 200 °C and 500 °C the dimples were more elongated than at 25 °C.

It is necessary to introduce a viscous drag stress component into the developed microstructure- and dislocation-based model developed here to take care of the upturn of flow stress at high strain rate. The accuracy of the microstructure- and dislocation-sensitive model developed here for predicting of flow stress was high with high values of correlation

© Central University of Technology, Free State

coefficient R^2 very close to 1 and absolute errors δ less than 6.0% for the model and experimental values.

11.2.4. Implementation, verification, and validation of constitutive model (Chapters 9 & 10)

The results from preliminary simulation of single element and multiple elements models at three loading conditions and two different temperatures, using VUHARD and VUMAT subroutines developed here, showed excellent correlation with the analytical solutions at the same conditions.

The comparison between the experimental and numerical results obtained here showed excellent correlation with the correlation coefficient and average absolute percentage errors at two selected values of equivalent strain of $>$ 0.97 and $<$ 4%, respectively. Different sets of J-C model were further used to model the SHPB test specimens and numerical test simulated at similar conditions as those of DMLS Ti6Al4V(ELI) samples. The model implemented into FE code ABAQUS/Explicit in this thesis offers advantage in that the average initial dislocation density and grain size, which greatly influence the properties of this alloy, together with two viscous drag curve-fitting parameters can be used to adequately describe the flow stress of various microstructures of DMLS Ti6Al4V(ELI). This is in contrast to the five parameters that are required to be determined for each microstructure in the J-C model.

11.3 RECOMMENDATIONS FOR FUTURE RESEARCH

As only the high strain rate properties of various forms of DMLS Ti6Al4V(ELI) were studied in this work, it is necessary for future research to focus on the low to moderate strain rate properties of the alloy, over a wide range of temperatures. It was noted in section 7.3.1 of Chapter 7 that direct evidence of dynamic recovery and recrystallisation could not be pointed out from the SEI images. Future work should focus on using more advanced microstructural characterisation techniques, such as EBSD and TEM, to study the microstructure along the ASBs. The type, size-level and spatial distribution of such defects emerging along the ASBs, due to possible dynamic recrystallisation, should also be studied using TEM.

© Central University of Technology, Free State

The performance of the VUHARD and VUMAT subroutines should also be tested in other complex dynamic simulations such as Taylor impact test and blast loading of plates. It was shown in section 9.4.2 of Chapter 9 that the flow stress curves saturated as the values of equivalent plastic strain increased, since the implemented model was not developed to incorporate unloading and damage evolution. The microstructure-sensitive model should be extended to include some form of failure criterion or damage model. The utility of the constitutive relations implemented for high-strain-rate numerical simulations in the present study should be extended to other metals and alloys, such as steel and aluminium, that show wide ranges of microstructures for varying heat treatment cycles.

© Central University of Technology, Free State

APPENDICES

APPENDIX A – THE IMPLICIT INTEGRATION SCHEME TO COMPUTE FOR EQUIVALENT PLASTIC STRAIN (ABAQUS 2020)

The deviatoric stress during plastic deformation can be expressed as (ABAQUS 2020):

$$S_{ij}^{(2)} = S_{ij}^{(1)} + 2\mu\Delta\varepsilon_{ij}^{e} = S_{ij}^{(1)} + 2\mu\left(\Delta\varepsilon_{kl} - \Delta\varepsilon_{kl}^{p}\right) = S_{ij}^{t} - 2\mu\Delta\varepsilon_{kl}^{p} \qquad A\text{-}1$$

where $S_{ij}^{(2)}$ and $S_{ij}^{(1)}$ are the new and old deviatoric stress, $\Delta\varepsilon_{ij}^{e}$, $\Delta\varepsilon_{kl}$ and $\Delta\varepsilon_{kl}^{p}$ are increment in deviatoric elastic strain, equivalent strain and equivalent plastic strain, respectively. S_{ij}^{t} is the trial stress and μ the shear modulus. The return stress from Equation A-1 is:

$$S_{ij}^{r} = 2\mu\Delta\varepsilon_{kl}^{p} \qquad A\text{-}2$$

To evaluate the value of the return stress S_{ij}^{r} and therefore deviatoric stress $S_{ij}^{(2)}$, the increment of the plastic component $\Delta\varepsilon_{kl}^{p}$ and therefore increment in equivalent plastic strain $\Delta\epsilon_{e}^{p}$ must be determined. Thus,

$$\Delta\varepsilon_{kl}^{p} = \left(\frac{\partial f}{\partial\sigma_{kl}}\right)\partial\epsilon^{p} = \frac{3}{2}\frac{S_{ij}^{(2)}}{q^{(2)}}\Delta\epsilon_{e}^{p} \qquad A\text{-}3$$

where $\partial\epsilon^{p}$ is the equivalent plastic strain increment and $q^{(2)}$ the new equivalent von Mises stress. Equations A-1 and A-3 can be combined into:

$$S_{ij}^{(2)} = S_{ij}^{t} - 2\mu\frac{3}{2}\frac{S_{ij}^{(2)}}{q^{(2)}}\Delta\epsilon_{e}^{p} = S_{ij}^{t} - 3\mu\frac{S_{ij}^{(2)}}{q^{(2)}}\Delta\epsilon_{e}^{p} \qquad A\text{-}4$$

Thus, the new deviatoric stress is given by:

$$S_{ij}^{(2)} = \frac{S_{ij}^{t}}{1+3\mu\frac{\partial\epsilon^{p}}{q^{(2)}}} \qquad A\text{-}5$$

The new equivalent von Mises stress can be obtained from Equation A-5, thus making Equation 2-44 of Chapter 2:

$$q^{(2)} = \sqrt{\frac{3}{2}S_{ij}^{2}S_{ij}^{2}} = \frac{\sqrt{\frac{3}{2}S_{ij}^{t}S_{ij}^{t}}}{1+3\mu\frac{\Delta\epsilon_{e}^{p}}{q^{(2)}}} = \frac{\sigma_{e}^{t}}{1+3\mu\frac{\Delta\epsilon_{e}^{p}}{q^{(2)}}} \qquad A\text{-}6$$

© Central University of Technology, Free State

Since at yielding surface $q^{(2)} = \sigma_y^{(2)}$ (where $\sigma_y^{(2)}$ is the new stress computed from constitutive equation) then:

$$\sigma_y^{(2)} = \sigma_e^t - 3\mu\Delta\epsilon_e^p \quad or \quad \sigma_e^t - 3\mu\Delta\epsilon_e^p - \sigma_y^{(2)} = 0 \qquad A\text{-}7$$

Equation A-7 is a non-linear yield function and the increment of plastic strain $\partial\epsilon^{\mathrm{p}}$ between states 1(old state) and 2 (new state) must be computed. The iteration method of finding solutions of non–linear functions, which were discussed in section 2.8 of Chapter 2, can be used to do this. Alternatively, a non-iteration method can be used to solve for $\partial\epsilon^{\mathrm{p}}$ (ABAQUS 2020) if the plastic flow stress occurring between the old and new state can be considered. The flow stress at new state can be expressed explicitly using the flow stress at old state as:

$$\sigma_y^{(2)} = \sigma_y^{(1)} + \boldsymbol{H}\Delta\epsilon_e^p \qquad A\text{-}8$$

where $\boldsymbol{H}$ denotes the rate of change in flow stress with plastic strain. Equations A-7 and A-8 can be combined to solve for $\partial\epsilon^p$, new deviatoric stress and stress tensor as:

$$\Delta\epsilon_e^p = \frac{\sigma_e^t - \sigma_y^{(1)}}{3\mu + \boldsymbol{H}} \qquad A\text{-}9$$

$$factor = \frac{\sigma_y^{(2)}}{\sigma_e^t} = \frac{\sigma_y^{(2)}}{\left(\sigma_y^{(2)} + 3\mu\Delta\epsilon_e^p\right)} \qquad A\text{-}10$$

$$S_{ij}^{new} = factor\ x\ S_{ij}^t \qquad A\text{-}11$$

$$\sigma_{ij}^{new} = S_{ij}^{new} + \sigma_m \qquad A\text{-}12$$

APPENDIX B – THEORY OF ONE-WAVE PROPAGATION IN SHPB TEST (GRAY 2000)

This section of the appendices presents the basic theory of the SHPB experiment. The derivation of the equations of stress, strain and strain rate are based on the theory of propagation of one-dimensional (1-D) elastic wave propagation in materials. In doing this, an SHPB experimental set-up consisting of a specimen sandwiched between two cylindrical pressure bars (as incident and transmitter bars) is considered.

One Dimension (1-D) Wave Propagation in an Elastic Material

In cases of 1-D wave propagation along the x-direction in a material that is represented by the relationship, $(\frac{\partial u}{\partial x})$, the stress induced in the material can be expressed as:

© Central University of Technology, Free State

$$\sigma = E\frac{\partial u}{\partial x} \qquad \textit{B-1}$$

where, the symbols E and u represent for the Young's modulus of the material and the displacement at a specific point in the material along the x-direction.

The equation for the motion of stress waves in 1-D in a particular direction (in this case the x-direction) can be expressed as:

$$\frac{\partial \sigma}{\partial x} = \rho\frac{\partial^2 u}{\partial t^2} \qquad \textit{B-2}$$

where symbol ρ stands for density of the material. The results of combining Equations B-1 and B-2 gives rise to the following equation:

$$E\frac{\partial^2 u}{\partial x^2} = \rho\frac{\partial^2 u}{\partial t^2} \qquad \textit{B-3}$$

The equation of motion in the bar for a wave of infinite wavelength along the x-direction, is given by:

$$C_o^2\frac{\partial^2 u}{\partial x^2} = \frac{\partial^2 u}{\partial t^2} \qquad \textit{B-4}$$

The symbol C_o in this equation represents the velocity of the propagating wave. Comparing Equations B-3 and B-4 allows the parameter C_o to be expressed as:

$$C_o = \sqrt{\frac{E}{\rho}} \qquad \textit{B-5}$$

D' Alembert's solution of the wave equation, Equation B-4, is given as:

$$u(x,t) = f(x - C_o t) + g(x + C_o t) \qquad \textit{B-6}$$

Functions f and g are arbitrary, but they are dependent on the initial conditions. The functions $f(x - C_o t)$ and $g(x + C_o t)$ correspond to waves travelling in negative and positive x-directions, respectively. Incident compressive and tensile pulses propagating in an elastic bar in the positive and negative x-directions, respectively, are represented as shown in Figure B-1.

© Central University of Technology, Free State

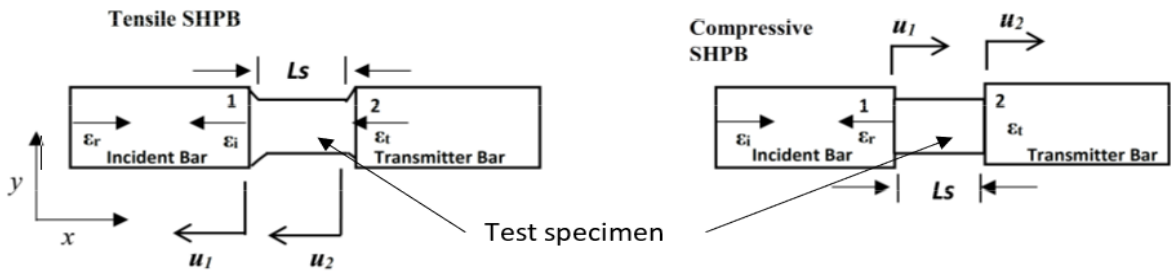

Figure B-1. Schematic diagram illustrating the tensile and compressive SHPB set up.

The general solution of the 1-D wave equation is of the form:

$$u = g(x - C_o t) \qquad \textit{B-7}$$

In this equation symbols t and C_o represent time and the longitudinal wave velocity. The strain (ϵ) in this is obtained by differentiating Equation B-7 with respect to x, thus:

$$\epsilon = \frac{\partial u}{\partial x} = g' \qquad \textit{B-8}$$

Similarly, the velocity is obtained by differentiating Equation B-7 with respect to the time as follows:

$$v = \frac{\partial u}{\partial t} = -C_o g' \qquad \textit{B-9}$$

The velocity can further be expressed as a function of the longitudinal wave velocity and strain, thus:

$$v = \frac{\partial u}{\partial t} = -C_o f' = -C_o \frac{\partial u}{\partial x} \qquad \textit{B-10}$$

It is evident from Equation B-10 that:

$$v = -C_0 \varepsilon \qquad \textit{B-11}$$

The 1-D longitudinal wave velocity in elastic materials is known to be dependent on the elastic modulus (E) and density (ρ) of the pressure bars and can be expressed as:

$$C_o = \sqrt{\frac{E}{\rho}} \qquad \therefore \qquad E = C_0^2 \rho \qquad \textit{B-12}$$

Equation B-11 and B-12, and the equation of linear elasticity, $\sigma = \varepsilon E$ can further be combined to give rise to:

© Central University of Technology, Free State

$$v = -C_o \frac{\sigma}{E} \quad \therefore \quad v = -\frac{\sigma}{C_o \rho} \implies \sigma = -\rho C_o v \qquad \textit{B-13}$$

The incident pulse is in the negative x-direction as shown by the negative sign in Equation B-13, to denote a tensile loading acting on the test specimen. The incident wave in the case of compressive loading travels in the opposite direction and therefore, Equation B-13 becomes:

$$\sigma = \rho C_o v \qquad \textit{B-14}$$

The velocity (v_{s1}) at interface labelled 1 in Figure B-1 can be expressed as the sum of the velocity due to the incident pulse (v_i) and the reflected pulse (v_r) thus:

$$v_{s1} = v_i + v_r \qquad \textit{B-15}$$

If compressive stresses are acting on the specimen, then velocity (v_i) is expressed as:

$$v_i = C_o \varepsilon_i \qquad \textit{B-16}$$

In this case the reflected wave in the input bar travels in the opposite direction, thus velocity (v_r) is expressed as:

$$v_r = -C_o \varepsilon_r \qquad \textit{B-17}$$

Equations B-16 and B-17 are substituted into Equation B-15 to give:

$$v_{s1} = -C_0(\varepsilon_r - \varepsilon_i) \qquad \textit{B-18}$$

Similarly, velocity (v_{s2}) at the interface labelled 2 in Figure B-1 is only a function of transmitted wave and can be expressed as:

$$v_{s2} = C_0 \varepsilon_t \qquad \textit{B-19}$$

The rate of change of strain (strain rate) acting on the test specimen is a function of the difference between velocities v_{s1} and v_{s2} , and the length of the test specimen expressed as:

$$\dot{\epsilon} = \frac{v_{s1} - v_{s2}}{l_s} \qquad \textit{B-20}$$

Equation B-20 can be rewritten based on Equations B-18 and B-19 as:

$$\dot{\varepsilon_s} = \frac{-C_o(\varepsilon_r - \varepsilon_i - \varepsilon_t)}{l_s} \qquad \textit{B-21}$$

© Central University of Technology, Free State

The force at the interface of the incident and specimen bars is the resultant sum of the forces due to the incident and reflected waves and can be presented as:

$$A_s\sigma_{s1} = (\sigma_i + \sigma_r)A_0 \qquad \textit{B-22-i}$$

In this Equation the symbols A_0, A_s, σ_{s1}, σ_i and σ_r denote the cross-sectional areas of the bars, the cross-sectional areas specimen, the specimen stress at the interface 1, the stress due to incident pulse and stress due reflected pulse, respectively.

Similarly, the stress at interface 2 in Figure B-1 can be expressed as:

$$A_s\sigma_{s2} = \sigma_t A_0 \qquad \textit{B-22-ii}$$

where σ_t is the stress due to transmitted wave.

After some time, due to reverberation of waves, the specimen attain an equilibrium state of stress where the equality of stresses, $\sigma_{s1} = \sigma_{s2}$, is satisfied. In this case then Equations B-22-i and B-22-ii can be equated to one another giving rise to:

$$\sigma_t = \sigma_i + \sigma_r \qquad \textit{B-23}$$

From Hooke's law i.e., $\sigma = E\epsilon$ Equation B-23 to be rewritten as:

$$\varepsilon_t = \varepsilon_i + \varepsilon_r \qquad \textit{B-24}$$

From Equation B-22-ii and the relationship $\sigma = E\varepsilon$, the stress acting on the test specimen $\sigma_s = \sigma_{s1} = \sigma_{s2}$ can be written as:

$$\sigma_s = \frac{EA_0\varepsilon_t}{A_s} \qquad \textit{B-25}$$

The rate of change in strain (strain rate) expressed in the form of Equation B-21 can be rewritten using Equation B-24 as:

$$\dot{\varepsilon_s} = \frac{2\varepsilon_r C_0}{l_s} \qquad \textit{B-26}$$

The strain in the loaded specimen can be obtained from the integration of Equation B-26 from the onset of testing at time *t*= 0 to any time *t* as follows:

$$\epsilon_s = 2\frac{C_0}{l_s}\int_0^t \epsilon_r\, dt \qquad \textit{B-27}$$

© Central University of Technology, Free State

APPENDIX C – THERMODYNAMICS OF SHPB TEST SPECIMENS

The following two general thermodynamic equations can be used to estimate the amount of time it takes for the temperature of the test sample to decrease by a given value:

$$\frac{Q}{t} = \frac{K\,A\Delta T}{d} \qquad C\text{-}1$$

$$Q = m\,Cp\Delta T \qquad C\text{-}2$$

In these two equations the symbols Q, t, A, ΔT, d, m, K and C_p denote the amount of heat energy lost, time in seconds, surface area of the test sample, change of temperature, width of the test specimen, coefficient of thermal conductivity, mass of the test specimen, and specific heat capacity of the specimen, respectively.

The thermal properties of C_p and K for Ti6Al4V(ELI) are known from the literature to be, 526.3 $J/Kg.k$ and 6.7 $w/m.K$, respectively, while the density is known as 4.43 g/cm^3 (ASM 2018).

The volume of cylindrical test samples with a radius and height of 3 mm and 6 mm, respectively is equal to $1.696\,x\,10^{-7}m^{-3}$. Therefore, the amount of heat energy lost for a temperature drop of 30 ℃ is equal to:

$$Q = 1.696\,x\,10^{-7} \times 4.43 \times 10^{3} \times 526.3 \times 30 = 11.86\,J \qquad C\text{-}3$$

The heat lost by the specimen for a given time t can be calculated from Equation C-1 as:

$$\frac{Q}{t} = \frac{11.86}{t} = \frac{6.7}{0.006}\,x\,((2\pi x 0.003\,x\,0.006) + (2\pi x 0.003^2))x\,30 \qquad C\text{-}4$$

Combining Equations C-3 and C-4 give rise to change in time as:

$$t = \frac{12.82}{1.608} = 7.9\,sec$$

APPENDIX D – INTEGRATION OF THE TAYLOR HARDENING LAW (Jonas *et al*. 2009)

The rate of increase of dislocations with plastic strain can be expressed as:

$$\frac{d\rho}{d\varepsilon_p} = (h - k_2\rho) \qquad D\text{-}1$$

© Central University of Technology, Free State

The change in plastic strain ε_p can be expressed from Equation D-1 as:

$$d\varepsilon_p = \left(\frac{d\rho}{h-k_2\rho}\right) \qquad D\text{-}2$$

The plastic strain at an instance therefore can be expressed as:

$$\varepsilon_p = \int \frac{d\rho}{(h-k_2\rho)} = -\frac{1}{k_2} ln(h - k_2\rho) + C \qquad D\text{-}3$$

Equation D-3 can further be simplified as:

$$-k_2(\varepsilon_p + C) = In(h - k_2\rho) \qquad D\text{-}4a$$

$$exp(-k_2\varepsilon_p + A) = h - k_2\rho \qquad D\text{-}4b$$

$$\rho = \frac{h}{k_2} - \frac{C_1}{k_2} exp\,(-k_2\varepsilon_p) \qquad D\text{-}4c$$

where C is integral constant and C_1 is the solution for $exp\ A$. At yielding condition, $\varepsilon_p = 0$ and the $\rho = \rho_o$, where ρ_o is the material initial dislocation density. Thus C_1 can be expressed as $h - \rho_o k_2$. Equation D-4c then becomes:

$$\rho = \frac{h}{k_2} - \frac{(h-\rho_o k_2)}{k_2} exp(-k_2\varepsilon_p) = \frac{h}{k_2}\left(1 - exp(-k_2\varepsilon_p)\right) + \rho_o exp\,(-k_2\varepsilon_p) \qquad D\text{-}5$$

The flow stress Equation 4-10 (in Chapter 4) now becomes:

$$\sigma - \sigma_y = \alpha\mu(T)bM\left(\frac{h}{k_2}\left(1 - exp(-k_2\varepsilon_p)\right) + \rho_o\, exp(-k_2\varepsilon_p)\right)^{\frac{1}{2}} \qquad D\text{-}6$$

The attractive feature of this expression is that only two constant parameters (h & k_2) are required to adequately describe dislocations evolution.

APPENDIX E – METHOD OF CALCULATING THE AVERAGE BURGERS VECTOR AND AVERAGE CONTRAST FACTOR

The method of calculating the average Burgers vector and average contrast factor is outlined in Ungar and Borbely (1996), Dragomir and Ungar (2002) and Takashi *et al.* (2010) for hexagonal crystal structures. The measured contrast factor of a material as a product of the average magnitude of the Burgers vector can be expressed as:

$$\overline{C_{hk.l}b^2}^{(m)} = \sum_{i=1}^{N} f_i\, \bar{C}^{(i)} {b_i}^2 \qquad E\text{-}1$$

© Central University of Technology, Free State

where the parameter N stands for the number of activated sub-slip systems ($N = 11$ as shown in Table 6-3) and f_i the fractions of the sub-systems ($\sum_{i=1}^{11} f_1 = 1$ and $f_i \geq 0$) and Equation E-1 can be expanded to give the following expression:

$$\overline{C_{hk.l}b^2}^{(m)} = {b_1}^2 \sum_{i=1}^{N<a>} f_i \overline{C^{(i)}}\, {b_1}^2 + {b_2}^2 \sum_{j=1}^{N<c>} f_i \overline{C^{(J)}} + {b_2}^2 \sum_{j=k}^{N<c+a>} f_i \overline{C^{(k)}} \qquad E\text{-}2$$

where the parameters $N < a >$, $N < c >$ and $N < c + a >$ are number of sub-slip systems with the Burgers vector types $< a >$, $< c >$ and $< c + a >$ respectively. Further assuming a particular Burgers vector type to be randomly distributed in different sub-slip systems, allows Equation E-2 to be written as:

$$\overline{b^2 C_{hk.l}}^{(m)} = \sum_{i=1}^{3} h_i \bar{C}^{(i)} {b_i}^2 \qquad E\text{-}3$$

where the parameters h_i represent the fractions of the dislocation-population in the material with the same Burgers vectors *i.e.*, $\mathbf{b_1}$, $\mathbf{b_2}$ and $\mathbf{b_3}$ and $\bar{C}^{(i)}$ are averaged over the sub-slips systems, each corresponding to the same Burgers vector type. Equation 6-6 (in Chapter 6) is substituted into Equation E-3 to give rise to:

$$\sum_{i=1}^{3} h_i \overline{C_{hk.0}}^{(m)} {b_i}^2 \left(1 + {q_1}^{(m)} x + {q_2}^{(m)} x^2\right) = \sum_{i=1}^{3} h_i \overline{C_{hk.0}}^{(i)} {b_i}^2 \left(1 + {q_1}^{(i)} x + {q_2}^{(i)} x^2\right) \qquad E\text{-}4$$

The measured values of ${q_1}^{(m)}$ and ${q_2}^{(m)}$ are written in terms of numerically calculated values of ${q_1}^{(i)}$, ${q_2}^{(i)}$ and average contrast factor ($\bar{C}^{(i)}$) represented in Table 6-3 (Chapter 6) of the i number of sub-slip systems as:

$${q_1}^{(m)} = \frac{1}{X} \sum_{i=1}^{3} h_i \bar{C}^{(i)} {b_i}^2 {q_1}^{(i)}\,,\ {q_2}^{(m)} = \frac{1}{X} \sum_{i=1}^{3} h_i \bar{C}^{(i)} {b_i}^2\ {q_2}^{(i)} \text{ and } \sum_{i=1}^{3} h_i = 1 \qquad E\text{-}5$$

where the parameter $X = \sum_{i=1}^{3} h_i \bar{C}^{(i)} {b_i}^2 = \overline{b^2 C_{hk.0}}^{(m)}$.

APPENDIX F (1) – CODE OF THE VUHARD SUBROUTINE DEVELOPED HERE

```
C **********************************************************************
      subroutine vuhard (
C Read only -
     *     nblock,
     *     jElem, kIntPt, kLayer, kSecPt,
     *     lAnneal, stepTime, totalTime, dt, cmname,
     *     nstatev, nfieldv, nprops,
     *     props, tempOld, tempNew, fieldOld, fieldNew,
```


© Central University of Technology, Free State

```
     *     stateOld,
     *     eqps, eqpsRate,
C Write only -
     *     yield, dyieldDtemp, dyieldDeqps,
     *     stateNew)
C
      include 'vaba_param.inc'
C
            dimension props(nprops), tempOld(nblock), tempNew(nblock),
     1    fieldOld(nblock,nfieldv), fieldNew(nblock,nfieldv),
     2    stateOld(nblock,nstatev), eqps(nblock), eqpsRate(nblock),
     3    yield(nblock), dyieldDtemp(nblock), dyieldDeqps(nblock,2),
     4    stateNew(nblock,nstatev), jElem(nblock)
C
        character*80 cmname
C
************************************************************************
C Print the constitutive model parameters
          kb3    = props(1)
          goi    = props(2)
         ddeqps0 = props(3)
          theta  = props(4)
          p      = props(5)
          q      = props(6)
          e0     = props(7)
          h      = props(8)
          k2     = props(9)
          abm    = props(10)
          Khp    = props(11)
          alpha  = props(12)
          ala    = props(13)
          t      = props(14)
          U0     = props(15)
          D      = props(16)
          T0     = props(17)
C*************************************************************************
C    Print out material properties.
C*************************************************************************
          write (*,*)'The model constant parameters'
          write (*,*)'kb3=',kb3
          write (*,*)'goi=',goi
          write (*,*)'ddeqps0=',ddeqps0
          write (*,*)'theta=',theta
          write (*,*)'p=',p
          write (*,*)'q=',q
          write (*,*)'e0=',e0
          write (*,*)'h=',h
          write (*,*)'k2=',k2
          write (*,*)'abm=',abm
          write (*,*)'Khp=',Khp
          write (*,*)'alpha=',alpha
          write (*,*)'ala=',ala
          write (*,*)'laths thickness=',t
          write (*,*)'U0=',U0
          write (*,*)'D=',D
          write (*,*)'T0=',T0
C
C The Hall-Petch relationship from the alpha length thickness (t)
C
          Khp_D=Khp/sqrt(t)
          write (*,*)'Khp_D=',Khp_D
```


© Central University of Technology, Free State

```
            do k = 1, nblock
               epps = eqps(k)
               temp = tempOld(k)
               write(*,*)'temp=',temp
C    Compute for Temperature dependent shear modulus
            if (temp.eq.0.D0) then
             U=U0
            else
             U=U0-((D/(exp(T0/temp)-1.0))) *10**3
           end if
             write (*,*),'U=',U
C
C    Compute for the thermal part of flow stress
C
          thermal1=1-((kb3*temp)/(goi*U)*log(ddeqps0/ddeqps))**(1.0/q)
           thermal2=theta*thermal1**(1.0/p) *U/U0
            write (*,*)'thermal1=',thermal1
             write (*,*)'thermal2=',thermal2
C

C    Compute for athermal part of flow stress
C
          athermal1=(1-exp(-k2*epps))*h/k2
            athermal2=e0*exp(-k2*epps)
              athermal3=ala*(1-exp(-alpha*ddeqps))
          athermal4=sqrt(athermal1+athermal2) *abm*U +athermal3 + Khp_D
           write (*,*)'athermal1=',athermal1
            write (*,*)'athermal2=',athermal2
             write (*,*)'athermal3=',athermal3
              write (*,*)'athermal4=',athermal4
C
C    Compute for Total flow stress at different level of epps
C
          flowstress=thermal2+athermal4
           write (*,*)'flowstress=',flowstress
C
C    Compute for Partial derivative of Total flowstress w.r.t epps
C
           dathermal1=abm*U/2*(athermal1+athermal2)**(-1.0/2)
            dathermal2=h*exp(-k2*epps)-(e0*k2*exp(-k2*epps))
           dathermal3=dathermal1*dathermal2
              write (*,*)'dathermal1=',dathermal1
               write (*,*)'dathermal2=',dathermal2
                write (*,*)'dathermal3=',dathermal3
C
C Assign an array of Partial derivative of Total flowstress w.r.t epps.
C
                  dyieldDeqps(k,1) = dathermal3
                   write(*,*)'dyieldDeqps(k,1)=',dyieldDeqps(k,1)
C
C Compute the Partial derivatives of Total flowstress w.r.t ddeqps.
C
           eqpsRate(k)= ddeqps
           p2=(1.0-p)/p
           q2=(1.0-q)/q
           ddthermal1=(theta*temp*kb3)/(p*q*U*ddeqps)
           ddthermal2=(1-(log(ddeqps0/ddeqps)      *kb3*temp/goi/U)**(1.0/q))
**p2
             ddthermal3=(log(ddeqps0/ddeqps) *kb3*temp/goi/U) **q2
              ddthermal4= alpha*exp(-alpha*ddeqps)
```


© Central University of Technology, Free State

```
          ddthermal5=ddthermal1*ddthermal2*ddthermal3+ddthermal4
          write (*,*)'ddthermal1=',ddthermal1
           write (*,*)'ddthermal2=',ddthermal2
            write (*,*)'ddthermal3=',ddthermal3
             write (*,*)'ddthermal4=',ddthermal4

C
C  Assign  an  array  for  partial  derivatives  of  Total  flowstress  w.r.t
ddeqps.
C
               dyieldDeqps(k,2) = ddthermal5
                write (*,*)' dyieldDeqps(k,2)=', dyieldDeqps(k,2)
C
C Compute and return the yield stress.
C
          yield(k) = flowstress

          write (*,*)' yield(k)=',  yield(k)
          write (*,*)'eqps=',eqps(k)
          write (*,*)'eqpsRate(k)=', eqpsRate(k)
           end do
         return
        end
```

APPENDIX F (2) – VUHARD SUBROUTINE USER-DEFINED MATERIAL PROPERTIES

Table F-1. The VUHARD subroutine and the ABAQUS material property definition

Variables	VUHARD	ABAQUS
K/b^3	Kb3	Props (1)
goi	goi	Props (2)
$\dot{\varepsilon}_o$	ddeqps0	Props (3)
σ^o	theta	Props (4)
p	p	Props (5)
q	q	Props (6)
ρ_o	e0	Props (7)
h	h	Props (8)
k2	k2	Props (9)
α x b x M	abm	Props (10)
K_{H-p}	Khp	Props (11)
α_1	alpha	Props (12)
ζ	ala	Props (13)
t	t	Props (14)
U_0	U0	Props (15)
D	D	Props (16)
T_0	T0	Props (17)

APPENDIX G (1) – CODE OF THE VUMAT SUBROUTINE DEVELOPED HERE

```
      subroutine vumat(
C Read only (unmodifiable)variables -
     1  nblock, ndir, nshr, nstatev, nfieldv, nprops, jInfoArray,
     2  stepTime, totalTime, dtArray, cmname, coordMp, charLength,
     3  props, density, strainInc, relSpinInc,
```


© Central University of Technology, Free State

```
     4  tempOld, stretchOld, defgradOld, fieldOld,
     5  stressOld, stateOld, enerInternOld, enerInelasOld,
     6  tempNew, stretchNew, defgradNew, fieldNew,
C Write only (modifiable) variables -
     7  stressNew, stateNew, enerInternNew, enerInelasNew )
C
      include 'vaba_param.inc'
      parameter (i_info_AnnealFlag = 1,
     *     i_info_Intpt    = 2, ! Integration station number
     *     i_info_layer  = 3, ! Layer number
     *     i_info_kspt   = 4, ! Section point number in current layer
     *     i_info_effModDefn = 5, ! =1 if Bulk/ShearMod need to be defined
     *    i_info_ElemNumStartLoc   = 6) ! Start loc of user element number
C
      dimension props(nprops), density(nblock), coordMp(nblock,*),
     1                  charLength(nblock),         dtArray(2*(nblock)+1),
strainInc(nblock,ndir+nshr),
     2  relSpinInc(nblock,nshr), tempOld(nblock),
     3  stretchOld(nblock,ndir+nshr),
     4  defgradOld(nblock,ndir+nshr+nshr),
     5  fieldOld(nblock,nfieldv), stressOld(nblock,ndir+nshr),
     6  stateOld(nblock,nstatev), enerInternOld(nblock),
     7  enerInelasOld(nblock), tempNew(nblock),
     8  stretchNew(nblock,ndir+nshr),
     8  defgradNew(nblock,ndir+nshr+nshr),
     9  fieldNew(nblock,nfieldv),
     1  stressNew(nblock,ndir+nshr), stateNew(nblock,nstatev),
     2  enerInternNew(nblock), enerInelasNew(nblock), jInfoArray(*)
C
      character*80 cmname
C
      pointer (ptrjElemNum, jElemNum)
      dimension jElemNum(nblock)
C
      lAnneal = jInfoArray(i_info_AnnealFlag)
      iLayer = jInfoArray(i_info_layer)
      kspt   = jInfoArray(i_info_kspt)
      intPt  = jInfoArray(i_info_Intpt)
      iUpdateEffMod = jInfoArray(i_info_effModDefn)
      iElemNumStartLoc = jInfoArray(i_info_ElemNumStartLoc)
      ptrjElemNum = loc(jInfoArray(iElemNumStartLoc))
C

C Material property definitions

            e      =  props(1)
            xnu    =  props(2)
            kb3    =  props(3)
            goi    =  props(4)
           ddeqps0 =  props(5)
            theta  =  props(6)
            p      =  props(7)
            q      =  props(8)
            e0     =  props(9)
            h      =  props(10)
            k2     =  props(11)
            abm    =  props(12)
            Khp    =  props(13)
            alpha  =  props(14)
            ala    =  props(15)
            t      =  props(16)
```


© Central University of Technology, Free State

```
                U0      =  props(17)
                D       =  props(18)
                T0      =  props(19)

C
C Find the shear and bulk modulus.
C
                  μ =e/(two*(one+xnu))
                  bulk=e/(three*(one-two*xnu))
                  alamda=e*xnu/((1+xnu) *(1-2*xnu))
                  write (*,*)'μ=',μ
                  write (*,*)'bulk=',bulk
                  write (*,*)'alamda=',alamda
C
         if ((stepTime+totalTime).eq.0.0) then
            do i=1,nblock
              trace=strainInc(i,1)+strainInc(i,2)+strainInc(i,3)
               write (*,*)'trace=',trace
C New stress tensor due to elastic behaviour

stressNew(i,1)=stressOld(i,1)+two*G*strainInc(i,1)+alamda*trace

stressNew(i,2)=stressOld(i,2)+two*G*strainInc(i,2)+alamda*trace

stressNew(i,3)=stressOld(i,3)+two*G*strainInc(i,3)+alamda*trace
                stressNew(i,4)=stressOld(i,4)+two*G*strainInc(i,4)
                if (nshr.gt.1) then
                stressNew(i,5)=stressOld(i,5)+two*G*strainInc(i,5)
                stressNew(i,6)=stressOld(i,6)+two*G*strainInc(i,6)
                end if
                      write(*,*)'stressNew(i,1)=',stressNew(i,1)
                      write(*,*)'stressNew(i,2)=',stressNew(i,2)
                      write(*,*)'stressNew(i,4)=',stressNew(i,4)
            end do
       else
             do i=1,nblock
C
C Initialize the yield stress, plastic strain, and strain rate of the last
C   increment.
C
                  deqps    = stateOld(i,1)
                  ddeqps   = stateOld(i,2)
                  yieldOld = stateOld(i,3)
                  Temp     = TempOld(i)
C The Hall-Petch relationship from the alpha length thickness (t)
           Khp_D=Khp/sqrt(t)
           write (*,*)'Khp_D=',Khp_D
C Initialize small initial plastic strain.
                  depl=1e-8
C Compute for Temperature dependent shear modulus
           if (temp.eq.0. D0) then
            U=U0
           else
               U=U0-((D/(exp(T0/temp)-1.0))) *10**3
          end if
            write (*,*),'U=',U
C
C  Compute for yielding: Athermal and thermal components from the
C   constitutive model.
C
C Thermal part of flow stress
```


© Central University of Technology, Free State

```
        thermal1=1-((kb3*temp)/(goi*U) *log(ddeqps0/(ddeqps))) **(1.0/q)
         thermal2=theta*thermal1**(1.0/p) *U/U0
            write(*,*)'thermal1=',thermal1
             write(*,*)'thermal2=',thermal2
C                   Athermal part of flow stress
         athermal1=(1-exp(-k2*deqps)) *h/k2
           athermal2=e0*exp(-k2*deqps)
             athermal3=ala*(1-exp(-alpha*(ddeqps)))
              athermal4=sqrt(athermal1+athermal2) *abm*U +athermal3 + Khp_D
          write (*,*)'athermal1=',athermal1
           write (*,*)'athermal2=',athermal2
            write (*,*)'athermal3=',athermal3
             write (*,*)'athermal4=',athermal4
C
C Compute for old yield stress
C
        yieldOld=thermal2+athermal4
         write (*,*)'yieldOld=',yieldOld
C Compute for Partial derivative of yield stress w.r.t equivalent plastic
C strain (hard).
C
          hard1=abm*U/2*(athermal1+athermal2) **(-1.0/2)
           hard2=h*exp(-k2*deqps) -(e0*k2*exp(-k2*deqps))
            hard=hard1*hard2
             write (*,*)'hard1=',hard1
              write (*,*)'hard2=',hard2
               write (*,*)'hard=', hard
C
C Find the new trace and stress tensor.
C
                  trace= strainInc(i,1) + strainInc(i,2) + strainInc(i,3)
                  s11= stressOld(i,1) + 2*G*strainInc(i,1) + alamda*trace
                  s22= stressOld(i,2) + 2*G*strainInc(i,2) + alamda*trace
                  s33= stressOld(i,3) + 2*G*strainInc(i,3) + alamda*trace
                  s12= stressOld(i,4) + 2*G*strainInc(i,4)
                  if (nshr.gt.1.0) then
                  s13= stressOld(i,5) + 2*G*strainInc(i,5)
                  s23= stressOld(i,6) + 2*G*strainInc(i,6)
                  end if
C Compute hydrostatic stress.
                  smean=(s11+s22+s33)/3.0
C
C Compute deviatoric stress from hydrostatic stress and stress tensor.
                  s1 = s11 - smean
                  s2 = s22 - smean
                  s3 = s33 - smean
                  s4 = s12
                  s5 = s13
                  s6 = s23
C Compute the equivalent mises stress from deviatoric stress.
               if (nshr.eq.1) then
                 vmises = sqrt(1.5*(s1**2+s2**2+s3**2+2*s4**2))
                else
               vmises= sqrt(1.5*(s1**2+s2**2+s3**2+2*(s4**2+s5**2+s6**2)))
                     write (*,*)'vmises=',vmises
                end if
C
                  sigdif = vmises - yieldOld
                  facyld = 0.0
                  if (sigdif.gt.0.0) facyld = 1.0
```


© Central University of Technology, Free State

```
                  deqps = facyld*sigdif/(3*G + hard)
                  write (*,*)'deqps=',deqps
                  write (*,*)'dt=',dtArray(1)
                  write (*,*)'sigdif=',sigdif
C
C Compute the initial the plastic strain rate from increment in plastic
C strain.
                  if (deqps.gt.0.0) then
                            ddeqps=deqps/dtArray (1)
                        else
                            ddeqps=1.0
                  end if
                  write (*,*)'ddeqps=',ddeqps

C
C Update the stress
                  yieldNew = yieldOld + hard* deqps
                  write (*,*)'yieldNew=',yieldNew
                  factor   = yieldNew/(yieldNew+3*G*deqps)
                  write (*,*)'factor=', factor
C
C Find new stress tensor.
C
                  stressNew(i,1) = s1*factor + smean
                  stressNew(i,2) = s2*factor + smean
                  stressNew(i,3) = s3*factor + smean
                  stressNew(i,4) = s4*factor
                  if (nshr.gt.1) then
                    stressNew(i,5) = s5*factor
                    stressNew(i,6) = s5*factor
                 end if
C
C New equivalent deviatoric stress and von Mises equivalent
                  s1=s1*factor
                  s2=s2*factor
                  s3=s3*factor
                  s4=s4*factor
                  s5=s5*factor
                  s6=s6*factor
C Update the state variables.
                  stateNew(i,1) = stateOld(i,1) + deqps
                  stateNew(i,2) = ddeqps
                  stateNew(i,3) = yieldOld
                  write(*,*)'stateNew(i,1)=', stateNew(i,1)
                  write(*,*)'stateNew(i,3)=', stateNew(i,3)
C
C Update the specific internal energy.
C
                  sp1=(stressOld(i,1) +stressNew(i,1)) *strainInc(i,1)
                  sp2=(stressOld(i,2) +stressNew(i,2)) *strainInc(i,2)
                  sp3=(stressOld(i,3) +stressNew(i,3)) *strainInc(i,3)
                  sp4=(stressOld(i,4) +stressNew(i,4)) *strainInc(i,4)
                  sp5=(stressOld(i,5) +stressNew(i,5)) *strainInc(i,5)
                  sp6=(stressOld(i,6) +stressNew(i,6)) *strainInc(i,6)
           if (nshr.eq.1) then
         stress Power =0.5*(sp1+sp2+sp3) +sp4
          else
          stress Power = 0.5*(sp1+sp2+sp3) +sp4+sp5+sp6
            end if
          enerInternNew(i) = enerInternOld(i)+ stressPower / density(i)
C
```


© Central University of Technology, Free State

```
C Update the dissipated inelastic energy.
C Transfer old value of inelastic specific energy
C         enerInelasNew(i) = enerInelasOld(i)
C
           plasticWorkInc=0.5*(yieldNew)*deqps
           write(*,*)'plasticWorkInc=', plasticWorkInc
           enerInelasNew(i)=enerInelasOld(i)+plasticWorkInc/density(i)

                  end do
          end if
      return
      end
```

APPENDIX G(2) – VUMAT USER-DEFINED MATERIAL PROPERTIES

Table G-1. The VUMAT subroutine and the ABAQUS material property definition

Variables	VUMAT	ABAQUS
Elastic modulus	e	Props (1)
Poisson's ratio	xnu	Props (2)
K/b^3	Kb3	Props (3)
goi	goi	Props (4)
$\dot{\varepsilon}_o$	ddeqps0	Props (5)
σ^o	theta	Props (6)
p	p	Props (7)
q	q	Props (8)
ρ_o	e0	Props (9)
h	h	Props (10)
k2	k2	Props (11)
α x b x M	abm	Props (12)
K_{H-p}	Khp	Props (13)
α_1	alpha	Props (14)
ζ	ala	Props (15)
t	t	Props (16)
U_0	U0	Props (17)
D	D	Props (18)
T_0	T0	Props (19)

© Central University of Technology, Free State

APPENDIX H(1) – COLLECTIVE RESULTS FOR SAMPLES D USING 8-NODE SINGLE BRICK ELEMENTS.

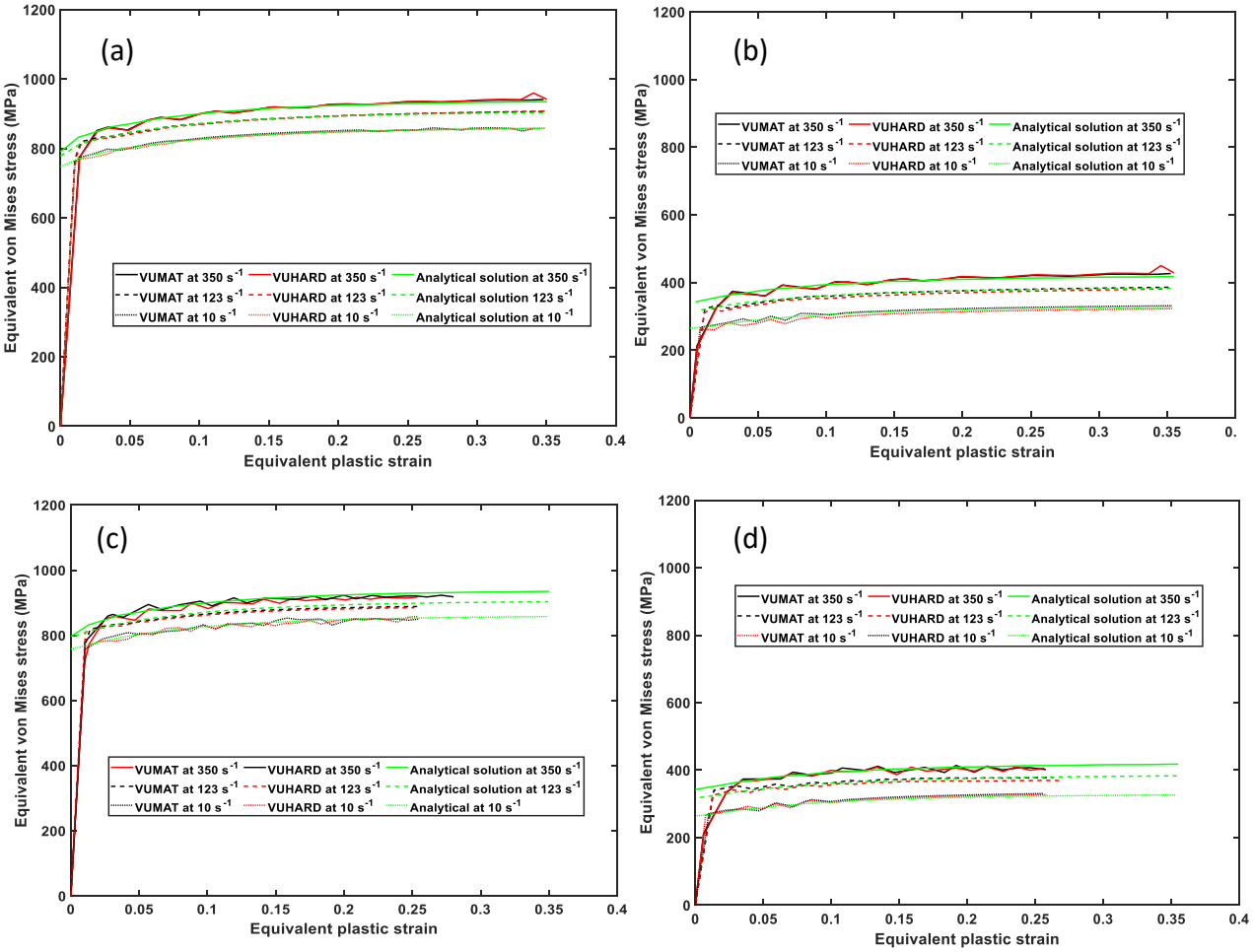

Figure H-1. Comparison between the analytical and numerical solutions in VUMAT and VUHARD at three different test velocities and temperatures of (a and c) 298 K and (b and d) 773 K for an 8-node linear brick element in (a and b) tension and (c and d) compression for samples D.

© Central University of Technology, Free State

APPENDIX H (2) – COLLECTIVE RESULTS FOR SAMPLES E USING 8-NODE SINGLE BRICK ELEMENTS

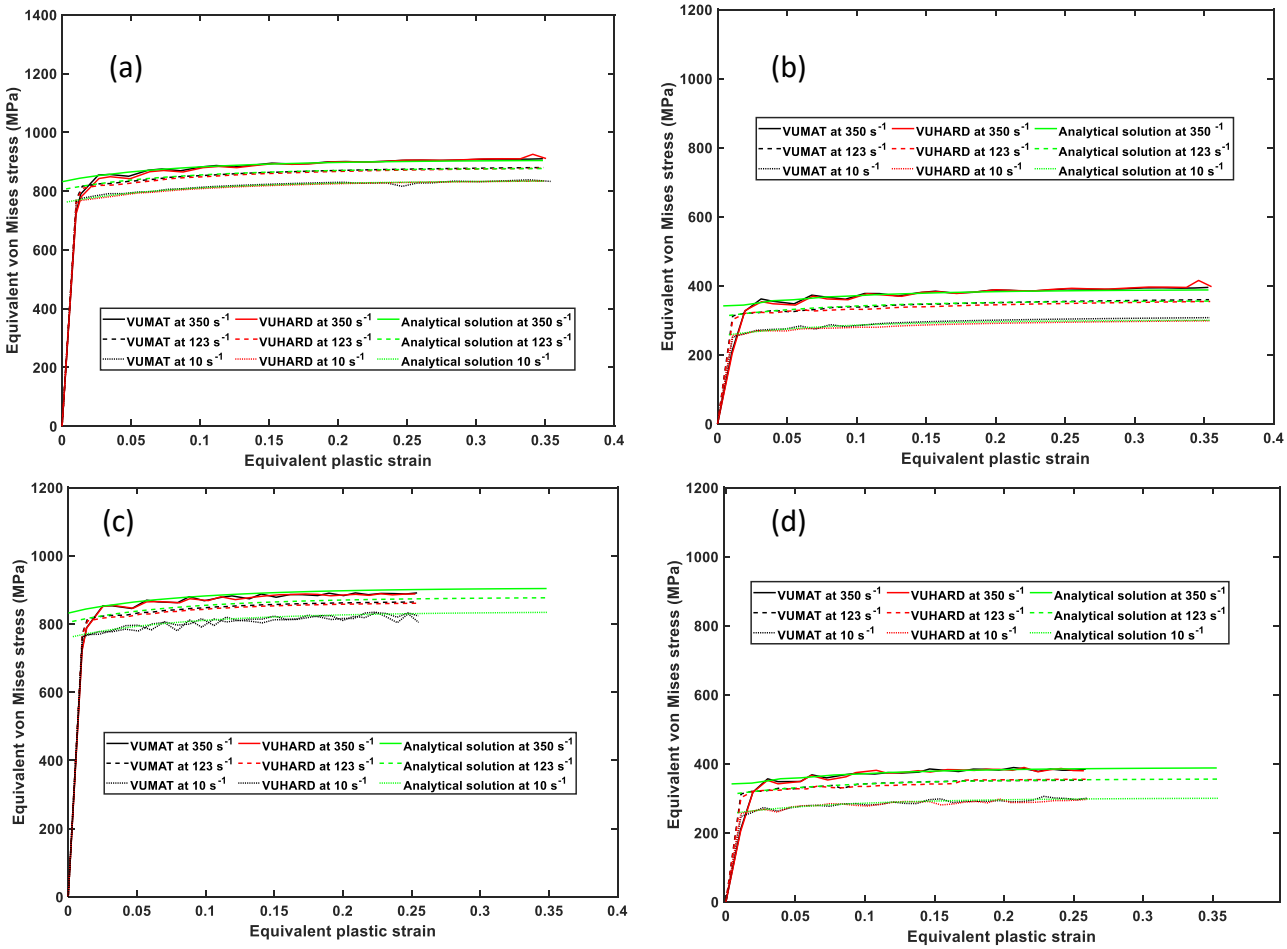

Figure H-2. Comparision between the analytical and numerical solutions in VUMAT and VUHARD at three different test velocities and temperatures of (a and c) 298 K and (b and d) 773 K for an 8-node linear brick element in (a and b) tension and (c and d) compression for samples E.

© Central University of Technology, Free State

APPENDIX I (1) – COLLECTIVE RESULTS FOR SAMPLES D USING 8-NODE BRICK MULTIPLE ELEMENTS

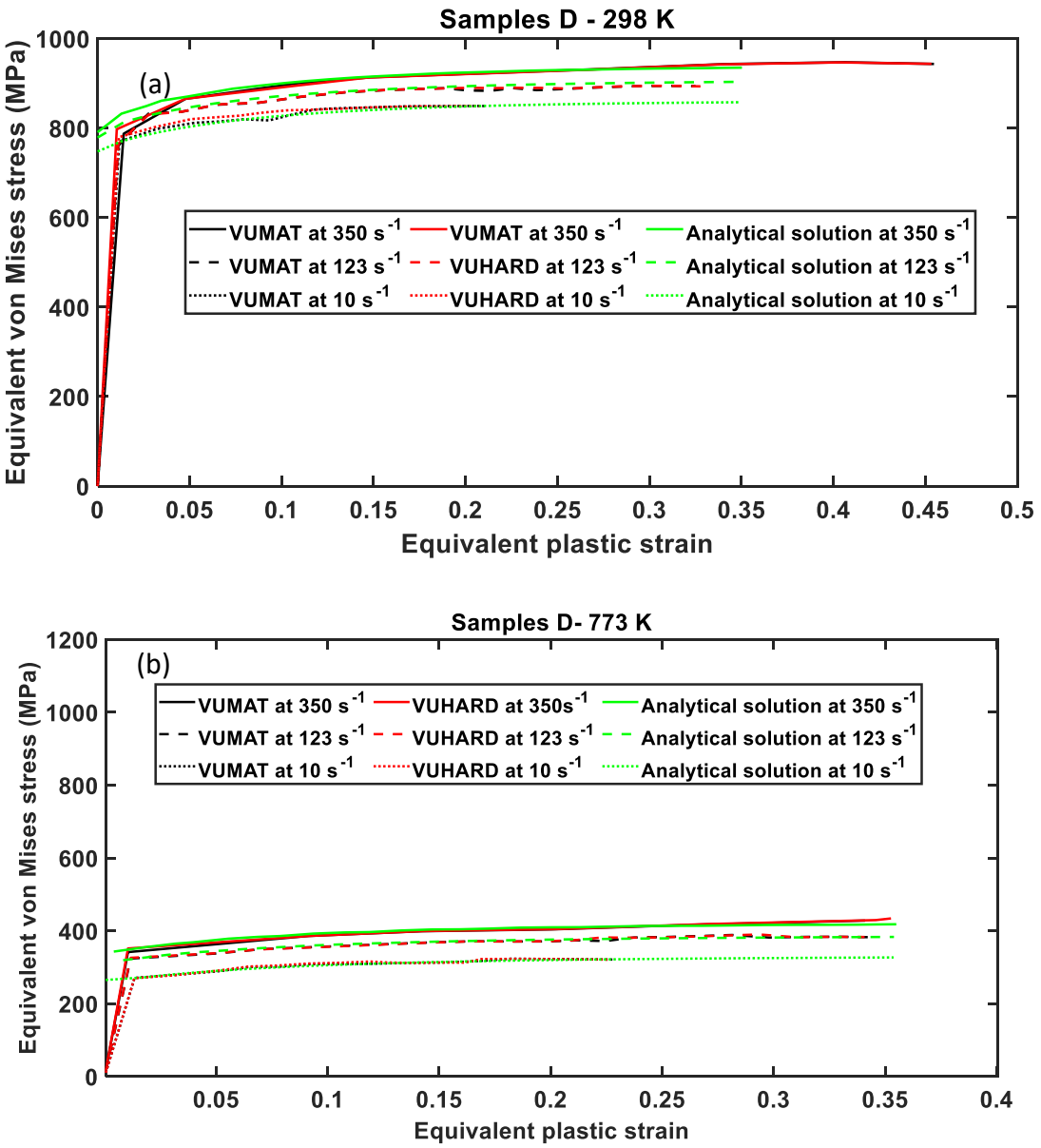

Figure I-1. Comparison between the analytical and numerical solutions in the VUMAT and VUHARD subroutines at three test velocities and a temperature of (a) 298 K and (b) 774 K for multiple elements cylindrical model of samples type D.

© Central University of Technology, Free State

APPENDIX I (2) – COLLECTIVE RESULTS FOR SAMPLES D USING 8-NODE BRICK MULTIPLE ELEMENTS

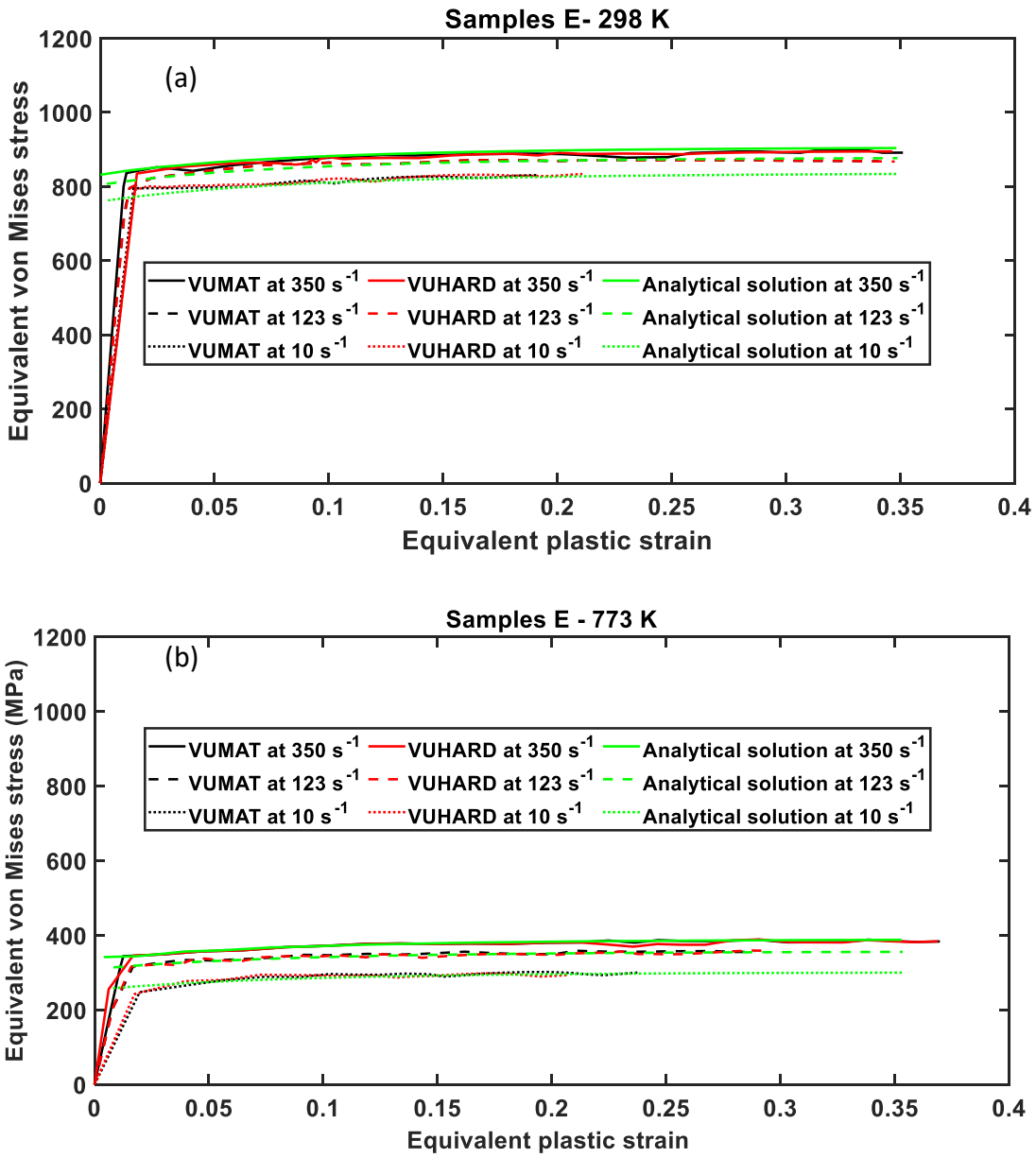

Figure I-2. Comparison between the analytical and numerical solutions in the VUMAT and VUHARD subroutines at three test velocities and a temperature of (a) 298 K and (b) 773K for multiple elements cylindrical model of samples type E.

© Central University of Technology, Free State